

# UC Berkeley

## UC Berkeley Electronic Theses and Dissertations

### Title

Gases, Liquids, Solids, and Reactions in Metal–Organic Frameworks

### Permalink

<https://escholarship.org/uc/item/0x00m9s1>

### Author

Gonzalez, Miguel Carlos Inocentes

### Publication Date

2017

Peer reviewed|Thesis/dissertation

Gases, Liquids, Solids, and Reactions in Metal–Organic Frameworks

By

Miguel Carlos Inocentes Gonzalez

A dissertation submitted in partial satisfaction of the

requirements for the degree of

Doctor of Philosophy

in

Chemistry

in the

Graduate Division

of the

University of California, Berkeley

Committee in charge:

Professor Jeffrey R. Long, Chair

Professor Richard A. Andersen

Professor Jeffrey A. Reimer

Fall 2017



## Abstract

### Gases, Liquids, Solids, and Reactions in Metal–Organic Frameworks

By

Miguel Carlos Inocentes Gonzalez

Doctor of Philosophy in Chemistry

University of California, Berkeley

Professor Jeffrey R. Long, Chair

Metal–organic frameworks have emerged as a class of porous materials with structures that can be defined by combining synthetic chemistry with precise characterization through crystallography. The work compiled in this dissertation pursues the study of these materials for many different applications, ranging from gas storage and molecular separations to cluster synthesis and catalysis. These investigations have all relied on single-crystal X-ray diffraction to provide insight into the influence of framework structure on adsorption properties and reactivity, ultimately leading to the discovery of new chemical species and behavior.

*Chapter 1* serves as a brief introduction to the role of single-crystal X-ray diffraction in advancing research on metal–organic frameworks. In particular, the reports discussed in this chapter exemplify experiments that have been critical in establishing that these materials can be designed to both retain porosity and bind guests through specific interactions. A few examples were chosen to feature relevant collaborative work conducted alongside the studies presented in the succeeding chapters.

*Chapter 2* describes the development of *in situ* single-crystal X-ray diffraction techniques that have enabled the direct observation of CO, CH<sub>4</sub>, N<sub>2</sub>, O<sub>2</sub>, Ar, and P<sub>4</sub> adsorption in the metal–organic framework Co<sub>2</sub>(dobdc) (dobdc<sup>4-</sup> = 2,5-dioxido-1,4-benzenedicarboxylate), which features a high density of coordinatively unsaturated cobalt(II) centers. These molecules exhibit such weak interactions with the high-spin cobalt(II) sites that no analogous molecular structures exist. Several of these structures have also led to the location of secondary and tertiary binding sites in the framework. Analysis of gas adsorption isotherms confirms that these gases bind to the cobalt(II) sites through mainly physisorptive interactions and that secondary binding sites become more relevant at elevated pressures.

While gas storage and gas separations have been the two most prominent applications for metal–organic frameworks, these materials have also shown promise as adsorbents for liquid-phase separations. *Chapter 3* reports the evaluation of Co<sub>2</sub>(dobdc) and its structural isomer Co<sub>2</sub>(*m*-dobdc) (*m*-dobdc<sup>4-</sup> = 4,6-dioxido-1,3-benzenedicarboxylate) for the separation of xylene isomers using single-component adsorption isotherms and multi-component breakthrough measurements. The framework Co<sub>2</sub>(dobdc) distinguishes among all four molecules, with binding affinities that follow the trend *o*-xylene > ethylbenzene > *m*-xylene > *p*-xylene. Structural characterization by single-crystal X-ray diffraction reveals that both frameworks facilitate the separation of these isomers through the extent of interaction between each C<sub>8</sub> guest molecule and two adjacent cobalt(II) centers, as well as the ability of each isomer to pack within the framework

pores. Moreover, in the presence of either *o*-xylene or ethylbenzene,  $\text{Co}_2(\text{dobdc})$  exhibits an unexpected structural distortion that increases its adsorption capacity for these guest molecules.

Metal–organic frameworks featuring ligands with open chelating sites have proven to be versatile platforms for the preparation of heterogeneous catalysts through post-synthetic metalation. *Chapter 4* details initial efforts toward the application of these frameworks as heterogeneous catalysts with crystallographically-defined active sites. In particular, a highly porous and thermally robust metal–organic framework,  $\text{Zr}_6\text{O}_4(\text{OH})_4(\text{bpydc})_6$  ( $\text{bpydc}^{2-} = 2,2'$ -bipyridine-5,5'-dicarboxylate), bears open bipyridine sites that readily react with a variety of solution- and gas-phase metal sources. Upon metalation, this framework undergoes a single-crystal-to-single-crystal transformation that enables precise structural determination of the resulting metal–linker complexes. Furthermore, the framework yields an active heterogeneous catalyst for arene C–H borylation when metalated with  $[\text{Ir}(\text{COD})_2]\text{BF}_4$  (COD = 1,5-cyclooctadiene).

*Chapter 5* builds upon the work in *Chapter 4* and leverages structural insight afforded by crystallography to investigate pore environment effects on ethylene oligomerization in the metal–organic frameworks  $\text{Zr}_6\text{O}_4(\text{OH})_4(\text{bpydc})_6$  and  $\text{Zr}_6\text{O}_4(\text{OH})_4(\text{bpydc})_{0.84}(\text{bpdc})_{5.16}$  ( $\text{bpdc}^{2-} = \text{bpdc}^{2-} = \text{biphenyl-4,4'-dicarboxylate}$ ). In these systems, the pore structure around the active nickel sites significantly influences their selectivity for formation of oligomers over polymer. Specifically, the single-crystal structure of  $\text{Zr}_6\text{O}_4(\text{OH})_4(\text{bpydc})_6(\text{NiBr}_2)_{5.64}$  indicates that neighboring metal–linker complexes enforce a steric environment on each nickel site that causes polymer formation to become favorable. Minimizing this steric congestion by isolating the nickel(II)–bipyridine complexes in the mixed-linker framework  $\text{Zr}_6\text{O}_4(\text{OH})_4(\text{bpydc})_{0.84}(\text{bpdc})_{5.16}$  markedly improves both catalytic activity and selectivity for oligomers. Furthermore, both frameworks give product mixtures that are enriched in shorter olefins ( $\text{C}_{4-10}$ ), leading to deviations from the expected Schulz-Flory distribution of oligomers. Although these deviations indicate possible pore confinement effects on selectivity, control experiments reveal that they likely arise at least in part from the presence of nickel species that are not ligated by the bipyridine within both frameworks.

Finally, *Chapter 6* demonstrates that a metal–organic framework can act as a multidentate ligand scaffold to template the formation of discrete inorganic clusters, enabling their stabilization within a porous crystalline support. The framework  $\text{Zr}_6\text{O}_4(\text{OH})_4(\text{bpydc})_6$  confines the growth of atomically-defined nickel(II) bromide, nickel(II) chloride, cobalt(II) chloride, and iron(II) chloride sheets through coordination of six chelating bipyridine linkers. Characterization by single-crystal X-ray diffraction reveals that each metal(II) halide sheet represents a fragment excised from a single layer in the bulk solid. Moreover, structures obtained at different precursor loadings allow for the observation of successive stages of cluster assembly. Magnetic susceptibility measurements demonstrate that the isolated clusters exhibit behavior distinct from that of their corresponding bulk materials.

## Table of Contents

List of Figures	iii
List of Tables	v
Acknowledgements	vi
<b>Chapter 1. Structural Studies on Metal–Organic Frameworks by Single-Crystal X-ray Diffraction</b>	<b>1</b>
1.1. Introduction	1
1.1. Structural evidence for permanent porosity	2
1.2. Characterization of framework–gas interactions	3
1.3. Post-synthetic metalation of metal–organic frameworks	8
1.4. Conclusions and outlook	9
1.5. References	10
<b>Chapter 2. Structural Characterization of Framework–Gas Interactions in the Metal–Organic Framework Co<sub>2</sub>(dobdc) by <i>in situ</i> Single-Crystal X-ray Diffraction</b>	<b>14</b>
2.1. Introduction	14
2.2. Experimental	16
2.2.1. Materials and Methods	16
2.2.2. Single-Crystal X-ray Diffraction	16
2.2.3. Gas Adsorption	18
2.3. Results and Discussion	19
2.3.4. Structural Characterization	19
2.3.5. Gas Adsorption	24
2.4. Conclusions and outlook	26
2.5. Acknowledgements	27
2.6. Supplementary Information	28
2.6.6. Supplementary Figures	28
2.6.7. Thermal ellipsoid plots and crystallographic tables	30
2.6.8. Langmuir fits for low-pressure gas adsorption isotherms of Co <sub>2</sub> (dobdc)	39
2.6.9. Low-coverage differential enthalpy of adsorption plots for Co <sub>2</sub> (dobdc)	47
2.7. References	48
<b>Chapter 3. Separation of Xylene Isomers through Multiple Metal Site Interactions in Metal–Organic Frameworks</b>	<b>53</b>
3.1. Introduction	53
3.2. Experimental	55
3.3. Results and Discussion	59
3.3.1. C <sub>8</sub> Isomer Adsorption Experiments	59
3.3.2. Structural Characterization of C <sub>8</sub> Isomer Adsorption	62
3.4. Conclusions	66
3.5. Acknowledgments	67
3.6. Supplementary Information	68
3.6.3. Supplementary Figures	68
3.6.4. Crystallographic Information	75
3.6.5. Single-Component C <sub>8</sub> Isomer Adsorption Isotherm Data	84

3.6.6.	C <sub>8</sub> Isomer Selectivities from Multi-Component Liquid-Phase Adsorption Data	88
3.6.7.	Powder X-ray Diffraction Data	89
3.7.	References	96
<b>Chapter 4. Single-Crystal-to-Single-Crystal Metalation of a Metal–Organic Framework: A Route toward Structurally Well-Defined Catalysts</b>		<b>100</b>
4.1.	Introduction	100
4.2.	Experimental	102
4.3.	Results and Discussion	107
4.4.	Conclusions and outlook	118
4.5.	Acknowledgements	119
4.6.	Supplementary Information	120
4.7.	References	168
<b>Chapter 5. Ethylene Oligomerization in Metal–Organic Frameworks Bearing Nickel(II) 2,2'-Bipyridine Complexes</b>		<b>171</b>
5.1.	Introduction	171
5.2.	Experimental	173
5.3.	Results and Discussion	177
5.3.1.	Synthesis and Metalation of Metal–Organic Frameworks	177
5.3.2.	Ethylene Oligomerization	179
5.4.	Conclusions	183
5.5.	Acknowledgements	183
5.6.	Supplementary Information	184
5.6.3.	Single-Crystal X-ray Diffraction Data	184
5.6.4.	Powder X-ray Diffraction Data	187
5.6.5.	Low-pressure Gas Adsorption Isotherms	197
5.6.6.	Thermogravimetric Analyses	204
5.6.7.	Ethylene Oligomerization Data	207
5.6.8.	Scanning Electron Microscopy Images	211
5.7.	References	214
<b>Chapter 6. Confinement of Atomically-Defined Metal Halide Sheets in a Metal–Organic Framework</b>		<b>217</b>
6.1.	Introduction	217
6.2.	Experimental	218
6.3.	Results and Discussion	222
6.4.	Conclusion	226
6.5.	Acknowledgements	227
6.6.	Supplementary Information	228
6.6.1.	Supplementary Figures	228
6.6.2.	Supplementary Tables	244
6.7.	References	249

## List of Figures

<b>Figure 1.1.</b>	Structures of $\text{Ni}_2(4,4'\text{-bpy})_3(\text{NO}_3)_4 \cdot 2\text{EtOH}$ and $\text{Ni}_2(4,4'\text{-bpy})_3(\text{NO}_3)_4$	2
<b>Figure 1.2.</b>	Structure of $\text{Zn}_4\text{O}(\text{bdc})_3$ or MOF-5	3
<b>Figure 1.3.</b>	Structure of $\text{Zn}_2(\text{atz})_2(\text{ox}) \cdot 1.30\text{CO}_2$	4
<b>Figure 1.4.</b>	Structures of $\text{Co}_2(\text{dobdc}) \cdot 4\text{CH}_3\text{OH}$ , $\text{Co}_2(\text{dobdc})$ , and $\text{Co}_2(\text{dobdc}) \cdot 2.9\text{CO}_2$ , depicting the activation of the framework and the adsorption of $\text{CO}_2$	5
<b>Figure 1.5.</b>	Structures of Co-BTTri- $\text{O}_2$ and Fe-BTTri-CO	6
<b>Figure 1.6.</b>	Cooperative $\text{CO}_2$ insertion into diamine-appended $\text{Zn}_2(\text{dobpdc})$	7
<b>Figure 1.7.</b>	Structure of $\text{Mn}_3(\text{L})_2(\text{L}')$ and $[\text{Mn}_3(\text{L})_2(\text{L}')(\text{Rh}(\text{CO})_2)][\text{Rh}(\text{CO})_2\text{Cl}_2]$ ( $\text{H}_2\text{L} = \text{bis}(4\text{-}(4\text{-carboxyphenyl})\text{-1H-3,5-dimethylpyrazolyl})\text{methane}$ )	8
<b>Figure 2.1.</b>	Structures CO, $\text{CO}_2$ , $\text{N}_2$ , $\text{O}_2$ , $\text{CH}_4$ , Ar, and $\text{P}_4$ in $\text{Co}_2(\text{dobdc})$	15
<b>Figure 2.2.</b>	Diagrams of the Advanced Light Source Beamline 11.3.1. gas cell and a capillary-dosing assembly	17
<b>Figure 2.3.</b>	Structures of $\text{Co}_2(\text{dobdc}) \cdot 0.58\text{CO}$ , $\text{Co}_2(\text{dobdc}) \cdot 2.9\text{CO}_2$ , $\text{Co}_2(\text{dobdc}) \cdot 5.9\text{O}_2$ , $\text{Co}_2(\text{dobdc}) \cdot 3.8\text{N}_2$ , $\text{Co}_2(\text{dobdc}) \cdot 2.0\text{CH}_4$ , $\text{Co}_2(\text{dobdc}) \cdot 2.0\text{Ar}$ , and $\text{Co}_2(\text{dobdc}) \cdot 1.3\text{P}_4$	21
<b>Figure 2.4.</b>	Low-pressure CO, $\text{CO}_2$ , $\text{CH}_4$ , $\text{N}_2$ , $\text{O}_2$ , and Ar adsorption isotherms and high-pressure CO, $\text{CO}_2$ , $\text{CH}_4$ , $\text{N}_2$ , and Ar adsorption isotherms for $\text{Co}_2(\text{dobdc})$	25
<b>Figure 3.1.</b>	Structures of $\text{Co}_2(\text{dobdc})$ and $\text{Co}_2(m\text{-dobdc})$	54
<b>Figure 3.2.</b>	Single-component vapor-phase $\text{C}_8$ isomer adsorption isotherms for $\text{Co}_2(\text{dobdc})$ and $\text{Co}_2(m\text{-dobdc})$ and multi-component $\text{C}_8$ isomer vapor-phase breakthrough measurements for $\text{Co}_2(\text{dobdc})$ and $\text{Co}_2(m\text{-dobdc})$	59
<b>Figure 3.3.</b>	Multi-component liquid-phase $\text{C}_8$ isomer adsorption measurements for $\text{Co}_2(\text{dobdc})$	61
<b>Figure 3.4.</b>	Structural distortion of $\text{Co}_2(\text{dobdc})$ upon adsorption of <i>o</i> -xylene	62
<b>Figure 3.5.</b>	Comparison of the <i>o</i> -xylene adsorption isotherms for $\text{Co}_2(\text{dobdc})$ at 50 °C and 150 °C	63
<b>Figure 3.6.</b>	Structures of <i>o</i> -xylene, ethylbenzene, <i>m</i> -xylene, and <i>p</i> -xylene in $\text{Co}_2(\text{dobdc})$	64
<b>Figure 3.7.</b>	Structures of <i>o</i> -xylene and ethylbenzene in $\text{Co}_2(m\text{-dobdc})$	66
<b>Figure 4.1.</b>	Structure of $\text{Zr}_6\text{O}_4(\text{OH})_4(\text{bpydc})_6$	101
<b>Figure 4.2.</b>	Structures of metalated $\text{Zr}_6\text{O}_4(\text{OH})_4(\text{bpydc})_6$	109



<b>Figure 4.3.</b> Comparison of the structures of $Zr_6O_4(OH)_4(bpydc)_6$ and $Zr_6O_4(OH)_4(bpydc)_6 (CuCl_2)_{5.8}$	110
<b>Figure 4.4.</b> Low-pressure $H_2$ adsorption isotherms for $Zr_6O_4(OH)_4(bpydc)_6$ and its metalated derivatives	113
<b>Figure 4.5.</b> Low-pressure CO adsorption isotherms for $Zr_6O_4(OH)_4(bpydc)_6$ and its metalated derivatives	114
<b>Figure 4.6.</b> Structure of $[Ir(dmbpydc)(COD)]BF_4$ , the molecular analog of $Zr_6O_4(OH)_4(bpydc)_6(Ir(COD)BF_4)_{4.7}$	115
<b>Figure 5.1.</b> Structure of $Zr_6O_4(OH)_4(bpydc)_6(NiBr_2)_{5.64}$	173
<b>Figure 5.2.</b> Space-filling model of the structure of $Zr_6O_4(OH)_4(bpydc)_6(NiBr_2)_{5.64}$	179
<b>Figure 5.3.</b> Average turnover frequency distribution plot for ethylene oligomerization reactions catalyzed by $Zr_6O_4(OH)_4(bpydc)_6(NiBr_2)_{5.64}$ , $Zr_6O_4(OH)_4(bpydc)_6(bpdc)(NiBr_2)_{0.84}$ , and $Zr_6O_4(OH)_4(bpdc)_6(NiBr_2)_{0.14}$	181
<b>Figure 6.1.</b> Structures of $Zr_6O_4(OH)_4(bpydc)_6(NiBr_2)_{5.64}$ and $Zr_6O_4(OH)_4(bpydc)_6(NiBr_2)_{5.64} (NiBr_2)_{15}$	218
<b>Figure 6.2.</b> Structures of $Zr_6O_4(OH)_4(bpydc)_6(NiCl_2)_{13}$ , $Zr_6O_4(OH)_4(bpydc)_6(CoCl_2)_{14}$ , and $Zr_6O_4(OH)_4(bpydc)_6(FeCl_2)_{17}$	222
<b>Figure 6.3.</b> Stages of nickel(II) halide cluster growth in $Zr_6O_4(OH)_4(bpydc)_6$	224
<b>Figure 6.4.</b> Dc magnetic susceptibility data for $Zr_6O_4(OH)_4(bpydc)_6(NiBr_2)_{12}$ , $Zr_6O_4(OH)_4(bpydc)_6(NiCl_2)_{18}$ , $Zr_6O_4(OH)_4(bpydc)_6(CoCl_2)_{18}$ , $Zr_6O_4(OH)_4(bpydc)_6(FeCl_2)_{19}$ and variable-temperature ac magnetic susceptibility data for $Zr_6O_4(OH)_4(bpydc)_6(FeCl_2)_{19}$	225

## List of Tables

<b>Table 2.1.</b>	Co–X <sub>gas</sub> distances and differential enthalpies of adsorption ( $\Delta h_{ad}$ ) of CO, CO <sub>2</sub> , CH <sub>4</sub> , N <sub>2</sub> , O <sub>2</sub> , and Ar in Co <sub>2</sub> (dobdc)	25
<b>Table 3.1.</b>	Physical Properties of the C <sub>8</sub> Alkylaromatics	53
<b>Table 3.2.</b>	C <sub>8</sub> Isomer Selectivities of Co <sub>2</sub> (dobdc)	61
<b>Table 4.1.</b>	Selected Properties of the Metal–Organic Frameworks Presented in Chapter 4	108
<b>Table 4.2.</b>	Control Experiments for Benzene C-H Borylation with HBpin	116
<b>Table 4.3.</b>	Control Experiments for Benzene C-H Borylation with B <sub>2</sub> pin <sub>2</sub>	116
<b>Table 4.4.</b>	Catalyst Cycling Experiments for Benzene C-H Borylation with Zr <sub>6</sub> O <sub>4</sub> (OH) <sub>4</sub> (bpydc) <sub>6</sub> (Ir(COD)BF <sub>4</sub> ) <sub>0.6</sub>	117
<b>Table 4.5.</b>	Selected Substrate Scope for C-H Borylation with HBpin	118
<b>Table 5.1.</b>	Nickel loading and surface areas of the metal–organic frameworks investigated in this work	177
<b>Table 5.2.</b>	Ethylene oligomerization results	180

## Acknowledgements

This work was supported through the Center for Gas Separations Relevant to Clean Energy Technologies, an Energy Frontier Research Center funded by the U.S. Department of Energy, Office of Science, Office of Basic Energy Sciences under Award DE-SC0001015, the Nanoporous Materials Genome Center, funded by the U.S. Department of Energy, Office of Basic Energy Sciences, Division of Chemical Sciences, Geosciences and Biosciences, under Award DE-FG02-12ER16362, the Laboratory Directed Research and Development Program of Lawrence Berkeley National Laboratory under U.S. Department of Energy Contract No. DE-AC02-05CH11231, and a Multidisciplinary University Research Initiatives Program funded by the U.S. Department of Defence, Office of Naval Research under Award N00014-15-1-2681. This research used resources of the Advanced Light Source and the Molecular Foundry, which are supported by the Director, Office of Science, Office of Basic Energy Sciences, of the U.S. Department of Energy under Contract No. DE-AC02-05CH11231. I thank Jeffrey R. Long, Eric D. Bloch, Jarad A. Mason, Simon J. Teat, Julia Oktawiec, Ari B. Turkiewicz, Matthew Kapelewski, Lucy E. Darago, Phillip J. Milner, Douglas A. Reed, Wendy L. Queen, Kevin J. Gagnon, Gregory Y. Morrison, Gokhan Barin, Matthew R. Hudson, Craig M. Brown, Rebecca L. Siegelman, Dianne J. Xiao, Dana J. Levine, Jordan C. Axelson, Mercedes K. Taylor, Colin A. Gould, Xiaowen Feng, Selvan Demir, A. Paulina Gómora-Figueroa, Alexander C. Forse, Jeffrey D. Martell, C. Michael McGuirk, David Gygi, Lucie Norel, David Z. Zee, Kristen A. Colwell, Kenji Sumida, Jonathan E. Bachman, Khetpakorn Chakarawet, Chung Jui Yu, Katie R. Meihaus, Joseph M. Zadrozny, Zoey R. Herm, Brian M. Wiers, Thomas M. McDonald, Michael L. Aubrey, Philip C. Bunting, Rodolfo T. Torres-Gavosto, Henry Z. Jiang, Michael E. Ziebel, Daniel Lussier, Jessee Park, Rebecca Khoo, Naomi Biggins, Ryan Murphy, Eugene Kim, Kaipeng Hou, Ever Velasquez, David Jaramillo, Maria Paley, Kaitlyn Engler, Adam Uliana, Alexander Vincent, Surya Parker, Ziting Zhu, Mary Anne Manumpil, David L. Rogow, Michael Nippe, Benjamin K. Keitz, Jeffrey Van Humbeck, Rob Ameloot, Elizabeth Montalvo, Kohei Takahashi, Christina M. Legendre, James R. Nasiaka, Jason S. Lee, Antonio DiPasquale, Greg Halder, Matthew Larsen, Carl Liskey, and Dante Valdez, for helpful discussions and experimental assistance.

# Chapter 1. Structural Studies on Metal–Organic Frameworks by Single-Crystal X-ray Diffraction

## 1.1. Introduction

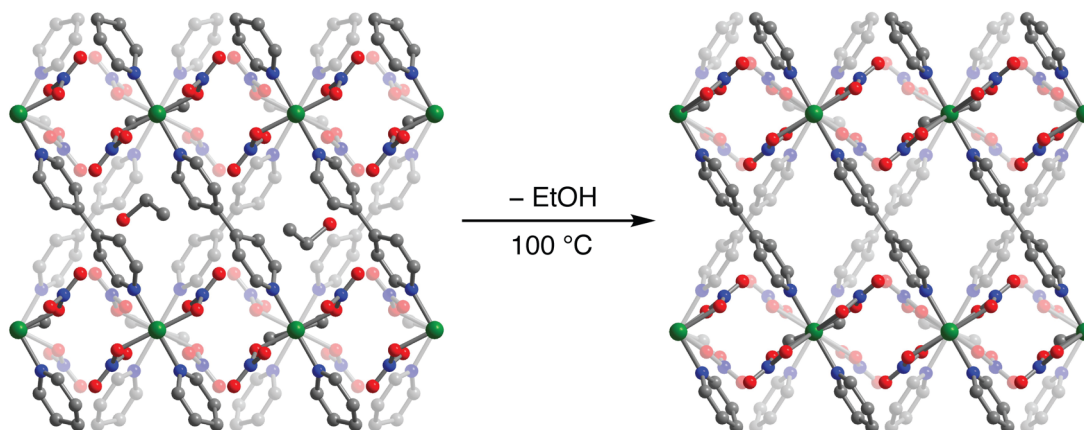
As porous materials assembled from metal ions or inorganic clusters connected in three dimensions by organic linkers, metal–organic frameworks readily adopt a variety of structures with well-defined pore environments.<sup>1–3</sup> Synthetic control over both the inorganic and organic components of these frameworks allows them to be tailored toward specific applications, leading to their growing potential in a broad range of technologies, such as gas storage,<sup>4,5</sup> molecular separations,<sup>6,7</sup> and catalysis.<sup>8–13</sup> The inherent crystallinity of these materials further complements these advantages by coupling the ability to engineer pore architecture and functionality with unparalleled structural characterization through crystallography. Indeed, the ease at which the structure of a metal–organic framework can be correlated to a desired property has been instrumental in driving the rapid advancement of the field.<sup>14</sup>

Although much can already be gleaned from simply obtaining the crystal structure of a metal–organic framework, an increasing number of reports have gone beyond routine structure determination by demonstrating that incorporated guests can be directly observed using diffraction techniques.<sup>15–58</sup> These studies reveal the location of adsorbed guest molecules and the resulting structural response of the framework, providing an intimate understanding of the underlying interactions that dictate adsorption behavior and reactivity. Such knowledge has not only proven to be essential in interpreting the chemical and physical properties of existing frameworks but has also guided the design and synthesis of new materials.

Aside from imparting practical insight into the adsorption or reaction of guest molecules within these materials, *in situ* diffraction methods also allow for the characterization of species that have been difficult to observe by conventional crystallography. For instance, much of the work on adsorbed molecules in metal–organic frameworks has led to the structural determination of interactions that have only been previously characterized by spectroscopy.<sup>48–57</sup> Furthermore, site-isolation within these materials has also been exploited in the study of active sites and reactive intermediates relevant to catalysis.<sup>18,27,59</sup>

While single-crystal X-ray diffraction has been an indispensable tool for characterizing new metal–organic frameworks, many of the *in situ* structural studies on these materials have relied on powder X-ray and neutron diffraction techniques.<sup>16–37,45,49–51</sup> This arises from the many challenges inherent to working with single crystals, such as their tendency to fracture upon removal or inclusion of guests and the sensitivity to contaminants associated with their small sample size. Despite these difficulties, *in situ* single-crystal X-ray diffraction studies have still played a significant role in furthering research on metal–organic frameworks, as exemplified by several key examples discussed in the succeeding sections of this chapter.

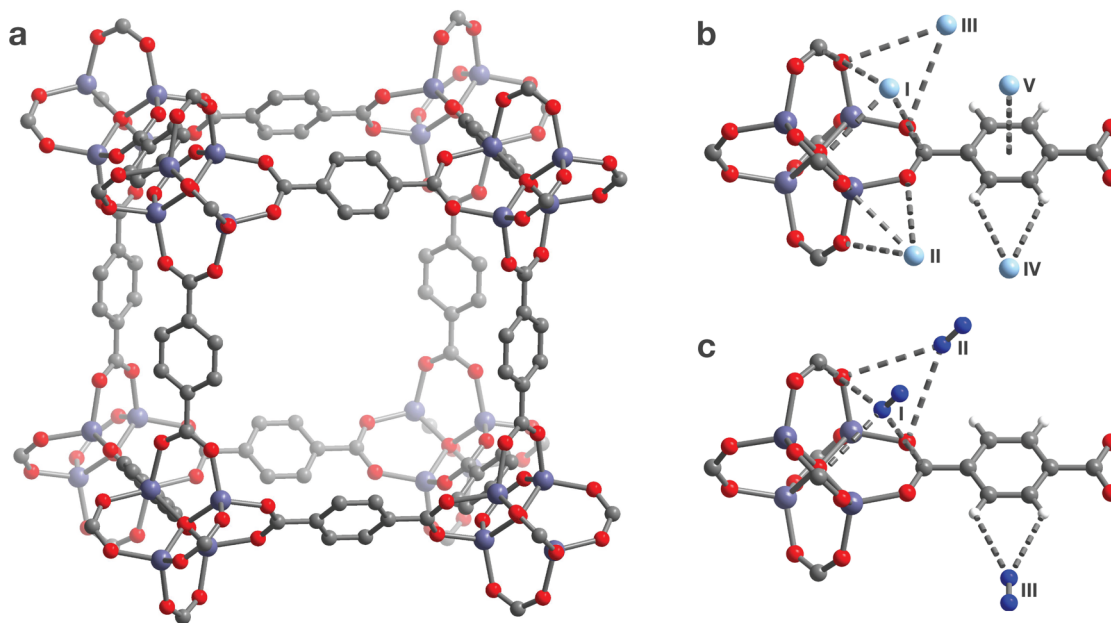
## 1.1. Structural evidence for permanent porosity



**Figure 1.1.** A portion of the crystal structures of  $\text{Ni}_2(4,4'\text{-bpy})_3(\text{NO}_3)_4 \cdot 2\text{EtOH}$  (left) and  $\text{Ni}_2(4,4'\text{-bpy})_3(\text{NO}_3)_4$  (right),<sup>60</sup> depicting structural changes upon complete removal of EtOH from the framework. Green, blue, red, and gray spheres represent Ni, N, O, and C atoms, respectively. Hydrogen atoms are omitted for clarity.

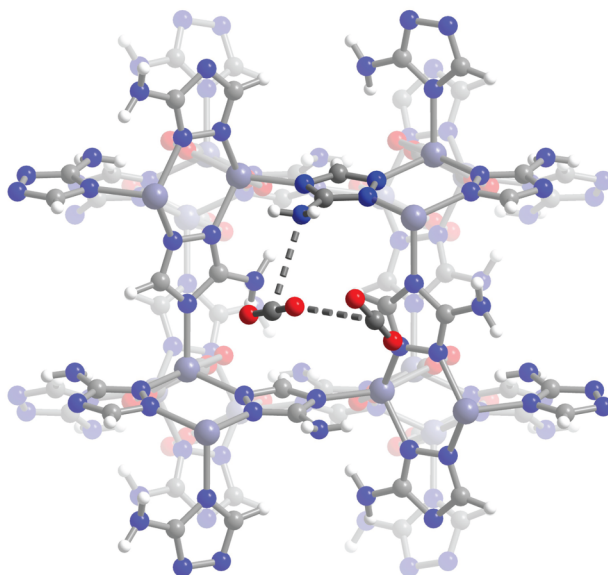
The ability to synthetically tune both the inorganic and organic building blocks of coordination solids imparts considerable structural versatility to these materials. Recognizing the tremendous potential in extending this advantage to porous materials, early research efforts focused on obtaining coordination solids with permanent porosity.<sup>61</sup> Much of the initial work showed through powder X-ray diffraction measurements that, in a number of these materials, guest solvent molecules could either be exchanged or removed without change or collapse of the structure.<sup>62,63</sup> One of the first instances of crystallographic characterization of a completely desolvated porous structure in a coordination solid was demonstrated in the compound  $\text{Ni}_2(4,4'\text{-bpy})_3(\text{NO}_3)_4$  (4,4'-bpy = 4,4'-bipyridine), which is built from interlocking sheets composed of nickel(II) centers bridged by 4,4'-bipyridine linkers.<sup>60</sup> The nickel(II) centers in this structure exhibit a pseudosquare pyramidal geometry with one apical and two basal bipyridine ligands in a meridional arrangement and two charge-balancing  $\text{NO}_3^-$  anions. The as-synthesized material contains two disordered ethanol molecules per formula unit, which were removed upon heating to 100 °C based on thermogravimetric analysis. *In situ* single-crystal X-ray diffraction experiments yielded the structure of the material both before and after desolvation under dry  $\text{N}_2$  at ~100 °C (Figure 1.1). Remarkably, the completely evacuated framework exhibited only a slight structural distortion and maintained its porous structure, clearly showing that permanent porosity could be realized in a coordination solid.

## 1.2. Characterization of framework–gas interactions



**Figure 1.2.** A portion of the crystal structure of  $\text{Zn}_4\text{O}(\text{bdc})_3$  ( $\text{bdc}^{2-} = 1,4\text{-benzenedicarboxylate}$ ) or MOF-5 (a) and structural characterization of the interactions of Ar (b) and  $\text{N}_2$  (c) with  $\text{Zn}_4\text{O}(\text{bdc})_3$  at 30 K,<sup>38</sup> as determined by single-crystal X-ray diffraction. Light purple, light blue, blue, red, gray, and white spheres represent Zn, Ar, N, O, C, and H atoms, respectively. Some hydrogen atoms are omitted for clarity.

With the development of design principles to achieve permanent porosity in metal–organic frameworks, the ability to obtain structures with high internal surface areas quickly emerged as a defining characteristic of these materials.<sup>3,64,65</sup> One of the earliest attempts to correlate high surface area with the presence of multiple gas binding sites employed *in situ* single-crystal X-ray diffraction to locate the Ar and  $\text{N}_2$  binding sites in  $\text{Zn}_4\text{O}(\text{bdc})_3$  ( $\text{bdc}^{2-} = 1,4\text{-benzenedicarboxylate}$ ) or MOF-5.<sup>38</sup> The framework features tetrahedral  $\text{Zn}_4\text{O}$  inorganic clusters bridged by an organic linker at each edge of the  $\text{Zn}_4$  tetrahedron to form a highly porous three-dimensional cubic structure (Figure 1.2a). Eight Ar adsorption sites were located in the framework at 30 K, five involving direct framework–Ar interactions (Figure 1.2b), while the remaining three constitute a secondary adsorption layer within the pore. Of the five sites on the framework, the strongest was found at the triangular faces of the  $\text{Zn}_4$  tetrahedron, where a single Ar atom interacts with three carboxylate groups and three zinc(II) centers, with  $\text{Ar}\cdots\text{C}_{\text{carboxylate}}$  distances of 3.572(4) Å and  $\text{Ar}\cdots\text{Zn}$  distances of 3.926(2) Å. The next strongest adsorption site is stabilized by  $\text{Ar}\cdots\text{O}$  contacts (3.49(3) Å) with three linker oxygen atoms, while the third site has  $\text{Ar}\cdots\text{O}$  contacts (3.792(19) Å) with two oxygen atoms. The Ar atoms located at the two remaining sites interact with the linker aromatic ring. Three adsorption sites were located in the structure of  $\text{N}_2$  in  $\text{Zn}_4\text{O}(\text{bdc})_3$  at 30 K (Figure 1.2c). The first is analogous to the primary Ar binding site, with  $\text{N}\cdots\text{C}_{\text{carboxylate}}$  distances of 3.379(3) Å and  $\text{N}\cdots\text{Zn}$  distances of 3.606(3) Å. Two carboxylate oxygen atoms interact with  $\text{N}_2$  at the second site with  $\text{N}\cdots\text{O}$  distances of 3.73(3) Å. At the third binding site,  $\text{N}_2$  interacts with edge of the linker aromatic ring. Taken together, these findings established that gas adsorption in metal–organic frameworks occurs at discrete binding sites stabilized by electrostatic interactions with the framework surface.

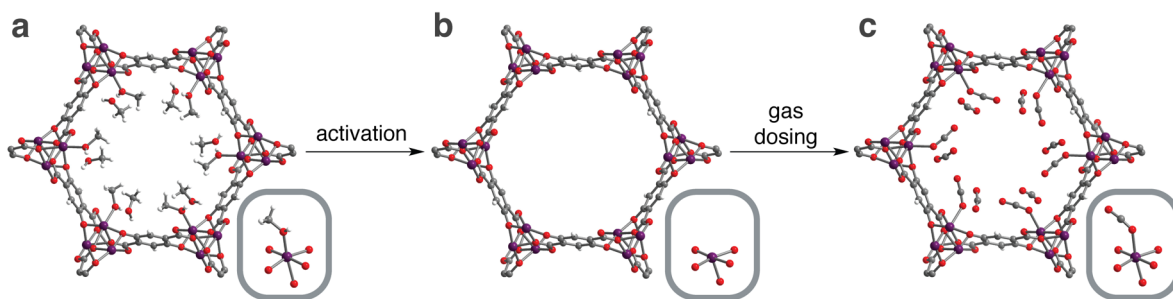


**Figure 1.3.** A portion of the crystal structure of  $\text{Zn}_2(\text{atz})_2(\text{ox}) \cdot 1.30\text{CO}_2$  at 173 K,<sup>66</sup> as determined by single-crystal X-ray diffraction. Light purple, blue, red, gray, and white spheres represent Zn, N, O, C, and H atoms, respectively.

As researchers turned to functionalizing metal–organic frameworks to enhance selectivity and capacity for specific gases, *in situ* diffraction experiments proved to be critical in confirming and studying the interaction of functional groups with adsorbate molecules.<sup>46,47,67</sup> One of the first of these studies was performed on the amine-functionalized framework  $\text{Zn}_2(\text{atz})_2(\text{ox})$  ( $\text{atz}^- = 3\text{-amino-1,2,4-triazolate}$ ;  $\text{ox}^{2-} = \text{oxalate}$ ), which is composed of Zn–triazolate sheets pillared by oxalate linkers.<sup>66</sup> The high and selective  $\text{CO}_2$  uptake and moderate  $\text{CO}_2$  adsorption enthalpy ( $-40.8 \text{ kJ/mol}$ ) of this framework was postulated to stem from physisorptive interactions resulting from  $\text{CO}_2$  binding to the moderately Lewis basic amines on the triazolate linkers of the framework. This hypothesis was later confirmed by *in situ* single-crystal X-ray diffraction measurements on the framework in the presence of  $\text{CO}_2$ . Two  $\text{CO}_2$  binding sites were located within the material at 173 K (Figure 1.3). The primary binding site features the anticipated interaction between an amine nitrogen atom and the electropositive carbon atom of  $\text{CO}_2$ , with a  $\text{C}\cdots\text{N}$  distance of  $3.151(8) \text{ \AA}$ . Additional weak interactions with neighboring aminotriazolate and oxalate linkers further stabilize  $\text{CO}_2$  bound at this site. Notably, the amine-bound  $\text{CO}_2$  molecule did not exhibit a strong deviation from linearity, consistent with only physisorption of  $\text{CO}_2$  within the material instead of chemisorption through the formation of ammonium carbamate species. In the second binding site,  $\text{CO}_2$  interacts with both the framework and the oxygen atom of  $\text{CO}_2$  at the first site. These experimental results were corroborated by molecular simulations, emphasizing the utility of combining both *in situ* diffraction experiments and computational studies in elucidating adsorption behavior in metal–organic frameworks.

Metal–organic frameworks bearing coordinatively unsaturated metal centers have been extensively investigated for applications in gas storage and gas separations, due to the ability of these exposed metal sites to bind and distinguish between gas molecules. While the metal–gas interactions responsible for the favorable adsorption properties of these materials were readily characterized by *in situ* powder X-ray diffraction, comparatively few studies have been

performed by single-crystal X-ray diffraction. This disparity arises from the propensity of open metal coordination sites to bind contaminants such as water, which is exacerbated by the small sample size of a single crystal.

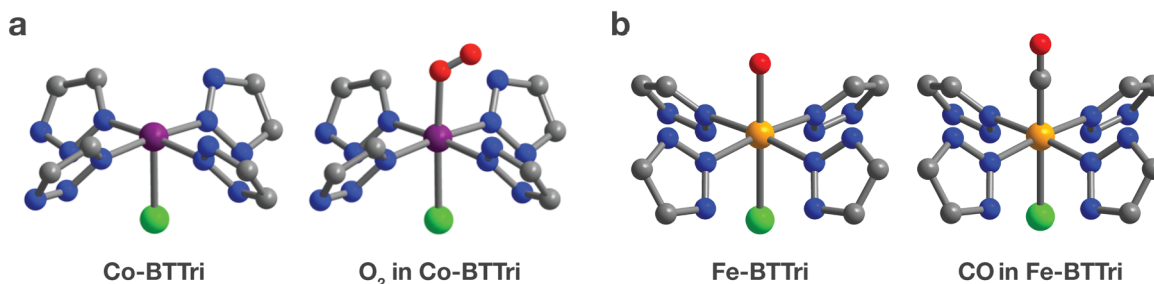


**Figure 1.4.** A portion of the single-crystal structures of  $\text{Co}_2(\text{dobdc})\cdot 4\text{CH}_3\text{OH}$  (a),  $\text{Co}_2(\text{dobdc})$  (b), and  $\text{Co}_2(\text{dobdc})\cdot 2.9\text{CO}_2$  (c),<sup>16</sup> depicting the activation of the framework (a to b) and the adsorption of  $\text{CO}_2$  (b to c). Insets detail the first coordination sphere of cobalt(II) in these structures. Purple, red, gray, and white sphere represent Co, O, C, and H atoms respectively.

The  $\text{M}_2(\text{dobdc})$  series of metal–organic frameworks ( $\text{dobdc}^{4-} = 2,5\text{-dioxido-1,4-benzenedicarboxylate}$ ;  $\text{M} = \text{Mg}^{\text{II}}, \text{Mn}^{\text{II}}, \text{Fe}^{\text{II}}, \text{Co}^{\text{II}}, \text{Ni}^{\text{II}}, \text{Cu}^{\text{II}}, \text{Zn}^{\text{II}}, \text{or Cd}^{\text{II}}$ ; also referred to as M-MOF-74 or CPO-27-M) have been intensely evaluated for gas storage and gas separations due to their high density of exposed metal sites.<sup>16-31,39,49-51,68,69</sup> Despite much earlier work employing *in situ* single-crystal X-ray diffraction to monitor the desolvation of  $\text{Co}_2(\text{dobdc})$  (Figure 1.4b),<sup>39</sup> the technique has only recently been employed to characterize metal–gas interactions in this material. In this study, *in situ* crystallography led to the observation of  $\text{CO}_2$  adsorption onto the cobalt(II) sites of  $\text{Co}_2(\text{dobdc})$  and, perhaps surprisingly, at nearby secondary binding sites (Figure 1.4c).<sup>16</sup> The structure shows  $\text{CO}_2$  bound to  $\text{Co}^{\text{II}}$  through an end-on coordination mode, with a  $\text{Co}-\text{O}_{\text{CO}_2}$  distance of 2.261(9) Å. The metal-bound  $\text{CO}_2$  tilts toward a nearby non-bridging carboxylate oxygen atom with a  $\text{C}_{\text{CO}_2}\cdots\text{O}$  separation of 3.29(7) Å and a  $\text{Co}-\text{O}-\text{C}$  angle of 133(3)°, which likely results from attraction between the partial positive charge of the  $\text{CO}_2$  carbon atom and the partial negative charge on the carboxylate oxygen. At the secondary binding site,  $\text{CO}_2$  interacts with two linker oxygen atoms with  $\text{C}_{\text{CO}_2}\cdots\text{O}$  distances of 3.21(5) Å and 3.29(8) Å. Finally, close  $\text{C}_{\text{CO}_2}\cdots\text{O}_{\text{CO}_2}$  contacts (2.74(7) Å) between  $\text{CO}_2$  molecules at the primary and secondary sites imply that  $\text{CO}_2$ – $\text{CO}_2$  interactions contribute to  $\text{CO}_2$  adsorption in this framework. These results corroborated structures solved from both powder neutron and X-ray diffraction data as well as those obtained from DFT calculations, which were all part of a comprehensive study on  $\text{CO}_2$  adsorption in the  $\text{M}_2(\text{dobdc})$  series of metal–organic frameworks ( $\text{M} = \text{Mg}^{\text{II}}, \text{Mn}^{\text{II}}, \text{Fe}^{\text{II}}, \text{Co}^{\text{II}}, \text{Ni}^{\text{II}}, \text{Cu}^{\text{II}}, \text{and Zn}^{\text{II}}$ ).<sup>16</sup> This study confirmed that  $\text{CO}_2$  uptake in  $\text{M}_2(\text{dobdc})$  occurs primarily through physisorptive interactions with significant contributions from adsorption at both the exposed metal sites and secondary adsorption sites.

Most metal–organic frameworks bearing metals with open coordination sites possess oxygen-based linkers that impose a weak ligand field on the metal center. As a result, the application of these materials for gas storage and gas separation has overwhelmingly relied on Lewis acidity alone to bind gas molecules.<sup>4-7</sup> Certain gases such as  $\text{O}_2$  and  $\text{CO}$ , however, can be adsorbed more selectively based on their capacity to accept electron density. Thus, materials featuring more electron-rich metal centers would be more effective at distinguishing between these gases than those that bind solely through electrostatic interactions.





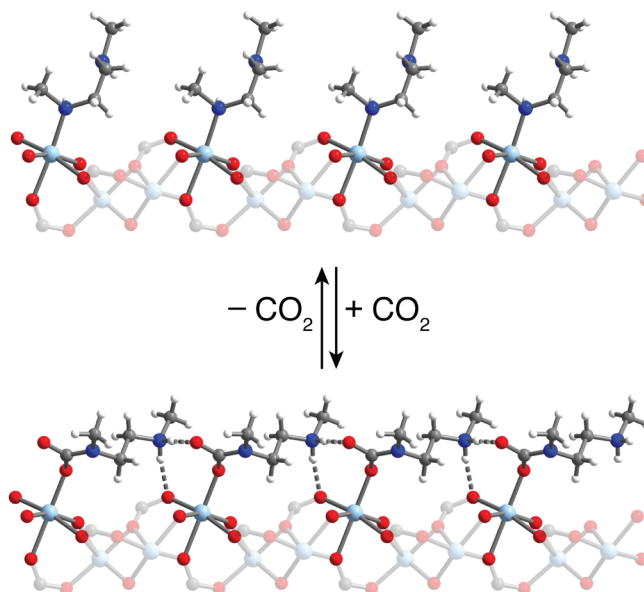
**Figure 1.5.** A portion of the structures of Co-BTtri–O<sub>2</sub> (M-BTtri = M<sub>3</sub>[(M<sub>4</sub>Cl)<sub>3</sub>(BTtri)<sub>8</sub>]<sub>2</sub>·DMF; H<sub>3</sub>BTtri = 1,3,5-tri(1H-1,2,3-triazol-5-yl)benzene); DMF = *N,N*-dimethylformamide) at 100 K<sup>54</sup> (a) and Fe-BTtri–CO at 100 K<sup>43</sup> (b), determined from single-crystal X-ray diffraction data. Purple, orange, blue, red, gray, and white spheres represent Co, Fe, N, O, C, and H atoms, respectively.

The metal–organic frameworks Co-BTtri (Figure 1.5a) and Co-BDTrip (M-BTtri = M<sub>3</sub>[(M<sub>4</sub>Cl)<sub>3</sub>(BTtri)<sub>8</sub>]<sub>2</sub>·DMF; H<sub>3</sub>BTtri = 1,3,5-tri(1H-1,2,3-triazol-5-yl)benzene; M-BDTrip = M<sub>3</sub>[(M<sub>4</sub>Cl)<sub>3</sub>(BDTriP)<sub>8</sub>]<sub>2</sub>·DMF; H<sub>3</sub>BDTriP = 5,5'-(5-(1H-pyrazol-4-yl)-1,3-phenylene)bis(1H-1,2,3-triazole); DMF = *N,N*-dimethylformamide) have been demonstrated to be promising materials for the separation of O<sub>2</sub> from air.<sup>54</sup> These anionic frameworks consist of square [Co<sup>II</sup><sub>4</sub>Cl]<sup>7+</sup> clusters connected by the tritopic linkers to form cubic expanded sodalite-type structures. Each cobalt(II) center in the [Co<sup>II</sup><sub>4</sub>Cl]<sup>7+</sup> cluster adopts a square pyramidal geometry with an apical chloride ligand and four azolate ligands on the basal plane (Figure 1.5a). The strong ligand field enforced by the triazolate or pyrazolate ligands result in the low-spin electronic configuration of the cobalt(II) centers. Significantly, these cobalt(II) sites were found to be sufficiently electron-rich to facilitate partial electron transfer upon binding O<sub>2</sub>, allowing for selective adsorption of O<sub>2</sub> over N<sub>2</sub>. Characterization of the O<sub>2</sub>-dosed frameworks by single-crystal X-ray diffraction at 100 K (Figure 1.5a) indicated that O<sub>2</sub> coordinates to cobalt through an end-on binding mode with slightly longer Co–O<sub>2</sub> distances (1.973(6) Å in Co-BTtri–O<sub>2</sub> and 1.967(8) Å in Co-BDTrip–O<sub>2</sub>) compared to molecular cobalt(III)–superoxo complexes, consistent with only partial electron transfer from Co<sup>II</sup> to O<sub>2</sub>. Both structures also exhibit contracted Co–N and Co–Cl bond distances in comparison to the bare frameworks, which also indicate reduced electron density at the cobalt center upon binding O<sub>2</sub>.

An analogous structural investigation was performed to determine the mechanism of CO adsorption in Fe-BTtri, the iron analogue of Co-BTtri.<sup>43</sup> In the structure of the DMF-solvated framework at 100 K (Figure 1.5b), the Fe–N distances were found to be 2.1424(14) Å, indicating that the iron(II) centers are high-spin. In contrast, the structure of Fe-BTtri–CO at 100 K (Figure 1.5b) displayed a short Fe–C<sub>CO</sub> distance (1.774(5) Å) and contraction of the Fe–N distances to 1.9843(19) Å. These results, in conjunction with spectroscopic and magnetic measurements, established that the favorable CO adsorption properties of Fe-BTtri arise from a reversible iron(II) spin state transition from a high-spin to a low-spin upon coordination of CO. As in Co-BTtri, the framework triazolate ligands increase the electron density and stabilize the low-spin state of the iron(II) centers in Fe-BTtri. Consequently, these sites form more stable Fe<sup>II</sup>–CO complexes due to enhanced  $\pi$  backbonding from Fe<sup>II</sup> to CO.

Similar studies have also been conducted on cobalt(II)- and iron(II)-metalated analogues of the framework Zr<sub>6</sub>O<sub>4</sub>(OH)<sub>10</sub>(H<sub>2</sub>O)<sub>6</sub>(tcpp)<sub>1.5</sub> (also referred to as PCN-224; H<sub>4</sub>tcpp = tetrakis(4-carboxyphenyl)porphyrin). Both the cobalt(II)- and iron(II)-metalated frameworks were found to weakly bind O<sub>2</sub> to form rare five-coordinate Co–O<sub>2</sub> and Fe–O<sub>2</sub> species.<sup>55,57</sup> Crystallographic

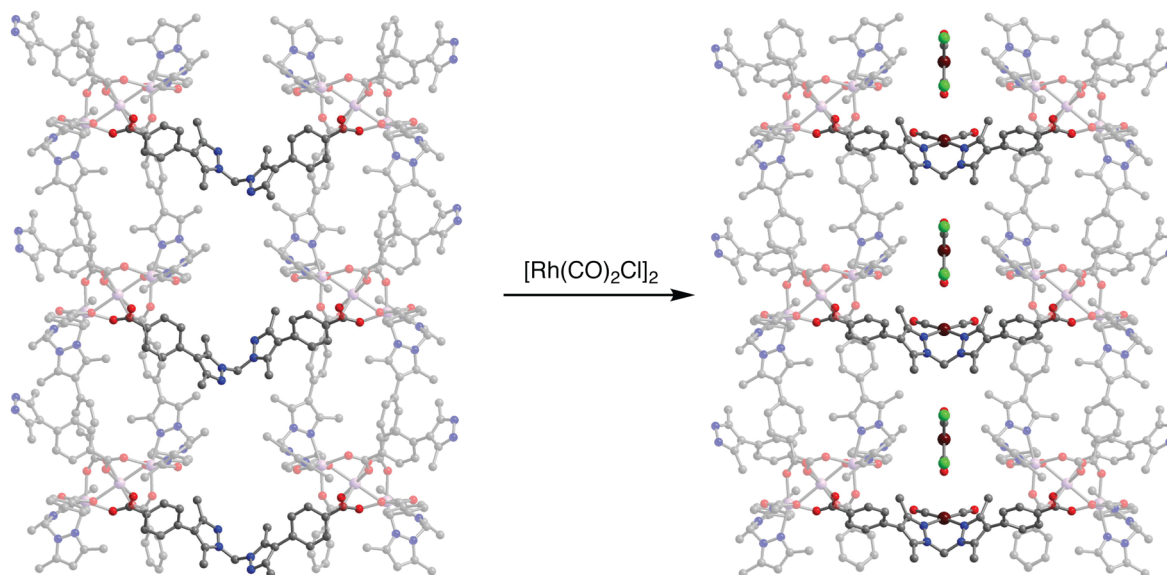
characterization of these complexes yielded a Co–O<sub>2</sub> distance of 1.93(4) Å and an Fe–O<sub>2</sub> distance of 1.79(1) Å, which are within the range of those reported for analogous metal(III)–superoxo complexes. The cobalt(II)-metalated variant was also reported to form either a monocarbonyl or dicarbonyl cobalt(II)–porphyrin complex in the presence of CO.<sup>56</sup> The monocarbonyl adduct was found to be the most stable species at 150 and 200 K, while significant population of the dicarbonyl species was observed at 8 and 80 K.



**Figure 1.6.** Cooperative CO<sub>2</sub> insertion into the metal-amine bonds of the framework m-2-m–Zn<sub>2</sub>(dobpdc) (m-2-m = *N,N'*-dimethylethylenediamine; dobpdc<sup>4-</sup> = 4,4'-dioxido-[1,1'-biphenyl]-3,3'-dicarboxylate) to form ammonium carbamate chains as observed by *in situ* single-crystal X-ray diffraction.<sup>58</sup> Light blue, red, blue, gray, and white spheres represent Zn, O, N, C, and H atoms, respectively.

Recent work has demonstrated that appending alkyldiamines to the open metal sites in M<sub>2</sub>(dobpdc) (dobpdc<sup>4-</sup> = 4,4'-dioxido-[1,1'-biphenyl]-3,3'-dicarboxylate; M = Mg, Mn, Fe, Co, Zn), an expanded analog of M<sub>2</sub>(dobdc), endows these materials with exceptional selectivity for CO<sub>2</sub>.<sup>70</sup> These materials also show unique step-shaped adsorption isotherms that can be leveraged to achieve very high working capacities for different CO<sub>2</sub> capture processes. These advantages arise from a cooperative adsorption mechanism involving insertion of CO<sub>2</sub> into the metal–amine bond to form ammonium carbamate chains that run along the framework pores (Figure 1.6).<sup>35</sup> The effects of amine structure on CO<sub>2</sub> adsorption in these materials were examined by correlating gas adsorption measurements with single-crystal structures of both the diamine and ammonium carbamate phase in diamine-appended Zn<sub>2</sub>(dobpdc).<sup>58</sup> These experiments uncovered how nuances in diamine structure dictate the thermodynamics of CO<sub>2</sub> adsorption in these materials by influencing the strength of the metal–amine bond, the steric repulsion between adjacent ammonium carbamate units, and the hydrogen-bonding and ion-pairing interactions available to the ammonium carbamate chains. In particular, lower CO<sub>2</sub> adsorption step pressures were observed when steric bulk on the diamine weakens the metal–amine bond and when multiple hydrogen-bonding and ion-pairing interactions stabilize the CO<sub>2</sub>-inserted phase. Conversely, higher CO<sub>2</sub> step pressures were achieved by adding bulky substituents at the terminal amine to destabilize the ion-pairing interactions between ammonium carbamate units.

### 1.3. Post-synthetic metalation of metal–organic frameworks



**Figure 1.7.** A portion of the structure of  $\text{Mn}_3(\text{L})_2(\text{L}')$  and  $[\text{Mn}_3(\text{L})_2(\text{L}')(\text{Rh}(\text{CO})_2)][\text{Rh}(\text{CO})_2\text{Cl}_2]$  ( $\text{H}_2\text{L}$  = bis(4-(4-carboxyphenyl)-1H-3,5-dimethylpyrazolyl)methane;  $\text{L}^{2-}$  and  $\text{L}'^{2-}$  are crystallographically distinct forms of deprotonated  $\text{H}_2\text{L}$ ) at 100 K,<sup>18,71</sup> determined from single-crystal X-ray diffraction data; pink, dark red, blue, red, and gray spheres represent Mn, Rh, N, O, and C atoms, respectively. Hydrogen atoms are omitted for clarity.

Post-synthetic metalation has proven to be a versatile approach toward expanding the coordination chemistry of metal–organic frameworks beyond their inorganic nodes.<sup>13,40,72-79</sup> Through this strategy, frameworks functionalized with coordinating groups can be employed as scaffolds to build a diverse array of metal complexes tailored to various applications, such as gas adsorption and catalysis. The coordination environment of these complexes, however, can often be impossible to resolve crystallographically in systems with significant disorder or very low metal site occupancies.<sup>80-82</sup> Nevertheless, several studies have demonstrated that structurally ordered metal species can be observed by single-crystal X-ray diffraction if the metalated framework possesses sufficiently low symmetry.<sup>18,40,59,71,79,83</sup>

A series of reports have featured the metalation of the chelating dipyrazole sites in the metal–organic framework  $\text{Mn}_3(\text{L})_2(\text{L}')$  ( $\text{H}_2\text{L}$  = bis(4-(4-carboxyphenyl)-1H-3,5-dimethylpyrazolyl)methane;  $\text{L}^{2-}$  and  $\text{L}'^{2-}$  are crystallographically distinct forms of deprotonated  $\text{H}_2\text{L}$ ).<sup>18,71,83</sup> Both the dipyrazole and carboxylate groups of the  $\text{L}^{2-}$  linkers bridge trinuclear  $\text{Mn}^{\text{II}}$  clusters to form two-dimensional  $\text{Mn}(\text{L})_2$  layers, which in turn are pillared by  $\text{L}'^{2-}$  linkers to generate a three-dimensional structure. The  $\text{L}'^{2-}$  linkers feature vacant dipyrazole chelating sites that allow for post-synthetic metalation of the framework. Upon metalation with a range of metal ions ( $\text{Mn}^{\text{II}}$ ,  $\text{Co}^{\text{II}}$ ,  $\text{Cu}^{\text{II}}$ ,  $\text{Zn}^{\text{II}}$ ,  $\text{Rh}^{\text{I}}$ , and  $\text{Cd}^{\text{II}}$ ), the low crystal symmetry of the framework results in the formation of crystallographically ordered metal–dipyrazole complexes, thereby allowing the coordination environment of these complexes to be precisely determined by single-crystal X-ray diffraction (Figure 1.7). Moreover, subsequent chemical transformations at these metal centers were also followed by crystallography, which enabled characterization of reactive intermediates in the Rh-catalyzed carbonylation of  $\text{CH}_3\text{Br}$  and  $\text{CH}_3\text{I}$ .<sup>18,71</sup>

#### **1.4. Conclusions and outlook**

As envisioned in initial efforts to endow coordination solids with permanent porosity, metal–organic frameworks have matured into a class of porous materials defined by the capacity to tailor both their inorganic and organic constituents. Research on these materials has increasingly relied on structural characterization by crystallography. Driven by this necessity, diffraction techniques have progressed substantially from conventional structure determination to the direct observation of the removal, inclusion, and reaction of molecular guests within these frameworks. As a result, these techniques have proven to be indispensable in establishing structure–property relationships that have ultimately led to the design of better materials. With the development and widespread adoption of crystallographic methods for porous materials, structural studies on metal–organic frameworks will not only continue to corroborate predicted behavior but also support the discovery of new chemical species and reactivity. The subsequent chapters of this thesis explore many aspects of the chemistry of metal–organic frameworks, encompassing work on framework–gas interactions, liquid-phase separations, catalysis, and the confinement of inorganic solids in these materials. In all these investigations, characterization by single-crystal X-ray diffraction has afforded vital insight into the influence of framework structure on guest incorporation and reactivity.

## 1.5. References

- (1) Tranchemontagne, D. J.; Mendoza-Cortes, J. L.; O’Keeffe, M.; Yaghi, O. M. *Chem. Soc. Rev.* **2009**, *38* (5), 1257–1283.
- (2) O’Keeffe, M.; Yaghi, O. M. *Chem. Rev.* **2012**, *112* (2), 675–702.
- (3) Yaghi, O. M.; O’Keeffe, M.; Ockwig, N. W.; Chae, H. K.; Eddaoudi, M.; Kim, J. *Nature* **2003**, *423* (6941), 705–714.
- (4) Murray, L. J.; Dincă, M.; Long, J. R. *Chem. Soc. Rev.* **2009**, *38* (5), 1294–1314.
- (5) Mason, J. A.; Veenstra, M.; Long, J. R. *Chem. Sci.* **2014**, *5* (1), 32–51.
- (6) Sumida, K.; Rogow, D. L.; Mason, J. A.; McDonald, T. M.; Bloch, E. D.; Herm, Z. R.; Bae, T.-H.; Long, J. R. *Chem. Rev.* **2012**, *112* (2), 724–781.
- (7) Herm, Z. R.; Bloch, E. D.; Long, J. R. *Chem. Mater.* **2014**, *26* (1), 323–338.
- (8) Ma, L.; Abney, C.; Lin, W. *Chem. Soc. Rev.* **2009**, *38* (5), 1248–1256.
- (9) Corma, A.; García, H.; Llabrés i Xamena, F. X. *Chem. Rev.* **2010**, *110* (8), 4606–4655.
- (10) Gascon, J.; Corma, A.; Kapteijn, F.; Llabrés i Xamena, F. X. *ACS Catal.* **2013**, 361–378.
- (11) Liu, J.; Chen, L.; Cui, H.; Zhang, J.; Zhang, L.; Su, C.-Y. *Chem. Soc. Rev.* **2014**, *43* (16), 6011–6061.
- (12) Wang, C.; Zheng, M.; Lin, W. *J. Phys. Chem. Lett.* **2011**, *2* (14), 1701–1709.
- (13) Cohen, S. M.; Zhang, Z.; Boissonnault, J. A. *Inorg. Chem.* **2016**, *55* (15), 7281–7290.
- (14) Gándara, F.; Bennett, T. D. *IUCrJ* **2014**, *1* (Pt 6), 563–570.
- (15) Zhang, J.-P.; Liao, P.-Q.; Zhou, H.-L.; Lin, R.-B.; Chen, X.-M. *Chem. Soc. Rev.* **2014**, *43* (16), 5789–5814.
- (16) Queen, W. L.; Hudson, M. R.; Bloch, E. D.; Mason, J. A.; Gonzalez, M. I.; Lee, J. S.; Gygi, D.; Howe, J. D.; Lee, K.; Darwish, T. A.; James, M.; Peterson, V. K.; Teat, S. J.; Smit, B.; Neaton, J. B.; Long, J. R.; Brown, C. M. *Chem. Sci.* **2014**, *5* (12), 4569–4581.
- (17) Lee, J. S.; Vlasisavljevich, B.; Britt, D. K.; Brown, C. M.; Haranczyk, M.; Neaton, J. B.; Smit, B.; Long, J. R.; Queen, W. L. *Adv. Mater.* **2015**, *27* (38), 5785–5796.
- (18) Bloch, W. M.; Burgun, A.; Coghlan, C. J.; Lee, R.; Coote, M. L.; Doonan, C. J.; Sumbly, C. J. *Nature Chemistry* **2014**, *6* (10), 906–912.
- (19) Dietzel, P. D. C.; Panella, B.; Hirscher, M.; Blom, R.; Fjellvåg, H. *Chem. Commun.* **2006**, No. 9, 959–961.
- (20) Dietzel, P. D. C.; Johnsen, R. E.; Fjellvåg, H.; Bordiga, S.; Groppo, E.; Chavan, S.; Blom, R. *Chem. Commun.* **2008**, No. 41, 5125–5127.
- (21) Liu, Y.; Kabbour, H.; Brown, C. M.; Neumann, D. A.; Ahn, C. C. *Langmuir* **2008**, *24* (9), 4772–4777.
- (22) McKinlay, A. C.; Xiao, B.; Wragg, D. S.; Wheatley, P. S.; Megson, I. L.; Morris, R. E. *J. Am. Chem. Soc.* **2008**, *130* (31), 10440–10444.
- (23) Dietzel, P. D. C.; Georgiev, P. A.; Eckert, J.; Blom, R.; Strässle, T.; Unruh, T. *Chem. Commun.* **2010**, *46* (27), 4962–4963.
- (24) Sumida, K.; Her, J.-H.; Dincă, M.; Murray, L. J.; Schloss, J. M.; Pierce, C. J.; Thompson, B. A.; FitzGerald, S. A.; Brown, C. M.; Long, J. R. *J. Phys. Chem. C* **2011**, *115* (16), 8414–8421.
- (25) Queen, W. L.; Bloch, E. D.; Brown, C. M.; Hudson, M. R.; Mason, J. A.; Murray, L. J.; Ramirez-Cuesta, A. J.; Peterson, V. K.; Long, J. R. *Dalton Trans.* **2012**, *41* (14), 4180–4188.
- (26) Geier, S. J.; Mason, J. A.; Bloch, E. D.; Queen, W. L.; Hudson, M. R.; Brown, C. M.;

- Long, J. R. *Chem. Sci.* **2013**, *4* (5), 2054–2061.
- (27) Xiao, D. J.; Bloch, E. D.; Mason, J. A.; Queen, W. L.; Hudson, M. R.; Planas, N.; Borycz, J.; Dzubak, A. L.; Verma, P.; Lee, K.; Bonino, F.; Crocellà, V.; Yano, J.; Bordiga, S.; Truhlar, D. G.; Gagliardi, L.; Brown, C. M.; Long, J. R. *Nature Chemistry* **2014**, *6* (7), 590–595.
- (28) Furukawa, H.; Gándara, F.; Zhang, Y.-B.; Jiang, J.; Queen, W. L.; Hudson, M. R.; Yaghi, O. M. *J. Am. Chem. Soc.* **2014**, *136* (11), 4369–4381.
- (29) Magdysyuk, O. V.; Adams, F.; Liermann, H.-P.; Spanopoulos, I.; Trikalitis, P. N.; Hirscher, M.; Morris, R. E.; Duncan, M. J.; McCormick, L. J.; Dinnebier, R. E. *Phys. Chem. Chem. Phys.* **2014**, *16* (43), 23908–23914.
- (30) Bloch, E. D.; Queen, W. L.; Chavan, S.; Wheatley, P. S.; Zadrozny, J. M.; Morris, R.; Brown, C. M.; Lamberti, C.; Bordiga, S.; Long, J. R. *J. Am. Chem. Soc.* **2015**, *137* (10), 3466–3469.
- (31) Ghose, S. K.; Li, Y.; Yakovenko, A.; Dooryhee, E.; Ehm, L.; Ecker, L. E.; Dippel, A.-C.; Halder, G. J.; Strachan, D. M.; Thallapally, P. K. *J. Phys. Chem. Lett.* **2015**, *6* (10), 1790–1794.
- (32) Murray, L. J.; Dincă, M.; Yano, J.; Chavan, S.; Bordiga, S.; Brown, C. M.; Long, J. R. *J. Am. Chem. Soc.* **2010**, *132* (23), 7856–7857.
- (33) Sumida, K.; Horike, S.; Kaye, S. S.; Herm, Z. R.; Queen, W. L.; Brown, C. M.; Grandjean, F.; Long, G. J.; Dailly, A.; Long, J. R. *Chem. Sci.* **2010**, *1* (2), 184–191.
- (34) Kapelewski, M. T.; Geier, S. J.; Hudson, M. R.; Stück, D.; Mason, J. A.; Nelson, J. N.; Xiao, D. J.; Hulvey, Z.; Gilmour, E.; FitzGerald, S. A.; Head-Gordon, M.; Brown, C. M.; Long, J. R. *J. Am. Chem. Soc.* **2014**, *136* (34), 12119–12129.
- (35) McDonald, T. M.; Mason, J. A.; Kong, X.; Bloch, E. D.; Gygi, D.; Dani, A.; Crocellà, V.; Giordanino, F.; Odoh, S. O.; Drisdell, W. S.; Vlaisavljevich, B.; Dzubak, A. L.; Poloni, R.; Schnell, S. K.; Planas, N.; Lee, K.; Pascal, T.; Wan, L. F.; Prendergast, D.; Neaton, J. B.; Smit, B.; Kortright, J. B.; Gagliardi, L.; Bordiga, S.; Reimer, J. A.; Long, J. R. *Nature* **2015**, *519* (7543), 303–308.
- (36) Hulvey, Z.; Vlaisavljevich, B.; Mason, J. A.; Tsivion, E.; Dougherty, T. P.; Bloch, E. D.; Head-Gordon, M.; Smit, B.; Long, J. R.; Brown, C. M. *J. Am. Chem. Soc.* **2015**, *137* (33), 10816–10825.
- (37) Gygi, D.; Bloch, E. D.; Mason, J. A.; Hudson, M. R.; Gonzalez, M. I.; Siegelman, R. L.; Darwish, T. A.; Queen, W. L.; Brown, C. M.; Long, J. R. *Chem. Mater.* **2016**, *28* (4), 1128–1138.
- (38) Rowsell, J. L. C.; Spencer, E. C.; Eckert, J.; Howard, J. A. K.; Yaghi, O. M. *Science* **2005**, *309* (5739), 1350–1354.
- (39) Dietzel, P. D. C.; Morita, Y.; Blom, R.; Fjellvåg, H. *Angew. Chem. Int. Ed.* **2005**, *44* (39), 6354–6358.
- (40) Gonzalez, M. I.; Bloch, E. D.; Mason, J. A.; Teat, S. J.; Long, J. R. *Inorg. Chem.* **2015**, *54* (6), 2995–3005.
- (41) Trickett, C. A.; Gagnon, K. J.; Lee, S.; Gándara, F.; Büergi, H.-B.; Yaghi, O. M. *Angew. Chem. Int. Ed.* **2015**, *54* (38), 11162–11167.
- (42) Marshall, R. J.; Griffin, S. L.; Wilson, C.; Forgan, R. S. *J. Am. Chem. Soc.* **2015**, *137* (30), 9527–9530.
- (43) Reed, D. A.; Xiao, D. J.; Gonzalez, M. I.; Darago, L. E.; Herm, Z. R.; Grandjean, F.; Long, J. R. *J. Am. Chem. Soc.* **2016**, *138* (17), 5594–5602.

- (44) Bhatt, P. M.; Belmabkhout, Y.; Cadiou, A.; Adil, K.; Shekhah, O.; Shkurenko, A.; Barbour, L. J.; Eddaoudi, M. *J. Am. Chem. Soc.* **2016**, *138* (29), 9301–9307.
- (45) Elsaidi, S. K.; Mohamed, M. H.; Simon, C. M.; Braun, E.; Pham, T.; Forrest, K. A.; Xu, W.; Banerjee, D.; Space, B.; Zaworotko, M. J.; Thallapally, P. K. *Chem. Sci.* **2017**, *8* (3), 2373–2380.
- (46) Liao, P.-Q.; Zhou, D.-D.; Zhu, A.-X.; Jiang, L.; Lin, R.-B.; Zhang, J.-P.; Chen, X.-M. *J. Am. Chem. Soc.* **2012**, *134* (42), 17380–17383.
- (47) Moreau, F.; da Silva, I.; Smail, Al, N. H.; Easun, T. L.; Savage, M.; Godfrey, H. G. W.; Parker, S. F.; Manuel, P.; Yang, S.; Schröder, M. *Nat Commun* **2017**, *8*, 14085.
- (48) Bloch, W. M.; Champness, N. R.; Doonan, C. J. *Angew. Chem. Int. Ed.* **2015**, *54* (44), 12860–12867.
- (49) Bloch, E. D.; Queen, W. L.; Krishna, R.; Zadrozny, J. M.; Brown, C. M.; Long, J. R. *Science* **2012**, *335* (6076), 1606–1610.
- (50) Bloch, E. D.; Hudson, M. R.; Mason, J. A.; Chavan, S.; Crocellà, V.; Howe, J. D.; Lee, K.; Dzubak, A. L.; Queen, W. L.; Zadrozny, J. M.; Geier, S. J.; Lin, L.-C.; Gagliardi, L.; Smit, B.; Neaton, J. B.; Bordiga, S.; Brown, C. M.; Long, J. R. *J. Am. Chem. Soc.* **2014**, *136* (30), 10752–10761.
- (51) Bloch, E. D.; Murray, L. J.; Queen, W. L.; Chavan, S.; Maximoff, S. N.; Bigi, J. P.; Krishna, R.; Peterson, V. K.; Grandjean, F.; Long, G. J.; Smit, B.; Bordiga, S.; Brown, C. M.; Long, J. R. *J. Am. Chem. Soc.* **2011**, *133* (37), 14814–14822.
- (52) Gonzalez, M. I.; Mason, J. A.; Bloch, E. D.; Teat, S. J.; Gagnon, K. J.; Morrison, G. Y.; Queen, W. L.; Long, J. R. *Chem. Sci.* **2017**, *8* (6), 4387–4398.
- (53) Lee, K.; Isley, W. C.; Dzubak, A. L.; Verma, P.; Stoneburner, S. J.; Lin, L.-C.; Howe, J. D.; Bloch, E. D.; Reed, D. A.; Hudson, M. R.; Brown, C. M.; Long, J. R.; Neaton, J. B.; Smit, B.; Cramer, C. J.; Truhlar, D. G.; Gagliardi, L. *J. Am. Chem. Soc.* **2014**, *136* (2), 698–704.
- (54) Xiao, D. J.; Gonzalez, M. I.; Darago, L. E.; Vogiatzis, K. D.; Haldoupis, E.; Gagliardi, L.; Long, J. R. *J. Am. Chem. Soc.* **2016**, *138* (22), 7161–7170.
- (55) Anderson, J. S.; Gallagher, A. T.; Mason, J. A.; Harris, T. D. *J. Am. Chem. Soc.* **2014**, *136* (47), 16489–16492.
- (56) Gallagher, A. T.; Malliakas, C. D.; Harris, T. D. *Inorg. Chem.* **2017**, *56* (8), 4654–4661.
- (57) Gallagher, A. T.; Kelty, M. L.; Park, J. G.; Anderson, J. S.; Mason, J. A.; Walsh, J. P. S.; Collins, S. L.; Harris, T. D. *Inorg. Chem. Front.* **2016**, *3* (4), 536–540.
- (58) Siegelman, R. L.; McDonald, T. M.; Gonzalez, M. I.; Martell, J.; Milner, P. J.; Mason, J. A.; Berger, A. H.; Bhowan, A. S.; Long, J. R. *J. Am. Chem. Soc.* **2017**.
- (59) Gonzalez, M. I.; Oktawiec, J.; Long, J. R. *Faraday Discuss.* **2017**.
- (60) Kepert, C. J.; Rosseinsky, M. J. *Chem. Commun.* **1999**, *0* (4), 375–376.
- (61) Schoedel, A.; Yaghi, O. M. In *Macrocyclic and Supramolecular Chemistry How Izatt–Christensen Award Winners Shaped the Field*; Izatt, R. M., Ed.; Macrocyclic and Supramolecular Chemistry: Chichester, UK, 2016; pp 200–219.
- (62) Venkataraman, D.; Gardner, G. B.; Lee, S.; Moore, J. S. *J. Am. Chem. Soc.* **1995**, *117* (46), 11600–11601.
- (63) Yaghi, O. M.; Li, G.; Li, H. *Nature* **1995**, *378* (6558), 703–706.
- (64) Li, H.; Eddaoudi, M.; O’Keeffe, M.; Yaghi, O. M. *Nature* **1999**, *402* (6759), 276–279.
- (65) Furukawa, H.; Ko, N.; Go, Y. B.; Aratani, N.; Choi, S. B.; Choi, E.; Yazaydin, A. O.; Snurr, R. Q.; O’Keeffe, M.; Kim, J.; Yaghi, O. M. *Science* **2010**, *329* (5990), 424–428.

- (66) Vaidhyanathan, R.; Iremonger, S. S.; Shimizu, G. K. H.; Boyd, P. G.; Alavi, S.; Woo, T. *K. Science* **2010**, *330* (6004), 650–653.
- (67) Vaidhyanathan, R.; Iremonger, S. S.; Shimizu, G. K. H.; Boyd, P. G.; Alavi, S.; Woo, T. *K. Science* **2010**, *330* (6004), 650–653.
- (68) Zhou, W.; Wu, H.; Yildirim, T. *J. Am. Chem. Soc.* **2008**, *130* (46), 15268–15269.
- (69) Caskey, S. R.; Wong-Foy, A. G.; Matzger, A. J. *J. Am. Chem. Soc.* **2008**, *130* (33), 10870–10871.
- (70) McDonald, T. M.; Lee, W. R.; Mason, J. A.; Wiers, B. M.; Hong, C. S.; Long, J. R. *J. Am. Chem. Soc.* **2012**, *134* (16), 7056–7065.
- (71) Burgun, A.; Coghlan, C. J.; Huang, D. M.; Chen, W.; Horike, S.; Kitagawa, S.; Alvino, J. F.; Metha, G. F.; Sumbly, C. J.; Doonan, C. J. *Angewandte Chemie* **2017**, *129* (29), 8532–8536.
- (72) Evans, J. D.; Sumbly, C. J.; Doonan, C. J. *Chem. Soc. Rev.* **2014**, *43* (16), 5933–5951.
- (73) Fei, H.; Cohen, S. M. *Chem. Commun.* **2014**, *50* (37), 4810–4812.
- (74) Dau, P. V.; Cohen, S. M. *Chem. Commun. (Camb.)* **2013**, *49* (55), 6128–6130.
- (75) Manna, K.; Zhang, T.; Greene, F. X.; Lin, W. *J. Am. Chem. Soc.* **2015**, *137* (7), 2665–2673.
- (76) Manna, K.; Zhang, T.; Lin, W. *J. Am. Chem. Soc.* **2014**, *136* (18), 6566–6569.
- (77) Zhang, T.; Manna, K.; Lin, W. *J. Am. Chem. Soc.* **2016**, *138* (9), 3241–3249.
- (78) Manna, K.; Zhang, T.; Carboni, M.; Abney, C. W.; Lin, W. *J. Am. Chem. Soc.* **2014**, *136* (38), 13182–13185.
- (79) Hou, Y.-L.; Yee, K.-K.; Wong, Y.-L.; Zha, M.; He, J.; Zeller, M.; Hunter, A. D.; Yang, K.; Xu, Z. *J. Am. Chem. Soc.* **2016**, jacs.6b09763–jacs.6b09764.
- (80) Wang, C.; deKrafft, K. E.; Lin, W. *J. Am. Chem. Soc.* **2012**, *134* (17), 7211–7214.
- (81) Falkowski, J. M.; Sawano, T.; Zhang, T.; Tsun, G.; Chen, Y.; Lockard, J. V.; Lin, W. *J. Am. Chem. Soc.* **2014**, *136* (14), 5213–5216.
- (82) Dau, P. V.; Kim, M.; Cohen, S. M. *Chem. Sci.* **2013**, *4* (2), 601.
- (83) Huxley, M. T.; Coghlan, C. J.; Bloch, W. M.; Burgun, A.; Doonan, C. J.; Sumbly, C. J. *Phil. Trans. R. Soc. A* **2017**, *375* (2084), 20160028–12.



## Chapter 2. Structural Characterization of Framework–Gas Interactions in the Metal–Organic Framework Co<sub>2</sub>(dobdc) by *in situ* Single-Crystal X-ray Diffraction

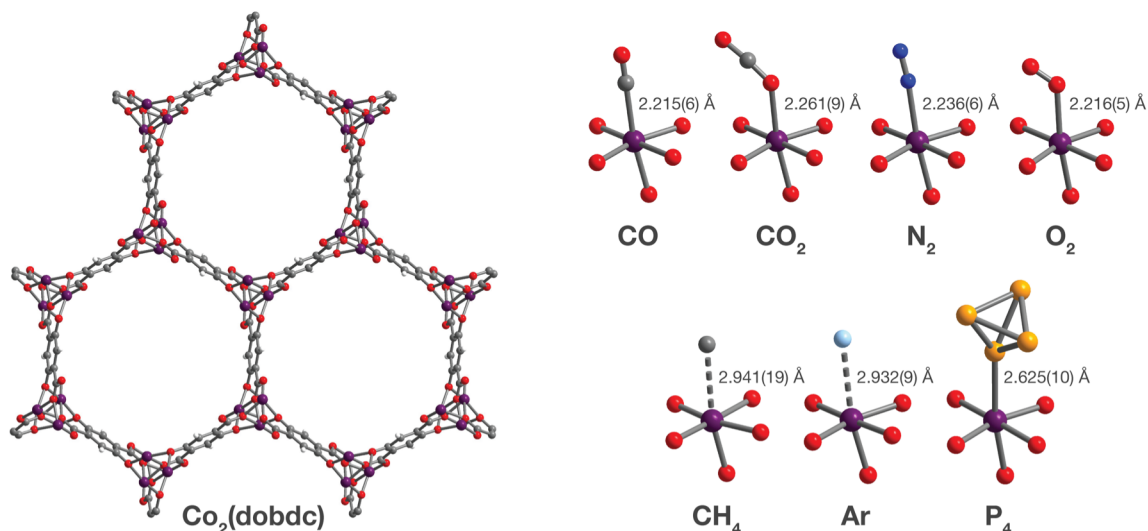
### 2.1. Introduction

*In situ* X-ray diffraction using single crystals as solid-state matrices has emerged as a powerful approach toward the direct observation of molecules and their reactivity.<sup>1-5</sup> The crystal lattice acts to both stabilize and align molecular guests, enabling their isolation and subsequent structural determination by crystallography. Amid many significant advances over the past two decades, these systems have found promising applications in the study of weakly interacting species, such as adsorbed gases,<sup>6-15</sup> which have been traditionally difficult to characterize crystallographically. Considerable work in this area has focused on conducting *in situ* X-ray diffraction experiments to investigate host-guest interactions and guest reactivity in molecular flasks, macromolecular hosts designed to encapsulate molecular guests.<sup>1,3</sup> Recognition that the chemistry of these systems extends to the capture and confinement of gas molecules has led to the characterization of a series of small gases within a molecular cavitand.<sup>15</sup> Recent work has featured single-crystal-to-single-crystal reactions of gas molecules with transition metal complexes. As particularly striking examples, this solid-gas reactivity has been leveraged to follow the exchange of small molecules (N<sub>2</sub>, CO, NH<sub>3</sub>, C<sub>2</sub>H<sub>4</sub>, H<sub>2</sub>, and O<sub>2</sub>) on an iridium pincer complex<sup>12</sup> and to isolate rhodium-alkane  $\sigma$ -complexes through the hydrogenation of their corresponding alkene complexes.<sup>16-18</sup> Although these reports reinforce the growing utility of molecular single-crystal matrices, their general applicability remains limited by the scarcity of structures that retain crystallinity upon binding and reaction of the molecular guests.<sup>2</sup> In addition, the tendency of molecules to pack closely in the crystalline state engenders only small or transient apertures in the crystal. This inability to support larger pore structures severely restricts the size of guests that can be incorporated.<sup>3</sup> The need to develop new crystalline matrices to address these challenges outlines an opportunity for alternative materials to contribute to the advancement of the field.

Metal–organic frameworks are a class of materials composed of inorganic clusters or metal ions connected in three dimensions by organic linkers. These materials exhibit the ability to adopt highly porous crystalline structures with well-defined pore architectures,<sup>19,20</sup> leading to their extensive evaluation for applications in gas storage,<sup>21,22</sup> gas separations,<sup>23,24</sup> and catalysis.<sup>25-28</sup> In contrast to the non-covalent interactions in molecular crystals, the coordinate-covalent bonds linking the inorganic and organic units in metal–organic frameworks give rise to their inherently greater thermal and chemical stability. Consequently, these materials are capable of maintaining porous structures that accommodate the removal, inclusion, exchange, or reaction of a more diverse selection of molecular guests over a wider range of conditions compared to molecular assemblies. In particular, frameworks that exhibit permanent and open porosity are uniquely suited to the study of gaseous species. Furthermore, these materials can be designed to facilitate explicit framework-guest interactions through synthetic control over pore size, shape, and functionality.

Indeed, research on metal–organic frameworks has increasingly relied on *in situ* diffraction experiments to provide critical insight into the contribution of the pore structure to adsorption behavior and reactivity.<sup>29-64</sup> Such studies also complement and validate computational efforts focused on understanding and predicting the properties of these materials.<sup>45,65-68</sup> Despite the greater accessibility, simplicity, and precision associated with single-crystal X-ray diffraction, the majority of work involving gases has been accomplished using powder X-ray and neutron

diffraction methods.<sup>29-52,55,64</sup> This primarily stems from the following challenges: (i) the difficulty in preparing single crystals of sufficient size and quality to be suitable for diffraction experiments, (ii) the tendency of some crystals to fracture under the evacuation or gas-dosing conditions, and (iii) the exceptionally high sensitivity to contaminants inherent to the small sample sizes used in single-crystal measurements (~500 ng for a typical 200- $\mu\text{m}$  wide single crystal). The third challenge is especially problematic in studying frameworks bearing metals with open coordination sites, due to the propensity of these sites to bind water over more weakly coordinating species. Nevertheless, several studies have proven to be successful in employing single-crystal X-ray diffraction experiments to observe framework-gas interactions.<sup>53,55,56,60-63,69</sup>



**Figure 2.1.** Structures determined by single-crystal X-ray diffraction. (Left) A portion of the crystal structure of Co<sub>2</sub>(dobdc) (dobdc<sup>4-</sup> = 2,5-dioxido-1,4-benzenedicarboxylate) at 296 K viewed along the *c* axis. (Right) First coordination spheres for Co<sup>II</sup> in the structures of CO, CO<sub>2</sub>,<sup>55</sup> N<sub>2</sub>, O<sub>2</sub>, CH<sub>4</sub>, Ar, and P<sub>4</sub> in Co<sub>2</sub>(dobdc) (at 150 K for CO<sub>2</sub>; at 100 K for N<sub>2</sub>, O<sub>2</sub>, CH<sub>4</sub>, and P<sub>4</sub>; at 90 K for CO and Ar); Purple, red, gray, blue, light blue, light orange, and white spheres represent Co, O, C, N, Ar, P, and H atoms, respectively. Note that the O<sub>2</sub> molecules bound to the Co<sup>II</sup> sites in Co<sub>2</sub>(dobdc)·5.9O<sub>2</sub> were found to be disordered over two orientations with relative occupancies of 73(3)% and 27(3)% (Figure 2.S8), but only one of these orientations (73(3)% occupancy) is shown for clarity. The structure of Co<sub>2</sub>(dobdc)·2.9CO<sub>2</sub> has been reported previously<sup>55</sup> and is shown here to facilitate comparisons.

The M<sub>2</sub>(dobdc) series of metal-organic frameworks (M = Mg<sup>II</sup>, Mn<sup>II</sup>, Fe<sup>II</sup>, Co<sup>II</sup>, Ni<sup>II</sup>, Cu<sup>II</sup>, Zn<sup>II</sup>, and Cd<sup>II</sup>; dobdc<sup>4-</sup> = 2,5-dioxido-1,4-benzenedicarboxylate; also referred to as M-MOF-74 or CPO-27(M)) have been intensely studied due to their high density of exposed metal(II) sites, which can interact favorably with guest molecules.<sup>29-46,54,55,70,71</sup> Much of the work evaluating the adsorption properties and reactivity of these materials has depended on powder X-ray or neutron diffraction for *in situ* characterization of gas binding.<sup>30-46,55</sup> Comparatively few studies have been performed using single-crystal X-ray diffraction<sup>54,55</sup> due to the intrinsic difficulty that accompanies *in situ* gas-dosing experiments on materials with open coordination sites and because only Co<sub>2</sub>(dobdc) and Zn<sub>2</sub>(dobdc) readily form single crystals. This work seeks to expand on these studies through techniques developed to dose gases into single crystals under rigorously air-free conditions. Herein, we report the direct structural characterization of CO, CH<sub>4</sub>, N<sub>2</sub>, O<sub>2</sub>, Ar, and P<sub>4</sub> adsorption in single crystals of Co<sub>2</sub>(dobdc) (Figure 2.1). The resulting structures confirm that each gas binds first to the exposed cobalt(II) sites and allow the identification of

secondary (for N<sub>2</sub>, O<sub>2</sub>, and Ar) and tertiary (for O<sub>2</sub>) binding sites within the framework. Remarkably, further inspection of Co<sup>II</sup>–gas distances reveals that binding occurs primarily through weak covalent (for CO) or non-covalent (for CH<sub>4</sub>, N<sub>2</sub>, O<sub>2</sub>, and Ar) interactions, which have never been observed by single-crystal X-ray diffraction. Finally, a combination of low- and high-pressure gas adsorption isotherms are used to evaluate the relationship between structure and adsorption behavior.

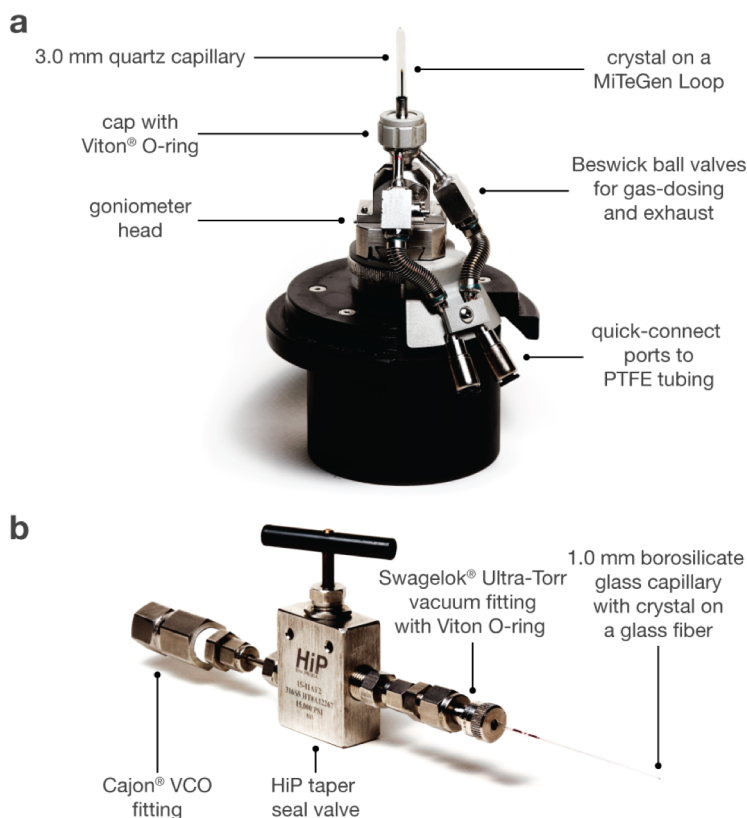
## 2.2. Experimental

### 2.2.1. Materials and Methods

*N,N*-dimethylformamide (DMF), ethanol, and methanol were obtained from commercial sources and used without further purification. Hexanes was deoxygenated by purging with Ar for 1 h and dried using a commercial solvent purification system designed by JC Meyer Solvent Systems. The compounds Co(NO<sub>3</sub>)<sub>2</sub>·6H<sub>2</sub>O and 2,5-dihydroxy-1,4-benzenedicarboxylic acid (H<sub>4</sub>dobdc) were purchased from Sigma-Aldrich and used as received. White phosphorus (P<sub>4</sub>) was prepared by heating red phosphorus under vacuum (~80 μbar) in a flame-sealed borosilicate glass tube over a Bunsen burner flame. The crude white phosphorus was then purified by recrystallization from hexanes. **Caution:** *white phosphorus is highly toxic and reacts violently with O<sub>2</sub> in air.* Single crystals of Co<sub>2</sub>(dobdc) were synthesized using a slight modification to a previously published procedure.<sup>71</sup> Briefly, a 100 mL Pyrex jar was charged with H<sub>4</sub>dobdc (198 mg, 1.00 mmol), Co(NO<sub>3</sub>)<sub>2</sub>·6H<sub>2</sub>O (970 mg, 3.34 mmol), and a 1:1:1 (v/v/v) mixture of DMF/ethanol/water (80 mL), and was then sealed with a Teflon cap. The resulting mixture was sonicated until all reactants were fully dissolved to form a violet solution. The reaction mixture was then placed in an oven that was preheated to 100 °C and kept at this temperature for 24 h, yielding violet needle-shaped single crystals. The crystals were soaked three times in 80 mL of DMF for 24 h at 120 °C, followed by soaking three times in 80 mL of methanol at 60 °C. The crystals were then stored in methanol in a 20 mL PTFE-capped vial prior to use for single-crystal X-ray diffraction experiments or gas-adsorption measurements. The Langmuir surface area of the sample used for gas adsorption measurements was determined to be 1400 ± 2 m<sup>2</sup>/g.

### 2.2.2. Single-Crystal X-ray Diffraction

**Gas dosing in the gas cell.** For Co<sub>2</sub>(dobdc), Co<sub>2</sub>(dobdc)·0.58CO, Co<sub>2</sub>(dobdc)·2.0CH<sub>4</sub>, and Co<sub>2</sub>(dobdc)·2.0Ar, a methanol-solvated crystal of Co<sub>2</sub>(dobdc) was mounted on a MiTeGen loop using a minimal amount of epoxy to ensure that the crystal pores remained accessible. The sample was then placed in a custom-made gas cell equipped with a quartz capillary, an O-ring seal, and Beswick ball valves for gas-dosing (Figure 2.2a). The cell was connected to a gas-dosing manifold using PTFE tubing, and was then evacuated under reduced pressure using a turbomolecular pump at an external temperature of 180 °C for 4–5 h to remove solvent molecules that fill the pores and coordinate to the exposed Co sites within the crystal. After obtaining the structure to confirm that the crystal was fully desolvated, the crystal was cooled to 25 °C and then dosed with the desired gas at a specified pressure (1.00 bar for CO and CH<sub>4</sub>; 1.14 bar for Ar).



**Figure 2.2.** (a) Diagram of the gas cell, which was designed and built at Advanced Light Source Beamline 11.3.1. (b) Diagram of a capillary-dosing assembly.

**Gas dosing in capillaries.** For  $\text{Co}_2(\text{dobdc})\cdot 5.9\text{O}_2$  and  $\text{Co}_2(\text{dobdc})\cdot 3.8\text{N}_2$ , methanol-solvated crystals of  $\text{Co}_2(\text{dobdc})$  were mounted on a borosilicate glass fiber using a minimal amount of epoxy, ensuring that the crystal pores remained accessible. The glass fiber was then inserted into a 1.0-mm borosilicate glass capillary, which was connected to a HiP Taper Seal valve using a Swagelok® Ultra-Torr vacuum fitting with a Viton® O-ring (Figure 2.2b). The capillary-dosing assembly was then attached to a port on a Micromeritics ASAP 2020 instrument using a Cajon® VCO fitting. The capillary was evacuated under reduced pressure at 180 °C for 24 h to remove solvent molecules that fill the pores and coordinate to the exposed Co sites within the crystal. The capillary was dosed with a specific gas at a specified pressure (0.8 bar for  $\text{N}_2$ ; 0.5 bar for  $\text{O}_2$ ), and was then flame-sealed with a methane/oxygen torch.

**Vapor dosing of  $\text{P}_4$ .** For  $\text{Co}_2(\text{dobdc})\cdot 1.3\text{P}_4$ , methanol-solvated  $\text{Co}_2(\text{dobdc})$  crystals (~20 mg) were desolvated in a glass tube under reduced pressure at 180 °C on a Micromeritics ASAP 2020 instrument. In an  $\text{N}_2$ -filled VAC Atmospheres glovebox, the desolvated crystals were transferred into a 4 mL vial, which was then placed in a 20 mL vial containing excess white phosphorus. **Caution:** white phosphorus is highly toxic and reacts violently with  $\text{O}_2$  in air. The 20 mL vial was sealed with a PTFE-lined cap then heated for 24 h at 80 °C. The  $\text{P}_4$ -dosed crystals were then coated with Paratone-N oil prior to use for single-crystal X-ray diffraction experiments.

**Data collection and refinement.** X-ray diffraction data for all samples were collected at Beamline 11.3.1 at the Advanced Light Source, Lawrence Berkeley National Laboratory using synchrotron radiation ( $\lambda = 0.7749 \text{ \AA}$  for  $\text{Co}_2(\text{dobdc})$ ,  $\text{Co}_2(\text{dobdc})\cdot 0.58\text{CO}$ ,  $\text{Co}_2(\text{dobdc})\cdot 1.19\text{CO}$ ,

Co<sub>2</sub>(dobdc)·2.0CH<sub>4</sub>, Co<sub>2</sub>(dobdc)·5.9O<sub>2</sub>, and Co<sub>2</sub>(dobdc)·1.3P<sub>4</sub>;  $\lambda = 0.6525 \text{ \AA}$  for Co<sub>2</sub>(dobdc)·2.0Ar;  $\lambda = 0.6199 \text{ \AA}$  for Co<sub>2</sub>(dobdc)·3.8N<sub>2</sub>) with either a Bruker AXS APEX II CCD detector (Co<sub>2</sub>(dobdc), Co<sub>2</sub>(dobdc)·0.58CO, Co<sub>2</sub>(dobdc)·1.2CO, Co<sub>2</sub>(dobdc)·2.0CH<sub>4</sub>, Co<sub>2</sub>(dobdc)·3.8N<sub>2</sub>, and Co<sub>2</sub>(dobdc)·2.0Ar) or a Bruker PHOTON100 CMOS detector (Co<sub>2</sub>(dobdc)·5.9O<sub>2</sub> and Co<sub>2</sub>(dobdc)·1.3P<sub>4</sub>) on a D8 diffractometer. The samples were cooled to a specified temperature (296 K for Co<sub>2</sub>(dobdc); 100 K for Co<sub>2</sub>(dobdc)·1.2CO, Co<sub>2</sub>(dobdc)·2.0CH<sub>4</sub>, Co<sub>2</sub>(dobdc)·3.8N<sub>2</sub>, Co<sub>2</sub>(dobdc)·5.9O<sub>2</sub>, and Co<sub>2</sub>(dobdc)·1.3P<sub>4</sub>; 90 K for Co<sub>2</sub>(dobdc)·0.58CO and Co<sub>2</sub>(dobdc)·2.0Ar) using an Oxford Cryosystems cryostream for data collection.

All crystals were found to be obverse/reverse twins based on analysis of their diffraction patterns. For each structure, CELL\_NOW<sup>72</sup> was used to determine the orientation matrices. Raw data for both twin matrices were integrated and corrected for Lorentz and polarization effects using Bruker AXS SAINT<sup>73</sup> software and corrected for absorption using TWINABS.<sup>74</sup> TWINABS was used to produce a merged HKLF4 file for structure solution and initial refinement and an HKLF5 file for final structure refinement. The structures were solved using direct methods with SHELXS<sup>75,76</sup> and refined using SHELXL<sup>75,77</sup> operated in the OLEX2 interface.<sup>78</sup> Thermal parameters were refined anisotropically for all non-hydrogen atoms. Disorder and thermal motion of the bound gas molecules required the use of displacement parameter (for Co<sub>2</sub>(dobdc)·1.2CO, Co<sub>2</sub>(dobdc)·5.9O<sub>2</sub>, Co<sub>2</sub>(dobdc)·3.8N<sub>2</sub>, Co<sub>2</sub>(dobdc)·2.0Ar, and Co<sub>2</sub>(dobdc)·1.3P<sub>4</sub>) and distance (for Co<sub>2</sub>(dobdc)·5.9O<sub>2</sub>, Co<sub>2</sub>(dobdc)·3.8N<sub>2</sub>, and Co<sub>2</sub>(dobdc)·1.3P<sub>4</sub>) restraints. All hydrogen atoms were refined using the riding model.

### 2.2.3. Gas Adsorption

**Low-pressure gas adsorption measurements.** Pure-component gas adsorption isotherms for pressures in the range 0–1.2 bar were measured by a volumetric method using Micromeritics ASAP2020 and ASAP2420 instruments. UHP-grade gases (99.999% purity He, Ar, N<sub>2</sub>, CO, CO<sub>2</sub>, and CH<sub>4</sub>; 99.998% purity CO<sub>2</sub>; 99.993% purity O<sub>2</sub>) were used for all measurements. A typical sample of 30–100 mg of Co<sub>2</sub>(dobdc) was transferred to a pre-weighed analysis tube, which was capped with a Micromeritics TranSeal and evacuated by heating at either 180 °C, reached by ramping at a rate of 1 °C/min, under dynamic vacuum until an outgas rate of less than 3  $\mu$ bar/min was achieved. The evacuated analysis tube containing the degassed sample was then carefully transferred to an electronic balance and weighed again to determine the mass of sample. The tube was then transferred back to the analysis port of the gas adsorption instrument. The outgas rate was again confirmed to be less than 3  $\mu$ bar/min. For all isotherms, warm and cold free space correction measurements were performed using ultra-high purity He gas. Nitrogen gas adsorption isotherms at 77 K were measured in liquid nitrogen using UHP-grade gas sources. Oil-free vacuum pumps and oil-free pressure regulators were used for all measurements to prevent contamination of the samples during the evacuation process or of the feed gases during the isotherm measurements. Langmuir surface areas were determined from N<sub>2</sub> adsorption data at 77 K using Micromeritics software, assuming a value of 16.2  $\text{\AA}^2$  for the molecular cross-sectional area of N<sub>2</sub>. Adsorption isotherms between 293 and 323 K were measured using a recirculating dewar connected to a Julabo F32-MC isothermal bath.

**High-pressure gas adsorption measurements.** High-pressure gas adsorption isotherms in the range of 0–100 bar were measured on an HPVA-II-100 from Particulate Systems, a Micromeritics company. In a typical measurement, 0.5–1.0 g of activated sample was loaded into a tared stainless steel sample holder inside a glovebox under a N<sub>2</sub> atmosphere. Prior to connecting the sample holder to the VCR fitting of the complete high-pressure assembly inside

the glovebox, the sample holder was weighed to determine the sample mass. The sample holder was then transferred to the HPVA-II-100 instrument, connected to the instrument's analysis port via an OCR fitting, and evacuated at room temperature for at least 2 h. The sample holder was placed inside an aluminum recirculating Dewar connected to a Julabo FP89-HL isothermal bath filled with Julabo Thermal C2 fluid. The temperature stability of the isothermal bath is  $\pm 0.02$  °C. Methods for accurately measuring the relevant sample free space, which involve the expansion of He from a calibrated volume at 0.7 bar and 25 °C to the evacuated sample holder, have been described in detail previously.<sup>22</sup> Non-ideality corrections were performed using the compressibility factors tabulated in the NIST REFPROP database<sup>79,80</sup> at each measured temperature and pressure.

**Adsorption isotherm fitting.** Low-pressure Ar, N<sub>2</sub>, and O<sub>2</sub> isotherms at 298, 308, and 318 K were fit with a single-site Langmuir equation, while low-pressure CH<sub>4</sub> isotherms at 293, 298, 303, 313, and 323 K were fit using a dual-site Langmuir equation (eq 1), where  $n$  is the total amount adsorbed in mmol/g,  $P$  is the pressure in bar,  $n_{\text{sat},i}$  is the saturation capacity in mmol/g, and  $b_i$  is the Langmuir parameter in bar<sup>-1</sup>.

$$n = \frac{n_{\text{sat},1}b_1P}{1+b_1P} + \frac{n_{\text{sat},2}b_2P}{1+b_2P} \quad (1)$$

$$b_i = e^{-S_i/R} e^{E_i \cdot 1000/RT} \quad (2)$$

The Langmuir parameter can be expressed using eq 2, where  $S_i$  is the site-specific integral entropy of adsorption in J/mol·K;  $E_i$  is the site-specific differential enthalpy of adsorption in kJ/mol,  $R$  is the gas constant in J/mol·K, and  $T$  is the temperature in K. For all gases, isotherms were fit both independently for each temperature (Figures S11, S13, S15, and S17) and simultaneously for all temperatures (Figures S12, S14, S16, and S18).

**Differential enthalpy of adsorption calculations.** Using the Langmuir fits, the differential enthalpy of adsorption,  $\Delta h_{\text{ad}}$ , can be calculated as a function of the total amount of gas adsorbed,  $n$ , by using the Clausius-Clapeyron equation (eq 3), where  $R$  is the gas constant in J/mol·K,  $T$  is the temperature in K,  $n$  is the total amount adsorbed in mmol/g, and  $P$  is the pressure in bar.

$$\Delta h_{\text{ad}} = -RT^2 \left( \frac{\partial \ln P}{\partial T} \right)_n \quad (3)$$

The Langmuir fits for each gas (fit independently for each temperature) were used to obtain the exact pressures that correspond to specific loadings at different temperatures (298, 308, and 318 K for N<sub>2</sub>, O<sub>2</sub>, and Ar; 293, 298, 303, 313, and 323 K for CH<sub>4</sub>). This was done at loading intervals of 0.05 mmol/g. At each loading, the slope of the best-fit line to  $\ln(P)$  versus  $1/T$  was calculated to obtain the differential enthalpies.

## 2.3. Results and Discussion

### 2.3.4. Structural Characterization

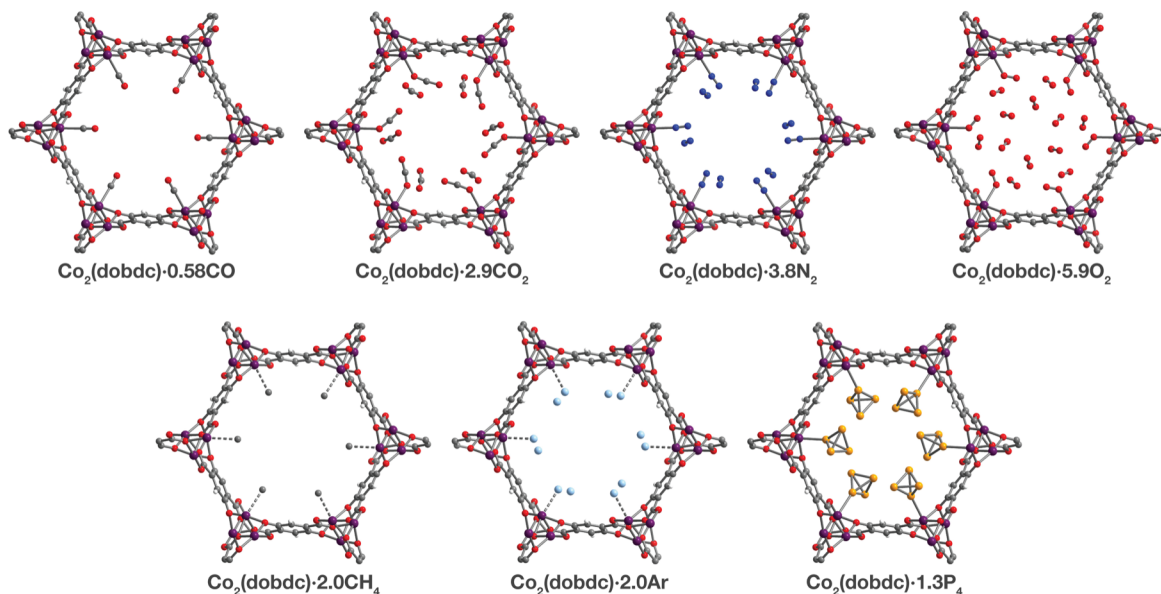
Two methods were developed for dosing gases into single crystals. The first involves using an environmental gas cell (Figure 2.2a), which was designed and built at ALS beamline 11.3.1. Similar to other gas cells that have recently been developed,<sup>81,82</sup> the cell allows the collection of single-crystal X-ray diffraction data on samples under vacuum or dosed with a desired gas. With

this method, the structure of the framework can be monitored throughout the evacuation and gas dosing of the crystal. This capability affords appreciable flexibility, as the temperature, gas pressure, and time can be changed at each stage of the experiment in response to structural data. As a result, the gas cell is especially useful for studying unfamiliar samples that still require experimental conditions to be optimized. Alternatively, a single crystal can be inserted into a borosilicate capillary, which is then heated under vacuum and subsequently dosed using a manifold or gas adsorption analyzer. The capillary is then flame-sealed with the crystal kept under a specified pressure of gas that is lower than 1 bar. Unlike the gas cell, using capillaries requires the evacuation time and temperature and the gas-dosing pressure to be determined prior to data collection. Although less versatile, the capillary method benefits from higher sample throughput compared to the gas cell because diffraction experiments are only conducted on gas-dosed samples. Consequently, this method can be preferable for samples that have established activation parameters and gas adsorption properties.

The metal–organic framework  $\text{Co}_2(\text{dobdc})$  crystallizes in the space group  $R\bar{3}$ , in which the special positions are exclusively situated along the one-dimensional helical chains of Co atoms, at the center of the organic linkers, and through the center of the hexagonal pores. This makes the framework particularly amenable to the crystallographic characterization of guest species as no crystallographic symmetry is enforced on sites above and within the vicinity of the coordinatively unsaturated cobalt(II) centers. This is evident in the exceptionally ordered structures of gases within  $\text{Co}_2(\text{dobdc})$  even in cases where the interactions are weak, as described previously<sup>32,39,54,55,68</sup> and discussed below.

Inspection of the structures of  $\text{Co}_2(\text{dobdc})\cdot 1.2\text{CO}$ ,  $\text{Co}_2(\text{dobdc})\cdot 0.58\text{CO}$ , and  $\text{Co}_2(\text{dobdc})\cdot 2.0\text{CH}_4$  (Figure 2.3), where only a single adsorption site is populated, shows that CO and  $\text{CH}_4$  first bind to the open coordination site of cobalt(II), confirming that this site has the greatest contribution to the adsorption of these gases in the material. Multiple adsorption sites could be located in the structures of  $\text{Co}_2(\text{dobdc})\cdot 3.8\text{N}_2$ ,  $\text{Co}_2(\text{dobdc})\cdot 5.9\text{O}_2$ ,  $\text{Co}_2(\text{dobdc})\cdot 2.0\text{Ar}$ , and  $\text{Co}_2(\text{dobdc})\cdot 1.3\text{P}_4$  (Figure 2.3), which complicates the determination of the primary adsorption sites. Comparison of relative site occupancies, displacement parameters, and framework-guest distances, however, indicates that  $\text{N}_2$ ,  $\text{O}_2$ , Ar, and  $\text{P}_4$  also bind primarily to the cobalt(II) sites. Remarkably, the secondary binding sites for  $\text{N}_2$ ,  $\text{O}_2$ , and Ar were found to have nearly identical locations (Figures 2.S1 and 2.S2), close to the non-bridging carboxylate and phenoxide oxygen atoms of  $\text{dobdc}^{4-}$ . Previous reports also identify the same secondary binding site in structures of  $\text{CO}_2$ <sup>55</sup> (Figure 2.3) and  $\text{H}_2\text{O}$ <sup>68</sup> in  $\text{Co}_2(\text{dobdc})$  (Figures 2.S1 and 2.S2). The similarity of these binding pockets likely arises from a slightly polarizing environment generated by the partial negative charges on surrounding linker oxygen atoms. In other metal–organic frameworks, the linker carboxylate oxygen atoms have been shown to facilitate similar weak interactions with gases.<sup>51,53</sup>

The structures of  $\text{Co}_2(\text{dobdc})\cdot 1.2\text{CO}$  at 100 K and  $\text{Co}_2(\text{dobdc})\cdot 0.58\text{CO}$  at 90 K (Figure 2.3) were obtained under 1.00 bar of CO in the gas cell. In these structures, CO loading was found to be lower than one per cobalt(II) site, which likely results from slow diffusion of CO as the crystals were rapidly cooled after CO dosing. Nevertheless, both structures display Co–C<sub>CO</sub> distances of 2.215(6) Å (Figure 2.1) and similar Co–C–O angles (175.7(12)° for  $\text{Co}_2(\text{dobdc})\cdot 1.2\text{CO}$  and 178.0(11)° for  $\text{Co}_2(\text{dobdc})\cdot 0.58\text{CO}$ ). These distances and angles are comparable to those previously obtained from powder neutron diffraction at 10 K, Co–C<sub>CO</sub> distance = 2.18(2) Å and Co–C–O angle = 171(2)°.<sup>39</sup> The long Co–C<sub>CO</sub> distance and deviation of the Co–C–O angle from 180° are both consistent with a weak interaction between cobalt(II) and



**Figure 2.3.** A portion of the crystal structures of  $\text{Co}_2(\text{dobdc})\cdot 0.58\text{CO}$  at 90 K,  $\text{Co}_2(\text{dobdc})\cdot 2.9\text{CO}_2$  at 150 K,<sup>55</sup>  $\text{Co}_2(\text{dobdc})\cdot 5.9\text{O}_2$  at 100 K,  $\text{Co}_2(\text{dobdc})\cdot 3.8\text{N}_2$  at 100 K,  $\text{Co}_2(\text{dobdc})\cdot 2.0\text{CH}_4$  at 100 K,  $\text{Co}_2(\text{dobdc})\cdot 2.0\text{Ar}$ , and  $\text{Co}_2(\text{dobdc})\cdot 1.3\text{P}_4$  at 100 K viewed along the  $c$  axis, as determined by single-crystal X-ray diffraction; purple, red, gray, blue, light blue, light orange, and white spheres represent Co, O, C, N, Ar, P, and H atoms, respectively. Note that the  $\text{O}_2$  molecules bound to the  $\text{Co}^{\text{II}}$  sites in  $\text{Co}_2(\text{dobdc})\cdot 5.9\text{O}_2$  were found to be disordered over two orientations with relative occupancies of 73(3)% and 27(3)% (Figure 2.S8), but only one of these orientations (73(3)% occupancy) is shown for clarity. In the structure of  $\text{Co}_2(\text{dobdc})\cdot 1.3\text{P}_4$ , the  $\text{P}_4$  molecules were found in two positions (Figure 2.S10), one with  $\text{P}_4$  molecules coordinated to the  $\text{Co}^{\text{II}}$  sites (45.5(10)% occupancy) and another 3.88(3) Å away from the  $\text{Co}^{\text{II}}$  sites centers (20.6(10)% occupancy), but only the coordinated  $\text{P}_4$  molecules are shown for clarity. The structure of  $\text{Co}_2(\text{dobdc})\cdot 2.9\text{CO}_2$  has been reported previously<sup>55</sup> and is shown here to facilitate comparisons.

CO with limited  $\text{Co}^{\text{II}}\text{--CO}$   $\pi$  backbonding. This is further supported by larger CO oxygen displacement parameters compared to carbon, which suggests that the bound CO is free to bend out of the axis along the  $\text{Co}^{\text{II}}\text{--CO}$  bond. Surveying the Cambridge Crystal Structure Database (CCSD),<sup>83</sup> single-crystal structures of cobalt carbonyl complexes with  $\text{Co}\text{--C}_{\text{CO}}$  distances longer than 2.0 Å are unprecedented. Examples of cobalt(II)–carbonyl complexes are exceedingly rare and all exhibit a low-spin configuration with  $\text{Co}\text{--C}_{\text{CO}}$  bond distances around 1.8 Å, which are typical to strong  $\text{Co}\text{--CO}$  bonds.<sup>84</sup> The weak-field  $\text{dobdc}^{4-}$  ligands in  $\text{Co}_2(\text{dobdc})$  impose a high-spin configuration for cobalt(II), which is maintained after binding CO.<sup>39</sup> Population of the antibonding cobalt(II) orbitals makes the  $\text{Co}\text{--CO}$   $\sigma$  interaction less favorable, lengthening the  $\text{Co}\text{--C}_{\text{CO}}$  distance. This diminishes  $\text{Co}^{\text{II}}\text{--CO}$   $\pi$  back-donation by preventing overlap between the Co  $3d$  and CO  $\pi^*$  orbitals. Together, these interdependent effects manifest in the exceptionally weak and fully reversible  $\text{M}\text{--CO}$  interaction in  $\text{Co}_2(\text{dobdc})$ , which has been shown to be a major advantage of  $\text{Co}_2(\text{dobdc})$  and its  $\text{Mg}^{\text{II}}$ ,  $\text{Mn}^{\text{II}}$ ,  $\text{Fe}^{\text{II}}$ ,  $\text{Ni}^{\text{II}}$ , and  $\text{Zn}^{\text{II}}$  analogs as prospective materials for industrial CO separations.<sup>39</sup>

X-ray analysis of a single crystal of  $\text{Co}_2(\text{dobdc})$  under 0.8 bar  $\text{N}_2$  at 100 K resulted in the structure of  $\text{Co}_2(\text{dobdc})\cdot 3.8\text{N}_2$  (Figure 2.3). The structure shows that  $\text{N}_2$  binds to cobalt(II) through an end-on interaction with a  $\text{Co}\text{--N}_{\text{N}_2}$  distance of 2.236(6) Å (Figure 2.1). This distance is comparable with the  $\text{Fe}\text{--N}_{\text{N}_2}$  distance of 2.30(1) Å obtained from the powder neutron



diffraction structure of N<sub>2</sub> in Fe<sub>2</sub>(dobdc).<sup>34</sup> Deviation of the Co–N–N angle (170.2(9)°) from 180° also suggests minimal  $\pi$  back-donation from Co<sup>II</sup> to N<sub>2</sub>. Of the cobalt dinitrogen complexes reported in the CCSD,<sup>83</sup> none have Co–N<sub>N2</sub> distances greater than 2.0 Å and only one of these features cobalt in its +2 oxidation state.<sup>85</sup> The long Co–N<sub>N2</sub> distance in Co<sub>2</sub>(dobdc)·3.8N<sub>2</sub> indicates a much weaker interaction between N<sub>2</sub> and the high-spin cobalt(II) centers in Co<sub>2</sub>(dobdc) compared to the Co–N<sub>2</sub> bonds formed in typical cobalt dinitrogen complexes.<sup>86–88</sup> The Co–N<sub>2</sub> bonds in these complexes are strengthened by significant Co–N<sub>2</sub>  $\pi$  back-donation, whereas N<sub>2</sub> can be thought to interact mainly through  $\sigma$  donation to cobalt(II) in Co<sub>2</sub>(dobdc). The secondary N<sub>2</sub> binding sites in Co<sub>2</sub>(dobdc)·3.8N<sub>2</sub> (Figure 2.3 and Figure 2.S1) display van der Waals interactions between N<sub>2</sub> and the oxygen atoms of dobdc<sup>4-</sup>, with N···O contacts ranging from 3.44(2) to 3.771(2) Å (Figure 2.S2). These sites are nearly identical to those located in the powder neutron diffraction structure of N<sub>2</sub> in Fe<sub>2</sub>(dobdc).<sup>34</sup> Full population of both binding sites to give four N<sub>2</sub> molecules adsorbed per formula unit in Co<sub>2</sub>(dobdc) corresponds surprisingly well to the estimated number of N<sub>2</sub> molecules adsorbed as a monolayer in the framework, which is ~4.3 based on a Brunauer–Emmett–Teller (BET) fit to 77 K N<sub>2</sub> adsorption isotherm data.<sup>55</sup>

To determine the structure of O<sub>2</sub> in Co<sub>2</sub>(dobdc), data was collected on a single crystal dosed with 0.5 bar of O<sub>2</sub> in a sealed capillary at 100 K. In the structure of Co<sub>2</sub>(dobdc)·5.9O<sub>2</sub> (Figure 2.3), O<sub>2</sub> is found to bind end-on with a Co–O<sub>O2</sub> distance of 2.216(5) Å (Figure 2.1). Disorder of the O<sub>2</sub> molecule results in two bent orientations with Co–O–O angles of 127.3(10)° and 128(3)° and relative occupancies of 73(3)% and 27(3)%, respectively (Figure 2.S8). The Co–O<sub>O2</sub> distance in Co<sub>2</sub>(dobdc)·5.9O<sub>2</sub> is unusually long. Structures of cobalt dioxygen complexes in the CCSD<sup>83</sup> and recently reported dioxygen adducts formed in other cobalt metal–organic frameworks,<sup>60,62</sup> all show Co–O<sub>O2</sub> distances that fall below 2.0 Å. This again suggests significant disparity between the Co–O<sub>2</sub> interaction in Co<sub>2</sub>(dobdc) and those in molecular cobalt complexes, where O<sub>2</sub> binding is characterized by electron transfer from one or two cobalt(II) centers to form superoxo or peroxo complexes, respectively.<sup>89,90</sup> In addition to the long Co–O<sub>O2</sub> distance, no significant difference in the average Co–O distances is apparent between cobalt(II) and dobdc<sup>4-</sup> in Co<sub>2</sub>(dobdc) (2.035(5) Å) and in Co<sub>2</sub>(dobdc)·5.9O<sub>2</sub> (2.036(5) Å). This further implies that partial oxidation of cobalt(II) does not occur upon O<sub>2</sub> binding, which is in contrast to partial oxidation of the iron(II) centers in Fe<sub>2</sub>(dobdc) to form either iron-superoxo species at 211 K or iron-peroxo species at 298 K.<sup>34</sup> Like in Co<sub>2</sub>(dobdc)·3.8N<sub>2</sub>, the secondary binding sites in Co<sub>2</sub>(dobdc)·5.9O<sub>2</sub> feature O<sub>2</sub> interacting with the dobdc<sup>4-</sup> oxygen atoms, with O···O contacts that range from 3.391(17) Å to 3.88(2) Å. Remarkably, tertiary binding sites for O<sub>2</sub> can also be identified in the structure, where O<sub>2</sub> interacts only with other O<sub>2</sub> molecules adsorbed on the primary and secondary sites. Similar sites were also observed by powder neutron diffraction in the structure of O<sub>2</sub> in Fe<sub>2</sub>(dobdc).<sup>34</sup> Experimental observation of these sites is particularly helpful to computational efforts focused on understanding the contribution of gas–gas interactions to adsorption in metal–organic frameworks and other porous materials.<sup>45,65,68,91,92</sup>

The structure of Co<sub>2</sub>(dobdc)·2.0CH<sub>4</sub> (Figure 2.3) was obtained by cooling a single crystal of Co<sub>2</sub>(dobdc) under 1 bar of CH<sub>4</sub> to 100 K in the gas cell. Although methane hydrogen atoms could not be located in the structure due to disorder and the difficulty in locating hydrogen atoms by X-ray diffraction, electron density corresponding to a methane carbon atom could be distinctly resolved above the framework cobalt sites with a Co<sup>II</sup>···C<sub>CH4</sub> distance of 2.941(19) Å (Figure 2.1). Significantly, this is the first M–CH<sub>4</sub> interaction that has been characterized by single-crystal X-ray diffraction. The Co···C<sub>CH4</sub> distance is comparable to distances characterized for metal–methane interactions in other metal–organic frameworks, which are generally close to

3 Å. The most relevant of these are from structures determined by powder neutron diffraction for CD<sub>4</sub> in Fe<sub>2</sub>(dobdc) (Fe···C<sub>CD4</sub> distance of 2.98(1) Å)<sup>66</sup> and in Mg<sub>2</sub>(dobdc) (Mg···C<sub>CD4</sub> distance of 3.04 Å).<sup>93</sup> The long M···C<sub>CH4</sub> distances in all of these structures are indicative of weak non-covalent interactions that stem from polarization of CH<sub>4</sub> by the partial positive charge on the metal center. These distances contrast with the relatively short M···C distances (around 2.4–2.5 Å) in alkane  $\sigma$ -complexes, which involve donation from the alkane C–H  $\sigma$  bond to the metal center.<sup>16–18</sup> Although the Co<sup>II</sup>–CH<sub>4</sub> interaction in Co<sub>2</sub>(dobdc) and analogous noncovalent M–CH<sub>4</sub> interactions should clearly be distinguished from the bonds formed in true metal–alkane  $\sigma$ -complexes, characterization of such weak M–CH<sub>4</sub> interactions has become increasingly important in the evaluation of materials for natural gas storage.<sup>22</sup>

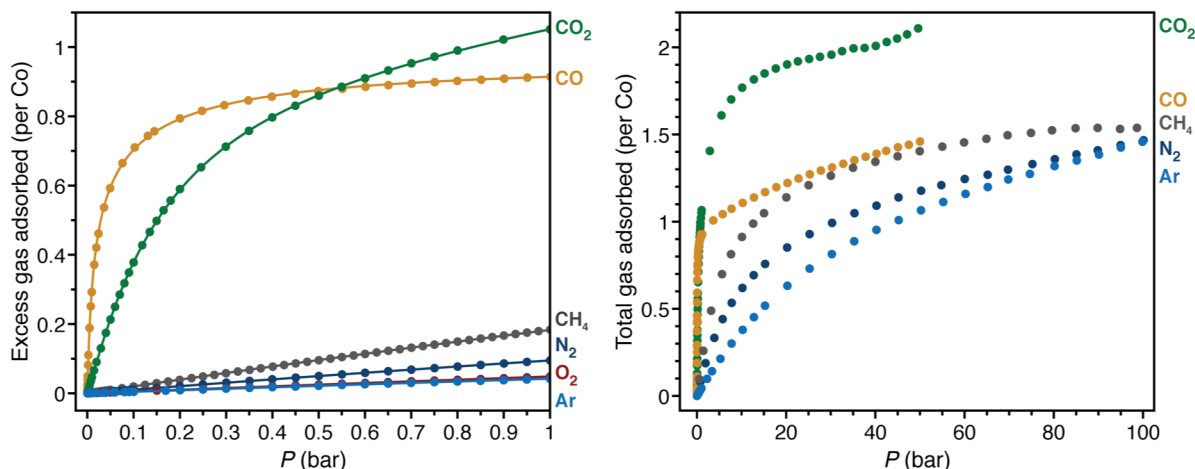
The inherent chemical stability of the noble gases has been thoroughly exploited for maintaining an inert environment for highly reactive species. As a result of this stability, isolation of molecular metal–noble gas species is exceedingly difficult. While no molecular metal–noble gas species other than metal–Xe<sup>94,95</sup> have been characterized crystallographically, computational methods and experimental techniques such as photodissociation spectroscopy and mass spectrometry have been employed to study these species.<sup>95–101</sup> Encouraged by the preceding results, attempts were made to characterize metal–Ar interactions, which have never been crystallographically observed, in Co<sub>2</sub>(dobdc). Under a pressure of 1.14 bar of Ar in the gas cell, no significant electron density could be observed over the cobalt(II) sites in Co<sub>2</sub>(dobdc) at 100 K. Upon cooling to 90 K, however, two binding sites for Ar were resolved, one directly above the metal center and another at a location similar to the secondary binding sites of N<sub>2</sub> and O<sub>2</sub> (Figures 2.2 and 2.S1). It is highly improbable that Ar occupies these adjacent sites simultaneously, because the distance between Ar molecules in the two sites (2.71(3) Å) is much shorter than twice the van der Waals radius of Ar (3.76 Å). In agreement with this, refinement of the Ar site occupancies results in site occupancies of 60.6(1.3)% for Ar interacting with cobalt(II) and 39.3(1.6)% for the second site, which give an overall formula of Co<sub>2</sub>(dobdc)·2.0Ar. These observations suggest that both sites have comparable affinities for Ar, resulting in an equilibrium between the two. Similar adsorption behavior has been observed for Kr and Xe in Ni<sub>2</sub>(dobdc) and Mg<sub>2</sub>(dobdc).<sup>42,46</sup> The interaction of Ar with the cobalt(II) centers in Co<sub>2</sub>(dobdc) is characterized by a Co–Ar distance of 2.932(9) Å (Figure 2.1), which represents the first metal–Ar interaction observed by crystallography. This distance compares well with M–Kr and M–Xe distances in Ni<sub>2</sub>(dobdc) and Mg<sub>2</sub>(dobdc) (Ni–Kr = 3.03(3) Å and 3.26(15) Å, Mg–Kr = 3.23(3) Å, Ni–Xe = 3.01(2) Å and 3.395(7) Å, Mg–Xe = 3.14(2) Å) obtained by powder X-ray diffraction.<sup>42,46</sup> The long distances between Ar, Kr, and Xe and the exposed metal sites in these frameworks is attributed to polarization induced by the partial positive charge on the metal centers. Like N<sub>2</sub> and O<sub>2</sub>, Ar interacts with the dobdc<sup>4-</sup> oxygen atoms in its second binding site (Figure 2.S2). Interactions between Ar and other noble gases with the linker oxygen atoms in other metal–organic frameworks have also been observed by both single-crystal<sup>10,53,69</sup> and powder X-ray diffraction.<sup>42,46</sup>

Motivated by previous work demonstrating the confinement of white phosphorus within a supramolecular cage<sup>102</sup> and a coordination solid,<sup>103</sup> we envisioned that Co<sup>II</sup>–P<sub>4</sub> species could be stabilized by leveraging the site-isolation of the open cobalt(II) coordination sites in Co<sub>2</sub>(dobdc). Heating activated single crystals of Co<sub>2</sub>(dobdc) in the presence of white phosphorus in a sealed vial at 80 °C resulted in adsorption of P<sub>4</sub> molecules to give Co<sub>2</sub>(dobdc)·1.3P<sub>4</sub> as determined by single-crystal X-ray diffraction. Initial refinement of the structure revealed clearly resolved P<sub>4</sub> tetrahedron exhibiting  $\eta^1$ -coordination to the cobalt(II) sites of the framework, with a Co<sup>II</sup>–P<sub>4</sub>

distance of  $\sim 2.6$  Å. The P<sub>4</sub> moiety, however, displayed highly prolate anisotropic displacement parameters and unusual P–P bond distances, long P<sub>apical</sub>–P<sub>basal</sub> bonds ( $\sim 2.6$  Å) and short P<sub>basal</sub>–P<sub>basal</sub> bonds ( $\sim 2.0$  Å), compared to the P–P bond distances in the crystal structure of P<sub>4</sub> (2.190(5)–2.212(5) Å).<sup>104</sup> Given the relatively long Co<sup>II</sup>–P bond distance and large displacement parameters, the apparent distortion of the coordinated P<sub>4</sub> likely resulted from disorder of the P<sub>4</sub> molecule rather than activation by the cobalt(II) center. Thus, the P<sub>4</sub> molecule was modelled to be disordered over two positions with all P–P distances restrained to be similar. The revised structure reveals that P<sub>4</sub> binds to only 45.5(10)% of the cobalt(II) sites with a long Co<sup>II</sup>–P<sub>4</sub> distance of 2.625(10) Å (Figures 2.1 and 2.3). The relative distance between P<sub>4</sub> molecules coordinated to adjacent cobalt(II) sites suggests that P<sub>4</sub> cannot coordinate to each cobalt(II) center because this would lead to P $\cdots$ P contacts (2.53(3) Å) that are much shorter than twice the van der Waals radius of P (3.90 Å). Consequently, the rest of the adsorbed P<sub>4</sub> populates a second site (20.6(10)% occupancy) 3.88 Å away from the cobalt(II) center (Figure 2.S10), where steric congestion prevents closer approach of the P<sub>4</sub> molecule to cobalt(II). Although rare, several molecular  $\eta^1$ -P<sub>4</sub> complexes have been prepared by employing transition metal precursors with an agostic interaction or weakly coordinated ligand that can be displaced by P<sub>4</sub> under mild reaction conditions.<sup>105,106</sup> In contrast to the long Co<sup>II</sup>–P<sub>4</sub> distance in Co<sub>2</sub>(dobdc)·1.3P<sub>4</sub>, molecular  $\eta^1$ -P<sub>4</sub> complexes reported in the CCSD<sup>83</sup> possess much shorter metal–P<sub>4</sub> distances that range from 2.1622(8)–2.464(3) Å and contain electron-rich metals capable of  $\pi$  backbonding to P<sub>4</sub>. These comparisons imply that, similar to the Co<sup>II</sup>–CO and Co<sup>II</sup>–N<sub>2</sub> interactions characterized in Co<sub>2</sub>(dobdc), the longer Co<sup>II</sup>–P<sub>4</sub> bond in Co<sub>2</sub>(dobdc)·1.3P<sub>4</sub> arises from the inability of the high-spin cobalt(II) centers to effectively support  $\pi$  back-donation to P<sub>4</sub>. Notably, the weaker cobalt(II)–P<sub>4</sub> complexes in Co<sub>2</sub>(dobdc) can be prepared and remain stable at much higher temperatures whereas most molecular  $\eta^1$ -P<sub>4</sub> complexes readily decompose at room temperature.<sup>105,106</sup> This thermal stability is attributed to the site-isolation of these Co<sup>II</sup>–P<sub>4</sub> species and their inability to decompose through oxidative addition of P<sub>4</sub>, due to the high-spin state and coordinative saturation of the framework cobalt(II) centers.

### 2.3.5. Gas Adsorption

Low-pressure gas adsorption isotherms at different temperatures were collected for CH<sub>4</sub>, N<sub>2</sub>, O<sub>2</sub>, and Ar, while the isotherms for CO and CO<sub>2</sub> were obtained from previous work<sup>39,55</sup> to relate the adsorption properties of these gases to the corresponding structures (Figures 2.3 and 2.S11–2.S18). To provide a quantitative comparison, the differential enthalpy of adsorption ( $\Delta h_{ad}$ ), a measure of the average binding energy for an adsorbate at a specific surface coverage, were calculated from isotherm data at low coverage of each gas (Table 2.1). In agreement with the crystal structures, the differential enthalpies of adsorption, which range from  $-48.8(2)$  (for CO) to  $-17(1)$  kJ/mol (for Ar), indicate relatively weak Co<sup>II</sup>–gas interactions compared to those characterized in molecular complexes. To place these values into context,  $-\Delta h_{ad}$  for CO in Co<sub>2</sub>(dobdc) is about one third of the bond dissociation energy for the first CO in CpCo(CO)<sub>2</sub> (148(2) kJ/mol; Cp<sup>-</sup> = cyclopentadienyl).<sup>107</sup>



**Figure 2.4.** Low-pressure gas adsorption isotherms for CO (yellow),<sup>39</sup> CO<sub>2</sub> (green),<sup>55</sup> CH<sub>4</sub> (gray), N<sub>2</sub> (dark blue), O<sub>2</sub> (red), and Ar (light blue) at 298 K (left). High-pressure gas adsorption isotherms for CO (yellow),<sup>39</sup> CO<sub>2</sub> (green), CH<sub>4</sub> (gray), N<sub>2</sub> (dark blue), and Ar (light blue) at 298 K (right). The filled circles and solid lines represent experimental data and corresponding Langmuir fits, respectively.

The trend in  $-\Delta h_{\text{ad}}$  values,  $\text{CO} > \text{CO}_2 > \text{N}_2 > \text{CH}_4 > \text{O}_2 > \text{Ar}$ , shows no clear correlation with the  $\text{Co}-X_{\text{gas}}$  distances obtained by single-crystal X-ray diffraction. As an approximate method to account for differences in the van der Waals radii among coordinated atoms, the sum of the ionic radius for high-spin cobalt(II) and the van der Waals radius of the coordinated atom can be subtracted from the  $\text{Co}-X_{\text{gas}}$  distances to give the parameter  $\Delta d$ . More negative values for  $\Delta d$  should correspond to stronger interactions. With the exception of CO<sub>2</sub> and CH<sub>4</sub>, the trend in  $\Delta d$  is consistent with that of  $-\Delta h_{\text{ad}}$ . In the structure of CO<sub>2</sub> on Co<sub>2</sub>(dobdc) (Figure 2.1), CO<sub>2</sub> coordinated to the cobalt(II) sites tilts towards one of the linker oxygen atoms to give a  $\text{C}_{\text{CO}_2} \cdots \text{O}$  distance of 3.29(7) Å.<sup>55</sup> This indicates that both direct interaction of CO<sub>2</sub> with the metal site and weak secondary interactions contribute to its enthalpy of adsorption. Conceivably, these

**Table 2.1.**  $\text{Co}-X_{\text{gas}}$  distances and differential enthalpies of adsorption ( $\Delta h_{\text{ad}}$ ) of CO, CO<sub>2</sub>, CH<sub>4</sub>, N<sub>2</sub>, O<sub>2</sub>, and Ar in Co<sub>2</sub>(dobdc).

gas	$d(\text{Co}-X_{\text{gas}})$ (Å)	$\Delta d^a$ (Å)	$-\Delta h_{\text{ad}}^b$ (kJ/mol)
CO	2.215(6) (Co-C)	-0.230(6)	48.8(2) <sup>39</sup>
CO <sub>2</sub>	2.261(9) <sup>55</sup> (Co-O) <sup>c</sup>	-0.004(9)	33.6(1) <sup>55</sup>
N <sub>2</sub>	2.236(6) (Co-N)	-0.059(6)	20.3(6)
O <sub>2</sub>	2.216(5) (Co-O)	-0.049(5)	18.56(3)
CH <sub>4</sub>	2.941(19) (Co $\cdots$ C)	—	19.21(9)
Ar	2.932(9) (Co-Ar)	0.307(9)	17(1)

<sup>a</sup> $\Delta d$  = the  $\text{Co}-X_{\text{gas}}$  distance minus the sum of the ionic radius for high-spin cobalt(II)<sup>108</sup> and the van der Waals radius of the coordinated atom.  $\Delta d$  was not calculated for CH<sub>4</sub> because the  $\text{Co} \cdots \text{C}$  distance is between Co and the central atom of CH<sub>4</sub>, not the coordinated hydrogen atoms, which makes it difficult to compare rigorously with the other gases. <sup>b</sup>Low-coverage differential enthalpies of adsorption were calculated at a loading of 0.5 mmol/g using independent Langmuir fits to low-pressure adsorption isotherms. <sup>c</sup>Although the structure of CO<sub>2</sub> in Co<sub>2</sub>(dobdc) was collected at a higher temperature (150 K) compared to the other structures (90 and 100 K), the  $\text{Co}-\text{O}_{\text{CO}_2}$  distance (2.23(4) Å) obtained at 10 K from powder neutron diffraction data shows that the  $\text{Co}-\text{O}_{\text{CO}_2}$  distance does not shorten significantly at lower temperatures.<sup>55</sup>

additional interactions cause CO<sub>2</sub> to be an outlier in the trend between  $\Delta d$  and  $-\Delta h_{\text{ad}}$ . Care should be exercised, however, in inferring relative binding strengths by comparing crystallographic distances. Overall, these results show that multiple factors contribute to the binding energy of a molecule and that interaction distances alone cannot adequately represent all of these factors, especially when considering different molecules. More reliable correlations can be drawn if distances are compared between the same molecule interacting with the same metal center.

The high-pressure adsorption isotherms for CO, CO<sub>2</sub>, CH<sub>4</sub>, N<sub>2</sub>, and Ar at 298 K (Figure 2.3) show that secondary adsorption sites become relevant at higher pressures, as the uptake for all gases eventually exceeds one gas molecule per cobalt site with increasing pressure. Qualitative comparison of the isotherms suggests that the secondary adsorption sites for CO<sub>2</sub> have the highest binding affinity with an uptake of  $\sim 2$  CO<sub>2</sub> molecules per Co at 40 bar. This likely results from the favorable interaction between the partial positive charge on the CO<sub>2</sub> carbon atom with linker oxygen atoms in the framework and intermolecular interactions between neighboring CO<sub>2</sub> molecules (Figure 2.S2). In contrast, CO, CH<sub>4</sub>, N<sub>2</sub>, and Ar have less pronounced adsorption at high pressures, with each showing an uptake of less than 1.5 molecules of gas per Co at 40 bar. Perhaps the most striking comparison lies between CO and CO<sub>2</sub>. As a polar molecule, CO has a stronger interaction with the cobalt(II) sites in the framework, which is clearly evident in its steeper low-pressure isotherm and more negative differential enthalpy of adsorption. At pressures beyond 0.55 bar, however, Co<sub>2</sub>(dobdc) adsorbs significantly larger amounts of CO<sub>2</sub>, demonstrating that distinct adsorption sites within a material can have considerably different selectivities depending on the nature of the gases adsorbed.

## 2.4. Conclusions and outlook

The foregoing results highlight the unique advantages of metal–organic frameworks as robust crystalline matrices that facilitate unhindered access of guest molecules, enabling for example the study of guest interactions with open metal coordination sites within the framework pores. Rigorously air-free gas-dosing methods were developed to overcome the challenges associated with studying weakly binding gases in single crystals. Through these methods, the interaction of CO, CH<sub>4</sub>, N<sub>2</sub>, O<sub>2</sub>, Ar, and P<sub>4</sub> with the metal–organic framework Co<sub>2</sub>(dobdc) were directly observed by single-crystal X-ray diffraction. The resulting structures reveal the location of the primary, secondary (for N<sub>2</sub>, O<sub>2</sub>, and Ar) and tertiary (for O<sub>2</sub>) binding sites for these gases within the framework. Moreover, examination of the Co<sup>II</sup>–gas distances shows that these Co<sup>II</sup>–gas interactions are distinctly weak compared to those found in molecular complexes. These unique interactions arise from the square pyramidal coordination geometry and the high-spin electronic configuration enforced by the framework on cobalt(II). As a result, this work represents the first report of the structural characterization of such species by single-crystal X-ray diffraction. Finally, differential enthalpies of adsorption determined from low-pressure gas adsorption isotherms corroborate the weak binding affinities inferred from the relatively long Co<sup>II</sup>–gas distances observed in the single crystal structures, while high-pressure gas adsorption isotherms at 298 K show significant contribution from secondary binding sites at pressures beyond 1 bar. Altogether, these results establish *in situ* single-crystal X-ray diffraction as a valuable technique, which imparts not only a practical understanding of gas adsorption in porous materials, but also new insights into the underlying interactions that give rise to their adsorption behavior.

Ongoing efforts are focused on developing *in situ* single-crystal X-ray diffraction methods that can be routinely employed in the evaluation of metal–organic frameworks for specific applications, such as gas separations and gas storage. In particular, techniques are being explored

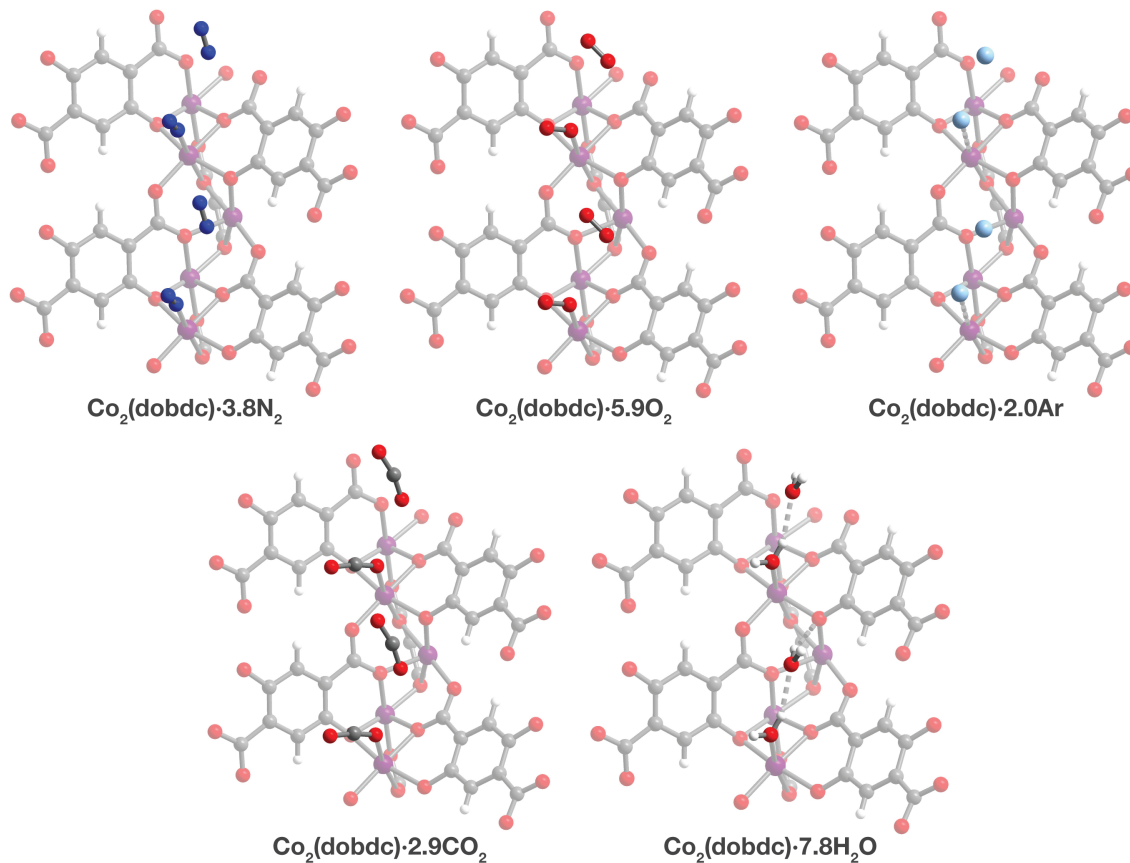
to enable (i) mounting crystals that decompose in air, (ii) systematic determination of the dependence of site occupancies for multiple binding sites on guest loading, (iii) collection of diffraction data at lower temperatures to lessen thermal disorder, and (iv) structural assessment of the absorptive properties of these materials in the presence of gas mixtures. Furthermore, it can be envisioned that these techniques can be used to isolate and observe reactive intermediates in metal–organic frameworks, providing a way to determine the structures of species that have only been amenable to characterization by spectroscopy.

## **2.5. Acknowledgements**

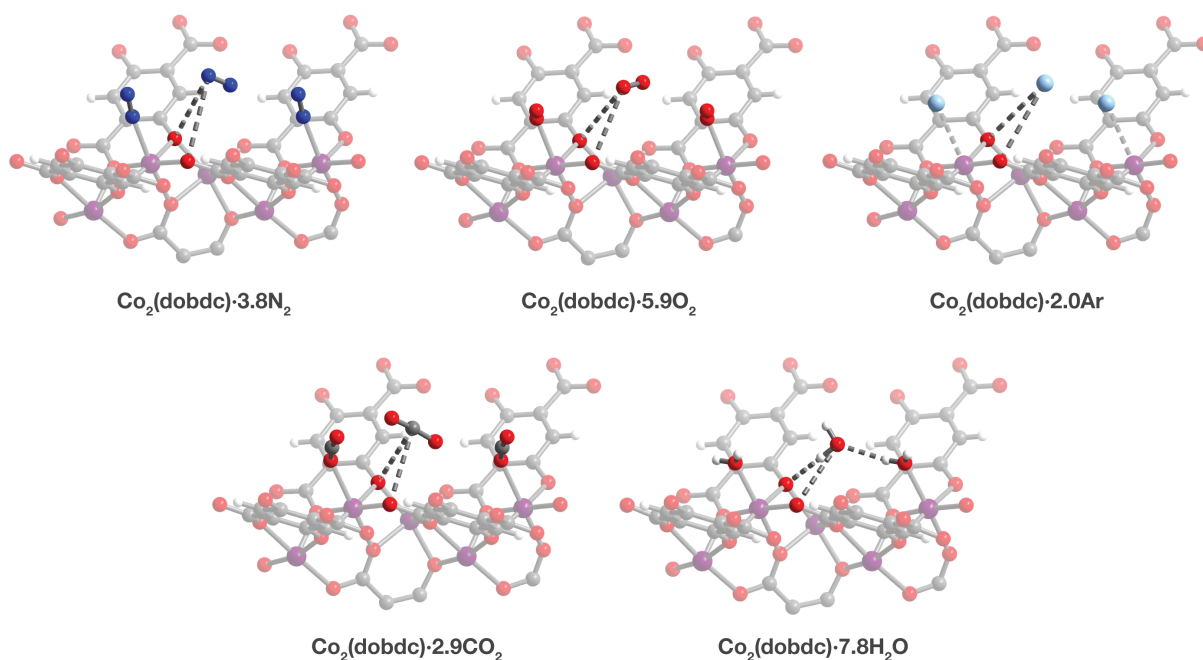
This work was supported through the Center for Gas Separations Relevant to Clean Energy Technologies, an Energy Frontier Research Center funded by the U.S. Department of Energy, Office of Science, Office of Basic Energy Sciences under Award DE-SC0001015. This research used resources of the Advanced Light Source and the Molecular Foundry, which are supported by the Director, Office of Science, Office of Basic Energy Sciences, of the U.S. Department of Energy under Contract No. DE-AC02-05CH11231. We thank Rebecca L. Siegelman, Julia Oktawiec, Dianne J. Xiao, James R. Nasiaka, Jason S. Lee, Kenji Sumida, David L. Rogow, and Dante Valdez for helpful discussions and experimental assistance.

## 2.6. Supplementary Information

### 2.6.6. Supplementary Figures



**Figure 2.S1.** Comparison of the secondary binding sites in the structures of  $\text{Co}_2(\text{dobdc})\cdot 3.8\text{N}_2$  at 100 K,  $\text{Co}_2(\text{dobdc})\cdot 5.9\text{O}_2$  at 100 K,  $\text{Co}_2(\text{dobdc})\cdot 2.0\text{Ar}$  at 90 K,  $\text{Co}_2(\text{dobdc})\cdot 2.9\text{CO}_2$ <sup>55</sup> at 150 K, and  $\text{Co}_2(\text{dobdc})\cdot 7.8\text{H}_2\text{O}$ <sup>68</sup> at 100 K as determined by single-crystal X-ray diffraction. Purple, red, gray, blue, light blue, and white spheres represent Co, O, C, N, Ar, and H atoms, respectively. The structures of  $\text{Co}_2(\text{dobdc})\cdot 2.9\text{CO}_2$  and  $\text{Co}_2(\text{dobdc})\cdot 7.8\text{H}_2\text{O}$  have been reported previously and are shown here to facilitate comparisons.

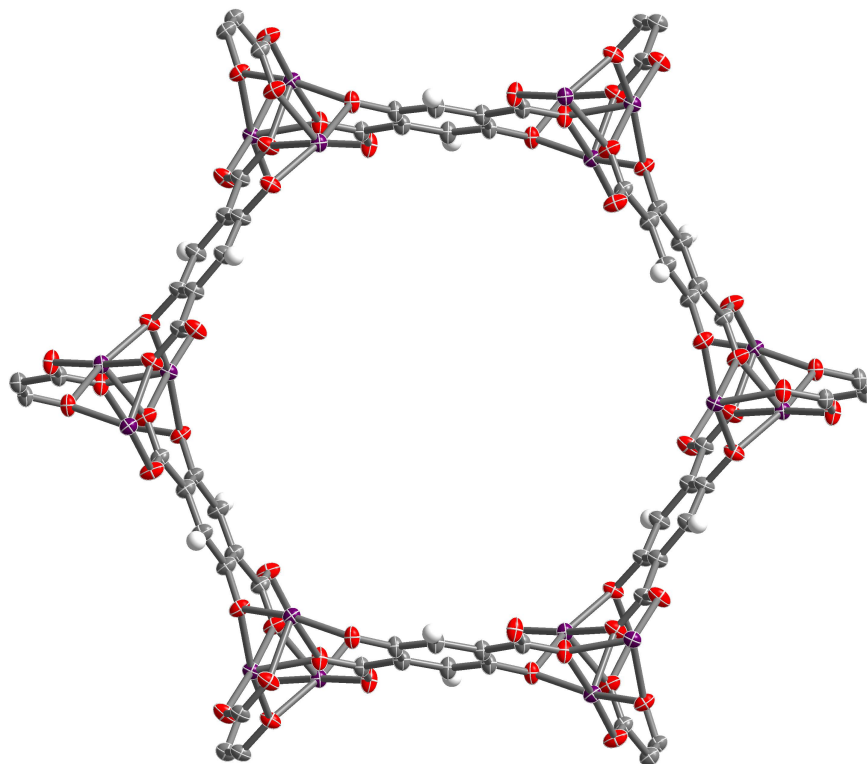


$\text{Co}_2(\text{dobdc})\cdot 3.8\text{N}_2$		$\text{Co}_2(\text{dobdc})\cdot 5.9\text{O}_2$		$\text{Co}_2(\text{dobdc})\cdot 2.0\text{Ar}$		$\text{Co}_2(\text{dobdc})\cdot 2.9\text{CO}_2^{55}$		$\text{Co}_2(\text{dobdc})\cdot 7.8\text{H}_2\text{O}^{68}$	
O1...N4	3.44(2) Å	O1...O7	3.391(17) Å	O1...Ar2	3.683(16) Å	O1...C6	3.21(5) Å	O1...H5a	2.15(3) Å
O3...N4	3.66(3) Å	O3...O7	3.376(18) Å	O3...Ar2	3.767(18) Å	O3...C6	3.29(8) Å	O3...O5	3.172(4) Å

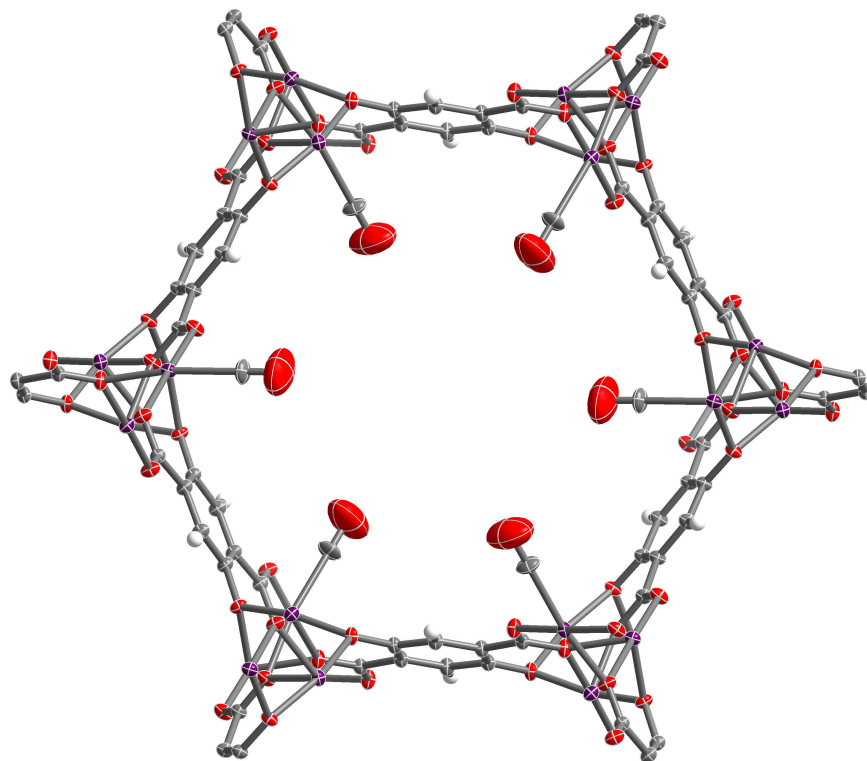
**Figure 2.S2.** Selected intermolecular contacts between the phenoxide oxygen (O1) and non-bridging carboxylate oxygen (O3) of the  $\text{dobdc}^{4-}$  linkers and gases bound at secondary binding sites in the structures of  $\text{Co}_2(\text{dobdc})\cdot 3.8\text{N}_2$  at 100 K,  $\text{Co}_2(\text{dobdc})\cdot 5.9\text{O}_2$  at 100 K,  $\text{Co}_2(\text{dobdc})\cdot 2.0\text{Ar}$  at 90 K,  $\text{Co}_2(\text{dobdc})\cdot 2.9\text{CO}_2^{55}$  at 150 K, and  $\text{Co}_2(\text{dobdc})\cdot 7.8\text{H}_2\text{O}^{68}$  at 100 K as determined by single-crystal X-ray diffraction. Purple, red, gray, blue, light blue, and white spheres represent Co, O, C, N, Ar, and H atoms, respectively. The structures of  $\text{Co}_2(\text{dobdc})\cdot 2.9\text{CO}_2$  and  $\text{Co}_2(\text{dobdc})\cdot 7.8\text{H}_2\text{O}$  have been reported previously and are shown here to facilitate comparisons.



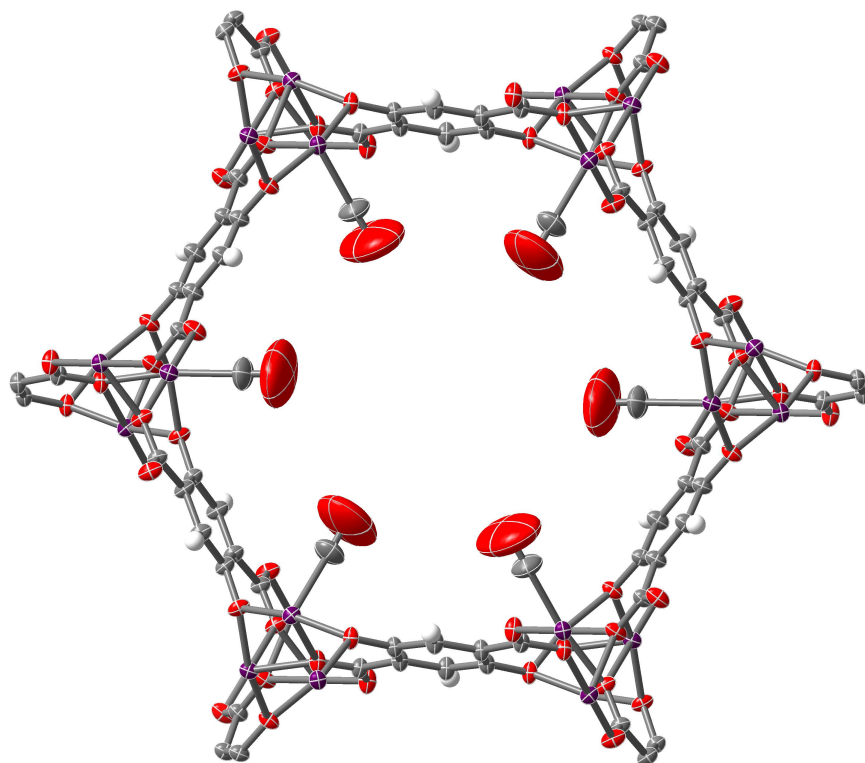
### 2.6.7. Thermal ellipsoid plots and crystallographic tables



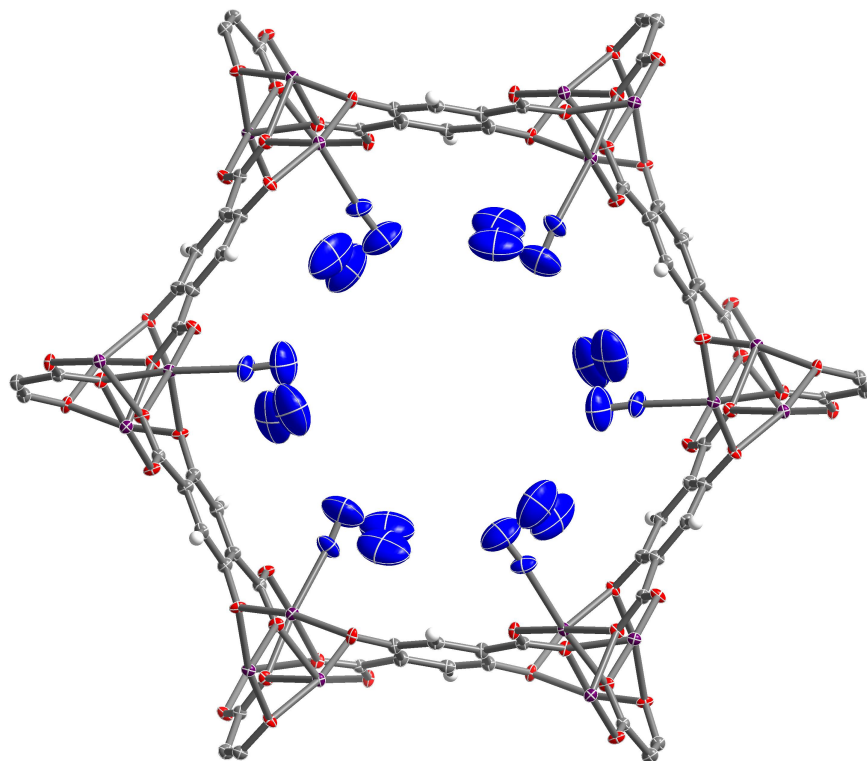
**Figure 2.S3.** Thermal ellipsoid plot of Co<sub>2</sub>(dobdc) at 298 K drawn at 50% probability level as determined by single-crystal X-ray diffraction; purple, red, gray and white ellipsoids represent Co, O, C, and H atoms, respectively.



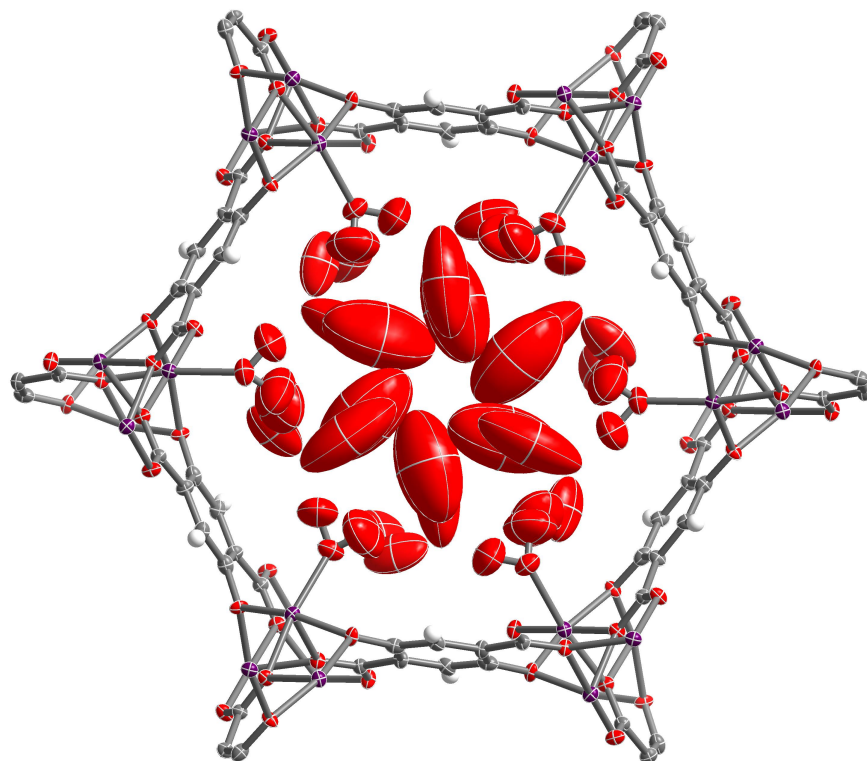
**Figure 2.S4.** Thermal ellipsoid plot of  $\text{Co}_2(\text{dobdc}) \cdot 0.58\text{CO}$  at 90 K drawn at 50% probability level as determined by single-crystal X-ray diffraction; purple, red, gray, and white ellipsoids represent Co, O, C, and H atoms, respectively.



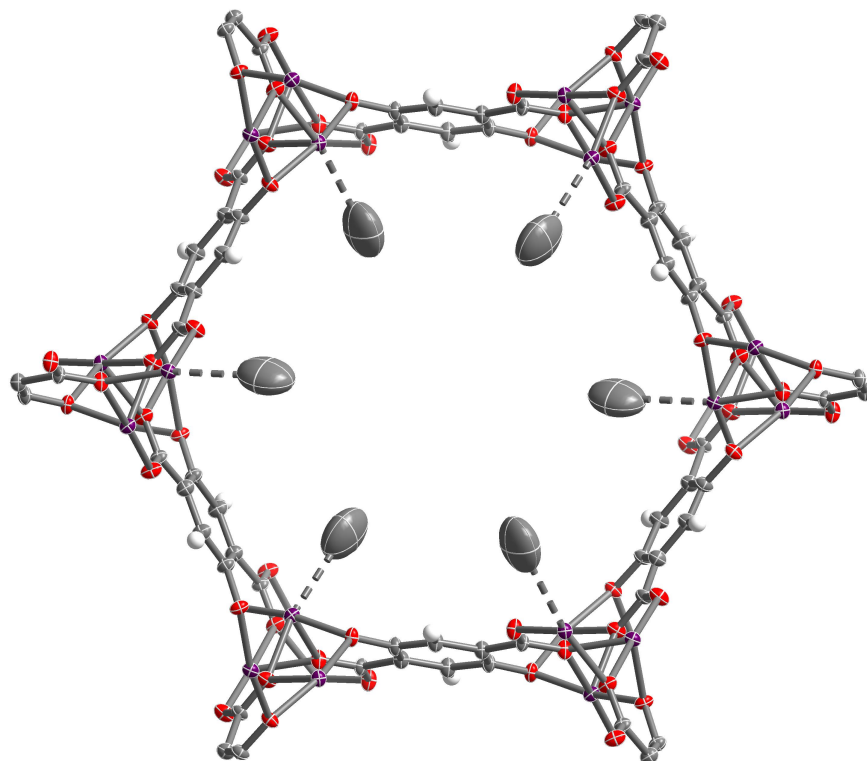
**Figure 2.S5.** Thermal ellipsoid plot of  $\text{Co}_2(\text{dobdc}) \cdot 1.2\text{CO}$  at 100 K drawn at 50% probability level as determined by single-crystal X-ray diffraction; purple, red, gray, and white ellipsoids represent Co, O, C, and H atoms, respectively.



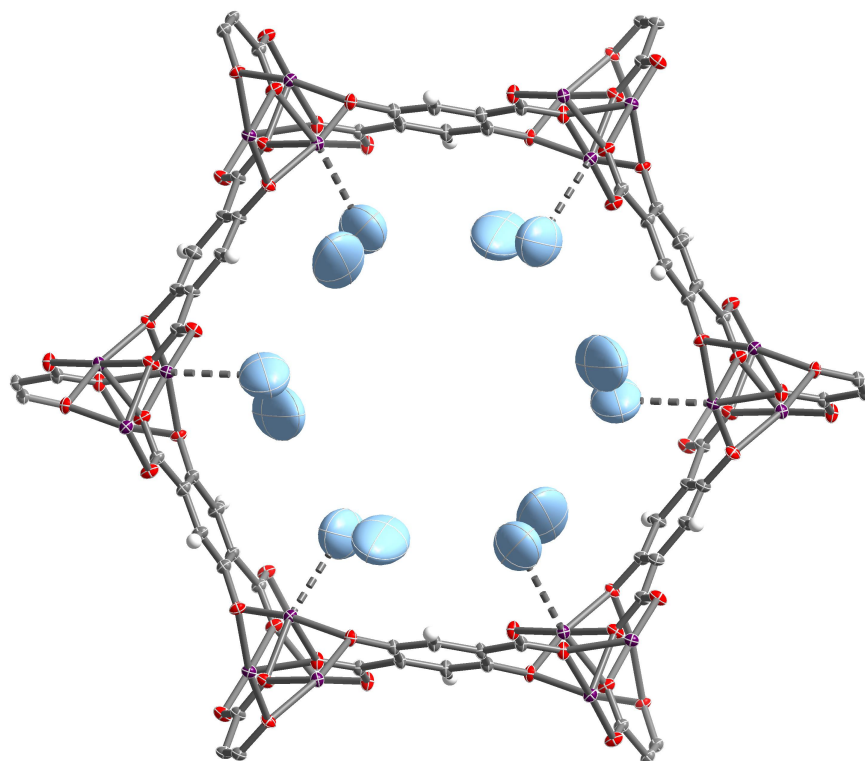
**Figure 2.S6.** Thermal ellipsoid plot of  $\text{Co}_2(\text{dobdc})\cdot 3.8\text{N}_2$  at 100 K drawn at 50% probability level as determined by single-crystal X-ray diffraction; purple, red, gray, blue, and white ellipsoids represent Co, O, C, N, and H atoms, respectively.



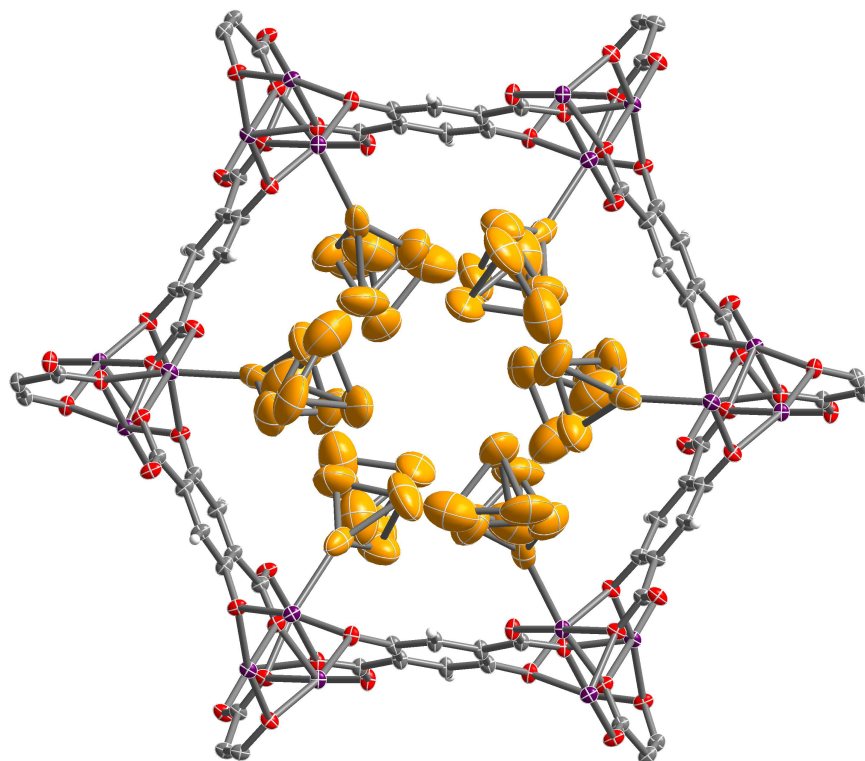
**Figure 2.S7.** Thermal ellipsoid plot of  $\text{Co}_2(\text{dobdc}) \cdot 5.9\text{O}_2$  at 100 K drawn at 50% probability level as determined by single-crystal X-ray diffraction; purple, red, gray, and white ellipsoids represent Co, O, C, and H atoms, respectively. Note,  $\text{O}_2$  bound to the  $\text{Co}^{\text{II}}$  sites were found to be disordered over two orientations with relative occupancies of 73(3)% and 27(3)%.



**Figure 2.S8.** Thermal ellipsoid plot of  $\text{Co}_2(\text{dobdc}) \cdot 2.0\text{CH}_4$  at 100 K drawn at 50% probability level as determined by single-crystal X-ray diffraction; purple, red, gray, and white ellipsoids represent Co, O, C, and H atoms, respectively.



**Figure 2.S9.** Thermal ellipsoid plot of  $\text{Co}_2(\text{dobdc}) \cdot 2.0\text{Ar}$  at 90 K drawn at 50% probability level as determined by single-crystal X-ray diffraction; purple, red, gray, light blue, and white ellipsoids represent Co, O, C, Ar, and H atoms, respectively.



**Figure 2.S10.** Thermal ellipsoid plot of  $\text{Co}_2(\text{dobdc})\cdot 1.3\text{P}_4$  at 100 K drawn at 50% probability level as determined by single-crystal X-ray diffraction; purple, red, gray, light orange, and white ellipsoids represent Co, O, C, P, and H atoms, respectively. Note, the  $\text{P}_4$  molecules were found in two positions, one with  $\text{P}_4$  molecules coordinated to the  $\text{Co}^{\text{II}}$  sites (45.5(10)% occupancy) and another 3.88(3) Å away from the  $\text{Co}^{\text{II}}$  sites centers (20.6(10)% occupancy).

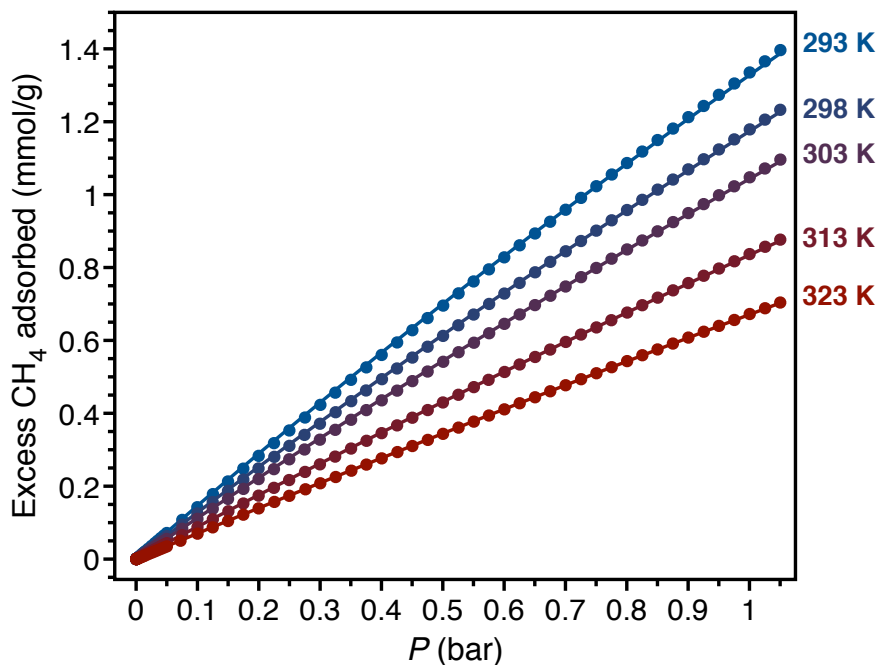


**Table 2.S1.** Crystallographic Data

	Co <sub>2</sub> (dobdc)	Co <sub>2</sub> (dobdc)-0.58CO	Co <sub>2</sub> (dobdc)-1.2CO	Co <sub>2</sub> (dobdc)-3.8N <sub>2</sub>	Co <sub>2</sub> (dobdc)-5.9O <sub>2</sub>	Co <sub>2</sub> (dobdc)-2.0CH <sub>4</sub>	Co <sub>2</sub> (dobdc)-2.0Ar	Co <sub>2</sub> (dobdc)-1.3P <sub>4</sub>
Formula	Co <sub>2</sub> C <sub>8</sub> H <sub>2</sub> O <sub>6</sub>	Co <sub>2</sub> C <sub>8.58</sub> H <sub>2</sub> O <sub>6.58</sub>	Co <sub>2</sub> C <sub>9</sub> H <sub>2</sub> O <sub>7.18</sub>	Co <sub>2</sub> C <sub>8</sub> H <sub>2</sub> N <sub>2.56</sub> O <sub>6</sub>	Co <sub>2</sub> C <sub>8</sub> H <sub>2</sub> O <sub>7.88</sub>	Co <sub>2</sub> C <sub>9</sub> H <sub>10</sub> O <sub>6</sub>	Co <sub>2</sub> C <sub>8</sub> H <sub>2</sub> O <sub>6</sub> Ar <sub>2</sub>	Co <sub>2</sub> C <sub>8</sub> H <sub>2</sub> O <sub>6</sub> P <sub>5.28</sub>
Temperature (K)	296(2)	90(2)	100(2)	100(2)	100(2)	100(2)	90(2)	100(2)
Crystal System	Trigonal	Trigonal	Trigonal	Trigonal	Trigonal	Trigonal	Trigonal	Trigonal
Space Group	$R\bar{3}$	$R\bar{3}$	$R\bar{3}$	$R\bar{3}$	$R\bar{3}$	$R\bar{3}$	$R\bar{3}$	$R\bar{3}$
a, b, c (Å)	25.892(4), 25.892(4), 6.8482(9)	25.8262(16), 25.8262(16), 6.8315(4)	25.853(3), 25.853(3), 6.8494(7)	25.810(8), 25.810(8), 6.901(2)	25.7599(9), 25.7599(9), 6.8766(3)	25.866(5), 25.866(5), 6.8457(12)	25.860(4), 25.860(4), 6.8678(10)	25.7348(8), 25.7348(8), 6.8385(2)
$\alpha, \beta, \gamma$ (°)	90, 90, 120	90, 90, 120	90, 90, 120	90, 90, 120	90, 90, 120	90, 90, 120	90, 90, 120	90, 90, 120
$V$ , (Å <sup>3</sup> )	3975.9(12)	3946.1(5)	3964.6(9)	3981(3)	3951.8(3)	3966.4(15)	3977.5(12)	3922.2(3)
Z	9	9	9	9	9	9	9	9
Radiation, $\lambda$ (Å)	Synchrotron, 0.7749	Synchrotron, 0.7749	Synchrotron, 0.7749	Synchrotron, 0.6199	Synchrotron, 0.7749	Synchrotron, 0.7749	Synchrotron, 0.6525	Synchrotron, 0.7749
2 $\theta$ Range for Data Collection	6.782 to 64.176	6.8 to 69.512	6.782 to 69.43	4.768 to 47.466	5.974 to 54.904	6.786 to 65.124	5.696 to 63.570	6.796 to 74.476
Completeness to 2 $\theta$	99.9% (2 $\theta$ = 55.412°)	99.0% (2 $\theta$ = 55.412°)	99.9% (2 $\theta$ = 55.412°)	99.9% (2 $\theta$ = 43.670°)	99.1% (2 $\theta$ = 54.904°)	99.8% (2 $\theta$ = 55.412°)	99.8% (2 $\theta$ = 46.096°)	99.9% (2 $\theta$ = 55.412°)
Data / Restraints / Parameters	2374 / 0 / 74	2857 / 0 / 92	2885 / 9 / 92	2040 / 8 / 110	1536 / 34 / 138	2442 / 0 / 83	3887 / 6 / 94	3479 / 216 / 148
Goodness of Fit on F <sup>2</sup>	1.116	1.070	1.051	1.190	1.015	1.064	1.072	1.198
R1 <sup>a</sup> , wR2 <sup>b</sup> (I > 2 $\sigma$ (I))	0.0485, 0.1370	0.0274, 0.0696	0.0389, 0.0978	0.0632, 0.1233	0.0481, 0.1045	0.0477, 0.1205	0.0513, 0.1272	0.0822, 0.2465
R1 <sup>a</sup> , wR2 <sup>b</sup> (all data)	0.0564, 0.1453	0.0317, 0.0718	0.0491, 0.1032	0.0805, 0.1328	0.0860, 0.1203	0.0558, 0.1271	0.0637, 0.1358	0.0902, 0.2530
Largest Diff. Peak and Hole (e Å <sup>-3</sup> )	0.990 and -0.519	0.578 and -0.391	0.454 and -0.432	0.688 and -0.753	0.826 and -0.587	0.777 and -0.482	1.740 and -0.956	2.388 and -1.557

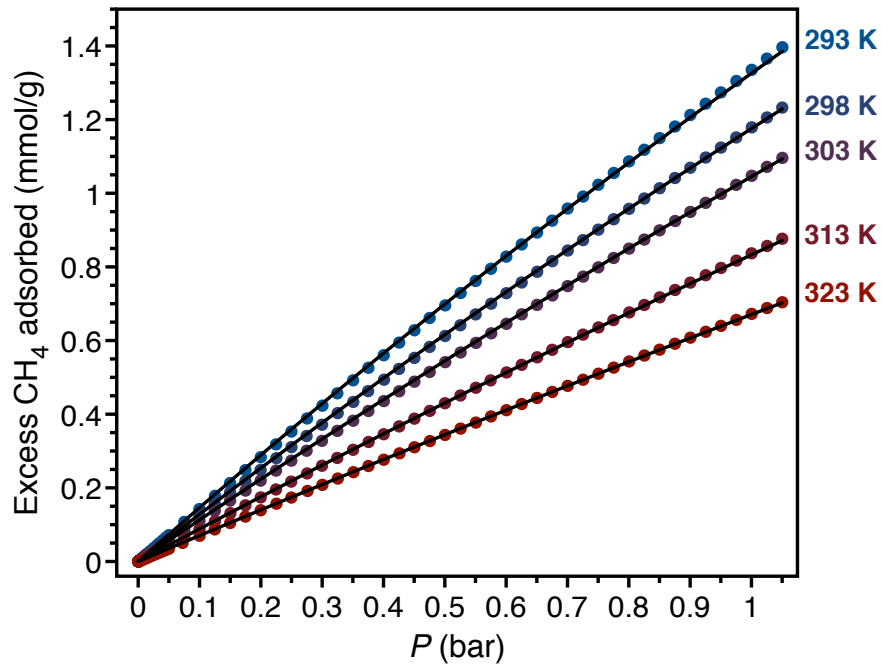
$$^a R1 = \frac{\sum |F_o| - |F_c|}{\sum |F_o|}, \quad ^b wR2 = \left\{ \frac{\sum [w(F_o^2 - F_c^2)]^2}{\sum [w(F_o^2)]^2} \right\}^{1/2}$$

### 2.6.8. Langmuir fits for low-pressure gas adsorption isotherms of Co<sub>2</sub>(dobdc)



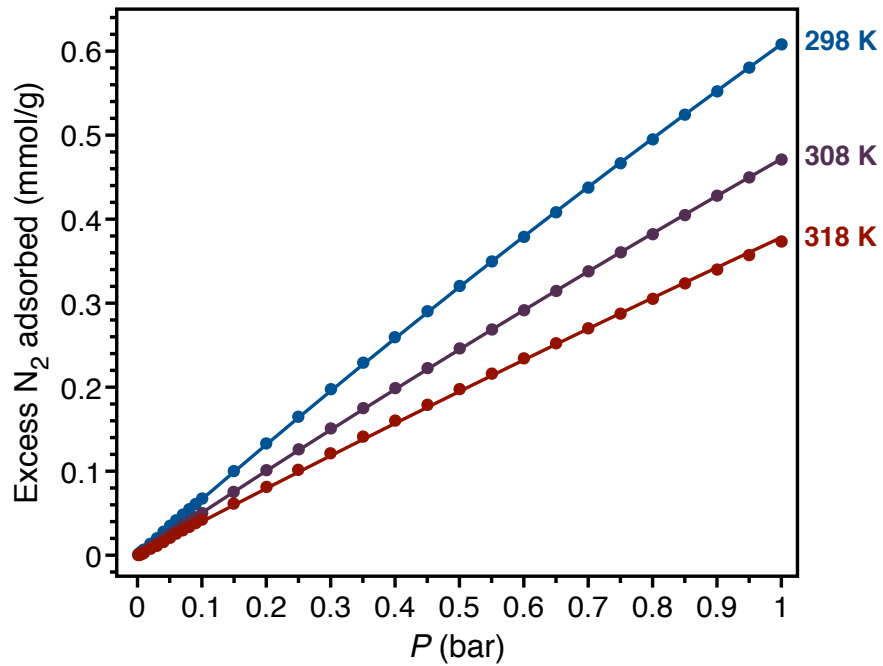
$T$ (K)	$n_{\text{sat},1}$ (mmol/g)	$S_1$ (R)	$-E_1$ (kJ/mol)	$n_{\text{sat},2}$ (mmol/g)	$S_2$ (R)	$-E_2$ (kJ/mol)
293.15	6.41	10.6	20.6	6.41	9.39	17.6
298.15	6.41	10.5	20.3	6.41	9.33	17.4
303.15	6.41	10.6	20.6	6.41	9.42	17.6
313.15	6.41	10.6	20.6	6.41	9.42	17.6
323.15	6.41	10.5	20.4	6.41	9.39	17.5

**Figure 2.S11.** Dual-site Langmuir fits and parameters for CH<sub>4</sub> adsorption isotherms of Co<sub>2</sub>(dobdc) at 293.15, 298.15, 303.15, 313.15, 323.15 K (fit independently for each temperature);  $T$  is the temperature,  $n_{\text{sat},i}$  is the saturation capacity,  $S_i$  is the site-specific molar entropy of adsorption,  $E_i$  is the site-specific binding energy, and R is the gas constant in J/mol·K.



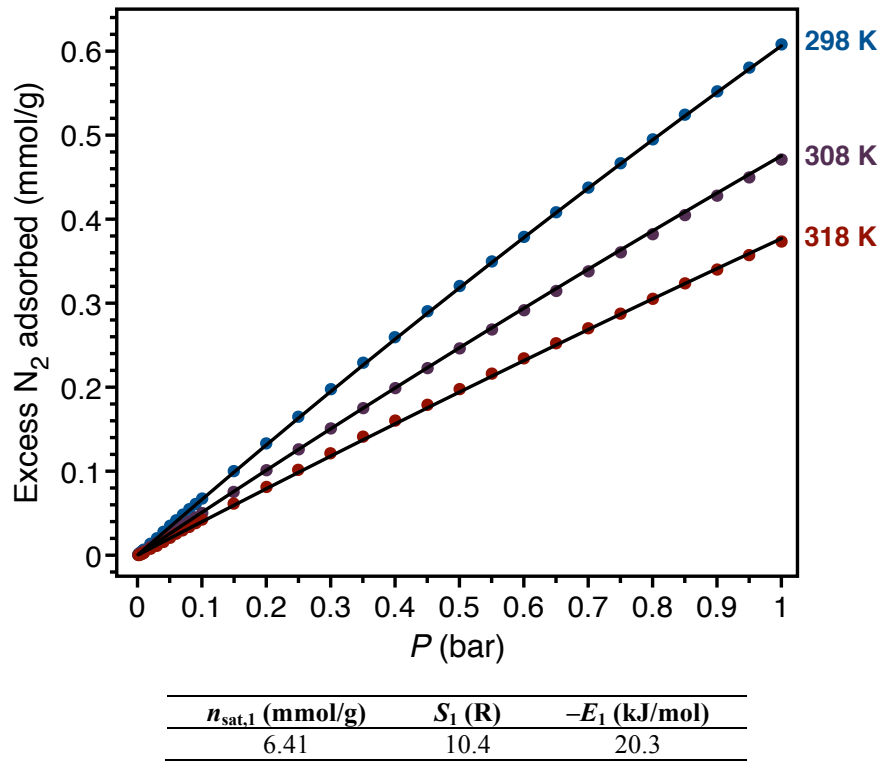
$n_{\text{sat},1}$ (mmol/g)	$S_1$ (R)	$-E_1$ (kJ/mol)	$n_{\text{sat},2}$ (mmol/g)	$S_2$ (R)	$-E_2$ (kJ/mol)
6.41	10.1	19.4	6.41	10.1	19.3

**Figure 2.S12.** Dual-site Langmuir fits and parameters for CH<sub>4</sub> adsorption isotherms of Co<sub>2</sub>(dobdc) at 293.15, 298.15, 303.15, 313.15, 323.15 K (fit simultaneously for all temperatures);  $n_{\text{sat},i}$  is the saturation capacity,  $S_i$  is the site-specific molar entropy of adsorption,  $E_i$  is the site-specific binding energy, and R is the gas constant in J/mol·K.

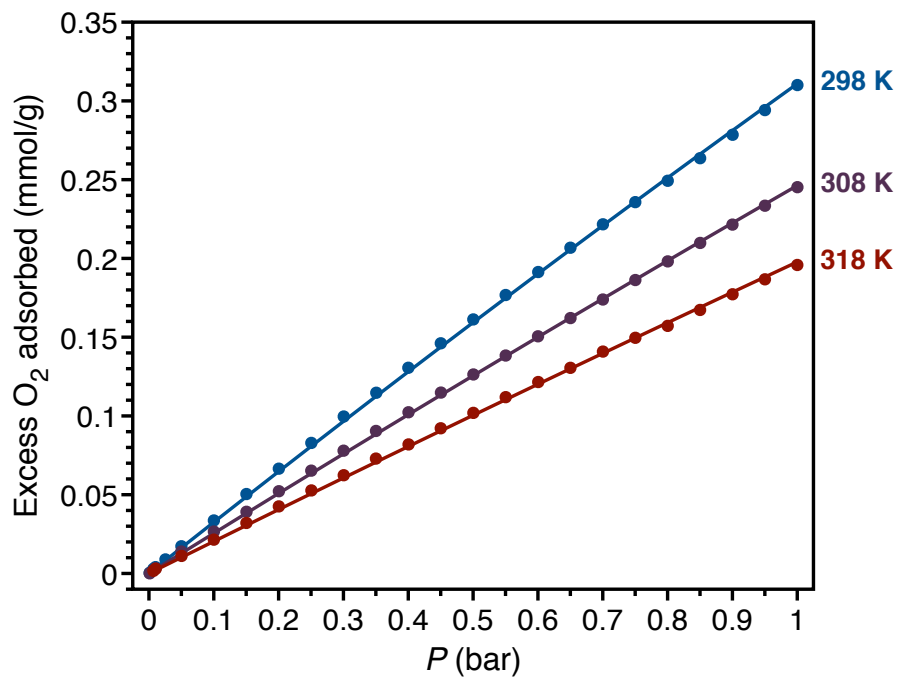


$T$ (K)	$n_{\text{sat},1}$ (mmol/g)	$S_1$ (R)	$-E_1$ (kJ/mol)
298.15	6.41	10.1	19.5
308.15	6.41	10.2	19.6
318.15	6.41	10.2	19.6

**Figure 2.S13.** Single-site Langmuir fits and parameters for N<sub>2</sub> adsorption isotherms of Co<sub>2</sub>(dobdc) at 298.15, 308.15, and 318.15 K (fit independently for each temperature);  $T$  is the temperature,  $n_{\text{sat},1}$  is the saturation capacity,  $S_i$  is the site-specific molar entropy of adsorption,  $E_i$  is the site-specific binding energy, and R is the gas constant in J/mol·K.

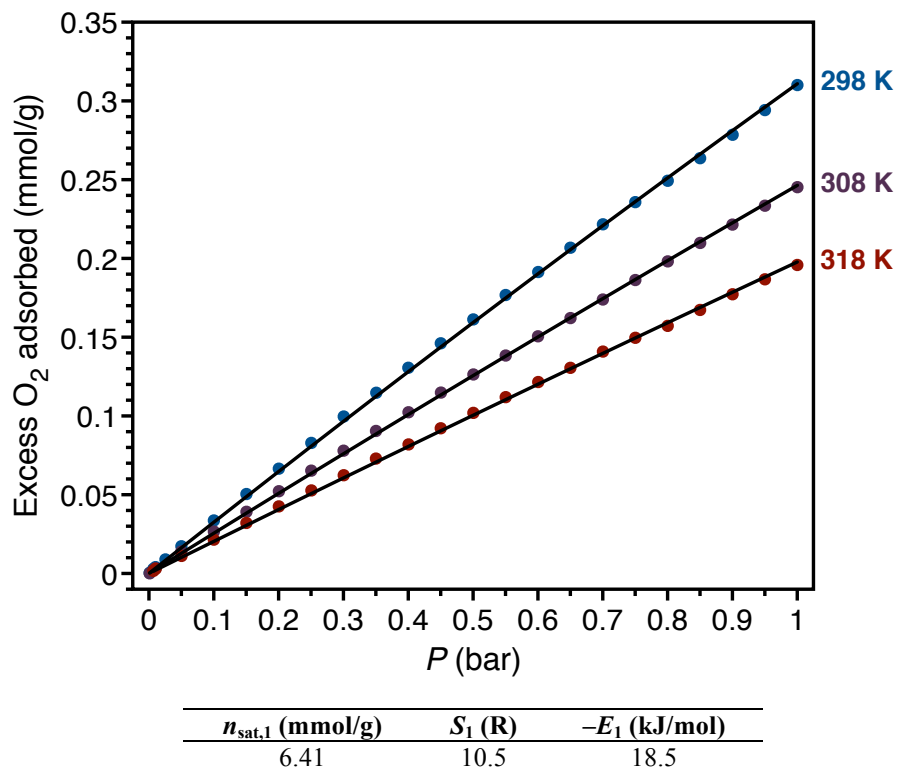


**Figure 2.S14.** Single-site Langmuir fit and parameters for  $\text{N}_2$  adsorption isotherms of  $\text{Co}_2(\text{dobdc})$  at 298.15, 308.15, and 318.15 K (fit simultaneously for all temperatures);  $n_{\text{sat},1}$  is the saturation capacity,  $S_1$  is the site-specific molar entropy of adsorption,  $E_1$  is the site-specific binding energy, and  $R$  is the gas constant in  $\text{J}/\text{mol}\cdot\text{K}$ .

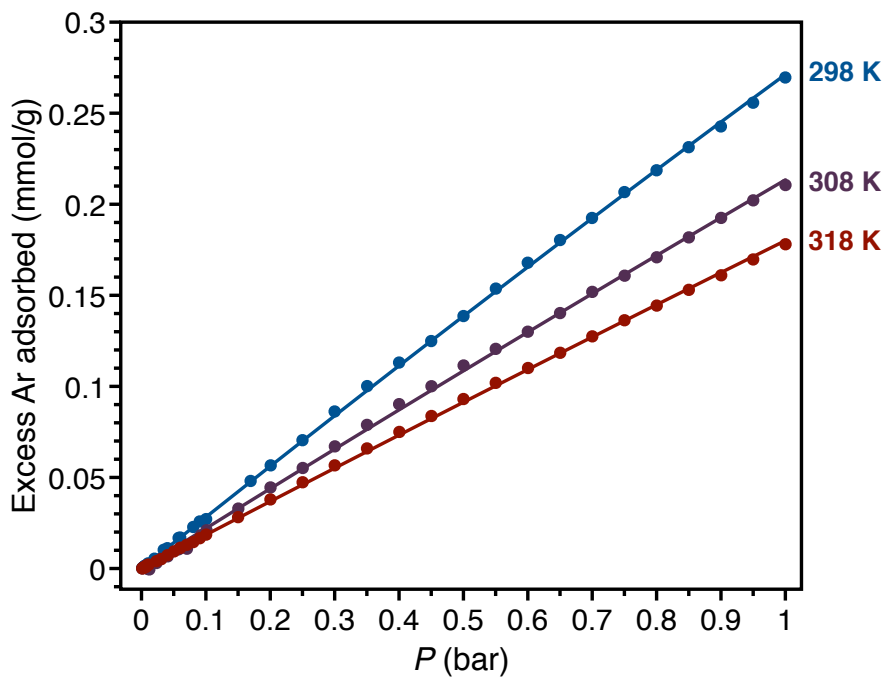


$T$ (K)	$n_{\text{sat},1}$ (mmol/g)	$S_1$ (R)	$-E_1$ (kJ/mol)
298.15	6.41	10.6	18.8
308.15	6.41	10.6	19.0
318.15	6.41	10.6	19.0

**Figure 2.S15.** Single-site Langmuir fits and parameters for O<sub>2</sub> adsorption isotherms of Co<sub>2</sub>(dobdc) at 298.15, 308.15, and 318.15 K (fit independently for each temperature);  $T$  is the temperature,  $n_{\text{sat},1}$  is the saturation capacity,  $S_i$  is the site-specific molar entropy of adsorption,  $E_i$  is the site-specific binding energy, and R is the gas constant in J/mol·K.



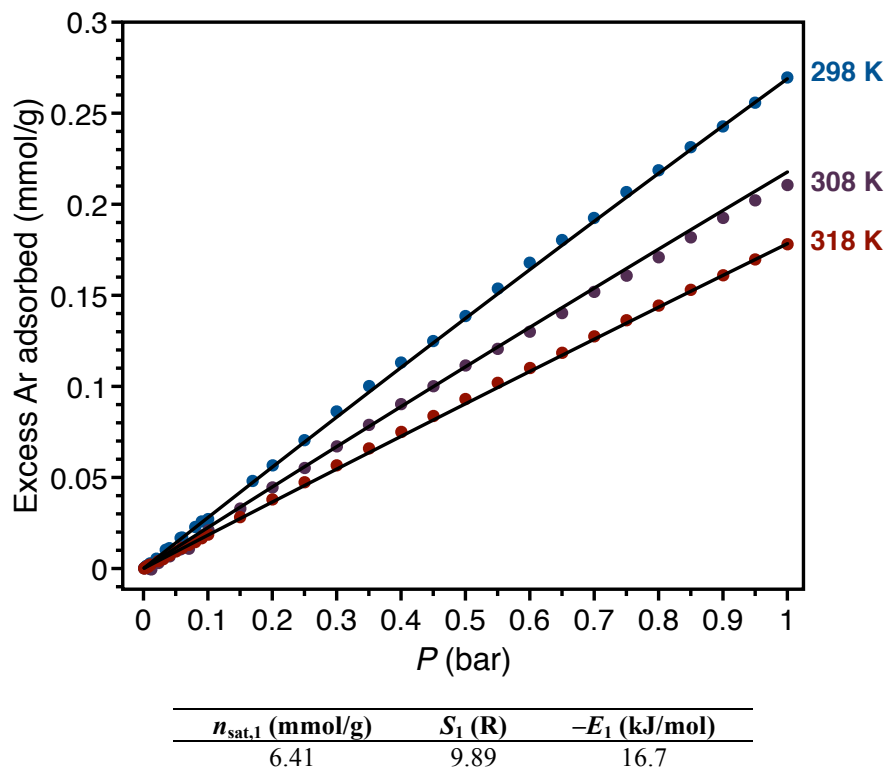
**Figure 2.S16.** Single-site Langmuir fits and parameters for  $\text{O}_2$  adsorption isotherms of  $\text{Co}_2(\text{dobdc})$  at 298.15, 308.15, and 318.15 K (fit simultaneously for all temperatures);  $n_{\text{sat},1}$  is the saturation capacity,  $S_i$  is the site-specific molar entropy of adsorption,  $E_i$  is the site-specific binding energy, and  $R$  is the gas constant in  $\text{J/mol}\cdot\text{K}$ .



$T$ (K)	$n_{\text{sat},1}$ (mmol/g)	$S_1$ (R)	$-E_1$ (kJ/mol)
298.15	6.41	9.88	16.8
308.15	6.41	9.90	16.7
318.15	6.41	9.82	16.6

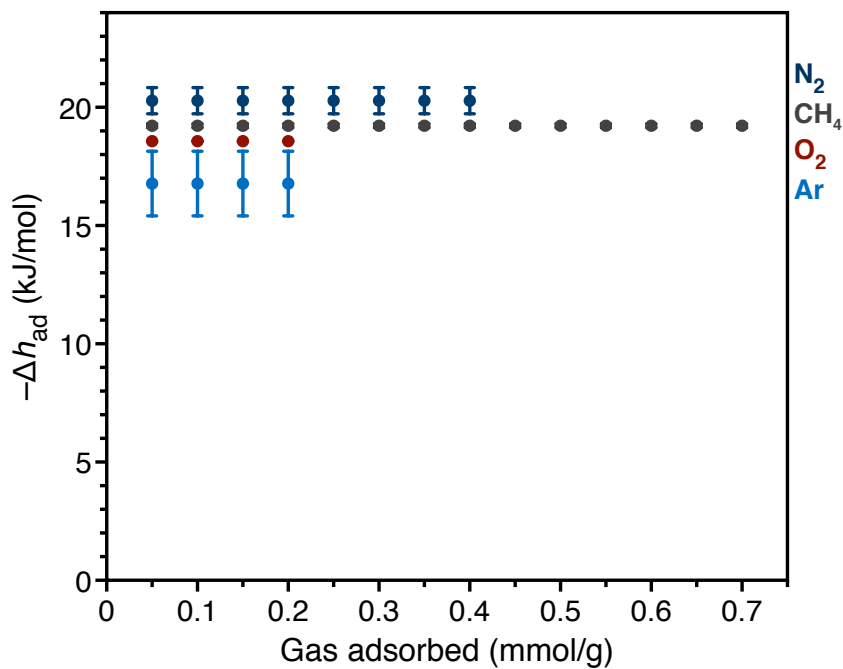
**Figure 2.S17.** Single-site Langmuir fits and parameters for Ar adsorption isotherms of  $\text{Co}_2(\text{dobdc})$  at 298.15, 308.15, and 318.15 K (fit independently for each temperature);  $T$  is the temperature,  $n_{\text{sat},1}$  is the saturation capacity,  $S_i$  is the site-specific molar entropy of adsorption,  $E_i$  is the site-specific binding energy, and  $R$  is the gas constant in  $\text{J/mol}\cdot\text{K}$ .





**Figure 2.S18.** Single-site Langmuir fits and parameters for Ar adsorption isotherms of  $\text{Co}_2(\text{dobdc})$  at 298.15, 308.15, and 318.15 K (fit simultaneously for all temperatures);  $n_{\text{sat},1}$  is the saturation capacity,  $S_1$  is the site-specific molar entropy of adsorption,  $E_1$  is the site-specific binding energy, and  $R$  is the gas constant in  $\text{J/mol}\cdot\text{K}$ .

### 2.6.9. Low-coverage differential enthalpy of adsorption plots for $\text{CO}_2(\text{dobdc})$



**Figure 2.S19.** Low-coverage differential enthalpy of adsorption ( $\Delta h_{\text{ad}}$ ) plots (calculated using independent Langmuir fits to low-pressure adsorption isotherms) for  $\text{CH}_4$  (gray),  $\text{N}_2$  (dark blue),  $\text{O}_2$  (red), and Ar (light blue) adsorption in  $\text{CO}_2(\text{dobdc})$ . Error bars for  $\text{CH}_4$  and  $\text{O}_2$  are smaller than the symbols used for the data.

## 2.7. References

- (1) Yoshizawa, M.; Klosterman, J. K.; Fujita, M. *Angew. Chem. Int. Ed.* **2009**, *48* (19), 3418–3438.
- (2) van der Boom, M. E. *Angew. Chem. Int. Ed.* **2011**, *50* (50), 11846–11848.
- (3) Inokuma, Y.; Kawano, M.; Fujita, M. *Nature Chemistry* **2011**, *3* (5), 349–358.
- (4) Pike, S. D.; Weller, A. S. *Philos Trans A Math Phys Eng Sci* **2015**, *373* (2037), 20140187–20140187.
- (5) Bloch, W. M.; Champness, N. R.; Doonan, C. J. *Angew. Chem. Int. Ed.* **2015**, *54* (44), 12860–12867.
- (6) Albrecht, M.; Lutz, M.; Spek, A.; van Koten, G. *Nature* **2000**, *406* (6799), 970–974.
- (7) Albrecht, M.; Lutz, M.; Schreurs, A. M. M.; Lutz, E. T. H.; Spek, A. L.; Van Koten, G. *J. Chem. Soc., Dalton Trans.* **2000**, No. 21, 3797–3804.
- (8) Atwood, J. L.; Barbour, L. J.; Jerga, A. *Science* **2002**, *296* (5577), 2367–2369.
- (9) O'Neil, A.; Wilson, C.; Webster, J. M.; Allison, F. J.; Howard, J. A. K.; Poliakov, M. *Angewandte Chemie* **2002**, *114* (20), 3950–3953.
- (10) Takamizawa, S.; Nakata, E.-I.; Saito, T.; Kojima, K. *CrystEngComm* **2003**, *5* (72), 411–413.
- (11) Zenkina, O. V.; Keske, E. C.; Wang, R.; Crudden, C. M. *Angew. Chem. Int. Ed.* **2011**, *50* (35), 8100–8104.
- (12) Huang, Z.; White, P. S.; Brookhart, M. *Nature* **2010**, *465* (7298), 598–601.
- (13) Takamizawa, S.; Akatsuka, T.; Ueda, T. *Angew. Chem. Int. Ed.* **2008**, *47* (9), 1689–1692.
- (14) Sundberg, J.; Cameron, L. J.; Southon, P. D.; Kepert, C. J.; McKenzie, C. J. *Chem. Sci.* **2014**, *5*, 4017–4025.
- (15) Kane, C. M.; Banisafar, A.; Dougherty, T. P.; Barbour, L. J.; Holman, K. T. *J. Am. Chem. Soc.* **2016**, *138* (13), 4377–4392.
- (16) Pike, S. D.; Thompson, A. L.; Algarra, A. G.; Apperley, D. C.; Macgregor, S. A.; Weller, A. S. *Science* **2012**, *337* (6102), 1648–1651.
- (17) Pike, S. D.; Chadwick, F. M.; Rees, N. H.; Scott, M. P.; Weller, A. S.; Krämer, T.; Macgregor, S. A. *J. Am. Chem. Soc.* **2015**, *137* (2), 820–833.
- (18) Chadwick, F. M.; Rees, N. H.; Weller, A. S.; Krämer, T.; Iannuzzi, M.; Macgregor, S. A. *Angew. Chem. Int. Ed.* **2016**, *55* (11), 3677–3681.
- (19) Eddaoudi, M.; Kim, J.; Rosi, N.; Vodak, D.; Wachter, J.; O'Keeffe, M.; Yaghi, O. M. *Science* **2002**, *295* (5554), 469–472.
- (20) Cohen, S. M. *Chem. Rev.* **2012**, *112* (2), 970–1000.
- (21) Murray, L. J.; Dincă, M.; Long, J. R. *Chem. Soc. Rev.* **2009**, *38* (5), 1294–1314.
- (22) Mason, J. A.; Veenstra, M.; Long, J. R. *Chem. Sci.* **2014**, *5* (1), 32–51.
- (23) Sumida, K.; Rogow, D. L.; Mason, J. A.; McDonald, T. M.; Bloch, E. D.; Herm, Z. R.; Bae, T.-H.; Long, J. R. *Chem. Rev.* **2012**, *112* (2), 724–781.
- (24) Herm, Z. R.; Bloch, E. D.; Long, J. R. *Chem. Mater.* **2014**, *26* (1), 323–338.
- (25) Ma, L.; Abney, C.; Lin, W. *Chem. Soc. Rev.* **2009**, *38* (5), 1248–1256.
- (26) Corma, A.; García, H.; Llabrés i Xamena, F. X. *Chem. Rev.* **2010**, *110* (8), 4606–4655.
- (27) Wang, C.; Zheng, M.; Lin, W. *J. Phys. Chem. Lett.* **2011**, *2* (14), 1701–1709.
- (28) Cohen, S. M.; Zhang, Z.; Boissonnault, J. A. *Inorg. Chem.* **2016**, *55* (15), 7281–7290.
- (29) Dietzel, P. D. C.; Panella, B.; Hirscher, M.; Blom, R.; Fjellvåg, H. *Chem. Commun.* **2006**, No. 9, 959–961.

- (30) Dietzel, P. D. C.; Johnsen, R. E.; Fjellvåg, H.; Bordiga, S.; Groppo, E.; Chavan, S.; Blom, R. *Chem. Commun.* **2008**, No. 41, 5125–5127.
- (31) Liu, Y.; Kabbour, H.; Brown, C. M.; Neumann, D. A.; Ahn, C. C. *Langmuir* **2008**, *24* (9), 4772–4777.
- (32) McKinlay, A. C.; Xiao, B.; Wragg, D. S.; Wheatley, P. S.; Megson, I. L.; Morris, R. E. *J. Am. Chem. Soc.* **2008**, *130* (31), 10440–10444.
- (33) Dietzel, P. D. C.; Georgiev, P. A.; Eckert, J.; Blom, R.; Strässle, T.; Unruh, T. *Chem. Commun.* **2010**, *46* (27), 4962–4963.
- (34) Bloch, E. D.; Murray, L. J.; Queen, W. L.; Chavan, S.; Maximoff, S. N.; Bigi, J. P.; Krishna, R.; Peterson, V. K.; Grandjean, F.; Long, G. J.; Smit, B.; Bordiga, S.; Brown, C. M.; Long, J. R. *J. Am. Chem. Soc.* **2011**, *133* (37), 14814–14822.
- (35) Sumida, K.; Her, J.-H.; Dincă, M.; Murray, L. J.; Schloss, J. M.; Pierce, C. J.; Thompson, B. A.; FitzGerald, S. A.; Brown, C. M.; Long, J. R. *J. Phys. Chem. C* **2011**, *115* (16), 8414–8421.
- (36) Bloch, E. D.; Queen, W. L.; Krishna, R.; Zadrozny, J. M.; Brown, C. M.; Long, J. R. *Science* **2012**, *335* (6076), 1606–1610.
- (37) Queen, W. L.; Bloch, E. D.; Brown, C. M.; Hudson, M. R.; Mason, J. A.; Murray, L. J.; Ramirez-Cuesta, A. J.; Peterson, V. K.; Long, J. R. *Dalton Trans.* **2012**, *41* (14), 4180–4188.
- (38) Geier, S. J.; Mason, J. A.; Bloch, E. D.; Queen, W. L.; Hudson, M. R.; Brown, C. M.; Long, J. R. *Chem. Sci.* **2013**, *4* (5), 2054–2061.
- (39) Bloch, E. D.; Hudson, M. R.; Mason, J. A.; Chavan, S.; Crocellà, V.; Howe, J. D.; Lee, K.; Dzubak, A. L.; Queen, W. L.; Zadrozny, J. M.; Geier, S. J.; Lin, L.-C.; Gagliardi, L.; Smit, B.; Neaton, J. B.; Bordiga, S.; Brown, C. M.; Long, J. R. *J. Am. Chem. Soc.* **2014**, *136* (30), 10752–10761.
- (40) Xiao, D. J.; Bloch, E. D.; Mason, J. A.; Queen, W. L.; Hudson, M. R.; Planas, N.; Borycz, J.; Dzubak, A. L.; Verma, P.; Lee, K.; Bonino, F.; Crocellà, V.; Yano, J.; Bordiga, S.; Truhlar, D. G.; Gagliardi, L.; Brown, C. M.; Long, J. R. *Nature Chemistry* **2014**, *6* (7), 590–595.
- (41) Furukawa, H.; Gándara, F.; Zhang, Y.-B.; Jiang, J.; Queen, W. L.; Hudson, M. R.; Yaghi, O. M. *J. Am. Chem. Soc.* **2014**, *136* (11), 4369–4381.
- (42) Magdysyuk, O. V.; Adams, F.; Liermann, H.-P.; Spanopoulos, I.; Trikalitis, P. N.; Hirscher, M.; Morris, R. E.; Duncan, M. J.; McCormick, L. J.; Dinnebier, R. E. *Phys. Chem. Chem. Phys.* **2014**, *16* (43), 23908–23914.
- (43) Bloch, W. M.; Burgun, A.; Coghlan, C. J.; Lee, R.; Coote, M. L.; Doonan, C. J.; Sumbly, C. J. *Nature Chemistry* **2014**, *6* (10), 906–912.
- (44) Bloch, E. D.; Queen, W. L.; Chavan, S.; Wheatley, P. S.; Zadrozny, J. M.; Morris, R.; Brown, C. M.; Lamberti, C.; Bordiga, S.; Long, J. R. *J. Am. Chem. Soc.* **2015**, *137* (10), 3466–3469.
- (45) Lee, J. S.; Vlaisavljevich, B.; Britt, D. K.; Brown, C. M.; Haranczyk, M.; Neaton, J. B.; Smit, B.; Long, J. R.; Queen, W. L. *Adv. Mater.* **2015**, *27* (38), 5785–5796.
- (46) Ghose, S. K.; Li, Y.; Yakovenko, A.; Dooryhee, E.; Ehm, L.; Ecker, L. E.; Dippel, A.-C.; Halder, G. J.; Strachan, D. M.; Thallapally, P. K. *J. Phys. Chem. Lett.* **2015**, *6* (10), 1790–1794.
- (47) Murray, L. J.; Dincă, M.; Yano, J.; Chavan, S.; Bordiga, S.; Brown, C. M.; Long, J. R. *J. Am. Chem. Soc.* **2010**, *132* (23), 7856–7857.

- (48) Sumida, K.; Horike, S.; Kaye, S. S.; Herm, Z. R.; Queen, W. L.; Brown, C. M.; Grandjean, F.; Long, G. J.; Dailly, A.; Long, J. R. *Chem. Sci.* **2010**, *1* (2), 184–191.
- (49) Kapelewski, M. T.; Geier, S. J.; Hudson, M. R.; Stück, D.; Mason, J. A.; Nelson, J. N.; Xiao, D. J.; Hulvey, Z.; Gilmour, E.; FitzGerald, S. A.; Head-Gordon, M.; Brown, C. M.; Long, J. R. *J. Am. Chem. Soc.* **2014**, *136* (34), 12119–12129.
- (50) McDonald, T. M.; Mason, J. A.; Kong, X.; Bloch, E. D.; Gygi, D.; Dani, A.; Crocellà, V.; Giordanino, F.; Odoh, S. O.; Drisdell, W. S.; Vlasisavljevich, B.; Dzubak, A. L.; Poloni, R.; Schnell, S. K.; Planas, N.; Lee, K.; Pascal, T.; Wan, L. F.; Prendergast, D.; Neaton, J. B.; Smit, B.; Kortright, J. B.; Gagliardi, L.; Bordiga, S.; Reimer, J. A.; Long, J. R. *Nature* **2015**, *519* (7543), 303–308.
- (51) Hulvey, Z.; Vlasisavljevich, B.; Mason, J. A.; Tsvion, E.; Dougherty, T. P.; Bloch, E. D.; Head-Gordon, M.; Smit, B.; Long, J. R.; Brown, C. M. *J. Am. Chem. Soc.* **2015**, *137* (33), 10816–10825.
- (52) Gygi, D.; Bloch, E. D.; Mason, J. A.; Hudson, M. R.; Gonzalez, M. I.; Siegelman, R. L.; Darwish, T. A.; Queen, W. L.; Brown, C. M.; Long, J. R. *Chem. Mater.* **2016**, *28* (4), 1128–1138.
- (53) Rowsell, J.; Spencer, E. C.; Eckert, J.; Howard, J. *Science* **2005**, *309* (5739), 1350–1354.
- (54) Dietzel, P. D. C.; Morita, Y.; Blom, R.; Fjellvåg, H. *Angew. Chem. Int. Ed.* **2005**, *44* (39), 6354–6358.
- (55) Queen, W. L.; Hudson, M. R.; Bloch, E. D.; Mason, J. A.; Gonzalez, M. I.; Lee, J. S.; Gygi, D.; Howe, J. D.; Lee, K.; Darwish, T. A.; James, M.; Peterson, V. K.; Teat, S. J.; Smit, B.; Neaton, J. B.; Long, J. R.; Brown, C. M. *Chem. Sci.* **2014**, *5* (12), 4569–4581.
- (56) Anderson, J. S.; Gallagher, A. T.; Mason, J. A.; Harris, T. D. *J. Am. Chem. Soc.* **2014**, *136* (47), 16489–16492.
- (57) Gonzalez, M. I.; Bloch, E. D.; Mason, J. A.; Teat, S. J.; Long, J. R. *Inorg. Chem.* **2015**, *54* (6), 2995–3005.
- (58) Trickett, C. A.; Gagnon, K. J.; Lee, S.; Gándara, F.; Buergi, H.-B.; Yaghi, O. M. *Angew. Chem. Int. Ed.* **2015**, *54* (38), 11162–11167.
- (59) Marshall, R. J.; Griffin, S. L.; Wilson, C.; Forgan, R. S. *J. Am. Chem. Soc.* **2015**, *137* (30), 9527–9530.
- (60) Xiao, D. J.; Gonzalez, M. I.; Darago, L. E.; Vogiatzis, K. D.; Haldoupis, E.; Gagliardi, L.; Long, J. R. *J. Am. Chem. Soc.* **2016**, *138* (22), 7161–7170.
- (61) Reed, D. A.; Xiao, D. J.; Gonzalez, M. I.; Darago, L. E.; Herm, Z. R.; Grandjean, F.; Long, J. R. *J. Am. Chem. Soc.* **2016**, *138* (17), 5594–5602.
- (62) Gallagher, A. T.; Kelty, M. L.; Park, J. G.; Anderson, J. S.; Mason, J. A.; Walsh, J. P. S.; Collins, S. L.; Harris, T. D. *Inorg. Chem. Front.* **2016**, *3* (4), 536–540.
- (63) Bhatt, P. M.; Belmabkhout, Y.; Cadiau, A.; Adil, K.; Shekhah, O.; Shkurenko, A.; Barbour, L. J.; Eddaoudi, M. *J. Am. Chem. Soc.* **2016**, *138* (29), 9301–9307.
- (64) Elsaidi, S. K.; Mohamed, M. H.; Simon, C. M.; Braun, E.; Pham, T.; Forrest, K. A.; Xu, W.; Banerjee, D.; Space, B.; Zaworotko, M. J.; Thallapally, P. K. *Chem. Sci.* **2017**, *8* (3), 2373–2380.
- (65) Lin, L.-C.; Lee, K.; Gagliardi, L.; Neaton, J. B.; Smit, B. *J Chem Theory Comput* **2014**, *10* (4), 1477–1488.
- (66) Lee, K.; Isley, W. C.; Dzubak, A. L.; Verma, P.; Stoneburner, S. J.; Lin, L.-C.; Howe, J. D.; Bloch, E. D.; Reed, D. A.; Hudson, M. R.; Brown, C. M.; Long, J. R.; Neaton, J.

- B.; Smit, B.; Cramer, C. J.; Truhlar, D. G.; Gagliardi, L. *J. Am. Chem. Soc.* **2014**, *136* (2), 698–704.
- (67) Lee, K.; Howe, J. D.; Lin, L.-C.; Smit, B.; Neaton, J. B. *Chem. Mater.* **2015**, *27* (3), 668–678.
- (68) Mercado, R.; Vlaisavljevich, B.; Lin, L.-C.; Lee, K.; Lee, Y.; Mason, J. A.; Xiao, D. J.; Gonzalez, M. I.; Kapelewski, M. T.; Neaton, J. B.; Smit, B. *J. Phys. Chem. C* **2016**, *120* (23), 12590–12604.
- (69) Chen, X.; Plonka, A. M.; Banerjee, D.; Krishna, R.; Schaef, H. T.; Ghose, S.; Thallapally, P. K.; Parise, J. B. *J. Am. Chem. Soc.* **2015**, *137* (22), 7007–7010.
- (70) Zhou, W.; Wu, H.; Yildirim, T. *J. Am. Chem. Soc.* **2008**, *130* (46), 15268–15269.
- (71) Caskey, S. R.; Wong-Foy, A. G.; Matzger, A. J. *J. Am. Chem. Soc.* **2008**, *130* (33), 10870–10871.
- (72) Sheldrick, G. M. *CELL NOW V2008/2*; Bruker AXS Inc, 2008.
- (73) Bruker Analytical X-ray Systems, Inc. *SAINTE and APEX 2 Software for CCD Diffractometers*; Bruker Analytical X-ray Systems, Inc.: Madison, WI, USA, 2000.
- (74) Sheldrick, G. M. *TWINABS, Version 2012/1*; University of Göttingen, 2012.
- (75) Sheldrick, G. M. *Acta Crystallogr., A, Found. Crystallogr.* **2008**, *64* (Pt 1), 112–122.
- (76) Sheldrick, G. M. *SHELXS*; University of Göttingen, Germany, 2014.
- (77) Sheldrick, G. M. *SHELXL*; University of Göttingen, Germany: University of Göttingen, Germany, 2014.
- (78) Dolomanov, O. V.; Bourhis, L. J.; Gildea, R. J.; Howard, J. A. K.; Puschmann, H. *Journal of Applied Crystallography* **2009**, *42* (2), 339–341.
- (79) Lemmon, E. W.; Huber, M. L.; McLinden, M. *Reference Fluid Thermodynamic and Transport Properties-REFPROP Version 8.0*; National Institute of Standards and Technology, Standard Reference Data Program: Gaithersburg, 2007.
- (80) Lemmon, E. W.; Span, R. *Journal of Chemical & Engineering Data* **2006**, *51* (3), 785–850.
- (81) Warren, J. E.; Pritchard, R. G.; Abram, D.; Davies, H. M.; Savarese, T. L.; Cash, R. J.; Raithby, P. R.; Morris, R.; Jones, R. H.; Teat, S. J. *Journal of Applied Crystallography* **2009**, *42* (3), 457–460.
- (82) Cox, J. M.; Walton, I. M.; Benson, C. A.; Chen, Y. S.; Benedict, J. B. *Journal of Applied Crystallography* **2015**, *48* (2), 578–581.
- (83) Groom, C. R.; Bruno, I. J.; Lightfoot, M. P.; Ward, S. C. *Acta Crystallogr Sect B Struct Crystallogr Cryst Chem* **2016**, *72* (2), 171–179.
- (84) Ghilardi, C. A.; Midollini, S.; Sacconi, L. *Journal of Organometallic Chemistry* **1980**, *186* (2), 279–287.
- (85) Fernández, P.; Sousa-Pedrares, A.; Romero, J.; Durán, M. L.; Sousa, A.; Pérez-Lourido, P.; García-Vázquez, J. A. *Eur. J. Inorg. Chem.* **2010**, No. 5, 814–823.
- (86) MacKay, B. A.; Fryzuk, M. D. *Chem. Rev.* **2004**, *104* (2), 385–402.
- (87) Fryzuk, M. D.; Johnson, S. A. *Coordination Chemistry Reviews* **2000**, *200-202*, 379–409.
- (88) Khoenkhoen, N.; de Bruin, B.; Reek, J. N. H.; Dzik, W. I. *Eur. J. Inorg. Chem.* **2015**, No. 4, 567–598.
- (89) Niederhoffer, E. C.; Timmons, J. H.; Martell, A. E. *Chem. Rev.* **1984**, *84* (2), 137–203.
- (90) Tovrog, B. S.; Kitko, D. J.; Drago, R. S. *J. Am. Chem. Soc.* **1976**, *98* (17), 5144–5153.
- (91) DeCoste, J. B.; Weston, M. H.; Fuller, P. E.; Tovar, T. M.; Peterson, G. W.; LeVan, M.

- D.; Farha, O. K. *Angew. Chem. Int. Ed.* **2014**, *53* (51), 14092–14095.
- (92) Meek, S. T.; Teich-McGoldrick, S. L.; Perry, J. J. *J. Phys. Chem. C* **2012**, *116* (37), 19765–19772.
- (93) Wu, H.; Zhou, W.; Yildirim, T. *J. Am. Chem. Soc.* **2009**, *131* (13), 4995–5000.
- (94) Seppelt, K. *Z. anorg. allg. Chem.* **2003**, *629* (14), 2427–2430.
- (95) Grochala, W. *Chem. Soc. Rev.* **2007**, *36* (10), 1632–1655.
- (96) Bellert, D.; Breckenridge, W. H. *Chem. Rev.* **2002**, *102* (5), 1595–1622.
- (97) Carnegie, P. D.; Bandyopadhyay, B.; Duncan, M. A. *J. Phys. Chem. A* **2008**, *112* (28), 6237–6243.
- (98) Carnegie, P. D.; Bandyopadhyay, B.; Duncan, M. A. *J. Phys. Chem. A* **2011**, *115* (26), 7602–7609.
- (99) Bandyopadhyay, B.; Duncan, M. A. *Chemical Physics Letters* **2012**, *530* (C), 10–15.
- (100) Lessen, D.; Brucat, P. J. *J. Chem. Phys.* **1989**, *90* (11), 6296–6305.
- (101) Perutz, R. N.; Turner, J. J. *J. Am. Chem. Soc.* **1975**, *97* (17), 4791–4800.
- (102) Mal, P.; Breiner, B.; Rissanen, K.; Nitschke, J. R. *Science* **2009**, *324* (5935), 1697–1699.
- (103) Choi, W.; Ohtsu, H.; Matsushita, Y.; Kawano, M. *Dalton Trans.* **2016**, *45* (15), 6357–6360.
- (104) Simon, A.; Borrmann, H.; Horakh, J. *Eur. J. Inorg. Chem.* **1997**, *130* (9), 1235–1240.
- (105) Peruzzini, M.; Gonsalvi, L.; Romerosa, A. *Chem. Soc. Rev.* **2005**, *34* (12), 1038.
- (106) Luis, P. L.; de los Rios, I.; Peruzzini, M. *Phosphorus Research Bulletin* **2001**, *12* (0), 167–180.
- (107) Sztáray, B.; Szepes, L.; Baer, T. *J. Phys. Chem. A* **2003**, *107* (44), 9486–9490.
- (108) Shannon, R. D. *Acta Crystallographica Section A* **1976**, *32* (5), 751–767.

## Chapter 3. Separation of Xylene Isomers through Multiple Metal Site Interactions in Metal–Organic Frameworks

### 3.1. Introduction

Industrial chemical separations account for 15% of the global energy demand.<sup>1</sup> As a consequence, the development of more energy-efficient separations using adsorbent- or membrane-based technologies represents a key pursuit toward mitigating the continuous rise in worldwide energy consumption.<sup>2</sup> One of the most difficult industrial mixtures to partition consists of the C<sub>8</sub> isomers *o*-xylene, *m*-xylene, *p*-xylene, and ethylbenzene, which are primarily obtained from either reformates or pyrolysis gasoline.<sup>3</sup> Both sources yield mixtures of the four isomers that do not match market demand. For example, of the 39.2 Mt of xylenes produced in 2008, 33.0 Mt was used as pure *p*-xylene, 3.6 Mt as *o*-xylene, 0.4 Mt as *m*-xylene, and the remainder was used directly without separation as mixed xylenes solvent.<sup>4</sup> The large need for pure *p*-xylene stems from its use as a precursor to terephthalic acid, a major feedstock in the production of polyesters and polyamides.<sup>5</sup> The second most valuable isomer, *o*-xylene, is mainly converted to phthalic anhydride, a precursor to plasticizers.<sup>6</sup> Current processes do not isolate ethylbenzene from the C<sub>8</sub> mixture, as the isomer is produced more economically by the alkylation of benzene with ethylene.<sup>7</sup> Optimizing output to meet economic demand requires separation of the desired isomers (mainly *p*-xylene and some *o*-xylene) followed by isomerization of the unwanted fraction back to the thermodynamic mixture.<sup>3</sup>

**Table 3.1.** Physical Properties of the C<sub>8</sub> Alkylaromatics<sup>3,8</sup>

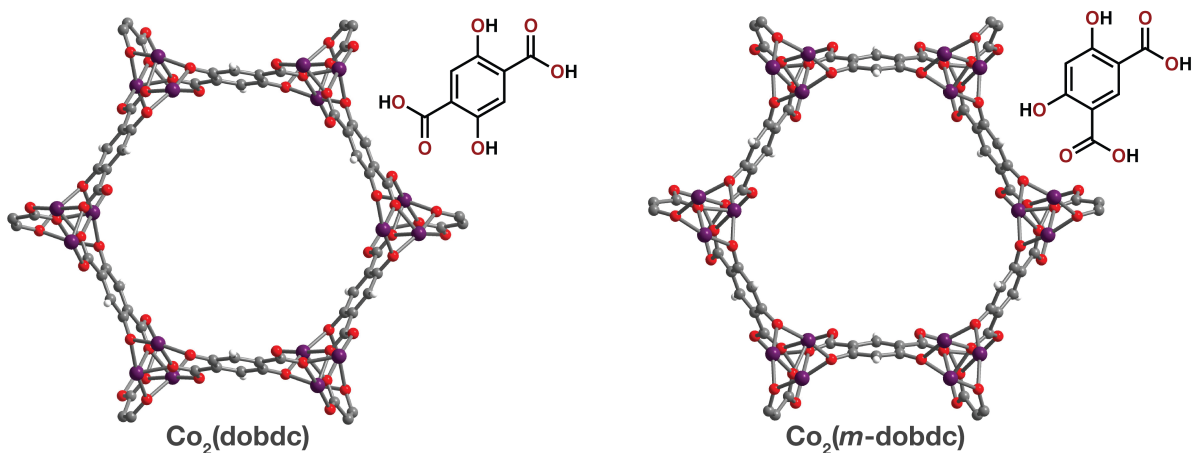
C <sub>8</sub> Isomer	Boiling point (°C)	Kinetic diameter (Å)	Dipole moment (× 10 <sup>18</sup> esu cm)	Polarizability (× 10 <sup>-25</sup> cm <sup>3</sup> )
<i>o</i> -xylene	144.4	6.8	0.649	141–149
<i>m</i> -xylene	139.1	6.8	0.36	142
<i>p</i> -xylene	138.4	5.8	0.1	137–149
ethylbenzene	136.2	5.8	0.59	142

The similar boiling points of the C<sub>8</sub> isomers makes distillative separation of all four nearly impossible, while their comparable sizes and polarizabilities limit the ability of adsorbents to distinguish between the different isomers (Table 3.1). Current state-of-the-art technology involves either crystallization (25% of production) or adsorption (75% of production) to effect separation. Industrial adsorption-based techniques for the production of pure *p*-xylene are carried out in the liquid phase with faujasite-type zeolites using simulated moving bed technology.<sup>5</sup> Although difficult, *o*-xylene can be separated by fractional distillation, while the *m*-xylene and ethylbenzene are obtained using other adsorption- and complexation-based processes, such as the commonly used Parex process from Honeywell UOP.<sup>9</sup> The isolation of all four isomers using a single process has yet to be implemented, prompting research efforts to pursue the development of more efficient technologies. Several studies have focused on improving adsorptive separations with zeolites,<sup>10-13</sup> while more recent work has highlighted membrane-based separations as competitive and less energy-intensive alternatives.<sup>14</sup>

Metal–organic frameworks have previously been studied for the separation of hydrocarbon mixtures such as ethane/ethylene, propane/propylene, and C<sub>6</sub> alkane mixtures, among many others.<sup>15</sup> In particular, some of these materials have been studied for the separation of xylene isomers based on size and shape selectivity.<sup>16-26</sup> For example, the framework V(O)(bdc) (H<sub>2</sub>bdc



= 1,4-benzenedicarboxylic acid) or MIL-47 affords separation based on packing differences and adsorbate–adsorbate interactions upon adsorption,<sup>17</sup> engendering many follow-up studies on both MIL-47<sup>18,19</sup> and its structural analogs M(OH)(bdc) or MIL-53-M (M = Al, Fe).<sup>20,26</sup> In addition, the flexible metal–organic framework Ce(Htcpb) (H<sub>4</sub>tcpb = 1,2,4,5-tetrakis(4-carboxyphenyl)benzene) has been demonstrated to effectively separate the four C<sub>8</sub> isomers through shape-selective conformational changes in response to specific isomers.<sup>25</sup>



**Figure 3.1.** A portion of the crystal structures of Co<sub>2</sub>(dobdc) and Co<sub>2</sub>(*m*-dobdc) (dobdc<sup>4-</sup> = 2,5-dioxido-1,4-benzenedicarboxylate; *m*-dobdc<sup>4-</sup> = 4,6-dioxido-1,3-benzenedicarboxylate); purple, red, gray, and white spheres represent Co, O, C, and H atoms, respectively.

Frameworks bearing coordinatively unsaturated metal centers have been extensively investigated as adsorbents for the separations of small gas molecules, due to the ability of their exposed metal sites to preferentially bind specific gases.<sup>15,27-38</sup> Despite considerable work demonstrating the ability of these materials to separate gas mixtures that are generally difficult to purify, only a limited number of studies have explored their use in the separation of larger molecules such as the C<sub>8</sub> alkylaromatics.<sup>17,24</sup> In one report, the metal–organic framework Ni<sub>2</sub>(dobdc) was shown to separate two-component mixtures of *o*-xylene, *m*-xylene, and *p*-xylene although the exposed nickel(II) coordination sites in this material were thought to play a minor role in the separation.<sup>24</sup> Here, we demonstrate through adsorption and breakthrough measurements coupled with structural characterization by single-crystal X-ray diffraction that the metal–organic frameworks Co<sub>2</sub>(dobdc) and Co<sub>2</sub>(*m*-dobdc) (Figure 3.1) facilitate the separation of the C<sub>8</sub> aromatics through subtle differences in the interaction of two coordinatively unsaturated metal centers with each C<sub>8</sub> molecule. Furthermore, Co<sub>2</sub>(dobdc) undergoes a structural distortion upon binding either *o*-xylene or ethylbenzene, which significantly increases its adsorption capacity for these isomers.

### 3.2. Experimental

**Materials and Methods.** *N,N*-dimethylformamide (DMF), tetrahydrofuran (THF), ethanol, and methanol were obtained from commercial sources and used without further purification. The solvent *n*-heptane, the internal standard *n*-undecane, and the C<sub>8</sub> isomers *o*-xylene, *m*-xylene, *p*-xylene, and ethylbenzene were purchased from Sigma-Aldrich, dried over sodium (*n*-heptane) or 3 Å molecular sieves (undecane, *o*-xylene, *m*-xylene, *p*-xylene, and ethylbenzene), degassed *via* three successive freeze–pump–thaw cycles, and then stored over 3 Å molecular sieves in an N<sub>2</sub>-filled glovebox. The compounds Co(NO<sub>3</sub>)<sub>2</sub>·6H<sub>2</sub>O, Co(acetate)<sub>2</sub>·4H<sub>2</sub>O and 2,5-dihydroxy-1,4-benzenedicarboxylic acid (H<sub>4</sub>dobdc) were purchased from Sigma-Aldrich and used as received. The metal-organic framework Co<sub>2</sub>(dobpdc) (dobpdc<sup>2-</sup> = 4,4'-dioxidobiphenyl-3,3'-dicarboxylate), which is the expanded analogue of Co<sub>2</sub>(dobdc) and the ligand 4,4'-dioxidobiphenyl-3,3'-dicarboxylic acid (H<sub>4</sub>dobpdc) were synthesized according to a previously published procedures as detailed in the Supporting Information.<sup>39</sup>

**Synthesis of H<sub>4</sub>(*m*-dobdc).** Resorcinol (1,3-dihydroxybenzene; 37.6 g, 0.340 mol) was ground and dried under vacuum. KHCO<sub>3</sub> (100 g, 1.00 mmol) was separately ground and dried under vacuum. The two powders were mixed together thoroughly and placed in a glass jar that was sealed in a Parr reaction bomb equipped with an internal thermocouple and a pressure gauge. The reaction bomb was evacuated under vacuum and then dosed with CO<sub>2</sub> to 40 bar pressure. The bomb was heated to 250 °C (measured by the internal thermocouple) in a sand bath for 24 h and then slowly cooled to room temperature. The pressure was vented and water (1 L) was added to the solid in the jar, which was broken up mechanically, followed by sonication of the mixture. This suspension was filtered and the filtrate was acidified with 12 M HCl until reaching a pH < 2 and white solid H<sub>4</sub>(*m*-dobdc) had precipitated. The solid product was collected by filtration. (Yield: 53.2 g, 79 %). <sup>1</sup>H NMR (400 MHz, DMSO-*d*<sub>6</sub>) δ 9.22 (br, 4H), 8.28 (s, 1H), 6.22 (s, 1H); <sup>13</sup>C NMR (400 MHz, DMSO-*d*<sub>6</sub>) δ 172.0, 167.7, 134.3, 107.3, 103.0.

**Synthesis of Co<sub>2</sub>(dobdc).** The framework Co<sub>2</sub>(dobdc) was synthesized using a slight modification to a previously published procedure.<sup>27</sup> A 1 L Pyrex jar was charged with H<sub>4</sub>dobdc (2.23 g, 11.3 mmol), Co(NO<sub>3</sub>)<sub>2</sub>·6H<sub>2</sub>O (10.9 g, 37.5 mmol), and a 1:1:1 (v/v/v) mixture of DMF/ethanol/water (900 mL), and then sealed with a PTFE-lined cap. The resulting mixture was sonicated until all reactants were fully dissolved to form a violet solution. The reaction mixture was then placed in an oven that was preheated to 100 °C and kept at this temperature for 24 h, yielding violet needle-shaped single crystals. The crystals were soaked three times in 1 L of DMF for 24 h at 120 °C, followed by soaking three times in 1 L of methanol at 60 °C. The crystals were then heated at 180 °C under dynamic vacuum for 24 h to give fully-desolvated Co<sub>2</sub>(dobdc). Langmuir surface area (N<sub>2</sub>, 77 K): 1413 m<sup>2</sup>/g.

All the single crystals obtained from the large-scale synthesis of Co<sub>2</sub>(dobdc) were found to exhibit obverse/reverse twinning, which complicated the analysis of structures that showed distortion of the lattice upon soaking with *o*-xylene or ethylbenzene. Non-twinned single-crystals were synthesized using a slight modification to a previously published procedure.<sup>40</sup> A solution of H<sub>4</sub>dobdc (74.3 mg, 0.375 mmol) in THF (2.5 mL) was added to a solution of Co(acetate)<sub>2</sub>·4H<sub>2</sub>O (93.4 mg, 0.375 mmol) in DI H<sub>2</sub>O (2.5 mL) in a PTFE-lined Parr-reactor. The reactor was placed in an oven that was preheated to 110 °C and kept at this temperature for 5 days to give pink needle-shaped single crystals. The crystals were soaked three times in 20 mL of DMF for 24 h at 120 °C, followed by soaking three times in 20 mL of methanol at 60 °C. Fully-desolvated Co<sub>2</sub>(dobdc) single crystals were obtained by heating at 180 °C under dynamic vacuum for 24 h.

**Synthesis of Co<sub>2</sub>(*m*-dobdc).** The framework Co<sub>2</sub>(*m*-dobdc) was synthesized according to literature procedures.<sup>41</sup> A 1 L three-neck round-bottom flask was charged with methanol (310 mL) and DMF (310 mL) and sparged with N<sub>2</sub> for 1 h while stirring. H<sub>4</sub>(*m*-dobdc) (2.00 g, 10.1 mmol) and CoCl<sub>2</sub> (3.27 g, 25.2 mmol) were added and the flask was equipped with a reflux condenser and sealed under N<sub>2</sub>, forming a blue-pink suspension. The reaction mixture was then stirred at 120 °C for 18 h, yielding a pink microcrystalline solid that was isolated by filtration. The powder was soaked in DMF (500 mL) at 60 °C for 24 h, followed by soaking thrice in methanol (500 mL each) for 24 h each at 60 °C. The resulting powder was collected by filtration then heated to 180 °C under dynamic vacuum for 24 h to give fully-desolvated Co<sub>2</sub>(*m*-dobdc). Langmuir surface area (N<sub>2</sub>, 77 K): 1498 m<sup>2</sup>/g.

Single crystals of Co<sub>2</sub>(*m*-dobdc) were prepared by adapting the procedure used for the large-scale synthesis of Co<sub>2</sub>(dobdc). A 100 mL Pyrex jar was charged with H<sub>4</sub>(*m*-dobdc) (198 mg, 1.0 mmol), Co(NO<sub>3</sub>)<sub>2</sub>·6H<sub>2</sub>O (970 mg, 3.33 mmol), and a 1:1:1 (v/v/v) mixture of DMF/ethanol/water (80 mL), and then sealed with a Teflon cap. The resulting mixture was sonicated until all reactants were fully dissolved to form a pink solution. The reaction mixture was then placed in an oven that was preheated to 100 °C and kept at this temperature for 24 h, yielding pink needle-shaped single crystals. The crystals were soaked three times in 100 mL of DMF for 24 h at 120 °C, followed by soaking three times in 100 mL of methanol at 60 °C. Fully desolvated Co<sub>2</sub>(*m*-dobdc) single crystals were obtained by heating at 180 °C under dynamic vacuum for 24 h.

**Synthesis of 4,4'-dihydroxy-(1,1'-biphenyl)-3,3'-dicarboxylic acid (H<sub>4</sub>dobpdc).** This compound was synthesized according to a previously reported procedure.<sup>39</sup> Briefly, 5-bromosalicylic acid (10.0 g, 46.1 mmol) was heated to reflux in methanol (300 mL) with sulfuric acid (10 mL) for 12 h and cooled to room temperature. The solvent was removed with a rotary evaporator, producing a white solid product (methyl 5-bromo-2-hydroxybenzoate). A 500 mL three-neck round bottom flask was then charged with methyl 5-bromo-2-hydroxybenzoate (8.00 g, 34.6 mmol), bi(pinacolato)diboron (8.79 g, 34.6 mmol), potassium acetate (10.2 g, 104 mmol), bis(triphenylphosphine)-palladium dichloride (1.21 g, 1.73 mmol), and 1,4-dioxane (300 mL). The reaction mixture was sparged with argon for 1 h, heated at reflux under inert gas while stirring for 24 h, and cooled to ambient temperature. The solution was filtered and the filtrate was extracted with diethyl ether (3 × 150 mL). Organic extracts were combined, dried over MgSO<sub>4</sub>, and the solvent was removed on a rotary evaporator to yield an off-white crystalline powder (methyl 2-hydroxy-5-(4,4,5,5-tetramethyl-1,3,2-dioxaborola-yl)benzoate).

A 500 mL three-neck round-bottom flask was charged with methyl 5-bromo-2-hydroxybenzoate (5.00 g, 21.6 mmol), methyl 2-hydroxy-5-(4,4,5,5-tetramethyl-1,3,2-dioxaborola-yl)benzoate (6.62 g, 23.8 mmol), potassium carbonate (6.58 g, 47.6 mmol), lithium chloride (0.101 mg, 2.38 mmol), 1,4-dioxane (150 mL), and water (150 mL) and sparged with argon for 1.5 h. Tetrakis(triphenylphosphine)palladium (0.826 g, 0.714 mmol) was added to the reaction mixture while still under argon and the reaction mixture was heated to reflux under inert atmosphere for 24 h, cooled to ambient temperature, and then filtered. The filtrate was acidified to pH = 1 using 12 M HCl, causing a white precipitate to form. This precipitate was collected by filtration to yield a white powder, which is the H<sub>4</sub>(dobpdc) product.

**Synthesis of Co<sub>2</sub>(dobpdc).** This compound was synthesized according to a previously reported procedure.<sup>42</sup> Briefly, H<sub>4</sub>(dobpdc) (41.1, 0.15 mmol), Co(NO<sub>3</sub>)<sub>2</sub>·6H<sub>2</sub>O (109 mg, 0.375 mmol), and 15 mL of 1:1:1 water/DMF/ethanol were added to a 20 mL scintillation vial. The vial was sealed with a PTFE-lined cap, placed in a well plate, and heated to 393 K for 36 h. The

reaction mixture was decanted and the remaining powder was soaked three times in DMF at 60 °C and then three times in methanol at 60 °C, each for 8 h. The pink solid was collected by filtration and desolvated by heating under dynamic vacuum (<10 μbar) at 523 K for 24 h, yielding the fully desolvated Co<sub>2</sub>(dobpdc).

**Single-component Vapor-phase Adsorption Experiments.** Approximately 150 mg of each sample was loaded into a preweighed sample tube in an N<sub>2</sub>-filled glovebox and the sample tubes were capped with a Transeal equipped with Kalrez O-rings. The samples were then transferred to a Micromeritics 2420 instrument degas manifold and heated at a rate of 0.2 °C/min to a temperature of 180 °C while each sample was under vacuum. When a degas rate of <1 μbar/min was achieved, each sample was considered activated. Following this procedure, the sample were transferred to a Micromeritics 3Flex instrument equipped with a vapor dosing tube for single-component xylene adsorption measurements. Each sample tube was subsequently immersed in a temperature-controlled oil bath that surrounded most of the tube. Each xylene was stored over 4 Å molecular sieves prior to being placed in the vapor dosing tube and degassed on the instrument via three freeze–pump–thaw cycles. The vapor dosing tube was then heated to 35 °C with a heating mantle and kept at this temperature for the duration of the experiments. The manifold of the instrument itself was heated to 45 °C to prevent condensation of liquid xylenes. Experiments were conducted with the instrument in fixed pressure incremental dose mode in increments of 0.1 mmol/g. Importantly, each dose was allowed to equilibrate until the change in pressure was below 0.01% of the average pressure measured over 90 s intervals to ensure full equilibration of each isomer with the metal–organic framework adsorbent.

**Multi-component Vapor-phase Breakthrough Experiments.** Breakthrough experiments were carried out using a custom-built breakthrough apparatus consisting of a Swagelok fittings and copper tubing connecting an N<sub>2</sub> cylinder, several valves, a sample holder, and a bubbler to a Perkin Elmer Clarus 500 gas chromatograph (GC). A mixture of *o*-xylene, *m*-xylene, *p*-xylene, and ethylbenzene was loaded into a glass bubbler connected to the setup. Nitrogen (N<sub>2</sub>, 99.999%) was flowed through the bubbler at a rate of 40 mL/min, which was controlled by an MRS mass flow controller. Composition of the four components in the bubbler was adjusted until a 1:1:1:1 mixture was achieved in the vapor phase, as detected by the GC equipped with a Supelco SCOT Bentone 34/DNDP capillary column. Each sample was then loaded into one vertical portion of a U-shaped Swagelok assembly equipped with a fritted gasket to hold the sample in place, then connected to the apparatus and heated to 125 °C. The C<sub>8</sub> mixture from the bubbler was carried by this nitrogen flow through the sample and to the GC, which sampled the effluent gas every 5 min. Peak integration of each sampling event allowed for the determination of the relative amounts of each component over time. Once all four of the C<sub>8</sub> isomers had broken through the column and the starting composition was detected, the flow was switched to pure N<sub>2</sub> and the temperature of the packed bed was increased to 225 °C at a rate of 1 °C/min, while continuing to monitor the eluent from the packed bed by GC.

**Multi-component Liquid-phase Adsorption Experiments.** In an N<sub>2</sub>-filled glovebox, equimolar stock solutions of *o*-xylene, *m*-xylene, *p*-xylene, and ethylbenzene (0.010–1.7 M for each isomer) in dry *n*-heptane were prepared with *n*-undecane (0.01 M) as an internal standard. For each concentration, a 250 μL aliquot of C<sub>8</sub> isomer solution was added to a pre-weighed (~20 mg in most cases) sample of Co<sub>2</sub>(dobdc) in a 4 mL vial. Each sample vial was sealed with a PTFE-lined cap and kept at 33 °C for 24 h. The concentrations of both the stock solution and the solution over the Co<sub>2</sub>(dobdc) were both analyzed by gas chromatography using an SRI instruments 8610V GC equipped with a Supelco SCOT Bentone 34/DNDP capillary column and

a Cobra autosampler. The amount of each isomer adsorbed was then calculated from the difference between the initial and equilibrium concentration of the isomer and the mass of the Co<sub>2</sub>(dobdc) sample. Two-component selectivities,  $S$ , were calculated according to eq 1, where  $q_i$  and  $q_j$  represent the quantity adsorbed for components  $i$  and  $j$ , respectively, while  $C_i$  and  $C_j$  represent the equilibrium concentration for components  $i$  and  $j$ , respectively.

$$S = \frac{q_i/q_j}{c_i/c_j} \quad (1)$$

**Single-crystal X-ray Diffraction.** In an N<sub>2</sub>-filled glovebox, fully-desolvated single crystals of either Co<sub>2</sub>(dobdc) or Co<sub>2</sub>(*m*-dobdc) were soaked in ~3 mL of *o*-xylene, *m*-xylene, *p*-xylene, or ethylbenzene for at least 24 h at 33 °C in 4 mL vials sealed with teflon-lined caps. Sample vials were kept sealed and taken out of the glove box prior to data collection. Immediately after opening the sample vial, crystals were coated with Paratone-N oil, mounted on MiTeGen loops, and then cooled to 100 K using an Oxford Cryostreams cryostrem for data collection. X-ray diffraction data for all samples were collected at Beamline 11.3.1 at the Advanced Light Source, Lawrence Berkeley National Laboratory using synchrotron radiation ( $\lambda = 0.8856 \text{ \AA}$  for Co<sub>2</sub>(dobdc)·0.99(*o*-xylene), Co<sub>2</sub>(dobdc)·0.36(ethylbenzene), Co<sub>2</sub>(dobdc)·0.82(*p*-xylene), and Co<sub>2</sub>(*m*-dobdc)(H<sub>2</sub>O)<sub>0.61</sub>·0.77(ethylbenzene);  $\lambda = 0.7749 \text{ \AA}$  for Co<sub>2</sub>(dobdc)·0.74(*m*-xylene), Co<sub>2</sub>(*m*-dobdc)·0.92(*o*-xylene)) with a Bruker D8 diffractometer equipped with a Bruker PHOTON100 CMOS detector.

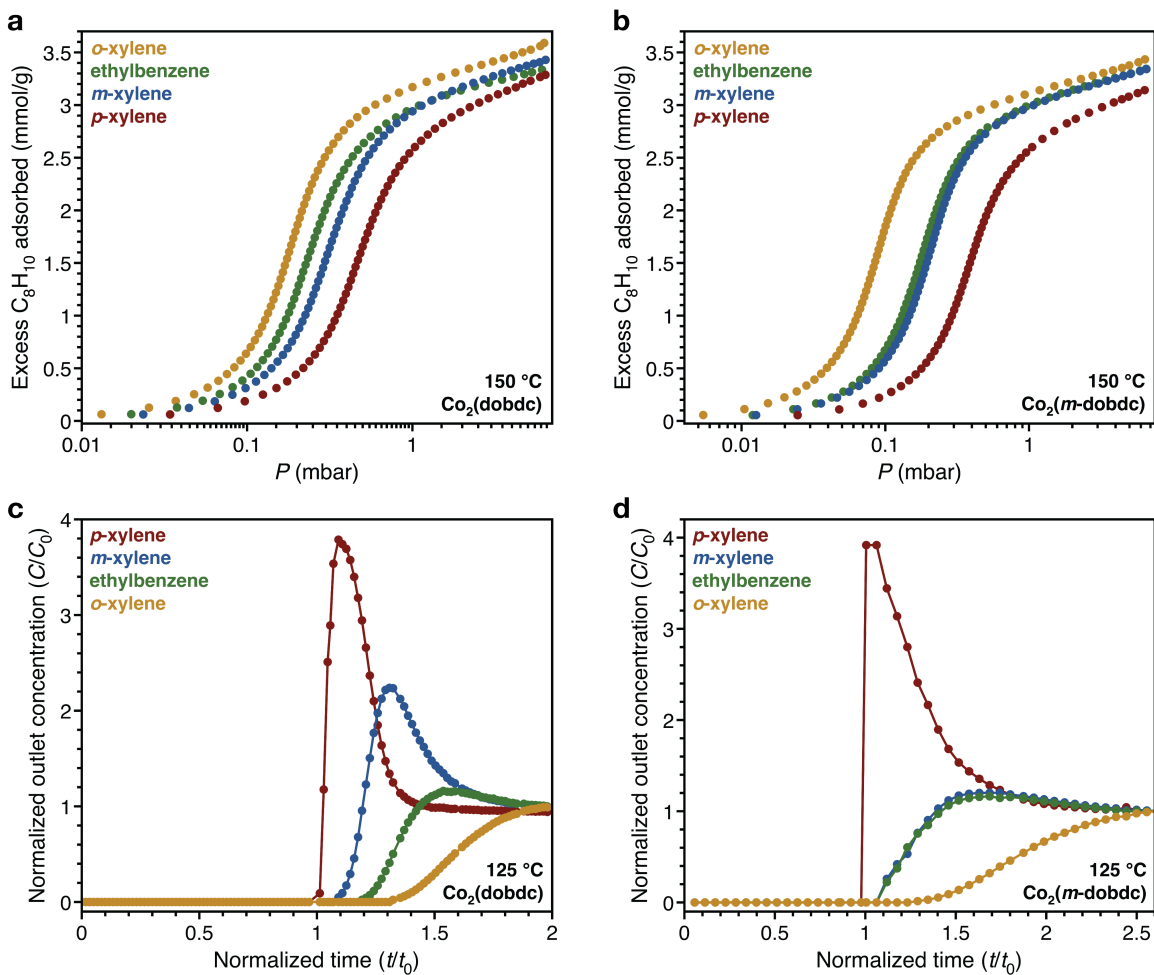
Raw data were integrated and corrected for Lorentz and polarization effects using Bruker AXS SAINT<sup>43</sup> software and corrected for absorption using SADABS.<sup>44</sup> The structures were solved using direct methods with SHELXS<sup>45,46</sup> or intrinsic phasing using SHELXT<sup>47</sup> and refined using SHELXL<sup>45,48</sup> operated in the OLEX2 interface.<sup>49</sup> Thermal parameters were refined anisotropically for all non-hydrogen atoms. In all structures, disorder of the C<sub>8</sub> isomers required the use of displacement parameter and distance restraints. In some cases, the disorder was so severe that geometric constraints were necessary to model the aromatic ring of the C<sub>8</sub> isomers. All hydrogen atoms were refined using the riding model. In the presence of either *o*-xylene or ethylbenzene, Co<sub>2</sub>(dobdc) undergoes a structural distortion that involves the elongation of three out of four hexagonal channels along the direction normal to two opposing walls of the pore. This distortion results in the formation of a supercell, characterized by the doubling of both the *a* and *b* edges of the undistorted structure. Refinement of the distorted structures (Co<sub>2</sub>(dobdc)·0.99(*o*-xylene) and Co<sub>2</sub>(dobdc)·0.36(ethylbenzene)) revealed significant residual electron density at positions that match the structure of the undistorted framework (Figures 3.S10 and 3.S11), suggesting that a small fraction of these crystals remain undistorted. This likely arises from defects in the crystals where the cobalt(II) sites are inaccessible, which has been reported in the M<sub>2</sub>(dobdc) series of metal–organic frameworks based on gas adsorption measurements.<sup>32</sup> A suitable structural model that accounts for this electron density could not be generated, leading to high *R*-factors for both structures.

**Powder X-ray Diffraction.** In an N<sub>2</sub>-filled glovebox, single crystals of Co<sub>2</sub>(dobdc) were ground into a microcrystalline powder and soaked for 24 h in 3 mL of *o*-xylene, *m*-xylene, *p*-xylene, or ethylbenzene. The soaked samples were then quickly filtered, taking care not to completely dry the powder, and loaded into 1.5 mm quartz capillaries that were flame-sealed. Powder X-ray diffraction data were collected on Beamline 17-BM-B at the Advanced Photon Source (APS) at Argonne National Laboratory with a wavelength of 0.75009 Å. A standard peak search, followed by indexing via the Single Value Decomposition approach,<sup>50</sup> as implemented in

TOPAS-Academic,<sup>51</sup> allowed the determination of approximate unit cell dimensions. Precise unit cell dimensions were determined by performing a structureless Le Bail refinement in TOPAS-Academic.

### 3.3. Results and Discussion

#### 3.3.1. C<sub>8</sub> Isomer Adsorption Experiments



**Figure 3.2.** Single-component vapor-phase *o*-xylene (yellow), ethylbenzene (green), *m*-xylene (blue), and *p*-xylene (red) adsorption isotherms for Co<sub>2</sub>(dobdc) (a) and Co<sub>2</sub>(*m*-dobdc) (b) at 150 °C. Multi-component vapor-phase breakthrough measurements for an equimolar mixture of *o*-xylene (yellow), ethylbenzene (green), *m*-xylene (blue), and *p*-xylene (red) vapor with Co<sub>2</sub>(dobdc) (c) and Co<sub>2</sub>(*m*-dobdc) (d) at 125 °C. To facilitate comparisons between the two breakthrough experiments, time is normalized by assigning the time of *p*-xylene breakthrough as  $t_0$ .

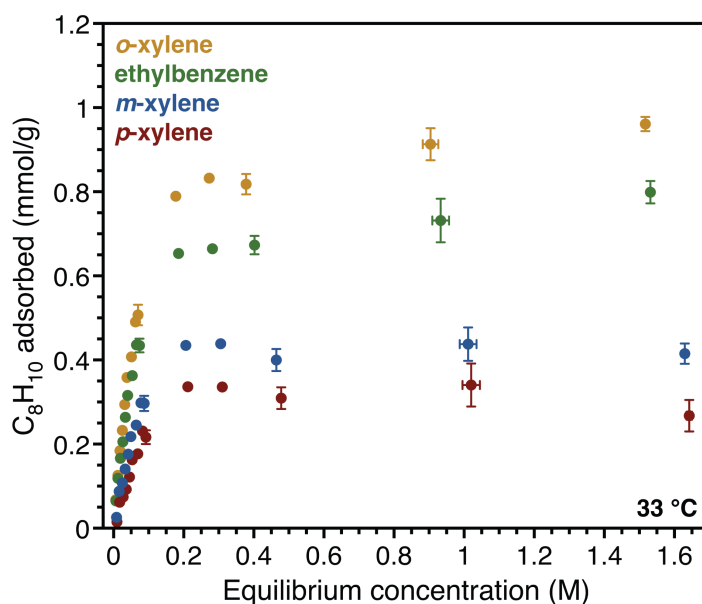
The isomeric metal–organic frameworks Co<sub>2</sub>(dobdc) and Co<sub>2</sub>(*m*-dobdc) both possess 1-D hexagonal channels lined with a high density of coordinatively unsaturated cobalt(II) centers.<sup>27,41</sup> To determine the ability of these frameworks to distinguish the four C<sub>8</sub> isomers, single-component adsorption isotherms were collected at 150 °C. Comparison of the adsorption isotherms for Co<sub>2</sub>(dobdc) (Figure 3.2a) reveals that the affinity of the framework for each isomer follows the trend *o*-xylene > ethylbenzene > *m*-xylene > *p*-xylene, suggesting that all four isomers can be separated by the framework. In contrast, the order of adsorption strength in

Co<sub>2</sub>(*m*-dobdc) is *o*-xylene > ethylbenzene ≈ *m*-xylene > *p*-xylene (Figure 3.2b), which indicates that the framework cannot discriminate between ethylbenzene and *m*-xylene despite having a structure similar to Co<sub>2</sub>(dobdc). Previous work has shown that Ni<sub>2</sub>(dobdc) exhibits the same trend in affinity for *o*-xylene, *m*-xylene, and *p*-xylene.<sup>24</sup> Both cobalt frameworks show saturation capacities that range from 3.1–3.6 mmol/g at ~7 mbar, which are much higher than those reported for the Ni variant (1.9–2.1 mmol/g), and correspond to the adsorption of one xylene molecule per two metal centers (3.2 mmol/g). Notably, Co<sub>2</sub>(dobdc) and Co<sub>2</sub>(*m*-dobdc) also display greater volumetric capacities (3.8–4.2 mmol/cm<sup>3</sup>) than those reported for the industrially relevant faujasite-type zeolites (2.4–2.8 mmol/cm<sup>3</sup> of NaY).<sup>5,24,52,53</sup> In general, the adsorption isotherms for the C<sub>8</sub> isomers in Co<sub>2</sub>(dobdc) and Co<sub>2</sub>(*m*-dobdc) show considerable uptake at low pressures (0.1 to 1 mbar) and relatively high temperature, indicating strong interactions between the framework and the alkylaromatics. Additional single-component isotherms were collected at 140, 150, and 160 °C (Figures 3.S18 and 3.S19) for each C<sub>8</sub> isomer in both frameworks to determine differential enthalpies of adsorption, which range from  $-63 \pm 4$  kJ/mol (for ethylbenzene) to  $-77 \pm 6$  kJ/mol (for *o*-xylene) in Co<sub>2</sub>(dobdc) and  $-67 \pm 2$  kJ/mol (for *p*-xylene) to  $-81 \pm 1$  kJ/mol (for ethylbenzene) in Co<sub>2</sub>(*m*-dobdc) at about half saturation capacity (Figure 3.S20). The large errors associated with the calculated enthalpies preclude meaningful comparisons between the different isomers, although these highly exothermic adsorption enthalpies are consistent with the steep adsorption isotherms and likely arise from a combination of multiple framework–guest interactions.

Multi-component vapor-phase breakthrough measurements were performed on Co<sub>2</sub>(dobdc) and Co<sub>2</sub>(*m*-dobdc) to evaluate their performance in separating an actual mixture of the four C<sub>8</sub> alkylaromatics. In these experiments, N<sub>2</sub> was bubbled through a mixture of *o*-xylene, *m*-xylene, *p*-xylene, and ethylbenzene to produce an equimolar vapor mixture that was subsequently flowed through approximately 1 g of each material at 125 °C. The components of the eluent from the sample columns were determined via gas chromatography and plotted as a function of normalized time (Figure 3.2c). Consistent with the order of adsorption strengths determined from the single-component adsorption isotherms, *p*-xylene breaks through the Co<sub>2</sub>(dobdc) column first followed by *m*-xylene, ethylbenzene, and finally *o*-xylene. In contrast, as predicted in the single-component adsorption isotherms, the breakthrough profile of Co<sub>2</sub>(*m*-dobdc) shows the elution of *p*-xylene first, followed by *m*-xylene and ethylbenzene simultaneously, then *o*-xylene last (Figure 3.2d). Overall, these experiments establish that a four-component mixture of the C<sub>8</sub> isomers can be partitioned in Co<sub>2</sub>(dobdc), whereas Co<sub>2</sub>(*m*-dobdc) can separate all isomers except ethylbenzene and *m*-xylene.

Although the breakthrough measurements clearly demonstrate separation of the four C<sub>8</sub> isomers in Co<sub>2</sub>(dobdc), this experiment was conducted under adsorbate concentrations (~9–13 mbar partial pressure for each isomer) that are much lower than those of current adsorption-based processes, which typically operate in the liquid phase.<sup>5</sup> As the selectivity of an adsorbent can show strong dependence on feed concentration,<sup>19</sup> Co<sub>2</sub>(dobdc) was further evaluated through liquid-phase batch adsorption experiments at 33 °C using equimolar solutions of the four isomers (0.040–6.8 M total concentration) in *n*-heptane. The results of these measurements confirm that Co<sub>2</sub>(dobdc) maintains its separation performance over a wide range of concentrations (Figure 3.3 and Figure 3.S22), even approaching that of a pure xylenes mixture (~8 M total concentration). The selectivities calculated from these liquid-phase adsorption experiments (Table 3.2) agree well with the trends observed in both the single-component vapor-phase adsorption experiments and the multi-component breakthrough experiments. At the highest total concentration (6.8 M;

1.7 M in each isomer),  $\text{Co}_2(\text{dobdc})$  is most selective for *o*-xylene over *p*-xylene ( $3.9 \pm 0.5$ ) and least selective for *o*-xylene over ethylbenzene ( $1.21 \pm 0.02$ ). Comparable values have been reported for two-component mixtures of *o*-xylene, *m*-xylene, and *p*-xylene in  $\text{Ni}_2(\text{dobdc})$ .<sup>24</sup>



**Figure 3.3.** Multi-component liquid-phase *o*-xylene (yellow), ethylbenzene (green), *m*-xylene (blue), and *p*-xylene (red) adsorption measurements for  $\text{Co}_2(\text{dobdc})$  at 33 °C using equimolar solutions of the four isomers in *n*-heptane. Data points with error bars (for measurements with initial  $\text{C}_8$  isomer concentrations of 0.010, 0.050, 0.10, 0.50, 1.0, and 1.7 M) were determined from an average of three replications. The error bars for data points obtained from measurements with an initial concentration of 0.010 M are smaller than the markers.

**Table 3.2.**  $\text{C}_8$  Isomer Selectivities of  $\text{Co}_2(\text{dobdc})^a$

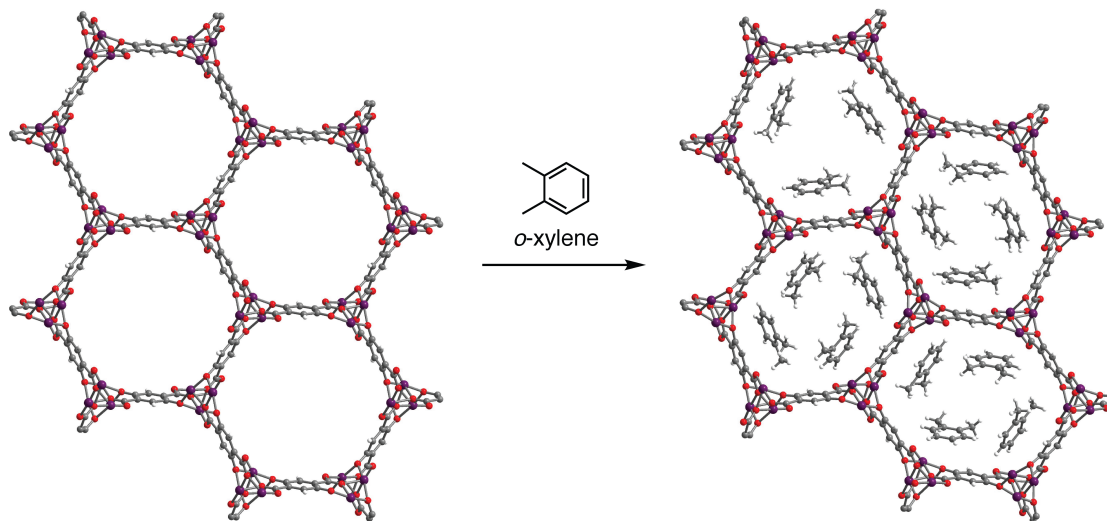
$\text{C}_8$ isomers	Selectivity
<i>o</i> -xylene/ <i>m</i> -xylene	$2.5 \pm 0.1$
<i>o</i> -xylene/ <i>p</i> -xylene	$3.9 \pm 0.5$
<i>o</i> -xylene/ethylbenzene	$1.21 \pm 0.02$
ethylbenzene/ <i>m</i> -xylene	$2.05 \pm 0.05$
ethylbenzene/ <i>p</i> -xylene	$3.21 \pm 0.4$
<i>m</i> -xylene/ <i>p</i> -xylene	$1.6 \pm 0.2$

<sup>a</sup>Determined from a multi-component liquid-phase adsorption experiment with equimolar amounts of the  $\text{C}_8$  isomers (1.7 M in each isomer; 6.8 M total concentration) in *n*-heptane at 33 °C.

The above data suggest that  $\text{Co}_2(\text{dobdc})$  could facilitate the separation of all four  $\text{C}_8$  isomers in a single industrial adsorption process, which would be especially useful for obtaining ethylbenzene from  $\text{C}_8$  mixtures. Although unable to separate all four isomers,  $\text{Co}_2(m\text{-dobdc})$  could conceivably be applicable in current xylenes separation processes, wherein the *p*-xylene and *o*-xylene are obtained by separation and the mixture of *m*-xylene and ethylbenzene are regioisomerized to the equilibrium mixture. In addition,  $\text{Co}_2(m\text{-dobdc})$  and its isostructural analogs with other metal cations also offer the advantage of combining high adsorption performance with low materials cost compared to that of other metal–organic frameworks.<sup>54</sup> The selectivity of both cobalt frameworks for the other isomers over *p*-xylene could even be used in the separation of these components from the 90+% *p*-xylene product mixtures of toluene disproportionation processes.<sup>55</sup>



### 3.3.2. Structural Characterization of C<sub>8</sub> Isomer Adsorption



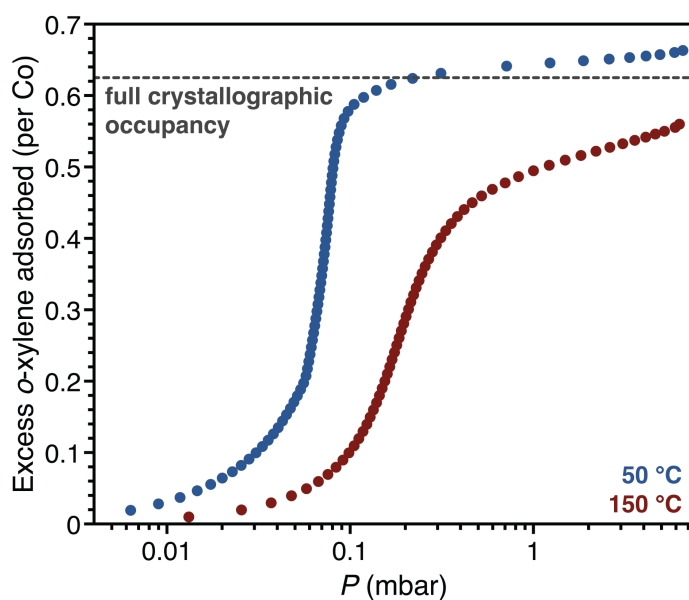
**Figure 3.4.** Structural distortion of Co<sub>2</sub>(dobdc) upon adsorption of *o*-xylene as determined by single-crystal X-ray diffraction at 100 K. Three out of four channels distort to accommodate an additional equivalent of *o*-xylene. The *o*-xylene molecules in the undistorted pore were found to be disordered over two sets of locations due to the  $\bar{3}$  symmetry of the framework, but only one set is shown here for clarity. Purple, red, gray, and white spheres represent Co, O, C, and H atoms, respectively.

Single-crystal X-ray diffraction studies were performed to elucidate the structural features that underlie the ability of these frameworks to bind and differentiate the C<sub>8</sub> isomers. In general, structures were obtained from data collected at 100 K on single crystals that were soaked for ~24 h in an aliquot of each C<sub>8</sub> alkylaromatic. Contrary to the structural rigidity maintained by the M<sub>2</sub>(dobdc) series of metal–organic frameworks upon adsorption of different small molecules,<sup>29-32,35,56-70</sup> Co<sub>2</sub>(dobdc) exhibits appreciable flexibility upon adsorption of the two strongest binding isomers, *o*-xylene and ethylbenzene. Upon binding either of these isomers, three out of every four pores in the framework elongate along the direction perpendicular to two opposing edges of a hexagonal channel (Figure 3.4). The arrangement of six deformed channels around a single undistorted channel maintains the  $R\bar{3}$  symmetry of the lattice but lowers its translational symmetry, which manifests in the formation of a supercell with *a* and *b* edges that are double that of the undistorted framework. Notably, these experimental results corroborate computational work predicting similar adsorbate-induced lattice distortions in expanded variants of this framework.<sup>71</sup>

Remarkably, the distorted pores in the *o*-xylene structure accommodate four xylene molecules relative to the three adsorbed in an undistorted channel, resulting in three distinct binding sites for *o*-xylene in the framework (Figure 3.4 and Figure 3.S3). Two cobalt(II) centers interact with a single *o*-xylene molecule at two of these sites, one located in a deformed channel and the other in an undistorted channel. In the third site, *o*-xylene binds to only a single cobalt(II) center through  $\eta^2$  coordination of the aromatic ring. Only one binding site was resolved in the structure of ethylbenzene in Co<sub>2</sub>(dobdc), which is located in the distorted pore of the framework (Figure 3.S5). In contrast, no framework distortion occurs when *m*-xylene or *p*-xylene bind to Co<sub>2</sub>(dobdc), and for these isomers only one xylene molecule is adsorbed for every two cobalt sites at full occupancy (Figure 3.S1 and 3.S2), consistent with the saturation capacities measured

from the single-component adsorption isotherms.

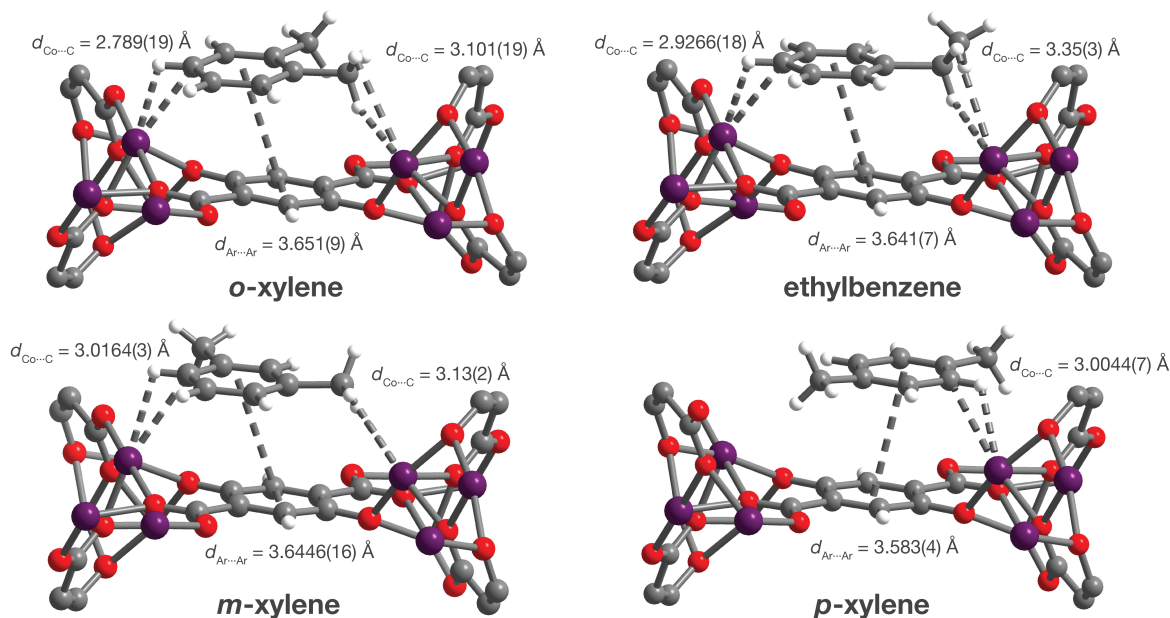
In the *o*-xylene and ethylbenzene structures, the two cobalt centers interacting with a single molecule in the distorted channels are brought  $\sim 0.2$  Å closer together than in the activated framework (7.854(2) Å with *o*-xylene and 7.897(3) Å with ethylbenzene compared to 8.0771(12) Å). This contraction leads to closer contact between the exposed cobalt sites and the adsorbate, resulting in greater stabilization of the adsorbed *o*-xylene or ethylbenzene. As framework distortion only occurs upon adsorption of the two strongest binding isomers, we can infer that this structural change requires sufficiently strong framework–guest interactions, while the tight packing of *o*-xylene molecules in the deformed channels also suggest that guest–guest interactions also play a key role. Altogether, these structural results indicate that distortion of the framework is governed by an interplay between the energetic penalty incurred upon deformation and the thermodynamic stability gained through enhanced framework–guest interactions and the adsorption of additional molecules upon distortion.



**Figure 3.5.** Comparison of the *o*-xylene adsorption isotherms for  $\text{Co}_2(\text{dobdc})$  at 50 °C (blue) and 150 °C (red). The saturation capacity at 50 °C corresponds well with full crystallographic occupancy of all the *o*-xylene sites in the structure of *o*-xylene in  $\text{Co}_2(\text{dobdc})$  at 100 K, whereas the capacity at 150 °C matches a loading of one *o*-xylene per two cobalt sites in an undistorted pore.

To determine if the structural distortion of  $\text{Co}_2(\text{dobdc})$  occurs at temperatures relevant of those used to evaluate  $\text{C}_8$  isomer separation, we carried out variable-temperature powder X-ray diffraction studies on *o*-xylene- and ethylbenzene-soaked samples of the framework from 27–127 °C (Figures 3.S23 and 3.S24). These experiments revealed that the distortion only happens at temperatures well below the those of the single-component adsorption isotherms (150 °C) and breakthrough measurements (125 °C). Specifically, *o*-xylene induces framework distortion at temperatures lower than or equal to 67 °C, while the ethylbenzene-soaked sample remained undistorted even as low as 27 °C. Moreover, diffraction experiments at 100 K on single crystals taken from the multi-component liquid-phase batch adsorption measurements showed no evidence of the distortion, indicating that the presence of the other isomers prevents *o*-xylene and ethylbenzene from distorting the framework. Thus, the observed separation performance of  $\text{Co}_2(\text{dobdc})$  under the conditions of the breakthrough and liquid-phase adsorption experiments

cannot be attributed to the flexibility of the framework. Comparing the *o*-xylene adsorption isotherms at 50 °C and 150 °C, however, demonstrates the distortion does impact the adsorption properties of the framework. Indeed, the saturation capacity at 150 °C corresponds to the loading of one *o*-xylene per two cobalt sites in the undistorted pore (3.2 mmol *o*-xylene), whereas the isotherm at 50 °C displays the anticipated 25% increase in capacity that accompanies the distortion (Figure 3.5).



**Table 3.3.** A portion of the structures of *o*-xylene, ethylbenzene, *m*-xylene, and *p*-xylene in Co<sub>2</sub>(dobdc) at 100 K as determined through analysis of single-crystal X-ray diffraction data, showing the interactions of each isomer with two exposed cobalt(II) sites and the linker arene ring. The structures shown for *o*-xylene and ethylbenzene correspond to binding sites within the distorted hexagonal channels. Two additional binding sites were located for *o*-xylene (Figure 3.S2). Purple, red, gray, and white spheres represent Co, O, C, and H atoms, respectively.

Comparison of the structures of the four isomers in Co<sub>2</sub>(dobdc) at 100 K reveals that each isomer interacts with both the exposed cobalt(II) sites and the linker aromatic rings (Figure 3.6). All four isomers display comparable arene  $\pi$ - $\pi$  interactions with the dobdc<sup>4-</sup> linker, with centroid-to-centroid distances that span from 3.583(4) Å (*p*-xylene) to 3.651(9) Å (*o*-xylene). The similarity of these distances and lack of an apparent trend with binding affinity suggest that  $\pi$ - $\pi$  interactions do not contribute significantly to the xylene isomer selectivity. In contrast, clear differences can be identified in the interactions of each isomer with the exposed cobalt(II) sites in the framework. Significantly, *o*-xylene, ethylbenzene, and *m*-xylene are capable of interacting with two cobalt(II) centers on opposite ends of a linker, whereas *p*-xylene, the weakest binding isomer, interacts with only a single metal site. Two of the binding sites for *o*-xylene feature the interaction of a methyl group and an aryl C-H group at the 1 and 4 positions of the *o*-xylene ring with two cobalt(II) centers on opposing sides of a dobdc<sup>4-</sup> linker (Figure 3.6 and Figure 3.S2), with Co $\cdots$ C<sub>methyl</sub> distances of 3.101(18) Å and 3.13(5) Å and Co $\cdots$ C<sub>aryl</sub> distances of 2.789(19) Å and 2.9130(18) Å, respectively. These distances are much longer than those observed for agostic interaction in alkyl and aryl complexes,<sup>72-78</sup> indicating that the xylene molecule binds through weak non-covalent interactions that arise from polarization by the exposed partial positive charge on the cobalt centers. We note that although another binding mode was identified for *o*-xylene in the distorted structure of Co<sub>2</sub>(dobdc) (Figure 3.S4), this site is less relevant as the distortion does

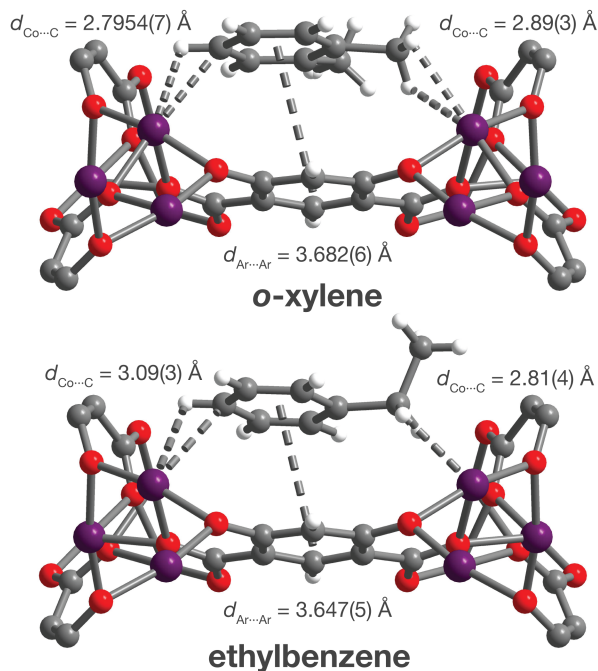
not occur under the conditions of the multi-component separation.

Ethylbenzene also interacts with two metal sites through a benzylic carbon and an opposing aryl C–H group. Both interactions are longer than those observed with *o*-xylene, in line with the lower affinity of Co<sub>2</sub>(dobdc) for ethylbenzene (Figure 3.6). These comparatively weaker Co<sup>II</sup>–ethylbenzene interactions likely result from the additional steric bulk of the ethyl group, which prevents closer approach of molecule to the cobalt sites and is evident in the much longer Co···C<sub>benzyl</sub> distance (3.35(3) Å) of ethylbenzene compared to the Co···C<sub>methyl</sub> distance of *o*-xylene (3.101(8) Å).

The second weakest adsorbing isomer, *m*-xylene, also binds to two cobalt(II) sites through opposing alkyl and aryl C–H groups. In comparison to *o*-xylene and ethylbenzene, *m*-xylene exhibits a longer Co···C<sub>aryl</sub> distance of 3.0164(3) Å, which is attributed to steric repulsion between the adjacent methyl group and a linker oxygen atom that is only 3.34(3) Å away. The longer Co···C<sub>aryl</sub> distance suggests that a weaker Co<sup>II</sup>–aryl interaction leads to the lower affinity of the framework for this isomer.

The 1,4 substitution of *p*-xylene causes it to be too long to adopt the same orientation as the other C<sub>8</sub> isomers, precluding its interaction with two metal sites. As a consequence, this isomer is only stabilized by the interaction of an aryl C–H group with a single cobalt(II) center and an arene π–π interaction with the linker. The absence of a second Co<sup>II</sup>–*p*-xylene interaction results in this isomer binding the weakest to Co<sub>2</sub>(dobdc). Single-component adsorption isotherms from an expanded analog of this material, Co<sub>2</sub>(dobpdc) (dobpdc<sup>4-</sup> = 4,4'-dioxidobiphenyl-3,3'-dicarboxylate),<sup>39</sup> corroborate that interaction with only a single metal site leads to weaker adsorption of the C<sub>8</sub> isomers, as the longer distances between the two cobalt(II) centers across each linker in this material prevent any of the four isomers from interacting with both cobalt sites (Figure 3.S21).

Interestingly, Co<sub>2</sub>(*m*-dobdc) does not exhibit pore distortion upon binding any of the isomers at the studied temperatures. The lack of any observed distortion likely arises from the closer distance of the cobalt(II) centers in Co<sub>2</sub>(*m*-dobdc) (7.7923(15) Å) compared to Co<sub>2</sub>(dobdc) (8.0771(12) Å). This difference of ~0.2 Å matches well with the observed change in Co···Co distance upon framework distortion in Co<sub>2</sub>(dobdc) and likely precludes the need for a distortion to maximize the interaction between two metal sites and a single C<sub>8</sub> molecule in Co<sub>2</sub>(*m*-dobdc). Furthermore, this difference in behavior between the isomeric frameworks highlights that subtle changes in structure can affect their properties. As in Co<sub>2</sub>(dobdc), *o*-xylene and ethylbenzene were also observed to bind to two cobalt(II) sites in Co<sub>2</sub>(*m*-dobdc) through the interaction of an alkyl group and an aryl C–H group (Figure 3.7), resulting in three binding sites in each hexagonal channel related by three-fold symmetry (Figures 3.S6 and 3.S7). The stronger binding isomer, *o*-xylene, displays a shorter Co···C<sub>aryl</sub> distance (2.7953(7) Å) and a similar Co···C<sub>alkyl</sub> distance (2.89(3) Å) compared to ethylbenzene (Co···C<sub>aryl</sub> = 3.09(3) Å; Co···C<sub>alkyl</sub> = 2.81(4) Å), suggesting that Co<sub>2</sub>(*m*-dobdc) also distinguishes between the two isomers through the strength of their interactions with two metal sites. Although sufficiently resolved structures of the other C<sub>8</sub> alkylaromatics in Co<sub>2</sub>(*m*-dobdc) could not be obtained due to severe disorder enforced by the mirror symmetry of the framework, the selectivity of Co<sub>2</sub>(*m*-dobdc) for the different isomers is expected to be controlled by similar factors as those identified in Co<sub>2</sub>(dobdc).



**Figure 3.6.** A portion of the structures of *o*-xylene and ethylbenzene in  $\text{Co}_2(m\text{-dobdc})$  at 100 K as determined through analysis of single-crystal X-ray diffraction data, showing the interactions of each isomer with two exposed cobalt(II) sites and the linker arene ring. The  $\text{C}_8$  isomers in both structures are disordered over two positions due to the mirror symmetry of the framework. Water was found to contaminate 30% of the cobalt(II) sites in the structure of ethylbenzene in  $\text{Co}_2(m\text{-dobdc})$ , but only ethylbenzene is shown here for clarity. Purple, red, gray, and white spheres represent Co, O, C, and H atoms, respectively.

### 3.4. Conclusions

We have demonstrated that the  $\text{C}_8$  alkylaromatics *o*-xylene, *m*-xylene, *p*-xylene, and ethylbenzene can be separated by the metal–organic frameworks  $\text{Co}_2(\text{dobdc})$  and  $\text{Co}_2(m\text{-dobdc})$  through the varied extent of interaction of each isomer with two adjacent coordinatively unsaturated cobalt(II) centers. Single-component adsorption isotherms, multi-component vapor-phase breakthrough measurements, and multi-component liquid-phase batch adsorption experiments show that  $\text{Co}_2(\text{dobdc})$  effectively separates all four isomers and has the strongest affinity for *o*-xylene, followed by ethylbenzene, *m*-xylene, and *p*-xylene. In contrast,  $\text{Co}_2(m\text{-dobdc})$  can only distinguish between three of the four isomers, due to its similar binding affinity for *m*-xylene and ethylbenzene.

Single-crystal X-ray diffraction experiments indicate that the strong adsorption of the  $\text{C}_8$  alkylaromatics arise from their interactions with a linker aromatic ring and exposed cobalt(II) sites in both  $\text{Co}_2(\text{dobdc})$  and  $\text{Co}_2(m\text{-dobdc})$ . In particular, a comparison of the structures of the four xylene isomers in  $\text{Co}_2(\text{dobdc})$  shows that the framework distinguishes among the isomers due to nuanced differences in the interaction of *o*-xylene, ethylbenzene, and *m*-xylene with two adjacent cobalt(II) centers and the inability of *p*-xylene to interact with a second metal site. Furthermore, the structures of *o*-xylene and ethylbenzene in  $\text{Co}_2(\text{dobdc})$  reveal that the framework undergoes an unprecedented structural distortion upon binding of these isomers, allowing the accommodation of additional adsorbate molecules.

Altogether, these results highlight that leveraging the interaction of multiple coordinatively

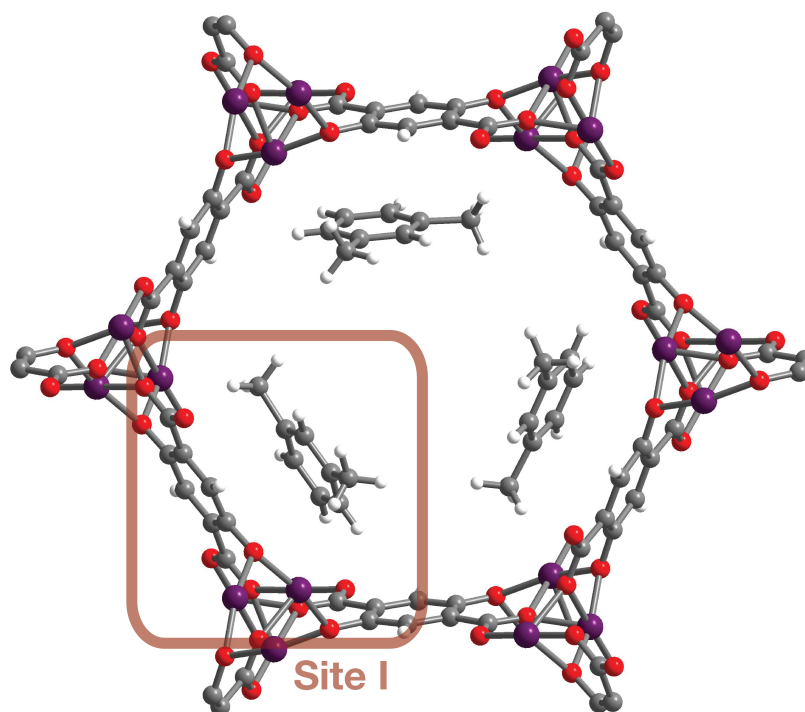
unsaturated metal centers with a single molecule allows for the design of new adsorbents for the separation of hydrocarbons. Altering the distance between the exposed metal sites in these materials could afford control over their selectivity for the different C<sub>8</sub> isomers and enable the separation of mixtures containing other adsorbates.

### **3.5. Acknowledgments**

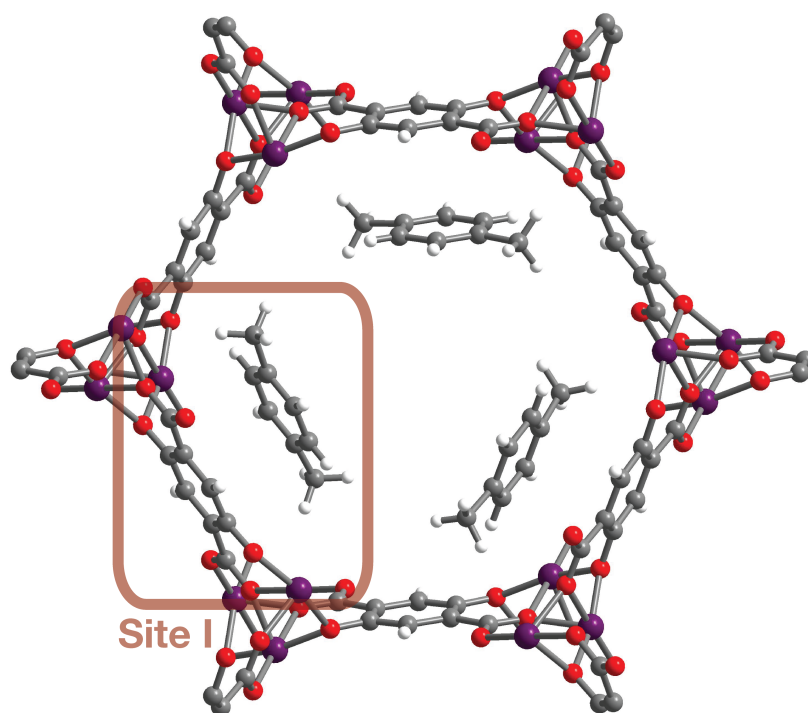
This work was supported through the Center for Gas Separations Relevant to Clean Energy Technologies, an Energy Frontier Research Center funded by the U.S. Department of Energy, Office of Science, Office of Basic Energy Sciences under Award DE-SC0001015. This research used resources of the Advanced Light Source, which is supported by the Director, Office of Science, Office of Basic Energy Sciences, of the U.S. Department of Energy under Contract No. DE-AC02-05CH11231, and the Advanced Photon Source, a DoE Office of Science User Facility operated by Argonne National Laboratory under Contract No. DE-AC02-06CH11357. We thank Greg Halder and the 17-BM-B staff for experimental assistance. We acknowledge Katie R. Meihaus for editorial assistance. We also thank Simon J. Teat and Rebecca L. Siegelman for helpful discussions.

## 3.6. Supplementary Information

### 3.6.3. Supplementary Figures

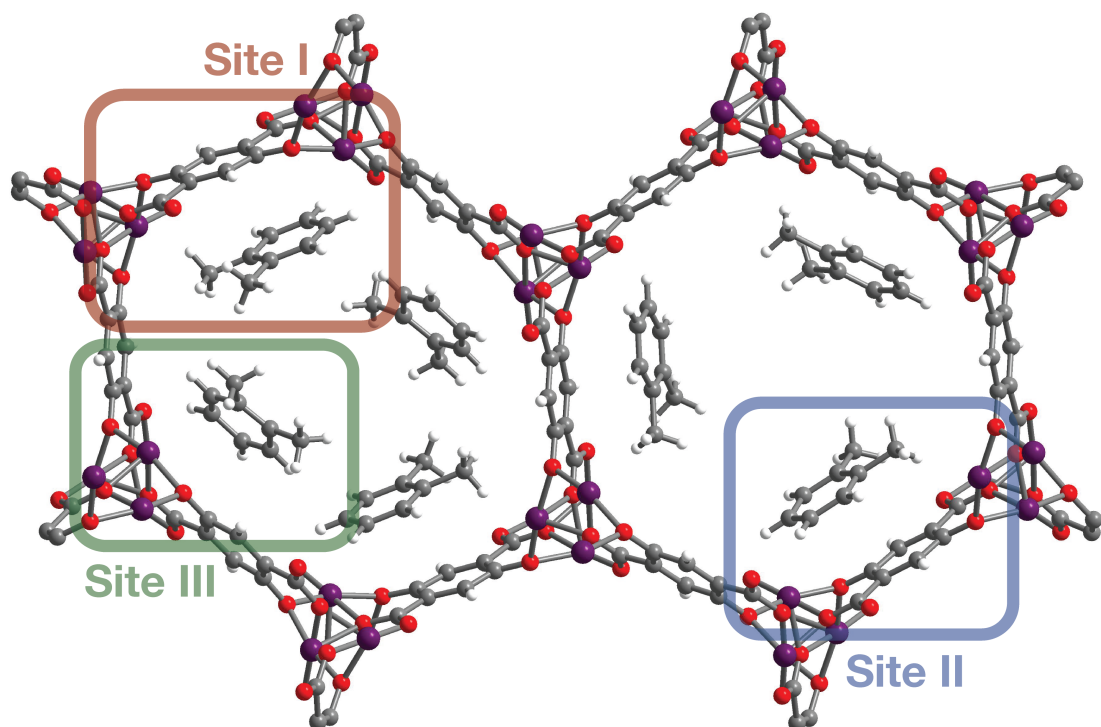


**Figure 3.S1.** A portion of the crystal structure of  $\text{Co}_2(\text{dobdc})\cdot 0.74(m\text{-xylene})$  at 100 K as determined through analysis of single-crystal X-ray diffraction data. The chemical occupancy for  $m$ -xylene were refined to be 74% (37% site occupancy). The  $m$ -xylene molecules were found to be disordered over two sets of locations due to the  $\bar{3}$  symmetry of the framework, but only one set is shown here for clarity. Purple, red, gray, and white spheres represent Co, O, C, and H atoms, respectively.

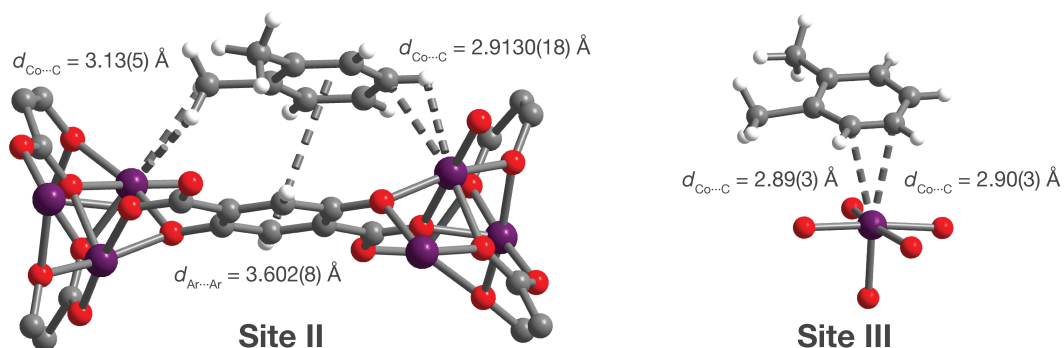


**Figure 3.S2.** A portion of the crystal structure of  $\text{Co}_2(\text{dobdc}) \cdot 0.82(p\text{-xylene})$  at 100 K as determined through analysis of single-crystal X-ray diffraction data. The chemical occupancy for  $p$ -xylene were refined to be 82% (41% site occupancy). The  $p$ -xylene molecules were found to be disordered over two sets of locations due to the  $\bar{3}$  symmetry of the framework, but only one set is shown here for clarity. Purple, red, gray, and white spheres represent Co, O, C, and H atoms, respectively.

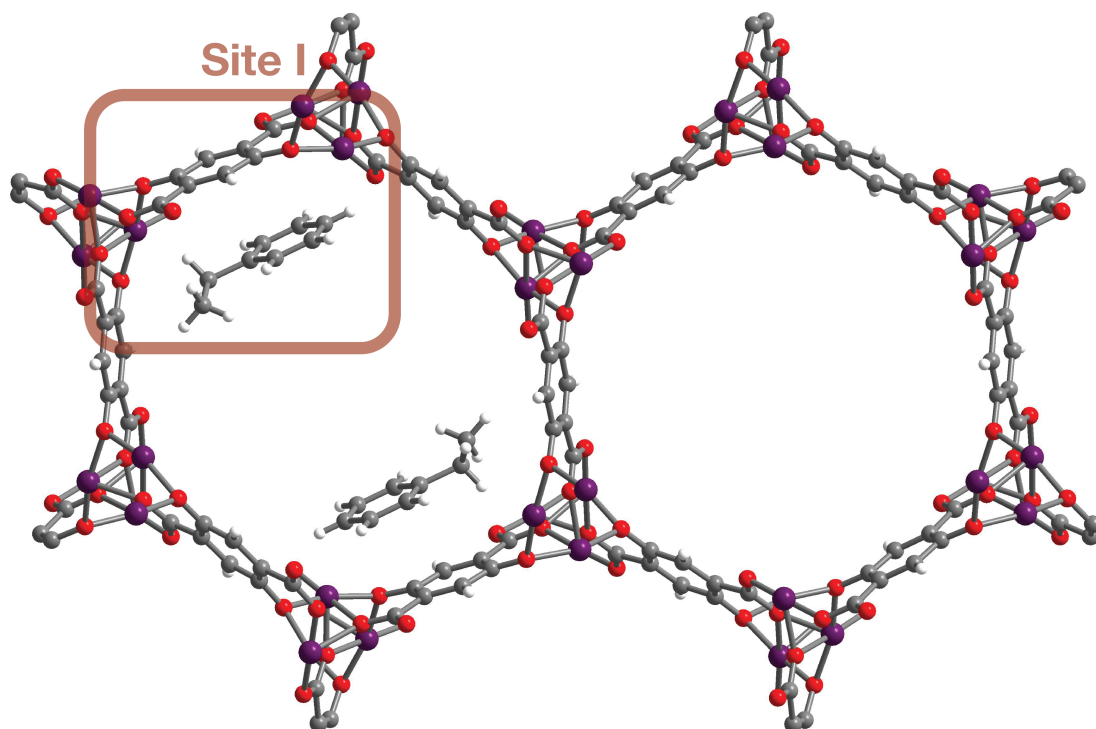




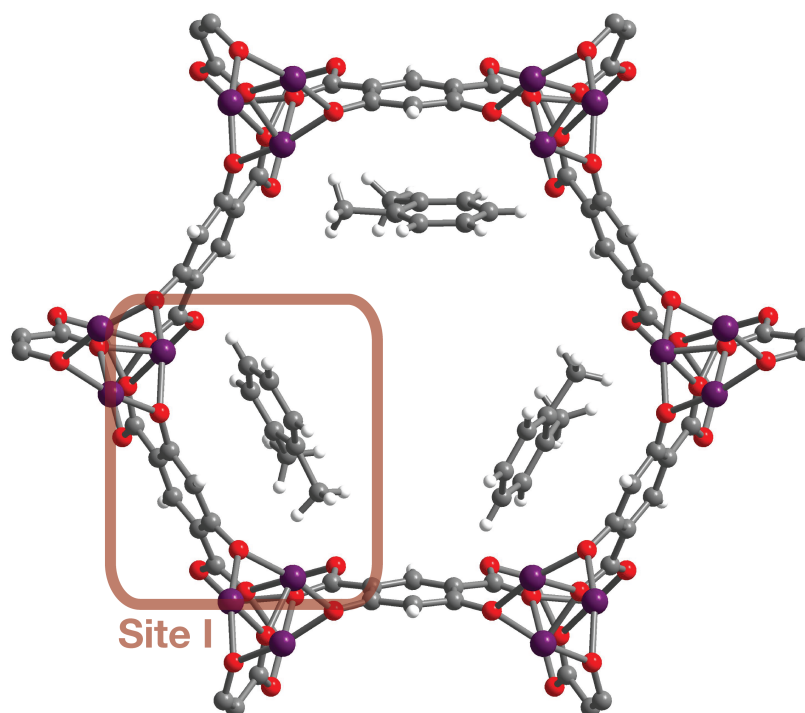
**Figure 3.S3.** A portion of the crystal structure of  $\text{Co}_2(\text{dobdc})\cdot 0.99(o\text{-xylene})$  at 100 K as determined through analysis of single-crystal X-ray diffraction data. In the structure, three out of four channels distort to accommodate an additional equivalent of *o*-xylene. The chemical occupancies for *o*-xylene were refined to be 89% for Site I, 78% for Site II, and 69% for Site III. The *o*-xylene molecules in the undistorted pore (Site II) were found to be disordered over two sets of locations due to the  $\bar{3}$  symmetry of the framework, but only one set is shown here for clarity. Purple, red, gray, and white spheres represent Co, O, C, and H atoms, respectively.



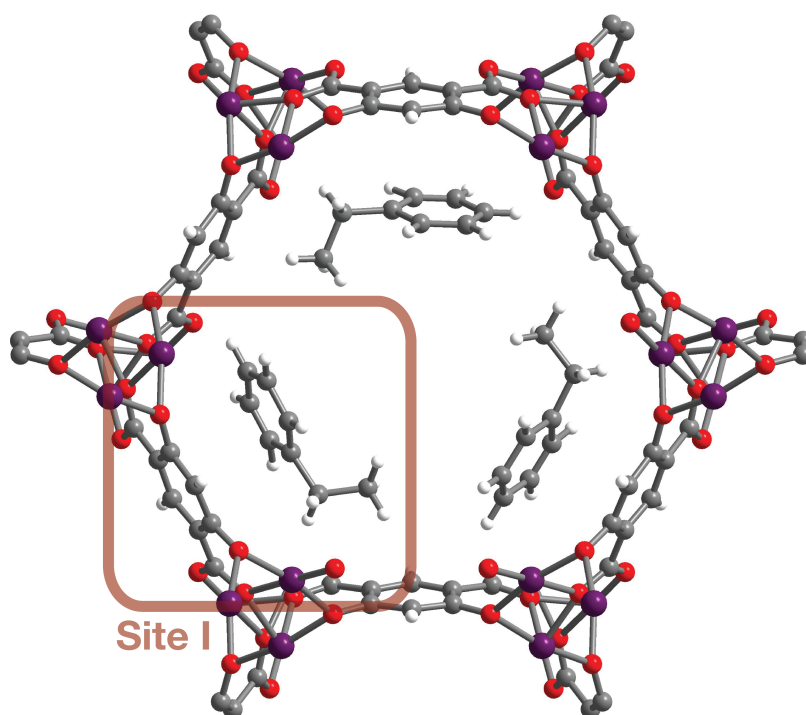
**Figure 3.S4.** Views of the single-crystal structure of *o*-xylene in  $\text{Co}_2(\text{dobdc})$  at 100 K showing two additional binding sites for *o*-xylene. Site II shows the interaction of *o*-xylene with two exposed cobalt(II) sites and the linker arene ring, whereas *o*-xylene at Site III interacts with only a single cobalt center. The *o*-xylene molecules in the undistorted pore (Site II) were found to be disordered over two sets of locations due to the  $\bar{3}$  symmetry of the framework, but only one set is shown here for clarity. Purple, red, gray, and white spheres represent Co, O, C, and H atoms, respectively.



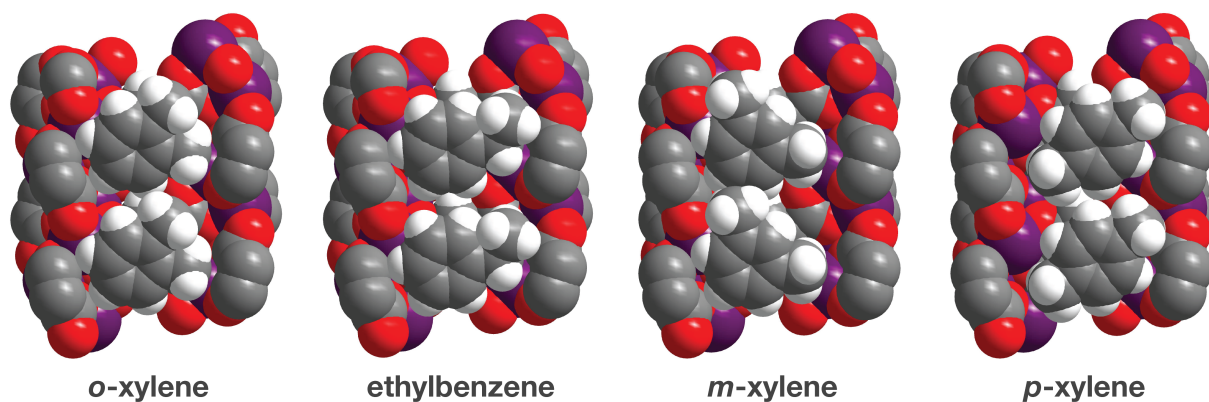
**Figure 3.S5.** A portion of the crystal structure of  $\text{Co}_2(\text{dobdc}) \cdot 0.36(\text{ethylbenzene})$  at 100 K as determined through analysis of single-crystal X-ray diffraction data. In the structure, three out of four channels distort. The chemical occupancy for ethylbenzene were refined to be 71%. Purple, red, gray, and white spheres represent Co, O, C, and H atoms, respectively.



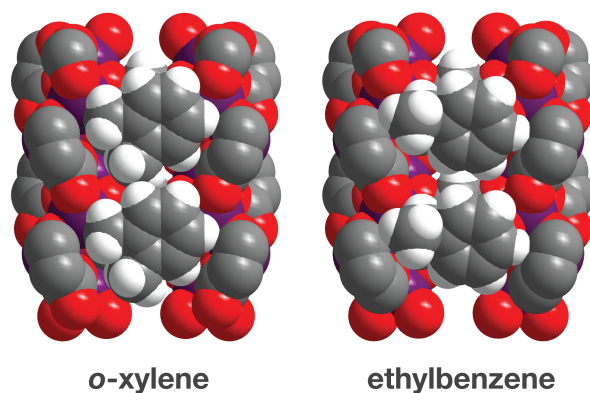
**Figure 3.S6.** A portion of the crystal structure of  $\text{Co}_2(m\text{-dobdc})\cdot 0.92(o\text{-xylene})$  at 100 K as determined through analysis of single-crystal X-ray diffraction data. The chemical occupancy for *p*-xylene were refined to be 92% (46% site occupancy). The *o*-xylene molecules were found to be disordered over two positions due to the mirror symmetry of the framework, but only one orientation is shown here for clarity. Purple, red, gray, and white spheres represent Co, O, C, and H atoms, respectively.



**Figure 3.S7.** A portion of the crystal structure of  $\text{Co}_2(m\text{-dobdc})(\text{H}_2\text{O})_{0.61}\cdot 0.77(\text{ethylbenzene})$  at 100 K as determined through analysis of single-crystal X-ray diffraction data. The chemical occupancies for ethylbenzene were refined to be 77% (38.5% site occupancy). The ethylbenzene molecules were found to be disordered over two positions due to the mirror symmetry of the framework, but only one orientation is shown here for clarity. Water was found to contaminate 30% of the cobalt(II) sites in the structure of ethylbenzene in  $\text{Co}_2(m\text{-dobdc})$ , but only ethylbenzene is shown here for clarity. Purple, red, gray, and white spheres represent Co, O, C, and H atoms, respectively.

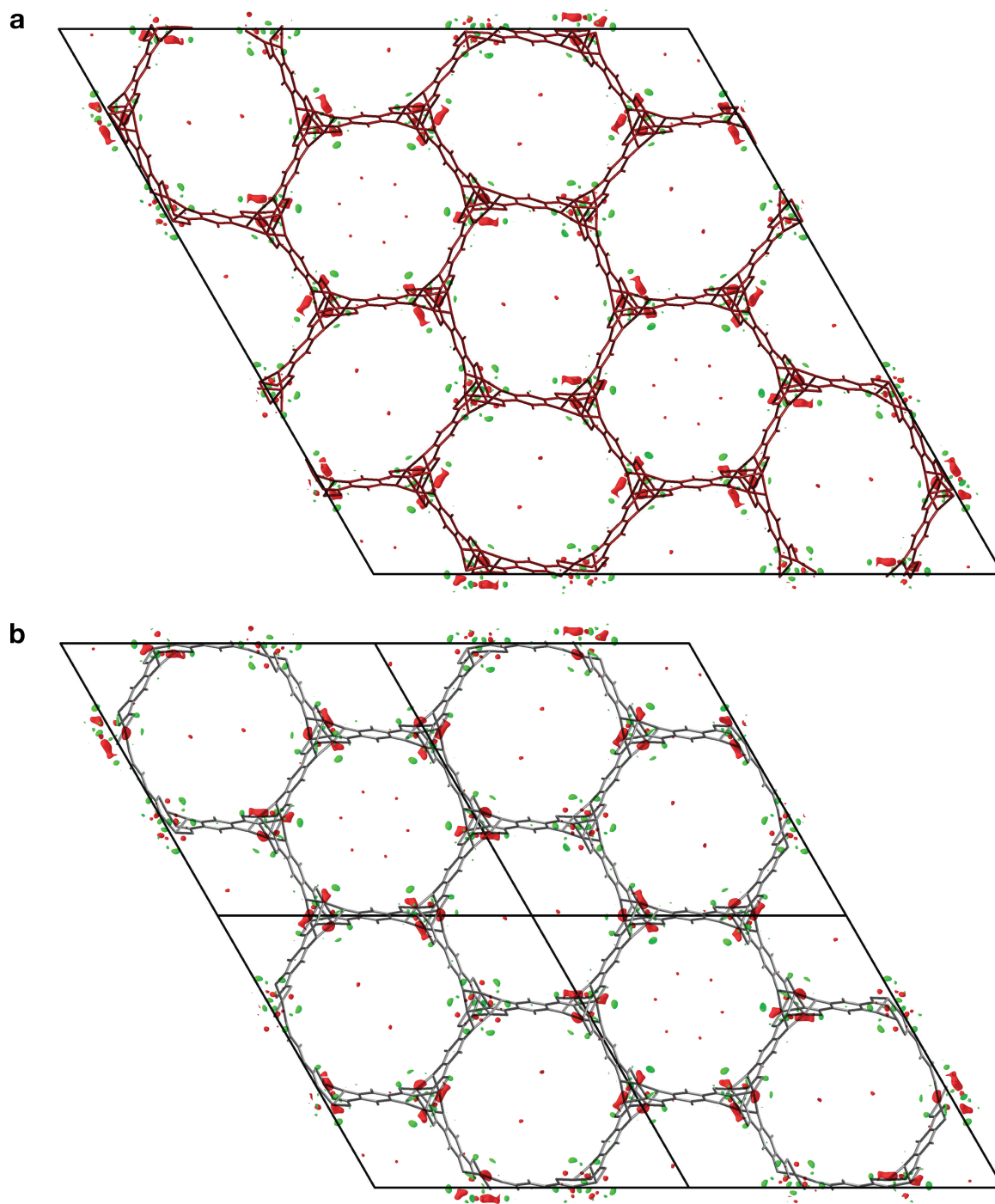


**Figure 3.S8.** Comparison of the space-filling models of the crystal structures of *o*-xylene, ethylbenzene, *m*-xylene, and *p*-xylene in  $\text{Co}_2(\text{dobdc})$  at 100 K. The structures shown for *o*-xylene and ethylbenzene correspond to binding sites within the distorted hexagonal channels. Two additional binding sites were located for *o*-xylene. Purple, red, gray, and white spheres represent Co, O, C, and H atoms, respectively.

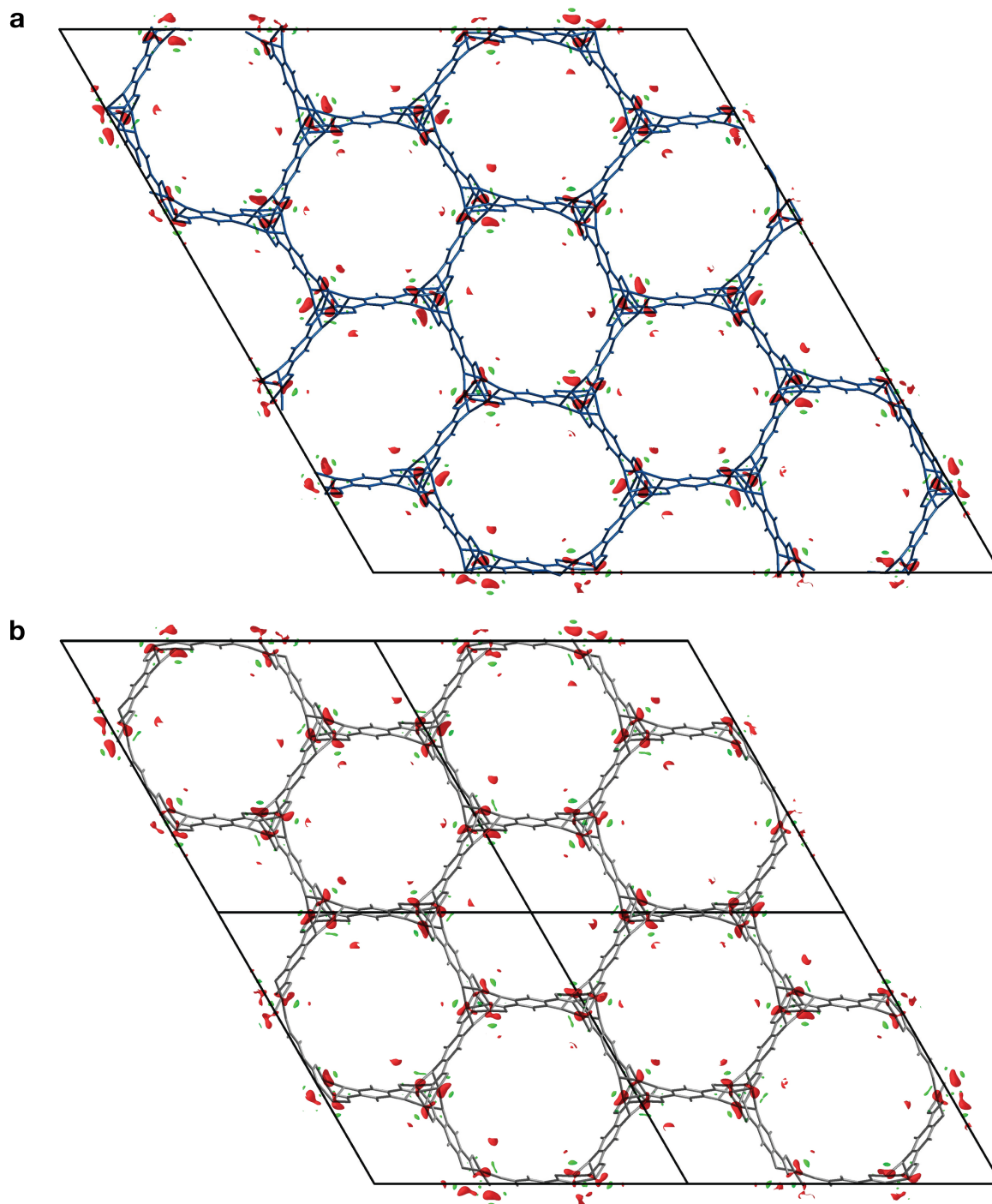


**Figure 3.S9.** Comparison of the space-filling models of the crystal structures of *o*-xylene and ethylbenzene in  $\text{Co}_2(\text{m-dobdc})$  at 100 K. Purple, red, gray, and white spheres represent Co, O, C, and H atoms, respectively.

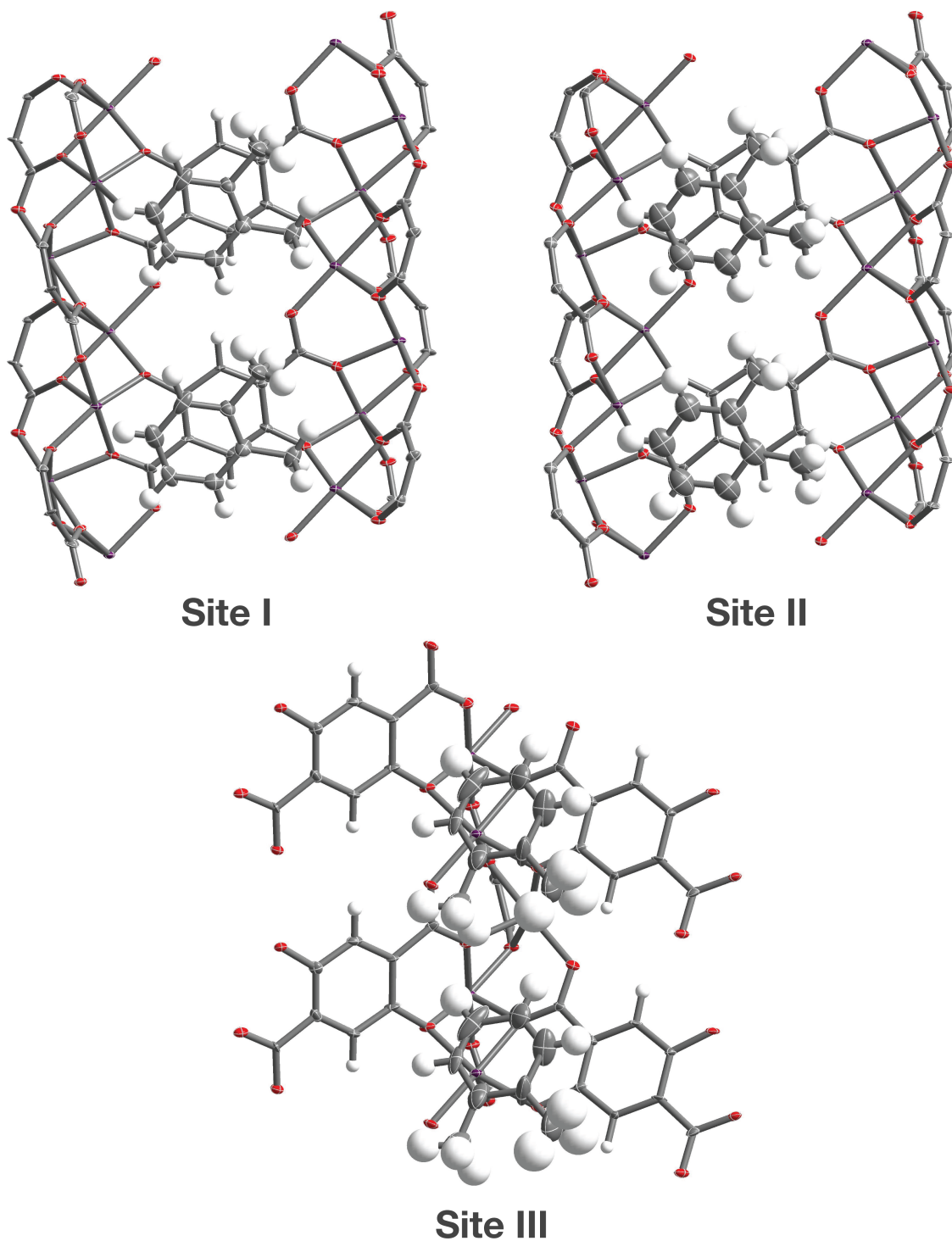
### 3.6.4. Crystallographic Information



**Figure 3.S10.** Overlay of the electron-density difference map of the structure of  $\text{Co}_2(\text{dobdc}) \cdot 0.99(o\text{-xylene})$  on the structural model for  $\text{Co}_2(\text{dobdc}) \cdot 0.99(o\text{-xylene})$  (red) (a) and  $\text{Co}_2(\text{dobdc})$  (gray) (b). Red surfaces correspond to regions of positive electron density, while green surfaces correspond to regions of negative electron density. Regions of electron density that are not accounted for by the model match the positions of the cobalt(II) atoms in the structure of the undistorted  $\text{Co}_2(\text{dobdc})$ .

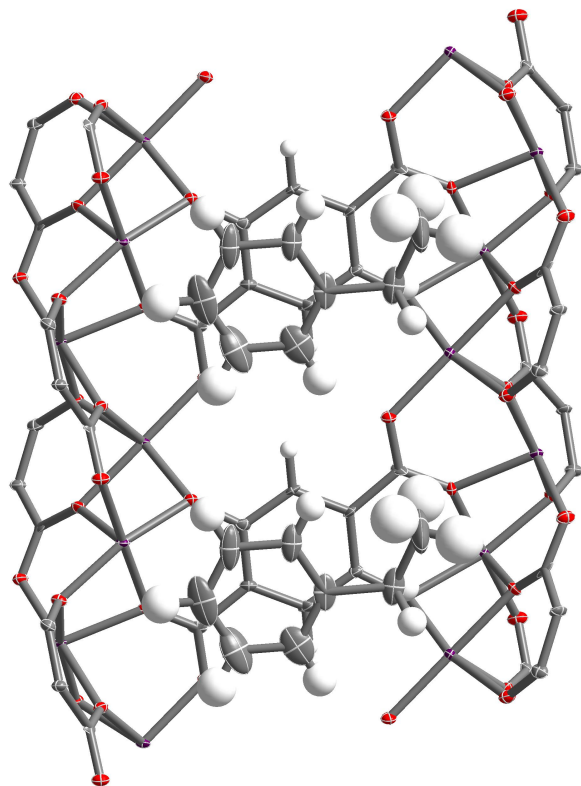


**Figure 3.S11.** Overlay of the electron-density difference map of the structure of  $\text{Co}_2(\text{dobdc}) \cdot 0.36(\text{ethylbenzene})$  on the structural model for  $\text{Co}_2(\text{dobdc}) \cdot 0.36(\text{ethylbenzene})$  (blue) (a) and  $\text{Co}_2(\text{dobdc})$  (gray) (b). Red surfaces correspond to regions of positive electron density, while green surfaces correspond to regions of negative electron density. Regions of electron density that are not accounted for by the model match the positions of the cobalt(II) atoms in the structure of the undistorted  $\text{Co}_2(\text{dobdc})$ .

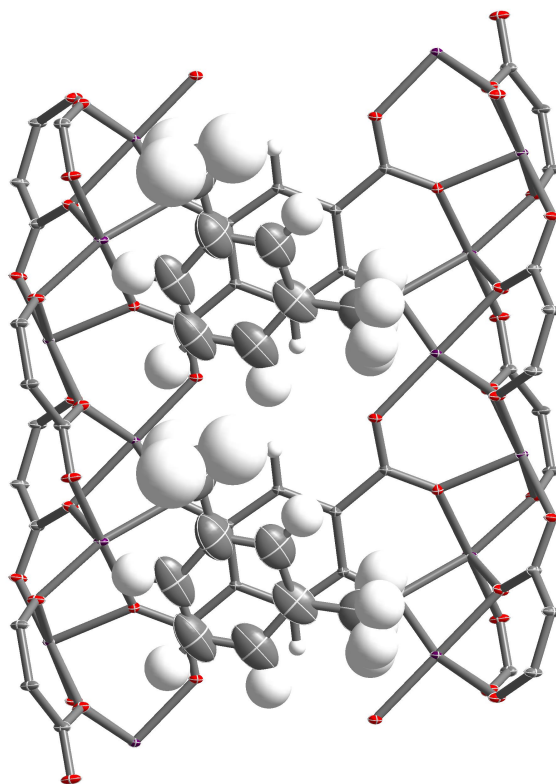


**Figure 3.S12.** Atomic displacement parameter plot for  $\text{Co}_2(\text{dobdc})\cdot 0.99(o\text{-xylene})$  at 100 K drawn at 50% probability level as determined by single crystal X-ray diffraction; purple, red, gray and white ellipsoids represent Co, O, C, and H atoms, respectively.

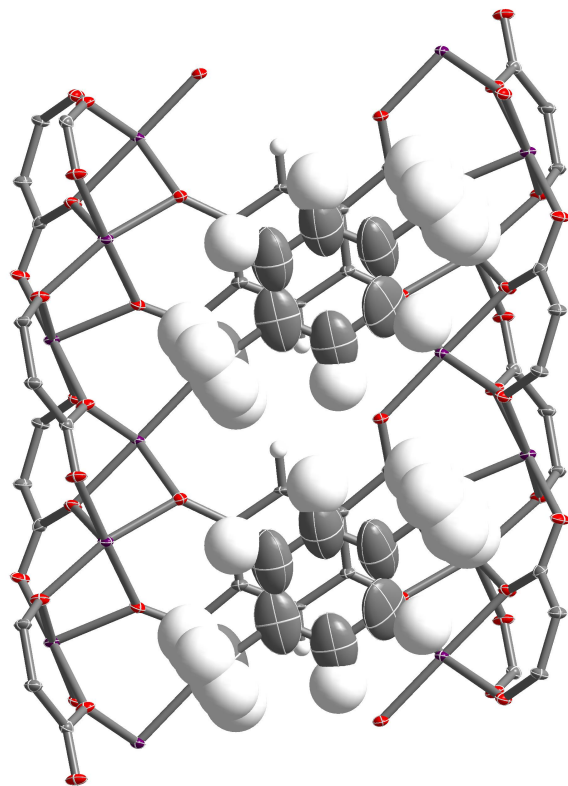




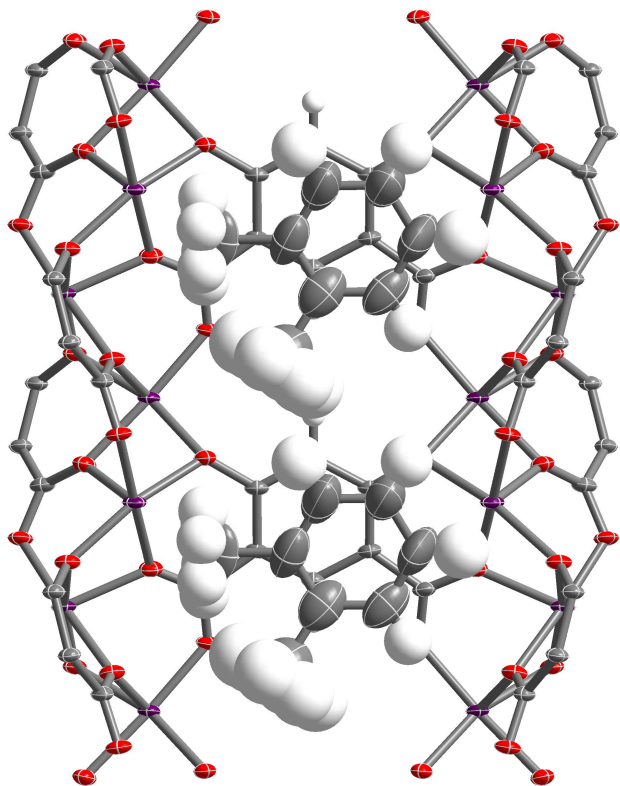
**Figure 3.S13.** Atomic displacement parameter plot for  $\text{Co}_2(\text{dobdc}) \cdot 0.36(\text{ethylbenzene})$  at 100 K drawn at 50% probability level as determined by single crystal X-ray diffraction; purple, red, gray and white ellipsoids represent Co, O, C, and H atoms, respectively.



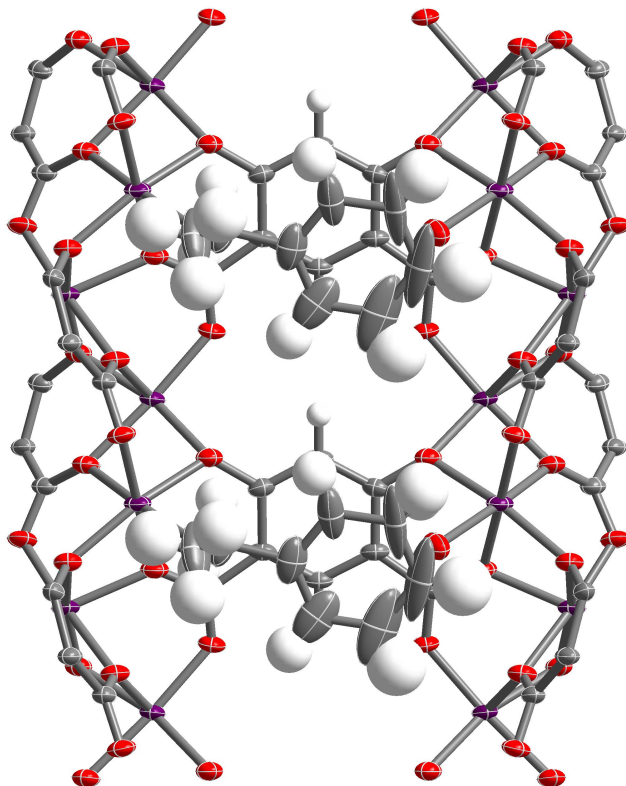
**Figure 3.S14.** Atomic displacement parameter plot for Co<sub>2</sub>(dobdc)·0.74(*m*-xylene) at 100 K drawn at 50% probability level as determined by single crystal X-ray diffraction; purple, red, gray and white ellipsoids represent Co, O, C, and H atoms, respectively.



**Figure 3.S15.** Atomic displacement parameter plot for  $\text{Co}_2(\text{dobdc})\cdot 0.82(p\text{-xylene})$  at 100 K drawn at 50% probability level as determined by single crystal X-ray diffraction; purple, red, gray and white ellipsoids represent Co, O, C, and H atoms, respectively.



**Figure 3.S16.** Atomic displacement parameter plot for  $\text{Co}_2(m\text{-dobdc}) \cdot 0.92(o\text{-xylene})$  at 100 K drawn at 50% probability level as determined by single crystal X-ray diffraction. The *o*-xylene molecules were found to be disordered over two positions due to the mirror symmetry of the framework, but only one orientation is shown here for clarity. Purple, red, gray and white ellipsoids represent Co, O, C, and H atoms, respectively.



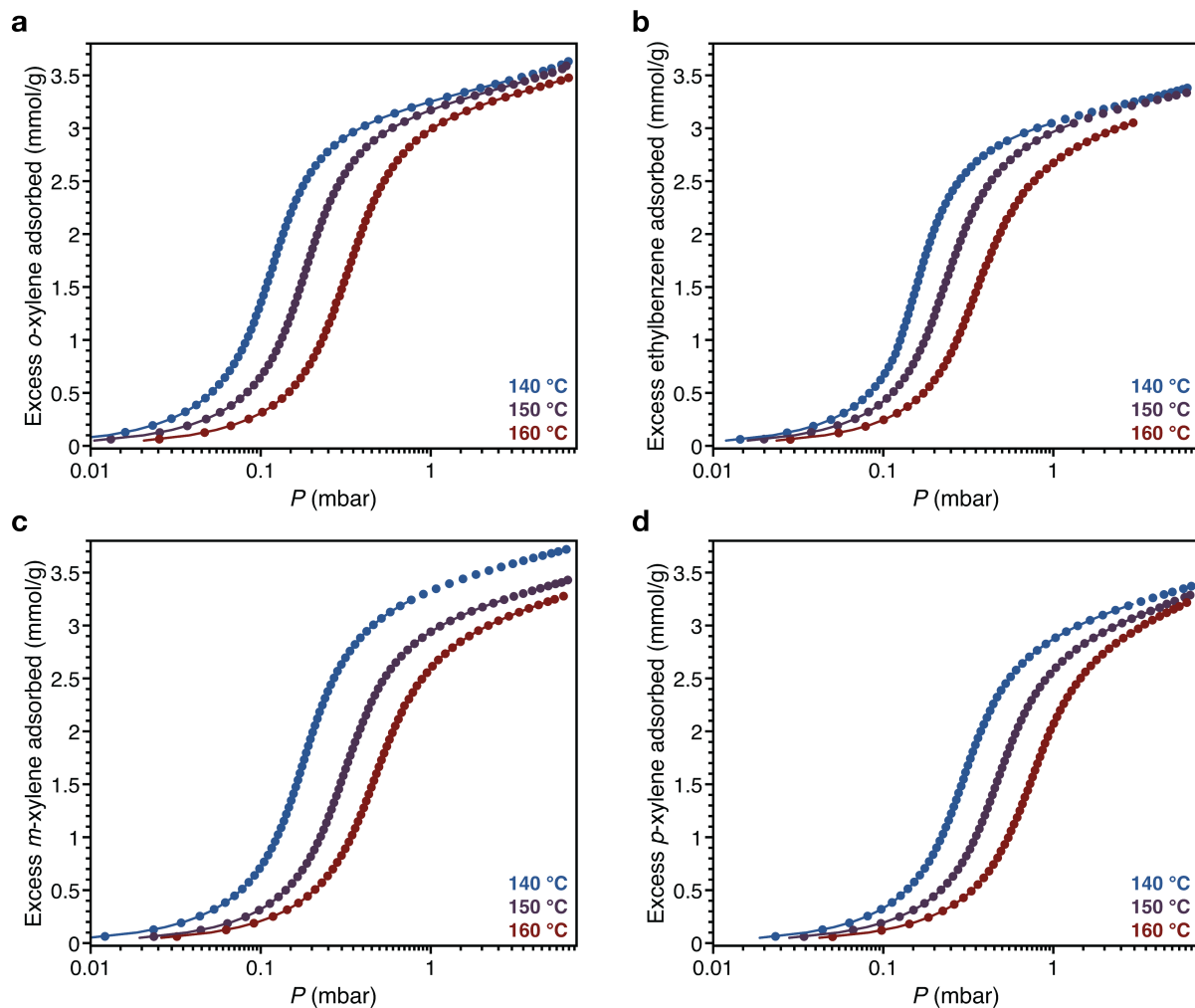
**Figure 3.S17.** Atomic displacement parameter plot for  $\text{Co}_2(m\text{-dobdc})(\text{H}_2\text{O})_{0.61}\cdot 0.77(\text{ethylbenzene})$  at 100 K drawn at 50% probability level as determined by single crystal X-ray diffraction. The ethylbenzene molecules were found to be disordered over two positions due to the mirror symmetry of the framework, but only one orientation is shown here for clarity. Purple, red, gray and white ellipsoids represent Co, O, C, and H atoms, respectively.

**Table 3.S1.** Crystallographic Data

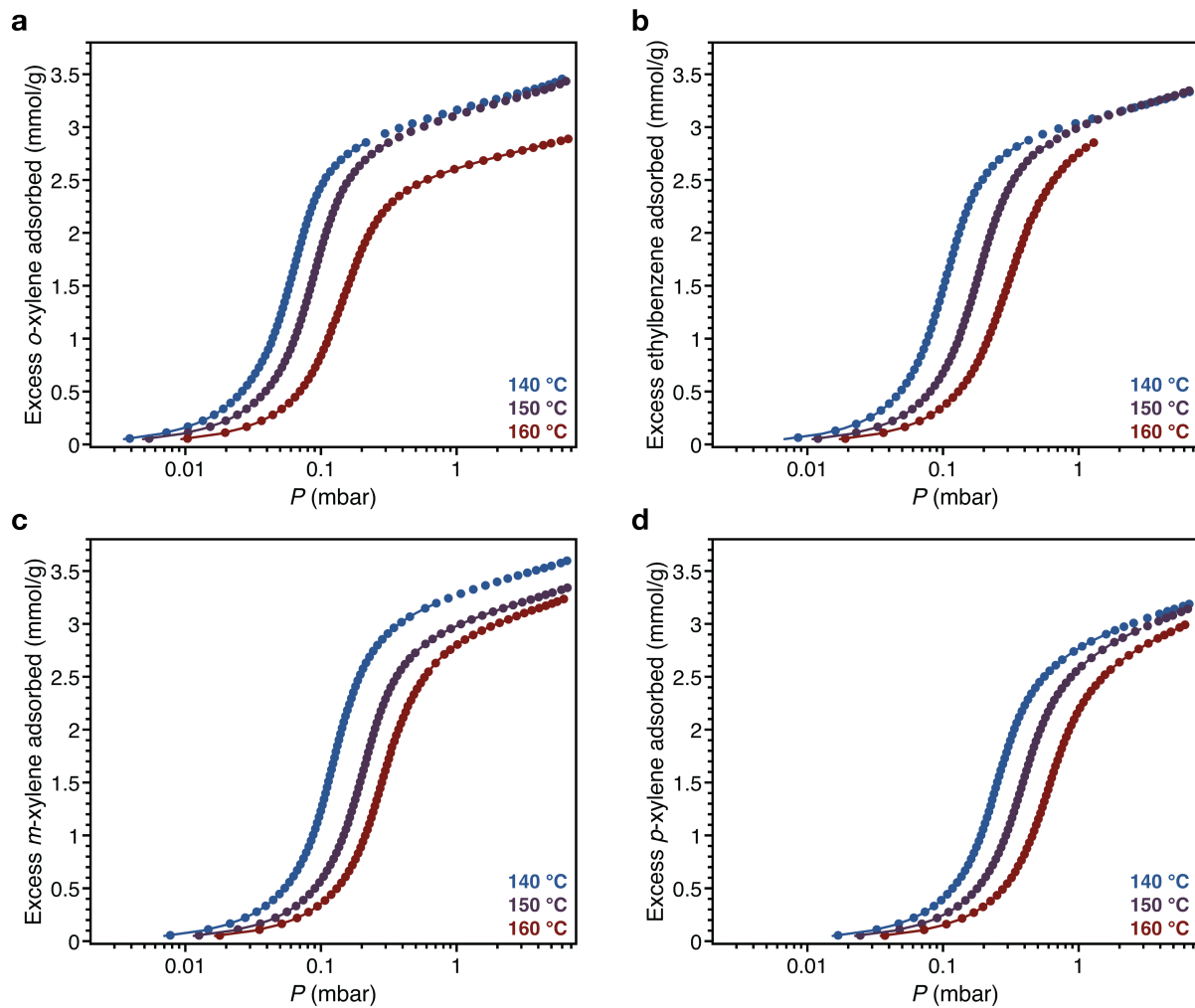
	Co <sub>2</sub> (dobdc)·0.99OX	Co <sub>2</sub> (dobdc)·0.36EB	Co <sub>2</sub> (dobdc)·0.74MX	Co <sub>2</sub> (dobdc)·0.82PX	Co <sub>2</sub> (m-dobdc)·0.92OX	Co <sub>2</sub> (m-dobdc)(H <sub>2</sub> O) <sub>0.61</sub> ·0.77EB
Formula	C <sub>15.90</sub> H <sub>11.88</sub> Co <sub>2</sub> O <sub>6</sub>	C <sub>10.84</sub> H <sub>5.56</sub> Co <sub>2</sub> O <sub>6</sub>	C <sub>13.89</sub> H <sub>9.36</sub> Co <sub>2</sub> O <sub>6</sub>	C <sub>14.53</sub> H <sub>10.17</sub> Co <sub>2</sub> O <sub>6</sub>	C <sub>15.39</sub> H <sub>11.23</sub> Co <sub>2</sub> O <sub>6</sub>	C <sub>14.15</sub> H <sub>10.91</sub> Co <sub>2</sub> O <sub>6.61</sub>
Temperature (K)	100(2)	100(2)	100(2)	100(2)	100(2)	100(2)
Crystal System	Trigonal	Trigonal	Trigonal	Trigonal	Trigonal	Trigonal
Space Group	$R\bar{3}$	$R\bar{3}$	$R\bar{3}$	$R\bar{3}$	$R3m$	$R3m$
<i>a</i> , <i>b</i> , <i>c</i> (Å)	51.6110(19), 51.6110(19), 6.8292(3)	51.7341(19), 51.7341(19), 6.8014(3)	25.8450(9), 25.8450(9), 6.8219(3)	25.9019(15), 25.9019(15), 6.8226(5)	25.812(3), 25.812(3), 6.8165(8)	25.8977(9), 25.8977(9), 6.7599(3)
<i>a</i> , <i>β</i> , <i>γ</i> (°)	90, 90, 120	90, 90, 120	90, 90, 120	90, 90, 120	90, 90, 120	90, 90, 120
<i>V</i> , (Å <sup>3</sup> )	15753.8(14)	15764.6(14)	3946.3(3)	3964.1(5)	3933.1(11)	3926.4(3)
<i>Z</i>	36	36	9	9	9	9
Radiation, <i>λ</i> (Å)	Synchrotron, 0.8856	Synchrotron, 0.8856	Synchrotron, 0.7749	Synchrotron, 0.8856	Synchrotron, 0.7749	Synchrotron, 0.8856
2 <i>θ</i> Range for Data Collection (°)	5.204 to 75.960	5.192 to 75.880	5.954 to 87.922	6.790 to 64.562	5.962 to 65.120	6.792 to 68.968
Completeness to 2 <i>θ</i>	99.7% (2 <i>θ</i> = 64.194°)	99.8% (2 <i>θ</i> = 64.194°)	99.9% (2 <i>θ</i> = 55.412°)	99.9% (2 <i>θ</i> = 64.194°)	99.9% (2 <i>θ</i> = 55.412°)	99.8% (2 <i>θ</i> = 64.194°)
Data / Restraints / Parameters	9711 / 139 / 498	9751 / 69 / 350	5205 / 104 / 135	1623 / 115 / 133	2569 / 112 / 137	2004 / 54 / 146
Goodness of Fit on <i>F</i> <sup>2</sup>	1.183	1.101	1.312	1.053	1.087	1.083
<i>R</i> <sub>1</sub> <sup><i>a</i></sup> , <i>wR</i> <sub>2</sub> <sup><i>b</i></sup> (I > 2σ(I))	0.1481, 0.3584	0.1631, 0.4703	0.0492, 0.1271	0.0538, 0.1390	0.0412, 0.1064	0.0399, 0.1080
<i>R</i> <sub>1</sub> <sup><i>a</i></sup> , <i>wR</i> <sub>2</sub> <sup><i>b</i></sup> (all data)	0.1508, 0.3593	0.1743, 0.4748	0.0536, 0.1287	0.0749, 0.1516	0.0477, 0.1098	0.0440, 0.1099
Largest Diff. Peak and Hole (e Å <sup>-3</sup> )	3.249 and -2.420	6.576 and -2.255	1.088 and -1.499	1.932 and -0.459	0.830 and -0.515	1.068 and -0.391

*OX* = *o*-xylene; *EB* = *o*-ethylbenzene; *MX* = *m*-xylene; *PX* = *p*-xylene.  $arR_1 = \sum |F_o| - |F_c| / \sum |F_o|$ ;  $bwR_2 = \sqrt{\sum w(F_o - F_c)^2} / \sum w(F_o)$

### 3.6.5. Single-Component C<sub>8</sub> Isomer Adsorption Isotherm Data



**Figure 3.S18.** Single-component vapor-phase *o*-xylene (a), ethylbenzene (b), *m*-xylene (c), and *p*-xylene (d) adsorption isotherms for CO<sub>2</sub>(dobdc) at 140 °C (blue), 150 °C (violet), and 160 °C (red). Filled circles represent experimental data, while solid lines represent corresponding fits obtained by spline interpolation.



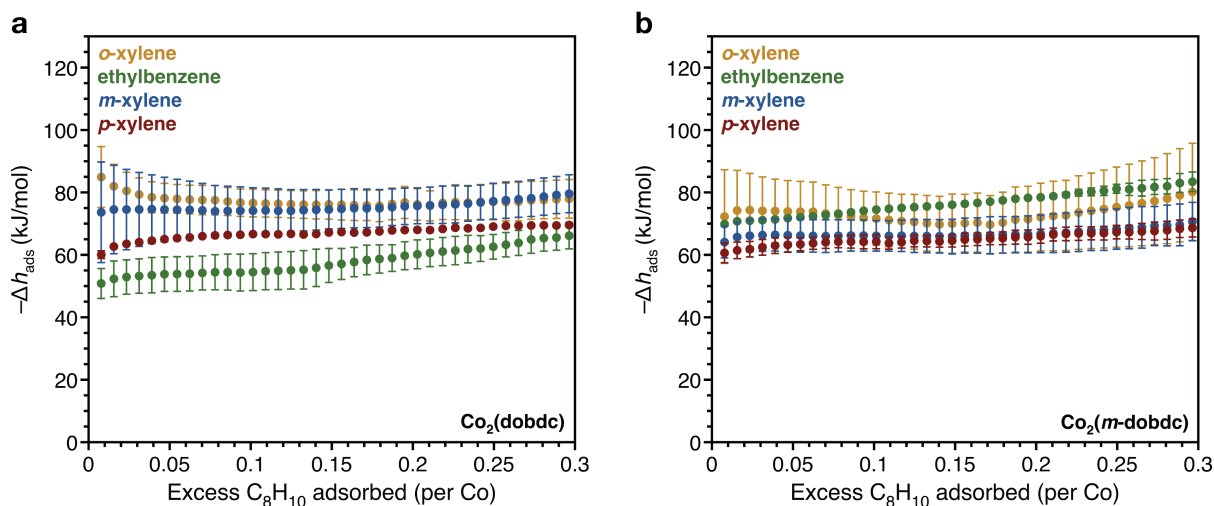
**Figure 3.S19.** Single-component vapor-phase *o*-xylene (a), ethylbenzene (b), *m*-xylene (c), and *p*-xylene (d) adsorption isotherms for  $\text{Co}_2(\text{dobdc})$  at 140 °C (blue), 150 °C (violet), and 160 °C (red). Filled circles represent experimental data, while solid lines represent corresponding fits obtained by spline interpolation.



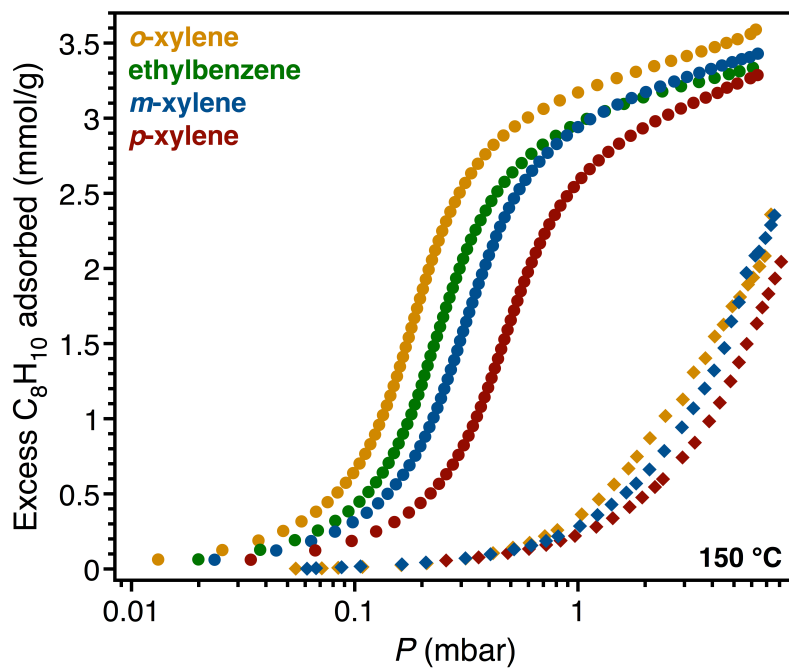
**Differential Enthalpy of Adsorption Calculations.** As suitable fits to the adsorption isotherm data could not be obtained with multi-site Langmuir equations, isotherms were fit independently by spline interpolation. Using the fits, the differential enthalpy of adsorption,  $\Delta h_{\text{ads}}$ , can be calculated as a function of the total amount of gas adsorbed,  $n$ , by using the the Clausius-Clapeyron equation (eq 2), where  $R$  is the gas constant in  $\text{J/mol}\cdot\text{K}$ ,  $T$  is the temperature in  $\text{K}$ ,  $n$  is the total amount adsorbed in  $\text{mmol/g}$ , and  $P$  is the pressure in bar.

$$\Delta h_{\text{ads}} = -RT^2 \left( \frac{\partial \ln P}{\partial T} \right)_n \quad (2)$$

The fits for each  $\text{C}_8$  isomer (fit independently for each temperature) were used to obtain the exact pressures that correspond to specific loadings at different temperatures ( $140\text{ }^\circ\text{C}$ ,  $150\text{ }^\circ\text{C}$ , and  $160\text{ }^\circ\text{C}$ ). This was done at loading intervals of  $0.05\text{ mmol/g}$ . At each loading, the slope of the best-fit line to  $\ln(P)$  versus  $1/T$  was calculated to obtain the differential enthalpy.

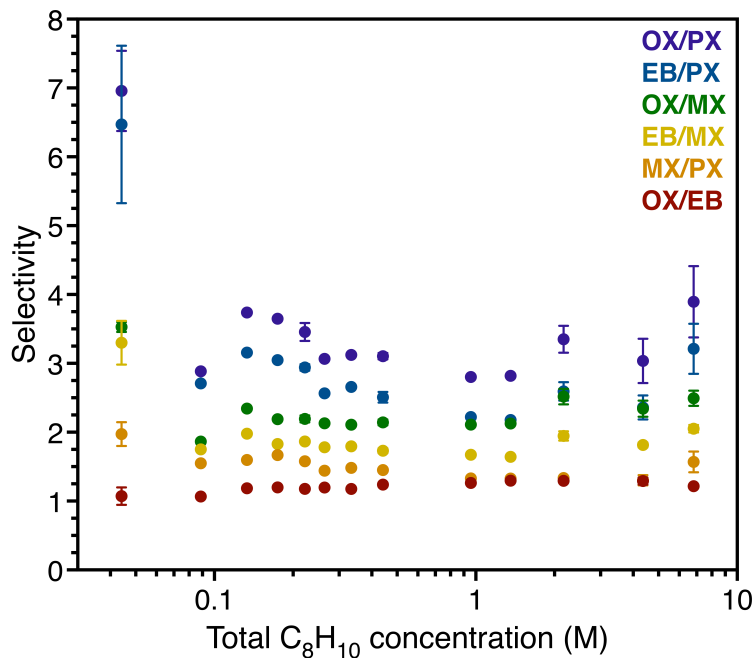


**Figure 3.S20.** Differential enthalpy of adsorption ( $\Delta h_{\text{ads}}$ ) plots (calculated from fits to the adsorption isotherms generated by spline interpolation) *o*-xylene (orange), ethylbenzene (green), *m*-xylene (blue), and *p*-xylene (red) adsorption in  $\text{Co}_2(\text{dobdc})$  (a) and  $\text{Co}_2(m\text{-dobdc})$  (b).



**Figure 3.S21.** Comparison of the single-component vapor-phase *o*-xylene (orange), ethylbenzene (green), *m*-xylene (blue), and *p*-xylene (red) adsorption isotherms for Co<sub>2</sub>(dobdc) (filled circles) and Co<sub>2</sub>(dobpdc) (filled diamonds) at 150 °C.

### 3.6.6. C<sub>8</sub> Isomer Selectivities from Multi-Component Liquid-Phase Adsorption Data

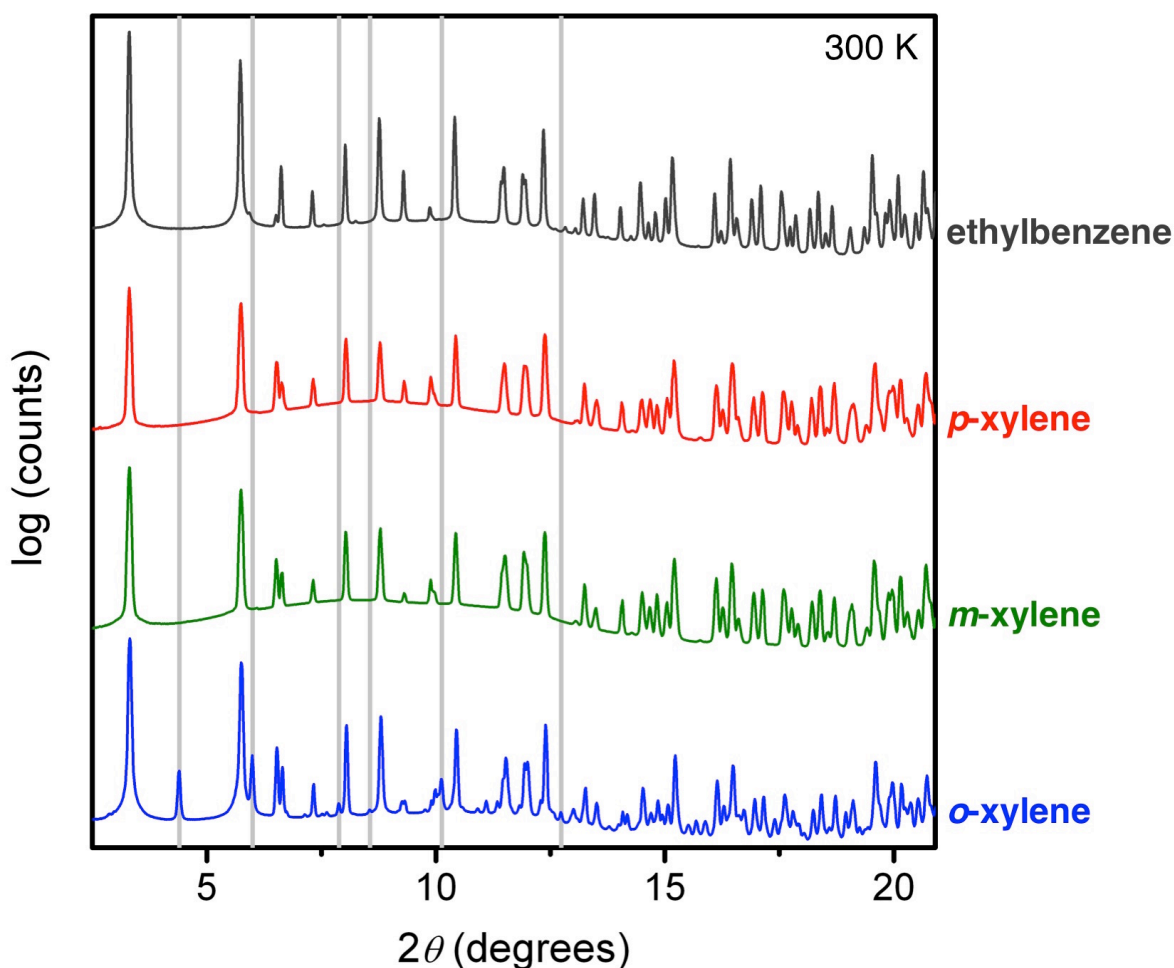


**Figure 3.S22.** Two-component selectivities for *o*-xylene/*p*-xylene (violet), ethylbenzene/*p*-xylene (blue), *o*-xylene/*m*-xylene (green), ethylbenzene/*m*-xylene (yellow), *m*-xylene/*p*-xylene (orange), and *o*-xylene/ethylbenzene (red) determined from a multi-component liquid-phase adsorption experiment with equimolar amounts of the C<sub>8</sub> isomers (0.1–1.7 M in each isomer; 0.4–6.8 M total concentration) in *n*-heptane at 33 °C. The selectivities are plotted over the initial total C<sub>8</sub> isomer concentration for each measurement. Data points with error bars (for measurements with initial total C<sub>8</sub> isomer concentrations of 0.044, 0.22, 0.44, 2.2, 4.4, and 6.8 M) were determined from an average of three replications.

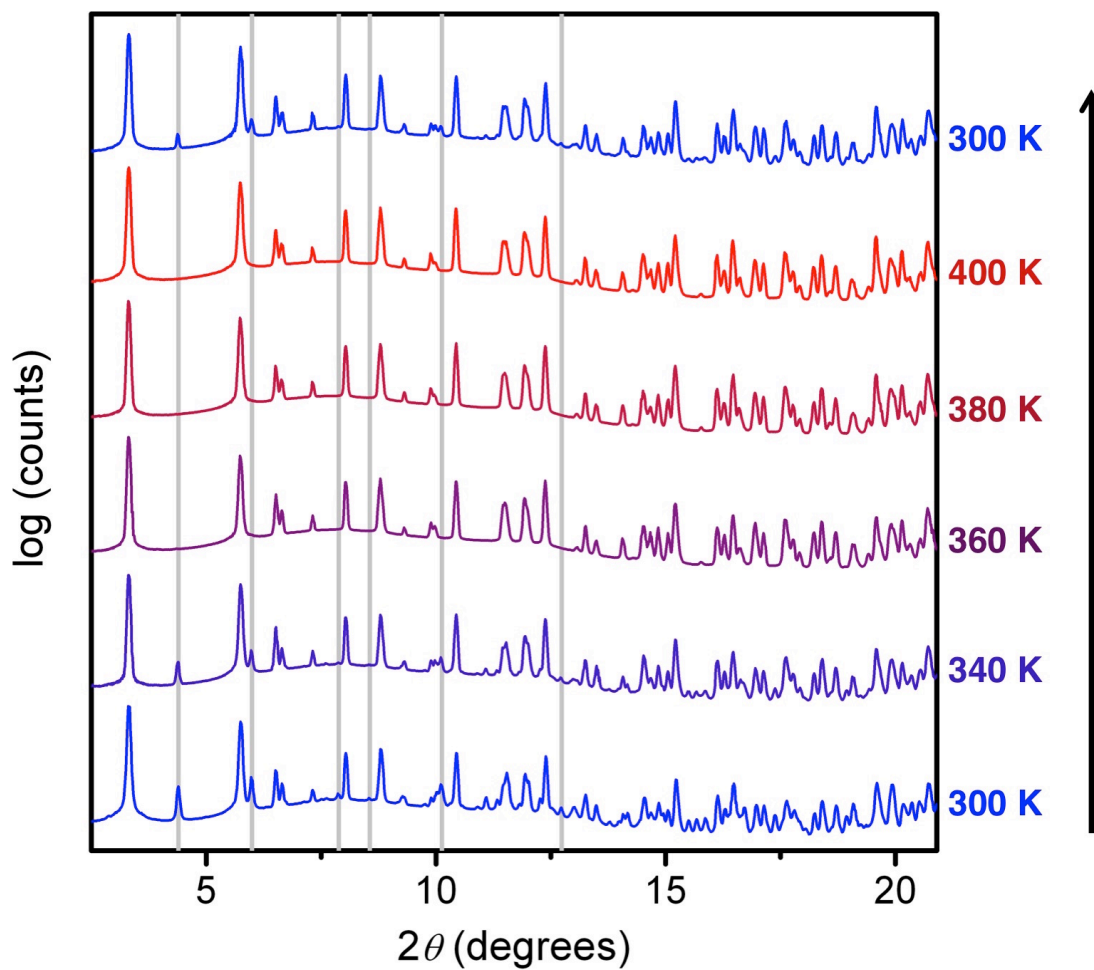
### 3.6.7. Powder X-ray Diffraction Data

**Table 3.S2.** Unit cell parameters for Co<sub>2</sub>(dobdc) powder samples.

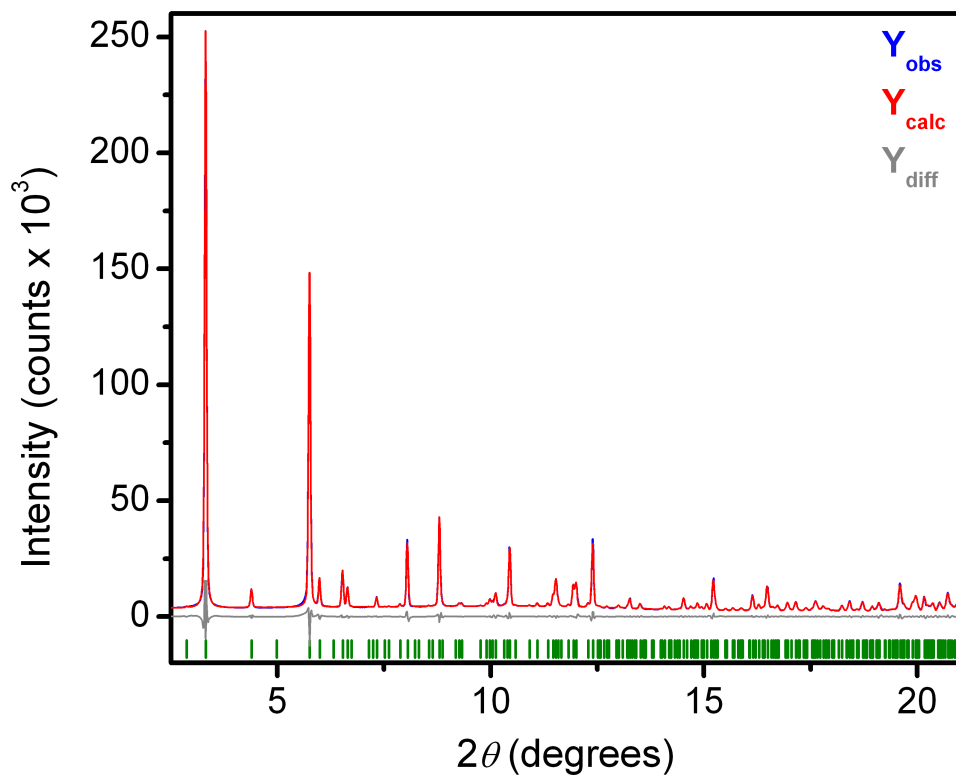
	Space Group	$T$ (K)	$a$ (Å)	$c$ (Å)	$V$ (Å <sup>3</sup> )
<i>o</i> -xylene	$R\bar{3}$	300	51.713(1)	6.8842(3)	15943(1)
<i>o</i> -xylene	$R\bar{3}$	400	25.873(1)	6.8973(3)	3998.4(4)
<i>m</i> -xylene	$R\bar{3}$	300	25.8808(6)	6.8923(2)	3998.1(2)
<i>p</i> -xylene	$R\bar{3}$	300	25.8916(9)	6.8853(3)	3997.4(3)
ethylbenzene	$R\bar{3}$	300	25.9580(3)	6.9065(1)	4030.2(1)



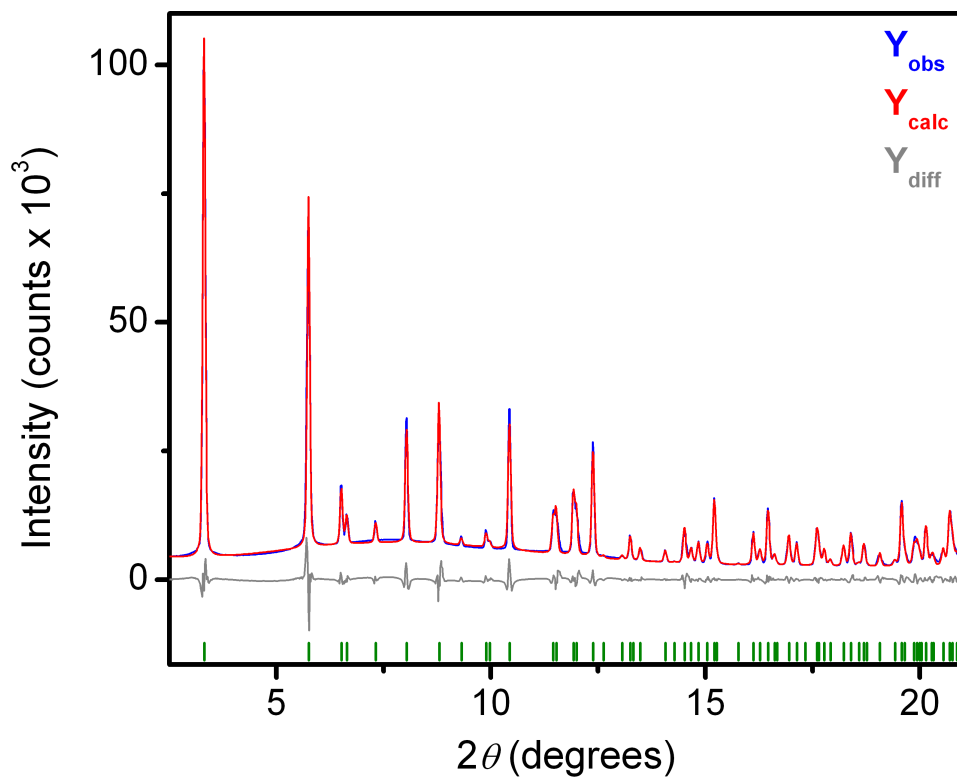
**Figure 3.S23.** Powder X-ray diffraction patterns ( $\lambda = 0.75009$  Å) at 300 K for Co<sub>2</sub>(dobdc) soaked in *o*-xylene (blue), *m*-xylene (green), *p*-xylene (red), and ethylbenzene (dark gray). Light gray lines indicate the positions of Bragg peaks that are only present in the distorted framework, where the dimensions of the  $a$  and  $b$  axes of the unit cell are doubled.



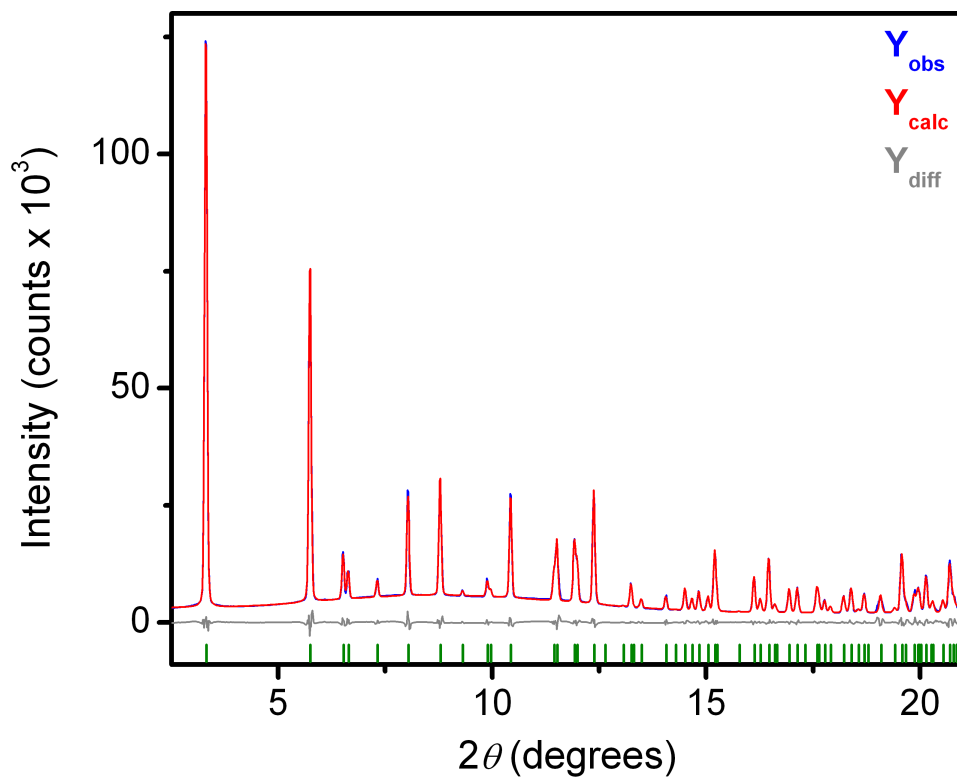
**Figure 3.S24.** Variable temperature powder X-ray diffraction patterns ( $\lambda = 0.75009 \text{ \AA}$ ) for  $\text{Co}_2(\text{dobdc})$  soaked in *o*-xylene from 300 K to 400 K. Light gray lines indicate the positions of Bragg peaks that are only present in the distorted framework, where the dimensions of the *a* and *b* axes of the unit cell are doubled.



**Figure 3.S25.** Structureless Le Bail refinement for X-ray powder diffraction data at 300 K of  $\text{Co}_2(\text{dobdc})$  soaked in *o*-xylene. Blue and red lines represent the observed and calculated diffraction patterns, respectively. The gray line represents the difference between observed and calculated patterns, and the green tick marks indicate calculated Bragg peak positions.  $R_{\text{wp}} = 0.049$ ,  $R_p = 0.035$ ,  $\lambda = 0.75009 \text{ \AA}$ .

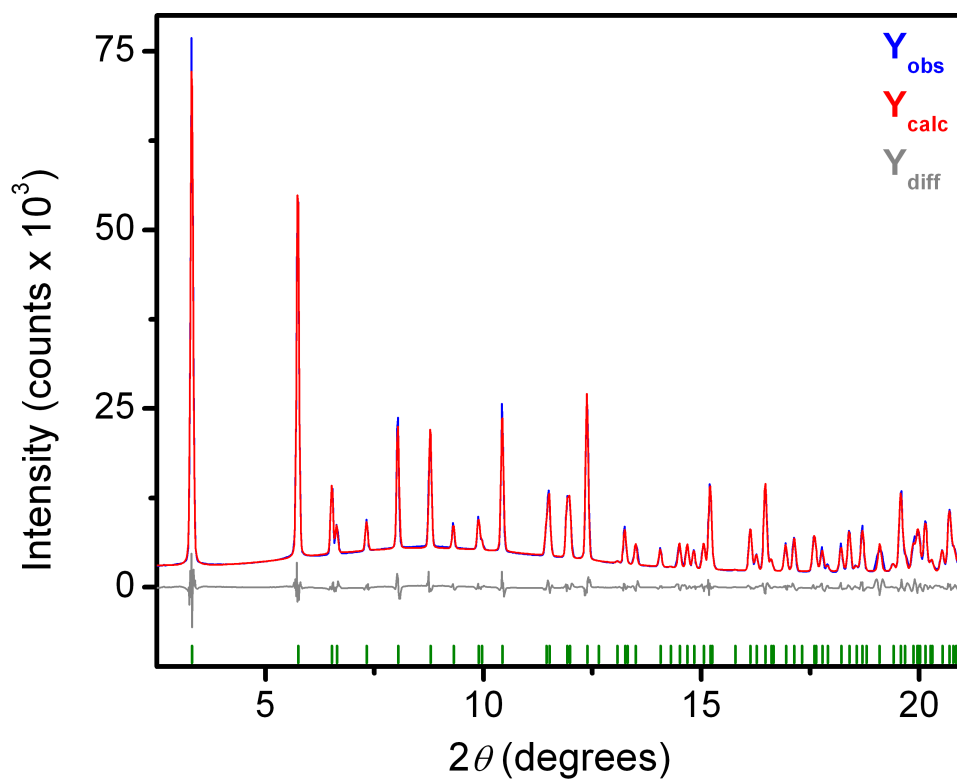


**Figure 3.S26.** Structureless Le Bail refinement for powder X-ray diffraction data at 400 K of  $\text{Co}_2(\text{dobdc})$  soaked in *o*-xylene. Blue and red lines represent the observed and calculated diffraction patterns, respectively. The gray line represents the difference between observed and calculated patterns, and the green tick marks indicate calculated Bragg peak positions.  $R_{\text{wp}} = 0.062$ ,  $R_{\text{p}} = 0.045$ ,  $\lambda = 0.75009 \text{ \AA}$ .

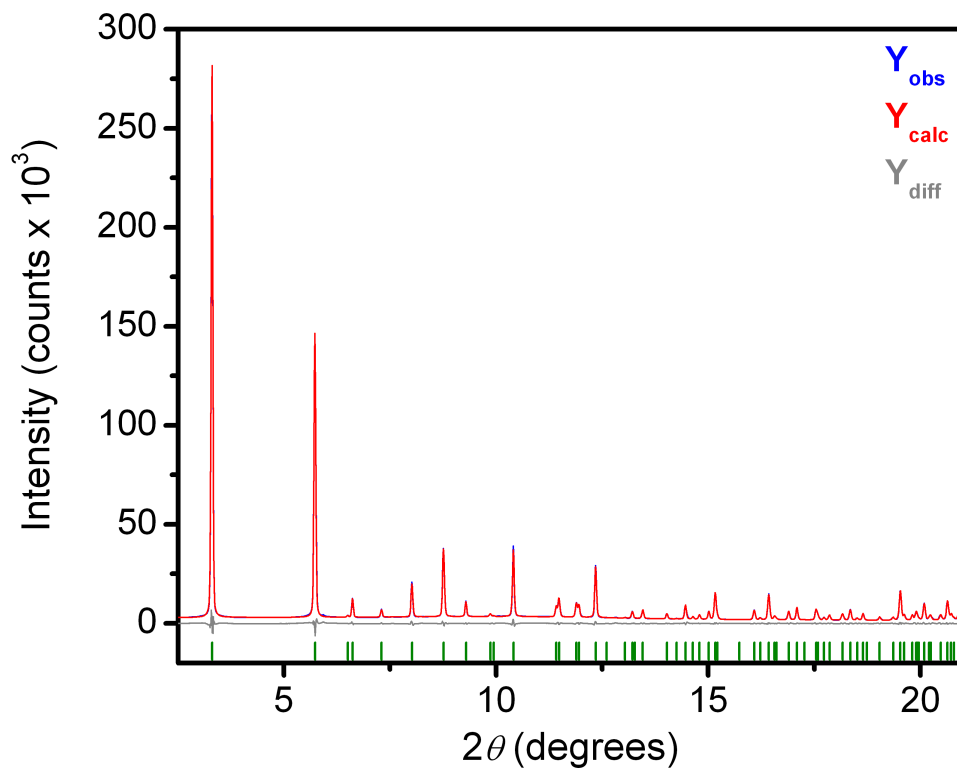


**Figure 3.S27.** Structureless Le Bail refinement for powder X-ray diffraction data at 300 K of Co<sub>2</sub>(dobdc) soaked in *m*-xylene. Blue and red lines represent the observed and calculated diffraction patterns, respectively. The gray line represents the difference between observed and calculated patterns, and the green tick marks indicate calculated Bragg peak positions.  $R_{wp} = 0.040$ ,  $R_p = 0.028$ ,  $\lambda = 0.75009 \text{ \AA}$ .





**Figure 3.S28.** Structureless Le Bail refinement for powder X-ray diffraction data at 300 K of Co<sub>2</sub>(dobdc) soaked in *p*-xylene. Blue and red lines represent the observed and calculated diffraction patterns, respectively. The gray line represents the difference between observed and calculated patterns, and the green tick marks indicate calculated Bragg peak positions.  $R_{wp} = 0.065$ ,  $R_p = 0.045$ ,  $\lambda = 0.75009$  Å.



**Figure 3.S29.** Structureless Le Bail refinement for powder X-ray diffraction data at 300 K of Co<sub>2</sub>(dobdc) soaked in ethylbenzene. Blue and red lines represent the observed and calculated diffraction patterns, respectively. The gray line represents the difference between observed and calculated patterns, and the green tick marks indicate calculated Bragg peak positions.  $R_{wp} = 0.033$ ,  $R_p = 0.025$ ,  $\lambda = 0.75009$  Å.

### 3.7. References

- (1) *Materials for Separation Technologies. Energy and Emission Reduction Opportunities*; U.S. Department of Energy, 2005.
- (2) Sholl, D. S.; Lively, R. P. *Nature* **2016**, 532 (7600), 435–437.
- (3) Fabri, J.; Graeser, U.; Simo, T. A. In *Ullman's Encyclopedia of Industrial Chemistry*; Wiley-VCH Verlag GmbH & Co. KGaA, 2000.
- (4) Denayer, J. F. M.; De Vos, D.; Leflaive, P. In *Metal-Organic Frameworks*; Farrusseng, D., Ed.; Applications from Catalysis to Gas Storage; Wiley-VCH Verlag GmbH & Co. KGaA: Weinheim, Germany, 2011; Vol. 83, pp 171–190.
- (5) Minceva, M.; Rodrigues, A. E. *AIChE J.* **2007**, 53 (1), 138–149.
- (6) Pellegrino, J. L. *Energy and Environmental Profile of the Chemicals Industry*; U.S. Department of Energy, 2000.
- (7) Welch, V. A.; Fallon, K. J.; Gelbke, H.-P. *Ethylbenzene*; Wiley-VCH Verlag GmbH & Co. KGaA: Weinheim, Germany, 2000; Vol. 13, pp 451–414.
- (8) Li, J.-R.; Kuppler, R. J.; Zhou, H.-C. *Chem. Soc. Rev.* **2009**, 38 (5), 1477–29.
- (9) Guo, G.-Q.; Chen, H.; Long, Y.-C. *Microporous Mesoporous Mater.* **2000**, 39 (1-2), 149–161.
- (10) Hulme, R.; Rosensweig, R. E.; Ruthven, D. M. *Ind. Eng. Chem. Res.* **1991**, 30 (4), 752–760.
- (11) Yan, T. Y. *Ind. Eng. Chem. Res.* **1989**, 28 (5), 572–576.
- (12) Ruthven, D. M.; Goddard, M. *Zeolites* **1986**, 6 (4), 275–282.
- (13) Santacesaria, E.; Morbidelli, M.; Servida, A.; Storti, G.; Carra, S. *Ind. Eng. Chem. Process Des. Dev.* **1982**, 21 (3), 446–451.
- (14) Koh, D.-Y.; McCool, B. A.; Deckman, H. W.; Lively, R. P. *Science* **2016**, 353 (6301), 804–807.
- (15) Herm, Z. R.; Bloch, E. D.; Long, J. R. *Chem. Mater.* **2014**, 26 (1), 323–338.
- (16) Van de Voorde, B.; Bueken, B.; Denayer, J.; De Vos, D. *Chem. Soc. Rev.* **2014**, 43 (16), 5766–5788.
- (17) Alaerts, L.; Kirschhock, C. E. A.; Maes, M.; van der Veen, M. A.; Finsy, V.; Depla, A.; Martens, J. A.; Baron, G. V.; Jacobs, P. A.; Denayer, J. F. M.; De Vos, D. E. *Angew. Chem. Int. Ed.* **2007**, 46 (23), 4293–4297.
- (18) Alaerts, L.; Maes, M.; Jacobs, P. A.; Denayer, J. F. M.; De Vos, D. E. *Phys. Chem. Chem. Phys.* **2008**, 10 (20), 2979–2985.
- (19) Finsy, V.; Verelst, H.; Alaerts, L.; De Vos, D.; Jacobs, P. A.; Baron, G. V.; Denayer, J. F. M. *J. Am. Chem. Soc.* **2008**, 130 (22), 7110–7118.
- (20) Alaerts, L.; Maes, M.; Giebler, L.; Jacobs, P. A.; Martens, J. A.; Denayer, J. F. M.; Kirschhock, C. E. A.; De Vos, D. E. *J. Am. Chem. Soc.* **2008**, 130 (43), 14170–14178.
- (21) Gu, Z.-Y.; Jiang, D.-Q.; Wang, H.-F.; Cui, X.-Y.; Yan, X.-P. *J. Phys. Chem. C* **2010**, 114 (1), 311–316.
- (22) Bárcia, P. S.; Guimarães, D.; Mendes, P. A. P.; Silva, J. A. C.; Guillerm, V.; Chevreau, H.; Serre, C.; Rodrigues, A. E. *Microporous Mesoporous Mater.* **2011**, 139 (1-3), 67–73.
- (23) Vermoortele, F.; Maes, M.; Moghadam, P. Z.; Lennox, M. J.; Ragon, F.; Boulhout, M.; Biswas, S.; Laurier, K. G. M.; Beurroies, I.; Denoyel, R.; Roeffaers, M.; Stock, N.; Düren, T.; Serre, C.; De Vos, D. E. *J. Am. Chem. Soc.* **2011**, 133 (46), 18526–18529.
- (24) Peralta, D.; Barthelet, K.; Pérez-Pellitero, J.; Chizallet, C.; Chaplais, G.; Simon-Masseron, A.; Pirngruber, G. D. *J. Phys. Chem. C* **2012**, 116 (41), 21844–21855.

- (25) Warren, J. E.; Perkins, C. G.; Jelfs, K. E.; Boldrin, P.; Chater, P. A.; Miller, G. J.; Manning, T. D.; Briggs, M. E.; Stylianou, K. C.; Claridge, J. B.; Rosseinsky, M. J. *Angew. Chem. Int. Ed.* **2014**, *53* (18), 4592–4596.
- (26) Osta, El, R.; Carlin-Sinclair, A.; Guillou, N.; Walton, R. I.; Vermoortele, F.; Maes, M.; De Vos, D.; Millange, F. *Chem. Mater.* **2012**, *24* (14), 2781–2791.
- (27) Caskey, S. R.; Wong-Foy, A. G.; Matzger, A. J. *J. Am. Chem. Soc.* **2008**, *130* (33), 10870–10871.
- (28) Dietzel, P. D. C.; Besikiotis, V.; Blom, R. *J. Mater. Chem.* **2009**, *19* (39), 7362–7370.
- (29) Bloch, E. D.; Murray, L. J.; Queen, W. L.; Chavan, S.; Maximoff, S. N.; Bigi, J. P.; Krishna, R.; Peterson, V. K.; Grandjean, F.; Long, G. J.; Smit, B.; Bordiga, S.; Brown, C. M.; Long, J. R. *J. Am. Chem. Soc.* **2011**, *133* (37), 14814–14822.
- (30) Bloch, E. D.; Queen, W. L.; Krishna, R.; Zadrozny, J. M.; Brown, C. M.; Long, J. R. *Science* **2012**, *335* (6076), 1606–1610.
- (31) Bloch, E. D.; Hudson, M. R.; Mason, J. A.; Chavan, S.; Crocellà, V.; Howe, J. D.; Lee, K.; Dzubak, A. L.; Queen, W. L.; Zadrozny, J. M.; Geier, S. J.; Lin, L.-C.; Gagliardi, L.; Smit, B.; Neaton, J. B.; Bordiga, S.; Brown, C. M.; Long, J. R. *J. Am. Chem. Soc.* **2014**, *136* (30), 10752–10761.
- (32) Queen, W. L.; Hudson, M. R.; Bloch, E. D.; Mason, J. A.; Gonzalez, M. I.; Lee, J. S.; Gygi, D.; Howe, J. D.; Lee, K.; Darwish, T. A.; James, M.; Peterson, V. K.; Teat, S. J.; Smit, B.; Neaton, J. B.; Long, J. R.; Brown, C. M. *Chem. Sci.* **2014**, *5* (12), 4569–4581.
- (33) Xiao, D. J.; Gonzalez, M. I.; Darago, L. E.; Vogiatzis, K. D.; Haldoupis, E.; Gagliardi, L.; Long, J. R. *J. Am. Chem. Soc.* **2016**, *138* (22), 7161–7170.
- (34) Reed, D. A.; Xiao, D. J.; Gonzalez, M. I.; Darago, L. E.; Herm, Z. R.; Grandjean, F.; Long, J. R. *J. Am. Chem. Soc.* **2016**, *138* (17), 5594–5602.
- (35) Geier, S. J.; Mason, J. A.; Bloch, E. D.; Queen, W. L.; Hudson, M. R.; Brown, C. M.; Long, J. R. *Chem. Sci.* **2013**, *4* (5), 2054–2061.
- (36) Bloch, E. D.; Queen, W. L.; Hudson, M. R.; Mason, J. A.; Xiao, D. J.; Murray, L. J.; Flacau, R.; Brown, C. M.; Long, J. R. *Angewandte Chemie* **2016**, *128* (30), 8747–8751.
- (37) Murray, L. J.; Dincă, M.; Yano, J.; Chavan, S.; Bordiga, S.; Brown, C. M.; Long, J. R. *J. Am. Chem. Soc.* **2010**, *132* (23), 7856–7857.
- (38) Sumida, K.; Rogow, D. L.; Mason, J. A.; McDonald, T. M.; Bloch, E. D.; Herm, Z. R.; Bae, T.-H.; Long, J. R. *Chem. Rev.* **2012**, *112* (2), 724–781.
- (39) Gygi, D.; Bloch, E. D.; Mason, J. A.; Hudson, M. R.; Gonzalez, M. I.; Siegelman, R. L.; Darwish, T. A.; Queen, W. L.; Brown, C. M.; Long, J. R. *Chem. Mater.* **2016**, *28* (4), 1128–1138.
- (40) Dietzel, P. D. C.; Morita, Y.; Blom, R.; Fjellvåg, H. *Angew. Chem. Int. Ed.* **2005**, *44* (39), 6354–6358.
- (41) Kapelewski, M. T.; Geier, S. J.; Hudson, M. R.; Stück, D.; Mason, J. A.; Nelson, J. N.; Xiao, D. J.; Hulvey, Z.; Gilmour, E.; FitzGerald, S. A.; Head-Gordon, M.; Brown, C. M.; Long, J. R. *J. Am. Chem. Soc.* **2014**, *136* (34), 12119–12129.
- (42) McDonald, T. M.; Mason, J. A.; Kong, X.; Bloch, E. D.; Gygi, D.; Dani, A.; Crocellà, V.; Giordanino, F.; Odoh, S. O.; Drisdell, W. S.; Vlaisavljevich, B.; Dzubak, A. L.; Poloni, R.; Schnell, S. K.; Planas, N.; Lee, K.; Pascal, T.; Wan, L. F.; Prendergast, D.; Neaton, J. B.; Smit, B.; Kortright, J. B.; Gagliardi, L.; Bordiga, S.; Reimer, J. A.; Long, J. R. *Nature* **2015**, *519* (7543), 303–308.
- (43) Bruker Analytical X-ray Systems, Inc. *SAINT and APEX 2 Software for CCD*

- Diffractionmeters*; Bruker Analytical X-ray Systems, Inc.: Madison, WI, USA, 2000.
- (44) Sheldrick, G. M. *SADABS*; Bruker Analytical X-ray Systems, Inc.: Madison, WI, USA, 2014.
- (45) Sheldrick, G. M. *Acta Crystallogr., A, Found. Crystallogr.* **2008**, *64* (Pt 1), 112–122.
- (46) Sheldrick, G. M. *SHELXS*; University of Göttingen, Germany, 2014.
- (47) Sheldrick, G. M. *Acta Crystallogr A Found Adv* **2015**, *71* (Pt 1), 3–8.
- (48) Sheldrick, G. M. *SHELXL*; University of Göttingen, Germany: University of Göttingen, Germany, 2014.
- (49) Dolomanov, O. V.; Bourhis, L. J.; Gildea, R. J.; Howard, J. A. K.; Puschmann, H. *Journal of Applied Crystallography* **2009**, *42* (2), 339–341.
- (50) Coelho, A. A. *Journal of Applied Crystallography* **2003**, *36* (1), 86–95.
- (51) Coelho, A. A. *TOPAS-Academic, Version 4.1*; Coelho Software: Brisbane, 2007.
- (52) Minceva, M.; Rodrigues, A. E. *Chemical Engineering Research and Design* **2004**, *82* (5), 667–681.
- (53) Bellat, J.-P.; Simonot-Grange, M.-H.; Jullian, S. *Zeolites* **1995**, *15* (2), 124–130.
- (54) DeSantis, D.; Mason, J. A.; James, B. D.; Houchins, C.; Long, J. R.; Veenstra, M. *Energy & Fuels* **2017**, *31* (2), 2024–2032.
- (55) Perego, C.; Pollesel, P. In *Advances in Nanoporous Materials*; Ernst, S., Ed.; Advances in Nanoporous Materials; Elsevier, 2010; Vol. 1, pp 97–149.
- (56) Dietzel, P. D. C.; Georgiev, P. A.; Eckert, J.; Blom, R.; Strässle, T.; Unruh, T. *Chem. Commun.* **2010**, *46* (27), 4962–4963.
- (57) Xiao, D. J.; Bloch, E. D.; Mason, J. A.; Queen, W. L.; Hudson, M. R.; Planas, N.; Borycz, J.; Dzubak, A. L.; Verma, P.; Lee, K.; Bonino, F.; Crocellà, V.; Yano, J.; Bordiga, S.; Truhlar, D. G.; Gagliardi, L.; Brown, C. M.; Long, J. R. *Nature Chemistry* **2014**, *6* (7), 590–595.
- (58) McKinlay, A. C.; Xiao, B.; Wragg, D. S.; Wheatley, P. S.; Megson, I. L.; Morris, R. E. *J. Am. Chem. Soc.* **2008**, *130* (31), 10440–10444.
- (59) Bloch, E. D.; Queen, W. L.; Chavan, S.; Wheatley, P. S.; Zadrozny, J. M.; Morris, R.; Brown, C. M.; Lamberti, C.; Bordiga, S.; Long, J. R. *J. Am. Chem. Soc.* **2015**, *137* (10), 3466–3469.
- (60) Sumida, K.; Her, J.-H.; Dincă, M.; Murray, L. J.; Schloss, J. M.; Pierce, C. J.; Thompson, B. A.; FitzGerald, S. A.; Brown, C. M.; Long, J. R. *J. Phys. Chem. C* **2011**, *115* (16), 8414–8421.
- (61) Queen, W. L.; Bloch, E. D.; Brown, C. M.; Hudson, M. R.; Mason, J. A.; Murray, L. J.; Ramirez-Cuesta, A. J.; Peterson, V. K.; Long, J. R. *Dalton Trans.* **2012**, *41* (14), 4180–4188.
- (62) Lee, J. S.; Vlasisavljevich, B.; Britt, D. K.; Brown, C. M.; Haranczyk, M.; Neaton, J. B.; Smit, B.; Long, J. R.; Queen, W. L. *Adv. Mater.* **2015**, *27* (38), 5785–5796.
- (63) Bloch, W. M.; Burgun, A.; Coghlan, C. J.; Lee, R.; Coote, M. L.; Doonan, C. J.; Sumbly, C. J. *Nature Chemistry* **2014**, *6* (10), 906–912.
- (64) Furukawa, H.; Gándara, F.; Zhang, Y.-B.; Jiang, J.; Queen, W. L.; Hudson, M. R.; Yaghi, O. M. *J. Am. Chem. Soc.* **2014**, *136* (11), 4369–4381.
- (65) Magdysyuk, O. V.; Adams, F.; Liermann, H.-P.; Spanopoulos, I.; Trikalitis, P. N.; Hirscher, M.; Morris, R. E.; Duncan, M. J.; McCormick, L. J.; Dinnebier, R. E. *Phys. Chem. Chem. Phys.* **2014**, *16* (43), 23908–23914.
- (66) Ghose, S. K.; Li, Y.; Yakovenko, A.; Dooryhee, E.; Ehm, L.; Ecker, L. E.; Dippel, A.-

- C.; Halder, G. J.; Strachan, D. M.; Thallapally, P. K. *J. Phys. Chem. Lett.* **2015**, *6* (10), 1790–1794.
- (67) Dietzel, P. D. C.; Johnsen, R. E.; Fjellvåg, H.; Bordiga, S.; Groppo, E.; Chavan, S.; Blom, R. *Chem. Commun.* **2008**, No. 41, 5125–5127.
- (68) Liu, Y.; Kabbour, H.; Brown, C. M.; Neumann, D. A.; Ahn, C. C. *Langmuir* **2008**, *24* (9), 4772–4777.
- (69) Gonzalez, M. I.; Mason, J. A.; Bloch, E. D.; Teat, S. J.; Gagnon, K. J.; Morrison, G. Y.; Queen, W. L.; Long, J. R. *Chem. Sci.* **2017**, *8* (6), 4387–4398.
- (70) Rosnes, M. H.; Sheptyakov, D.; Franz, A.; Frontzek, M.; Dietzel, P. D. C.; Georgiev, P. A. *Phys. Chem. Chem. Phys.* **2017**, *103*, 2347.
- (71) Jawahery, S.; Simon, C. M.; Braun, E.; Witman, M.; Tiana, D.; Vlaisavljevich, B.; Smit, B. *Nat Commun* **2016**, *8*, 1–9.
- (72) Pike, S. D.; Thompson, A. L.; Algarra, A. G.; Apperley, D. C.; Macgregor, S. A.; Weller, A. S. *Science* **2012**, *337* (6102), 1648–1651.
- (73) Pike, S. D.; Chadwick, F. M.; Rees, N. H.; Scott, M. P.; Weller, A. S.; Krämer, T.; Macgregor, S. A. *J. Am. Chem. Soc.* **2015**, *137* (2), 820–833.
- (74) Chadwick, F. M.; Rees, N. H.; Weller, A. S.; Krämer, T.; Iannuzzi, M.; Macgregor, S. A. *Angew. Chem. Int. Ed.* **2016**, *55* (11), 3677–3681.
- (75) Vigalok, A.; Uzan, O.; Shimon, L. J. W.; Ben-David, Y.; Martin, J. M. L.; Milstein, D. *J. Am. Chem. Soc.* **1998**, *120* (48), 12539–12544.
- (76) Dani, P.; Karlen, T.; Gossage, R. A.; Smeets, W. J. J.; Spek, A. L.; Van Koten, G. *J. Am. Chem. Soc.* **1997**, *119* (46), 11317–11318.
- (77) Gusev, D. G.; Madott, M.; Dolgushin, F. M.; Lyssenko, K. A.; Antipin, M. Y. *Organometallics* **2000**, *19* (9), 1734–1739.
- (78) Stępień, M.; Latos-Grażyński, L.; Szterenberga, L.; Panek, J.; Latajka, Z. *J. Am. Chem. Soc.* **2004**, *126* (14), 4566–4580.

## Chapter 4. Single-Crystal-to-Single-Crystal Metalation of a Metal–Organic Framework: A Route toward Structurally Well-Defined Catalysts

### 4.1. Introduction

The synthesis of catalysts with highly tunable and well-defined active sites remains an enduring goal in the field of heterogeneous catalysis, as the development of new catalysts has been largely limited by the structural ambiguity and non-uniformity in typical heterogeneous catalysts.<sup>1,2</sup> Although molecular catalysts exhibit tremendous advantages in the ability to design and characterize their active sites, approximately 80% of catalytic processes still adopt heterogeneous systems.<sup>3</sup> This strong industrial preference for heterogeneous catalysts arises from their inherent stability and ease of recovery, which allows more efficient catalyst separation and reuse. Significant advances in preparing and characterizing heterogeneous catalysts with distinct site-isolated active species have been achieved by grafting molecular catalysts onto solid supports coupled with characterization via a comprehensive array of spectroscopic techniques.<sup>1,2</sup> Molecular systems, however, still maintain a considerably higher degree of structural control and are typically more amenable to characterization than heterogeneous materials. In particular, the ability to systematically change the ligand environment of the catalytically active metal site and determine molecular structure by X-ray diffraction remains unrealized in these supported catalysts.

Metal–organic frameworks exhibit the exceptional capability of adopting crystalline structures with both high porosity<sup>4</sup> and specific pore environments,<sup>5,6</sup> resulting in their extensive evaluation for applications in gas storage and gas separation.<sup>7-10</sup> As readily functionalized porous structures, these materials are uniquely suited to combine the structural control available to homogeneous molecular catalysts with the inherent ease of separation and reuse of heterogeneous catalysts. Similar to molecular catalysts, metal–organic frameworks can be easily tailored to give optimal catalytic activity and selectivity.<sup>11-13</sup> Moreover, active site isolation within a solid framework can impart stability to reactive species by preventing intermolecular decomposition pathways, allowing their characterization and use for productive chemistry.<sup>14-18</sup> Finally, the ability to determine the structures of these frameworks through X-ray diffraction enables facile correlation of structure to catalytic activity.<sup>14,19</sup> Altogether, these distinct advantages open up a promising avenue towards the design of robust catalysts with isolated and well-defined active sites.

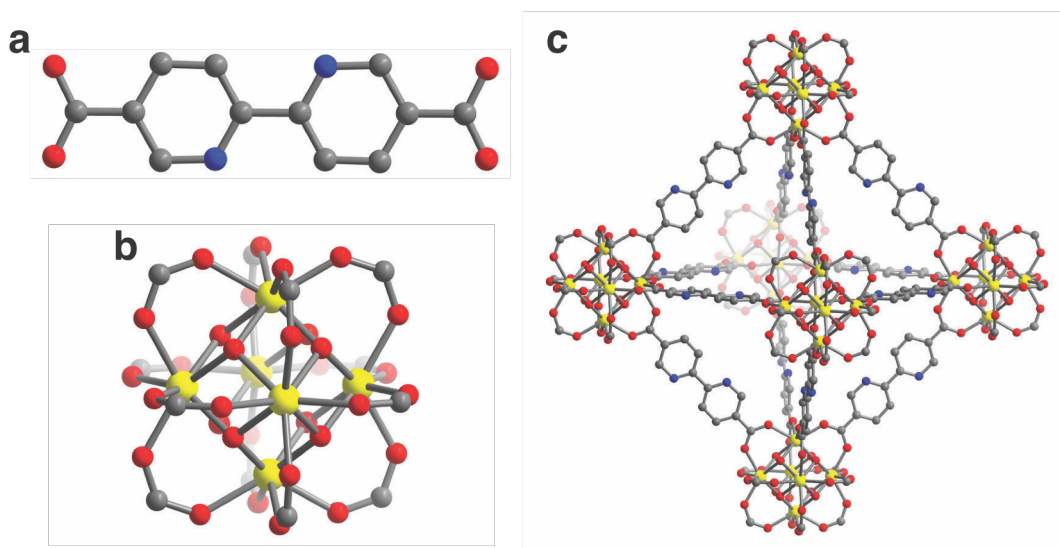
Much of the research on metal–organic framework catalysis has focused on reactions facilitated by the metal nodes.<sup>14,20-23</sup> In comparison to molecular catalysts, however, achieving tunability in these systems has been challenging, as only a few metal and linker combinations lead to frameworks with metal sites that are accessible for catalysis. This limits the range of metal sites and coordination environments available to evaluate as potential catalytically active sites. To overcome these limitations, alternative strategies have been developed to allow greater opportunity for catalyst design, such as the encapsulation of catalytically active metal species<sup>24-26</sup> and the use of functionalized linkers to build catalysts into the framework.<sup>13,17,27-30</sup> Among these methods, post-synthetic metalation has emerged as a versatile way to produce materials with isolated and well-defined catalytically active sites.<sup>31-37</sup>

In analogy to how a single ligand family is used to make a diverse set of molecular catalysts, we envisioned using a metal–organic framework with bridging linkers featuring accessible chelating sites as a platform to synthesize catalysts for a variety of reactions. Through judicious choice of the metal source used for post-synthetic metalation, one could potentially prepare a

wide range of catalytically-active species based not only on the identity of the metal cation but also the coordinated ancillary ligands.

The synthesis of metal–organic frameworks with open chelating sites requires a strategy that prevents metalation of the chelating site during framework synthesis. This has previously been achieved by using a linker with hard carboxylate donors and a softer chelating moiety, allowing selective metal coordination based on their hard/soft acid properties.<sup>19,38</sup> The hard carboxylate groups preferentially bind to hard oxophilic metal ions to form a porous framework, while the chelating sites remain available for post-synthetic metalation. Metal–organic frameworks derived from the  $\text{Zr}_6\text{O}_4(\text{OH})_4(\text{bpdc})_6$  ( $\text{bpdc}^{2-}$  = biphenyl-4,4'-dicarboxylate) or UiO-67<sup>39</sup> represent ideal systems for this strategy due to their inherent thermal and chemical stability and the strong preference of  $\text{Zr}^{\text{IV}}$  for hard oxygen donors. We anticipated that  $\text{Zr}_6\text{O}_4(\text{OH})_4(\text{bpydc})_6$  ( $\text{bpydc}^{2-}$  = and 2,2'-bipyridine-5,5'-dicarboxylate), the bipyridine analog of  $\text{Zr}_6\text{O}_4(\text{OH})_4(\text{bpdc})_6$ , could be synthesized and employed as a platform for building an array of heterogeneous catalysts through post-synthetic metalation (Figure 4.1). Indeed, while this manuscript was in preparation, recent reports have demonstrated the synthesis of this compound and its application in gas separation,<sup>40</sup>  $\text{H}_2\text{S}$  removal,<sup>41</sup> and catalysis.<sup>32,33</sup>

In addition to being a versatile route towards new heterogeneous catalysts, the structural determination of the resulting metalated frameworks can provide insight that is critical to both understanding the mechanism of catalysis and precise tuning of catalyst structure to obtain ideal activity and selectivity. This would demonstrate the ability to characterize and tailor a heterogeneous catalyst to a degree previously only possible for molecular systems. In practice, however, it can be very challenging to determine the structures of the metal-linker complexes formed from post-synthetic metalation, because the high symmetry of most metal–organic frameworks leads to disorder of these sites.<sup>18,30,34,42</sup> Recent work, however, has shown that structurally ordered metal-linker complexes can be achieved if a metal–organic framework has



**Figure 4.1.** Structure of  $\text{bpydc}^{2-}$  linkers (a) and the octahedral  $\text{Zr}_6$  inorganic nodes (b) in **1**. A portion of the crystal structure of **1** (c) as determined by analysis of single-crystal X-ray diffraction data. The bipyridine nitrogen atoms were found to be disordered over two positions in the crystal structure, but are represented here in specific positions. Yellow, red, blue, and gray spheres represent Zr, O, N, and C atoms, respectively; H atoms are omitted for clarity.



sufficiently low symmetry.<sup>19</sup>

Herein, we report the synthesis of  $\text{Zr}_6\text{O}_4(\text{OH})_4(\text{bpydc})_6$  (**1**) and its subsequent metalation with solution- and gas-phase metal precursors. We demonstrate the unprecedented single-crystal-to-single-crystal metalation of **1** and characterization of the resulting metalated frameworks,  $\mathbf{1}\cdot(\text{CuCl}_2)_{5.8}$ ,  $\mathbf{1}\cdot(\text{CuCl})_{6.8}$ ,  $\mathbf{1}\cdot(\text{CoCl}_2)_{5.5}$ ,  $\mathbf{1}\cdot(\text{FeBr}_2)_{6.1}$ , and  $\mathbf{1}\cdot(\text{Cr}(\text{CO})_4)_{5.6}$ , by single-crystal X-ray diffraction. Remarkably, metalation of the framework leads to a structural transition to a lower symmetry space group, allowing the structural characterization of the metal-bipyridine complexes within the pores. Furthermore, **1** shows catalytic activity in arene C–H borylation upon metalation with  $[\text{Ir}(\text{COD})_2]\text{BF}_4$ . These results highlight the unique potential of metal–organic frameworks as heterogeneous catalysts with well-defined site-isolated active sites that can be precisely characterized structurally.

## 4.2. Experimental

**Materials and Methods.** All manipulations were performed under an  $\text{N}_2$  atmosphere in a VAC Atmospheres glovebox or using standard Schlenk techniques. Acetonitrile, benzene, toluene, hexanes, diethyl ether, and 1,2-difluorobenzene were deoxygenated by purging with argon for 1 h and dried using a commercial solvent purification system designed by JC Meyer Solvent Systems. The compounds 1,3-dimethylbenzene and 1,3-dimethoxybenzene were purchased from Sigma-Aldrich, dried over Na/benzophenone, and degassed via three successive freeze–pump–thaw cycles. Bis(pinacolato)diboron was purchased from Strem and purified by recrystallization from hexanes followed by sublimation at 80 °C and 60 mTorr. The compounds 2,2'-bipyridine-5,5'-dicarboxylic acid ( $\text{H}_2\text{bpydc}$ ) and dimethyl [2,2'-bipyridine]-5,5'-dicarboxylate ( $\text{dmbpydc}$ ) were synthesized using a previously published procedure.<sup>29</sup> The compounds  $\text{ZrCl}_4$ , 5,5'-dimethyl-2,2'-bipyridine, 1,3,5-trimethoxybenzene, triphenyl-phosphine ( $\text{PPh}_3$ ), and tricyclohexylphosphine ( $\text{PCy}_3$ ) were purchased from Sigma-Aldrich and used as received. The compounds  $[\text{Ir}(\text{COD})_2]\text{BF}_4$ ,  $\text{FeBr}_2$ ,  $\text{CoCl}_2$ ,  $\text{CuCl}$ , and  $\text{CuCl}_2$  were purchased from Strem and used as received. All other chemicals were purchased from commercial vendors and used as received unless otherwise noted.

Thermogravimetric analyses were carried out with a TA Instruments TGA Q5000 operating at a ramp rate of 1 °C/min under a 25 mL/min  $\text{N}_2$  flow. Air-sensitive samples were prepared as a slurry in hexanes to temporarily protect the sample from oxygen and moisture and quickly loaded into the instrument. Samples were then heated to 100 °C at a rate of 1 °C/min and held at that temperature for 1 h to evaporate the hexanes prior to analysis. Infrared spectra were collected on a Perkin Elmer Avatar Spectrum 400 FTIR spectrophotometer equipped with a Pike attenuated total reflectance accessory (ATR) accessory. UV-vis spectra were recorded on a Carry 5000 spectrophotometer equipped with a reflectance sphere for diffuse reflectance spectra. Scanning electron microscopy (SEM) samples were prepared by dispersing crystals in dichloromethane and drop casting onto a silicon chip. In order to dissipate charge, the samples were sputter coated with ~3 nm of Au (Denton Vacuum, LLC). Crystals were imaged at 5keV/12 $\mu\text{A}$  by field emission SEM (JEOL FSM6430). Elemental analyses were obtained from the Microanalytical Laboratory of the University of California, Berkeley using a Perkin-Elmer 2400 Series II combustion analyzer. NMR spectra were acquired on Bruker AVB-400 and AVQ-400 instruments at the University of California, Berkeley NMR facility. All chemical shifts are given in relation to residual solvent peaks or tetramethylsilane. NMR yields were determined by  $^1\text{H}$  NMR spectroscopy with 1,3,5-trimethoxybenzene as an internal standard.

**Zr<sub>6</sub>O<sub>4</sub>(OH)<sub>4</sub>(bpydc)<sub>6</sub> (1).** H<sub>2</sub>bpydc (3.09 g, 12.5 mmol) and benzoic acid (125 g, 1000 mmol), and *N,N*-dimethylformamide (DMF; 1 L) from a newly opened bottle were placed into a three-neck 2-L round bottom flask equipped with a Schlenk adapter, glass stoppers, and a magnetic stir bar and the resulting mixture was purged with dry nitrogen for 30 min. Solid ZrCl<sub>4</sub> (2.96 g, 12.5 mmol) was then added and the mixture was purged with dry nitrogen for an additional 30 min. Deionized water (410 μL, 22.8 mmol) was then added and the mixture was heated with magnetic stirring for 5 days at 120 °C under a nitrogen atmosphere. After allowing the mixture to cool to room temperature, the solvent was decanted and the resulting white microcrystalline powder was washed by soaking three times in 500-mL aliquots fresh DMF for 24 h at 120 °C, followed by solvent exchange with tetrahydrofuran (THF) via Soxhlet extraction for 3 days. The THF solvated powder was filtered under dry N<sub>2</sub>, followed by heating at 120 °C under dynamic vacuum for 24 h to give fully-desolvated Zr<sub>6</sub>O<sub>4</sub>(OH)<sub>4</sub>(bpydc)<sub>6</sub>. Yield: 3.70 g, 82%. Anal. Calc. for C<sub>72</sub>H<sub>36</sub>N<sub>12</sub>O<sub>32</sub>Zr<sub>6</sub>: C, 40.55; H, 1.98; N, 7.88. Found: C, 41.72; H, 1.98; N, 7.52. IR (solid-ATR): 3205 (br, w), 1653 (m), 1591 (s), 1536 (m), 1403 (s), 1167 (w), 1014 (w), 839 (2), 802 (w), 770 (s), 720 (w), 653 (s), 455 (s).

**Single Crystals of Zr<sub>6</sub>O<sub>4</sub>(OH)<sub>4</sub>(bpydc)<sub>6</sub> (1).** H<sub>2</sub>bpydc (247 mg, 1.00 mmol), benzoic acid (9.89 g, 80.0 mmol), and anhydrous DMF (80 mL) were placed into a 100-mL Teflon-capped jar and sonicated for 1 min. Solid ZrCl<sub>4</sub> (466 mg, 2.00 mmol) was then added and the mixture was sonicated for 1 min. Deionized water (128 μL) was added and the resulting solution was placed in an oven that was pre-heated to 120 °C, and the vessel was kept at that temperature for 5 days, yielding colorless octahedron-shaped single crystals on the walls of the jar. The crystals were soaked three times in fresh DMF for 24 h at 120 °C, followed by soaking three times in dry deoxygenated THF for 24 h at 70 °C in a Schlenk flask under N<sub>2</sub> atmosphere. The crystals were then kept in THF and stored in a glove box under N<sub>2</sub> atmosphere. Characterization of the crystals was performed using single-crystal X-ray diffraction.

**General Procedure for Metalation of 1 with Solution-Phase Metal Precursors.** Microcrystalline **1** (50–500 mg), the desired metal source (0.10–1.0 equivalents per bpydc), and acetonitrile (3 mL) were mixed in a 20-mL Teflon-capped vial. The resulting mixture was then heated for a week on a hot plate at 80 °C to afford a colored powder. After cooling to room temperature, the solvent was decanted and the powder was soaked three times in fresh acetonitrile for 24 h at 80 °C in order to remove any unreacted metal source. The solvent was then removed under reduced pressure at 80 °C to give the corresponding metalated framework. Metal insertion reduces the stability of the framework to moisture. Thus, metalation and subsequent manipulations were carried out under an inert atmosphere.

Single crystals of **1** in THF were placed in a 4-mL Teflon-capped vial. Most of the solvent was pipetted out, followed by addition of excess (10–20 mg) metal source in acetonitrile. The mixture was allowed to react for 7 days at 80 °C, resulting in a color change of the crystals. Most of the solution was removed by pipette and the crystals were subsequently soaked three times in fresh acetonitrile at 80 °C for 24 h, and were then used for single-crystal X-ray diffraction experiments.

**Metalation of 1 with Cr(CO)<sub>6</sub>.** Microcrystalline powder of Zr<sub>6</sub>O<sub>4</sub>(OH)<sub>4</sub>(bpydc)<sub>6</sub> (10-50 mg) in a 4 mL vial were placed in a 20 mL vial containing excess Cr(CO)<sub>6</sub>. The 20-mL vial was sealed with a Teflon cap and heated for 7 days at 80 °C. The resulting dark green solid was washed three times with benzene at 80 °C to remove any unreacted Cr(CO)<sub>6</sub>, and was then heated at 80 °C under reduced pressure for 24 h to give **1**·(Cr(CO)<sub>4</sub>)<sub>5.6</sub>.

Single crystals of  $\text{Zr}_6\text{O}_4(\text{OH})_4(\text{bpydc})_6$  in THF or benzene were placed in a 4-mL Teflon-capped vial. Most of the solvent was pipetted out and the 4-mL vial was placed within a 20-mL vial containing excess  $\text{Cr}(\text{CO})_6$ . The 20-mL vial was sealed with a Teflon cap and heated for 7 days at 80 °C. The resulting dark green crystals were either used directly or soaked in acetonitrile then used for single-crystal X-ray diffraction experiments.

**$\text{Zr}_6\text{O}_4(\text{OH})_4(\text{bpdc})_6$  (2).** This material was synthesized by substituting  $\text{H}_2\text{bpydc}$  with  $\text{H}_2\text{bpdc}$  in the synthetic procedure for **1** above. Anal. Calc. for  $\text{C}_{84}\text{H}_{52}\text{O}_{32}\text{Zr}_6$ : C, 47.58; H, 2.47; N, 0. Found: C, 47.85; H, 2.11; N, 0.

**$[\text{Ir}(\text{dmbpydc})(\text{COD})]\text{BF}_4$  (3).** In a 20-mL vial,  $\text{dmbpydc}$  (22.0 mg, 0.0808 mmol) was added to a solution of  $[\text{Ir}(\text{COD})_2]\text{BF}_4$  (40.2 mg, 0.0811 mmol) in acetonitrile (3 mL). The initially yellow solution immediately turned dark green upon addition of  $\text{dmbpydc}$ . The vial was sealed with a Teflon cap and allowed to stir at room temperature for 12 h. The resulting dark green solution was then concentrated under reduced pressure. Layering or slow diffusion of diethyl ether over the concentrated solution afforded dark green crystals, which were suitable for single-crystal X-ray analysis. After carefully decanting the solvent, the crystals were washed with diethyl ether and dried under reduced pressure to give  $[\text{Ir}(\text{dmbpydc})(\text{COD})]\text{BF}_4$ . Yield: 38.2 mg, 72%. Anal. Calc. for  $\text{C}_{22}\text{H}_{24}\text{BF}_4\text{IrN}_2\text{O}_4$ : C, 40.07; H, 3.67; N, 4.25. Found: C, 39.62; H, 3.40; N, 4.72.  $^1\text{H}$  NMR (400 MHz,  $\text{CD}_3\text{CN}$ )  $\delta$  8.778 (dd, 2H), 8.703 (d, 2H), 8.537 (d, 2H), 4.406 (m, 4H), 3.971 (s, 6H), 2.405 (m, 4H), 2.035 (m, 4H). IR (solid-ATR): 3121 (w), 3067 (w), 3000 (w), 2958 (w), 2894 (w), 2841 (w), 1721 (m), 1611 (2), 1427 (w), 1296 (m), 1276 (m), 1191 (w), 1128 (m), 1027 (br, m), 867 (w), 760 (m), 523 (w), 484 (w).

**General Procedure for Metal Content Analysis via ICP-OES.** Roughly 10 mg of activated material was placed in a 20 mL plastic vial and digested with 2 mL concentrated HF and diluted with 18 mL 5%  $\text{HNO}_3$  in Millipore water. The resulting solution was transferred to a 100 mL volumetric flask and diluted to mark with 5% (v/v) aqueous  $\text{HNO}_3$  in Millipore water to give a stock solution that contained roughly 25 ppm Zr from the sample. The stock sample solution (10 mL) and 2.5 ppm Y (1 mL) were added to a 25 mL volumetric flask and diluted to mark with 5% (v/v) aqueous  $\text{HNO}_3$  to give sample solution that is roughly 10 ppm Zr with 0.1 ppm Y as an internal standard. Standard solutions with 0.1, 1, 5, 10, and 15 ppm of the metals of interest and 0.1 ppm Y as an internal standard were prepared for the calibration curve.

**Low-Pressure Gas Adsorption Measurements.** Gas adsorption isotherms for pressures in the range 0–1.2 bar were measured by a volumetric method using Micromeritics ASAP2020 and ASAP2420 instruments. A typical sample of ca. 100 mg of metal–organic framework was transferred to a pre-weighed analysis tube, which was capped with a Micromeritics TranSeal and evacuated by heating at either 120 °C (**1** and **2**) or 80 °C (**1**•( $\text{CuCl}_2$ )<sub>5.8</sub>, **1**•( $\text{CuCl}$ )<sub>6.8</sub>, **1**•( $\text{CoCl}_2$ )<sub>5.5</sub>, **1**•( $\text{FeBr}_2$ )<sub>6.1</sub>, and **1**•( $\text{Cr}(\text{CO})_4$ )<sub>5.6</sub>) at a ramp rate of 1 °C/min under dynamic vacuum until an outgas rate of less than 3  $\mu\text{bar}/\text{min}$  was achieved. The evacuated analysis tube containing the degassed sample was then carefully transferred to an electronic balance and weighed again to determine the mass of sample. The tube was then transferred back to the analysis port of the gas adsorption instrument. The outgas rate was again confirmed to be less than 3  $\mu\text{bar}/\text{min}$ . For all isotherms, warm and cold free space correction measurements were performed using ultra-high purity He gas (99.999% purity);  $\text{N}_2$  and  $\text{H}_2$  isotherms at 77 K and 298 K were measured in liquid nitrogen and water baths, respectively, using UHP-grade gas sources. Oil-free vacuum pumps and oil-free pressure regulators were used for all measurements to prevent contamination of the samples during the evacuation process or of the feed gases during the isotherm measurements.

Langmuir surface areas were determined from N<sub>2</sub> adsorption data at 77 K using Micromeritics software.

**Powder X-ray diffraction.** Diffraction data were collected with 0.02° steps using a Bruker AXS D8 Advance diffractometer equipped with Cu-K $\alpha$  radiation ( $\lambda = 1.5418 \text{ \AA}$ ), a Göbel mirror, a Lynxeye linear position-sensitive detector, and mounting the following optics: fixed divergence slit (0.6 mm), receiving slit (3 mm), and secondary beam Soller slits (2.5°). The generator was set at 40 kV and 40 mA. Samples were either loaded on zero background sample holders, in a custom-built airfree stage, or packed into air-free capillaries in a nitrogen-filled glovebox and mounted using a capillary stage.

While it was not possible to collect a single crystal structure of activated **1**•(CuCl<sub>2</sub>)<sub>5.8</sub>, a high-resolution X-ray diffraction pattern was collected at 11-BM at the Advanced Photon Source at Argonne National Laboratory via the rapid access mail-in program. Approximately 5 mg of activated CuCl<sub>2</sub> microcrystalline powder was loaded in a glass capillary inside a glovebox under a dinitrogen atmosphere. The capillary was fully evacuated, then backfilled with 10 mbar of He and flame-sealed. The wavelength for the X-ray diffraction experiment was 0.413746 Å, and the temperature was 100 K.

A standard peak search, followed by indexing through the Single Value Decomposition approach,<sup>43</sup> as implemented in TOPAS-Academic,<sup>44</sup> allowed the determination of approximate unit cell parameters. The space group was assigned as  $Pa\bar{3}$  on the basis of systematic absences. The unit cell and space group were verified by a structureless Le Bail refinement and confirmed by successful structure solution and Rietveld refinement. Initially, the solvated crystal structure of **1**•(CuCl<sub>2</sub>)<sub>5.8</sub> was used as a starting model for the Rietveld refinement of CuCl<sub>2</sub>.

During the Rietveld refinement process, a rigid, idealized model was employed for the full 2,2'-bipyridine-5,5'-dicarboxylic acid ligand. Initially, all bond distances in the rigid body were fixed, and just the position ( $x, y, z$ ) and orientation ( $\alpha, \beta, \gamma$ ) of rigid body was refined. In the final stages of the refinement, all aromatic C–C bond distances were refined, but constrained to be equal. Aromatic C–N bond distances were refined, but constrained to be equal. Carboxylate C–O bond distances were refined but constrained to be equal. The C–C distances between the carboxylates and bipyridine were also refined, but constrained to be equal. The C–C distance between the two pyridine rings was fully refined. All aromatic C–H distances were fixed at 0.95 Å and not refined. The rotation angles between each carboxylate and the bipyridine were refined independently. A rotation angle about the axis perpendicular to the center of the bipyridine was defined and fully refined to account for any distortion of the ligand upon metal binding. Note that there is likely some slightly rotational disorder in the orientation of the ligand with respect to the Zr clusters, which is not modeled in this refinement. This likely explains the slight displacement of the Cu atom from the plane of the bipyridine. Rigid bodies were also defined for the two acetonitrile molecules interacting with the Zr cluster, and these C–C and C–N bond distances were fixed throughout the refinement. All other atomic positions were refined independently with no restraints.

The occupancies of the Cu and Cl atoms were refined, but constrained to be equal. The occupancies of each acetonitrile molecule were refined independently. Similar to the solvated single crystal structure, the occupancies of the all ligand atoms were constrained to be equal and refined to account for ligand vacancy defects. The occupancy of Cu and Cl atoms were restrained to be less than or equal to the occupancy of the ligand atoms. Note that terminal OH and H<sub>2</sub>O molecules were modeled at each ligand defect site (O1w, O2w, O3w, O4w), and their occupancy was fixed to 1 minus the ligand occupancy.

A single refined isotropic thermal parameter was assigned to each atom. The Zr and Cu thermal parameters were free to vary. The Cl thermal parameters were constrained to be the same. The thermal parameters for the cluster O atoms (O5a, O5b, O6a, O6b) were constrained to be the same. The thermal parameters for all ligand atoms were constrained to be the same. The thermal parameters for O1w, O2w, O3w, and O4w were constrained to be the same. The thermal parameters for the C and N atoms of each acetonitrile were also constrained to be the same. The calculated diffraction pattern for the final structural model of  $\mathbf{1}\cdot(\text{CuCl}_2)_{5.8}$  is in excellent agreement with the experimental diffraction pattern (Figure 4.S16).

**Single-Crystal X-ray Diffraction.** X-ray diffraction analyses were performed on single crystals coated with Paratone-N oil and mounted on MiTeGen loops. Crystals were frozen at a temperature of 100 K by an Oxford Cryosystems Cryostream 700 plus. Data for  $\mathbf{1}$  were collected using MoK $\alpha$  radiation ( $\lambda = 0.71073 \text{ \AA}$ ) and a Bruker QUAZAR diffractometer equipped with a Bruker AXS APEX II detector. Data for  $\mathbf{1}\cdot(\text{CuCl}_2)_{5.8}$ ,  $\mathbf{1}\cdot(\text{CuCl})_{6.8}$ ,  $\mathbf{1}\cdot(\text{CoCl}_2)_{5.5}$ ,  $\mathbf{1}\cdot(\text{FeBr}_2)_{6.1}$ ,  $\mathbf{1}\cdot(\text{Cr}(\text{CO})_4)_{5.6}$ ,  $\mathbf{1}\cdot(\text{Cr}(\text{CO})_4)_{5.6}$  (solvated), and  $\mathbf{3}$  were collected at Beamline 11.3.1 at the Advanced Light Source, Lawrence Berkeley National Laboratory using synchrotron radiation ( $\lambda = 0.7749 \text{ \AA}$  for  $\mathbf{1}\cdot(\text{CuCl}_2)_{5.8}$ ,  $\mathbf{1}\cdot(\text{CuCl})_{6.8}$ ,  $\mathbf{1}\cdot(\text{CoCl}_2)_{5.5}$ ,  $\mathbf{1}\cdot(\text{FeBr}_2)_{6.1}$ ,  $\mathbf{1}\cdot(\text{Cr}(\text{CO})_4)_{5.6}$  (solvated), and  $\mathbf{3}$ ;  $\lambda = 0.8856 \text{ \AA}$  for  $\mathbf{1}\cdot(\text{Cr}(\text{CO})_4)_{5.6}$ ) with a Bruker AXS APEX II CCD detector on a D85 diffractometer. Raw data were integrated and corrected for Lorentz and polarization effects using Bruker AXS SAINT software.<sup>45</sup> Absorption corrections were applied using SADABS.<sup>46</sup> Space group assignments were determined by examination of systematic absences, E-statistics, and successive refinement of the structures for  $\mathbf{1}$  and  $\mathbf{3}$ . Space group assignment for  $\mathbf{1}\cdot(\text{CuCl}_2)_{5.8}$ ,  $\mathbf{1}\cdot(\text{CuCl})_{6.8}$ ,  $\mathbf{1}\cdot(\text{CoCl}_2)_{5.5}$ ,  $\mathbf{1}\cdot(\text{FeBr}_2)_{6.1}$ , and  $\mathbf{1}\cdot(\text{Cr}(\text{CO})_4)_{5.6}$  is described in the succeeding paragraph. The structures were solved using direct methods with SHELXS<sup>47,48</sup> and refined using SHELXL<sup>49</sup> operated in the OLEX2<sup>50</sup> interface. None of the crystals showed significant decay during data collection. Thermal parameters were refined anisotropically for all non-hydrogen atoms. Hydrogen atoms were placed in ideal positions and refined using a riding model for all structures. Acetonitrile hydrogens that could neither be found or placed were omitted from the refinement but not in the formula. The oxygen atoms of the oxo and hydroxo groups on the zirconium clusters in all structures were disordered, so their site occupancy factors were fixed to give a chemical occupancy of 50%. Extensive solvent disorder that could not be modeled was found in the pores for  $\mathbf{1}$ ,  $\mathbf{1}\cdot(\text{CuCl}_2)_{5.8}$ ,  $\mathbf{1}\cdot(\text{CuCl})_{6.8}$ ,  $\mathbf{1}\cdot(\text{CoCl}_2)_{5.5}$ ,  $\mathbf{1}\cdot(\text{FeBr}_2)_{6.1}$ ,  $\mathbf{1}\cdot(\text{Cr}(\text{CO})_4)_{5.6}$ , and  $\mathbf{1}\cdot(\text{Cr}(\text{CO})_4)_{5.6}$  (solvated). A solvent mask was applied as implemented in OLEX2 for  $\mathbf{1}$  to account for unassigned electron density within the pores. The solvent masking procedure could not be applied to the other structures, due to the twin laws used in their refinement.

X-ray analysis of single crystals of  $\mathbf{1}\cdot(\text{CuCl}_2)_{5.8}$ ,  $\mathbf{1}\cdot(\text{CuCl})_{6.8}$ ,  $\mathbf{1}\cdot(\text{CoCl}_2)_{5.5}$ ,  $\mathbf{1}\cdot(\text{FeBr}_2)_{6.1}$ , and  $\mathbf{1}\cdot(\text{Cr}(\text{CO})_4)_{5.6}$  revealed that the unit cell of  $\mathbf{1}$  changes from face-centered cubic to primitive cubic upon metalation. Initial evaluation of the diffraction data suggested that the space group had changed to  $P2_13$ . Attempts to solve and refine the structures in  $P2_13$ , however, generally resulted in unsatisfactory refinement. Careful analysis of the apparent symmetry of preliminary structure solutions in  $P2_13$  and the symmetry of intermediate subgroups that relate  $Fm\bar{3}m$  to  $P2_13$  through maximal subgroup chains led to the selection of  $Pa\bar{3}$  as a possible space group. Solution and refinement of the data in  $Pa\bar{3}$  required significantly less restraints in structure refinement and gave much lower values for R1 compared to those solved in  $P2_13$ . Going from  $Fm\bar{3}m$  to  $Pa\bar{3}$  upon metalation results in two twin domains related by the lost mirror symmetry. Consequently, a twin law (TWIN 0 1 0 1 0 0 0 0 -1 2; BASF  $\approx$  0.50) was required for the structural refinement of  $\mathbf{1}\cdot(\text{CuCl}_2)_{5.8}$ ,  $\mathbf{1}\cdot(\text{CuCl})_{6.8}$ ,  $\mathbf{1}\cdot(\text{CoCl}_2)_{5.5}$ ,  $\mathbf{1}\cdot(\text{FeBr}_2)_{6.1}$ ,  $\mathbf{1}\cdot(\text{Cr}(\text{CO})_4)_{5.6}$ ,

and  $\mathbf{1}\cdot(\text{Cr}(\text{CO})_4)_{5.6}$  (solvated). Disorder of the solvent in  $\mathbf{1}\cdot(\text{CuCl}_2)_{5.8}$ ,  $\mathbf{1}\cdot(\text{CoCl}_2)_{5.5}$ ,  $\mathbf{1}\cdot(\text{FeBr}_2)_{6.1}$ , and  $\mathbf{1}\cdot(\text{Cr}(\text{CO})_4)_{5.6}$  (solvated) and of the metalated linkers in  $\mathbf{1}\cdot(\text{CuCl})_{6.8}$ ,  $\mathbf{1}\cdot(\text{CoCl}_2)_{5.5}$ ,  $\mathbf{1}\cdot(\text{FeBr}_2)_{6.1}$ , and  $\mathbf{1}\cdot(\text{Cr}(\text{CO})_4)_{5.6}$  required the use of restraints and independent free variables during refinement. Voids in the structures that result from disordered solvent that could not be modeled and large anisotropic displacement parameters that result from linker and solvent disorder gave rise to several A and B level alerts from checkCIF. Responses addressing these alerts have been included in the CIFs and can be read in reports generated by checkCIF.

**General Procedure for Arene C–H Borylation.**  $\mathbf{1}\cdot(\text{Ir}(\text{COD})(\text{BF}_4))_{0.6}$  (5.0 mg, 0.0013 mmol Ir), an arene (3.0 mL), and either HBpin (256.0 mg, 2.000 mmol) or  $\text{B}_2\text{pin}_2$  (157.2 mg, 0.6190 mmol) were mixed in a 20 mL Teflon-capped vial. The resulting mixture was heated at 80 °C with magnetic stirring for 24 hours. After allowing the reaction mixture to cool the solid was separated by centrifugation followed by filtration to give a colorless solution. The recovered solid was washed with 1.5 mL arene to extract any remaining products then separated from the mixture by centrifugation followed by filtration. Excess arene from the combined product solutions was then removed under reduced pressure to give the crude product. An internal standard, 1,3,5-trimethoxybenzene (20.0 mg, 0.119 mmol) was added to the product and the resulting solution was analyzed by  $^1\text{H}$  NMR.

**Control Experiments.** The general procedure for arene C-H borylation was implemented with the substitution of  $\mathbf{1}\cdot(\text{Ir}(\text{COD})(\text{BF}_4))_{0.6}$  with a catalyst control (**1**,  $[\text{Ir}(\text{COD})_2]\text{BF}_4$  or **2** with  $[\text{Ir}(\text{COD})_2]\text{BF}_4$ ).

**Surface Poisoning Experiments.** The general procedure for arene C-H borylation was implemented with the substitution of the arene with 3 mL of a 0.44 mM solution of  $\text{PPh}_3$  in benzene or 3 mL of a 0.43 mM solution of  $\text{PCy}_3$  in benzene.

**Catalyst Cycling Experiments.** The general procedure for arene C-H borylation was implemented over five cycles by resuspending the recovered catalyst in a fresh solution of reactants.

**Determination of Average Turnover Frequency.**  $\mathbf{1}\cdot(\text{Ir}(\text{COD})(\text{BF}_4))_{0.6}$  (4.0 mg, 0.0010 mmol Ir), benzene (7.0 mL), HBpin (562.5 mg, 4.395 mmol), and 1,3,5-trimethoxybenzene (39.5 mg, 0.235 mmol) were mixed in a 20 mL Teflon-capped vial and heated at 80 °C with magnetic stirring. Aliquots (0.5 mL) were taken from the reaction mixture at 0.5 h intervals from 0–2.5 h. The suspended solid from each aliquot was separated by centrifugation followed by filtration to give a colorless solution. Excess arene was then removed under reduced pressure to give the crude product, which was analyzed by  $^1\text{H}$  NMR.

**Hot Filtration Experiment.**  $\mathbf{1}\cdot(\text{Ir}(\text{COD})(\text{BF}_4))_{0.6}$  (5.0 mg, 0.0013 mmol Ir), benzene (7.0 mL), HBpin (555.9 mg, 4.344 mmol), and 1,3,5-trimethoxybenzene (41.0 mg, 0.244 mmol) were mixed in a 20 mL Teflon-capped vial and heated at 80 °C with magnetic stirring. After one hour all the solids in reaction mixture were removed by filtration and the filtrate was kept at 80 °C to allow any further reaction. Aliquots (0.5 mL) were taken from the reaction mixture at 0.5 h intervals from 0–2.5 h. The resulting mixture was heated at 80 °C with magnetic stirring for 24 hours. The suspended solid from each aliquot was separated by centrifugation followed by filtration to give a colorless solution. Excess arene was then removed under reduced pressure to give the crude product, which was analyzed by  $^1\text{H}$  NMR.

### 4.3. Results and Discussion

**Synthesis of  $\text{Zr}_6\text{O}_4(\text{OH})_4(\text{bpydc})_6$ .** Reaction of  $\text{ZrCl}_4$  with  $\text{H}_2\text{bpydc}$  in the presence of 80 equivalents of benzoic acid and 1.8 equivalents of water in DMF at 120 °C for 5 days affords **1**

as a white microcrystalline solid. Powder X-ray diffraction data show that **1** is isostructural to  $\text{Zr}_6\text{O}_4(\text{OH})_4(\text{bpdc})_6$  (Figure 4.S8). Thermogravimetric analysis data collected for the as-synthesized material (Figure 4.S32) shows a 41% mass loss from 40 to 120 °C, which is associated with framework desolvation. No further mass loss is observed until the framework decomposes at temperatures above 450 °C, which suggests that **1** has comparable thermal stability to  $\text{Zr}_6\text{O}_4(\text{OH})_4(\text{bpdc})_6$ .<sup>39,51</sup> The fully desolvated material exhibits Langmuir and BET surface areas of 2772 m<sup>2</sup>/g and 2730 m<sup>2</sup>/g, respectively, which are close to 3000 m<sup>2</sup>/g, the reported Langmuir surface area of  $\text{Zr}_6\text{O}_4(\text{OH})_4(\text{bpdc})_6$ .<sup>39</sup> SEM images of the bulk powder sample of **1** (Figure 4.S39) reveal that the material forms well-faceted octahedron-shaped crystals roughly 0.5–1 μm on an edge.

Benzoic acid is critical to the synthesis of highly crystalline **1**. Attempts to synthesize it in the absence of benzoic acid result in powders with poor crystallinity. Powder X-ray diffraction analysis reveals that increasing the amount of benzoic acid (0–80 equivalents per linker) leads to more crystalline material (Figure 4.S10), which is in agreement with results reported in a similar study for  $\text{Zr}_6\text{O}_4(\text{OH})_4(\text{bpdc})_6$ .<sup>51</sup> This effect is thought to arise from competition between benzoic acid and the dicarboxylic acid linkers during framework assembly, making framework formation more reversible.<sup>51</sup> In addition, having more benzoic acid present in the reaction mixture also requires longer reaction times. As an example, precipitate formation can be observed within a few hours if no benzoic acid is added, while it takes 2–3 days for the solid product to be observed in the presence of 80 equivalents of benzoic acid per linker. Attempts to synthesize the material with the addition of 100 or greater equivalents of benzoic acid per linker yielded no observable precipitate over 5 days.

The synthesis of X-ray quality single crystals of **1** required more careful control of the reaction conditions. In particular, both the amount of water added and the metal-to-ligand ratio had significant effects on the size and quality of the crystals. Though highly crystalline and porous **1** can be reproducibly synthesized using commercially available DMF, reproducible formation of single crystals requires the addition of a precise amount of water to anhydrous DMF

**Table 4.1.** Selected Properties of the Metal–Organic Frameworks Presented in this Work

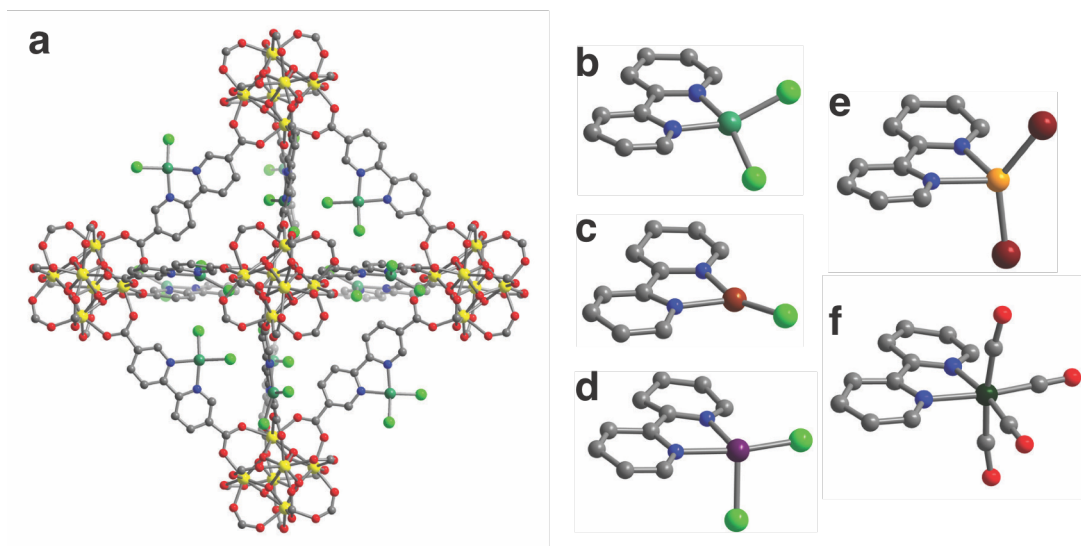
Compound	Color	Metal Loading <sup>a</sup> (%)	SA <sub>Lang.</sub> <sup>b</sup> (m <sup>2</sup> /g)	SA <sub>BET</sub> <sup>c</sup> (m <sup>2</sup> /g)
<b>1</b>	white		2772	2730
<b>2</b>	white		2805	2625
<b>1</b> ·(CuCl <sub>2</sub> ) <sub>5.8</sub>	green	96(1)	1253	1101
<b>1</b> ·(CuCl) <sub>6.8</sub>	light brown	114(3)	835	701
<b>1</b> ·(CoCl <sub>2</sub> ) <sub>5.5</sub>	pale blue	92(1)	1282	1204
<b>1</b> ·(FeBr <sub>2</sub> ) <sub>6.1</sub>	red-violet	101.1(7)	1073	971
<b>1</b> ·(Cr(CO) <sub>4</sub> ) <sub>5.6</sub>	dark green	93(2)	1065	934

<sup>a</sup>Metal loading was determined by ICP-OES based on the molar ratio of the inserted metal relative to Zr in the framework. <sup>b</sup>SA<sub>Lang.</sub> = Langmuir surface area. <sup>c</sup>SA<sub>BET</sub> = Brunauer-Emmett-Teller (BET) surface area.

obtained from a solvent purification system. Reaction conditions that use anhydrous DMF alone fail to yield any precipitate, which is consistent with the requirement of water to form the  $\mu_3$ -O and  $\mu_3$ -OH groups of the  $Zr_6$  octahedral nodes.<sup>51</sup> Interestingly, the addition of two equivalents of  $ZrCl_4$  per linker yields isolated and regularly-shaped octahedral crystals. In contrast, conditions that employ stoichiometric amounts of  $ZrCl_4$  per linker produce crystals that are intergrown.

X-ray analysis of an as-synthesized single crystal of **1** further confirmed that the framework is isostructural to  $Zr_6O_4(OH)_4(bpdc)_6$  (Figure 4.1). The calculated powder diffraction pattern obtained from the crystal structure agrees well with the experimental powder pattern, indicating that the crystal structure is representative of the bulk material (Figure 4.S9). As expected, the bipyridine units show disorder over two positions due to the  $Fm\bar{3}m$  symmetry of the structure. While this manuscript was in preparation, similar results were reported from X-ray analysis of crystals of **1** grown under slightly different conditions.<sup>40</sup> Refinement of the linker occupancy in the structure revealed that 86% of the ligand was present, corresponding to the absence of roughly 1/6 of the linkers. When the ligand is not present, the vacancies on the cluster have been suggested to be occupied with water or hydroxide,<sup>52-54</sup> which can be identified as weak electron density peaks 2.18(4) Å away from Zr.

**Metalation of  $Zr_6O_4(OH)_4(bpydc)_6$ .** Transition metal halides were first considered for the metalation of **1**, as these were expected to form solvated metal species that would easily fit through the triangular windows of the framework, which have an incircle of  $\sim 8$  Å in diameter.<sup>39</sup> Soaking microcrystalline powders of **1** in acetonitrile solutions of metal halide salts (typically one equivalent per bipyridine linker) at 80 °C for 5 days results in a color change (Table 4.1) of

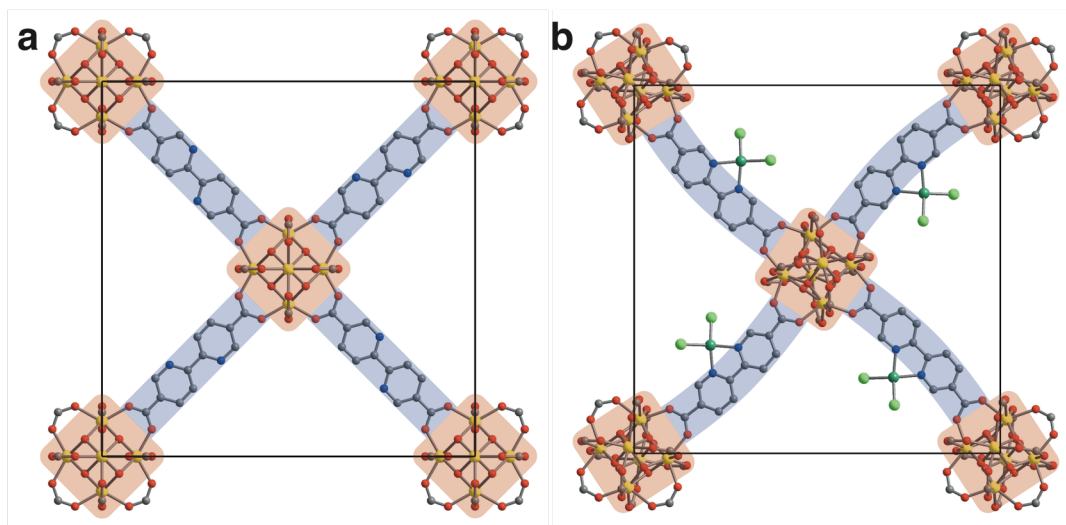


**Figure 4.2.** A portion of the crystal structure of  $1 \cdot (CuCl_2)_{5.8}$  (**a**) as determined by analysis of single-crystal X-ray diffraction data. Structures of the bipyridine metal complexes in  $1 \cdot (CuCl_2)_{5.8}$  (**b**),  $1 \cdot (CuCl)_{6.8}$  (**c**),  $1 \cdot (CoCl_2)_{5.5}$  (**d**),  $1 \cdot (FeBr_2)_{6.1}$  (**e**), and  $1 \cdot (Cr(CO)_4)_{5.6}$  (**f**), as determined from single-crystal X-ray diffraction data. Yellow, green, brown, purple, light orange, dark green, light green, dark red, red, blue, and gray spheres represent  $Zr^{IV}$ ,  $Cu^{II}$ ,  $Cu^I$ ,  $Co^{II}$ ,  $Fe^{II}$ ,  $Cr^0$ , Cl, Br, O, N, and C atoms, respectively; H atoms and acetonitrile molecules in the pores are omitted for clarity. Note that 53% of the Cu–bipyridine complexes in  $1 \cdot (CuCl)_{6.8}$  were found to have  $[CuCl_2]^-$  as a counteranion instead of  $Cl^-$  (Figure 4.S1), while the bipyridine complexes in  $1 \cdot (CoCl_2)_{5.5}$  and  $1 \cdot (FeBr_2)_{6.1}$  exist in different coordination geometries due to different degrees of solvation. (Figure 4.S2–4.S3) The coordinated solvent molecules in  $1 \cdot (CoCl_2)_{5.5}$  and  $1 \cdot (FeBr_2)_{6.1}$  could not be modeled due to disorder and weak scattering of the solvent molecules in comparison to the halide ligands.



the powders over the course of the reaction. The powders remain colored after three acetonitrile washes at 80 °C, suggesting successful metalation of the framework. The powder X-ray diffraction patterns of the metalated frameworks  $\mathbf{1}\cdot(\text{CuCl}_2)_{5.8}$ ,  $\mathbf{1}\cdot(\text{CuCl})_{6.8}$ ,  $\mathbf{1}\cdot(\text{CoCl}_2)_{5.5}$ , and  $\mathbf{1}\cdot(\text{FeBr}_2)_{6.1}$  show additional peaks compared to that of  $\mathbf{1}$ , indicating a possible change in space group upon metalation. Metal to zirconium ratios determined by ICP-OES analysis (Table 4.1) indicate a close to stoichiometric reaction of the bipyridine sites. Thermogravimetric analyses of the resulting powders generally showed slight decreases in thermal stability of the framework upon metalation (Figures 4.S33–4.S38). This is likely due to weakened carboxylate-Zr bonds that result from less electron density being available to the linker carboxylate groups, as well as to strain induced by arching of the linker upon coordination of the linker bipyridine moiety to a metal center, as discussed below.

Metal insertion in single crystals of  $\mathbf{1}$  was carried out under the same conditions used for the bulk microcrystalline samples, with the exception of using excess metal precursor. Similar to the powders, the crystals change color with no visible loss in crystal quality after metalation. Analysis of the crystals by single-crystal X-ray diffraction revealed a lowering of the framework symmetry from  $Fm\bar{3}m$  to  $Pa\bar{3}$ . Remarkably, the metalated bipyridine linkers were crystallographically ordered, allowing structural determination of the metal complexes formed within the framework (Figure 4.2).



**Figure 4.3.** Comparison of the crystal structures of  $\mathbf{1}$  (a) and  $\mathbf{1}\cdot(\text{CuCl}_2)_{5.8}$  (b) viewed along the  $[100]$  direction; unit cell edges are shown as black lines. The bare framework exhibits mirror symmetry along the body diagonals of its unit cell and face-centering translations that relate the zirconium clusters at the ends of each linker. In the metallated structure, the mirror symmetry is removed by the ordering of the linkers, while the face-centering is lost because the clusters at the ends of each linker are tilted in opposite directions.

Closer inspection of the structures shows that each bipyridine unit forms an arch to chelate the metal, presumably facilitating better orbital overlap with the metal (Figure 4.3). The zirconium clusters at the ends of each linker rotate slightly to accommodate the arching, while linkers around each cluster orient accordingly to conform to the direction of the cluster rotation. These distortions from the unmetalated structure collectively result in an ordering of the linker-metal complexes as they go from a site that has three mirror planes in  $Fm\bar{3}m$  to a site with no symmetry in  $Pa\bar{3}$ .

Although there are several examples of the structural characterization of post-synthetically metalated metal–organic frameworks, most structures fail to resolve the complete ligand environment around the metal centers due to extensive disorder of the metalated linkers.<sup>30,34,42</sup> Recent work has emphasized that full characterization of metal-linkers complexes formed via post-synthetic metalation requires low symmetry at the location of the open chelating site in the crystal, which can be achieved by starting with a metal–organic framework with low crystal symmetry.<sup>19</sup> The crystallographic ordering of the linkers in **1** after post-synthetic metalation demonstrates that the structural characterization of the metalated linkers in high-symmetry metal–organic frameworks can be achieved if the framework has a pathway to lower symmetry during metalation. To the best of our knowledge, this is the first reported example of this phenomenon in a metal–organic framework.

X-ray analysis of **1**·(CuCl<sub>2</sub>)<sub>5.8</sub> revealed significant ordering of both the framework and the acetonitrile molecules within the pores, which enabled reliable measurement of interatomic distances and angles for the (bpy)CuCl<sub>2</sub> units (Figure 4.2b). Interestingly, the Cu<sup>II</sup> centers do not have acetonitrile bound, despite the presence of additional acetonitrile in the pores. The Cu–N distances of 1.993(4) Å and 2.007(4) Å and Cu–Cl distances of 2.2101(15) Å and 2.2126(16) Å in the complex were found to be very close to reported bond distances for the analogous molecular complex, Cu(tbbpy)Cl<sub>2</sub> (tbbpy = 4,4'-bis(*tert*-butyl)-2,2'-bipyridine)<sup>55</sup> The Cu<sup>II</sup> centers exhibit a distorted square planar geometry, with the Cl–Cu–Cl plane tilted 33° away from the N–Cu–N plane, which is likely a result of steric repulsion between the Cl<sup>−</sup> ligands and neighboring bipyridine H atoms. This distortion from planarity is common in molecular (bpy)CuCl<sub>2</sub> complexes and has been shown to vary with crystal packing.<sup>55</sup> While it was not possible to collect a single crystal structure of activated **1**·(CuCl<sub>2</sub>)<sub>5.8</sub>, a structure was obtained from high-resolution powder X-ray diffraction data (Figure 4.S16). In the activated structure, the Cu<sup>II</sup> centers are in a similar coordination geometry, with the Cl–Cu–Cl plane tilted 45° away from the N–Cu–N plane.

Structural determination of the bipyridine metal complexes was more challenging for **1**·(CuCl)<sub>6.8</sub>, **1**·(CoCl<sub>2</sub>)<sub>5.5</sub>, and **1**·(FeBr<sub>2</sub>)<sub>6.1</sub>, due to the disorder attributed to rotation of the linkers and variation in the degree of solvation of the metal complexes. The linkers in **1**·(CuCl)<sub>6.8</sub> show rotational disorder over two positions tilted 27° away from each other. Although the Cu<sup>I</sup> complexes in **1**·(CuCl)<sub>6.8</sub> were modeled as distorted trigonal planar complexes with Cl<sup>−</sup> as a coordinated counteranion (Figure 4.2c), residual electron density close to the Cu<sup>I</sup> center suggests that 53% of the complexes actually have linear [CuCl<sub>2</sub>]<sup>−</sup> units as a bound counteranion (Figure 4.S1). Molecular complexes that are analogous to the (bpy)CuCl structural model exist.<sup>56,57</sup> The closest analogs to the (bpy)Cu(CuCl<sub>2</sub>) structural model contain phenanthroline- or bipyridine-Cu<sup>I</sup> units bridged by [CuCl<sub>2</sub>]<sup>−</sup> anions,<sup>58,59</sup> which cannot form in the framework due to the isolation of the bipyridine sites.

Similar to the structure of **1**·(CuCl)<sub>6.8</sub>, the linkers in **1**·(CoCl<sub>2</sub>)<sub>5.5</sub> displayed rotational disorder over two positions, tilted 14° away from each other. The bipyridine-CoCl<sub>2</sub> adducts were clearly located and appear to be square planar in one of the disordered positions (Figure 4.2d) and distorted square planar in the other (Figure 4.S2). Residual electron density close to the Co<sup>II</sup> centers, however, indicates that solvent is likely bound to Co<sup>II</sup> and that the complexes are actually in octahedral and trigonal bipyramidal geometries (Figure 4.S2), which are more consistent with published structures.<sup>60,61</sup> The square planar sites can be assigned to be octahedral with the bipyridine and Cl<sup>−</sup> ligands coplanar and solvent on the axial sites, while the distorted square planar sites can be assigned as partially trigonal bipyramidal with the N and Cl on the

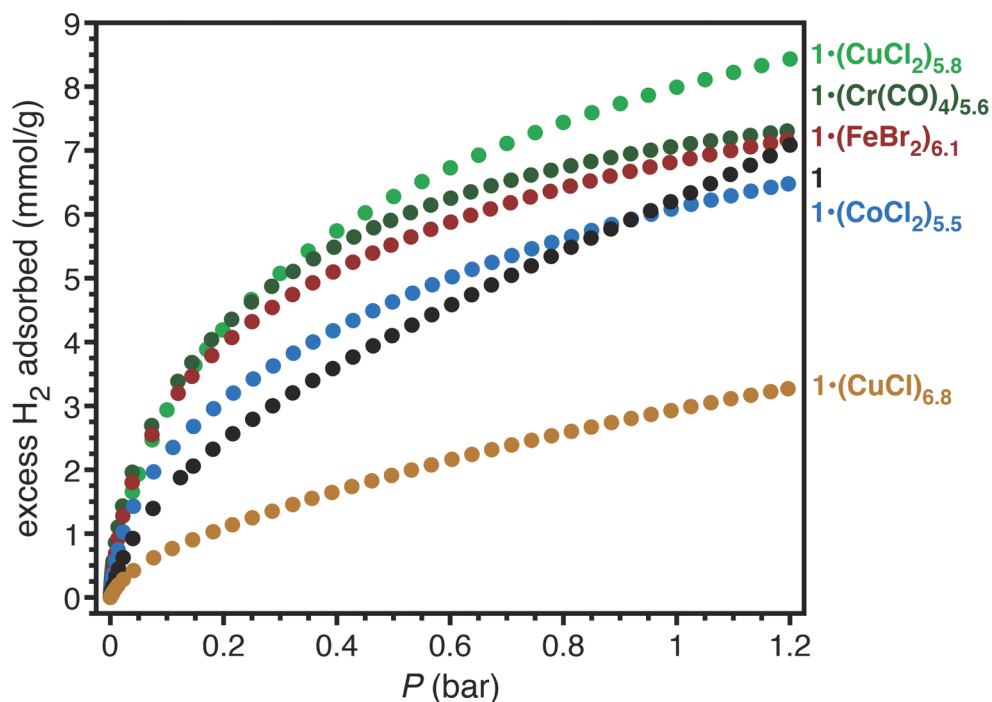
axial sites and N, Cl, and solvent on the equatorial sites. Unfortunately, the disorder and weak scattering from the bound solvent molecules prevent a more accurate assignment of the Co<sup>II</sup> complex geometries.

X-ray diffraction data for **1**·(FeBr<sub>2</sub>)<sub>6.1</sub> collected on single crystals that were washed with acetonitrile alone gave structures with poorly resolved FeBr<sub>2</sub> moieties. The disorder in the structures can be attributed to the Fe<sup>II</sup> complexes being in multiple states of solvation. Consequently, crystals were further washed with benzene at 80 °C in an attempt to fully desolvate the Fe<sup>II</sup> centers. X-ray analysis of one of these crystals gives a much more ordered structure, with the Fe<sup>II</sup> centers predominantly in a pseudotetrahedral geometry (Figure 4.2e), which is reasonable for FeBr<sub>2</sub> complexes with nitrogen-based chelating ligands.<sup>62</sup> Additional electron density peaks found near to the Fe<sup>II</sup> centers suggests that a fraction of the complexes have the Br<sup>-</sup> ligands closer to the Fe-bipyridine plane. Similar to **1**·(CoCl<sub>2</sub>)<sub>5.5</sub>, solvent may still be bound to on a fraction of the Fe<sup>II</sup> sites, forcing them into what appears to be a pseudooctahedral geometry with the bipyridine and Br<sup>-</sup> ligands on the equatorial sites and solvent on the axial sites (Figure 4.S3). The geometry of these Fe<sup>II</sup> sites, however, cannot be accurately assigned due to the disorder and the weak scattering from the coordinated solvent molecules on the Fe<sup>II</sup> sites in comparison to the Br<sup>-</sup> ligands.

Given the permanent porosity of **1**, we explored the possibility of using framework to chelate metals from reagents introduced in the gas phase. Heating a microcrystalline sample of **1** in a sealed vial with excess Cr(CO)<sub>6</sub> at 80 °C over 7 days results in gradual color change of the framework from white to dark green over the course of the reaction, consistent with the metalation of the bipyridine sites. Analysis of the resulting framework by infrared spectroscopy shows CO stretches at 2012, 1897, 1870, and 1845 cm<sup>-1</sup> (Figure 4.S43), consistent with the formation of (bpy)Cr(CO)<sub>4</sub> complexes within the framework.<sup>63</sup> Remarkably, single crystals of **1** can also be metalated and analyzed by X-ray diffraction, leading to structural confirmation that the complexes formed are indeed (bpy)Cr(CO)<sub>4</sub> (Figure 4.2f). These results emphasize the unique ability to perform and characterize gas phase reactions in metal–organic frameworks due to their inherent porosity and crystallinity.

The structures obtained for single crystals of **1**·(Cr(CO)<sub>4</sub>)<sub>6</sub> from data collected directly after metalation show rotational disorder of the (bpy)Cr(CO)<sub>4</sub> units within the framework. Interestingly, soaking crystals of **1**·(Cr(CO)<sub>4</sub>)<sub>6</sub> in acetonitrile results in ordering of the linkers, conceivably due to restriction of the rotational freedom of the linkers as the pores are filled with solvent. The Cr–N distances of 2.102(4) Å and 2.105(4) Å, equatorial Cr–C distances of 1.842(7) Å and 1.842(7) Å, and equatorial C–O distances of 1.173(8) Å and 1.167(9) Å are all in good agreement with analogous complexes in the literature.<sup>64</sup> In contrast, the axial Cr–C distances of 1.77(1) Å and 1.78(2) Å and C–O distances of 1.29(2) Å and 1.24(2) Å are comparatively shorter, which may be an artifact of slight disorder of the (bpy)Cr(CO)<sub>4</sub> complexes along the direction of these bonds.

**Gas Adsorption.** Low-pressure N<sub>2</sub> adsorption data (Figure 4.S17) collected at 77 K for metalated frameworks reveal a considerable decrease in surface area upon metalation of **1** (Table 4.1). These results are consistent with loss of accessible pore surface due to the metal-linker complexes occupying additional space in the pores. In line with this, frameworks with bulkier metal complexes exhibit lower surface areas, with the exception of **1**·(CuCl)<sub>6.8</sub>. The low surface area of **1**·(CuCl)<sub>6.8</sub> relative to the other metal halide metalated frameworks may be attributed to some of the Cu sites in **1**·(CuCl)<sub>6.8</sub> possessing the much larger [CuCl<sub>2</sub>]<sup>-</sup> as a counteranion instead of the Cl<sup>-</sup>.

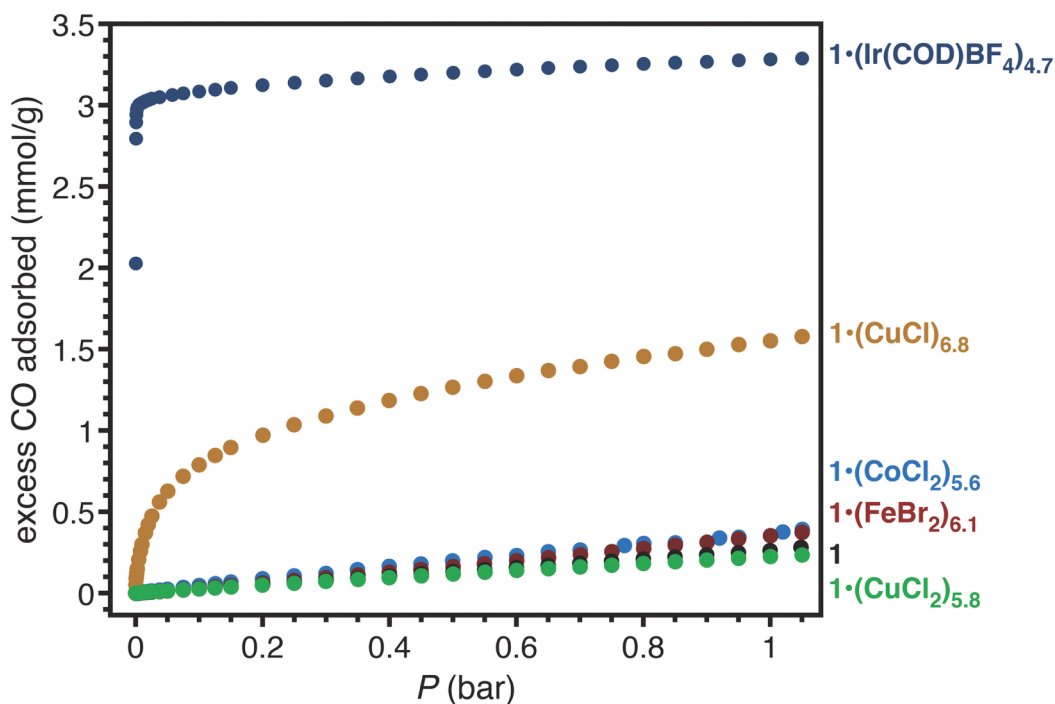


**Figure 4.4.** Low-pressure H<sub>2</sub> adsorption isotherms for **1**, **1·(CuCl<sub>2</sub>)<sub>5.8</sub>**, **1·(CuCl)<sub>6.8</sub>**, **1·(CoCl<sub>2</sub>)<sub>5.5</sub>**, **1·(FeBr<sub>2</sub>)<sub>6.1</sub>**, and **1·(Cr(CO)<sub>4</sub>)<sub>5.6</sub>** at 77 K.

To determine the accessibility of the metal sites in **1·(CuCl<sub>2</sub>)<sub>5.8</sub>**, **1·(CuCl)<sub>6.8</sub>**, **1·(CoCl<sub>2</sub>)<sub>5.5</sub>**, **1·(FeBr<sub>2</sub>)<sub>6.1</sub>**, and **1·(Cr(CO)<sub>4</sub>)<sub>5.6</sub>**, low-pressure H<sub>2</sub> adsorption measurements were performed at 77 K (Figure 4.4). All metalated frameworks except **1·(CuCl)<sub>6.8</sub>** displayed improved gravimetric H<sub>2</sub> uptake over the bare framework at low pressures, despite their lower surface areas and increased formula weights. The isotherms, however, did not show any steep uptake at very low pressures characteristic of strong interaction with open metal sites.<sup>65</sup> Instead, the increased H<sub>2</sub> capacity likely arises from the introduction of additional weakly polarizing sites and the formation of tighter binding pockets within the pores of the framework. Similar results have been reported for CO<sub>2</sub> adsorption in metalated samples of another bipyridine-containing framework, Al(OH)(bpydc).<sup>38</sup>

Although there is ample space in the coordination sphere of the metal-linker complexes in **1·(CuCl<sub>2</sub>)<sub>5.8</sub>** and **1·(CuCl)<sub>6.8</sub>**, these metal centers only show weak interaction with additional ligands, preferring lower coordination as a result of their filled d shells. While the Co<sup>II</sup> and Fe<sup>II</sup> centers in **1·(CoCl<sub>2</sub>)<sub>5.5</sub>** and **1·(FeBr<sub>2</sub>)<sub>6.1</sub>** should be able to achieve higher coordination, these complexes have the propensity to form tetrahedral complexes after desolvation. Weakly coordinating gases such as H<sub>2</sub> cannot bind to these metal centers, most likely because the resulting binding energy would not compensate for the reorganization energy required for conversion to geometries that support a higher coordination number.

Carbon monoxide adsorption experiments were performed on **1·(CuCl<sub>2</sub>)<sub>5.8</sub>**, **1·(CuCl)<sub>6.8</sub>**, **1·(CoCl<sub>2</sub>)<sub>5.5</sub>**, and **1·(FeBr<sub>2</sub>)<sub>6.1</sub>** at 298 K to probe the interaction of the metal sites with a more coordinating gas (Figure 4.5). Surprisingly, only **1·(CuCl)<sub>6.8</sub>** showed significant uptake of CO, reaching a level of approximately 0.4 per copper center at 0.2 bar. Here, coordination of CO to the Cu<sup>I</sup> centers is confirmed by the observation of a peak at 2093 cm<sup>-1</sup> in the infrared spectrum, which agrees with reported CO stretching frequencies in similar molecular Cu<sup>I</sup>-CO complexes



**Figure 4.5.** Low-pressure CO adsorption isotherms for **1**,  $1 \cdot (\text{CuCl}_2)_{5.8}$ ,  $1 \cdot (\text{CuCl})_{6.8}$ ,  $1 \cdot (\text{CoCl}_2)_{5.5}$ ,  $1 \cdot (\text{FeBr}_2)_{6.1}$  and  $1 \cdot (\text{Ir}(\text{COD})\text{BF}_4)_{4.8}$  at 298 K.

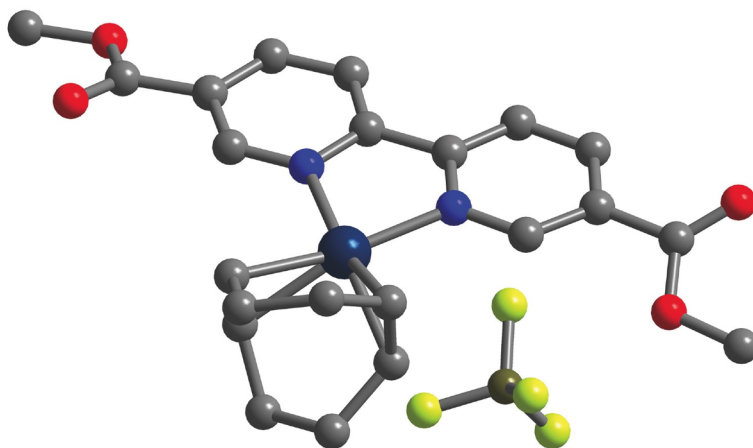
(Figure 4.S42).<sup>66</sup> The CO stretching frequency in the CO adduct of  $1 \cdot (\text{CuCl})_{6.8}$  is shifted  $50 \text{ cm}^{-1}$  lower relative to free CO, indicating modest  $\pi$  backbonding from  $\text{Cu}^{\text{I}}$  to CO. Substoichiometric uptake of CO per  $\text{Cu}^{\text{I}}$  suggests that CO binds to only one type of  $\text{Cu}^{\text{I}}$  center among the three determined in the single-crystal structure (Figure 4.S1). In contrast, the lack of any strong interaction between CO and  $1 \cdot (\text{CuCl}_2)_{5.8}$ ,  $1 \cdot (\text{CoCl}_2)_{5.5}$ , or  $1 \cdot (\text{FeBr}_2)_{6.1}$  suggests that the metal centers in these materials have insufficient  $\pi$  backbonding capability to form stable adducts with CO, which is attributed to the higher formal oxidation state of the metal centers in the bipyridine- $\text{M}^{\text{II}}$  complexes.

**Arene C–H Borylation.** Iridium-catalyzed C–H borylation has proven to be a practical and efficient way of functionalizing inert feedstock chemicals to make valuable products that are widely used in fine chemicals synthesis.<sup>67</sup> Among the many catalysts studied for this reaction, iridium complexes supported by chelating N-donor ligands have been shown to be very capable systems for the C–H borylation of arenes with either 4,4,4',4',5,5,5',5'-octamethyl-2,2'-bi-1,3,2-dioxaborolane ( $\text{B}_2\text{pin}_2$ ) or 4,4,5,5-tetramethyl-1,3,2-dioxaborolane (HBpin).<sup>68–71</sup> Inspired by the considerable amount of work on homogeneous systems, recent efforts have been directed towards making heterogeneous analogs of these catalysts.<sup>33,72,73</sup> Given that  $\text{Ir}^{\text{I}}$  precursors in combination with 2,2'-bipyridine ligands lead to highly active homogeneous systems, we investigated whether **1** would show similar activity when metalated with iridium.

Considering the size of the pore apertures in **1**,  $[\text{Ir}(\text{COD})_2]\text{BF}_4$  (COD = 1,5-cyclooctadiene) was selected as an metalation agent, as it forms a relatively compact complex,  $[\text{Ir}(\text{COD})(\text{MeCN})_2]^+$ , in acetonitrile.<sup>74</sup> Metalation of a microcrystalline powder of **1** with  $[\text{Ir}(\text{COD})_2]\text{BF}_4$  following the procedure used for the metal halides indeed yields  $1 \cdot (\text{Ir}(\text{COD})\text{BF}_4)_{4.7}$  as an olive green powder. ICP-OES analysis of the powder indicates 78% Ir loading of the framework, which is much lower than the loading determined for the frameworks

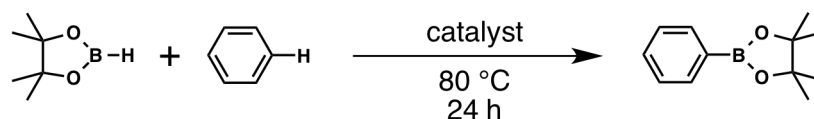
metalated with first-row transition metal halides. X-ray analysis of the metalated single crystals revealed no change in space group and less than 10% occupancy of Ir at the bipyridine sites. Consequently, the ancillary ligands on Ir could not be identified. Disparity between the Ir loading in the powder and single crystal samples implies that the extent of metalation at the framework surface is greater than that of the interior. Compared to  $\sim 60 \mu\text{m}$  single crystals, the  $\sim 0.5\text{-}1 \mu\text{m}$  crystals in the powder sample have a much larger crystal surface area to volume ratio, which would result in higher Ir loading in the powder. The Ir source may be blocking the pore windows upon metalation, obstructing the diffusion of additional Ir complexes to sites within the framework. This may be due to the larger size of the Ir precursor compared to the first row transition metal halides. In addition, Ir forms much more stable complexes with bipyridine, making it less likely to reversibly dissociate from the bipyridine sites and travel deeper into the pore structure.

To provide insight into the structure of the Ir centers formed in  $\mathbf{1}\cdot(\text{Ir}(\text{COD})\text{BF}_4)_{4.7}$ , CO adsorption measurements were performed. These indicate substantial irreversible binding of CO with uptake of roughly two CO molecules per Ir center by 0.001 bar CO. This presumably occurs through the substitution of CO for COD on the Ir center to form  $\mathbf{1}\cdot(\text{Ir}(\text{CO})_2\text{BF}_4)_{4.7}$ . After CO adsorption, the resulting yellow material features two new peaks in the infrared spectrum at 2088 and 2026  $\text{cm}^{-1}$  (Figure 4.S41), which can be assigned to the asymmetric and symmetric CO stretching modes of the (bpy)Ir(CO)<sub>2</sub> complex. These frequencies agree with those reported for similar cationic Ir<sup>I</sup> dicarbonyl complexes.<sup>75,76</sup>



**Figure 4.6.** Crystal structure of **3**, the molecular analog of  $\mathbf{1}\cdot(\text{Ir}(\text{COD})\text{BF}_4)_{4.7}$  as determined by single-crystal X-ray diffraction. Dark blue, yellow green, olive green, red, blue, and gray spheres represent Ir<sup>I</sup>, F, B, O, N, and C atoms, respectively; H atoms are omitted for clarity.

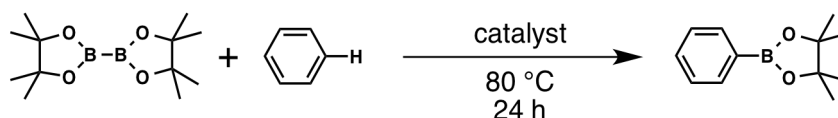
The compound  $[\text{Ir}(\text{dmbpydc})(\text{COD})]\text{BF}_4$  (**3**) was also synthesized as a molecular analog and characterized by single-crystal X-ray diffraction. The structure of **3** (see Figure 4.6) supports the initial description of the Ir complexes in  $\mathbf{1}\cdot(\text{Ir}(\text{COD})\text{BF}_4)_{4.7}$ , with dmbpydc and COD bound to Ir in a square planar geometry and  $\text{BF}_4^-$  as a non-coordinating anion. The UV-vis spectrum of  $\mathbf{1}\cdot(\text{Ir}(\text{COD})\text{BF}_4)_{4.7}$  (Figure 4.S44) reveals a shoulder at 466 nm and a peak at 594 nm, which likely correspond to the metal-to-ligand charge transfer bands of the Ir-bpy units in the framework. These correspond well to peaks at 466 nm and 602 nm in the UV-vis spectrum of **3**. Furthermore, infrared spectra of  $\mathbf{1}\cdot(\text{Ir}(\text{COD})\text{BF}_4)_{4.7}$  (Figure 4.S41) exhibits peaks between 2922–2841  $\text{cm}^{-1}$ , which are assigned to the aliphatic  $\nu(\text{C-H})$  of the coordinated COD moieties, and a



**Table 4.2.** Control Experiments for Benzene C-H Borylation with HBpin

Catalyst	Amount (mol%)	Yield <sup>a</sup> (%)
<b>1</b> ·(Ir(COD)(BF <sub>4</sub> )) <sub>0.6</sub>	0.065 (Ir)	100 <sup>b</sup>
<b>1</b>	0.68 (Zr)	0
[Ir(COD) <sub>2</sub> ]BF <sub>4</sub>	0.18 (Ir)	0.9
<b>2</b> + 0.6[Ir(COD) <sub>2</sub> ]BF <sub>4</sub>	0.84 (Zr)	0.03
<b>1</b> ·(Ir(COD)(BF <sub>4</sub> )) <sub>0.6</sub> + 0.6PPh <sub>3</sub>	0.065 (Ir)	4
<b>1</b> ·(Ir(COD)(BF <sub>4</sub> )) <sub>0.6</sub> + 0.6PCy <sub>3</sub>	0.069 (Ir)	4

<sup>a</sup>Yields were determined by <sup>1</sup>H NMR using 1,3,5-trimethoxybenzene as an internal standard. <sup>b</sup>Determined as an average of three replications.



**Table 4.3.** Control Experiments for Benzene C-H Borylation with B<sub>2</sub>pin<sub>2</sub>

Catalyst	Amount (mol%)	Yield <sup>a</sup> (%)
<b>1</b> ·(Ir(COD)(BF <sub>4</sub> )) <sub>0.6</sub>	0.21 (Ir)	94 <sup>b</sup>
<b>1</b>	2.4 (Zr)	0
[Ir(COD) <sub>2</sub> ]BF <sub>4</sub>	0.71 (Ir)	0.9
<b>2</b> + 0.6[Ir(COD) <sub>2</sub> ]BF <sub>4</sub>	2.3 (Zr)	0
<b>1</b> ·(Ir(COD)(BF <sub>4</sub> )) <sub>0.6</sub> + 0.6PPh <sub>3</sub>	0.21 (Ir)	0.05
<b>1</b> ·(Ir(COD)(BF <sub>4</sub> )) <sub>0.6</sub> + 0.6PCy <sub>3</sub>	0.20 (Ir)	0

<sup>a</sup>Yields were determined by <sup>1</sup>H NMR spectroscopy using 1,3,5-trimethoxybenzene as an internal standard.

<sup>b</sup>Determined as an average of three replications.

broad peak at 1056 cm<sup>-1</sup>, which is assigned to ν(B–F) of the BF<sub>4</sub><sup>-</sup> anion. Both features can also be observed in the same regions in the infrared spectrum of **3**. These results suggest that the structure of **3** is representative of the Ir-bipyridine complexes in **1**·(Ir(COD)BF<sub>4</sub>)<sub>4.7</sub>.

Borylation reactions were generally conducted over 24 h at 80 °C in neat arene using either B<sub>2</sub>pin<sub>2</sub> or HBpin as a boron reagent. To ensure that the Ir sites in the framework are accessible and to achieve catalyst loadings below 1 mol% Ir, only 10% of the bipyridine sites were metalated in the samples employed for catalysis. The Ir-metalated framework, **1**·(Ir(COD)BF<sub>4</sub>)<sub>0.6</sub>, proved to be a highly active catalyst for the C-H borylation of benzene to form 4,4,5,5-tetramethyl-2-phenyl-1,3,2-dioxaborolane (PhBpin) in good yield at a very low catalyst loading (Tables 4.2 and 4.3). Comparison of the powder X-ray diffraction patterns of the material before and after catalysis reveal no loss in crystallinity, suggesting that the material is stable under the conditions used for catalysis. Following conversion of benzene to PhBpin by <sup>1</sup>H NMR spectroscopy, the average turnover frequency of the catalyst was determined to be 860 mol PhBpin mol Ir<sup>-1</sup> h<sup>-1</sup> at 80 °C (Figure 4.S45), which is within an order of magnitude of that reported for the best molecular systems.<sup>69</sup> Note that supporting ligands that are stronger electron donors are better at stabilizing the proposed Ir<sup>V</sup> intermediate that forms upon C-H activation of the arene,<sup>67,69,71</sup> which is often the rate determining step of the reaction. Thus, the bipyridine-Ir units in **1**·(Ir(COD)BF<sub>4</sub>)<sub>0.6</sub> are expected to be less active in comparison to the best molecular Ir catalysts with more electron-rich supporting ligands, such as 4,4'-di-*tert*-butylbipyridine or 3,4,7,8-tetramethylphenanthroline.<sup>69,71</sup>

Several control experiments were performed to establish that catalysis is indeed facilitated by the Ir-bipyridine complexes in framework (Tables 4.2 and 4.3). As predicted,  $[\text{Ir}(\text{COD})_2]\text{BF}_4$  and **1** both display limited or no catalytic activity. The metal–organic framework  $\text{Zr}_6\text{O}_4(\text{OH})_4(\text{bpd})_6$  was synthesized and treated with  $[\text{Ir}(\text{COD})_2]\text{BF}_4$  following the same procedure used for **1**. The Ir-treated biphenyl framework did not show significant catalytic activity, excluding the possibility of catalysis by adventitious Ir species that may form upon interaction with the framework. A hot filtration experiment was performed to determine if any catalytic activity was due to soluble Ir species that may have formed during the reaction. No further increase in turnover number was observed after  $\mathbf{1}\cdot(\text{Ir}(\text{COD})\text{BF}_4)_{0.6}$  was filtered from the reaction mixture (Figure 4.S46), which further supports that catalysis is facilitated by the Ir-bipyridine complexes bound within the material.

To determine if catalysis occurs within the pores or only on the surface of the metal–organic framework crystallites, reactions were carried out in the presence of bulky coordinating groups, which can selectively poison the surface Ir sites due to their large size (Table 4.3).<sup>74</sup> Addition of one equivalent of either  $\text{PPh}_3$  or  $\text{PCy}_3$  per Ir to the reaction mixture led to drastically reduced yields, suggesting that catalysis occurs primarily at the surface of the material. This is consistent with Ir binding to only surface bipyridine sites and not to those within the pores.

**Table 4.4.** Catalyst Cycling Experiments for Benzene C-H Borylation with  $\text{Zr}_6\text{O}_4(\text{OH})_4(\text{bpydc})_6(\text{Ir}(\text{COD})\text{BF}_4)_{0.6}$

Boron Reagent	Yield <sup>a</sup> (%)				
	1	2	3	4	5
HBpin <sup>b</sup>	96	100	100	100	96
B <sub>2</sub> pin <sub>2</sub> <sup>c</sup>	94	91	90	80	54

<sup>a</sup>Yields were determined by <sup>1</sup>H NMR using 1,3,5-trimethoxybenzene as an internal standard. <sup>b</sup>Reaction conditions: 1.3 mmol HBpin, 3.0 mL benzene, 0.10 mol% Ir, 80 °C, 24 h. <sup>c</sup>Reaction conditions: 0.65 mmol B<sub>2</sub>pin<sub>2</sub>, 3.0 mL benzene, 0.20 mol% Ir, 80 °C, 24 h.


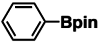
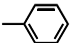
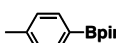
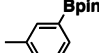
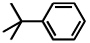
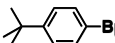
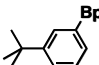
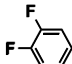
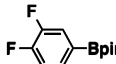
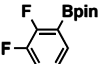
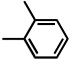
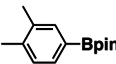
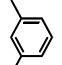
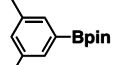

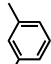
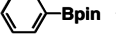
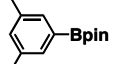
Catalyst cycling experiments indicated no significant loss in activity over five cycles when HBpin was employed, although activity decreased substantially after the third and fourth cycles when B<sub>2</sub>pin<sub>2</sub> was used (Table 4.4). The much lower catalyst stability with B<sub>2</sub>pin<sub>2</sub> may be attributed to impurities such as trace moisture in the B<sub>2</sub>pin<sub>2</sub> that can poison the catalytic sites. It has previously been reported that the maximum turnover number of the catalyst is highly dependent on the purity of the B<sub>2</sub>pin<sub>2</sub> used.<sup>68,69</sup> If the catalyst were inherently unstable to the reaction conditions, decreased activity after each cycle should have also been observed when HBpin was used as a boron reagent.

The activity of  $\mathbf{1}\cdot(\text{Ir}(\text{COD})(\text{BF}_4))_{0.6}$  in the borylation of several substituted arenes reveals that the catalyst exhibits size selectivity. Reaction with toluene, or 1,2-difluorobenzene results in nearly quantitative borylation, whereas substantially lower activity is observed using *tert*-butylbenzene, *o*-xylene, and *m*-xylene as substrates (Table 4.5). Assuming that the catalytic sites are predominantly on the surface, as suggested by surface poisoning experiments and low Ir loading after metalation, the unexpected size selectivity suggests that the local steric environment of the catalytic sites on the framework surface can prevent access to the Ir centers or destabilize ideal transition state conformations when bulkier substrates are used. A substrate competition experiment between benzene and *m*-xylene in 1:1 mixture showed that the catalyst has 95% selectivity for benzene, further suggesting that the lower yields observed for bulkier arenes are due to size or shape selectivity and not catalyst instability or poisoning from trace impurities in these solvents. Although size selectivity is not necessarily ideal for this specific



reaction, which has applications that require the ability to functionalize a broad scope of substrates, it is intriguing to observe that size selectivity still occurs even if the catalytic sites are likely on the surface of the particles. This implies that size selectivity in metal–organic frameworks does not have to arise solely from restriction of substrate access to catalytic sites by the pore apertures, but can also be influenced by the local steric environment around the catalytic sites, as dictated by the unique pore structure of a specific framework.

**Table 4.5.** Selected Substrate Scope for C-H Borylation with HBpin<sup>a</sup>

Substrates	Products	Product Ratio <sup>b</sup>	Conversion <sup>b</sup> (%)
		–	100 <sup>c</sup>
	 	40:60	96
	 	29:71	38
	 	67:33	96
		–	4
		–	27
  1:1	 	95:5	97

<sup>a</sup>Reaction conditions: 2.0 mmol HBpin, 3 mL arene or arene mixture, 0.065 mol% Ir, 80 °C, 24 h. <sup>b</sup>Product ratios and conversions were determined by <sup>1</sup>H NMR using 1,3,5-trimethoxybenzene as an internal standard.

<sup>c</sup>Determined as an average of three replications.

While this manuscript was in preparation, a recent paper reported the similar application of Zr<sub>6</sub>O<sub>4</sub>(OH)<sub>4</sub>(bpydc)<sub>6</sub> using [Ir(COD)(OMe)]<sub>2</sub> as an Ir source and B<sub>2</sub>pin<sub>2</sub> as the boron source.<sup>33</sup> Interestingly, the catalyst described in the report maintained activity after 20 cycles using B<sub>2</sub>pin<sub>2</sub> and displayed no pronounced size selectivity. The disparity between the reported results and the results in this work may be due to differences in particle size, surface morphology, and metal loading of the material, which indicates that these properties may have unexpected and profound effects on catalysis and, thus, should be more carefully studied.

#### 4.4. Conclusions and outlook

The foregoing results demonstrate that Zr<sub>6</sub>O<sub>4</sub>(OH)<sub>4</sub>(bpydc)<sub>6</sub>, a metal–organic framework featuring open 2,2'-bipyridine sites, can readily be metalated by a host of solution- and gas-phase metal reagents. Moreover, single-crystal-to-single-crystal metalation of the framework results in the ordering of the metal-linker complexes, enabling structural characterization by single-crystal X-ray diffraction. This remarkable structural ordering arises from a transition from *Fm* $\bar{3}$ *m* to

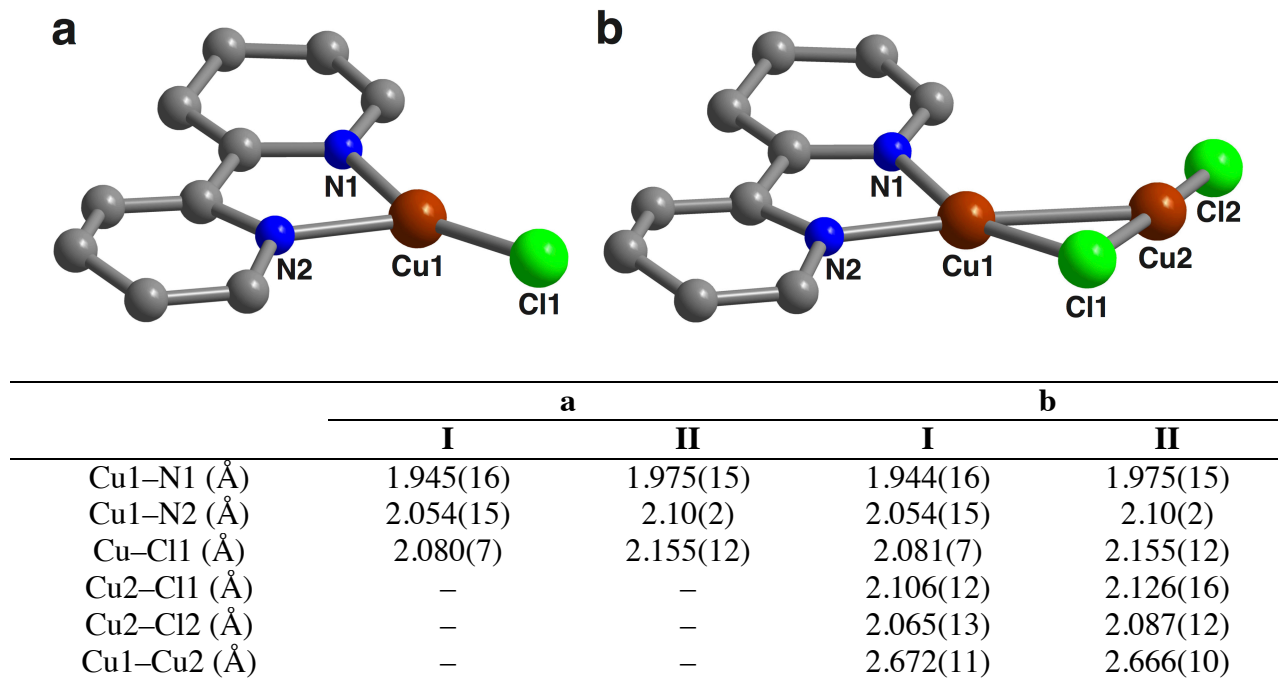
$Pa\bar{3}$  symmetry induced by the collective distortion of the framework linkers upon metal chelation. These findings emphasize that structural determination of the metal complexes in post-synthetically metalated metal–organic frameworks can be achieved if a high-symmetry framework can transition to a lower symmetry upon metal insertion. Furthermore, the  $[\text{Ir}(\text{COD})_2]\text{BF}_4$ -metalated framework is a highly active and recyclable catalyst for arene C–H borylation.

Ongoing efforts are directed towards finding other frameworks that display similar structural transitions upon metalation, as well as to developing methods to limit disorder due to linker rotation and variable solvation of the metal. In addition, the *in situ* structural observation of reactions at the metal sites in these frameworks by X-ray diffraction is being pursued. Finally, efforts are underway to demonstrate that post-synthetic metalation of metal–organic frameworks can be used to design catalysts with unparalleled reactivity and selectivity through judicious choice of metal node, chelating linker, and metal precursor. Altogether, these results exemplify the distinct advantages that metal–organic frameworks hold as highly tunable, well-defined platforms for catalysis and the exceptional ability to structurally characterize these materials through X-ray diffraction.

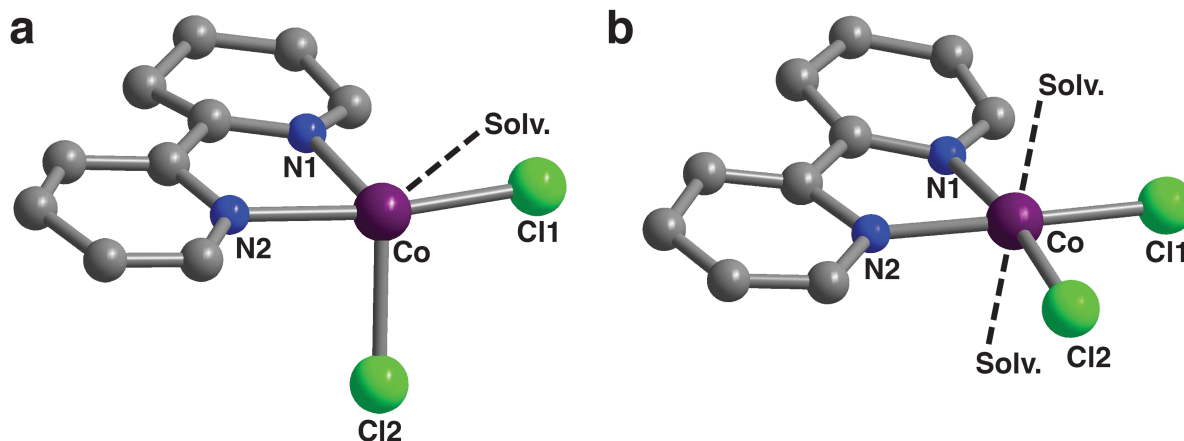
#### 4.5. Acknowledgements

This work was supported by the Laboratory Directed Research and Development Program of Lawrence Berkeley National Laboratory under U.S. Department of Energy Contract No. DE-AC02-05CH11231. The Advanced Light Source is supported by the Director, Office of Science, Office of Basic Energy Sciences, of the U.S. Department of Energy under Contract no. DE-AC02-05CH11231. We thank the 11-BM staff at the Advanced Photon Source at Argonne National Laboratory for assisting with powder X-ray diffraction experiments. Use of the Advanced Photon Source at Argonne National Laboratory was supported by the U. S. Department of Energy, Office of Science, Office of Basic Energy Sciences, under Contract No. DE-AC02-06CH11357. We are grateful for the assistance of Antonio DiPasquale and Kevin J. Gagnon with single-crystal X-ray diffraction experiments and Jonathan Bachman with SEM measurements. We also thank Kohei Takahashi, Matthew Larsen, and Carl Liskey for fruitful discussions.

#### 4.6. Supplementary Information

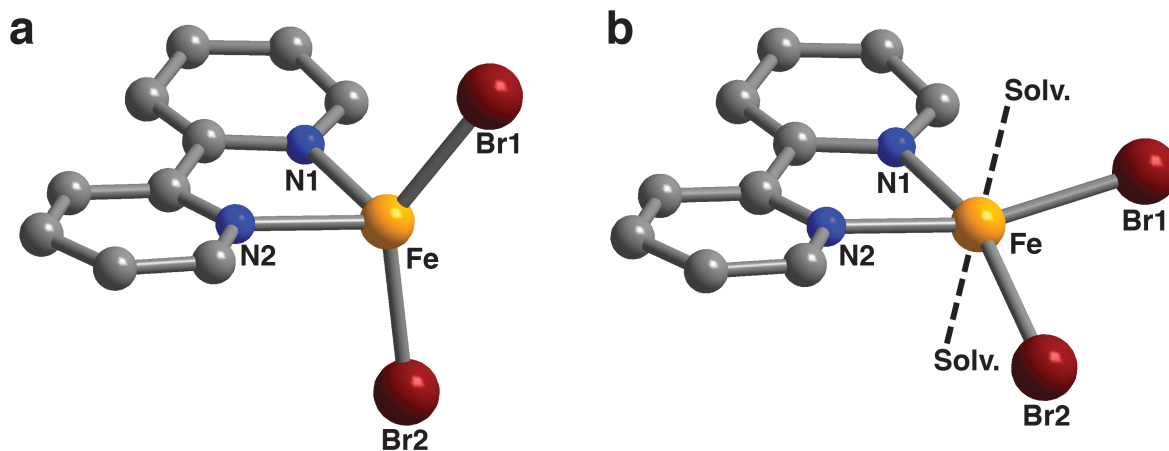


**Figure 4.S1.** Structure with selected bond distances of the (bpy)CuCl (a) and (bpy)Cu(CuCl<sub>2</sub>) (b) complexes in **1**•(CuCl)<sub>6.8</sub> as determined by single-crystal X-ray diffraction. The bipyridine-Cu<sup>I</sup> complexes show rotational disorder over two positions, which are labeled as **I** and **II**.



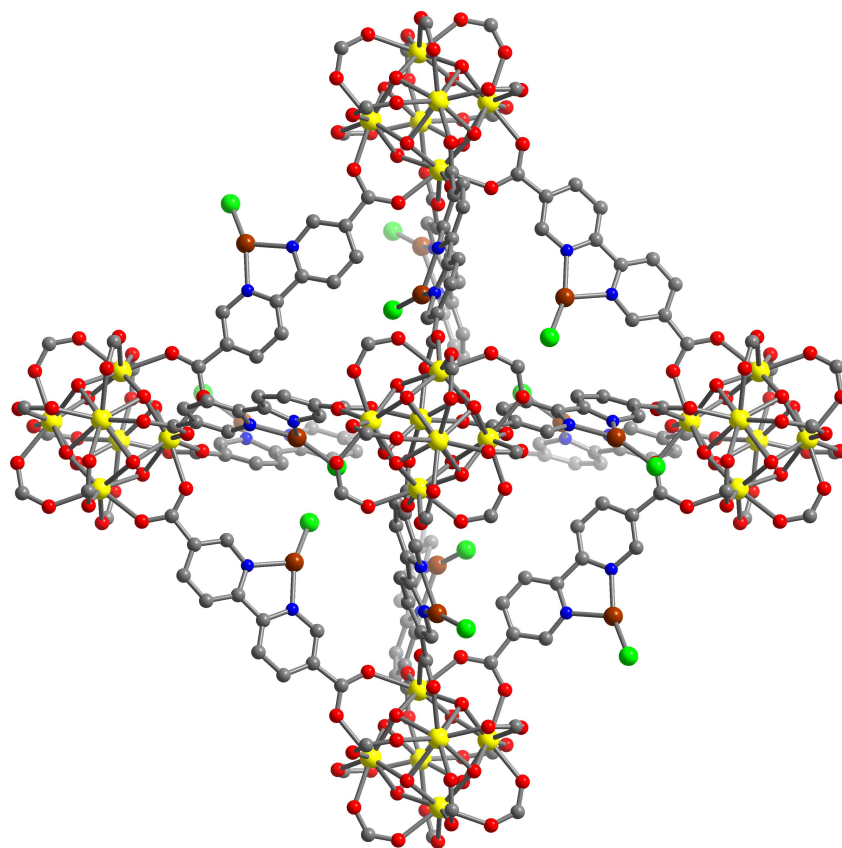
	<b>a</b>	<b>b</b>
Co–N1 (Å)	2.093(19) (eq)	2.13(2)
Co–N2 (Å)	2.166(15) (ax)	2.01(2)
Co–Cl1 (Å)	2.270(8) (ax)	2.273(16)
Co–Cl2 (Å)	2.330(11) (eq)	2.305(7)
Cl1–Co–Cl2 (°)	99.2(4)	92.4(5)
Cl1–Co–N2 (°)	171.5(6)	167.3(10)
N1–Co–Cl2 (°)	119.1(6)	171.6(7)
Angle between N1–Co–N2 and Cl1–Co–Cl2 planes (°)	120	4

**Figure 4.S2.** Structure with selected bond distances and angles of the (bpy)CoCl<sub>2</sub> complexes in **1**•(CoCl<sub>2</sub>)<sub>5.5</sub> as determined by single-crystal X-ray diffraction. The complexes are assigned to have trigonal bipyramidal (**a**) and octahedral (**b**) geometries with unresolved coordinated solvent at an equatorial site in the trigonal bipyramidal structure (**a**) and at axial sites in the octahedral structure (**b**).

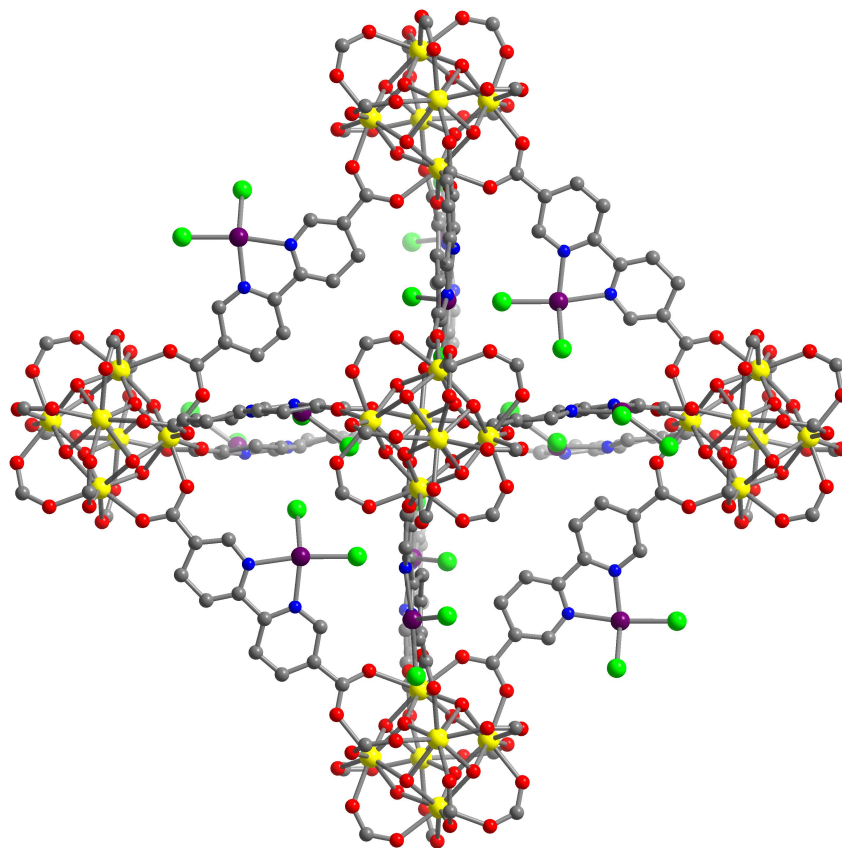


	<b>a</b>	<b>b</b>
Fe–N1 (Å)	2.173(9)	2.173(9)
Fe–N2 (Å)	2.104(9)	2.104(9)
Fe–Br1 (Å)	2.378(9)	2.501(14)
Fe–Br2 (Å)	2.356(7)	2.468(14)
Angle between N1–Fe–N2 and Br1–Fe–Br2 planes (°)	79	25

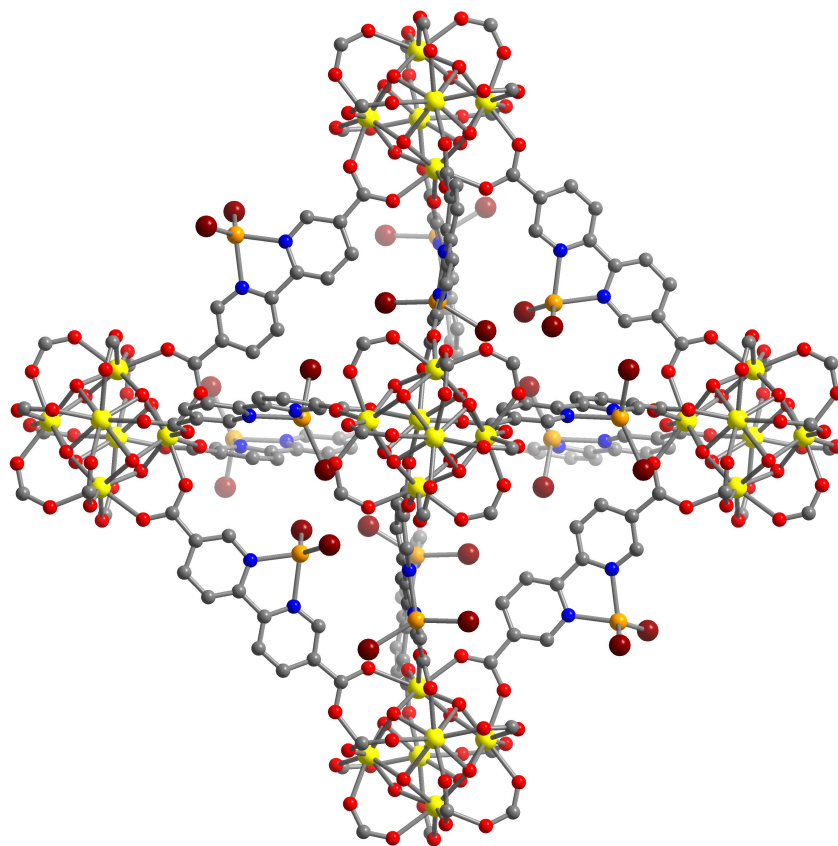
**Figure 4.S3.** Structure with selected bond distances and angles of the (bpy)FeBr<sub>2</sub> complexes in **1**•(FeBr<sub>2</sub>)<sub>6.1</sub> as determined by single-crystal X-ray diffraction. The complexes are assigned to have tetrahedral (**a**) and octahedral (**b**) geometries with unresolved coordinated solvent at the axial sites in the octahedral structure (**b**).



**Figure 4.S4.** A portion of the crystal structure of  $1 \cdot (\text{CuCl})_{6.8}$  as determined by analysis of single-crystal X-ray diffraction data; brown, light green, red, blue, and gray spheres represent Cu, Cl, O, N, and C atoms, respectively. The metalated linkers exist as  $\text{bpy}(\text{CuCl})$  and  $\text{bpy}(\text{Cu}(\text{CuCl}_2))$  units, but are represented here as  $\text{bpy}(\text{CuCl})$ . Hydrogen atoms are omitted for clarity.

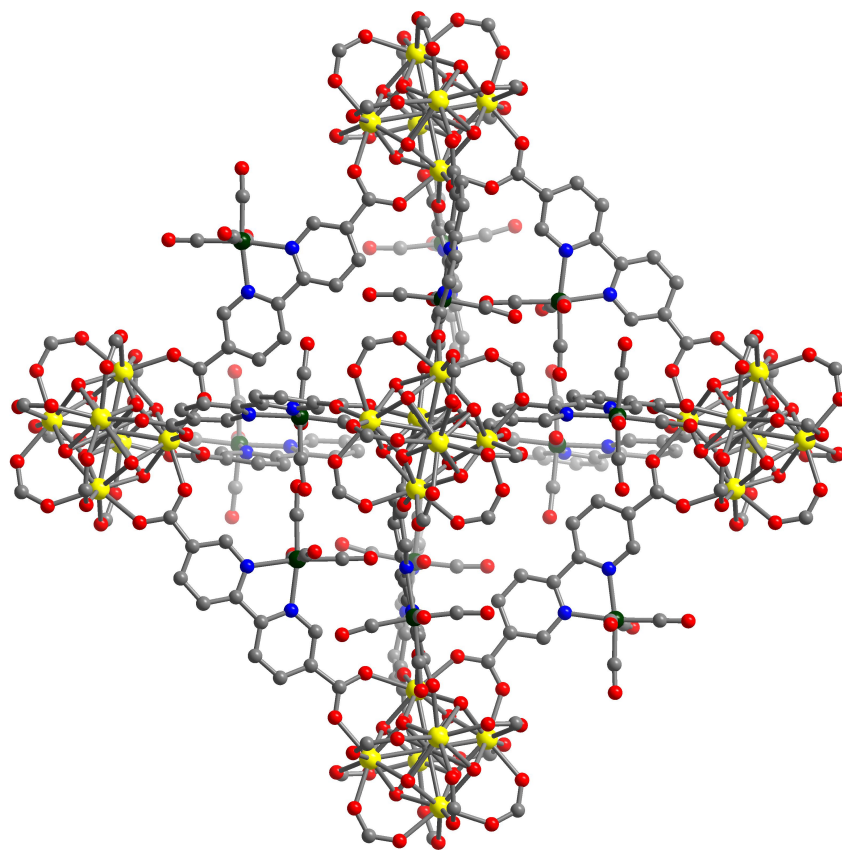


**Figure 4.S5.** A portion of the crystal structure of  $1 \cdot (\text{CoCl}_2)_{5.5}$  as determined by analysis of single-crystal X-ray diffraction data; purple, light green, red, blue, and gray spheres represent Co, Cl, O, N, and C atoms, respectively. The metalated linkers are disordered over two positions, but are represented here in only one orientation. Acetonitrile in the pores and hydrogen atoms are omitted for clarity.



**Figure 4.S6.** A portion of the crystal structure of  $1 \cdot (\text{FeBr}_2)_{6.1}$  as determined by analysis of single-crystal X-ray diffraction data; orange, dark red, red, blue, and gray spheres represent Fe, Br, O, N, and C atoms, respectively. The metalated linkers are disordered over two positions, but are represented here in only one orientation. Acetonitrile in the pores and hydrogen atoms are omitted for clarity.



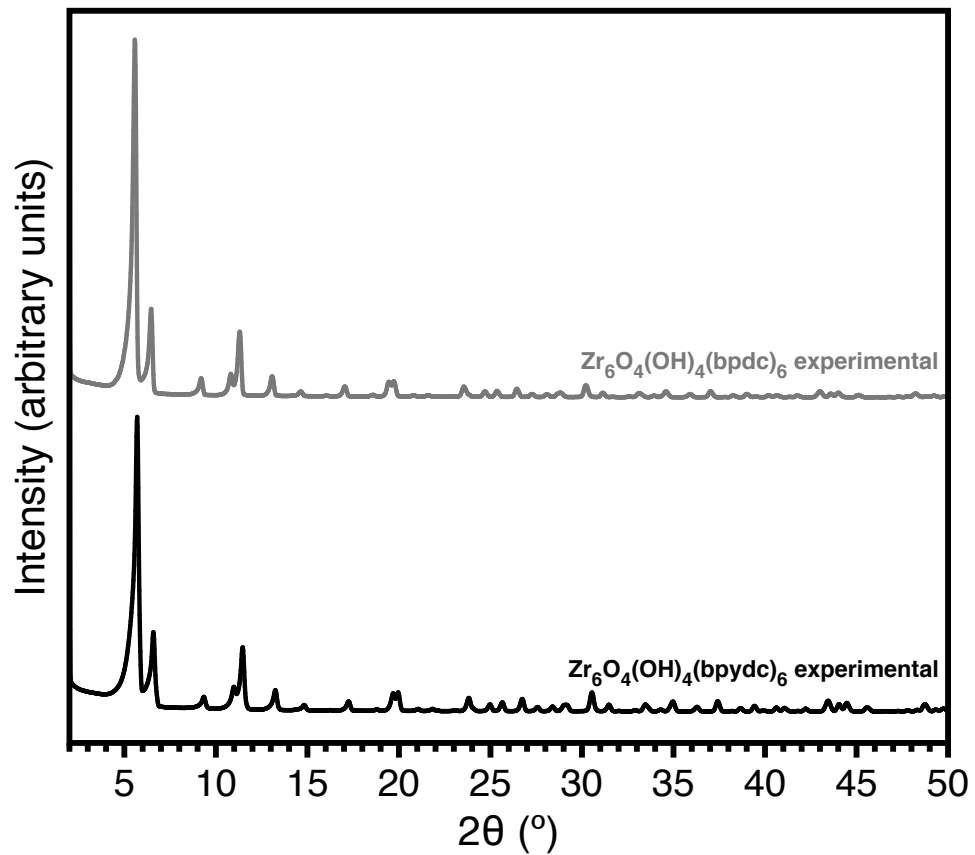


**Figure 4.S7.** A portion of the crystal structure of  $1 \cdot (\text{Cr}(\text{CO})_4)_{5,6}$  (solvated) as determined by analysis of single-crystal X-ray diffraction data; dark green, red, blue, and gray spheres represent Cr, O, N, and C atoms, respectively. Acetonitrile molecules in the pores and hydrogen atoms are omitted for clarity.

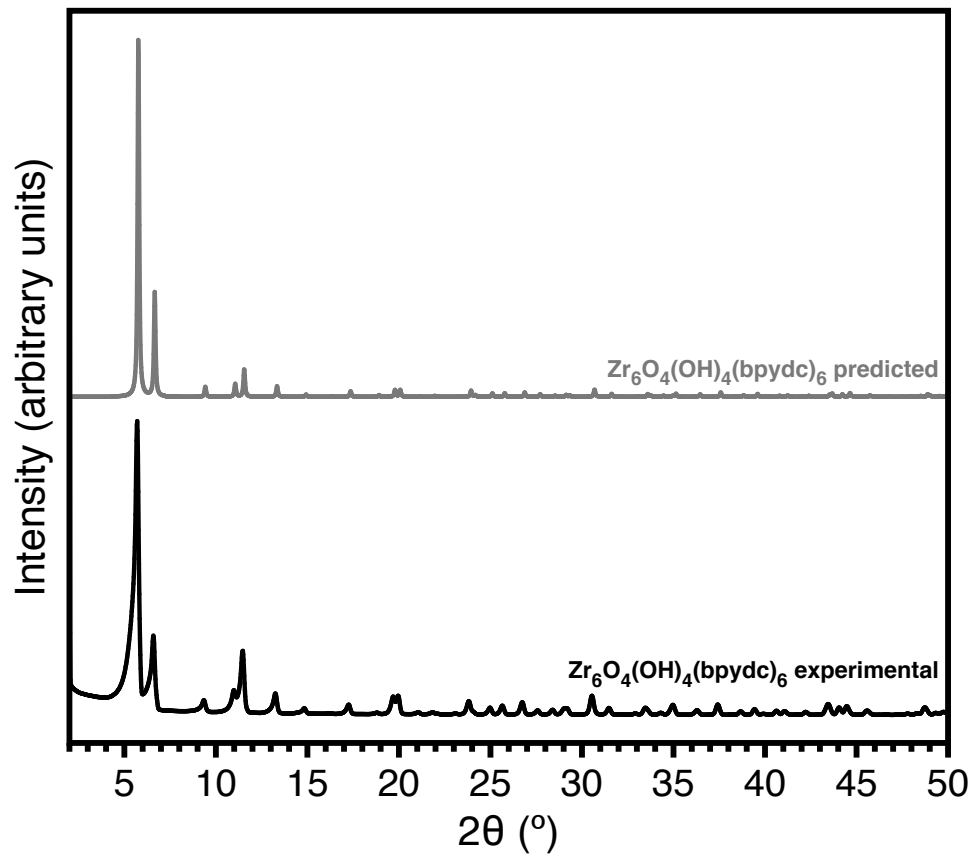
**Table 4.S1.** Crystallographic Data

	<b>1</b>	<b>1•(CuCl<sub>2</sub>)<sub>5,8</sub></b>	<b>1•(CuCl)<sub>6,1</sub></b>	<b>1•(CoCl<sub>2</sub>)<sub>5,5</sub></b>	<b>1•(FeBr<sub>2</sub>)<sub>6,1</sub></b>	<b>1•(Cr(CO)<sub>4</sub>)<sub>5,6</sub></b> (solvated)	<b>3</b>
Formula	C <sub>61.92</sub> H <sub>37.05</sub> N <sub>10.32</sub> O <sub>32</sub> Zr <sub>6</sub>	C <sub>83.76</sub> H <sub>65.17</sub> Cl <sub>10.44</sub> Cu <sub>5.22</sub> N <sub>21</sub> O <sub>32</sub> Zr <sub>6</sub>	C <sub>70.56</sub> H <sub>39.28</sub> Cl <sub>8.34</sub> Cu <sub>8.34</sub> N <sub>11.76</sub> O <sub>31.5</sub> Zr <sub>6</sub>	C <sub>66.52</sub> H <sub>39.70</sub> Cl <sub>9.12</sub> Co <sub>4.56</sub> N <sub>11.9</sub> O <sub>29.36</sub> Zr <sub>6</sub>	C <sub>67.2</sub> H <sub>40.72</sub> Br <sub>8.4</sub> Fe <sub>4.2</sub> N <sub>12.24</sub> O <sub>29.36</sub> Zr <sub>6</sub>	C <sub>86.31</sub> H <sub>39.04</sub> Cr <sub>4.95</sub> N <sub>11.68</sub> O <sub>49.8</sub> Zr <sub>6</sub>	C <sub>22</sub> H <sub>24</sub> BF <sub>4</sub> IrN <sub>2</sub> O <sub>4</sub>
Crystal System	Cubic	Cubic	Cubic	Cubic	Cubic	Cubic	Monoclinic
Space Group	<i>Fm</i> $\bar{3}$ <i>m</i>	<i>Pa</i> $\bar{3}$	<i>Pa</i> $\bar{3}$	<i>Pa</i> $\bar{3}$	<i>Pa</i> $\bar{3}$	<i>Pa</i> $\bar{3}$	<i>C2/c</i>
a, b, c (Å)	26.520(2)	26.0483(7)	26.1490(8)	26.0729(6)	26.255(4)	26.0205(7)	25.624(3), 11.6022(11), 14.5330(14)
$\alpha, \beta, \gamma$ (°)	90	90	90	90	90	90	90, 97.6110(10), 90
<i>V</i> , (Å <sup>3</sup> )	18652(4)	17674.1(14)	17879.9(16)	17724.3(12)	18098(8)	17617.6(14)	4282.5(7)
Z	4	4	4	4	4	4	8
Radiation,	MoK $\alpha$ ,	Synchrotron,	Synchrotron,	Synchrotron,	Synchrotron,	Synchrotron,	Synchrotron,
$\lambda$ (Å)	0.71073	0.7749	0.7749	0.7749	0.7749	0.8856	0.7749
R1 <sup>a</sup> , wR2 <sup>b</sup> (I>2 $\sigma$ (I))	0.0329, 0.0984	0.0380, 0.1134	0.0722, 0.2341	0.0574, 0.1904	0.0683, 0.2029	0.0539, 0.1644	0.0282, 0.0754
R1 <sup>a</sup> , wR2 <sup>b</sup> (all data)	0.0396, 0.0997	0.0428, 0.1189	0.0761, 0.2376	0.0664, 0.2014	0.0742, 0.2074	0.0562, 0.1666	0.0297, 0.0767

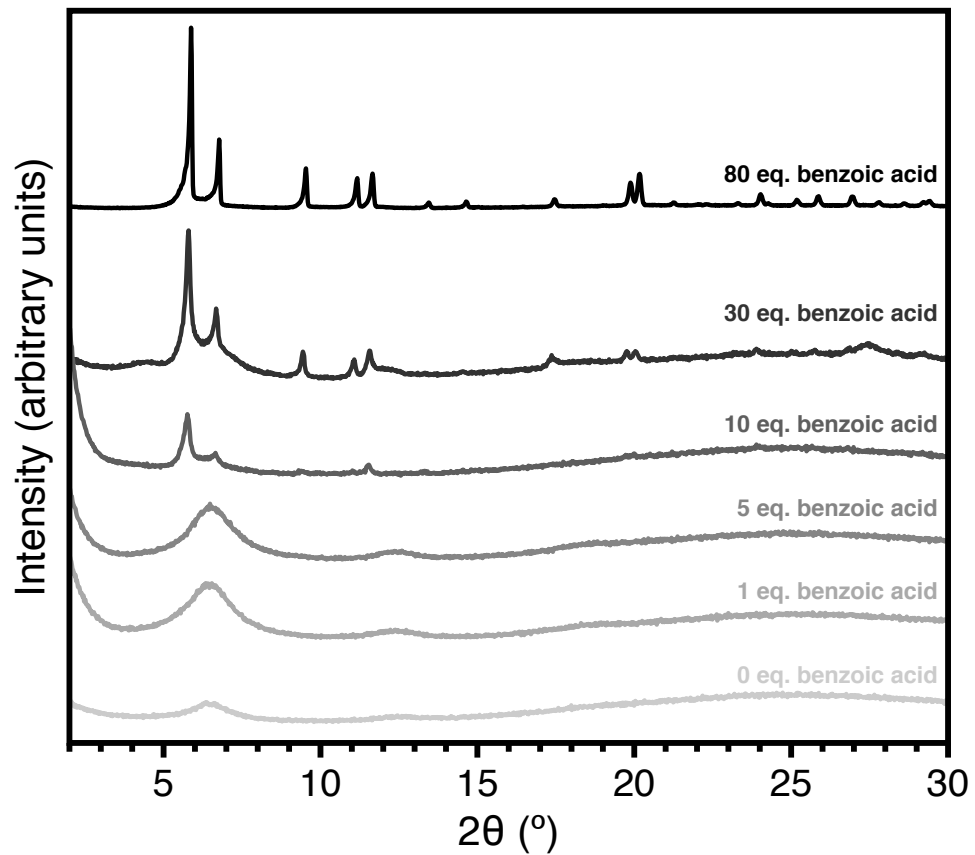
<sup>a</sup>R<sub>1</sub> =  $\sum ||F_o| - |F_c|| / \sum |F_o|$ , <sup>b</sup>wR<sub>2</sub> =  $\{ \sum [w(F_o^2 - F_c^2)]^2 / \sum [w(F_o^2)] \}^{1/2}$ .



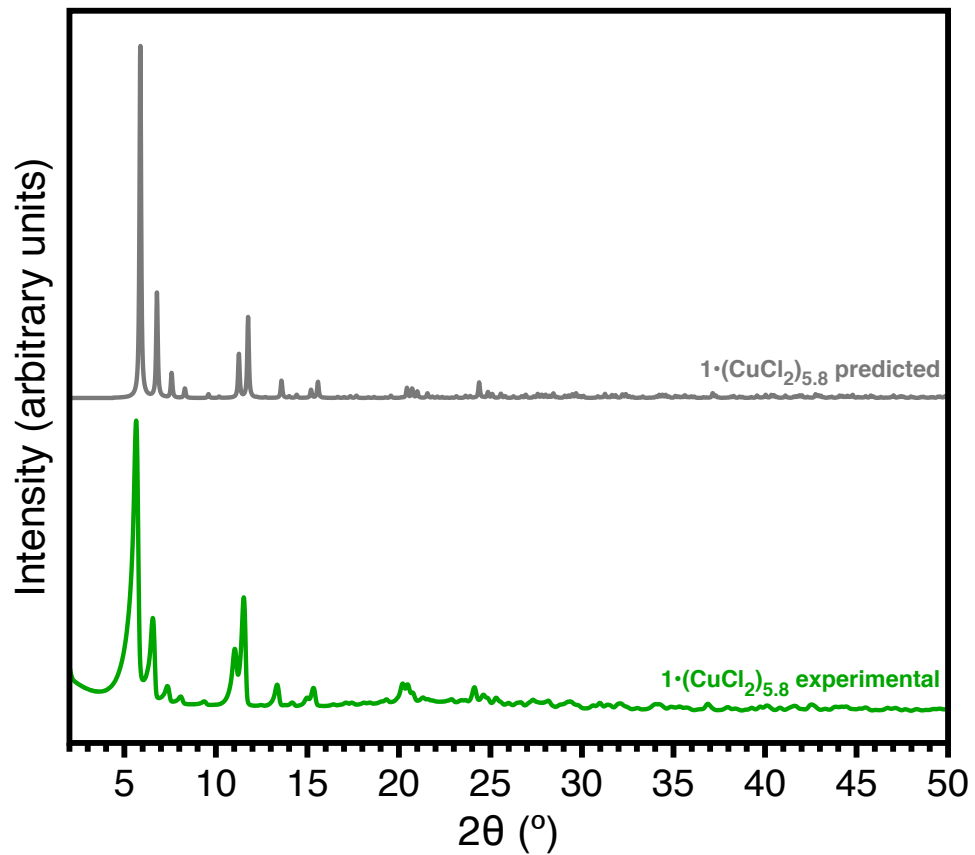
**Figure 4.S8.** Comparison of the powder X-ray diffraction patterns for  $\text{Zr}_6\text{O}_4(\text{OH})_4(\text{bpydc})_6$  (1) (black) and  $\text{Zr}_6\text{O}_4(\text{OH})_4(\text{bpdc})_6$  (2) (light gray).



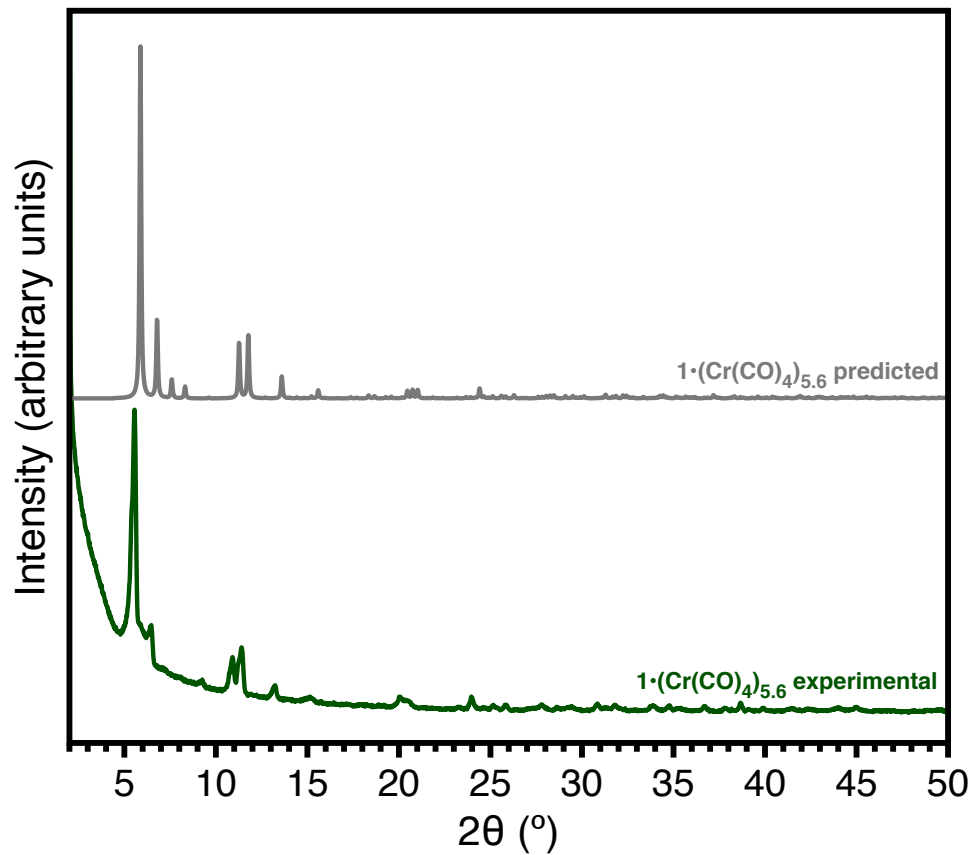
**Figure 4.S9.** Comparison of the predicted (light gray) and experimental (black) powder X-ray diffraction patterns for  $\text{Zr}_6\text{O}_4(\text{OH})_4(\text{bpydc})_6$  (1).



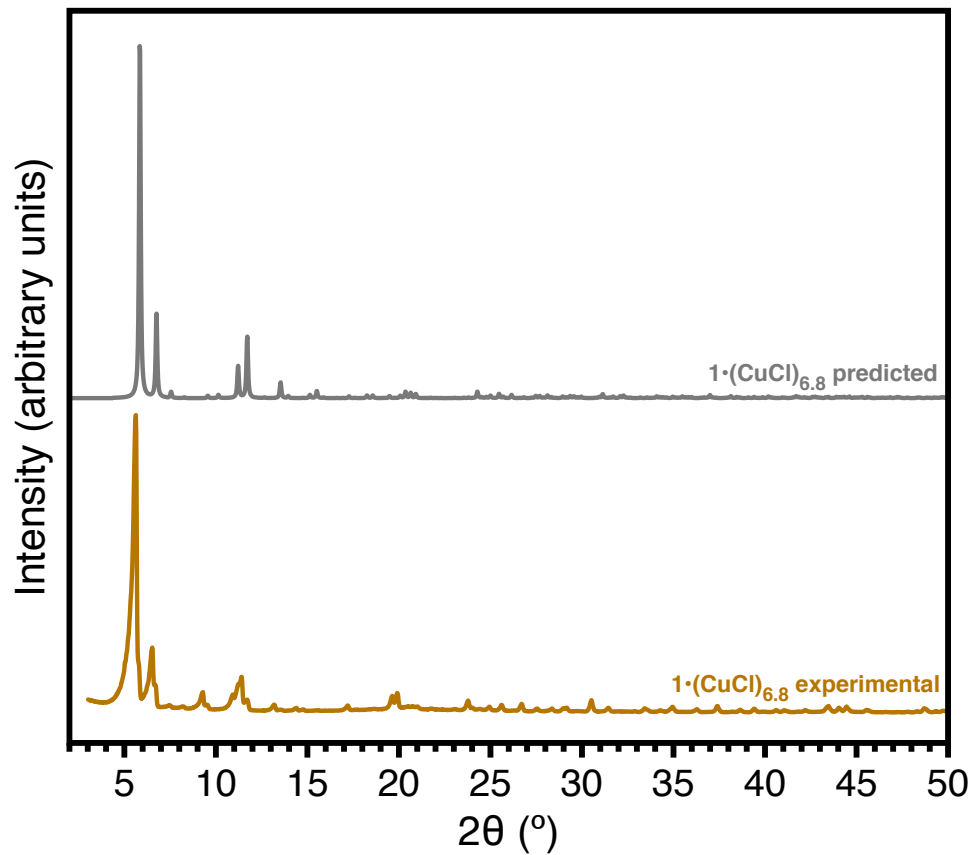
**Figure 4.S10.** Comparison of the powder X-ray diffraction patterns of **1** synthesized in the presence of 0, 1, 5, 10, 30, and 80 equivalents of benzoic acid (light gray to black).



**Figure 4.S11.** Comparison of the predicted (light gray) and experimental (light green) powder X-ray diffraction patterns for  $1\cdot(\text{CuCl}_2)_{5.8}$ .

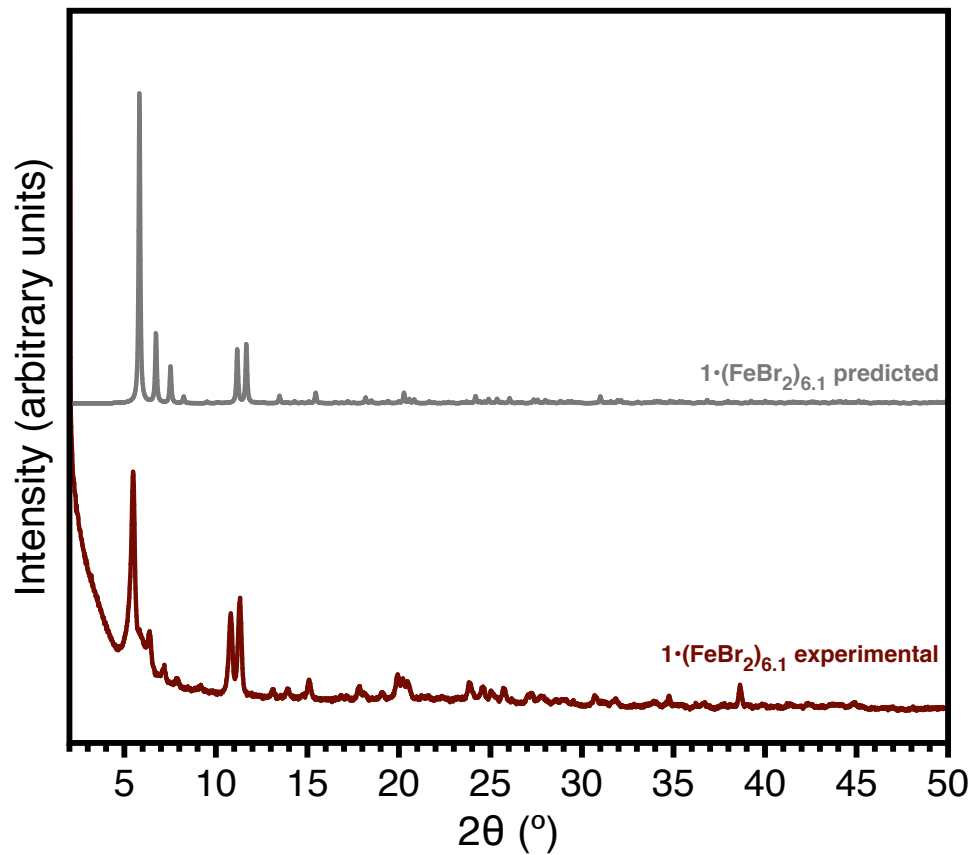


**Figure 4.S12.** Comparison of the predicted (light gray) and experimental (dark green) powder X-ray diffraction patterns for  $1 \cdot (\text{Cr}(\text{CO})_4)_{5.6}$ .

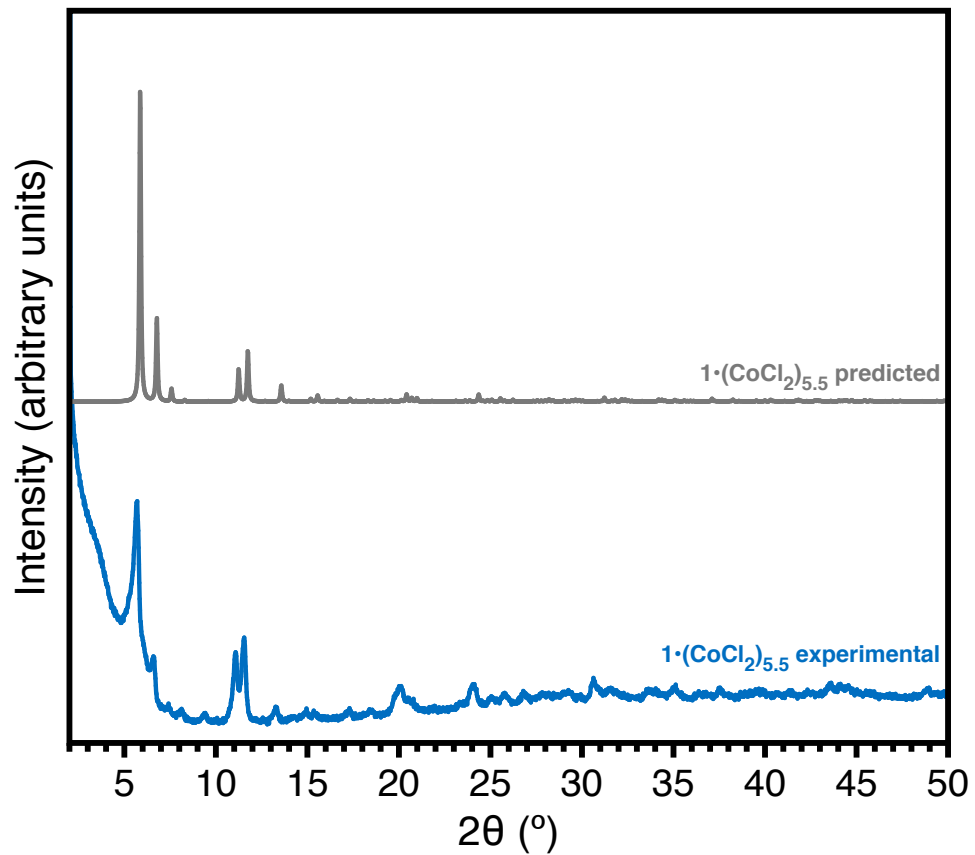


**Figure 4.S13.** Comparison of the predicted (light gray) and experimental (orange) powder X-ray diffraction patterns for  $1\cdot(\text{CuCl})_{6.8}$ .





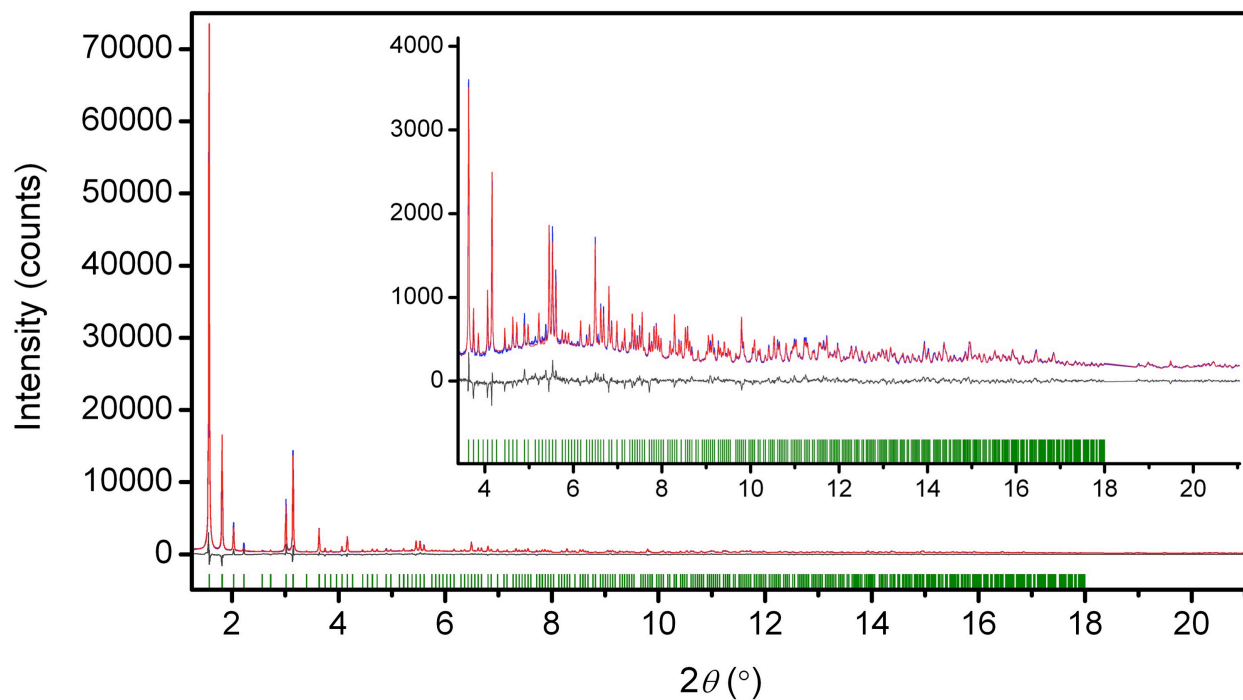
**Figure 4.S14.** Comparison of the predicted (light gray) and experimental (dark red) powder X-ray diffraction patterns for 1·(FeBr<sub>2</sub>)<sub>6.1</sub>.



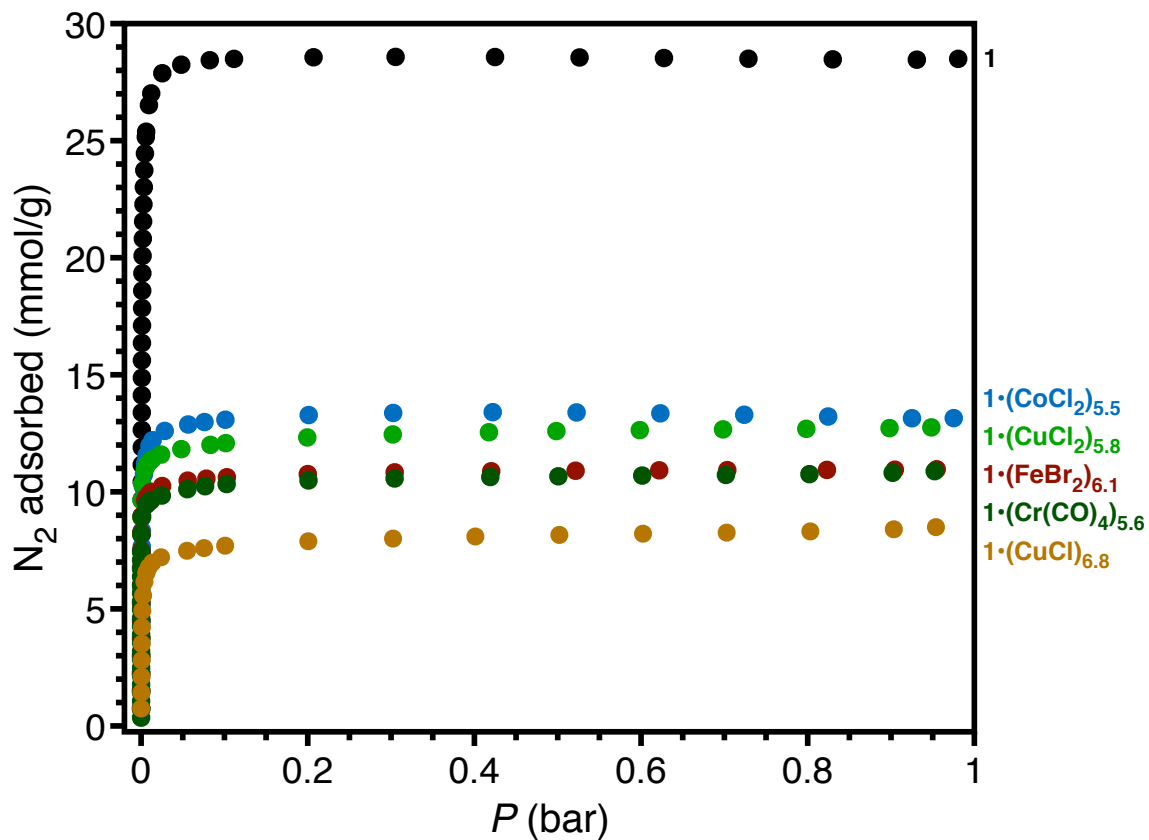
**Figure 4.S15.** Comparison of the predicted (light gray) and experimental (blue) powder X-ray diffraction patterns for  $1\cdot(\text{CoCl}_2)_{5.5}$ .

**Table 4.S2.** Rietveld Refinement of  $\mathbf{1} \cdot (\text{CuCl}_2)_{5.8}$  dosed with 10 mbar He. Values in parenthesis indicate one standard deviation from the parameter value. Temperature = 100 K,  $\lambda = 0.413746 \text{ \AA}$ , space group  $Pa\bar{3}$ ,  $a = 26.0887(4) \text{ \AA}$ ,  $V = 17756.4(8) \text{ \AA}^3$ . Goodness-of-fit parameters:  $R_{\text{wp}} = 6.90\%$ ,  $R_p = 5.58\%$ ,  $\chi^2 = 1.44$ .

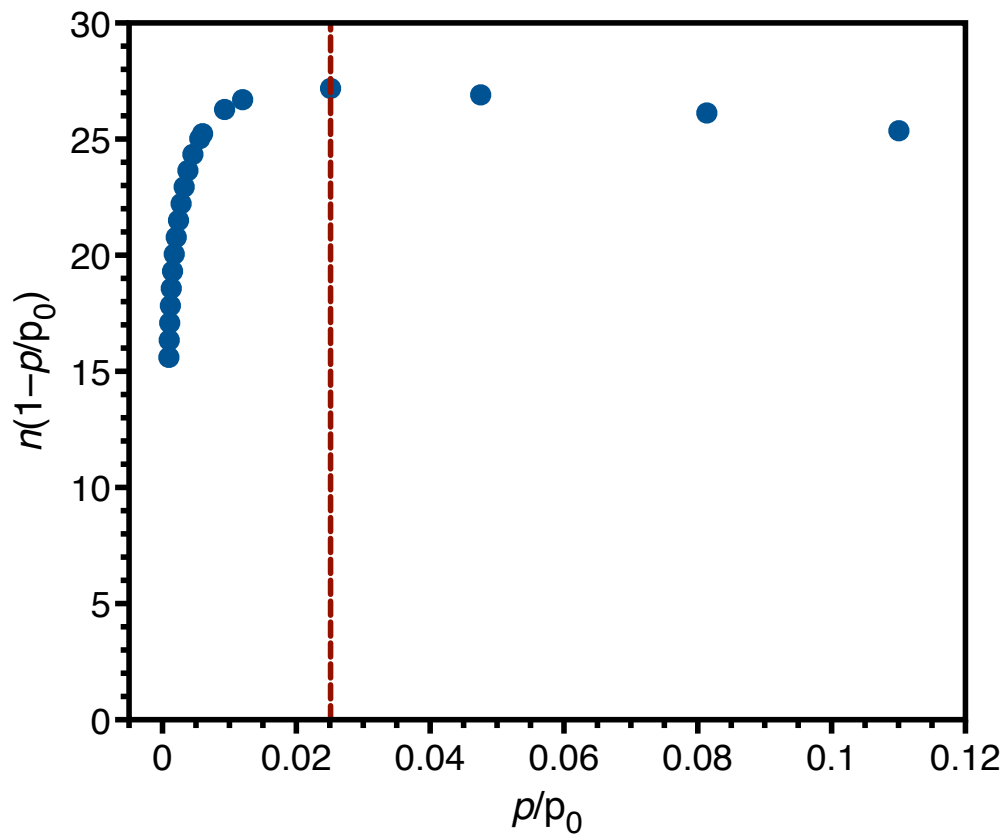
<i>atom</i>	<i>x</i>	<i>y</i>	<i>z</i>	<i>multiplicity</i>	<i>occupancy</i>	$U_{\text{iso}} (\text{\AA}^2)$
Zr	0.5154(2)	0.4836(2)	0.4088(1)	24	1	0.012
Cu	0.2075(5)	0.4805(4)	0.2884(4)	24	0.819(4)	0.077
Cl1	0.145(1)	0.533(1)	0.290(1)	24	0.819(4)	0.21
Cl2	0.203(1)	0.462(1)	0.366(1)	24	0.819(4)	0.17
C1	0.304	0.468	0.232	24	0.819(4)	0.019
C2	0.355	0.456	0.228	24	0.819(4)	0.019
C3	0.386	0.463	0.270	24	0.819(4)	0.019
C4	0.366	0.480	0.316	24	0.819(4)	0.019
C5	0.315	0.492	0.319	24	0.819(4)	0.019
N1	0.284	0.485	0.278	24	0.819(4)	0.019
C6	0.264	0.466	0.200	24	0.819(4)	0.019
C7	0.271	0.450	0.150	24	0.819(4)	0.019
C8	0.230	0.448	0.118	24	0.819(4)	0.019
C9	0.182	0.463	0.134	24	0.819(4)	0.019
C10	0.175	0.479	0.184	24	0.819(4)	0.019
N2	0.215	0.480	0.216	24	0.819(4)	0.019
C11	0.399	0.487	0.360	24	0.819(4)	0.019
O1	0.381	0.504	0.402	24	0.819(4)	0.019
O2	0.446	0.477	0.360	24	0.819(4)	0.019
C12	0.139	0.461	0.100	24	0.819(4)	0.019
O3	0.093	0.463	0.117	24	0.819(4)	0.019
O4	0.146	0.456	0.052	24	0.819(4)	0.019
H1	0.368	0.444	0.197	24	0.819(4)	0.019
H2	0.422	0.455	0.268	24	0.819(4)	0.019
H3	0.301	0.504	0.351	24	0.819(4)	0.019
H4	0.304	0.440	0.139	24	0.819(4)	0.019
H5	0.234	0.437	0.083	24	0.819(4)	0.019
H6	0.142	0.489	0.196	24	0.819(4)	0.019
O5a	0.465(2)	0.465(2)	0.465(2)	8	0.5	0.010
O5b	0.446(2)	0.446(2)	0.446(2)	8	0.5	0.010
O6a	0.539(3)	0.448(3)	0.470(3)	24	0.5	0.010
O6b	0.554(3)	0.430(3)	0.472(3)	24	0.5	0.010
O1w	0.368(6)	0.511(7)	0.409(5)	24	0.181(4)	0.019
O2w	0.452(6)	0.495(6)	0.353(6)	24	0.181(4)	0.019
O3w	0.087(6)	0.465(7)	0.130(7)	24	0.181(4)	0.019
O4w	0.154(6)	0.469(6)	0.042(6)	24	0.181(4)	0.019
N1s	0.149	0.585	0.109	24	0.23(1)	0.038
C1s	0.468	0.604	0.144	24	0.23(1)	0.038
C2s	0.193	0.630	0.187	24	0.23(1)	0.038
N2s	0.383	0.383	0.383	8	0.59(2)	0.16
C3s	0.348	0.366	0.360	24	0.59(2)	0.16
C4s	0.304	0.346	0.333	24	0.59(2)	0.16



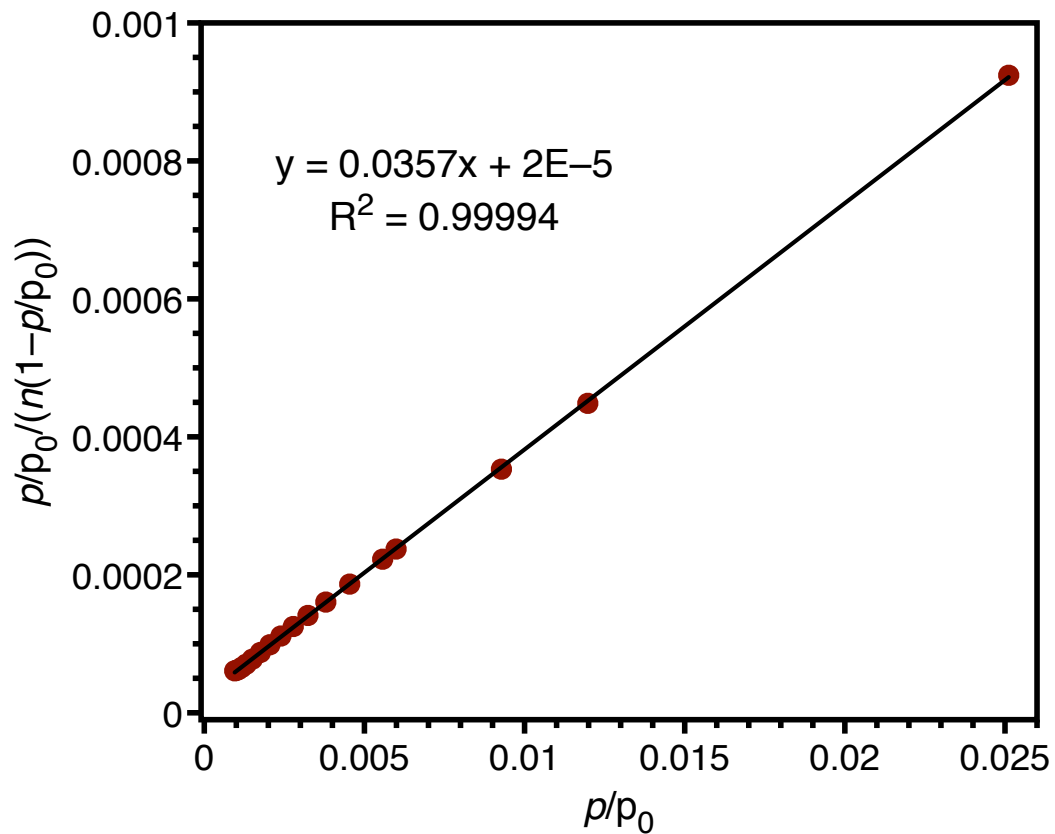
**Figure 4.S16.** Rietveld refinement of  $1 \cdot (\text{CuCl}_2)_{5.8}$  at 100 K dosed with 10 mbar He. The blue and red lines represent the experimental and calculated diffraction patterns, respectively; the gray line represents the difference between the experimental and calculated patterns; the green tick marks represent the calculated Bragg peak positions.



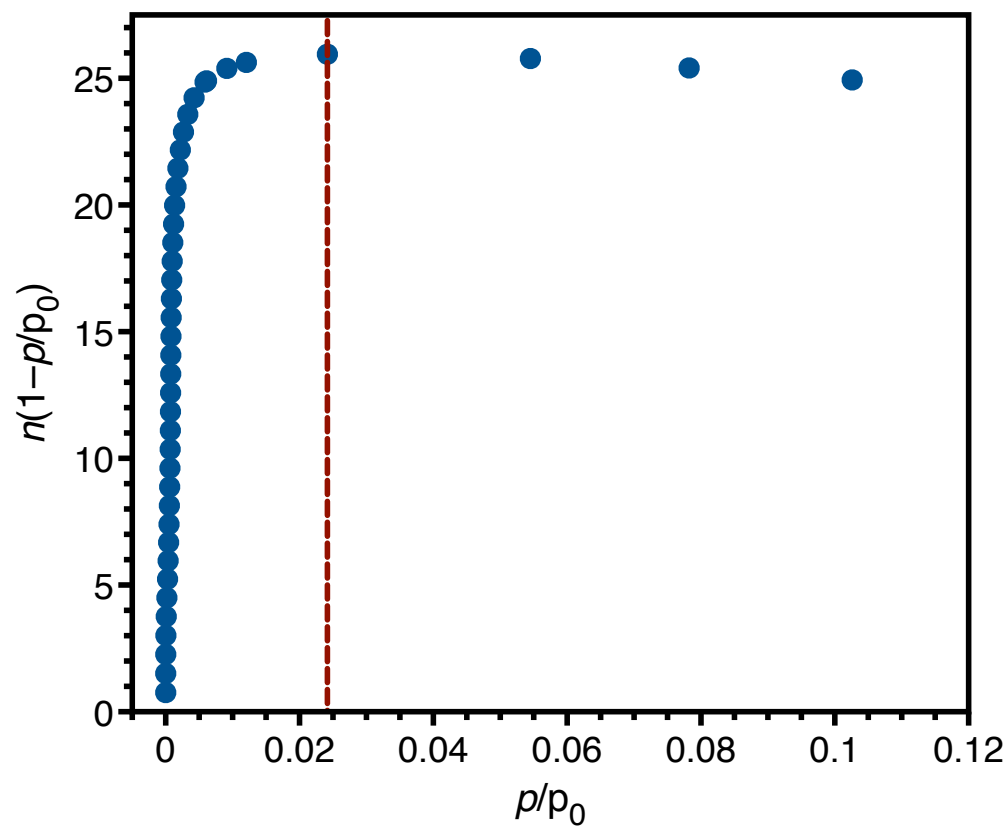
**Figure 4.S17.** Low-pressure N<sub>2</sub> adsorption isotherms for 1, 1•(CuCl<sub>2</sub>)<sub>5.8</sub>, 1•(CuCl)<sub>6.8</sub>, 1•(CoCl<sub>2</sub>)<sub>5.5</sub>, 1•(FeBr<sub>2</sub>)<sub>6.1</sub>, and 1•(Cr(CO)<sub>4</sub>)<sub>5.6</sub> at 77 K.



**Figure 4.S18.** Plot of  $n(1-p/p_0)$  vs.  $p/p_0$  for 1 to determine the maximum  $p/p_0$  used in the BET linear fit according to the first BET consistency criterion.<sup>77</sup>

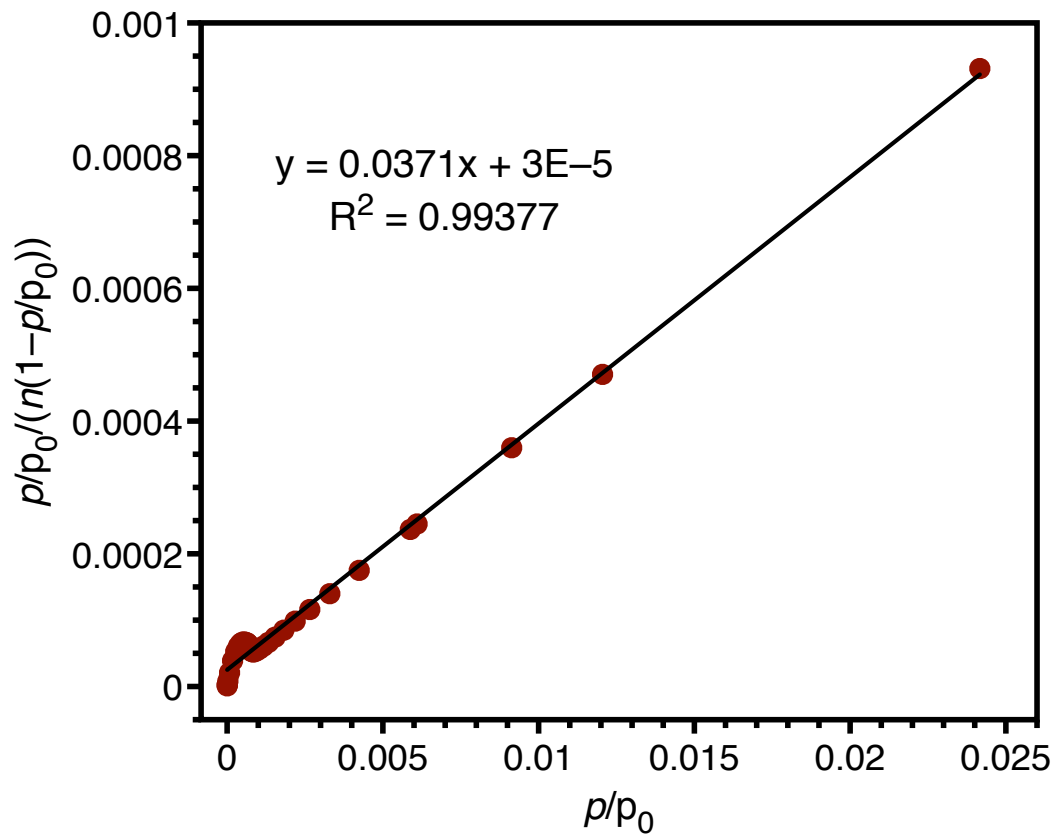


**Figure 4.S19.** Plot of  $p/p_0 / (n(1-p/p_0))$  vs.  $p/p_0$  for **1** to determine the BET surface area.<sup>77</sup> The slope of the best fit line for  $p/p_0 < 0.03$  is 0.0357, and the y-intercept is  $2.5 \times 10^{-5}$ , which satisfies the second BET consistency criterion. This results in a saturation capacity of 28.0 mmol/g and a BET surface area of 2730 m<sup>2</sup>/g.

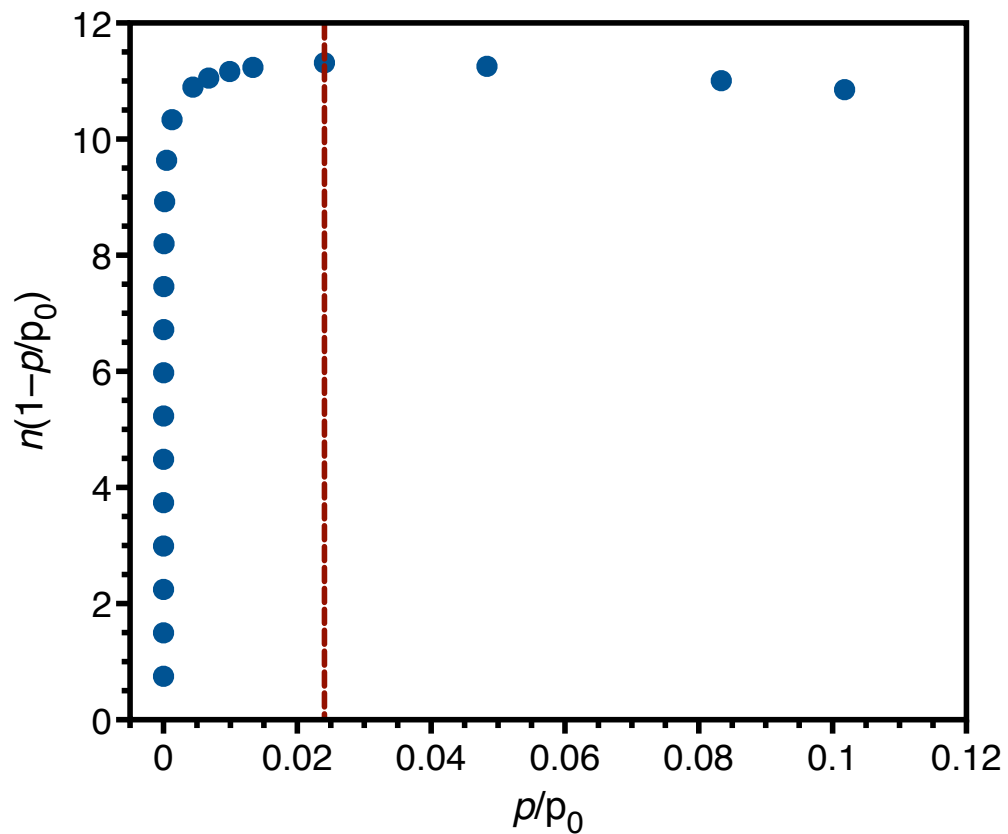


**Figure 4.S20.** Plot of  $n(1-p/p_0)$  vs.  $p/p_0$  for  $Zr_6O_4(OH)_4(bpdc)_6$  to determine the maximum  $p/p_0$  used in the BET linear fit according to the first BET consistency criterion.<sup>77</sup>

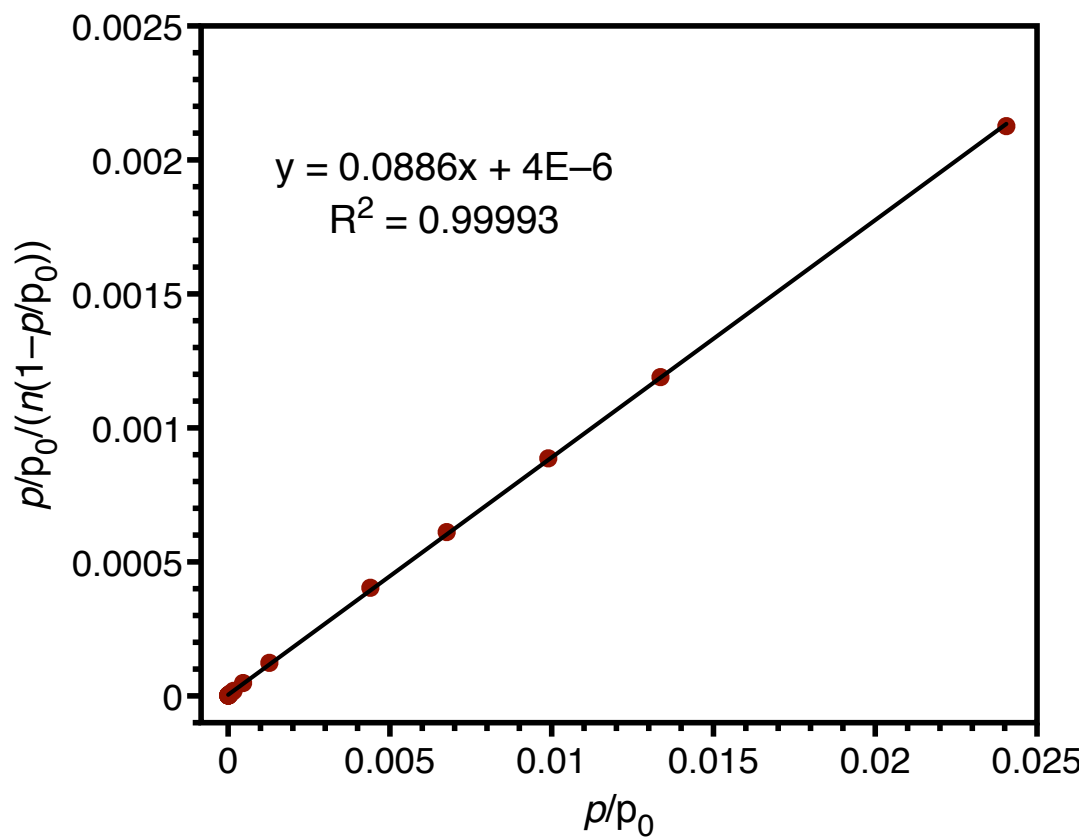




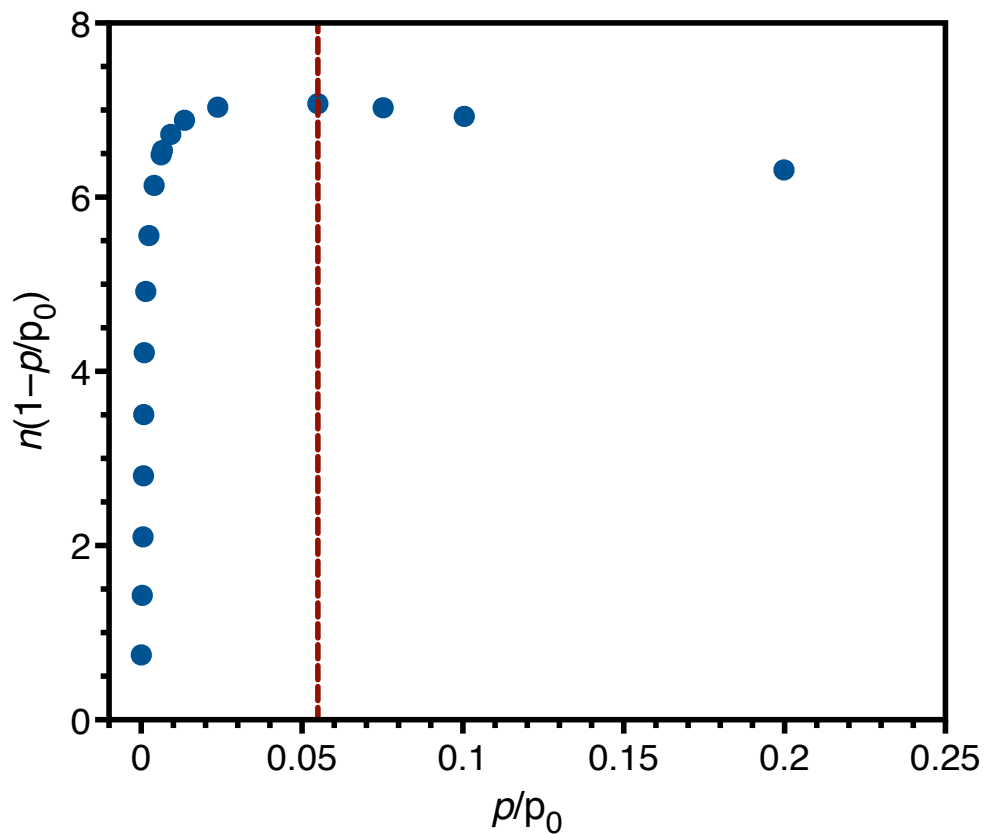
**Figure 4.S21.** Plot of  $p/p_0 / (n(1-p/p_0))$  vs.  $p/p_0$  for **1** to determine the BET surface area.<sup>77</sup> The slope of the best fit line for  $p/p_0 < 0.03$  is 0.0371, and the y-intercept is  $2.5 \times 10^{-5}$ , which satisfies the second BET consistency criterion. This results in a saturation capacity of 26.9 mmol/g and a BET surface area of 2625 m<sup>2</sup>/g.



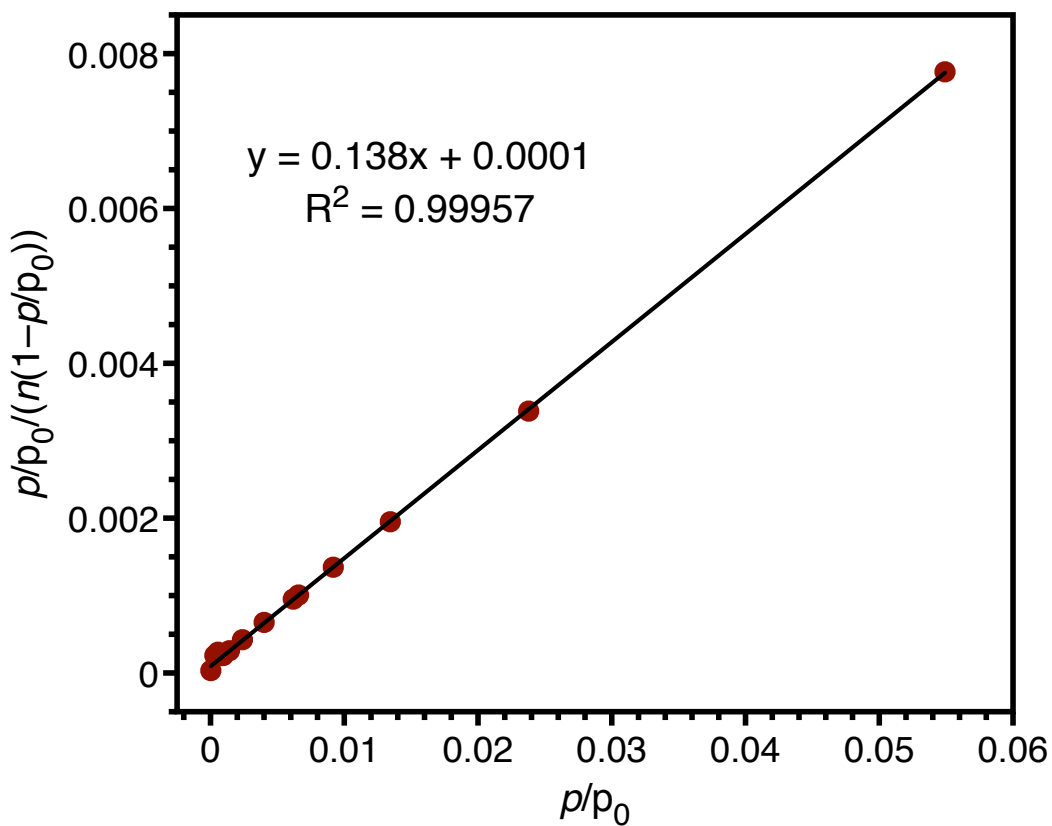
**Figure 4.S22.** Plot of  $n(1-p/p_0)$  vs.  $p/p_0$  for  $\mathbf{1} \cdot (\text{CuCl}_2)_{5.8}$  to determine the maximum  $p/p_0$  used in the BET linear fit according to the first BET consistency criterion.<sup>77</sup>



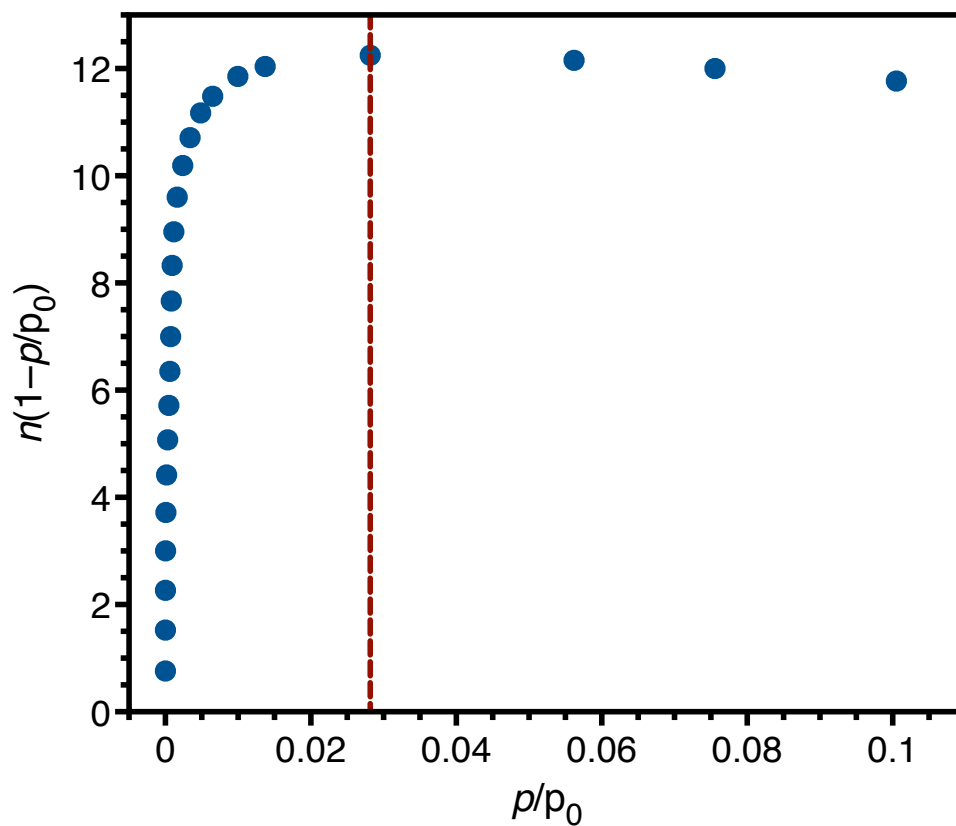
**Figure 4.S23.** Plot of  $p/p_0/(n(1-p/p_0))$  vs.  $p/p_0$  for  $1 \cdot (\text{CuCl}_2)_{5.8}$  to determine the BET surface area.<sup>77</sup> The slope of the best fit line for  $p/p_0 < 0.03$  is 0.0886, and the y-intercept is  $4.1 \times 10^{-6}$ , which satisfies the second BET consistency criterion. This results in a saturation capacity of 11.3 mmol/g and a BET surface area of 1101  $\text{m}^2/\text{g}$ .



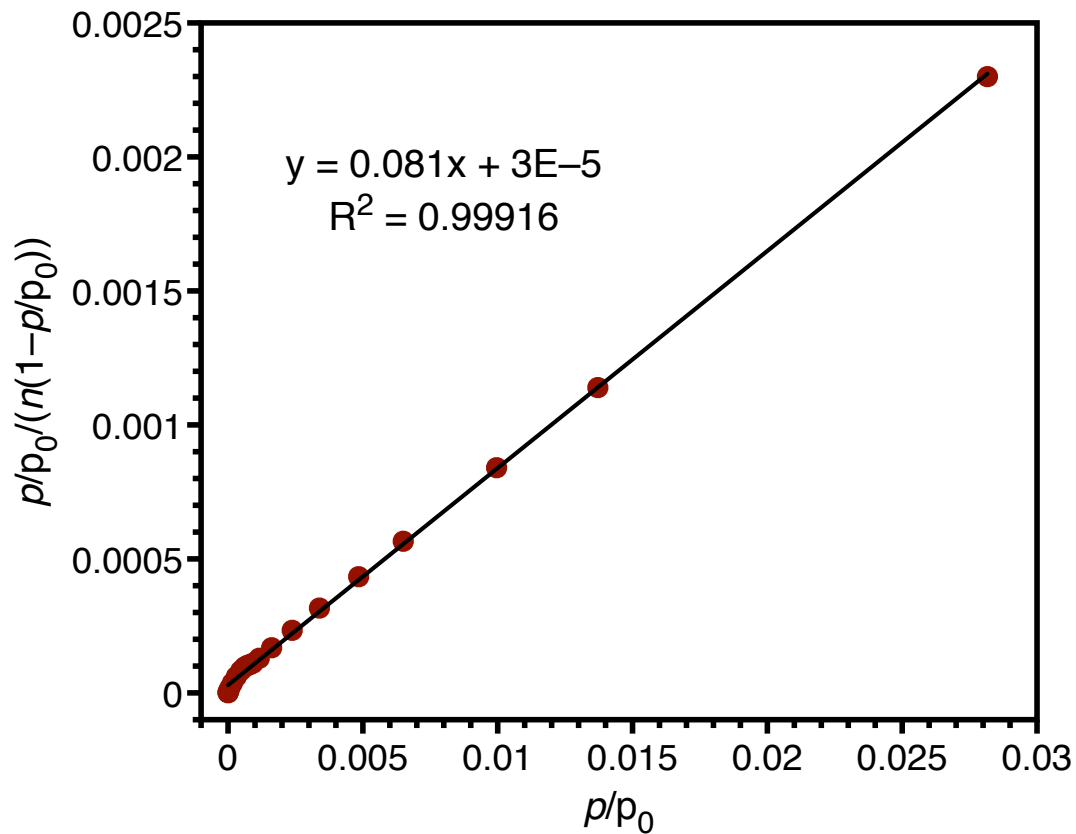
**Figure 4.S24.** Plot of  $n(1-p/p_0)$  vs.  $p/p_0$  for  $1 \cdot (\text{CuCl})_{6.8}$  to determine the maximum  $p/p_0$  used in the BET linear fit according to the first BET consistency criterion.<sup>77</sup>



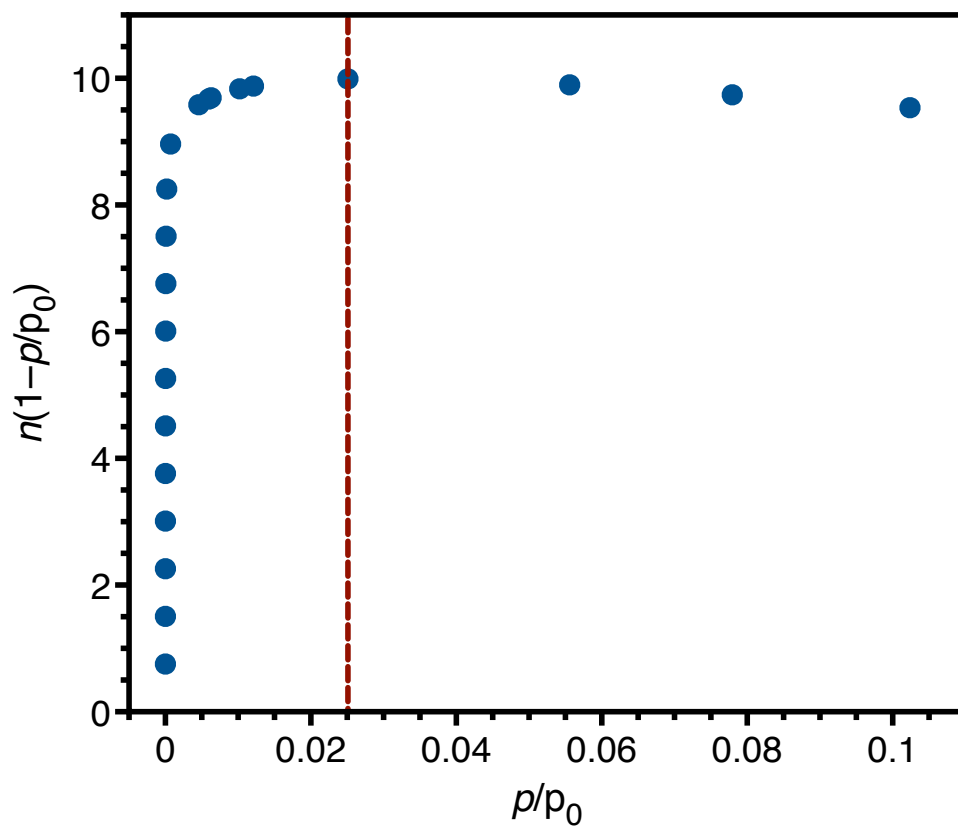
**Figure 4.S25.** Plot of  $p/p_0/(n(1-p/p_0))$  vs.  $p/p_0$  for  $1 \cdot (\text{CuCl})_{6.8}$  to determine the BET surface area.<sup>77</sup> The slope of the best fit line for  $p/p_0 < 0.06$  is 0.1389, and the y-intercept is  $1.1 \times 10^{-4}$ , which satisfies the second BET consistency criterion. This results in a saturation capacity of 7.2 mmol/g and a BET surface area of 701  $\text{m}^2/\text{g}$ .



**Figure 4.S26.** Plot of  $n(1-p/p_0)$  vs.  $p/p_0$  for  $1 \cdot (\text{CoCl}_2)_{5.5}$  to determine the maximum  $p/p_0$  used in the BET linear fit according to the first BET consistency criterion.<sup>77</sup>

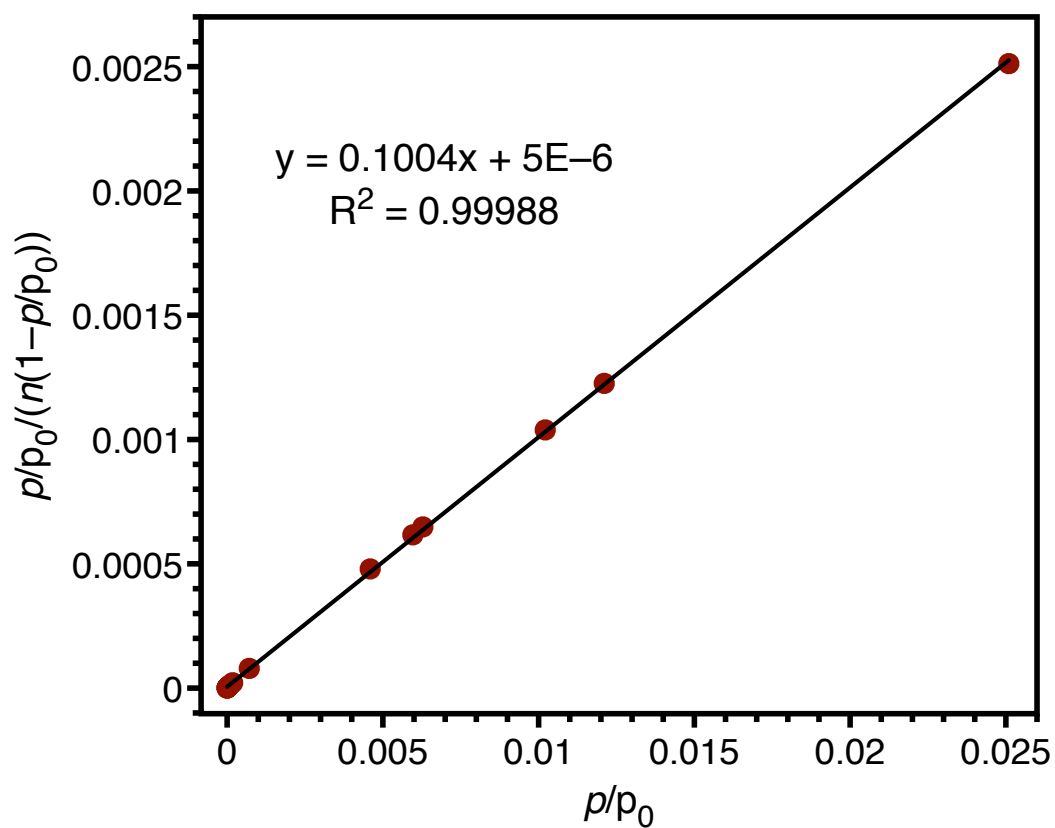


**Figure 4.S27.** Plot of  $p/p_0/(n(1-p/p_0))$  vs.  $p/p_0$  for  $1 \cdot (\text{CoCl}_2)_{5.5}$  to determine the BET surface area.<sup>77</sup> The slope of the best fit line for  $p/p_0 < 0.03$  is 0.0810, and the y-intercept is  $2.9 \times 10^{-5}$ , which satisfies the second BET consistency criterion. This results in a saturation capacity of 12.3 mmol/g and a BET surface area of 1204 m<sup>2</sup>/g.

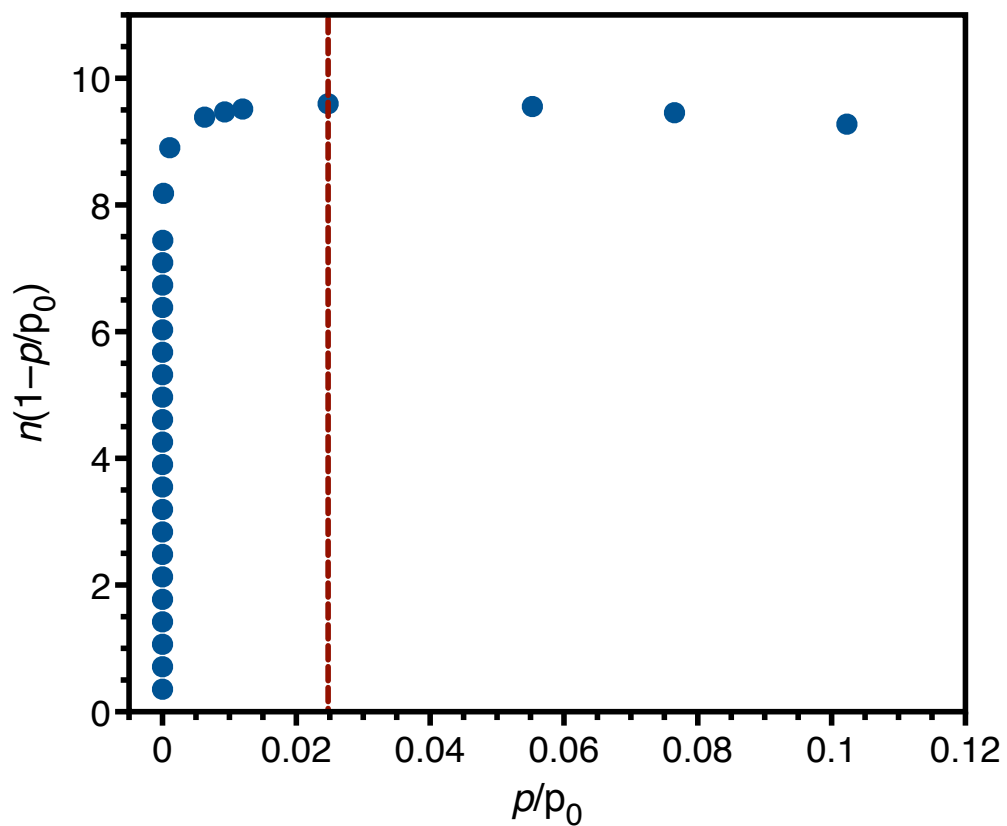


**Figure 4.S28.** Plot of  $n(1-p/p_0)$  vs.  $p/p_0$  for  $1 \cdot (\text{FeBr}_2)_{6.1}$  to determine the maximum  $p/p_0$  used in the BET linear fit according to the first BET consistency criterion.<sup>77</sup>

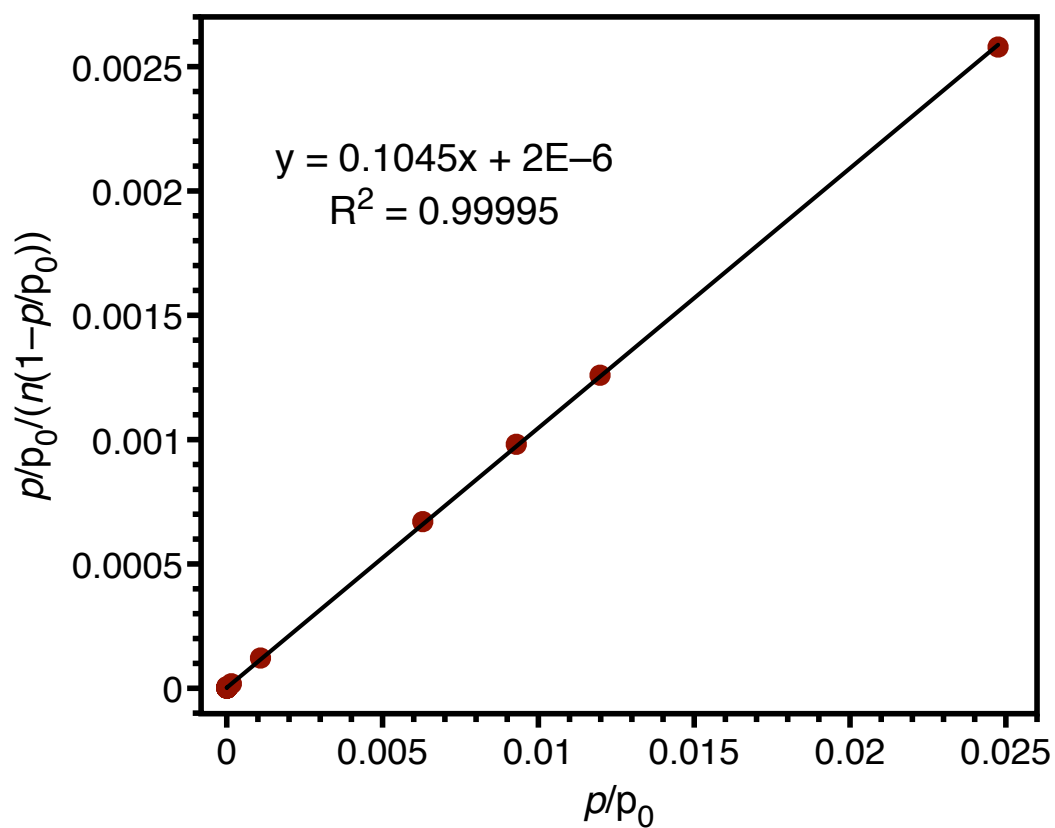




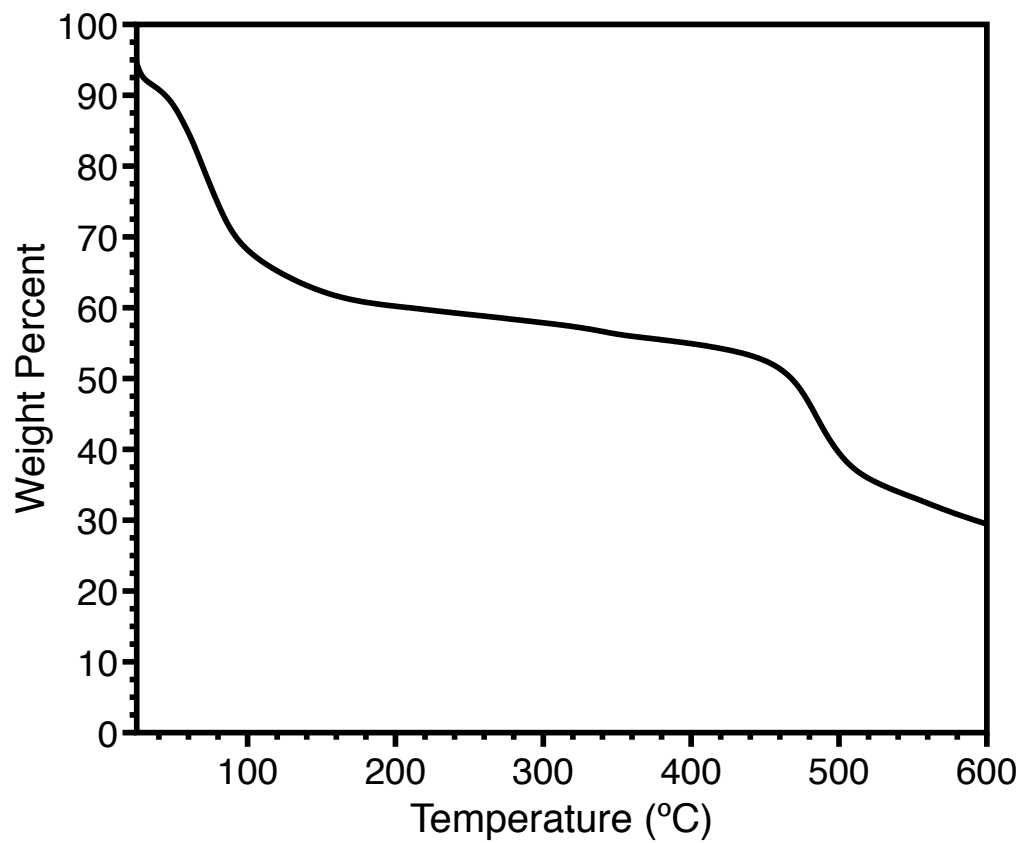
**Figure 4.S29.** Plot of  $p/p_0/(n(1-p/p_0))$  vs.  $p/p_0$  for  $1 \bullet (\text{FeBr}_2)_{6.1}$  to determine the BET surface area.<sup>77</sup> The slope of the best fit line for  $p/p_0 < 0.03$  is 0.10434, and the y-intercept is  $5.3 \times 10^{-6}$ , which satisfies the second BET consistency criterion. This results in a saturation capacity of 10.0 mmol/g and a BET surface area of 971  $\text{m}^2/\text{g}$ .



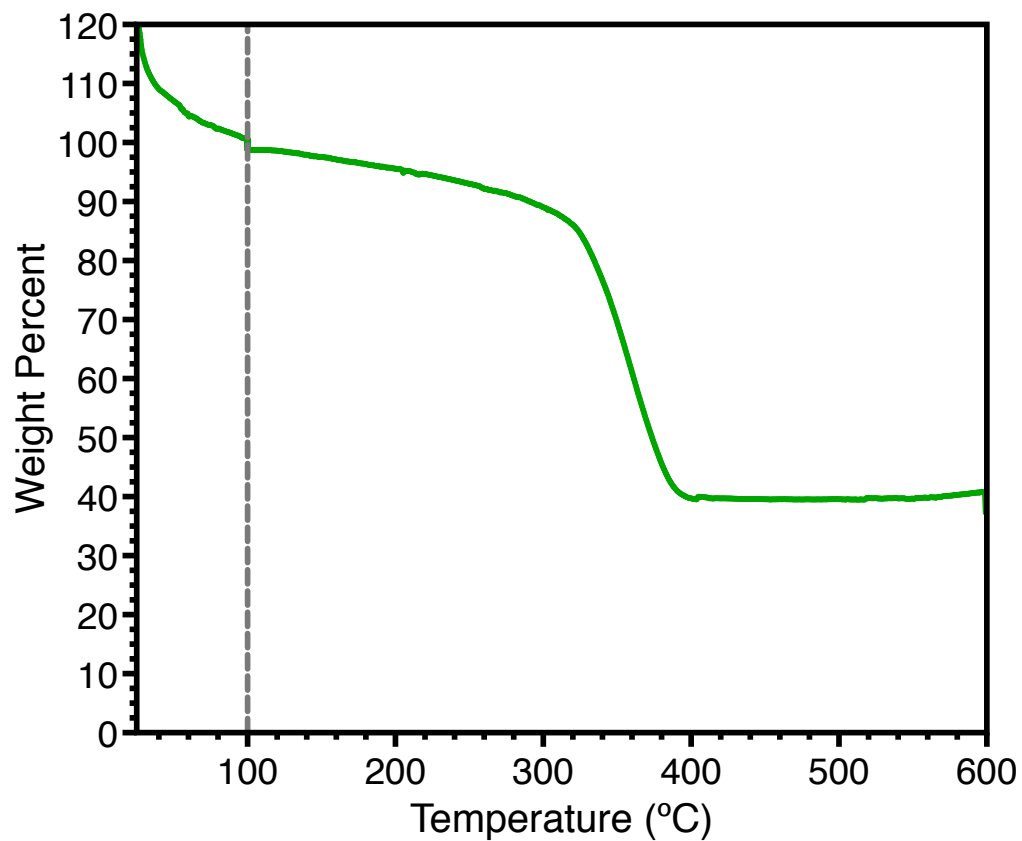
**Figure 4.S30.** Plot of  $n(1-p/p_0)$  vs.  $p/p_0$  for  $1 \cdot (\text{Cr}(\text{CO})_4)_{5,6}$  to determine the maximum  $p/p_0$  used in the BET linear fit according to the first BET consistency criterion.<sup>77</sup>



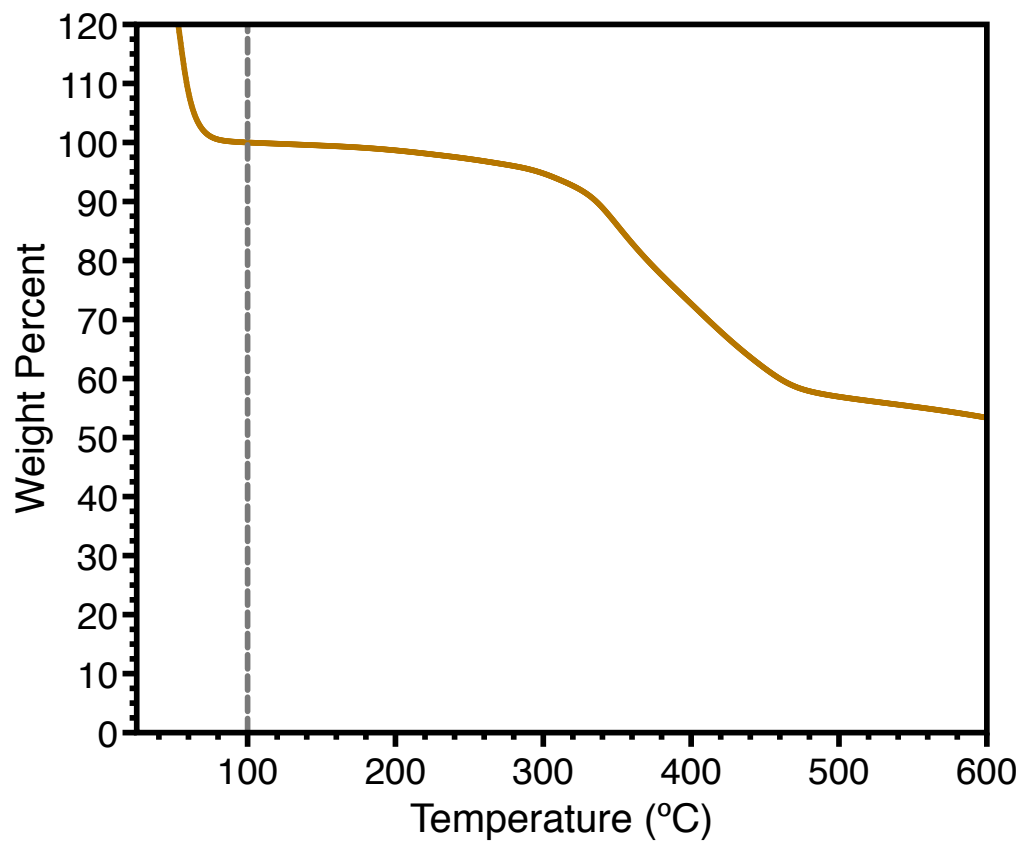
**Figure 4.S31.** Plot of  $p/p_0/(n(1-p/p_0))$  vs.  $p/p_0$  for  $1 \cdot (\text{Cr}(\text{CO})_4)_{5.6}$  to determine the BET surface area.<sup>77</sup> The slope of the best fit line for  $p/p_0 < 0.03$  is 0.10446, and the y-intercept is  $2.2 \times 10^{-6}$ , which satisfies the second BET consistency criterion. This results in a saturation capacity of 9.6 mmol/g and a BET surface area of 934  $\text{m}^2/\text{g}$ .



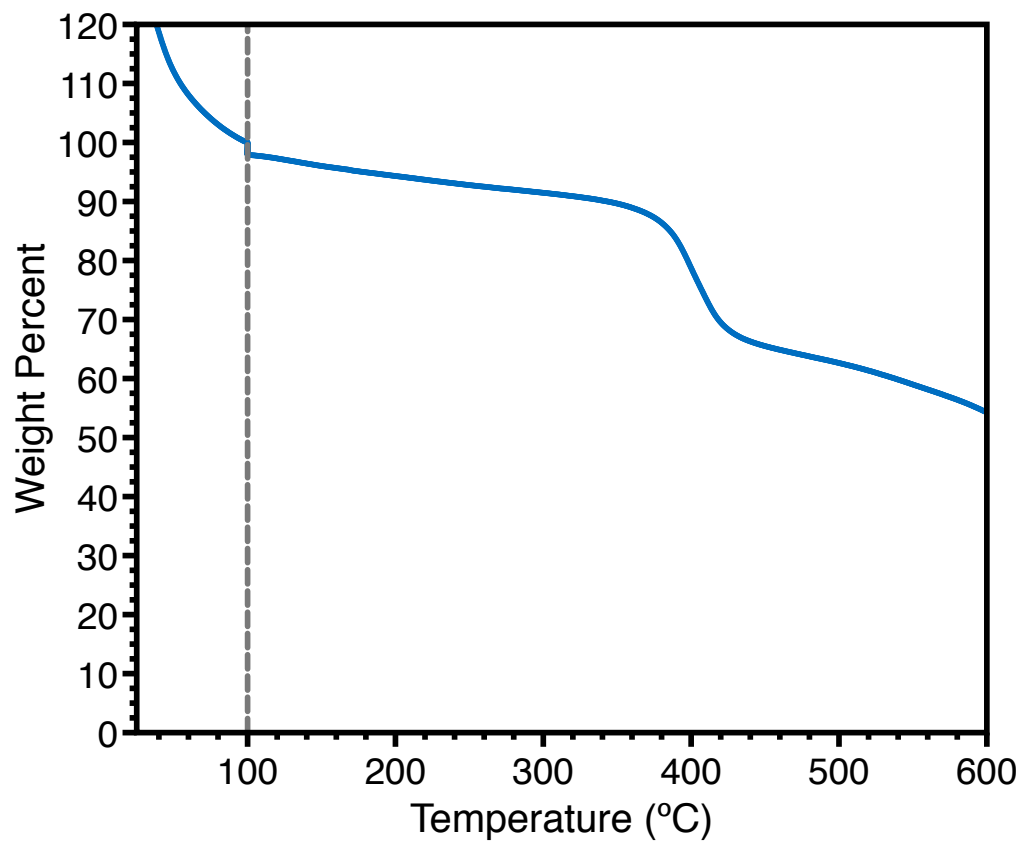
**Figure 4.S32.** Thermogravimetric analysis of THF solvated 1, heated at a ramp rate of 1 °C per minute.



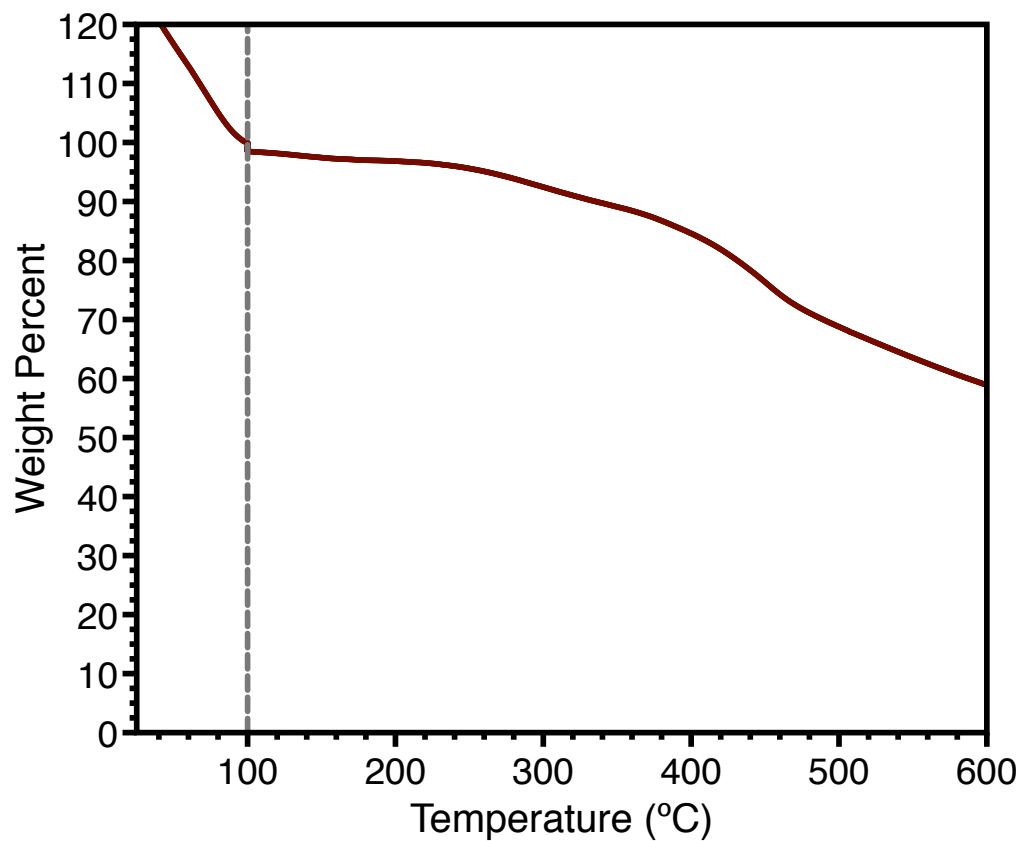
**Figure 4.S33.** Thermogravimetric analysis of a slurry of  $1 \cdot (\text{CuCl}_2)_{5.8}$  in n-hexane. The sample was heated at a ramp rate of  $1^\circ\text{C}$  per minute to  $100^\circ\text{C}$ , then held at this temperature for 1 hour (dashed gray line) to evaporate any remaining n-hexane. It was then heated at a ramp rate of  $1^\circ\text{C}$  per minute to  $600^\circ\text{C}$ .



**Figure 4.S34.** Thermogravimetric analysis of a slurry of  $1 \cdot (\text{CuCl})_{6.1}$  in n-hexane. The sample was heated at a ramp rate of  $1 \text{ }^\circ\text{C}$  per minute to  $100 \text{ }^\circ\text{C}$ , then held at this temperature for 1 hour (dashed gray line) to evaporate any remaining n-hexane. It was then heated at a ramp rate of  $1 \text{ }^\circ\text{C}$  per minute to  $600 \text{ }^\circ\text{C}$ .

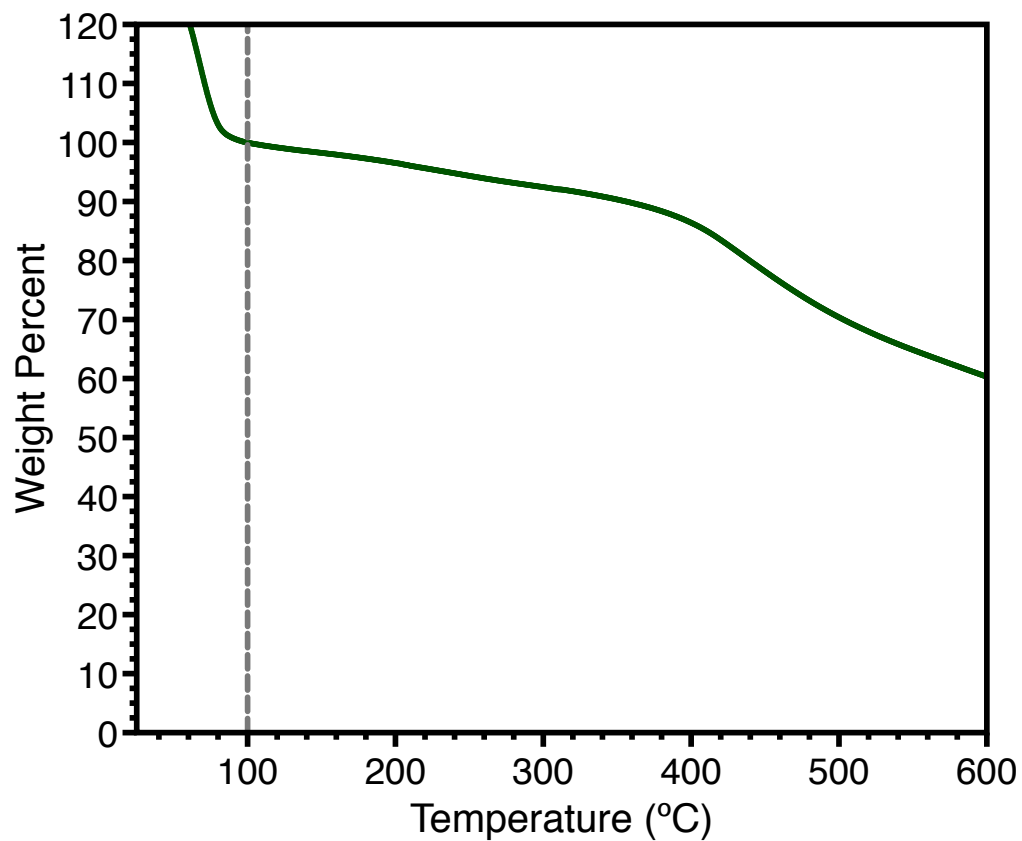


**Figure 4.S35.** Thermogravimetric analysis of a slurry of  $1 \cdot (\text{CoCl}_2)_{5.6}$  in n-hexane. The sample was heated at a ramp rate of  $1^\circ\text{C}$  per minute to  $100^\circ\text{C}$ , then held at this temperature for 1 hour (dashed gray line) to evaporate any remaining n-hexane. It was then heated at a ramp rate of  $1^\circ\text{C}$  per minute to  $600^\circ\text{C}$ .

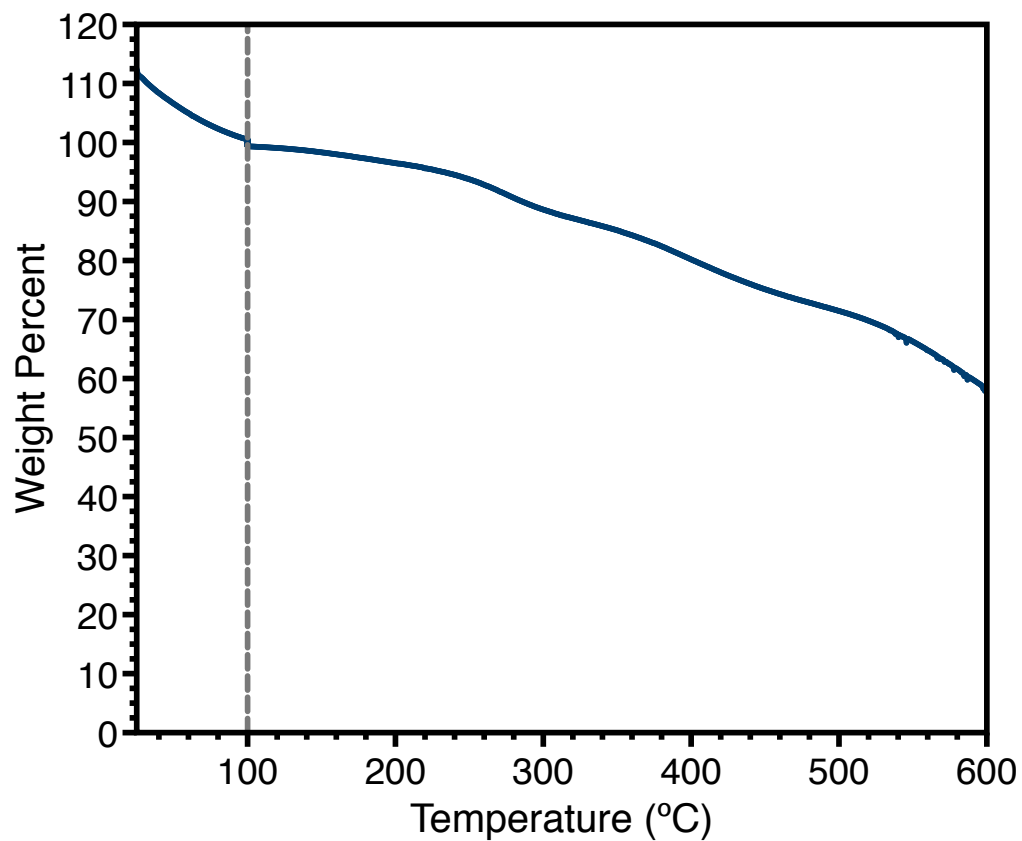


**Figure 4.S36.** Thermogravimetric analysis of a slurry of  $1 \cdot (\text{FeBr}_2)_{6.1}$  in n-hexane. The sample was heated at a ramp rate of 1 °C per minute to 100 °C, then held at this temperature for 1 hour (dashed gray line) to evaporate any remaining n-hexane. It was then heated at a ramp rate of 1 °C per minute to 600 °C.

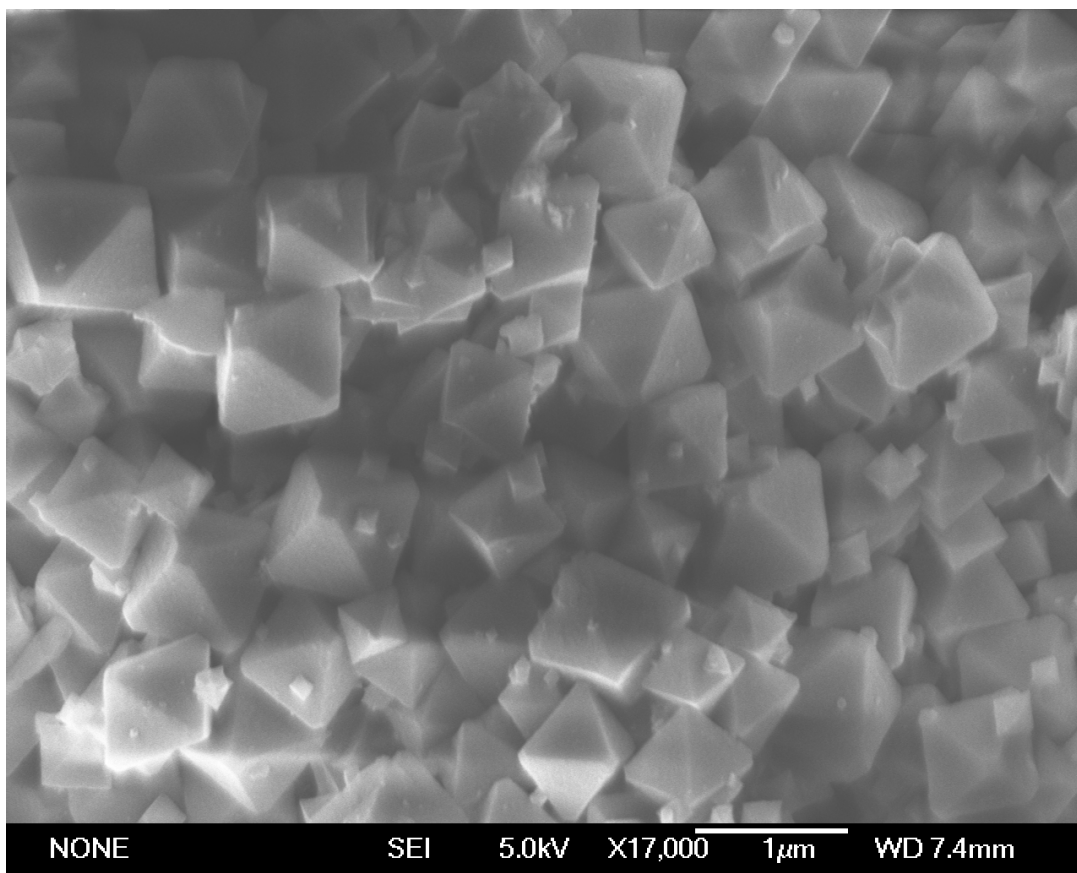




**Figure 4.S37.** Thermogravimetric analysis of a slurry of  $1 \cdot (\text{Cr}(\text{CO})_4)_{5,6}$  in n-hexane. The sample was heated at a ramp rate of  $1^\circ\text{C}$  per minute to  $100^\circ\text{C}$ , then held at this temperature for 1 hour (dashed gray line) to evaporate any remaining n-hexane. It was then heated at a ramp rate of  $1^\circ\text{C}$  per minute to  $600^\circ\text{C}$ .



**Figure 4.S38.** Thermogravimetric analysis of a slurry of  $1 \cdot (\text{Ir}(\text{COD})\text{BF}_4)_{4.7}$  in n-hexane. The sample was heated at a ramp rate of 1 °C per minute to 100 °C, then held at this temperature for 1 hour (dashed gray line) to evaporate any remaining n-hexane. It was then heated at a ramp rate of 1 °C per minute to 600 °C.



**Figure 4.S39.** SEM micrograph of Zr<sub>6</sub>O<sub>4</sub>(OH)<sub>4</sub>(bpydc)<sub>6</sub> (bulk sample).

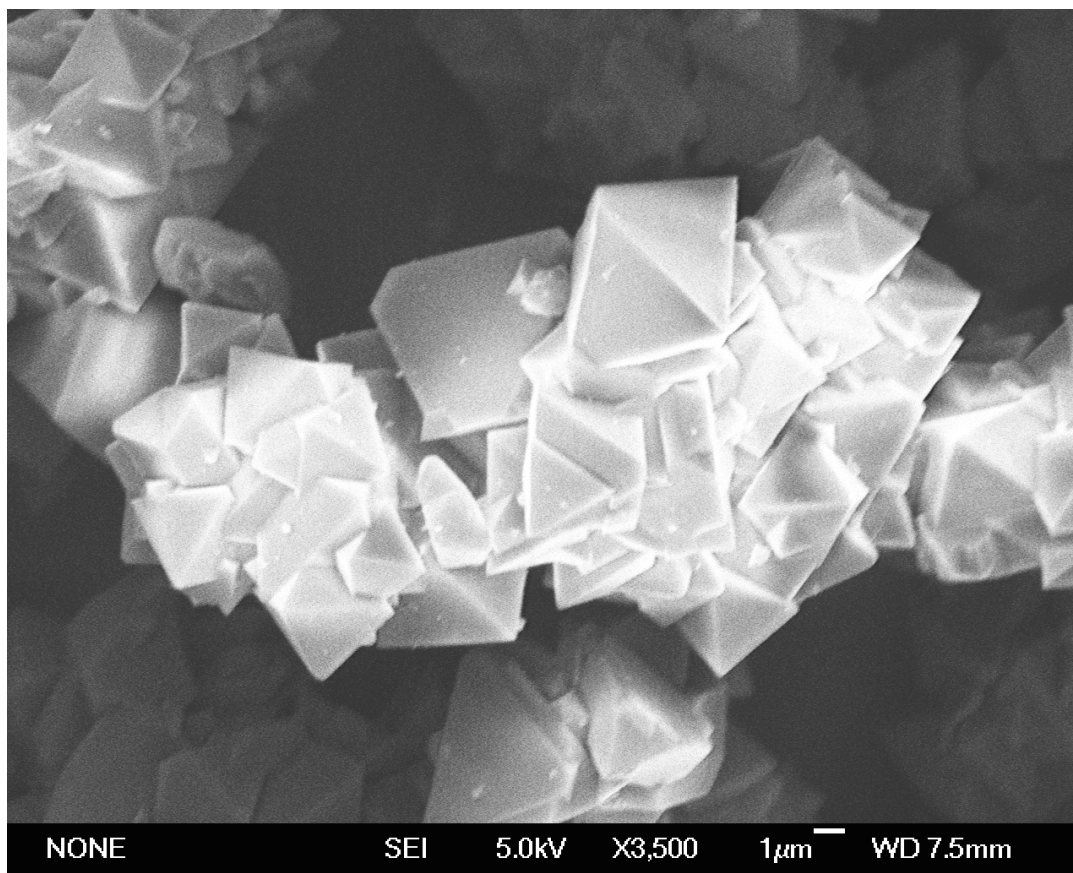
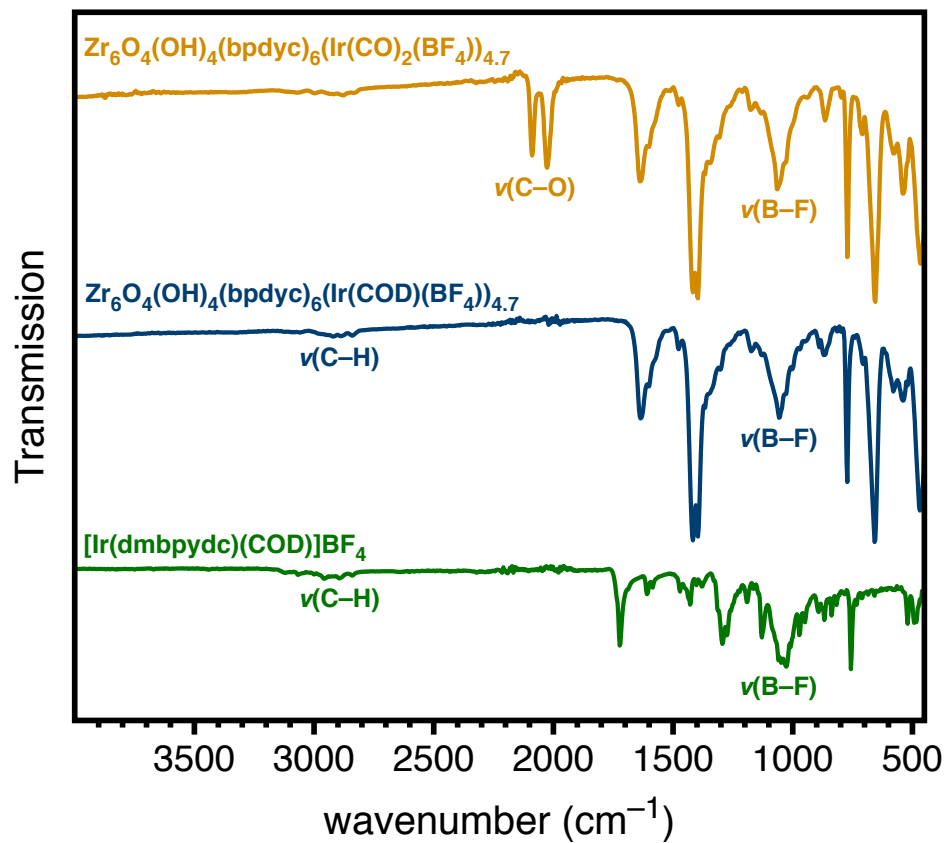
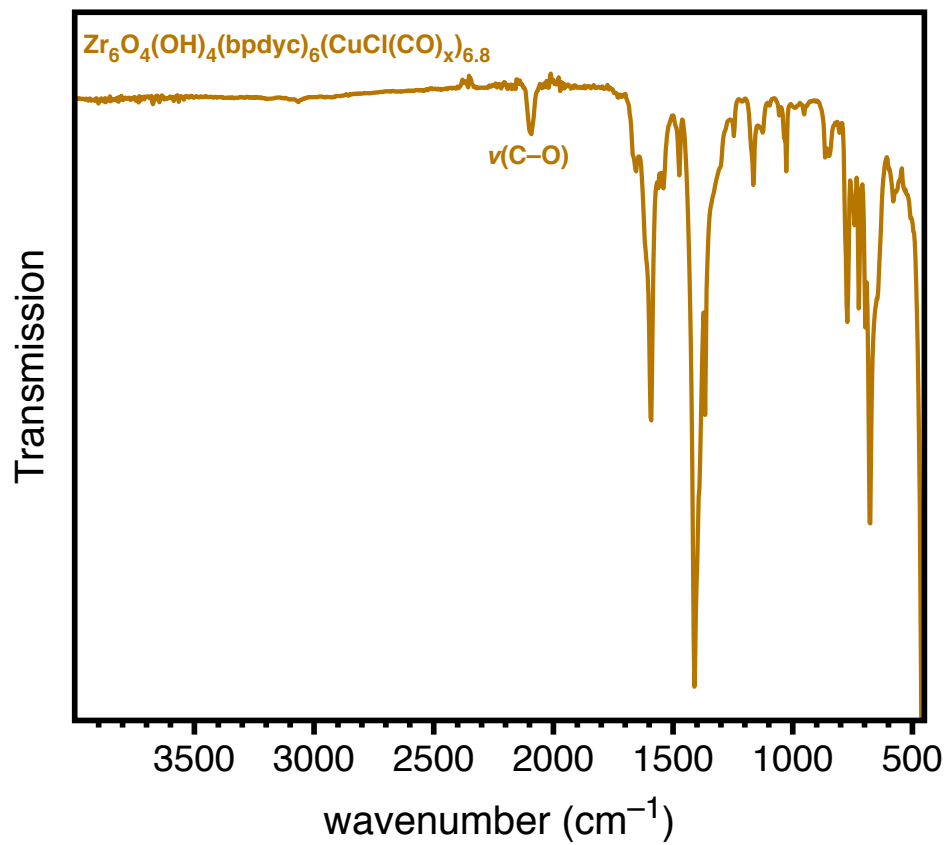


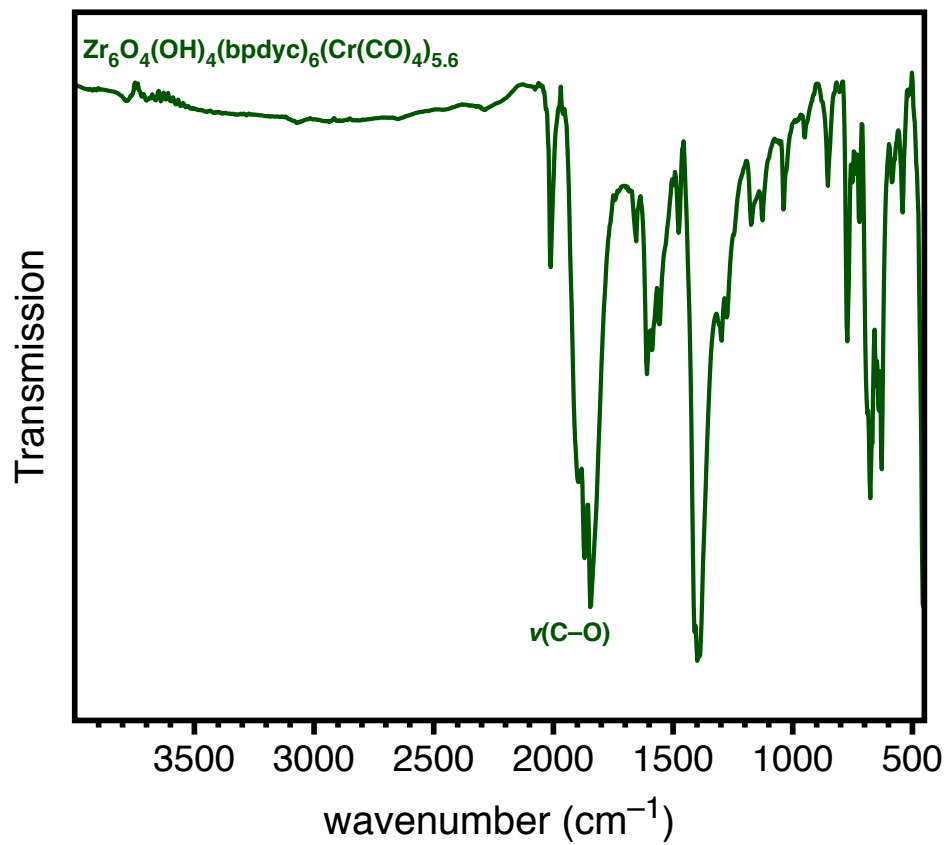
Figure 4.S40. SEM micrograph of  $Zr_6O_4(OH)_4(bpdc)_6$ .



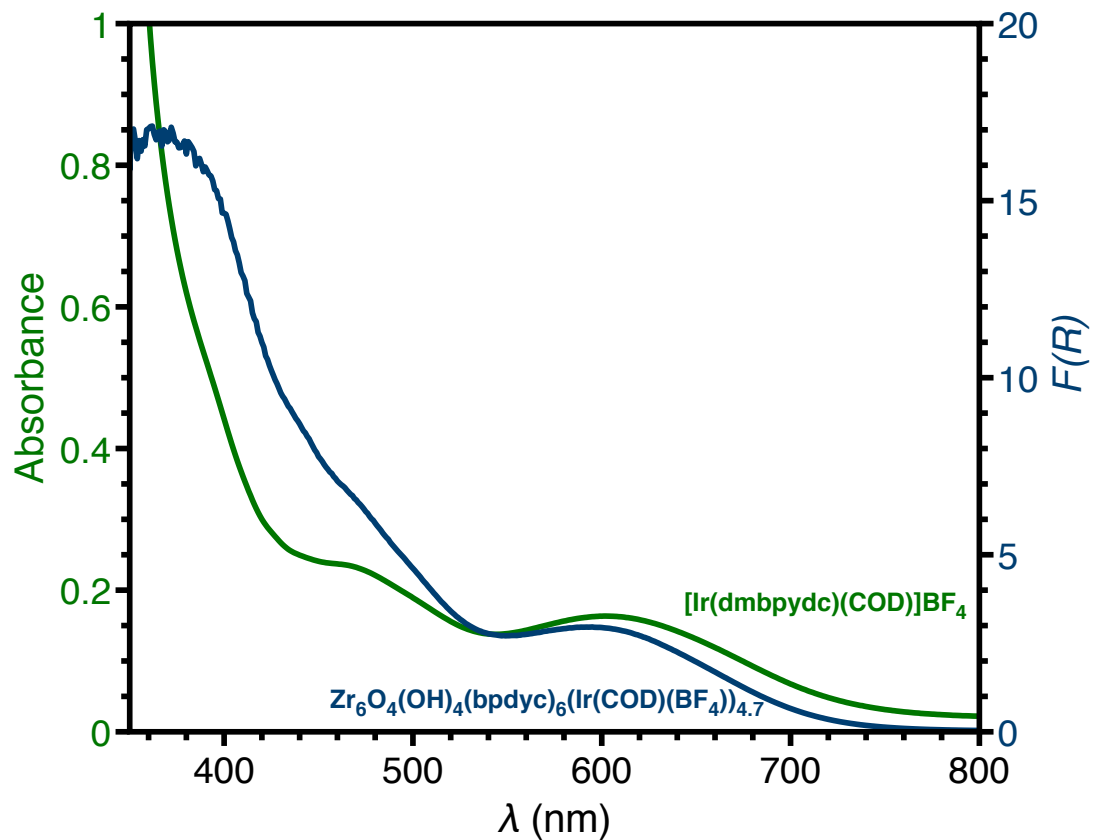
**Figure 4.S41.** FTIR spectra of  $\text{Zr}_6\text{O}_4(\text{OH})_4(\text{bpydc})_6(\text{Ir}(\text{CO})_2(\text{BF}_4))_{4.7}$ ,  $\text{Zr}_6\text{O}_4(\text{OH})_4(\text{bpydc})_6(\text{Ir}(\text{COD})(\text{BF}_4))_{4.7}$ ,  $[\text{Ir}(\text{dmbpydc})(\text{COD})]\text{BF}_4$ .



**Figure 4.S42.** FTIR spectra of  $\text{Zr}_6\text{O}_4(\text{OH})_4(\text{bpydc})_6(\text{CuCl}(\text{CO})_x)_{6.8}$ .

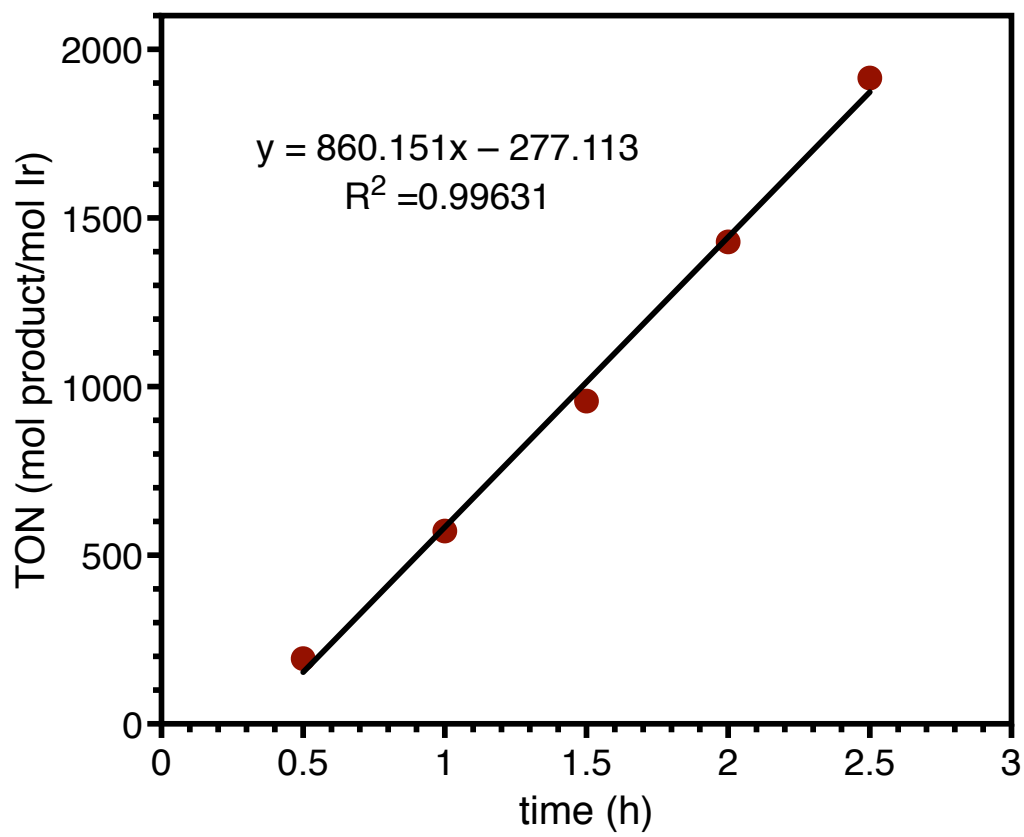


**Figure 4.S43.** FTIR spectra of  $\text{Zr}_6\text{O}_4(\text{OH})_4(\text{bpydc})_6(\text{Cr}(\text{CO})_4)_{5.6}$ .

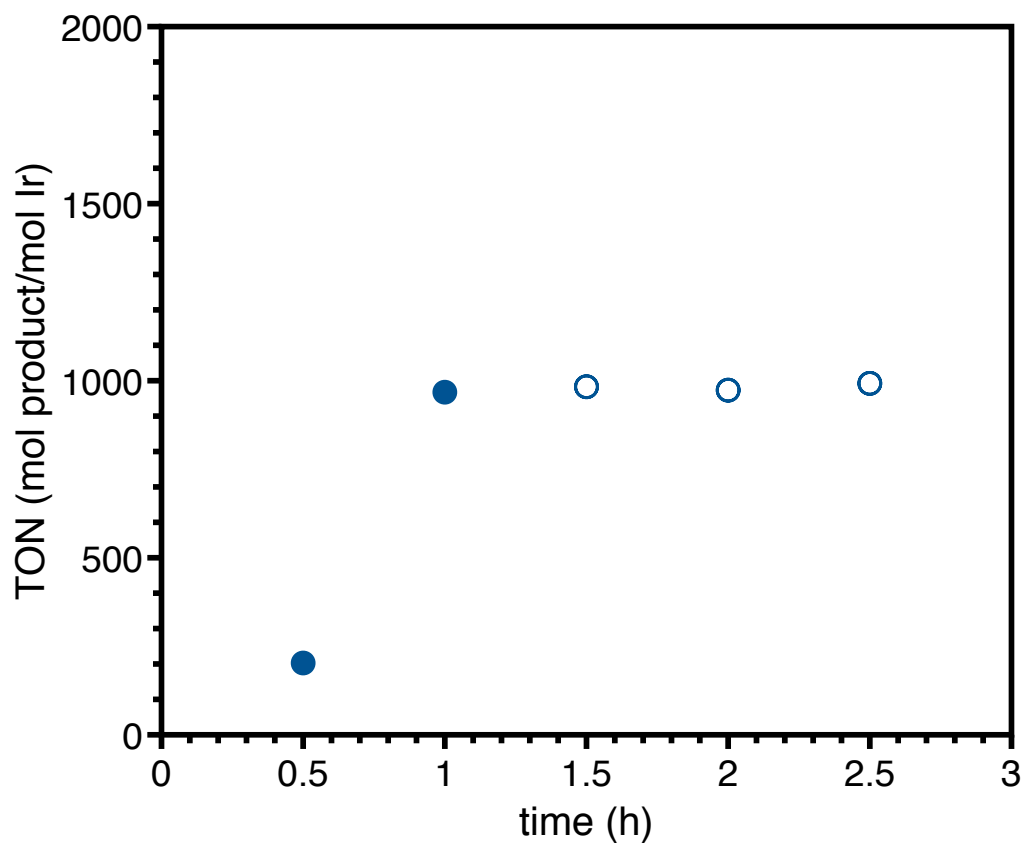


**Figure 4.S44.** Comparison of the UV-Vis spectrum for  $[\text{Ir}(\text{dmbpydc})(\text{COD})]\text{BF}_4$  and the diffuse reflectance UV-Vis spectrum for  $\text{Zr}_6\text{O}_4(\text{OH})_4(\text{bpydc})_6(\text{Ir}(\text{COD})(\text{BF}_4))_{4.7}$ .





**Figure 4.S45.** Plot of turnover number (TON) versus time used to determine the average turnover frequency (TOF) for benzene C-H borylation with  $1 \cdot (\text{Ir}(\text{COD})(\text{BF}_4))_{0.6}$  as a catalyst.



**Figure 4.S46.** Plot of turnover number (TON) versus time for the hot filtration experiment conducted for benzene C-H borylation with  $1 \cdot (\text{Ir}(\text{COD})(\text{BF}_4))_{0.6}$  as a catalyst. Shaded blue circles correspond to data obtained from aliquots collected while  $1 \cdot (\text{Ir}(\text{COD})(\text{BF}_4))_{0.6}$  was still present in the reaction mixture. Empty blue circles correspond to data points collected after removal of  $1 \cdot (\text{Ir}(\text{COD})(\text{BF}_4))_{0.6}$  by filtration.

#### 4.7. References

- (1) Serna, P.; Gates, B. C. *Acc. Chem. Res.* **2014**, *47* (8), 2612–2620.
- (2) Wegener, S. L.; Marks, T. J.; Stair, P. C. *Acc. Chem. Res.* **2012**, *45* (2), 206–214.
- (3) Hagen, J. *Industrial Catalysis*; Wiley-VCH Verlag GmbH & Co. KGaA: Weinheim, 2006.
- (4) Furukawa, H.; Ko, N.; Go, Y. B.; Aratani, N.; Choi, S. B.; Choi, E.; Yazaydin, A. O.; Snurr, R. Q.; O’Keeffe, M.; Kim, J.; Yaghi, O. M. *Science* **2010**, *329* (5990), 424–428.
- (5) Eddaoudi, M.; Kim, J.; Rosi, N.; Vodak, D.; Wachter, J.; O’Keeffe, M.; Yaghi, O. M. *Science* **2002**, *295* (5554), 469–472.
- (6) Cohen, S. M. *Chem. Rev.* **2012**, *112* (2), 970–1000.
- (7) Murray, L. J.; Dincă, M.; Long, J. R. *Chem. Soc. Rev.* **2009**, *38* (5), 1294–1314.
- (8) Sumida, K.; Rogow, D. L.; Mason, J. A.; McDonald, T. M.; Bloch, E. D.; Herm, Z. R.; Bae, T.-H.; Long, J. R. *Chem. Rev.* **2012**, *112* (2), 724–781.
- (9) Herm, Z. R.; Bloch, E. D.; Long, J. R. *Chem. Mater.* **2014**, *26* (1), 323–338.
- (10) Mason, J. A.; Veenstra, M.; Long, J. R. *Chem. Sci.* **2014**, *5* (1), 32–51.
- (11) Corma, A.; García, H.; Llabrés i Xamena, F. X. *Chem. Rev.* **2010**, *110* (8), 4606–4655.
- (12) Wang, C.; Zheng, M.; Lin, W. *J. Phys. Chem. Lett.* **2011**, *2* (14), 1701–1709.
- (13) Ma, L.; Abney, C.; Lin, W. *Chem. Soc. Rev.* **2009**, *38* (5), 1248–1256.
- (14) Xiao, D. J.; Bloch, E. D.; Mason, J. A.; Queen, W. L.; Hudson, M. R.; Planas, N.; Borycz, J.; Dzubak, A. L.; Verma, P.; Lee, K.; Bonino, F.; Crocellà, V.; Yano, J.; Bordiga, S.; Truhlar, D. G.; Gagliardi, L.; Brown, C. M.; Long, J. R. *Nature Chemistry* **2014**, *6* (7), 590–595.
- (15) Pullen, S.; Fei, H.; Orthaber, A.; Cohen, S. M.; Ott, S. *J. Am. Chem. Soc.* **2013**, *135* (45), 16997–17003.
- (16) Fei, H.; Shin, J.; Meng, Y. S.; Adelhardt, M.; Sutter, J.; Meyer, K.; Cohen, S. M. *J. Am. Chem. Soc.* **2014**, *136* (13), 4965–4973.
- (17) Feng, D.; Gu, Z.-Y.; Li, J.-R.; Jiang, H.-L.; Wei, Z.; Zhou, H.-C. *Angew. Chem. Int. Ed.* **2012**, *51* (41), 10307–10310.
- (18) Anderson, J. S.; Gallagher, A. T.; Mason, J. A.; Harris, T. D. *J. Am. Chem. Soc.* **2014**, *136* (47), 16489–16492.
- (19) Bloch, W. M.; Burgun, A.; Coghlan, C. J.; Lee, R.; Coote, M. L.; Doonan, C. J.; Sumbly, C. J. *Nature Chemistry* **2014**, *6* (10), 906–912.
- (20) Dhakshinamoorthy, A.; Alvaro, M.; Garcia, H. *Catal. Sci. Technol.* **2011**, *1* (6), 856.
- (21) Dhakshinamoorthy, A.; Alvaro, M.; Garcia, H. *Chem. Commun.* **2012**, *48* (92), 11275.
- (22) Dhakshinamoorthy, A.; Opanasenko, M.; Čejka, J.; Garcia, H. *Catal. Sci. Technol.* **2013**.
- (23) Horike, S.; Dincă, M.; Tamaki, K.; Long, J. R. *J. Am. Chem. Soc.* **2008**, *130* (18), 5854–5855.
- (24) Juan-Alcañiz, J.; Gascon, J.; Kapteijn, F. *J. Mater. Chem.* **2012**, *22* (20), 10102.
- (25) Genna, D. T.; Wong-Foy, A. G.; Matzger, A. J.; Sanford, M. S. *J. Am. Chem. Soc.* **2013**, *135* (29), 10586–10589.
- (26) Meilikhov, M.; Yusenko, K.; Esken, D.; Turner, S.; Van Tendeloo, G.; Fischer, R. A. *Eur. J. Inorg. Chem.* **2010**, *2010* (24), 3701–3714.
- (27) Li, L.; Matsuda, R.; Tanaka, I.; Sato, H.; Kanoo, P.; Jeon, H. J.; Foo, M. L.; Wakamiya, A.; Murata, Y.; Kitagawa, S. *J. Am. Chem. Soc.* **2014**, *136* (21), 7543–7546.
- (28) Hasegawa, S.; Horike, S.; Matsuda, R.; Furukawa, S.; Mochizuki, K.; Kinoshita, Y.;

- Kitagawa, S. *J. Am. Chem. Soc.* **2007**, *129* (9), 2607–2614.
- (29) Wang, C.; Xie, Z.; deKrafft, K. E.; Lin, W. *J. Am. Chem. Soc.* **2011**, *133* (34), 13445–13454.
- (30) Wang, C.; deKrafft, K. E.; Lin, W. *J. Am. Chem. Soc.* **2012**, *134* (17), 7211–7214.
- (31) Dau, P. V.; Cohen, S. M. *Chem. Commun. (Camb.)* **2013**, *49* (55), 6128–6130.
- (32) Fei, H.; Cohen, S. M. *Chem. Commun.* **2014**, *50* (37), 4810–4812.
- (33) Manna, K.; Zhang, T.; Lin, W. *J. Am. Chem. Soc.* **2014**, *136* (18), 6566–6569.
- (34) Falkowski, J. M.; Sawano, T.; Zhang, T.; Tsun, G.; Chen, Y.; Lockard, J. V.; Lin, W. *J. Am. Chem. Soc.* **2014**, *136* (14), 5213–5216.
- (35) Manna, K.; Zhang, T.; Carboni, M.; Abney, C. W.; Lin, W. *J. Am. Chem. Soc.* **2014**, *136* (38), 13182–13185.
- (36) Valvekens, P.; Bloch, E. D.; Long, J. R.; Ameloot, R. *Catalysis Today* **2014**, *246*, 55–59.
- (37) Evans, J. D.; Sumbly, C. J.; Doonan, C. J. *Chem. Soc. Rev.* **2014**, *43* (16), 5933–5951.
- (38) Bloch, E. D.; Britt, D.; Lee, C.; Doonan, C. J.; Uribe-Romo, F. J.; Furukawa, H.; Long, J. R.; Yaghi, O. M. *J. Am. Chem. Soc.* **2010**, *132* (41), 14382–14384.
- (39) Cavka, J. H.; Jakobsen, S.; Olsbye, U.; Guillou, N.; Lamberti, C.; Bordiga, S.; Lillerud, K. P. *J. Am. Chem. Soc.* **2008**, *130* (42), 13850–13851.
- (40) Li, L.; Tang, S.; Wang, C.; Lv, X.; Jiang, M.; Wu, H.; Zhao, X. *Chem. Commun.* **2014**, *50* (18), 2304–2307.
- (41) Nickerl, G.; Leistner, M.; Helten, S.; Bon, V.; Senkovska, I.; Kaskel, S. *Inorg. Chem. Front.* **2014**, *1* (4), 325–330.
- (42) Dau, P. V.; Kim, M.; Cohen, S. M. *Chem. Sci.* **2013**, *4* (2), 601.
- (43) Coelho, A. A. *Journal of Applied Crystallography* **2003**, *36* (1), 86–95.
- (44) Coelho, A. A. *TOPAS-Academic, Version 4.1*; Coelho Software: Brisbane, 2007.
- (45) Bruker Analytical X-ray Systems, Inc. *SAINT and APEX 2 Software for CCD Diffractometers*; Bruker Analytical X-ray Systems, Inc.: Madison, WI, USA, 2000.
- (46) Sheldrick, G. M. *SADABS*; Bruker Analytical X-ray Systems, Inc.: Madison, WI, USA, 2014.
- (47) Sheldrick, G. M. *SHELXS*; University of Göttingen, Germany, 2014.
- (48) Sheldrick, G. M. *Acta Crystallogr., A, Found. Crystallogr.* **2008**, *64* (Pt 1), 112–122.
- (49) Sheldrick, G. M. *SHELXL*; University of Göttingen, Germany: University of Göttingen, Germany, 2014.
- (50) Dolomanov, O. V.; Bourhis, L. J.; Gildea, R. J.; Howard, J. A. K.; Puschmann, H. *Journal of Applied Crystallography* **2009**, *42* (2), 339–341.
- (51) Schaate, A.; Roy, P.; Godt, A.; Lippke, J.; Waltz, F.; Wiebcke, M.; Behrens, P. *Chem. Eur. J.* **2011**, *17* (24), 6643–6651.
- (52) Valenzano, L.; Civalleri, B.; Chavan, S.; Bordiga, S.; Nilsen, M. H.; Jakobsen, S.; Lillerud, K. P.; Lamberti, C. *Chem. Mater.* **2011**, *23* (7), 1700–1718.
- (53) Katz, M. J.; Brown, Z. J.; Colón, Y. J.; Siu, P. W.; Scheidt, K. A.; Snurr, R. Q.; Hupp, J. T.; Farha, O. K. *Chem. Commun.* **2013**, *49* (82), 9449.
- (54) Shearer, G. C.; Chavan, S.; Ethiraj, J.; Vitillo, J. G.; Svelle, S.; Olsbye, U.; Lamberti, C.; Bordiga, S.; Lillerud, K. P. *Chem. Mater.* **2014**, *26* (14), 4068–4071.
- (55) Awad, D. J.; Schilde, U.; Strauch, P. *Inorganica Chimica Acta* **2011**, *365* (1), 127–132.
- (56) Healy, P. C.; Pakawatchai, C.; White, A. H. *J. Chem. Soc., Dalton Trans.* **1985**, No. 12, 2531–2539.

- (57) Hong, J.; Li, X.-Y.; Ng, S. W. *Acta Crystallographica Section E-Structure Reports Online* **2011**, *67* (9), M1322–U1496.
- (58) Xiao, L. N.; Wang, Y.; Pan, C. L.; Xu, J. N.; Wang, T. G.; Ding, H. *CrystEngComm* **2011**, *13* (15), 4878.
- (59) Cui, Y.; Chen, J.; Chen, G.; Ren, J.; Yu, W.; Qian, Y. *Acta Crystallogr C* **2001**, *57* (4), 349–351.
- (60) Desroches, C.; Ohrström, L. *Acta Crystallogr C* **2007**, *63* (Pt 5), m190–m192.
- (61) Brewer, B.; Brooks, N. R.; Sykes, A. G. *Journal of Chemical Crystallography* **2003**, *33* (9), 663–668.
- (62) Volbeda, J.; Meetsma, A.; Bouwkamp, M. W. *Organometallics* **2009**, *28* (1), 209–215.
- (63) Vlcek, A.; Grevels, F. W.; Snoeck, T. L.; Stufkens, D. J. *Inorganica Chimica Acta* **1998**, *278* (1), 83–90.
- (64) Baxter, P. N. W.; Connor, J. A.; Wallis, J. D.; Povey, D. C.; Powell, A. K. *Polyhedron* **1992**, *11* (14), 1771–1777.
- (65) Zhou, W.; Wu, H.; Yildirim, T. *J. Am. Chem. Soc.* **2008**, *130* (46), 15268–15269.
- (66) Ugozzoli, F.; Lanfredi, A. M. M.; Marsich, N.; Camus, A. *Inorganica Chimica Acta* **1997**, *256* (1), 1–7.
- (67) Mkhalid, I. A. I.; Barnard, J. H.; Marder, T. B.; Murphy, J. M.; Hartwig, J. F. *Chem. Rev.* **2010**, *110* (2), 890–931.
- (68) Ishiyama, T.; Takagi, J.; Ishida, K.; Miyaura, N.; Anastasi, N. R.; Hartwig, J. F. *J. Am. Chem. Soc.* **2002**, *124* (3), 390–391.
- (69) Boller, T. M.; Murphy, J. M.; Hapke, M.; Ishiyama, T.; Miyaura, N.; Hartwig, J. F. *J. Am. Chem. Soc.* **2005**, *127* (41), 14263–14278.
- (70) Tajuddin, H.; Harisson, P.; Bitterlich, B.; Collings, J. C.; Sim, N.; Batsanov, A. S.; Cheung, M. S.; Kawamorita, S.; Maxwell, A. C.; Shukla, L.; Morris, J.; Lin, Z.; Marder, T. B.; Steel, P. G. *Chem. Sci.* **2012**, *3* (12), 3505.
- (71) Larsen, M. A.; Hartwig, J. F. *J. Am. Chem. Soc.* **2014**, *136* (11), 4287–4299.
- (72) Waki, M.; Maegawa, Y.; Hara, K.; Goto, Y.; Shirai, S.; Yamada, Y.; Mizoshita, N.; Tani, T.; Chun, W.-J.; Muratsugu, S.; Tada, M.; Fukuoka, A.; Inagaki, S. *J. Am. Chem. Soc.* **2014**, *136* (10), 4003–4011.
- (73) Wu, F.; Feng, Y.; Jones, C. W. *ACS Catal.* **2014**, 1365–1375.
- (74) Green, M.; Kuc, T. A.; Taylor, S. H. *J. Chem. Soc., A* **1971**, No. 0, 2334–2337.
- (75) Rahaman, S. M. W.; Dinda, S.; Ghatak, T.; Bera, J. K. *Organometallics* **2012**, *31* (15), 5533–5540.
- (76) Harding, D. A. J.; Hope, E. G.; Singh, K.; Solan, G. A. *Polyhedron* **2012**, *33* (1), 360–366.
- (77) Walton, K. S.; Snurr, R. Q. *J. Am. Chem. Soc.* **2007**, *129* (27), 8552–8556.

## Chapter 5. Ethylene Oligomerization in Metal–Organic Frameworks Bearing Nickel(II) 2,2'-Bipyridine Complexes

### 5.1. Introduction

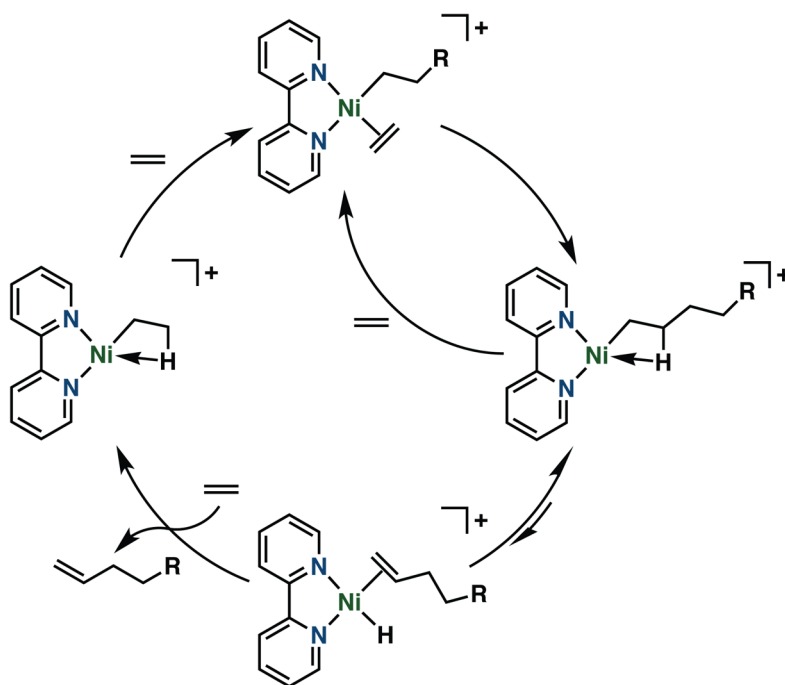
Heterogeneous catalysts maintain a dominant role in industrial synthesis, accounting for approximately 80% of all catalytic processes.<sup>1</sup> This preference for solid catalysts arises from their greater stability and ease of recovery, which enable higher throughput and lower cost of catalyst separation and replacement. Several key industrial transformations, however, still rely on molecular catalysts to achieve requisite reactivity or selectivity.<sup>2,3</sup> Among these processes, the oligomerization of ethylene to linear  $\alpha$ -olefins stands as one of the largest-scale homogeneously-catalyzed reactions, with over 4 million tons of linear  $\alpha$ -olefins produced each year as essential precursors to a wide variety of industrial products.<sup>4</sup> Short linear  $\alpha$ -olefins ( $C_4$ – $C_8$ ) are used as comonomers in the industrial synthesis of linear low-density polyethylene. These products are obtained through the highly-selective oligomerization of ethylene to 1-butene (the IFP/Sabic AlphaButol process), 1-hexene (the Chevron–Phillips trimerization process), or 1-octene (the Sasol tetramerization process). On the other hand, higher molecular weight oligomers remain important intermediates in the production of plasticizers ( $C_6$ – $C_{10}$ ), lubricants ( $C_{10}$ – $C_{12}$ ), and detergents ( $C_{12}$ – $C_{16}$ )<sup>4–6</sup> and are derived from less selective ethylene oligomerization in processes such as the Shell Higher Olefin Process (SHOP). With the intention of providing more practical, economical, and sustainable alternatives to these processes, considerable work has been directed toward developing heterogeneous oligomerization catalysts by immobilization of molecular catalysts on solid supports or ion-exchange in porous inorganic materials.<sup>7–10</sup> Despite these efforts, conventional heterogeneous systems have yet to match both the selectivity and activity of the best molecular catalysts,<sup>11–17</sup> highlighting the need for new materials in developing heterogeneous ethylene oligomerization catalysts.

Metal–organic frameworks, a class of porous crystalline materials, have proven to be exceptionally suited to the design of catalysts that bridge the gap between conventional heterogeneous and homogeneous catalysis. The high crystallinity, well-defined structure, and synthetic diversity of these materials enables control over active sites with a precision approaching that of molecular catalysts.<sup>18–22</sup> Furthermore, isolation of these sites within a porous rigid framework can impart stability to reactive species while maintaining their accessibility to substrates.<sup>23–26</sup> Taking advantage of these attributes, several metal–organic frameworks demonstrate promising activity for ethylene oligomerization,<sup>25–32</sup> with most reports focusing on the selective formation of 1-butene.<sup>26–29,32</sup> Notably, one of these materials, nickel(II)-exchanged  $Zn_5Cl_4(\text{btdd})_3$  ( $H_2\text{btdd} = \text{bis}(1H\text{-}1,2,3\text{-triazolo}[4,5\text{-}b],[4',5'\text{-}i])\text{dibenzo}[1,4]\text{dioxin}$ ) or Ni-MFU-4l, has been shown to achieve the highest activity for ethylene dimerization for a heterogeneous catalyst, with a selectivity for 1-butene that exceeds that of its molecular analog.<sup>26</sup>

Similar to analogous homogeneous catalysts, the active sites in these frameworks are generally thought to operate through the Cossee–Arlman mechanism (Scheme 1).<sup>27,33,34</sup> Here, chain growth involves successive ethylene insertion into a metal-alkyl intermediate and chain termination occurs through  $\beta$ -H elimination of the alkyl chain followed by substitution of the resulting olefin by ethylene. The relative rates of chain termination and chain growth govern product selectivity in these systems; catalysts with rates of chain termination that exceed the rate of chain growth selectively form butene, while those with comparable rates of chain termination and growth produce a Schulz–Flory chain length distribution of oligomers. The latter is characterized by an exponential decay in the mole fraction of each oligomer with increasing

chain length.<sup>33,35</sup>

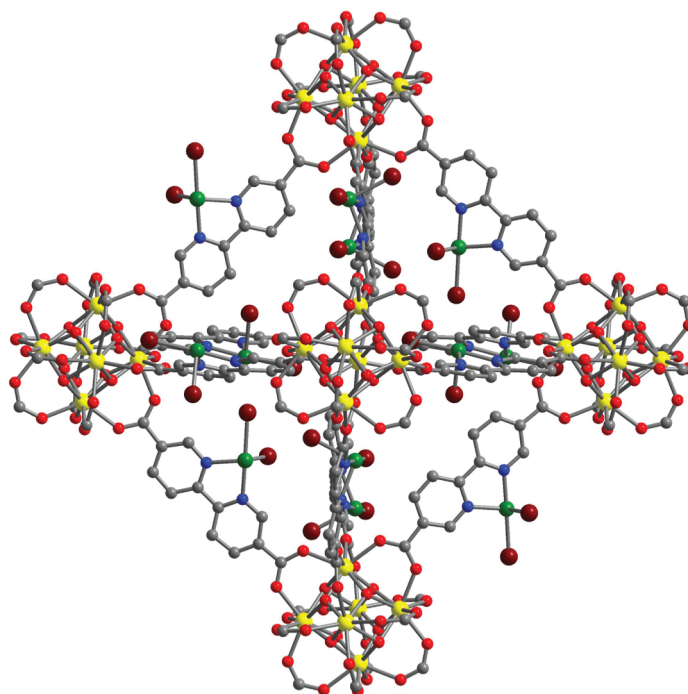
Given the continued industrial relevance of C<sub>4</sub>–C<sub>10</sub> α-olefins, we sought to develop new heterogeneous catalysts for the production of higher molecular weight olefins by designing metal–organic frameworks with active sites that give a Schulz–Flory distribution of oligomers. Moreover, because these systems produce intermediates of increasing chain length, the framework pore environment could potentially be used to influence the product selectivity. This influence offers an additional level of structural control over reactivity and has in fact been demonstrated to be a distinct advantage of metal–organic frameworks over molecular systems.<sup>36,37</sup> Conceivably, the metal-alkyl intermediates in these frameworks can grow sufficiently long for confinement within the pore to disfavor further ethylene insertion, resulting in selectivity for shorter oligomers. This selectivity would manifest as deviations from the expected Schulz–Flory product distribution, providing a convenient probe for confinement effects imparted by enclosing the active sites within a rigid framework.



**Scheme 5.1** Cossee–Arlman mechanism for ethylene oligomerization or polymerization catalyzed by nickel(II) bipyridine or α-diimine complexes.

The post-synthetic metalation of metal–organic frameworks has been extensively employed as a versatile strategy for engineering catalytic active sites within these materials.<sup>18–22,24,38–40</sup> Drawing upon the extensive work on ethylene oligomerization using molecular nickel(II) α-diimine and bipyridine complexes,<sup>34,35,41,42</sup> we envisioned that similar nickel(II) complexes could be installed into the 2,2′-bipyridine sites of the previously reported metal–organic framework Zr<sub>6</sub>O<sub>4</sub>(OH)<sub>4</sub>(bpydc)<sub>6</sub> (**1**).<sup>18,19,22,43</sup> As functionalized and expanded variants of the thermally and chemically stable framework Zr<sub>6</sub>O<sub>4</sub>(OH)<sub>4</sub>(bdc)<sub>6</sub> or UiO-66,<sup>44</sup> **1** and its metalated derivatives have been evaluated for applications in gas separation and catalysis.<sup>18,19,21,22,45</sup> The three-dimensional pore network of this framework should also accommodate diffusion of both reactants and products, while its ~13 Å-wide octahedral cages should be sufficiently small to induce

confinement effects on oligomerization. In addition, the ability to characterize the metal complexes formed in this framework by single-crystal X-ray diffraction provides an invaluable handle in correlating structure to observed reactivity.<sup>18</sup>



**Figure 5.1.** A portion of the crystal structure of  $\text{Zr}_6\text{O}_4(\text{OH})_4(\text{bpydc})_6(\text{NiBr}_2)_{5.64}$  at 100 K as determined by analysis of single-crystal X-ray diffraction data; yellow, green, dark red, red, blue, and gray spheres represent Zr, Ni, Br, O, N, and C atoms, respectively. The  $\text{Ni}^{\text{II}}$  centers are disordered over two positions (Figure 5.S1), but are represented here in only one orientation. Coordinated solvent molecules that complete the  $\text{Ni}^{\text{II}}$  coordination sphere could not be modeled due to disorder and weak scattering compared to the  $\text{Br}^-$  ligands. Hydrogen atoms are omitted for clarity.

Herein, we show that metalation of **1** with  $\text{Ni}(\text{DME})\text{Br}_2$  yields  $\mathbf{1}(\text{NiBr}_2)_6$ , which catalyzes the formation of a mixture of oligomers and polymer from ethylene with  $\text{Et}_2\text{AlCl}$  as an activating agent. Characterization of this framework by single-crystal X-ray diffraction (Figure 5.1) suggests that steric crowding of the nickel(II)-linker complexes causes these sites to favor production of polyethylene over ethylene oligomers. Both catalytic activity and selectivity can be appreciably enhanced through dispersion of the nickel active sites in the mixed-linker framework  $\mathbf{2}(\text{NiBr}_2)_{0.84}$ . Finally, the oligomer mixtures produced by these frameworks show deviations from the expected Schulz–Flory distribution, which may be an indication of confinement effects in these reactions. Control experiments reveal, however, that these deviations are at least partially due to the presence of adventitious nickel species.

## 5.2. Experimental

**Materials and Methods.** All manipulations were performed under an  $\text{N}_2$  atmosphere in a VAC Atmospheres glovebox or using standard Schlenk techniques. Cyclohexane was deoxygenated by purging with argon for 1 h and dried using a commercial solvent purification system designed by JC Meyer Solvent Systems. The solvents 1,2-dimethoxyethane (DME) and 1-methoxy-2-(2-methoxyethoxy)ethane (diglyme) were purchased from Sigma-Aldrich, dried



over Na/benzophenone (for DME) or 4A molecular sieves (for diglyme), and degassed via three successive freeze-pump-thaw cycles. The compound 2,2'-bipyridine-5,5'-dicarboxylic acid (H<sub>2</sub>bpydc) was synthesized using a previously published procedure.<sup>46</sup> The compounds ZrCl<sub>4</sub> and Ni(DME)Br<sub>2</sub> were purchased from Sigma-Aldrich and used as received. The compound biphenyl-4,4'-dicarboxylic acid (H<sub>2</sub>bpdc) was purchased from TCI and used as received. Analytical standards for undecane, 1-butene, 1-decene, 1-dodecene, 1-tetradecene, 1-hexadecene, and 1-octadecene were purchased from Sigma-Aldrich and used as received. Analytical standards for 1-hexene and 1-octene were purchased from TCI and used as received. All other chemicals were purchased from commercial vendors and used as received unless otherwise noted.

Thermogravimetric analyses were carried out with a TA Instruments TGA Q5000 operating at a ramp rate of 1 °C/min under a 25 mL/min N<sub>2</sub> flow. All samples were prepared as a slurry in hexanes to minimize exposure to oxygen and moisture during loading into the furnace. Samples were then heated to 100 °C at a rate of 1 °C/min and held at that temperature for 1 h to evaporate the hexanes prior to analysis. Scanning electron microscopy (SEM) samples were prepared by dispersing crystals in dichloromethane and drop casting onto a silicon chip. In order to dissipate charge, the samples were sputter coated with ~3 nm of Au (Denton Vacuum, LLC). Crystals were imaged at 5 keV/12 μA by field emission SEM (JEOL FSM6430). NMR spectra were acquired on Bruker AVB-400 or AVQ-400 instruments at the University of California, Berkeley NMR facility. All chemical shifts are given in relation to residual solvent peaks or tetramethylsilane. Gas chromatographic analysis was performed using an SRI Instruments 8610V GC equipped with an MXT-1 capillary column (60 m long; 0.53 mm internal diameter; 5.0 μm film thickness) and a Cobra autosampler.

**Zr<sub>6</sub>O<sub>4</sub>(OH)<sub>4</sub>(bpydc)<sub>6</sub> (1).** This material was synthesized as a microcrystalline powder using a slight modification to a previously published procedure.<sup>18</sup> Briefly, H<sub>2</sub>bpydc (6.11 g, 25.0 mmol), benzoic acid (224 g, 2.00 mol), and *N,N*-dimethylformamide (DMF; 1.00 L) from a newly opened bottle were placed into a three-neck 2-L round bottom flask equipped with a Schlenk adapter, glass stoppers, and a magnetic stir bar. The resulting mixture was purged with dry N<sub>2</sub> for 30 min. Solid ZrCl<sub>4</sub> (5.83 g, 25.0 mmol) was then added and the mixture was purged with dry N<sub>2</sub> for an additional 30 min. Deionized water (820 μL, 45.5 mmol) was then added and the mixture was heated with magnetic stirring for 5 days at 120 °C under an N<sub>2</sub> atmosphere. After allowing the mixture to cool to room temperature, the solvent was decanted and the resulting white microcrystalline powder was washed by soaking three times in 1-L aliquots of fresh DMF for 24 h at 120 °C, followed by solvent exchange with tetrahydrofuran (THF) via Soxhlet extraction for 3 days. The THF-solvated powder was filtered under dry N<sub>2</sub>, followed by heating at 120 °C under dynamic vacuum for 24 h to give fully desolvated Zr<sub>6</sub>O<sub>4</sub>(OH)<sub>4</sub>(bpydc)<sub>6</sub>. Langmuir surface area: 2743 ± 2 m<sup>2</sup>/g.

Single crystals of **1** were synthesized following a previously reported procedure.<sup>18</sup> Characterization of the crystals was performed by single-crystal X-ray diffraction.

**Zr<sub>6</sub>O<sub>4</sub>(OH)<sub>4</sub>(bpydc)<sub>0.84</sub>(bpdc)<sub>5.16</sub> (2).** This material was synthesized as a microcrystalline powder by substituting H<sub>2</sub>bpydc with a mixture composed of a 1:9 molar ratio of H<sub>2</sub>bpydc and H<sub>2</sub>bpdc in the synthetic procedure for **1** above. The precise linker composition was determined to be 14% bpydc<sup>2-</sup> and 86% bpdc<sup>2-</sup> by <sup>1</sup>H NMR analysis of a sample digested in a solution of 10 μL HF in 2 mL of DMSO-*d*<sub>6</sub>. Langmuir surface area: 2634 ± 2 m<sup>2</sup>/g. BET surface area: 2430 ± 20 m<sup>2</sup>/g.

**Zr<sub>6</sub>O<sub>4</sub>(OH)<sub>4</sub>(bpdC)<sub>6</sub> (3).** This material was taken from the same batch of sample synthesized for a previous report.<sup>18</sup>

**General Procedure for Metalation with Ni(DME)Br<sub>2</sub>.** Microcrystalline **1** or **2** (50–500 mg), Ni(DME)Br<sub>2</sub> (1.0 equivalent per bpydc<sup>2-</sup>), and DME (7.5 mL) were mixed in a 20-mL Teflon-capped vial. The resulting mixture was then heated for one week on a hot plate at 80 °C to afford a pale yellow powder. After cooling to room temperature, the supernatant solution was decanted and the powder was soaked three times in 15 mL fresh DME for 24 h at 80 °C to remove any unreacted metal source. The solvent was then removed under reduced pressure at 80 °C to give the corresponding metalated framework. Due to an observed reduction in stability of the framework to moisture upon metalation, the metalation and subsequent manipulations were carried out under an inert atmosphere.

Single crystals of **1** suspended in diglyme were transferred into a 4-mL Teflon-capped vial. Most of the solvent was decanted, followed by addition of microcrystalline **1** (10 mg), Ni(DME)Br<sub>2</sub> (1.0 equivalent per bpydc<sup>2-</sup> in microcrystalline **1**) and diglyme. The mixture was allowed to react for 1 month at 120 °C, resulting in a color change of both the crystals and the powder to pale yellow. Most of the solution was removed by pipette and the crystals were subsequently soaked three times in 3 mL of fresh diglyme at 120 °C for 24 h, after which they were used for single-crystal X-ray diffraction experiments.

**Single-Crystal X-ray Diffraction.** X-ray diffraction analysis was performed on a single crystal of **1**(NiBr<sub>2</sub>)<sub>5,64</sub> coated with Paratone-N oil and mounted on a MiTeGen loop. The crystal was frozen at a temperature of 100 K by an Oxford Cryosystems Cryostream 700 Plus. Data were collected at Beamline 11.3.1 at the Advanced Light Source at Lawrence Berkeley National Laboratory using synchrotron radiation ( $\lambda = 0.8856 \text{ \AA}$ ) on a Bruker D8 diffractometer equipped with a Bruker PHOTON100 CMOS detector. Raw data were integrated and corrected for Lorentz and polarization effects using Bruker AXS SAINT software.<sup>47</sup> Absorption corrections were applied using SADABS.<sup>48</sup> Initial evaluation of the diffraction data suggested that metalation induced a change of space group from  $Fm\bar{3}m$  to  $P2_13$ . Attempts to solve and refine the structure in  $P2_13$ , however, resulted in unsatisfactory refinement. Solution and refinement in the space group  $Pa\bar{3}$  was instead attempted based on previous work describing the change in space group of **1** upon metalation. In the end, this space group gave the most satisfactory refinement. The structure was solved using direct methods with SHELXS<sup>49,50</sup> and refined using SHELXL<sup>51</sup> operated in the OLEX2<sup>52</sup> interface. No significant significant crystal decay was observed during data collection. Thermal parameters were refined anisotropically for all non-hydrogen atoms. Hydrogen atoms were placed in ideal positions and refined using a riding model for all structures. Moving from  $Fm\bar{3}m$  to  $Pa\bar{3}$  results in two twin domains related by the lost mirror symmetry. Consequently, a twin law (TWIN 0 1 0 1 0 0 0 0 -1 2; BASF = 0.500(2)) was required for the structural refinement. The oxygen atoms of the oxo and hydroxo groups on the zirconium clusters in the structure were disordered, so their site occupancy factors were fixed to give a chemical occupancy of 50%. Hydrogen atoms on the hydroxo groups could neither be found nor placed and were omitted from the refinement but not from the formula. Disorder of the linker-NiBr<sub>2</sub> complexes required the use of geometric and displacement parameter restraints. Extensive solvent disorder was found in the pores for **1**(NiBr<sub>2</sub>)<sub>5,64</sub> and could not be modeled. Consequently, the unassigned electron density was accounted for using SQUEEZE<sup>53</sup> as implemented in the PLATON<sup>54</sup> interface. Refinement before SQUEEZE was applied gave an R1 of 10.10% (wR2 = 32.24%), while applying SQUEEZE resulted in an R1 of 6.51% (wR2 = 20.46%).

**Powder X-ray Diffraction.** Diffraction data were collected with 0.02° steps using a Bruker

AXS D8 Advance diffractometer equipped with Ni-filtered Cu-K $\alpha$  radiation ( $\lambda = 1.5418 \text{ \AA}$ ), a Göbel mirror, a Lynxeye linear position-sensitive director, and mounting the following optics: a fixed divergence slit (0.6 mm), a receiving slit (3 mm), and a secondary beam Soller slits (2.5°). The generator was set at 40 kV and 40 mA. Samples were either directly loaded on zero background sample holders or packed into capillaries in a nitrogen-filled glovebox and flame-sealed before data was collected by means of scans in the  $2\theta$  range of 2–50°. For **1**(NiBr<sub>2</sub>)<sub>6</sub>, **2**(NiBr<sub>2</sub>)<sub>0.84</sub>, and **3**(NiBr<sub>2</sub>)<sub>0.14</sub>, a standard peak search, followed by indexing through the Single Value Decomposition approach,<sup>55</sup> as implemented in TOPAS-Academic,<sup>56</sup> allowed the determination of approximate unit cell parameters. Analysis of **1**(NiBr<sub>2</sub>)<sub>6</sub> led to the assignment of the space group  $P\bar{a}3$  on the basis of systematic absences. The unit cell and space group were verified by a structureless Pawley refinement. Likewise, samples **2**(NiBr<sub>2</sub>)<sub>0.84</sub> and **3**(NiBr<sub>2</sub>)<sub>0.13</sub> were also examined, and the space group of the frameworks were found to have remained as  $Fm\bar{3}m$ .

**Low-Pressure Gas Adsorption Measurements.** Gas adsorption isotherms for pressures in the range 0–1.2 bar were measured by a volumetric method using a Micromeritics ASAP2420 instrument. A typical sample, consisting of ~100 mg of material was transferred to a pre-weighed analysis tube, which was capped with a Micromeritics *TranSeal* and evacuated by heating at either 120 °C (**1** and **2**) or 80 °C (**1**(NiBr<sub>2</sub>)<sub>6</sub>, **2**(NiBr<sub>2</sub>)<sub>0.84</sub>, and **3**(NiBr<sub>2</sub>)<sub>0.14</sub>) at a ramp rate of 1 °C/min under dynamic vacuum until an outgas rate of less than 3  $\mu\text{bar}/\text{min}$  was achieved. The evacuated analysis tube containing the degassed sample was then carefully transferred to an electronic balance and weighed again to determine the mass of sample. The tube was then transferred back to the analysis port of the gas adsorption instrument. The outgas rate was again confirmed to be less than 3  $\mu\text{bar}/\text{min}$ . For all isotherms, warm and cold free space correction measurements were performed using ultra-high purity He gas (99.999% purity); N<sub>2</sub> isotherms at 77 K were measured in liquid N<sub>2</sub> baths using UHP-grade gas sources. Oil-free vacuum pumps and oil-free pressure regulators were used for all measurements to prevent contamination of the samples during the evacuation process or of the feed gases during the isotherm measurements. Langmuir and Brunauer–Emmet–Teller (BET) surface areas were determined from N<sub>2</sub> adsorption data at 77 K using Micromeritics software.

**Ethylene Oligomerization Reactions.** In an N<sub>2</sub>-filled glovebox, microcrystalline powder of activated material (5–30 mg) was placed in a reactor built from a Swagelok® 10-mL stainless steel sample cylinder and a Swagelok® stainless steel ball valve. Cyclohexane, Et<sub>2</sub>AlCl (100 equivalents per Ni or Zr), undecane (internal standard), and a PTFE stir bar were added, ensuring that the total volume was consistently 5.0 mL. The reactor was sealed, removed from the glovebox, weighed, and then attached to a custom-built stainless steel high-pressure manifold kept under dynamic vacuum. Once the headspace was fully evacuated, the manifold was pressurized with 59 bar of ethylene. The sample cylinders were then carefully pressurized by partially opening the ball valves and heated at 55 °C for 1 h with magnetic stirring. At this time, the reactors were immediately sealed and cooled for 20 min. in a dry ice/isopropanol bath. With the reactor valve partially opened, the manifold was gradually vented to atmospheric pressure. The reactor was warmed to room temperature with the valve closed to prevent bumping of the reaction mixture into the manifold. After the pressure was carefully relieved, the reactor was sealed, detached from the manifold, and then weighed again to determine the total amount of ethylene consumed. The reaction mixture was then added to 1.0 mL of a 6.8% aqueous HCl solution kept in an ice bath. Once the excess Et<sub>2</sub>AlCl was fully quenched, a 1.0-mL aliquot of the cyclohexane layer was withdrawn and filtered through a 0.2- $\mu\text{m}$  PTFE syringe filter, and then

analyzed by gas chromatography. Note that, prior to each experiment, the reactors were thoroughly washed with successive ~10-mL aliquots of a 34% aqueous HNO<sub>3</sub> solution and deionized water to remove residual contaminants, which were found to cause background catalytic activity.

**General procedure for metal content analysis via ICP-OES.** Roughly 10 mg of activated material was placed in a 20-mL plastic vial and digested with 10  $\mu$ L of concentrated HF in 2 mL of dimethylsulfoxide and diluted with 18 mL of 5% HNO<sub>3</sub> in Millipore water. The resulting solution was transferred to a 100-mL volumetric flask and diluted to mark with 5% (v/v) aqueous HNO<sub>3</sub> in Millipore water to give a stock solution that contained roughly 25 ppm Zr from the sample. The stock sample solution (10 mL) and 2.5 ppm Y (1 mL) were added to a 25-mL volumetric flask and diluted to mark with 5% (v/v) aqueous HNO<sub>3</sub> to give sample solution that is roughly 10 ppm Zr with 0.1 ppm Y as an internal standard. Standard solutions with 0.1, 1, 5, 10, and 15 ppm Zr and Ni with 0.1 ppm Y as an internal standard were prepared for the calibration curve.

### 5.3. Results and Discussion

#### 5.3.1. Synthesis and Metalation of Metal–Organic Frameworks

The metal–organic framework Zr<sub>6</sub>O<sub>4</sub>(OH)<sub>4</sub>(bpydc)<sub>6</sub> (**1**) was prepared by a slight modification to a previously published procedure, and the resulting product was found to display a powder X-ray diffraction pattern and Langmuir surface area (Table 5.1) consistent with those previously reported.<sup>18</sup> With the intent of synthesizing a framework with a lower concentration of uniformly dispersed bipyridine sites relative to **1**, the mixed-linker framework Zr<sub>6</sub>O<sub>4</sub>(OH)<sub>4</sub>(bpydc)<sub>0.84</sub>(bpdc)<sub>5.16</sub> (**2**) was synthesized by reacting ZrCl<sub>4</sub> with a 1:9 mixture of H<sub>2</sub>bpydc and H<sub>2</sub>bpdc in the presence of benzoic acid, following the same synthetic method developed for **1**. Powder X-ray diffraction data show that **2** is isostructural to **1** (Figure 5.S3). Analysis of a sample of **2** digested in a solution of HF and DMSO-*d*<sub>6</sub> by <sup>1</sup>H NMR revealed that 14% of the linkers correspond to bpydc<sup>2-</sup>. Fully-desolvated **2** exhibits Langmuir and BET surface areas of 2630 m<sup>2</sup>/g and 2430 m<sup>2</sup>/g (Table 5.1), respectively, which are slightly lower than the reported surface areas of **1**. Thermogravimetric analysis of the thermal decomposition of **2** under flowing N<sub>2</sub> (Figure 5.S17) showed that, after desolvation, the framework remains stable at temperatures up to 450 °C, at which point a sharp decrease in mass associated with framework decomposition occurs.

**Table 5.1.** Nickel loading and surface areas of the metal–organic frameworks investigated in this work.

compound	Ni loading <sup>a</sup> (%)	SA <sub>Lang</sub> <sup>b</sup> (m <sup>2</sup> /g)	SA <sub>BET</sub> <sup>c</sup> (m <sup>2</sup> /g)
<b>1</b>	—	2743 ± 2, 2772 (ref. 18)	2730 (ref. 18)
<b>2</b>	—	2634 ± 2	2430 ± 20
<b>3</b>	—	2805 (ref. 18)	2625 (ref. 18)
<b>1</b> (NiBr <sub>2</sub> ) <sub>6</sub>	101 ± 2	650 ± 8	545 ± 3
<b>2</b> (NiBr <sub>2</sub> ) <sub>0.84</sub>	14.1 ± 0.2	2467 ± 2	2300 ± 20
<b>3</b> (NiBr <sub>2</sub> ) <sub>0.14</sub>	2.30 ± 0.06	2450 ± 10	—

<sup>a</sup>Nickel loading was determined by ICP-OES analysis based on the molar ratio of Ni relative to Zr in the framework. <sup>b</sup>SA<sub>Lang</sub> = Langmuir surface area. <sup>c</sup>SA<sub>BET</sub> = Brunauer–Emmet–Teller (BET) surface area.

Molecular nickel(II) bipyridine and  $\alpha$ -diimine precatalysts studied for ethylene oligomerization are generally synthesized by reaction of the corresponding ligand with Ni(DME)Br<sub>2</sub> in CH<sub>2</sub>Cl<sub>2</sub> at room temperature for 18 h.<sup>35,57</sup> Post-synthetic metalation of metal-organic frameworks, however, often requires higher temperatures and longer reaction times to achieve high metal loadings. Thus, DME was selected as a solvent for metalation to allow for higher reaction temperatures without significantly changing the coordination environment of the nickel(II) complexes in the metalated frameworks. In addition, the DME-solvated NiBr<sub>2</sub> complexes are sufficiently small to fit through the triangular windows of the frameworks, which have an incircle diameter of  $\sim 8$  Å. Thus, suspending microcrystalline powders of **1** or **2** with one equivalent of Ni(DME)Br<sub>2</sub> per bipyridine linker at 80 °C for 5 days yielded **1**(NiBr<sub>2</sub>)<sub>6</sub> and **2**(NiBr<sub>2</sub>)<sub>0.84</sub>, respectively, as pale yellow powders. These microcrystalline powders retain their color after three 24-h DME washes, suggesting the successful metalation of the frameworks. Determination of the nickel to zirconium ratios by ICP-OES analysis confirmed the full metalation of the bipyridine sites in both **1** and **2** (Table 5.1). Low-pressure N<sub>2</sub> adsorption data collected at 77 K for the metalated frameworks show the expected decrease in surface area (Table 5.1) with increasing nickel loading.

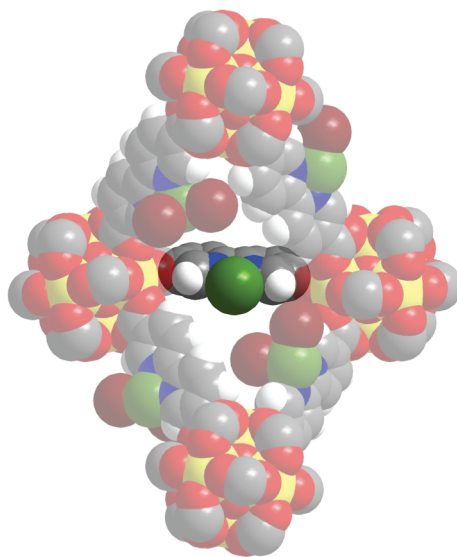
Based on thermogravimetric analysis (Figures 5.S18–19), **1**(NiBr<sub>2</sub>)<sub>6</sub> and **2**(NiBr<sub>2</sub>)<sub>0.84</sub> remain intact up to 350 °C and 400 °C, respectively. The lower thermal stability of these frameworks compared to **1** and **2** is consistent with what has been observed for metalated derivatives of **1**.<sup>18</sup> Analysis of the powder X-ray diffraction patterns of **1**(NiBr<sub>2</sub>)<sub>6</sub> and **2**(NiBr<sub>2</sub>)<sub>0.84</sub> (Figures 5.S4–5) reveals that both frameworks maintain crystallinity after metalation. The space group of **2** remains *Fm* $\bar{3}$ *m* upon metalation to form **2**(NiBr<sub>2</sub>)<sub>0.84</sub> (Table 5.S2 and Figure 5.S8). In this space group, crystallographic symmetry imposes disorder of the bipyridine complexes over at least two positions, making their structural characterization exceedingly difficult. Metalation of **1**, however, was found to induce a change in space group from *Fm* $\bar{3}$ *m* to the lower-symmetry space group *Pa* $\bar{3}$  (Table 5.S7 and Figure 5.S8), which has been previously reported to be caused by the crystallographic ordering of the metal-bipyridine complexes within the framework.<sup>18</sup>

In contrast to the powder sample, single crystals of **1** treated with the same metalation conditions do not show a change in space group and were found to have very low nickel loading. This disparity has been previously observed and can be attributed to slow diffusion of the metal source into the crystal interior.<sup>18</sup> To address this problem, higher reaction temperatures were attempted, requiring the replacement of DME with the higher-boiling solvent diglyme. Reaction with one equivalent of Ni(DME)Br<sub>2</sub> in diglyme at 120 °C for one month results in the single-crystal-to-single-crystal metalation of **1** to form **1**(NiBr<sub>2</sub>)<sub>5.64</sub>. Characterization of **1**(NiBr<sub>2</sub>)<sub>5.64</sub> by single-crystal X-ray diffraction revealed that the space group changed to *Pa* $\bar{3}$ , accompanied by ordering of linker-NiBr<sub>2</sub> complexes in the framework (Figure 5.1). The nickel(II) centers were found to be disordered over two positions tilted 23° apart, with site occupancies of 64% and 30% (Figure 5.S1). In addition to the bipyridine linkers, the Br<sup>-</sup> ligands could also be resolved but were disordered over several nickel(II) coordination sites. The relative positions and site occupancies of these ligands indicate that 87% of the nickel sites adopt a pseudooctahedral coordination geometry, while the remaining sites appear to be square pyramidal (Figure 5.S1). Residual electron density suggests that solvent molecules complete the nickel(II) coordination spheres. These ligands, however, could not be resolved due to disorder and weaker scattering compared to the Br<sup>-</sup> ligands. Thus, the nickel coordination geometries cannot be assigned with complete accuracy. These nickel centers likely adopt a tetrahedral geometry, upon desolvation of the framework.

### 5.3.2. Ethylene Oligomerization

In general, ethylene oligomerization reactions were conducted under 59 bar of ethylene at 55 °C for 1 h, which are similar conditions to those reported for molecular nickel(II) bipyridine catalysts.<sup>35</sup> Diethylaluminum chloride was selected as an activating reagent in place of the more commonly used methylaluminoxane (MAO) because it is more likely to fit through the triangular windows of **1** and **2**. Additionally, nickel(II)  $\alpha$ -diimine complexes have been found to exhibit comparable activity for ethylene oligomerization with either Et<sub>2</sub>AlCl or MAO as activating agents.<sup>34</sup>

The framework **1**(NiBr<sub>2</sub>)<sub>6</sub> reacts with ethylene to give a range of oligomers (C<sub>4</sub>–C<sub>18</sub>+) in the presence of Et<sub>2</sub>AlCl. Surprisingly, C<sub>4</sub>–C<sub>18</sub> oligomers only accounted for 23 ± 1% of the ethylene consumed, while a considerable amount of polymer was recovered from the reaction mixture. Nickel(II)  $\alpha$ -diimine catalysts for ethylene polymerization require ligands that enforce steric bulk around positions axial to the square planar active species.<sup>58,59</sup> Blocking these sites inhibits chain termination by preventing the associative substitution of the olefin chain by ethylene (Scheme 1), leading to the formation of polymer instead of oligomers. Bipyridine-based nickel(II) catalysts, however, typically lack the necessary steric bulk to facilitate polymerization,<sup>35,57</sup> suggesting that the formation of polyethylene in **1**(NiBr<sub>2</sub>)<sub>6</sub> is an effect of the immediate pore environment and not the ligand.

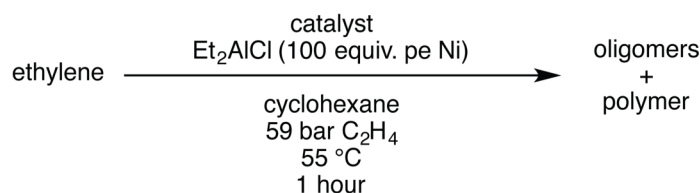


**Figure 5.2.** Space-filling model of a section of the crystal structure of Zr<sub>6</sub>O<sub>4</sub>(OH)<sub>4</sub>(bpydc)<sub>6</sub>(NiBr<sub>2</sub>)<sub>5.64</sub> emphasizing the pore environment around the nickel(II)–linker complexes as determined by analysis of single-crystal X-ray diffraction data; yellow, green, dark red, red, blue, and gray spheres represent Zr, Ni, Br, O, N, and C atoms, respectively. The Ni<sup>II</sup> centers are disordered over two positions (Figure 5.S1), but are represented here in only one orientation. Coordinated solvent molecules that complete the Ni<sup>II</sup> coordination sphere could not be modeled due to disorder and weak scattering compared to the Br<sup>−</sup> ligands. Bromine atoms on one of the nickel(II)–linker complexes are omitted for clarity.

Indeed, further examination of the single-crystal structure of **1** reveals that nearby linker–NiBr<sub>2</sub> complexes (within 6 Å) surround the sites above and below each nickel(II) center (Figure 5.2). This steric environment coupled with the presence of additional charge-balancing anions can act to impede displacement of the growing alkyl chain, making polymer formation more favorable. In addition, **1**(NiBr<sub>2</sub>)<sub>6</sub> consumes ethylene at a relatively low average turnover

frequency (TOF) of  $4300 \pm 400 \text{ mol}_{\text{ethylene}} \text{ mol}_{\text{Ni}}^{-1} \text{ h}^{-1}$  (Table 5.2) under oligomerization conditions. In contrast, molecular nickel(II) bipyridine catalysts selectively produce a Schulz–Flory distribution of oligomers with much higher activities.<sup>35,57</sup> The lower activity of **1**(NiBr<sub>2</sub>)<sub>6</sub> compared to its molecular analog Ni(bpy)Br<sub>2</sub> (TOF =  $\sim 63000 \text{ mol}_{\text{ethylene}} \text{ mol}_{\text{Ni}}^{-1} \text{ h}^{-1}$ )<sup>35</sup> likely originates from incomplete activation of the framework nickel(II) complexes by Et<sub>2</sub>AlCl. Full metalation of **1** constricts the pore apertures in the framework and decreases its porosity (Table 5.1), which would in turn hinder diffusion of Et<sub>2</sub>AlCl to sites in the crystal interior. This problem is further aggravated upon reaction with Et<sub>2</sub>AlCl, because the proposed cationic nickel active species that forms (Scheme 1) requires a non-coordinating alkyl aluminium halide anion for charge balance.

**Table 5.2.** Ethylene oligomerization results.



catalyst	average TOF <sup>a</sup> ( $\text{mol}_{\text{ethylene}} \text{ mol}_{\text{Ni}}^{-1} \text{ h}^{-1}$ )	activity <sup>a</sup> ( $\text{g}_{\text{product}} \text{ g}_{\text{catalyst}}^{-1} \text{ h}^{-1}$ )	weight % <sup>a</sup> (C <sub>4–18</sub> olefins)
<b>1</b> (NiBr <sub>2</sub> ) <sub>6</sub>	4300 ± 400	220 ± 20	23 ± 1
<b>2</b> (NiBr <sub>2</sub> ) <sub>0.84</sub>	36000 ± 3000	370 ± 30	73 ± 6
<b>3</b> (NiBr <sub>2</sub> ) <sub>0.14</sub>	25000 ± 2000	44 ± 3	91 ± 20

<sup>a</sup>Determined as an average of three replications.

Initial attempts to relieve the steric congestion around the nickel active sites in **1** by metalation with only 0.1 equivalents Ni(DME)Br<sub>2</sub> gave rise to only a negligible improvement in selectivity for oligomers. Suspecting that surface linker sites were being preferentially metalated, resulting in ineffective dispersion of the nickel active sites, we synthesized the mixed-linker framework **2** to obtain a material with more uniformly dispersed nickel(II)-bipyridine complexes. Gratifyingly, the Ni-metalated framework **2**(NiBr<sub>2</sub>)<sub>0.84</sub> exhibits dramatically increased activity and selectivity for oligomers over polymer (Table 5.2). Under oligomerization conditions, this material consumes ethylene with an average TOF of  $36000 \pm 3000 \text{ mol}_{\text{ethylene}} \text{ mol}_{\text{Ni}}^{-1} \text{ h}^{-1}$  and produces 73 ± 6 weight % C<sub>4–18</sub> oligomers, which approach the activity of the molecular analog.<sup>35,57</sup> Importantly, **2**(NiBr<sub>2</sub>)<sub>0.84</sub> also exhibits higher activity per gram of catalyst compared to **1**(NiBr<sub>2</sub>)<sub>6</sub>, indicating that achieving high metal loadings may not always lead to optimal activity in porous catalysts. The greater activity and selectivity afforded by **2**(NiBr<sub>2</sub>)<sub>0.84</sub> compared to **1**(NiBr<sub>2</sub>)<sub>6</sub> cannot be attributed to differences in particle size, as SEM images (Figures 5.S26–27) confirm that both frameworks possess similar particle size distributions ( $\sim 0.2$ – $2.0 \mu\text{m}$ ). These results demonstrate that active site dilution improves mass transport within the framework and prevents crowding of the active sites, with both effects enabling higher activity and selectivity for oligomers.

To probe for possible pore environment effects on oligomerization selectivity, the product mixtures from these reactions were analyzed for deviations from the expected Schulz–Flory distribution (Figure 5.3). In product mixtures that follow this distribution, the ratio of moles produced for oligomers with a chain length of  $n$  carbons ( $\text{mol } C_n$ ) and that of an oligomer that is one ethylene unit shorter ( $\text{mol } C_{n-2}$ ) is equal to the probability of chain propagation ( $\alpha$ ) (eq 1).

This distribution can also be mathematically described using the Schulz–Flory formula (eq 2; where  $\sum mol C_n$  is the total molar amount of oligomers), which gives a straight line in the logarithmic plot of  $mol C_n$  versus chain length  $n$ . As a consequence, any deviations from the Schulz–Flory distribution can easily be identified if the product mixture does not follow this linear trend.

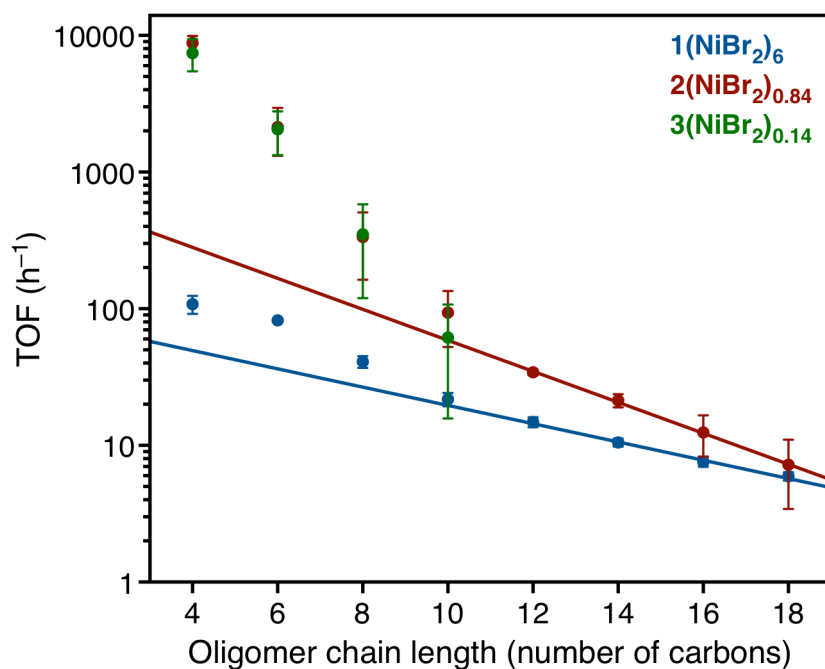
$$\frac{mol C_n}{mol C_{n-2}} = \alpha = \frac{r_{\text{chain growth}}}{r_{\text{chain growth}} + r_{\text{chain termination}}} \quad (1)$$

$$mol C_n = (\sum mol C_n)(1 - \alpha)\alpha^{n-1} \quad (2)$$

To facilitate comparison of the relative activities for each catalyst over the entire range of oligomer chain lengths, eq 2 can also be expressed in terms of average turnover frequency for each oligomer chain length ( $TOF C_n$ ), which is in units of  $mol_{\text{oligomer}} / mol_{\text{Ni}} / \text{hour}$  (eq 3).

$$TOF C_n = (\sum TOF C_n)(1 - \alpha)\alpha^{n-1} \quad (3)$$

Remarkably, consistent with the anticipated impact of pore confinement upon oligomerization, both **1**(NiBr<sub>2</sub>)<sub>6</sub> and **2**(NiBr<sub>2</sub>)<sub>0.84</sub> show enhanced selectivity for shorter oligomers, resulting in deviations from the Schulz–Flory distribution (Figure 5.3). Specifically, the C<sub>12–18</sub> oligomer fractions follow the expected linear trend, while the average turnover frequencies for the C<sub>4–10</sub> oligomer fractions are higher than expected. From these observations, we reasoned that active sites on the outer surfaces of the crystals might give rise to a Schulz–Flory distribution of oligomers, while sites located in the crystal interior exhibit selectivity for shorter oligomers due



**Figure 5.3.** Average turnover frequency ( $mol_{\text{oligomer}} / mol_{\text{Ni}} / \text{h}^{-1}$ ) distribution plot for C<sub>4–18</sub> oligomers produced in ethylene oligomerization reactions catalyzed by **1**(NiBr<sub>2</sub>)<sub>6</sub> (blue), **2**(NiBr<sub>2</sub>)<sub>0.84</sub> (red), and **3**(NiBr<sub>2</sub>)<sub>0.14</sub> (green). The filled circles represent experimental data and the solid lines represent fits to the data for the C<sub>12–18</sub> oligomer fractions using the Schulz–Flory equation.



to confinement within the pore. In agreement with this hypothesis, a more pronounced deviation was observed for reactions catalyzed by  $\mathbf{2}(\text{NiBr}_2)_{0.84}$ , in which a greater fraction of nickel sites within the crystal interior are accessible.

Examination of the relative amount of  $\alpha$ -olefin in each oligomer fraction (Table 5.S3) further corroborates that the pore environment influences oligomerization selectivity. The Schulz–Flory ( $\text{C}_{12-18}$ ) region of the oligomer mixture produced by  $\mathbf{1}(\text{NiBr}_2)_6$  contains higher fractions of  $\alpha$ -olefins (~83–86%) compared to that of its molecular analog (~55%).<sup>35</sup> This higher selectivity for  $\alpha$ -olefins suggests stronger inhibition of chain termination from the internal olefin nickel(II) complexes that form upon isomerization compared to that of  $\alpha$ -olefin complexes due to the steric environment around the active nickel sites. Instead, the internal olefins isomerize back to form  $\alpha$ -olefins that either continue chain growth or undergo chain termination. Conversely,  $\mathbf{2}(\text{NiBr}_2)_{0.84}$  displays lower selectivity (~50%) for  $\alpha$ -olefins in the  $\text{C}_{12-18}$  fraction, agreeing with the description of the dispersed linker–nickel(II) complexes in this framework as sites that behave like molecular bipyridine nickel(II) oligomerization catalysts. Both  $\mathbf{1}(\text{NiBr}_2)_6$  and  $\mathbf{2}(\text{NiBr}_2)_{0.84}$ , however, exhibit much lower selectivities for  $\alpha$ -olefins in fractions that show significant deviation from the Schulz–Flory distribution. The decreased selectivity for  $\alpha$ -olefins is consistent with a higher probability for chain isomerization at sites that predominantly produce short oligomers, which can be attributed to slower chain growth brought about by active site confinement within the pores of these frameworks.

Recognizing that the observed product distributions could also arise from the presence of more than one nickel active species in the framework, we performed control experiments to determine if the nickel(II)-bipyridine sites were solely responsible for the observed catalytic activity. No conversion of ethylene to either oligomers or polymer was observed using  $\mathbf{1}$ , confirming that the framework zirconium sites are inactive. The biphenyl variant of  $\mathbf{1}$ ,  $\text{Zr}_6\text{O}_4(\text{OH})_4(\text{bpdc})_6$  ( $\mathbf{3}$ ), was then prepared and subjected to the same metalation conditions, to check whether any adventitious Ni species that could be forming at other sites in the framework. Surprisingly, the Ni-treated framework  $\mathbf{3}(\text{NiBr}_2)_{0.14}$  was found to contain  $2.30 \pm 0.06\%$  Ni for each Zr center by ICP-OES (Table 5.1), even after extensive washing with DME. Additionally,  $\mathbf{3}(\text{NiBr}_2)_{0.14}$  selectively oligomerizes ethylene to produce only  $\text{C}_{4-10}$  oligomers (Table 5.2) with poor selectivity for  $\alpha$ -olefins. This unexpected activity likely originates from active nickel species coordinated to water and hydroxide ligands that occupy vacant linker sites on the zirconium cluster.<sup>60-62</sup> Similar metal binding sites on the zirconium cluster have been previously reported and studied for catalysis in other frameworks.<sup>25,63,64</sup> For instance, the framework NU-1000, which possesses four vacant linker coordination sites on its zirconium clusters, has been shown to be active for ethylene oligomerization upon metalation of these sites with nickel salts.<sup>25</sup>

These control experiments strongly suggest that the observed deviations from the Schulz–Flory distribution in  $\mathbf{1}(\text{NiBr}_2)_6$  and  $\mathbf{2}(\text{NiBr}_2)_{0.84}$  result in part from the formation of at least two different types of active sites, nickel(II)-bipyridine complexes and nickel species similar to those present in  $\mathbf{3}(\text{NiBr}_2)_{0.14}$ . Assuming, however, that the same amount of the nickel species in  $\mathbf{3}(\text{NiBr}_2)_{0.14}$  also exist in  $\mathbf{2}(\text{NiBr}_2)_{0.84}$  (17% of the  $\text{Ni}^{\text{II}}$  sites), activity from these sites would only account for around  $16 \pm 4\%$  by mass of the oligomers formed in excess of the amounts estimated from the Schulz–Flory distribution (Figure 5.S20). Thus, the contribution of pore confinement effects to the selectivity for  $\text{C}_{4-10}$  oligomers in these frameworks cannot be ruled out entirely, as it may be possible that the nickel(II)-bipyridine complexes in  $\mathbf{2}(\text{NiBr}_2)_{0.84}$  produce the rest of the oligomers associated with the deviation. The presence of two active species, however, precludes the rigorous investigation of such effects in these materials.

## 5.4. Conclusions

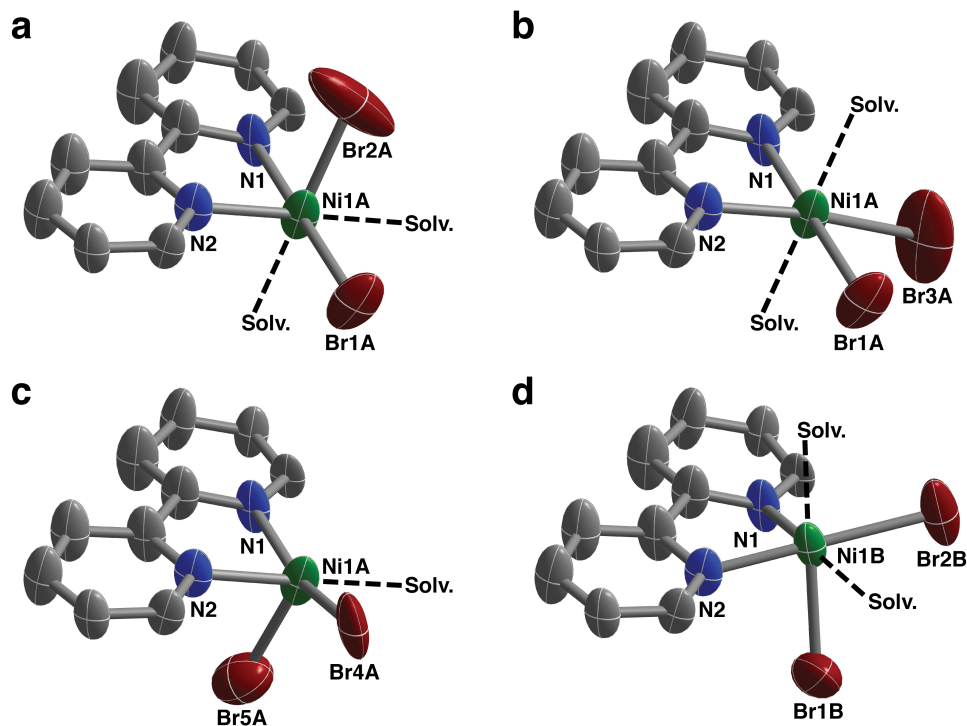
Metal–organic frameworks extend the degree of synthetic control and structural characterization available to molecular chemistry to the design of porous solids. These capabilities are distinctly advantageous in the development of heterogeneous systems for industrial processes that currently require homogeneous catalysts. Here, porous solid catalysts featuring active sites derived from molecular nickel(II) bipyridine ethylene oligomerization catalysts have been synthesized through the post-synthetic metalation of the metal–organic frameworks  $Zr_6O_4(OH)_4(bpydc)_6$  and  $Zr_6O_4(OH)_4(bpydc)_{0.84}(bpdc)_{5.16}$  using  $Ni(DME)Br_2$ . The pore environment in these materials substantially alters the reactivity of the nickel(II) bipyridine active sites. Specifically,  $Ni^{II}$ -metalated  $Zr_6O_4(OH)_4(bpydc)_6$  produces considerable amounts of polymer, which contrasts with the selectivity of molecular analogs for oligomers. This unexpected reactivity is ascribed to steric bulk from nearby linker– $NiBr_2$  complexes that block sites axial to the nickel(II) centers, thereby mimicking the steric environment found in molecular nickel(II)  $\alpha$ -diimine polymerization catalysts. Relieving the steric congestion around the active sites by dispersing the nickel(II) bipyridine complexes within the mixed-linker framework  $Zr_6O_4(OH)_4(bpydc)_{0.84}(bpdc)_{5.16}$ , leads to significantly greater activity and higher selectivity for oligomer formation. Furthermore, both  $Ni^{II}$ -metalated frameworks exhibit increased selectivity for  $C_{4-10}$  oligomers, giving rise to deviations from the expected Schulz–Flory product distribution. The results of key control experiments show, however, that the combined activity of the nickel(II)–bipyridine complexes and adventitious nickel sites partly account for this unusual product distribution. While confinement effects may still contribute to selectivity for shorter oligomers in these frameworks, the presence of two active sites severely complicates the study of such effects. Altogether, these results serve to emphasize that the apparent active site structure does not necessarily solely dictate reactivity in metal–organic frameworks, as well as that the pore environment around these sites can have profound influences on catalytic behavior.

## 5.5. Acknowledgements

The work was supported by the Nanoporous Materials Genome Center, funded by the U.S. Department of Energy, Office of Basic Energy Sciences, Division of Chemical Sciences, Geosciences and Biosciences, under Award DE-FG02-12ER16362. Single-crystal X-ray diffraction experiments were conducted at Beamline 11.3.1 at the Advanced Light Source, which is supported by the Director, Office of Science, Office of Basic Energy Sciences, of the U.S. Department of Energy under Contract No. DE-AC02-05CH11231. We are grateful for the assistance of Kristen A. Colwell with SEM measurements. We thank Phillip J. Milner, Dianne J. Xiao, David Z. Zee, Jeffrey D. Martell, and Rebecca L. Siegelman for helpful discussions.

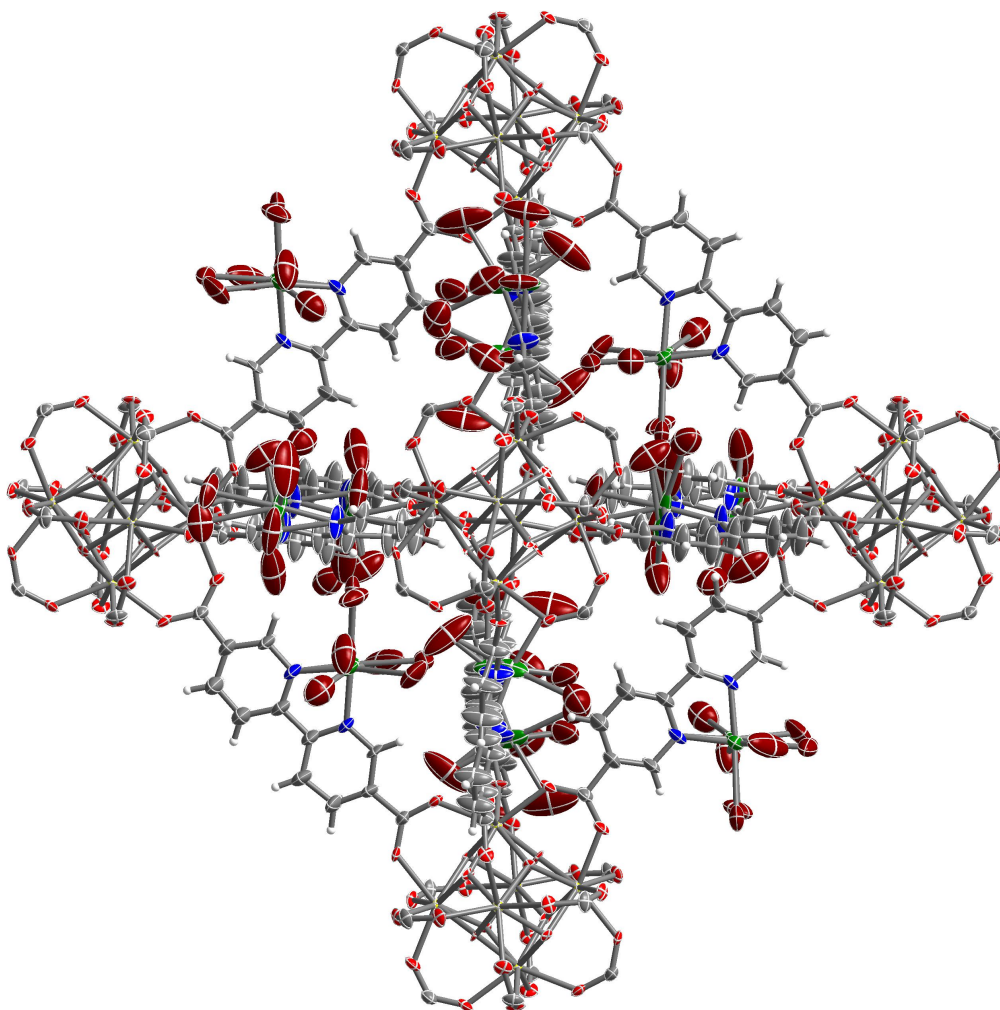
## 5.6. Supplementary Information

### 5.6.3. Single-Crystal X-ray Diffraction Data



	a	b	c	d			
occupancy	40%	occupancy	12%	occupancy	12%	occupancy	30%
Ni1A–N1	2.021(11) Å	Ni1A–N1	2.021(11) Å	Ni1A–N1	2.021(11) Å	Ni1B–N1	2.095(14) Å
Ni1A–N2	2.078(11) Å	Ni1A–N2	2.078(11) Å	Ni1A–N2	2.078(11) Å	Ni1B–N2	2.009(14) Å
Ni1A–Br1A	2.466(6) Å	Ni1A–Br1A	2.466(6) Å	Ni1A–Br4A	2.76(2) Å	Ni1A–Br1B	2.584(14) Å
Ni1A–Br2A	2.474(11) Å	Ni1A–Br3A	2.55(3) Å	Ni1A–Br5A	2.58(3)	Ni1A–Br2B	2.478(12)
Br1A–Ni1A–Br2A	94.8(3)°	Br1A–Ni1A–Br3A	86.2(6)°	Br4A–Ni1A–Br5A	118.4(8)°	Br1B–Ni1B–Br2B	95.7(5)°
Br1A–Ni1A–N2	80.0(4)°	Br1A–Ni1A–N2	80.0(4)°	Br4A–Ni1A–N2	89.3(5)°	Br1B–Ni1B–N1	90.4(6)°
Br2A–Ni1A–N1	96.8(4)°	Br3A–Ni1A–N1	84.0(7)°	Br5A–Ni1A–N1	95.0(7)°	Br1B–Ni1B–N2	82.5(5)°
Br2A–Ni1A–N2	82.4(5)°			Br5A–Ni1A–N2	95.8(7)°	Br2B–Ni1B–N1	81.7(5)°

**Figure 5.S1.** Structures and selected parameters of the (bpy)NiBr<sub>2</sub> complexes in Zr<sub>6</sub>O<sub>4</sub>(OH)<sub>4</sub>(bpydc)<sub>6</sub>(NiBr<sub>2</sub>)<sub>5.64</sub> at 100 K as determined by single-crystal X-ray diffraction; green, dark red, blue, and gray spheres represent Ni, Br, N, and C atoms, respectively. The Ni<sup>II</sup> centers are disordered over two positions. One position (Ni1A) is assigned to have pseudo-octahedral (a and b) and square pyramidal (c) geometries, while the other position (Ni1B) is pseudo-octahedral (d). Coordinating solvent molecules that complete the nickel coordination spheres could not be resolved, due to disorder and weak scattering compared to the Br<sup>-</sup> ligands. Hydrogen atoms are omitted for clarity.



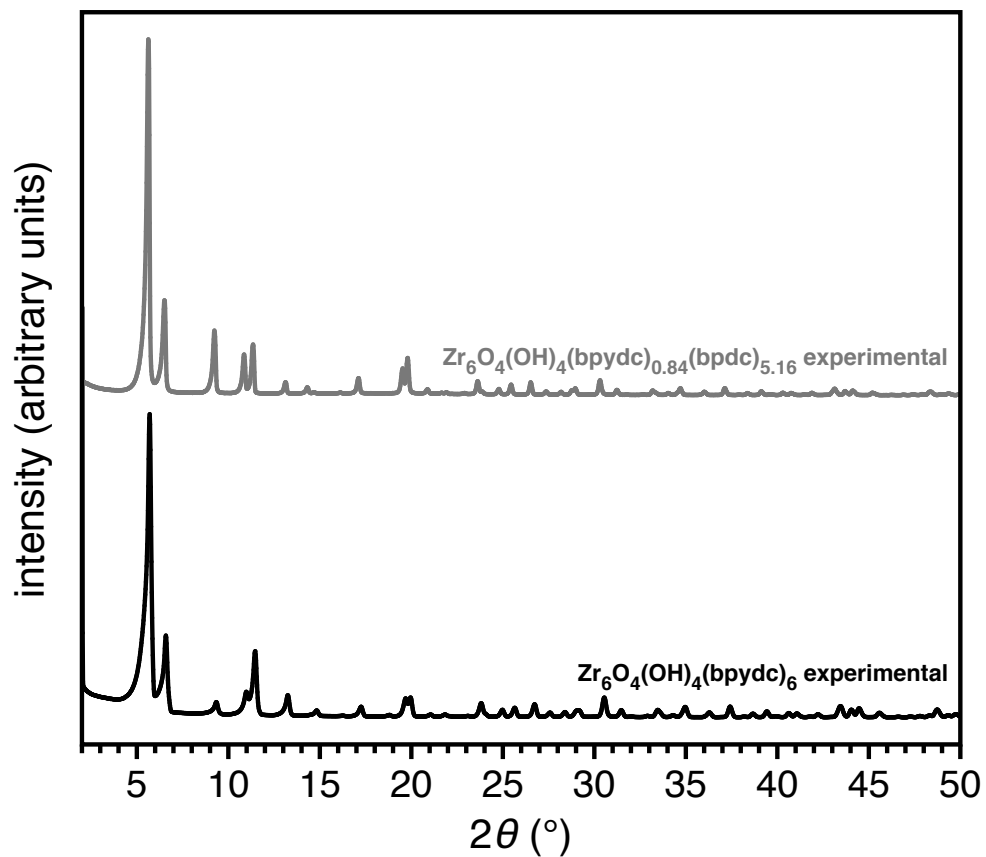
**Figure 5.S2.** Thermal ellipsoid plot of  $\text{Zr}_6\text{O}_4(\text{OH})_4(\text{bpydc})_6(\text{NiBr}_2)_{5.64}$  at 100 K drawn at 50% probability level as determined by single-crystal X-ray diffraction; yellow, green, dark red, red, blue, gray, and white ellipsoids represent Zr, Ni, Br, O, N, C, and H atoms, respectively.

**Table 5.S1.** Crystallographic Data for  $Zr_6O_4(OH)_4(bpydc)_6(NiBr_2)_{5.64}$ **Figure S1.**

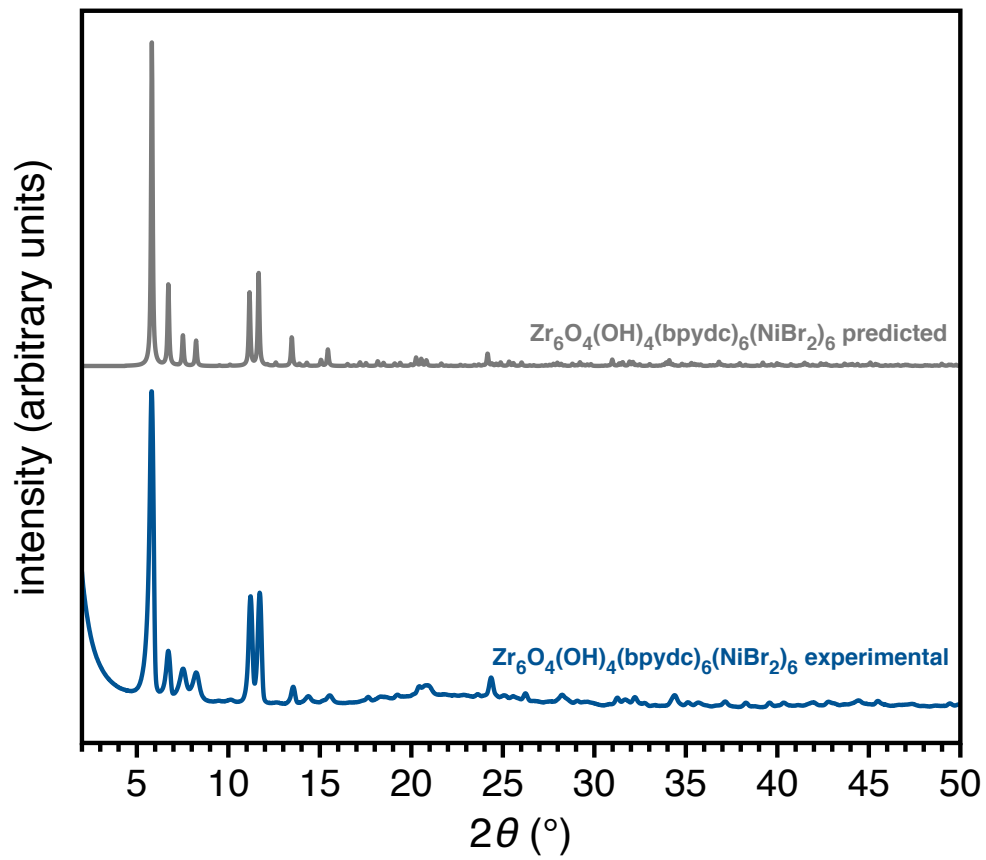
Formula	$Zr_6O_{30.56}C_{67.68}N_{11.28}H_{33.84}Ni_{5.64}Br_{11.28}$
Temperature (K)	100(2)
Crystal System	Cubic
Space Group	$Pa\bar{3}$
$a, b, c$ (Å)	26.2758(8)
$\alpha, \beta, \gamma$ (°)	90
$V$ (Å <sup>3</sup> )	18141.3(17)
$Z$	4
Radiation, $\lambda$ (Å)	Synchrotron, 0.8856
$2\theta$ Range for Data Collection (°)	4.320 to 59.612
Completeness to $2\theta$	100.0% ( $2\theta = 59.612^\circ$ )
Data / Restraints / Parameters	4662 / 705 / 278
Goodness of Fit on $F^2$	1.151
$R1^a, wR2^b$ ( $I > 2\sigma(I)$ )	0.0651, 0.2002
$R1^a, wR2^b$ (all data)	0.0715, 0.2046
Largest Diff. Peak and Hole (e Å <sup>-3</sup> )	1.044 and -0.677

$$^a R_1 = \frac{\sum ||F_o| - |F_c||}{\sum |F_o|}, \quad ^b wR_2 = \left\{ \frac{\sum [w(F_o^2 - F_c^2)^2]}{\sum [w(F_o^2)^2]} \right\}^{1/2}.$$

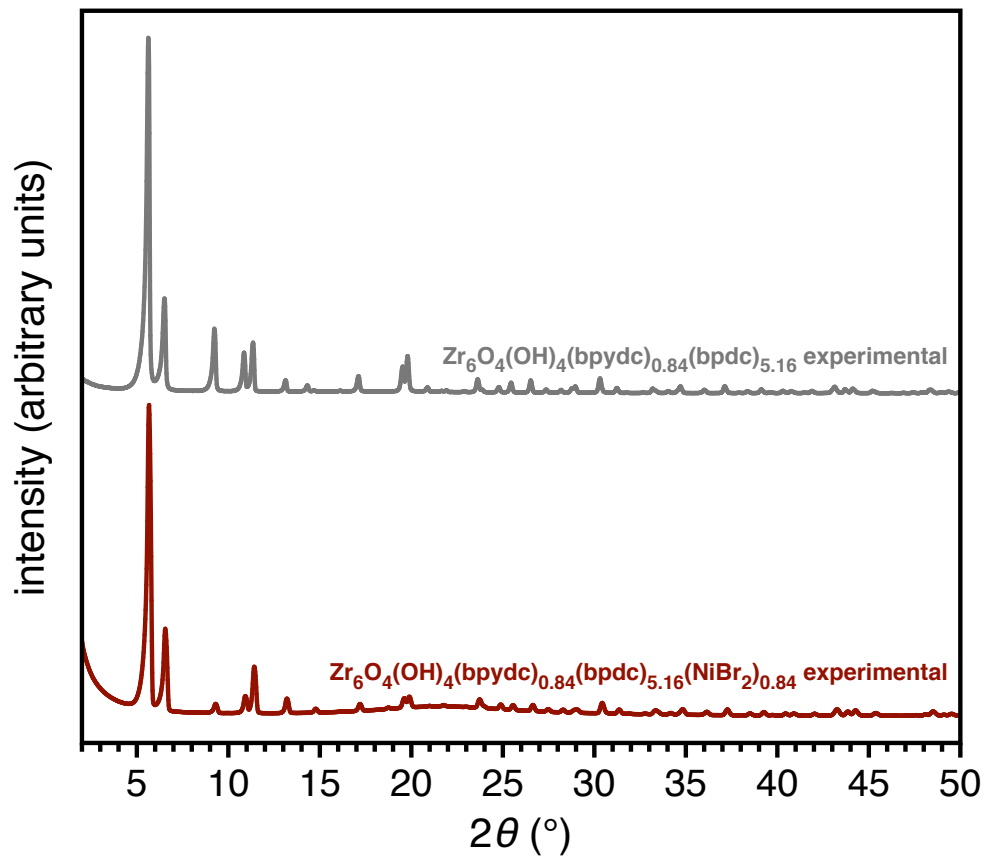
#### 5.6.4. Powder X-ray Diffraction Data



**Figure 5.S3.** Comparison of the powder X-ray diffraction patterns for  $\text{Zr}_6\text{O}_4(\text{OH})_4(\text{bpydc})_6$  (1; black) and  $\text{Zr}_6\text{O}_4(\text{OH})_4(\text{bpydc})_{0.84}(\text{bpdc})_{5.16}$  (2; light gray) at 298 K with a wavelength of 1.5418 Å.

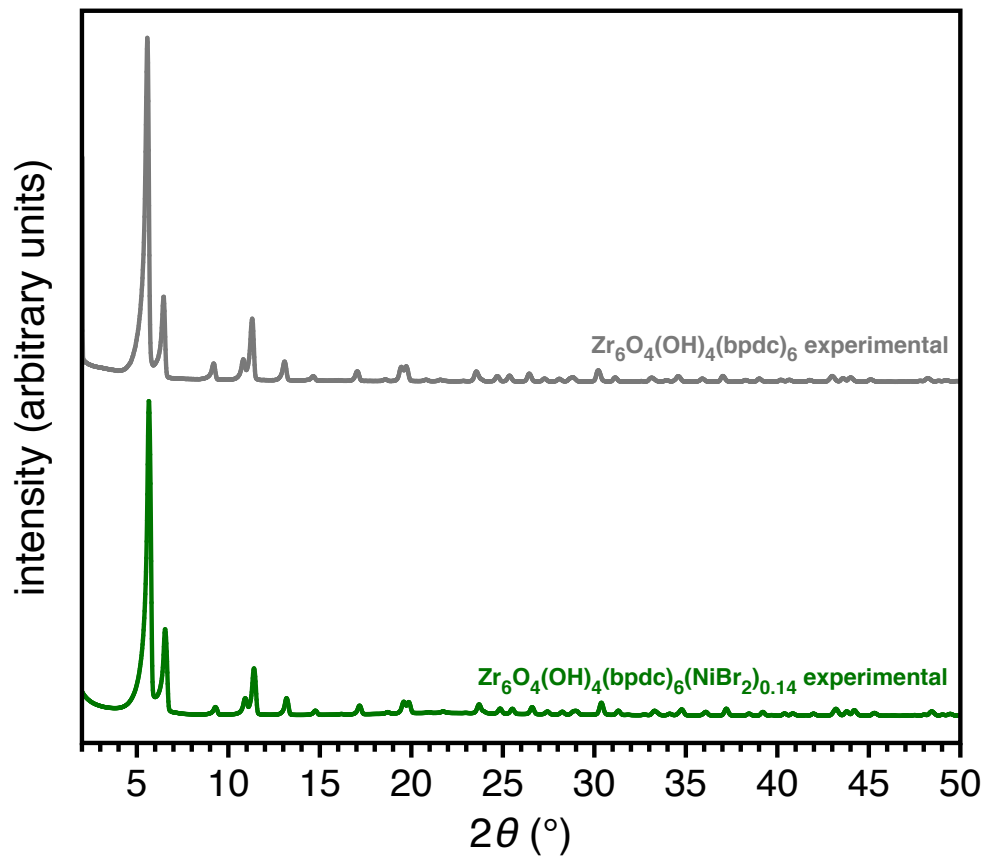


**Figure 5.S4.** Comparison of the predicted (light gray) and experimental (blue) powder X-ray diffraction patterns for  $\text{Zr}_6\text{O}_4(\text{OH})_4(\text{bpydc})_6(\text{NiBr}_2)_6$  (**1**( $\text{NiBr}_2$ )<sub>6</sub>) at 298 K with a wavelength of 1.5418 Å.

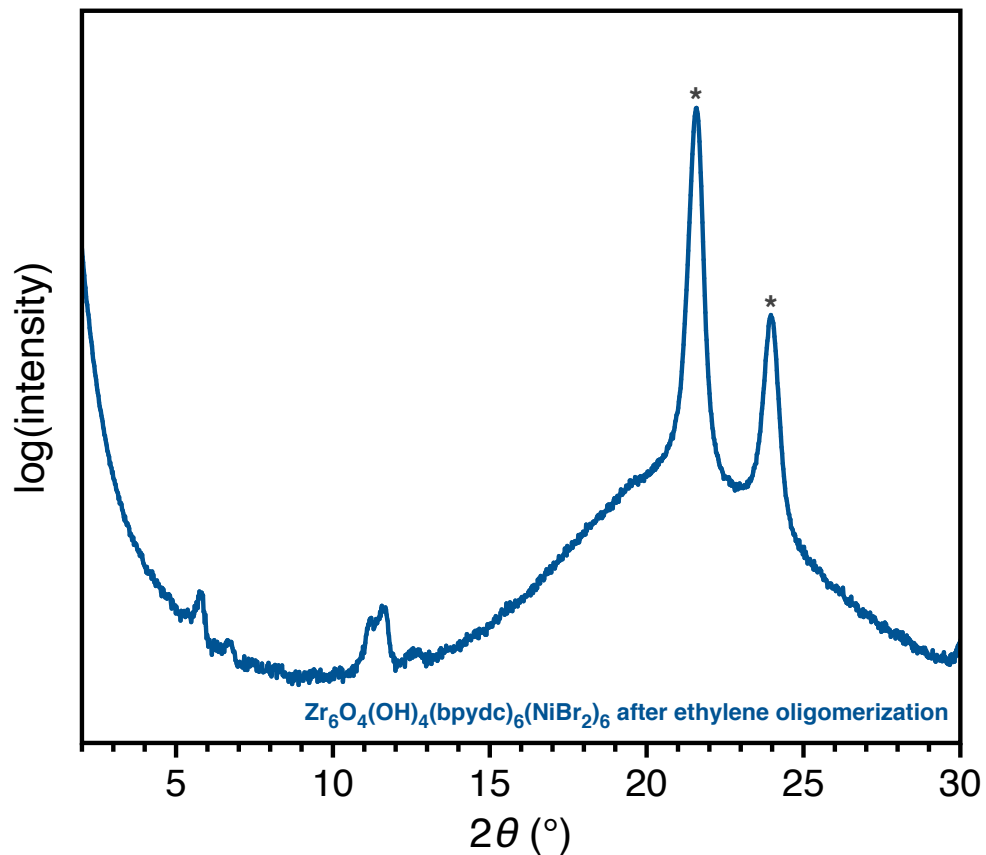


**Figure 5.S5.** Comparison of the powder X-ray diffraction patterns for  $\text{Zr}_6\text{O}_4(\text{OH})_4(\text{bpydc})_{0.84}(\text{bpdc})_{5.16}$  (**2**; light gray) and  $\text{Zr}_6\text{O}_4(\text{OH})_4(\text{bpydc})_{0.84}(\text{bpdc})_{5.16}(\text{NiBr}_2)_{0.84}$  (**2**(NiBr<sub>2</sub>)<sub>0.84</sub>; red) at 298 K with a wavelength of 1.5418 Å.

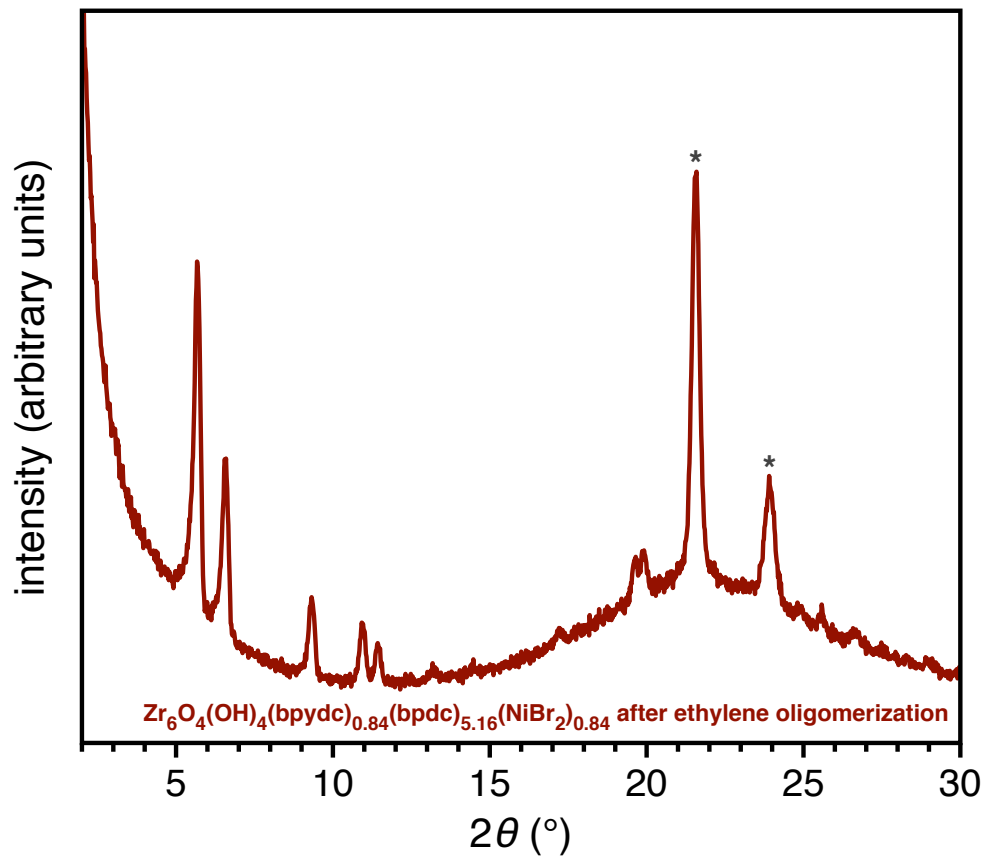




**Figure 5.S6.** Comparison of the powder X-ray diffraction patterns for  $\text{Zr}_6\text{O}_4(\text{OH})_4(\text{bpdc})_6$  (**3**; light gray) and  $\text{Zr}_6\text{O}_4(\text{OH})_4(\text{bpdc})_6(\text{NiBr}_2)_{0.14}$  (**3**(NiBr<sub>2</sub>)<sub>0.14</sub>; green) at 298 K with a wavelength of 1.5418 Å.



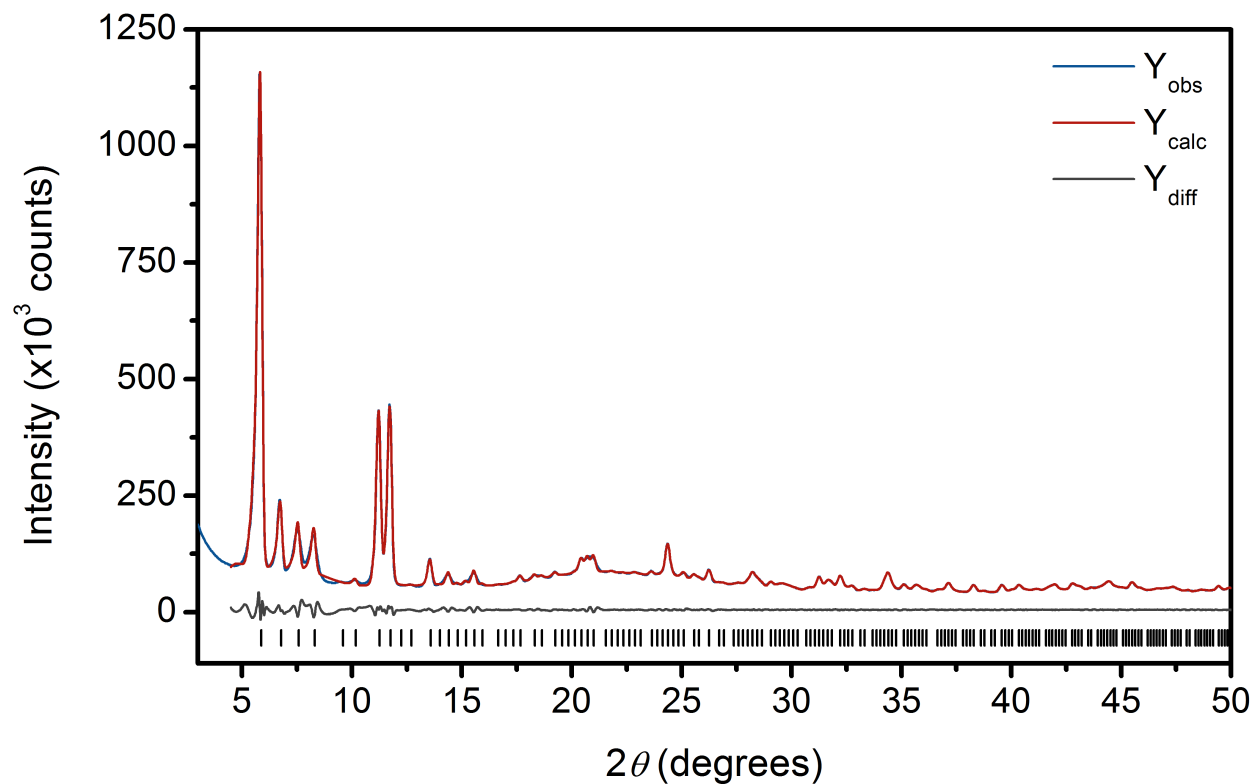
**Figure 5.S7.** Powder X-ray diffraction pattern (at 298 K) of the solid recovered from an ethylene oligomerization reaction with  $\text{Zr}_6\text{O}_4(\text{OH})_4(\text{bpydc})_6(\text{NiBr}_2)_6$  (**1**( $\text{NiBr}_2$ )<sub>6</sub>; blue) taken at 298 K with a wavelength of 1.5418 Å. Peaks corresponding to polyethylene are marked by gray asterisks. Note that the intensity is plotted on a logarithmic scale because the metal–organic framework was found to be embedded in a considerable amount of polyethylene (~5 mg metal–organic framework in 1 g of polyethylene).



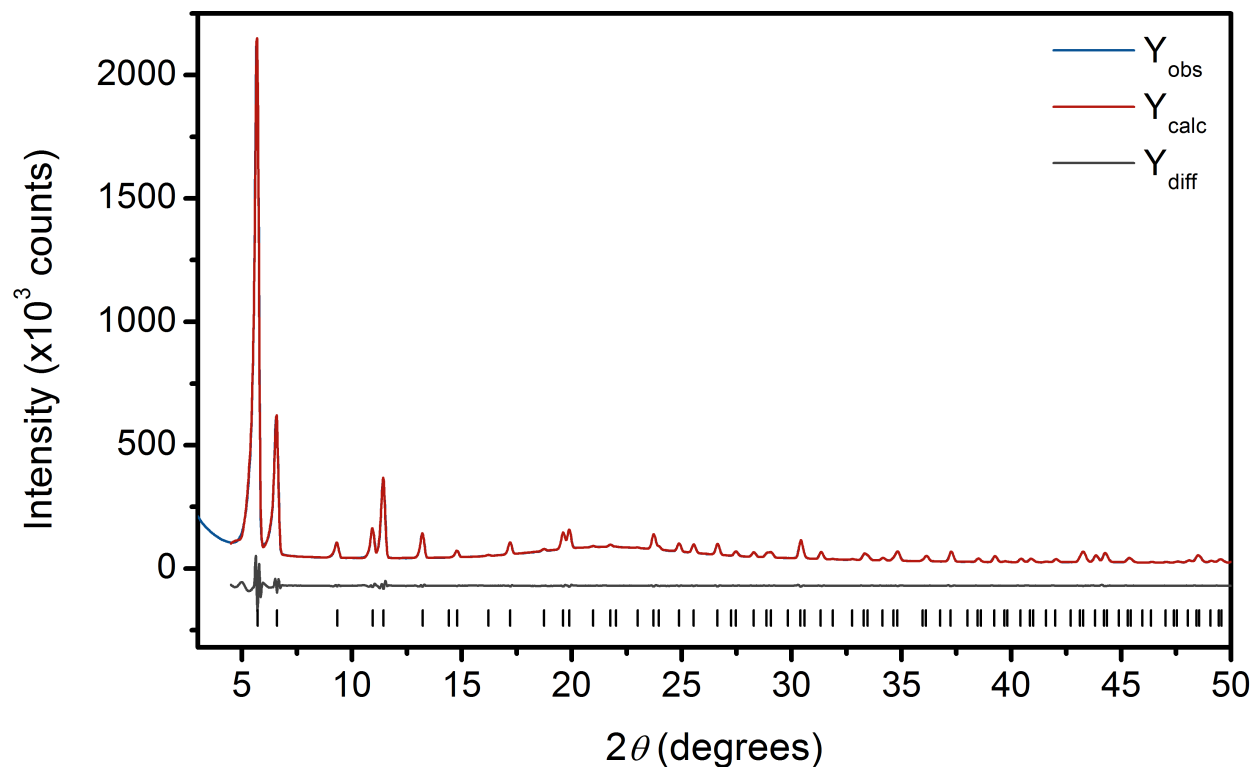
**Figure 5.S8.** Powder X-ray diffraction pattern of the solid recovered from an ethylene oligomerization reaction with  $\text{Zr}_6\text{O}_4(\text{OH})_4(\text{bpydc})_{0.84}(\text{bpdc})_{5.16}(\text{NiBr}_2)_{0.84}$  ( $\mathbf{2}(\text{NiBr}_2)_{0.84}$ ; red) taken at 298 K with a wavelength of 1.5418 Å. Peaks corresponding to polyethylene are marked by gray asterisks.

**Table 5.S2.** Unit cell parameters determined *via* Pawley fitting of powder X-ray diffraction data.

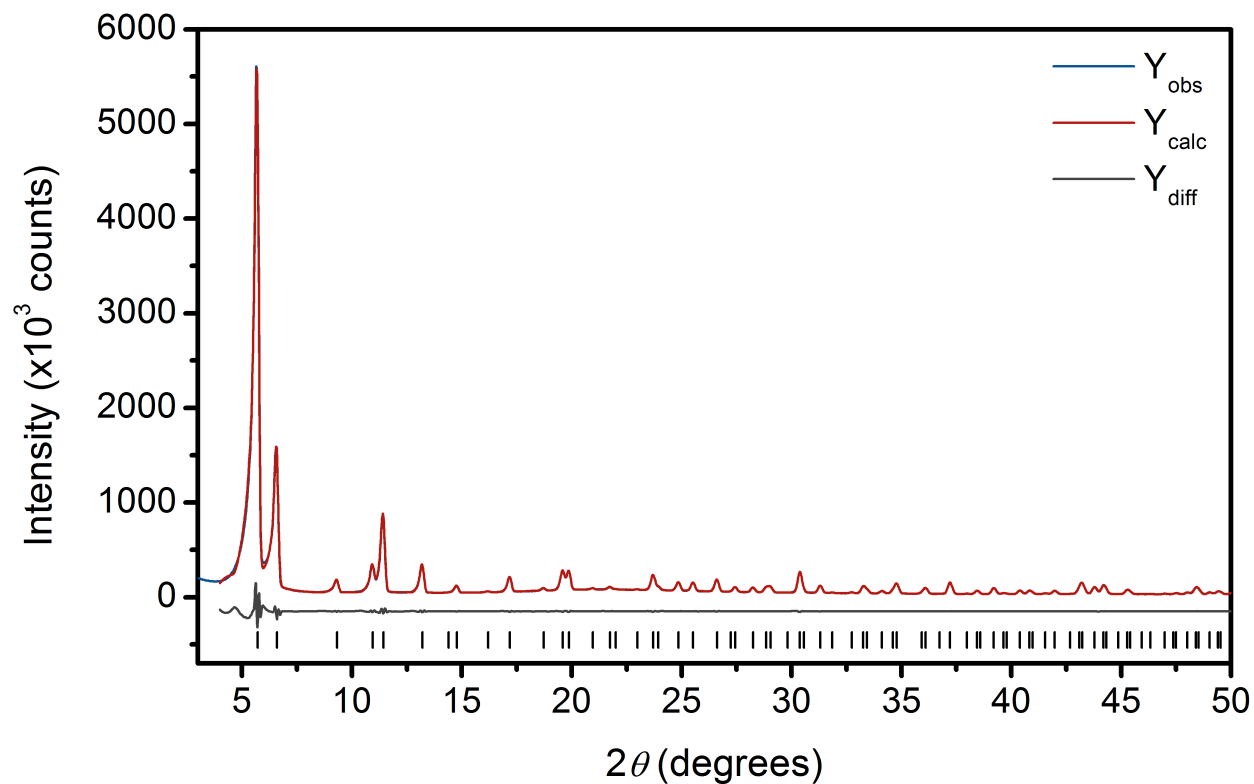
	<b>1(NiBr<sub>2</sub>)<sub>6</sub></b>	<b>2(NiBr<sub>2</sub>)<sub>0.84</sub></b>	<b>3(NiBr<sub>2</sub>)<sub>0.14</sub></b>
Space group	<i>Pa</i> $\bar{3}$	<i>Fm</i> $\bar{3}m$	<i>Fm</i> $\bar{3}m$
<i>a</i> (Å)	26.048(2)	26.7418(6)	26.7836(6)
<i>V</i> (Å <sup>3</sup> )	17674(4)	19123.7(14)	19213.4(12)
<i>R</i> <sub>exp</sub>	0.310	0.364	0.266
<i>R</i> <sub>wp</sub>	3.280	3.068	3.743
<i>R</i> <sub>p</sub>	1.933	2.028	2.639
Wavelength (Å)	1.5418	1.5418	1.5418
Temperature (K)	298	298	298



**Figure 5.S9.** Pawley refinement of  $1(\text{NiBr}_2)_6$  from  $2^\circ$  to  $50^\circ$ , as implemented by TOPAS-Academic.<sup>56</sup> The experimental powder pattern of  $1(\text{NiBr}_2)_6$  was taken on a Bruker D8 Advance powder X-ray diffractometer at 298 K with a wavelength of 1.5418 Å. Blue, red, and gray lines represent experimental data, calculated fits, and the difference between the two, respectively; black tick marks represent calculated Bragg peak positions. The broad hump observed at approximately  $20\text{--}25^\circ$  is due to diffuse scattering of the borosilicate capillary the sample was packed into.

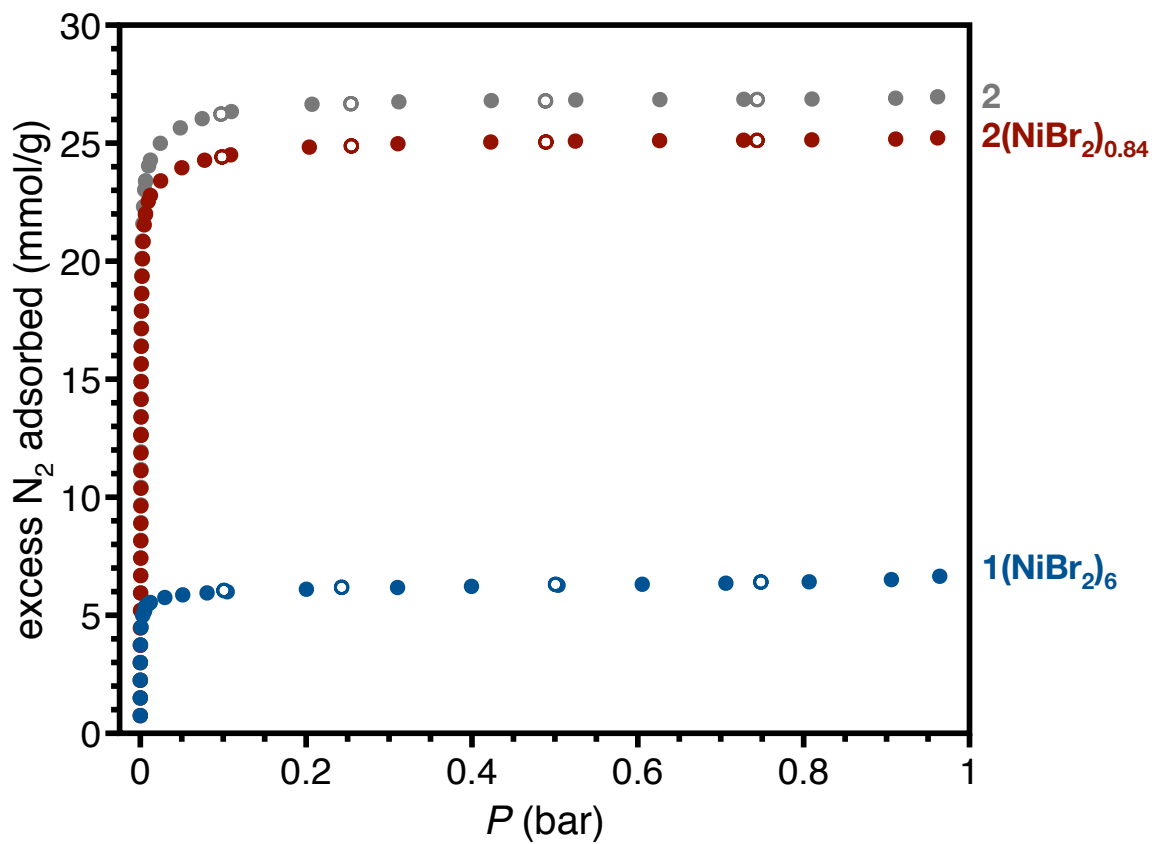


**Figure 5.S10.** Pawley refinement of  $2(\text{NiBr}_2)_{0.84}$  from  $2^\circ$  to  $50^\circ$ , as implemented by TOPAS-Academic.<sup>56</sup> The experimental powder pattern of  $2(\text{NiBr}_2)_{0.84}$  was taken on a Bruker D8 Advance powder X-ray diffractometer at 298 K with a wavelength of 1.5418 Å. Blue, red, and gray lines represent experimental data, calculated fits, and the difference between the two, respectively; black tick marks represent calculated Bragg peak positions. The broad hump observed at approximately  $20\text{--}25^\circ$  is due to diffuse scattering of the borosilicate capillary the sample was packed into.



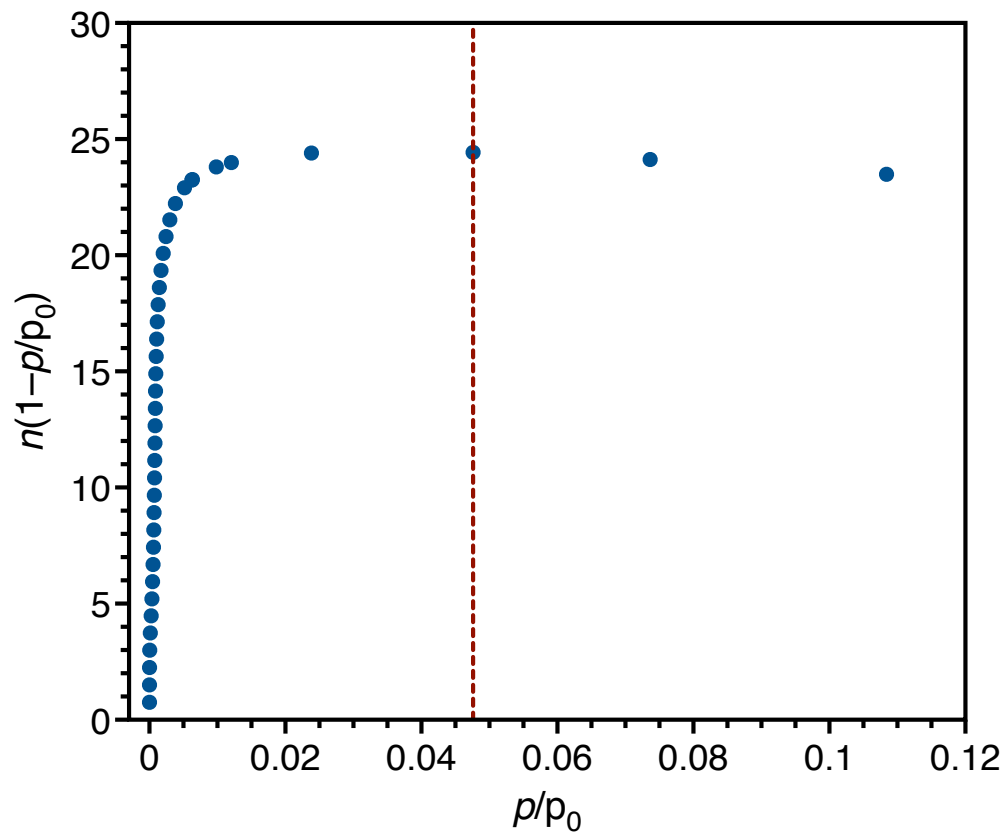
**Figure 5.S11.** Pawley refinement of  $3(\text{NiBr}_2)_{0.14}$  from  $2^\circ$  to  $50^\circ$ , as implemented by TOPAS-Academic.<sup>56</sup> The experimental powder pattern of  $3(\text{NiBr}_2)_{0.14}$  was taken on a Bruker D8 Advance powder X-ray diffractometer at 298 K with a wavelength of 1.5418 Å. Blue, red, and gray lines represent experimental data, calculated fits, and the difference between the two, respectively; black tick marks represent calculated Bragg peak positions. The broad hump observed at approximately  $20\text{--}25^\circ$  is due to diffuse scattering of the borosilicate capillary the sample was packed into.

### 5.6.5. Low-pressure Gas Adsorption Isotherms

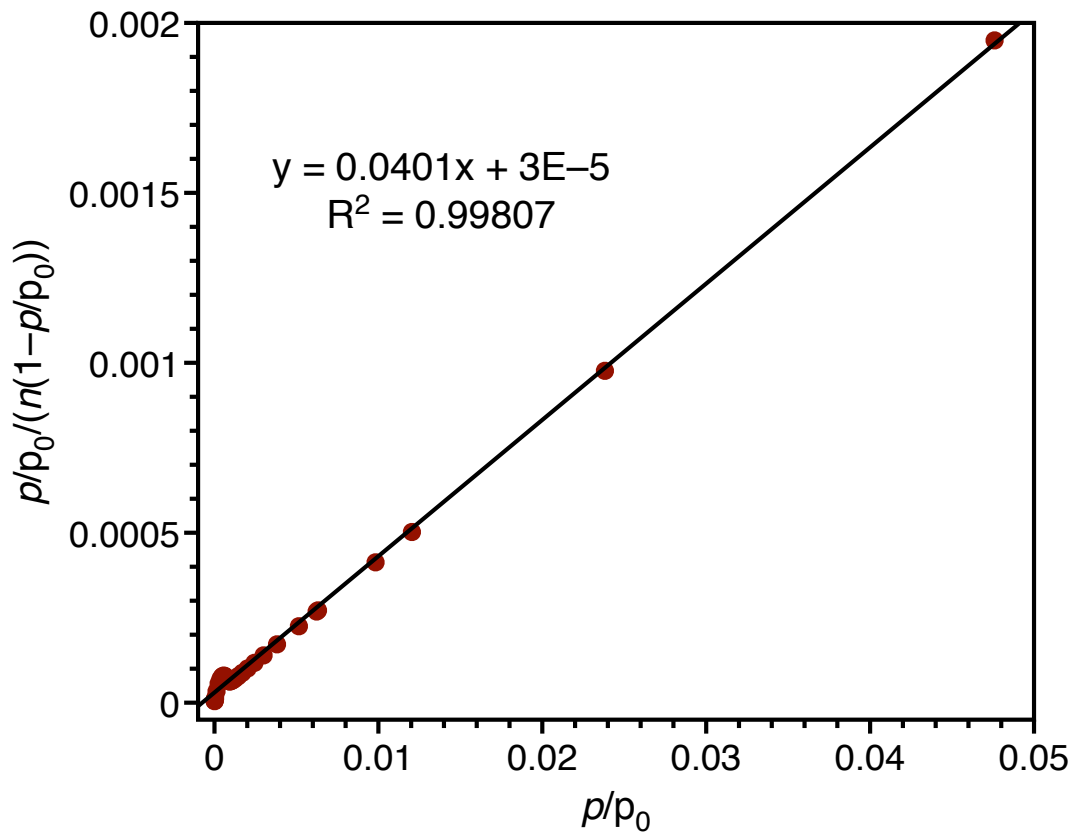


**Figure 5.S12.** Low-pressure N<sub>2</sub> adsorption isotherms for 2, 2(NiBr<sub>2</sub>)<sub>0.84</sub>, and 1(NiBr<sub>2</sub>)<sub>6</sub> at 77 K. Filled circles represent adsorption, while open circles represent desorption.

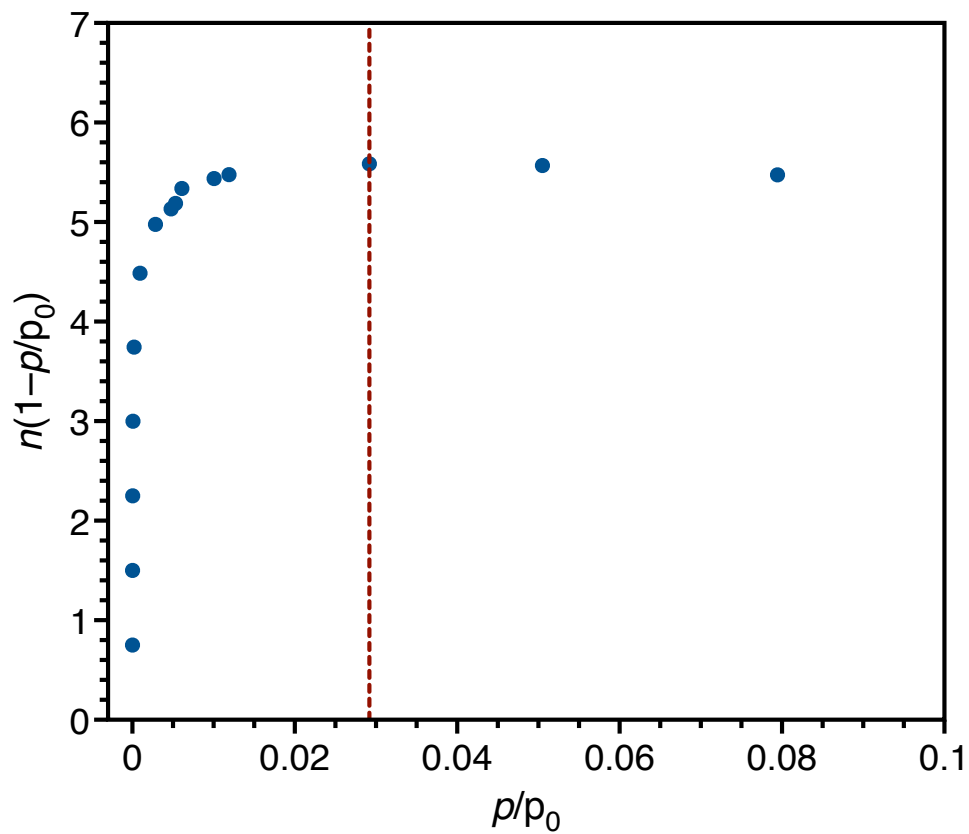




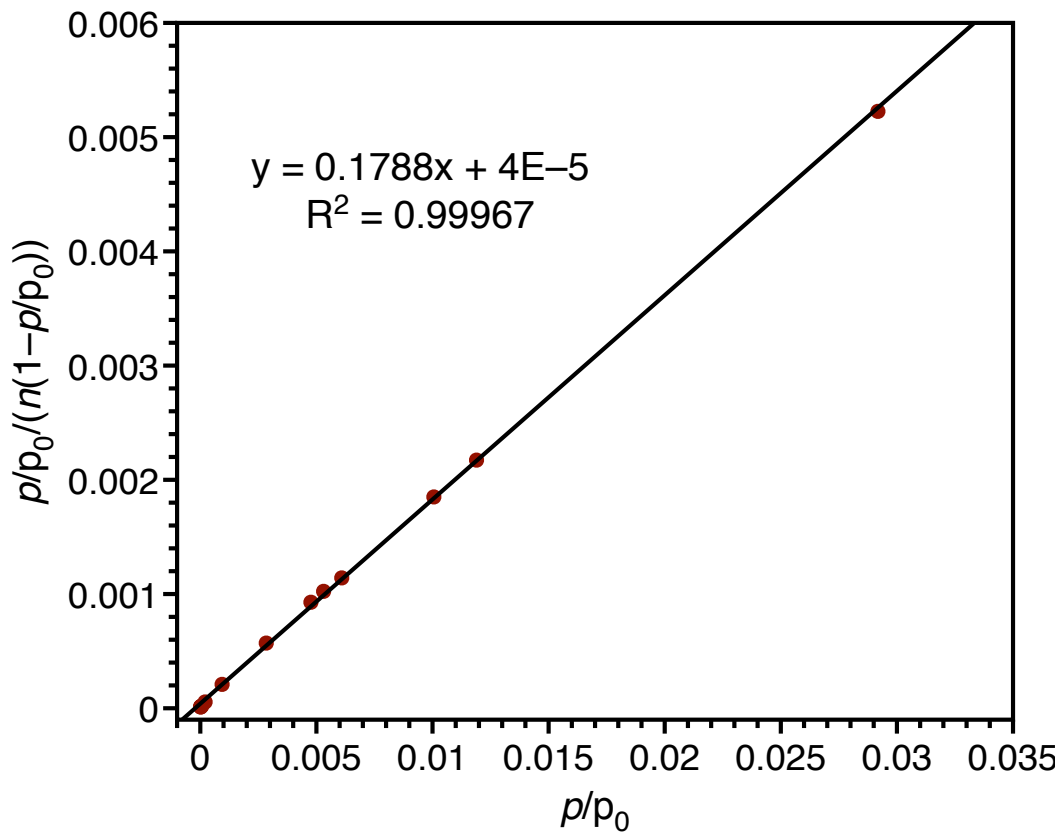
**Figure 5.S13.** Plot of  $n(1-p/p_0)$  vs.  $p/p_0$  for **2** to determine the maximum  $p/p_0$  used in the BET linear fit according to the first BET consistency criterion.<sup>65</sup>



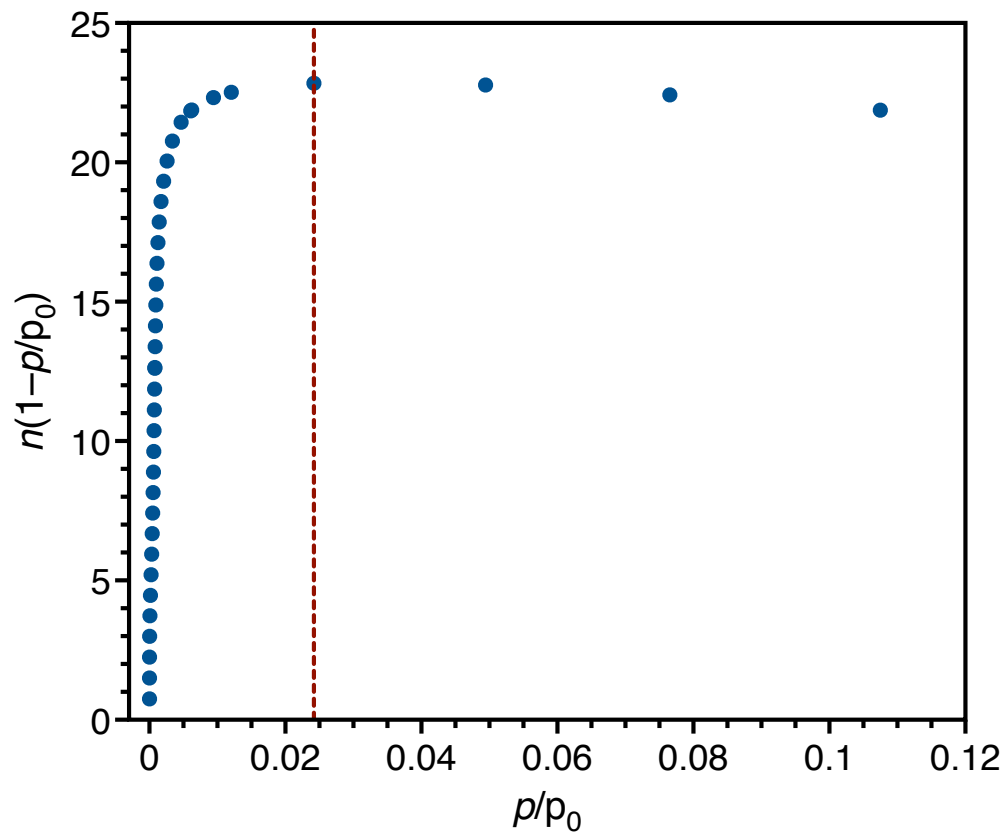
**Figure 5.S14.** Plot of  $p/p_0/(n(1-p/p_0))$  vs.  $p/p_0$  for **2** to determine the BET surface area.<sup>65</sup> The slope of the best fit line for  $p/p_0 < 0.03$  is 0.0401, and the y-intercept is  $3 \times 10^{-5}$ , which satisfies the second BET consistency criterion. This results in a saturation capacity of 24.9 mmol/g and a BET surface area of  $2430 \pm 20 \text{ m}^2/\text{g}$ .



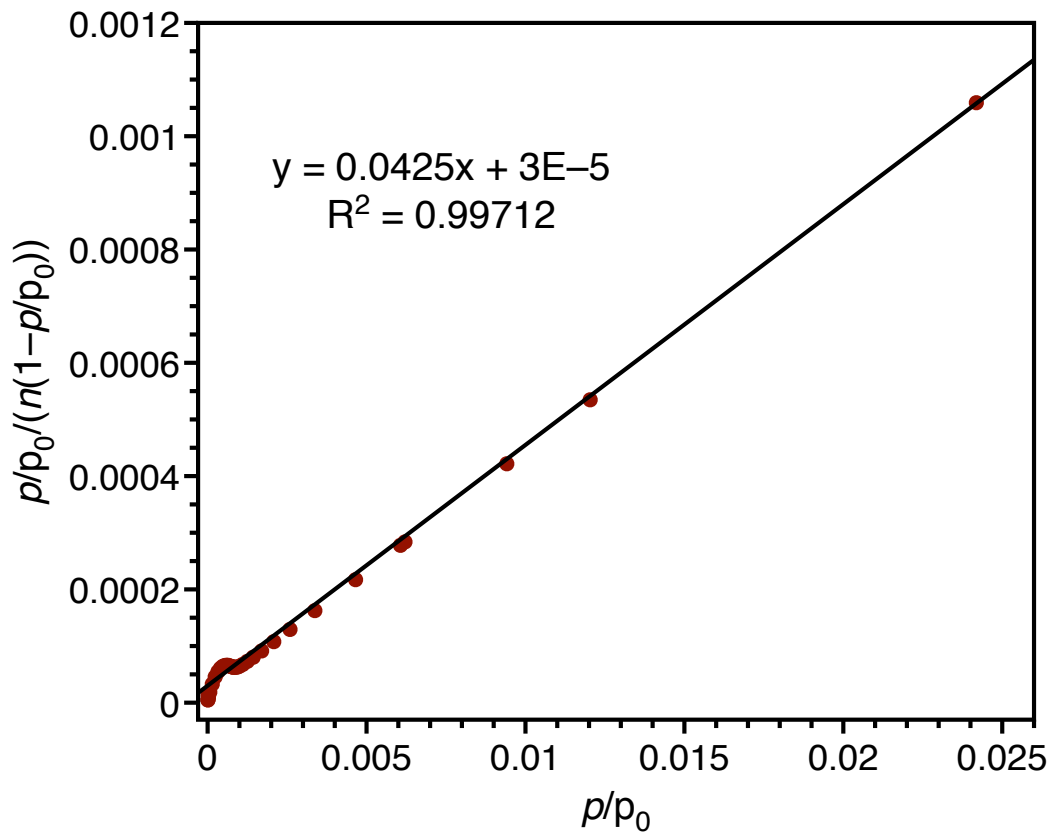
**Figure 5.S15.** Plot of  $n(1-p/p_0)$  vs.  $p/p_0$  for  $\mathbf{1}(\text{NiBr}_2)_6$  to determine the maximum  $p/p_0$  used in the BET linear fit according to the first BET consistency criterion.<sup>65</sup>



**Figure 5.S16.** Plot of  $p/p_0/(n(1-p/p_0))$  vs.  $p/p_0$  for  $1(\text{NiBr}_2)_6$  to determine the BET surface area.<sup>65</sup> The slope of the best fit line for  $p/p_0 < 0.03$  is 0.1788, and the y-intercept is  $4 \times 10^{-5}$ , which satisfies the second BET consistency criterion. This results in a saturation capacity of 5.6 mmol/g and a BET surface area of  $545 \pm 3 \text{ m}^2/\text{g}$ .

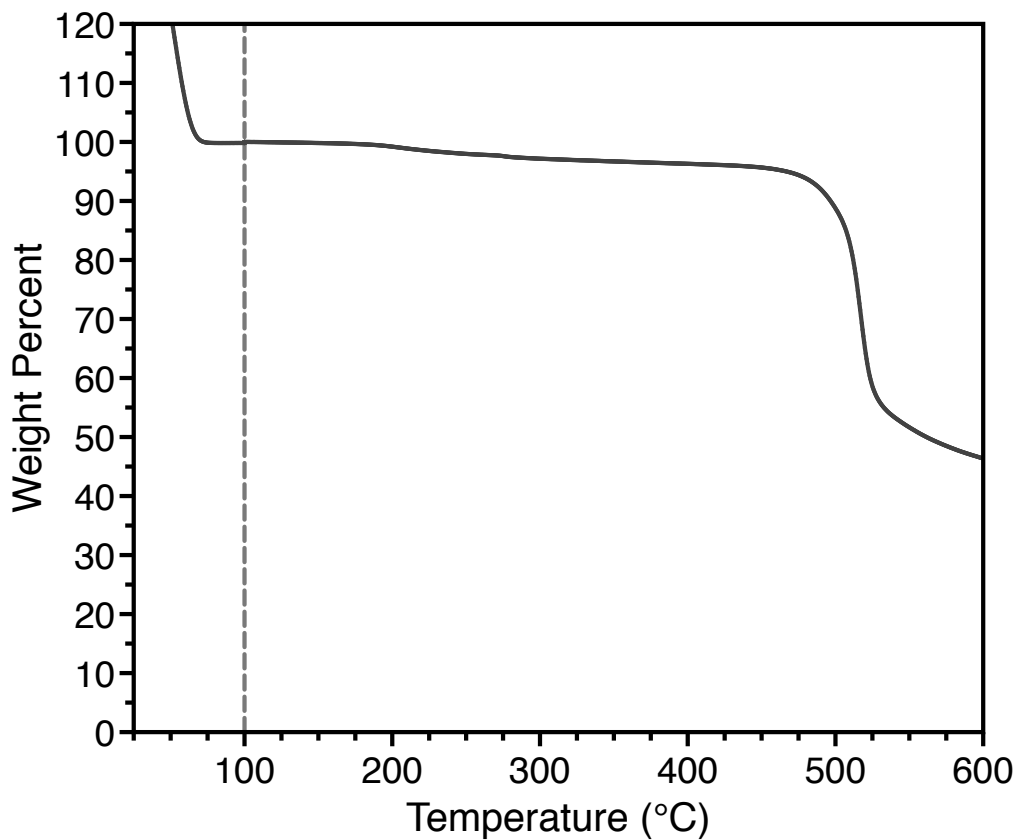


**Figure 5.S17.** Plot of  $n(1-p/p_0)$  vs.  $p/p_0$  for  $2(\text{NiBr}_2)_{0.84}$  to determine the maximum  $p/p_0$  used in the BET linear fit according to the first BET consistency criterion.<sup>65</sup>

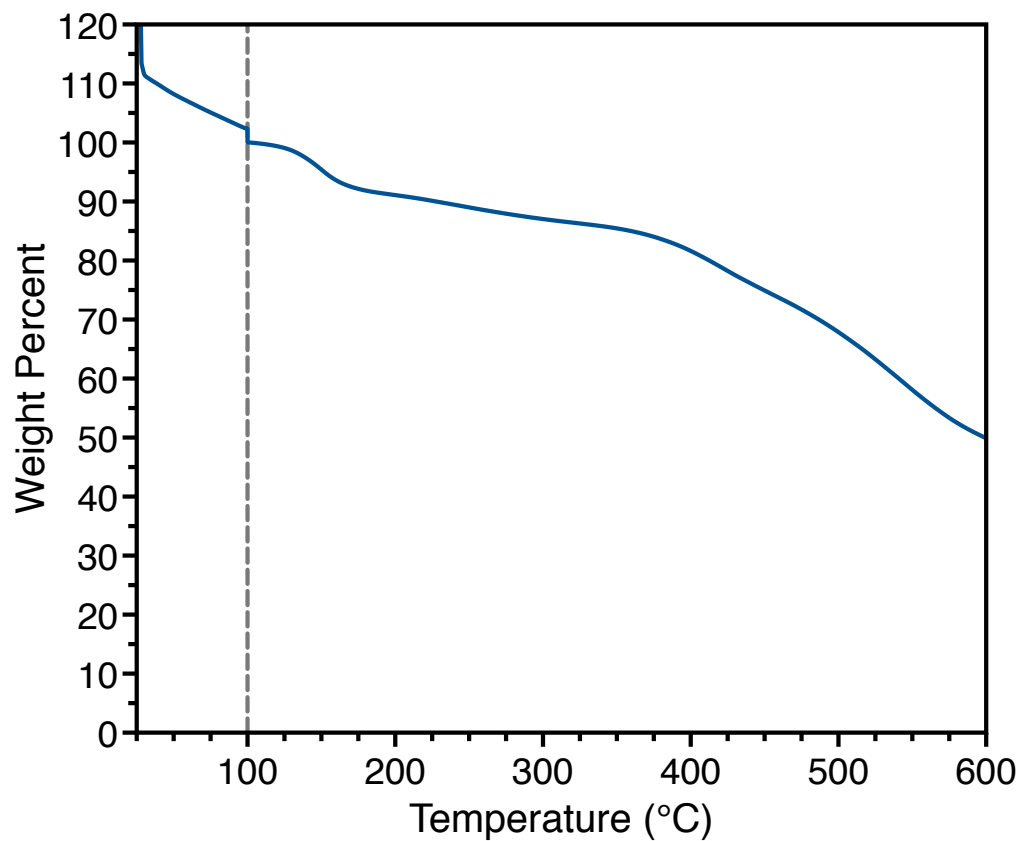


**Figure 5.S18.** Plot of  $p/p_0/(n(1-p/p_0))$  vs.  $p/p_0$  for  $2(\text{NiBr}_2)_{0.84}$  to determine the BET surface area.<sup>65</sup> The slope of the best fit line for  $p/p_0 < 0.03$  is 0.0425, and the y-intercept is  $3 \times 10^{-5}$ , which satisfies the second BET consistency criterion. This results in a saturation capacity of 23.5 mmol/g and a BET surface area of  $2300 \pm 20 \text{ m}^2/\text{g}$ .

### 5.6.6. Thermogravimetric Analyses

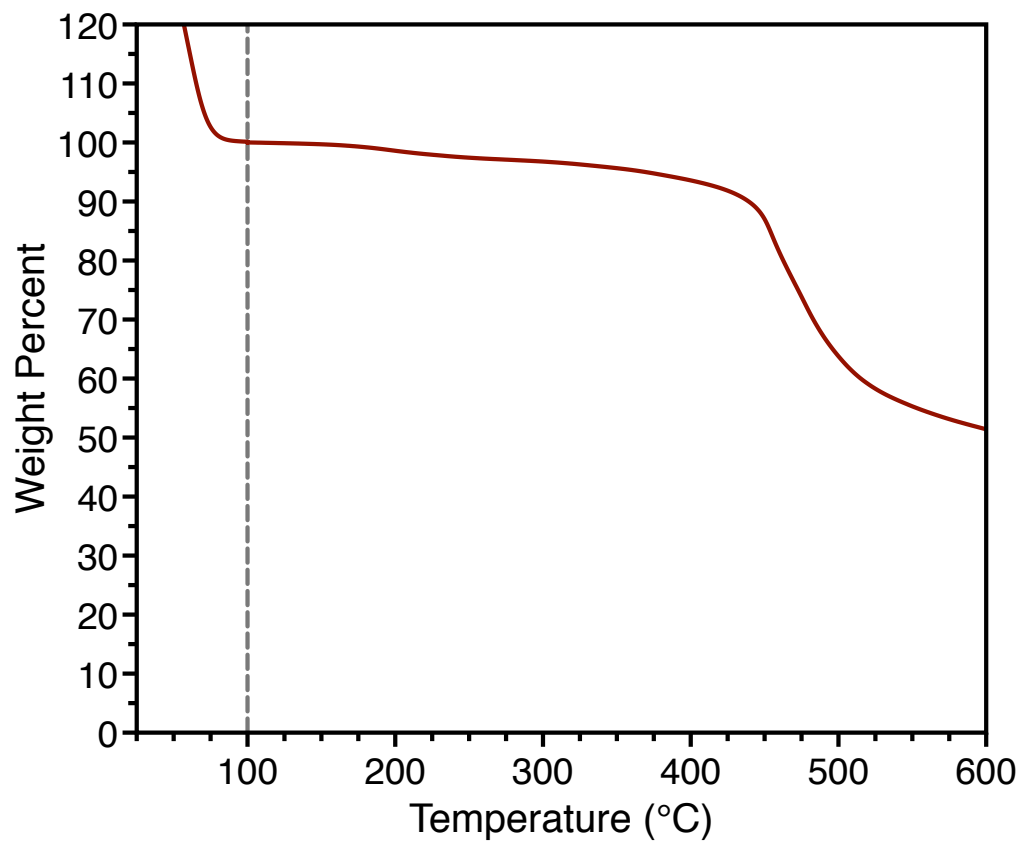


**Figure 5.S19.** Thermogravimetric analysis of a slurry of **2** in n-hexane. The sample was heated at a ramp rate of 1 °C/min. to 100 °C, then held at this temperature for 1 hour (dashed gray line) to evaporate any remaining n-hexane. The sample was then heated at a ramp rate of 1 °C/min. to 600 °C.



**Figure 5.S20.** Thermogravimetric analysis of a slurry of  $1(\text{NiBr}_2)_6$  in n-hexane. The sample was heated at a ramp rate of  $1\text{ }^\circ\text{C}/\text{min.}$  to  $100\text{ }^\circ\text{C}$ , then held at this temperature for 1 hour (dashed gray line) to evaporate any remaining n-hexane. The sample was then heated at a ramp rate of  $1\text{ }^\circ\text{C}/\text{min.}$  to  $600\text{ }^\circ\text{C}$ .





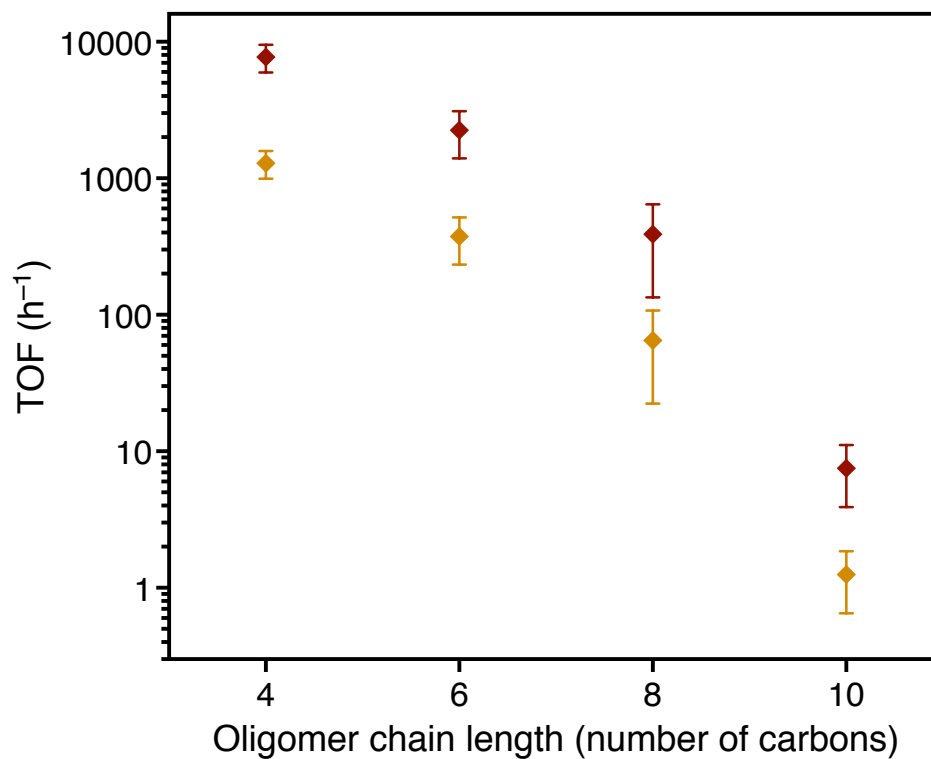
**Figure 5.S21.** Thermogravimetric analysis of a slurry of  $2(\text{NiBr}_2)_{0.84}$  in n-hexane. The sample was heated at a ramp rate of  $1\text{ }^\circ\text{C}/\text{min.}$  to  $100\text{ }^\circ\text{C}$ , then held at this temperature for 1 hour (dashed gray line) to evaporate any remaining n-hexane. The sample was then heated at a ramp rate of  $1\text{ }^\circ\text{C}/\text{min.}$  to  $600\text{ }^\circ\text{C}$ .

### 5.6.7. Ethylene Oligomerization Data

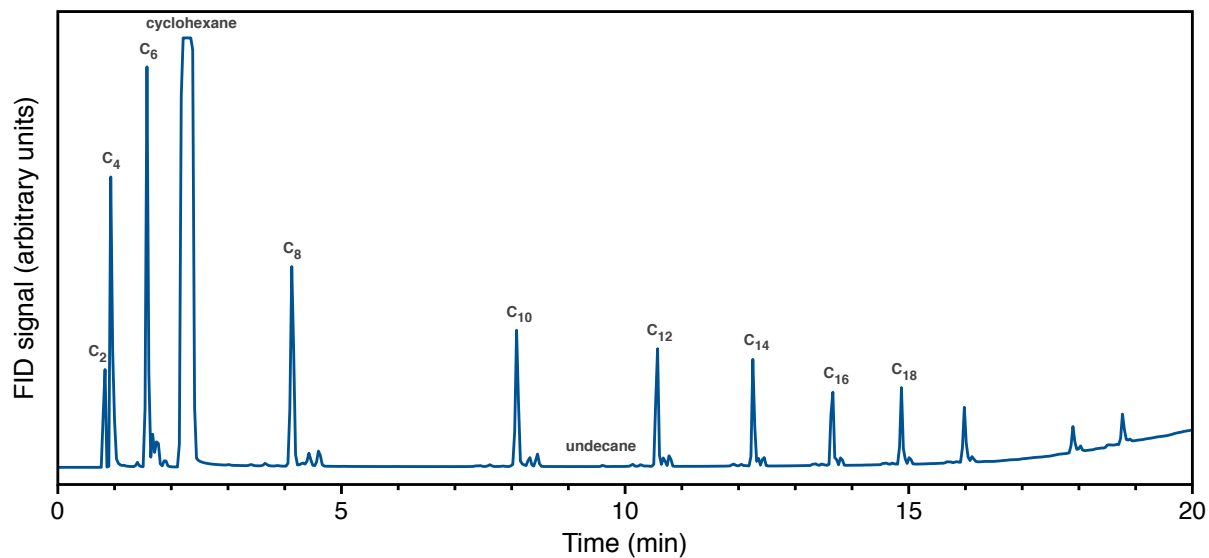
**Table 5.S3.** Amount of C<sub>4-18</sub> oligomers produced from ethylene oligomerization reactions catalyzed by 1·(NiBr<sub>2</sub>)<sub>6</sub>, 2·(NiBr<sub>2</sub>)<sub>6</sub>, and 3·(NiBr<sub>2</sub>)<sub>0.14</sub>.

ethylene oligomer	1·(NiBr <sub>2</sub> ) <sub>6</sub>		2·(NiBr <sub>2</sub> ) <sub>0.84</sub>		3·(NiBr <sub>2</sub> ) <sub>0.14</sub>	
	mol% <sup>a</sup>	wt%	mol% <sup>a</sup>	wt%	mol% <sup>a</sup>	wt%
C <sub>4</sub>	37(4)	5.0(9)	77(9)	48(6)	75(8)	60(10)
C <sub>6</sub>	28.2(8)	5.7(4)	19(7)	18(7)	21(6)	30(10)
C <sub>8</sub>	14(2)	3.8(2)	3(2)	4(2)	4(2)	6(4)
C <sub>10</sub>	7.5(1)	2.5(2)	0.8(4)	1.3(6)	0.10(3)	0.2(1)
C <sub>12</sub>	5.1(5)	2.1(2)	0.30(1)	0.57(3)		
C <sub>14</sub>	3.6(3)	1.7(1)	0.19(2)	0.41(1)		
C <sub>16</sub>	2.6(3)	1.4(1)	0.11(3)	0.3(1)		
C <sub>18</sub>	2.0(2)	1.2(1)	0.06(3)	0.2(1)		

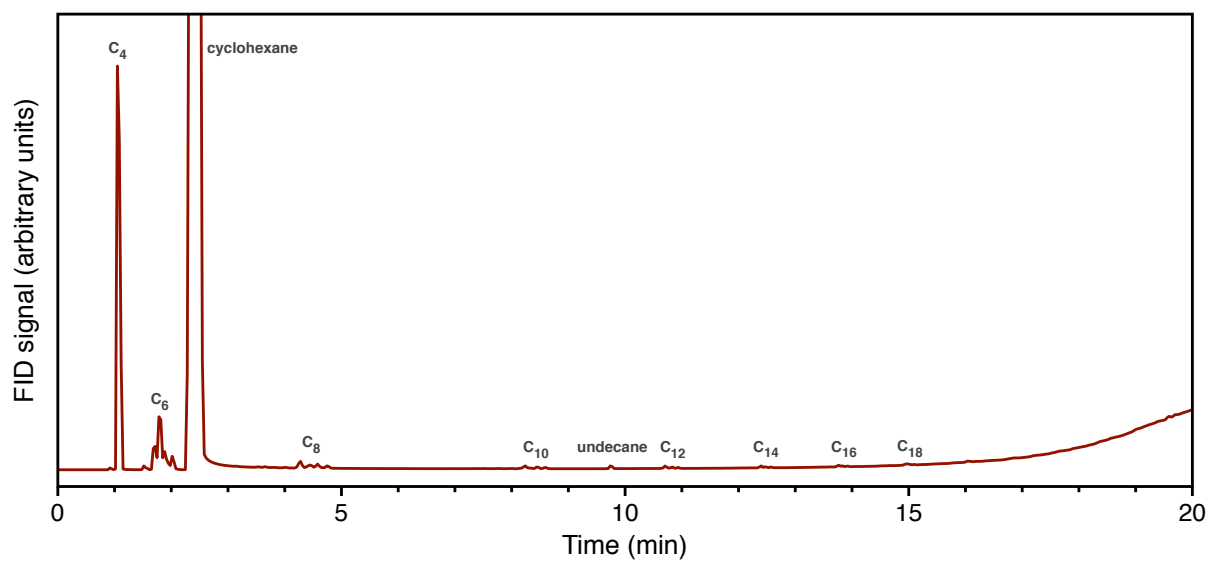
<sup>a</sup>Calculated for the C<sub>4-18</sub> product fraction.



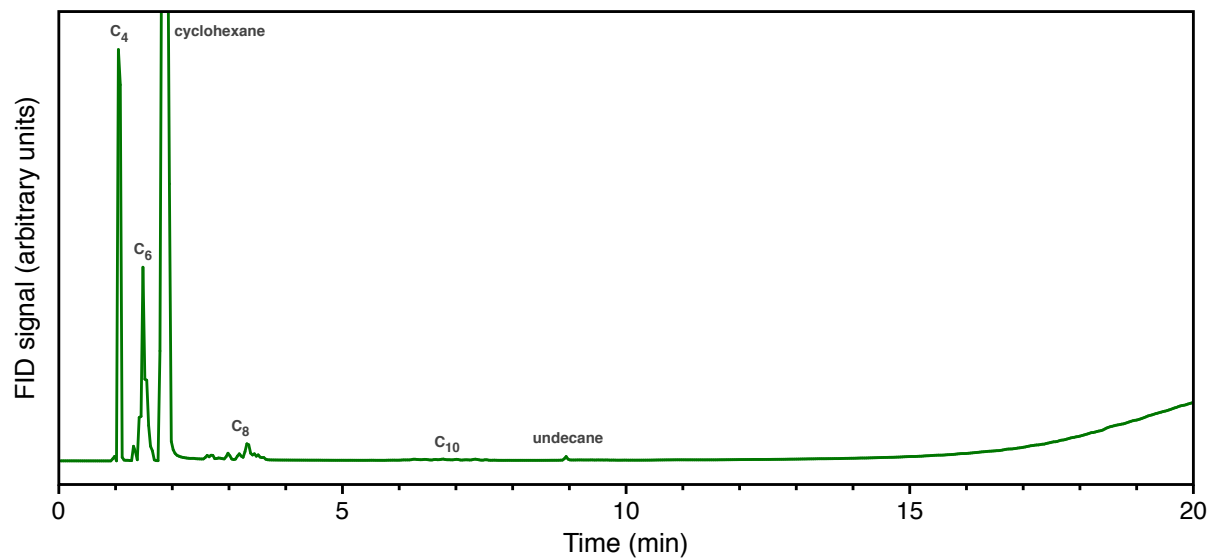
**Figure 5.S22.** Comparison of the non-Schulz-Flory contribution to the average turnover frequencies ( $\text{mol}_{\text{oligomer}} \text{mol}_{\text{Ni}}^{-1} \text{h}^{-1}$ ) for  $\text{C}_{4-10}$  oligomers produced in  $\mathbf{2}(\text{NiBr}_2)_{0.84}$  (red) and the estimated average turnover frequencies for oligomers generated from adventitious nickel sites in  $\mathbf{2}(\text{NiBr}_2)_{0.84}$  (yellow), assuming that  $\mathbf{2}(\text{NiBr}_2)_{0.84}$  contains the same number of adventitious sites per zirconium as  $\mathbf{3}(\text{NiBr}_2)_{0.14}$  (~17% of the nickel sites in  $\mathbf{2}(\text{NiBr}_2)_{0.84}$ ).



**Figure 5.S23.** Representative gas chromatogram for the product mixture obtained from ethylene oligomerization catalyzed by  $1(\text{NiBr}_2)_6$ .

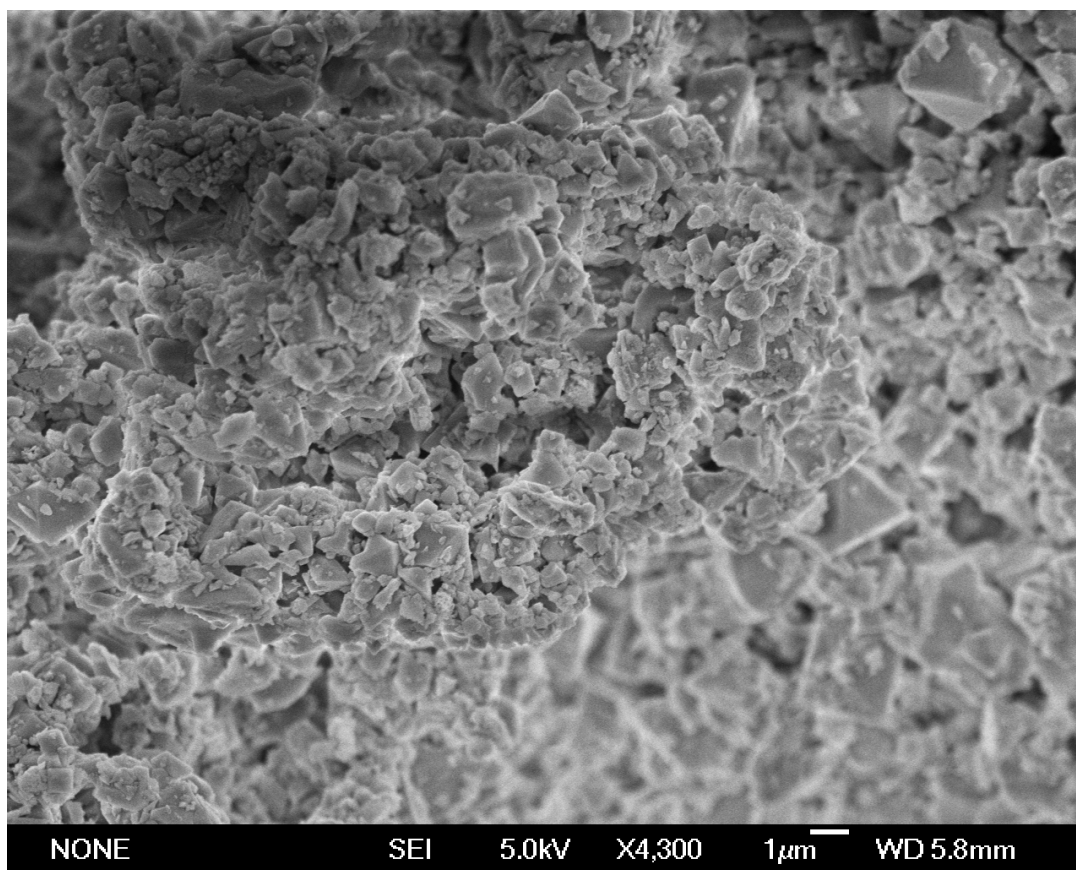


**Figure 5.S24.** Representative gas chromatogram for the product mixture obtained from ethylene oligomerization catalyzed by  $2(\text{NiBr}_2)_{0.84}$ .



**Figure 5.S25.** Representative gas chromatogram for the product mixture obtained from ethylene oligomerization catalyzed by  $3(\text{NiBr}_2)_{0.14}$ .

### 5.6.8. Scanning Electron Microscopy Images



**Figure 5.S26.** SEM micrograph of 1(NiBr<sub>2</sub>)<sub>6</sub> (bulk sample).

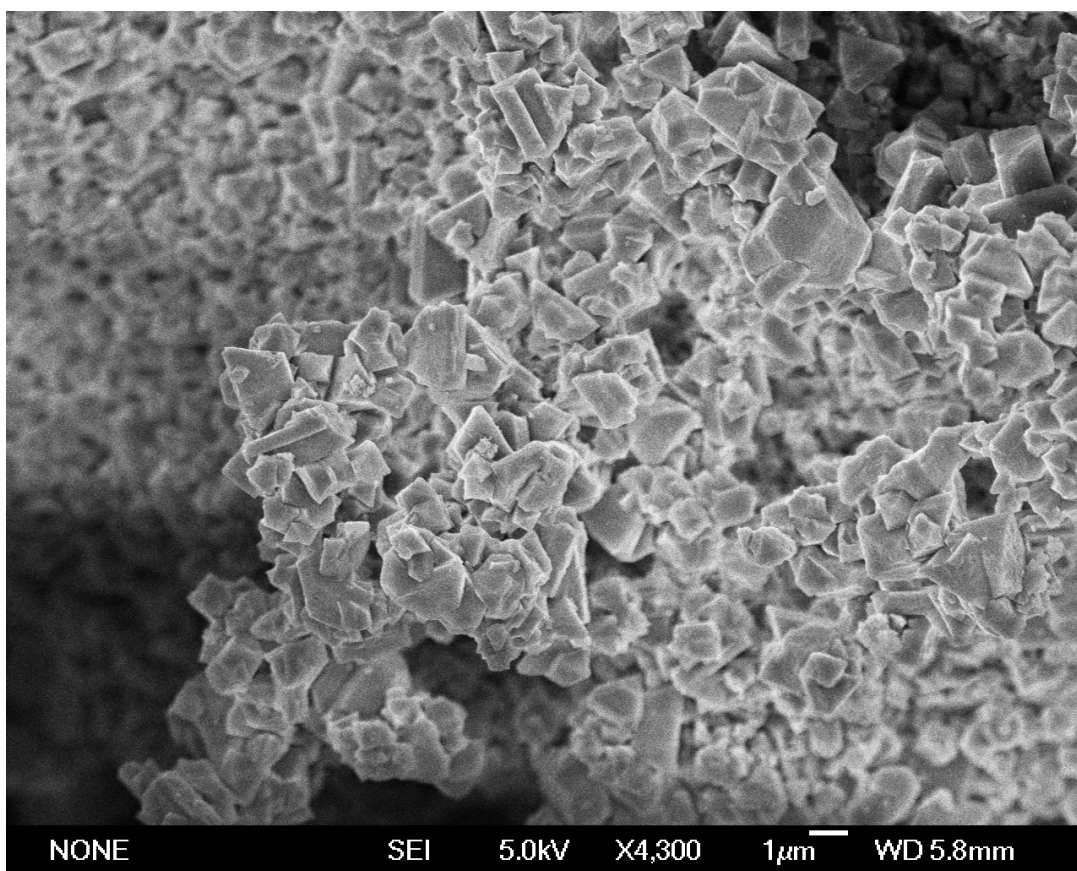


Figure 5.S27. SEM micrograph of  $2(\text{NiBr}_2)_{0.84}$ .

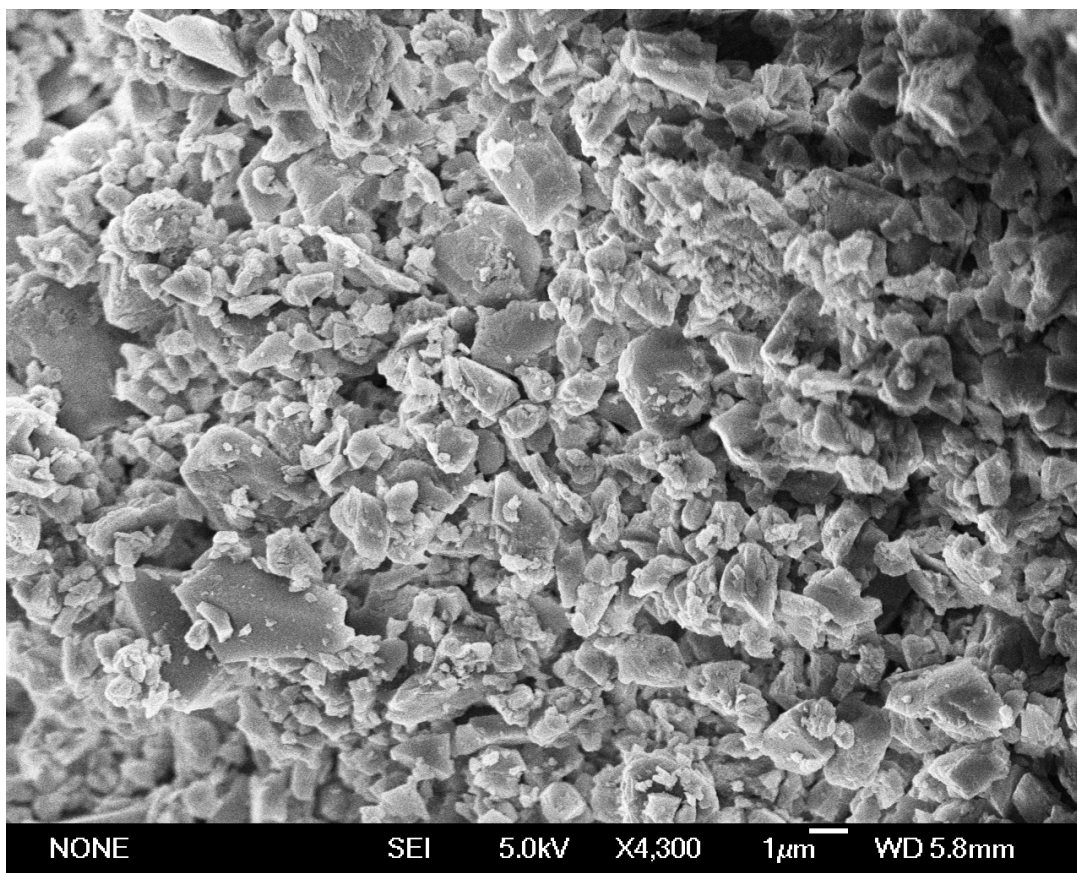


Figure 5.S28. SEM micrograph of  $3(\text{NiBr}_2)_{0.14}$ .



## 5.7. References

- (1) Hagen, J. *Industrial Catalysis*; Wiley-VCH Verlag GmbH & Co. KGaA: Weinheim, 2006.
- (2) Behr, A. In *Ullman's Encyclopedia of Industrial Chemistry*; Wiley-VCH: Weinheim, 2012; Vol. 7, pp 223–269.
- (3) Bhaduri, S.; Mukesh, D. *Homogeneous Catalysis: Mechanisms and Industrial Applications*; John Wiley & Sons, Inc., 2000; pp 1–12.
- (4) Forestière, A.; Olivier-Bourbigou, H. *Oil & Gas Science and Technology - Revue de l'IFP* **2009**, *64* (6), 649–667.
- (5) Belov, G. P.; Matkovsky, P. E. *Petroleum Chemistry* **2010**, *50* (4), 283–289.
- (6) van Leeuwen, P. W. N. M.; Clément, N. D.; Tschan, M. J. L. *Coordination Chemistry Reviews* **2011**, *255* (13-14), 1499–1517.
- (7) Finiels, A.; Fajula, F.; Hulea, V. *Catal. Sci. Technol.* **2014**, *4* (8), 2412–2415.
- (8) Galletti, A.; Geri, G.; Sbrana, G.; Marchionna, M. *Journal of Molecular Catalysis A: Chemical* **1996**, *111* (3), 273–280.
- (9) Braca, G.; Galletti, A.; Di Girolamo, M.; Sbrana, G. *Journal of Molecular Catalysis. A, Chemical* **1995**, *96* (3), 203–213.
- (10) Toulhoat, H.; Lontsi Fomena, M.; de Bruin, T. *J. Am. Chem. Soc.* **2011**, *133* (8), 2481–2491.
- (11) Keim, W. *Angew. Chem. Int. Ed.* **1990**, *29* (3), 235–244.
- (12) Keim, W. *Angew. Chem. Int. Ed.* **2013**, *52* (48), 12492–12496.
- (13) Small, B. L.; Brookhart, M. *J. Am. Chem. Soc.* **1998**, *120* (28), 7143–7144.
- (14) Speiser, F.; Braunstein, P.; Saussine, L. *Acc. Chem. Res.* **2005**, *38* (10), 784–793.
- (15) McGuinness, D. S. *Chem. Rev.* **2011**, *111* (3), 2321–2341.
- (16) Agapie, T. *Coordination Chemistry Reviews* **2011**, *255* (7-8), 861–880.
- (17) Dixon, J. T.; Green, M. J.; Hess, F. M.; Morgan, D. H. *Journal of Organometallic Chemistry* **2004**, *689* (23), 3641–3668.
- (18) Gonzalez, M. I.; Bloch, E. D.; Mason, J. A.; Teat, S. J.; Long, J. R. *Inorg. Chem.* **2015**, *54* (6), 2995–3005.
- (19) Manna, K.; Zhang, T.; Lin, W. *J. Am. Chem. Soc.* **2014**, *136* (18), 6566–6569.
- (20) Manna, K.; Zhang, T.; Carboni, M.; Abney, C. W.; Lin, W. *J. Am. Chem. Soc.* **2014**, *136* (38), 13182–13185.
- (21) Manna, K.; Zhang, T.; Greene, F. X.; Lin, W. *J. Am. Chem. Soc.* **2015**, *137* (7), 2665–2673.
- (22) Fei, H.; Cohen, S. M. *Chem. Commun.* **2014**, *50* (37), 4810–4812.
- (23) Xiao, D. J.; Bloch, E. D.; Mason, J. A.; Queen, W. L.; Hudson, M. R.; Planas, N.; Borycz, J.; Dzubak, A. L.; Verma, P.; Lee, K.; Bonino, F.; Crocellà, V.; Yano, J.; Bordiga, S.; Truhlar, D. G.; Gagliardi, L.; Brown, C. M.; Long, J. R. *Nature Chemistry* **2014**, *6* (7), 590–595.
- (24) Zhang, T.; Manna, K.; Lin, W. *J. Am. Chem. Soc.* **2016**, *138* (9), 3241–3249.
- (25) Li, Z.; Schweitzer, N. M.; League, A. B.; Bernales, V.; Peters, A. W.; Getsoian, A. B.; Wang, T. C.; Miller, J. T.; Vjunov, A.; Fulton, J. L.; Lercher, J. A.; Cramer, C. J.; Gagliardi, L.; Hupp, J. T.; Farha, O. K. *J. Am. Chem. Soc.* **2016**, *138* (6), 1977–1982.
- (26) Metzger, E. D.; Brozek, C. K.; Comito, R. J.; Dincă, M. *ACS Cent Sci* **2016**, *2* (3), 148–153.
- (27) Metzger, E. D.; Comito, R. J.; Hendon, C. H.; Dincă, M. *J. Am. Chem. Soc.* **2017**, *139*

- (2), 757–762.
- (28) Canivet, J.; Aguado, S.; Schuurman, Y.; Farrusseng, D. *J. Am. Chem. Soc.* **2013**, *135* (11), 4195–4198.
- (29) Madrahimov, S. T.; Gallagher, J. R.; Zhang, G.; Meinhart, Z.; Garibay, S. J.; Delferro, M.; Miller, J. T.; Farha, O. K.; Hupp, J. T.; Nguyen, S. T. *ACS Catal.* **2015**, 6713–6718.
- (30) Liu, B.; Jie, S.; Bu, Z.; Li, B.-G. *RSC Adv.* **2014**, *4* (107), 62343–62346.
- (31) Liu, S.; Zhang, Y.; Han, Y.; Feng, G.; Gao, F.; Wang, H. *Organometallics* **2017**, *36* (3), 632–638.
- (32) Mlinar, A. N.; Keitz, B. K.; Gygi, D.; Bloch, E. D.; Long, J. R.; Bell, A. T. *ACS Catal.* **2014**, *4* (3), 717–721.
- (33) Britovsek, G. J. P.; Malinowski, R.; McGuinness, D. S.; Nobbs, J. D.; Tomov, A. K.; Wadsley, A. W.; Young, C. T. *ACS Catal.* **2015**, 6922–6925.
- (34) Svejda, S. A.; Brookhart, M. *Organometallics* **1999**, *18* (1), 65–74.
- (35) Killian, C. M.; Johnson, L. K.; Brookhart, M. *Organometallics* **1997**, *16* (10), 2005–2007.
- (36) Xiao, D. J.; Oktawiec, J.; Milner, P. J.; Long, J. R. *J. Am. Chem. Soc.* **2016**, *138* (43), 14371–14379.
- (37) Kutzscher, C.; Nickerl, G.; Senkowska, I.; Bon, V. *Chem. Mater.* **2016**, *28* (8), 2573–2580.
- (38) Evans, J. D.; Sumbly, C. J.; Doonan, C. J. *Chem. Soc. Rev.* **2014**, *43* (16), 5933–5951.
- (39) Cohen, S. M.; Zhang, Z.; Boissonnault, J. A. *Inorg. Chem.* **2016**, *55* (15), 7281–7290.
- (40) Dau, P. V.; Cohen, S. M. *Chem. Commun. (Camb.)* **2013**, *49* (55), 6128–6130.
- (41) Kinnunen, T.-J. J.; Haukka, M.; Pakkanen, T. T.; Pakkanen, T. A. *Journal of Organometallic Chemistry* **2000**, *613* (2), 257–262.
- (42) Helldörfer, M.; Milius, W.; Alt, H. G. *Journal of Molecular Catalysis. A, Chemical* **2003**, 1–13.
- (43) Li, L.; Tang, S.; Wang, C.; Lv, X.; Jiang, M.; Wu, H.; Zhao, X. *Chem. Commun.* **2014**, *50* (18), 2304–2307.
- (44) Cavka, J. H.; Jakobsen, S.; Olsbye, U.; Guillou, N.; Lamberti, C.; Bordiga, S.; Lillerud, K. P. *J. Am. Chem. Soc.* **2008**, *130* (42), 13850–13851.
- (45) Fei, H.; Sampson, M. D.; Lee, Y.; Kubiak, C. P.; Cohen, S. M. *Inorg. Chem.* **2015**, *54* (14), 6821–6828.
- (46) Rama, G.; Ardá, A.; Maréchal, J.-D.; Gamba, I.; Ishida, H.; Jiménez-Barbero, J.; Vázquez, M. E.; Vázquez López, M. *Chem. Eur. J.* **2012**, *18* (23), 7030–7035.
- (47) Bruker Analytical X-ray Systems, Inc. *SAINTE and APEX 2 Software for CCD Diffractometers*; Bruker Analytical X-ray Systems, Inc.: Madison, WI, USA, 2000.
- (48) Sheldrick, G. M. *SADABS*; Bruker Analytical X-ray Systems, Inc.: Madison, WI, USA, 2014.
- (49) Sheldrick, G. M. *SHELXS*; University of Göttingen, Germany, 2014.
- (50) Sheldrick, G. M. *Acta Crystallogr., A, Found. Crystallogr.* **2008**, *64* (Pt 1), 112–122.
- (51) Sheldrick, G. M. *SHELXL*; University of Göttingen, Germany: University of Göttingen, Germany, 2014.
- (52) Dolomanov, O. V.; Bourhis, L. J.; Gildea, R. J.; Howard, J. A. K.; Puschmann, H. *Journal of Applied Crystallography* **2009**, *42* (2), 339–341.
- (53) Spek, A. L. *Acta Crystallogr C Struct Chem* **2015**, *71* (Pt 1), 9–18.

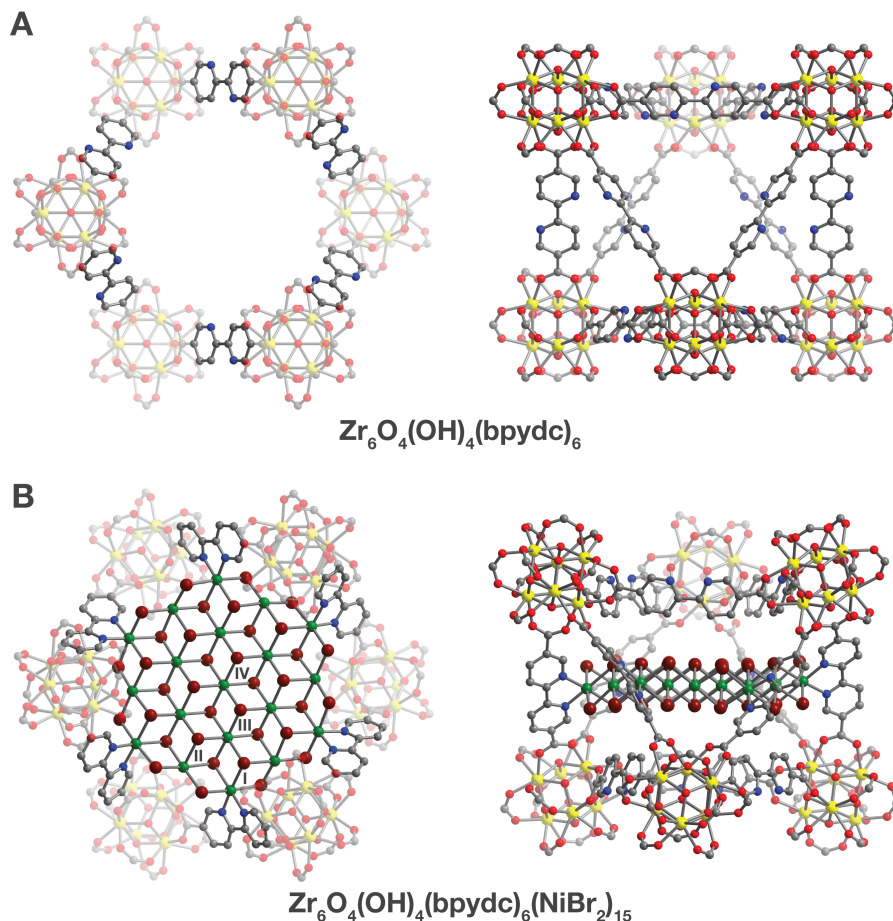
- (54) Spek, A. L. *Journal of Applied Crystallography* **2003**, *36* (1), 7–13.
- (55) Coelho, A. A. *Journal of Applied Crystallography* **2003**, *36* (1), 86–95.
- (56) Coelho, A. A. *TOPAS-Academic, Version 4.1*; Coelho Software: Brisbane, 2007.
- (57) Kinnunen, T.; Haukka, M.; Pakkanen, T. T. *Journal of Organometallic Chemistry* **2000**, *613* (2), 257–262.
- (58) Johnson, L. K.; Killian, C. M.; Brookhart, M. *J. Am. Chem. Soc.* **1995**, *117* (23), 6414–6415.
- (59) Ittel, S. D.; Johnson, L. K.; Brookhart, M. *Chem. Rev.* **2000**, *100* (4), 1169–1204.
- (60) Shearer, G. C.; Chavan, S.; Bordiga, S.; Svelle, S.; Olsbye, U.; Lillerud, K. P. *Chem. Mater.* **2016**, *28* (11), 3749–3761.
- (61) Trickett, C. A.; Gagnon, K. J.; Lee, S.; Gándara, F.; Büergi, H.-B.; Yaghi, O. M. *Angew. Chem. Int. Ed.* **2015**, *54* (38), 11162–11167.
- (62) Shearer, G. C.; Chavan, S.; Ethiraj, J.; Vitillo, J. G.; Svelle, S.; Olsbye, U.; Lamberti, C.; Bordiga, S.; Lillerud, K. P. *Chem. Mater.* **2014**, *26* (14), 4068–4071.
- (63) Manna, K.; Ji, P.; Greene, F. X.; Lin, W. *J. Am. Chem. Soc.* **2016**, *138* (24), 7488–7491.
- (64) Yuan, S.; Chen, Y.-P.; Qin, J.; Lu, W.; Wang, X.; Zhang, Q.; Bosch, M.; Liu, T.-F.; Lian, X.; Zhou, H.-C. *Angewandte Chemie* **2015**, *127* (49), 14909–14913.
- (65) Walton, K. S.; Snurr, R. Q. *J. Am. Chem. Soc.* **2007**, *129* (27), 8552–8556.

## Chapter 6. Confinement of Atomically-Defined Metal Halide Sheets in a Metal–Organic Framework

### 6.1. Introduction

The size- and shape-dependent characteristics that distinguish nanoscale materials from bulk solids inherently arise from constraining the dimensions of an inorganic structure.<sup>1-3</sup> As a consequence, many studies have focused on rationally shaping these materials to influence and enhance their optical, electronic, magnetic, and catalytic properties.<sup>4-6</sup> Of particular interest is the cluster size regime around 1 nm, where these properties are highly sensitive to cluster topology.<sup>7,8</sup> Although a select number of stable clusters can typically be synthesized within this regime, isolating clusters of a predetermined size and shape remains a challenge. In principle, confinement within a metal–organic framework can define the structure and composition of these species and allow for their precise characterization by crystallography. Motivated by these potential capabilities, researchers have increasingly explored metal–organic frameworks as solid supports for both nanoparticles and inorganic clusters.<sup>9,10</sup> Several reports have demonstrated the uniform incorporation of nanoparticles or clusters through encapsulation of preformed particles or serendipitous self-assembly during framework synthesis.<sup>9-12</sup> Constraining cluster formation within framework pores has proven to be more difficult, as the absence of sufficiently stabilizing interactions in most metal–organic frameworks leads to nonselective agglomeration and unrestricted growth.<sup>9,10</sup> Recent work, however, has highlighted that frameworks bearing coordinating groups encourage site-specific nucleation, affording improved control over cluster size and distribution.<sup>13-16</sup>

Simple capping agents have been widely used to stabilize nanoparticles and metal clusters,<sup>1,5,6</sup> while biological<sup>17</sup> and molecular<sup>18</sup> scaffolds take this chemistry further by precisely orienting multiple ligands to direct cluster assembly. We envisioned that a metal–organic framework could act as a preorganized array of ligands to template the growth of discrete inorganic clusters. Thus, we selected the framework  $Zr_6O_4(OH)_4(bpydc)_6$  (Figure 6.1A;  $bpydc^{2-} = 2,2'$ -bipyridine-5,5'-dicarboxylate), which features  $\sim 1.3$  nanometer-wide octahedral cages lined with chelating sites that readily bind a variety of metal sources.<sup>14-16,19,20</sup> Metalation of this framework induces a single-crystal-to-single-crystal transformation that results in crystallographic ordering of the metal–linker complexes,<sup>19,20</sup> thereby enabling their structural determination by crystallography. In the metalated framework, six bipyridine linkers point toward the center of each octahedral cage, creating a multidentate scaffold for cluster growth. Anticipating the importance of reversibility in promoting uniform cluster formation, we selected the first-row transition metal halides as precursors due to the lability of their metal–halide bonds. In addition, many of these metal halides form bulk structures comprised of stacked layers of edge-sharing octahedra that display unique physical properties upon separation into monolayers.<sup>21,22</sup> Here, we report the confinement of atomically-defined metal(II) halide (nickel(II) bromide, nickel(II) chloride, cobalt(II) chloride, and iron(II) chloride) sheets in  $Zr_6O_4(OH)_4(bpydc)_6$  (**1**) and their characterization by single-crystal X-ray diffraction. Furthermore, the structures of these species at different metal halide loadings shed light on the mechanisms of cluster growth, while magnetic measurements on the isolated sheets expose magnetic properties that are inaccessible in the bulk material.



**Figure 6.1.** A portion of the crystal structures of **1** (**A**) and **1**(NiBr<sub>2</sub>)<sub>15</sub> (**B**) at 100 K as determined by single-crystal X-ray diffraction. The four crystallographically distinct Ni sites in the structure of **1**(NiBr<sub>2</sub>)<sub>15</sub> are labeled with roman numerals on their top right. Yellow, green, dark red, red, blue, and gray spheres represent Zr, Ni, Br, O, N, and C atoms, respectively. Hydrogen atoms are omitted for clarity.

## 6.2. Experimental

**Materials and Methods:** All manipulations were performed under an N<sub>2</sub> atmosphere in a VAC Atmospheres glovebox or under an N<sub>2</sub> or Ar atmosphere using standard Schlenk techniques. The solvent 1,2-difluorobenzene (DFB) was deoxygenated by purging with argon for 1 h and dried using a commercial solvent purification system designed by JC Meyer Solvent Systems. The solvents 1,2-dimethoxyethane (DME) and bis(2-methoxyethyl) ether (diglyme) were purchased from Sigma-Aldrich, dried over Na/benzophenone (for DME) or 4 Å molecular sieves (for diglyme), and degassed via three successive freeze-pump-thaw cycles. The compound 2,2'-bipyridine-5,5'-dicarboxylic acid (H<sub>2</sub>bpydc) was synthesized using a previously published procedure.<sup>23</sup> The compounds ZrCl<sub>4</sub>, Ni(DME)Br<sub>2</sub>, Ni(DME)Cl<sub>2</sub>, NiBr<sub>2</sub>, CoCl<sub>2</sub>, and FeCl<sub>2</sub> were purchased from commercial vendors (Sigma-Aldrich for ZrCl<sub>4</sub>, Ni(DME)Br<sub>2</sub>, and Ni(DME)Cl<sub>2</sub>; Strem for NiBr<sub>2</sub>, CoCl<sub>2</sub>, and FeCl<sub>2</sub>) and used as received. All other chemicals were purchased from commercial vendors and used as received unless otherwise noted.

NMR spectra were acquired on Bruker AVB-400 or AVQ-400 instruments at the University

of California, Berkeley NMR facility. All chemical shifts are given in relation to residual solvent peaks or tetramethylsilane. Powder X-ray diffraction patterns were collected on microcrystalline powder samples loaded into 1.0 mm boron-rich glass capillaries inside a N<sub>2</sub>-filled glovebox and then flame-sealed. High-resolution synchrotron X-ray powder diffraction data were subsequently collected at 298 K with a wavelength of 0.45241 Å at beamline 17-BM-B at the Advanced Photon Source at Argonne National Laboratory. Transmission electron microscopy (TEM) was performed on an FEI Titan 80–300kV microscope at the National Center for Electron Microscopy. Annular dark field scanning TEM images and energy dispersive X-ray spectroscopy (EDS) maps were acquired using a beam current of 100–300 pA at room temperature. The four EDS SDD detectors had a collection solid angle of approximately 0.7 steradian. Images were acquired before and after the EDS map to confirm that the sample did not damage visibly due to the electron beam. Inductively coupled plasma optical emission spectrometry (ICP-OES) analysis was performed on a Perkin Elmer Optima 7000 DV instrument at the University of California, Berkeley, microanalytical facility.

**Zr<sub>6</sub>O<sub>4</sub>(OH)<sub>4</sub>(bpydc)<sub>6</sub> (1).** This material was synthesized as a microcrystalline powder using a previously published procedure.<sup>20</sup> Typically, a 2-L round bottom flask equipped with a Schlenk adapter, glass stoppers, and a magnetic stir bar was charged with H<sub>2</sub>bpydc (6.11 g, 25. mmol), benzoic acid (224 g, 2.00 mol), and *N,N*-dimethylformamide (DMF; 1.00 L) from a newly opened bottle. The resulting mixture was purged with dry Ar for 30 min. Solid ZrCl<sub>4</sub> (5.83 g, 25.0 mmol) was then added, after which the mixture was purged with dry Ar for an additional 30 min. Deionized water (820 μL, 45.5 mmol) was added and the mixture was heated with magnetic stirring for 5 days at 120 °C under an N<sub>2</sub> atmosphere. After allowing the mixture to cool to room temperature, the solvent was decanted and the resulting white microcrystalline powder was washed by soaking three times in 1-L aliquots of fresh DMF for 24 h at 120 °C, followed by solvent exchange with tetrahydrofuran (THF) via Soxhlet extraction for 3 days. The THF-solvated powder was filtered under dry Ar, followed by heating at 120 °C under dynamic vacuum for 24 h to give fully desolvated **1**. The powder X-ray diffraction pattern and Langmuir surface area (2700 m<sup>2</sup>/g; N<sub>2</sub>, 77 K) of the material were found to be consistent with those reported in the literature.<sup>20</sup>

Single crystals of **1** were synthesized following a previously reported procedure<sup>19</sup> and characterized by single-crystal X-ray diffraction.

**General Procedure for Loading 1 with NiX<sub>2</sub> (X<sup>-</sup> = Cl<sup>-</sup>, Br<sup>-</sup>) in Diglyme.** Single crystals of **1** (< 0.1 mg) suspended in diglyme were transferred into a 4 mL PTFE-capped vial. Most of the solvent was decanted, followed by addition excess metal source (Ni(DME)Cl<sub>2</sub>, Ni(DME)Br<sub>2</sub>, or NiBr<sub>2</sub>; 5–10 mg; > 50 equiv) and diglyme (3 mL). The mixture was allowed to react for 1 month at 120 °C, resulting in a color change of the crystals to pale yellow. The crystals were then characterized by single-crystal X-ray diffraction.

Stoichiometric reactions were performed on microcrystalline powder samples of **1** in the presence of single crystals that were later characterized by crystallography. Single crystals of **1** (< 0.1 mg) suspended in diglyme were transferred into a 4-mL PTFE-capped vial. Most of the solvent was decanted, followed by addition of microcrystalline **1** (60 mg), metal source (1.0–3.25 equiv Ni(DME)Cl<sub>2</sub>, Ni(DME)Br<sub>2</sub>, or NiBr<sub>2</sub> per bpydc<sup>2-</sup> in microcrystalline **1**) and diglyme. The mixture was allowed to react for 1 month at 120 °C, resulting in a color change of both the crystals and the powder to pale yellow. Most of the solution was removed by pipette and the crystals were subsequently soaked three times in 3 mL of fresh DME at room temperature (~32 °C) for 24 h. In cases where unreacted metal halide solids were observed, these were

removed by carefully transferring a slurry of the framework into a new vial prior to each wash. A slurry containing most of the microcrystalline powder was separated from the crystals and pipetted into a new vial, after which the solvent was removed under reduced pressure at 80 °C to give a microcrystalline powder sample of the NiX<sub>2</sub>-loaded framework. The remaining single crystals were then used for single-crystal X-ray diffraction experiments.

**General Procedure for Loading 1 with MX<sub>2</sub> (MX<sub>2</sub> = FeCl<sub>2</sub>, CoCl<sub>2</sub>, and NiBr<sub>2</sub>) in 10% (v/v) DME in DFB.** Single crystals of **1** (< 0.1 mg) suspended in diglyme were transferred into a thick-walled borosilicate tube. Most of the solvent was decanted, followed by addition excess metal source (FeCl<sub>2</sub>, CoCl<sub>2</sub>, or Ni(DME)Br<sub>2</sub>; 5–10 mg; > 50 equiv), DME (0.30 mL), and DFB (2.70 mL). The reaction mixture was degassed by three freeze–pump–thaw cycles, after which the tube was flame-sealed and then placed in an oven preheated to 120 °C. The mixture was allowed to react for 1 month at this temperature, resulting in a color change of the crystals (purple for FeCl<sub>2</sub>, blue for CoCl<sub>2</sub>, and pale yellow for Ni(DME)Br<sub>2</sub>). The crystals were then characterized by single-crystal X-ray diffraction.

Stoichiometric reactions were performed on microcrystalline powder samples of **1** in the presence of single crystals that were later characterized by crystallography. Single crystals of **1** (< 0.1 mg) suspended in diglyme were transferred into a thick-walled borosilicate tube. Most of the solvent was decanted, followed by addition of microcrystalline **1** (60 mg), metal source (3.25 equiv FeCl<sub>2</sub>, CoCl<sub>2</sub>, or Ni(DME)Br<sub>2</sub>), DME (0.30 mL), and DFB (2.70 mL). The reaction mixture was degassed by three freeze–pump–thaw cycles, after which the tube was flame-sealed and then placed in an oven preheated to 120 °C. The mixture was allowed to react for 1 month at this temperature, resulting in a color change of the both the crystals and the powder (purple for FeCl<sub>2</sub>, blue for CoCl<sub>2</sub>, and pale yellow for Ni(DME)Br<sub>2</sub>). Most of the solution was removed by pipette and the crystals were subsequently soaked three times in 3 mL of fresh DME at room temperature (~32 °C) for 24 h. In cases where unreacted metal halide solids were observed, these were removed by carefully transferring a slurry of the framework into a new vial prior to each wash. A slurry containing most of the microcrystalline powder was separated from the crystals and pipetted into a new vial, after which the solvent was removed under reduced pressure at 80 °C to give a microcrystalline powder sample of the NiX<sub>2</sub>-loaded framework. The remaining single crystals were then used for single-crystal X-ray diffraction experiments.

**Single-Crystal X-ray Diffraction.** X-ray diffraction analysis was performed on single crystals coated with Paratone-N oil and mounted on a MiTeGen loops. The crystals were frozen at a temperature of 100 K by an Oxford Cryosystems Cryostream 700 Plus. Data were collected at Beamline 11.3.1 at the Advanced Light Source at Lawrence Berkeley National Laboratory using synchrotron radiation ( $\lambda = 0.8856 \text{ \AA}$  and  $0.9537 \text{ \AA}$ ) on a Bruker D8 diffractometer equipped with either a Bruker PHOTON100 CMOS detector or a Bruker PHOTON II CMOS detector. Raw data were integrated and corrected for Lorentz and polarization effects using Bruker AXS SAINT software.<sup>24</sup> Absorption corrections were applied using SADABS.<sup>25</sup> Initial evaluation of the diffraction data suggested that Zr<sub>6</sub>O<sub>4</sub>(OH)<sub>4</sub>(bpydc)<sub>6</sub> undergoes a change of space group from *Fm* $\bar{3}$ *m* to *P2*<sub>1</sub>*3* upon loading with NiBr<sub>2</sub>, NiCl<sub>2</sub>, CoCl<sub>2</sub>, or FeCl<sub>2</sub>. Based on previous work,<sup>19</sup> attempts to solve and refine these structures in *P2*<sub>1</sub>*3* result in unsatisfactory refinement, thus solution and refinement in the space group *Pa* $\bar{3}$  was instead attempted. In the end, this space group gave the most satisfactory refinement. The structure was solved using direct methods with SHELXS<sup>26,27</sup> and refined using SHELXL<sup>28</sup> operated in the OLEX2<sup>29</sup> interface. No significant crystal decay was observed during data collection. Thermal parameters were refined anisotropically for all non-hydrogen atoms. Hydrogen atoms were placed in ideal

positions and refined using a riding model for all structures. Moving from  $Fm\bar{3}m$  to  $Pa\bar{3}$  results in two twin domains related by the lost mirror symmetry along the body diagonals of the unit cell. Consequently, a twin law (TWIN 0 1 0 1 0 0 0 0 -1 2; BASF  $\approx$  0.50) was required for the structural refinement. The oxygen atoms of the oxo and hydroxo groups on the zirconium clusters in the structure were disordered and, in cases where this disorder could be modeled, the site occupancy factors of these oxygen atoms were fixed to give a chemical occupancy of 50%. Hydrogen atoms on the hydroxo groups could neither be found nor placed and were omitted from the refinement but not from the formula. Disorder of the linkers and the metal halides in some of the structures required the use of geometric and displacement parameter restraints. Extensive solvent disorder was found in the pores for most of the structures and could not be modeled. Consequently, the unassigned electron density in these structures was accounted for using SQUEEZE<sup>30</sup> as implemented in the PLATON<sup>31</sup> interface.

**Low-Pressure Gas Adsorption Measurements.** Gas adsorption isotherms for pressures in the range 0–1.2 bar were measured by a volumetric method using a Micromeritics ASAP2420 instrument. A typical sample, consisting of  $\sim$ 100 mg of material was transferred to a pre-weighed analysis tube, which was capped with a Micromeritics *TranSeal* and evacuated by heating at 120 °C for 1 or 80 °C for all samples loaded with metal(II) halides at a ramp rate of 1 °C/min under dynamic vacuum until an outgas rate of less than 3  $\mu$ bar/min was achieved. The evacuated analysis tube containing the degassed sample was then carefully transferred to an electronic balance and weighed again to determine the mass of sample. The tube was then transferred back to the analysis port of the gas adsorption instrument. The outgas rate was again confirmed to be less than 3  $\mu$ bar/min. For all isotherms, warm and cold free space correction measurements were performed using ultra-high purity He gas (UHP, 99.999% purity); N<sub>2</sub> isotherms at 77 K were measured in liquid N<sub>2</sub> baths using UHP-grade gas sources. Oil-free vacuum pumps and oil-free pressure regulators were used for all measurements to prevent contamination of the samples during the evacuation process or of the feed gases during the isotherm measurements. Langmuir and Brunauer–Emmet–Teller (BET) surface areas were determined from N<sub>2</sub> adsorption data at 77 K.

**Magnetic Measurements.** Samples were prepared by adding crystalline powder to a 5 mm inner diameter quartz tube containing a raised quartz platform. Solid eicosane was added to cover the sample to prevent crystallite torquing and provide good thermal contact between the sample and the cryostat. The tubes were fitted with Teflon sealable adapters, evacuated on a Schlenk line, and flame-sealed under static vacuum. Following flame sealing, the solid eicosane was melted in a water bath held at 40 °C. Magnetic susceptibility measurements were performed using a Quantum Design MPMS2 SQUID magnetometer. Dc magnetic susceptibility measurements were collected in the temperature range 2–300 K under applied magnetic fields of 0.01 T, 0.1 T, and 1 T. Magnetic hysteresis measurements were performed at a sweep rate of 9 mT/s. Diamagnetic corrections were applied to the data using Pascal's constants.

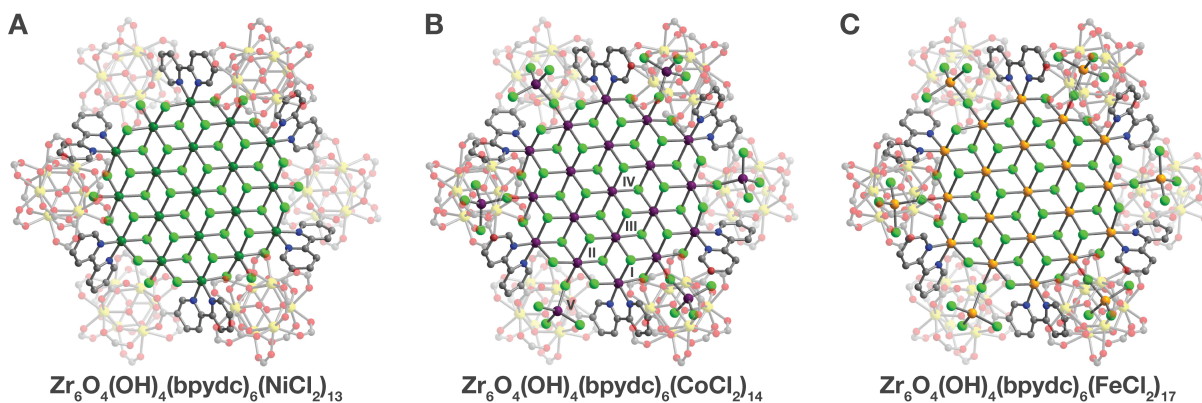
**General procedure for metal content analysis via ICP-OES.** Roughly 10 mg of activated material was placed in a 20-mL plastic vial and digested with 10  $\mu$ L of concentrated HF in 2 mL of dimethylsulfoxide and diluted with 18 mL of 5% HNO<sub>3</sub> in Millipore water. The resulting solution was transferred to a 100-mL volumetric flask and diluted to mark with 5% (v/v) aqueous HNO<sub>3</sub> in Millipore water to give a stock solution that contained roughly 25 ppm Zr from the sample. The stock sample solution (10.0 mL) and 2.50 ppm Y (1.00 mL) were added to a 25.0-mL volumetric flask and diluted to mark with 5% (v/v) aqueous HNO<sub>3</sub> to give sample solution that is  $\sim$ 10 ppm Zr with 0.100 ppm Y as an internal standard. Standard solutions with 0.100, 1.00,



5.00, 10.0, and 15.0 ppm Zr, Ni, Fe, and Co with 0.100 ppm Y as an internal standard were prepared for the calibration curve.

### 6.3. Results and Discussion

Reaction of **1** with Ni(DME)Br<sub>2</sub> (DME = 1,2-dimethoxyethane) in bis(2-methoxyethyl) ether (diglyme) at 120 °C affords the framework **1**(NiBr<sub>2</sub>)<sub>9.9</sub>. Structural characterization of NiBr<sub>2</sub>-loaded single crystals at 100 K reveals the growth of isolated nickel(II) bromide sheets within the octahedral cages of the framework (Figures 6.1B and 6.S1). Coordination of six bipyridine linkers to edge nickel sites constrains the diameter of each sheet to ~1.5 nm while the octahedral cages distort to accommodate the slightly larger sheet dimensions. At full occupancy, each cluster represents a monolayer of 19 edge-sharing nickel octahedra, which closely resembles a portion of the layered structure of bulk NiBr<sub>2</sub>.<sup>32</sup> Each cluster contains four crystallographically distinct nickel(II) sites. Two of these sites correspond to twelve nickel centers that define the edges of the sheet, alternating between nickel centers bound by bipyridine (Site I) and sites at edges facing the tetrahedral cages of the framework (Site II). The third and fourth sites form the interior of the sheet, comprising six symmetrically equivalent nickel octahedra (Site III) surrounding a central nickel site (Site IV). Nickel site occupancies in the **1**(NiBr<sub>2</sub>)<sub>9.9</sub> structure decrease from 78.4(1)% for Site I and 43.2(9)% for Site II at the edges of the sheet to 39.9(9)% for Site III and 23.3(17)% for Site IV at the center. Overall, these occupancies amount to only 52.2(5)% of the expected loading for a Ni<sub>19</sub>Br<sub>38</sub> cluster and suggest that complete sheets fill 23% of the framework cages and partial sheets take up 20%, while a combination of mononuclear bipyridine–NiBr<sub>2</sub> complexes and unmetalated linkers likely occupy the remaining cages. Optimizing the reaction conditions by lowering the concentration of coordinating solvent, further discussed below, led to a higher overall Ni occupancy (80.5(3)%) in the structure of **1**(NiBr<sub>2</sub>)<sub>15</sub>. The average nearest Ni···Ni separation (3.723(18) Å) in this structure agrees well with the separation in bulk NiBr<sub>2</sub> (3.723(10) Å), further confirming the similarity of these sheets to those in the bulk structure.



**Figure 6.2.** A portion of the crystal structures of **1**(NiCl<sub>2</sub>)<sub>13</sub> (A), **1**(CoCl<sub>2</sub>)<sub>14</sub> (B), and **1**(FeCl<sub>2</sub>)<sub>17</sub> at 100 K as determined by single-crystal X-ray diffraction. The five crystallographically distinct metal sites in the structure of **1**(CoCl<sub>2</sub>)<sub>14</sub> are labeled with roman numerals on their top right. Yellow, green, purple, orange, light green, red, blue, and gray spheres represent Zr, Ni, Co, Fe, Cl, O, N, and C atoms, respectively. Hydrogen atoms are omitted for clarity.

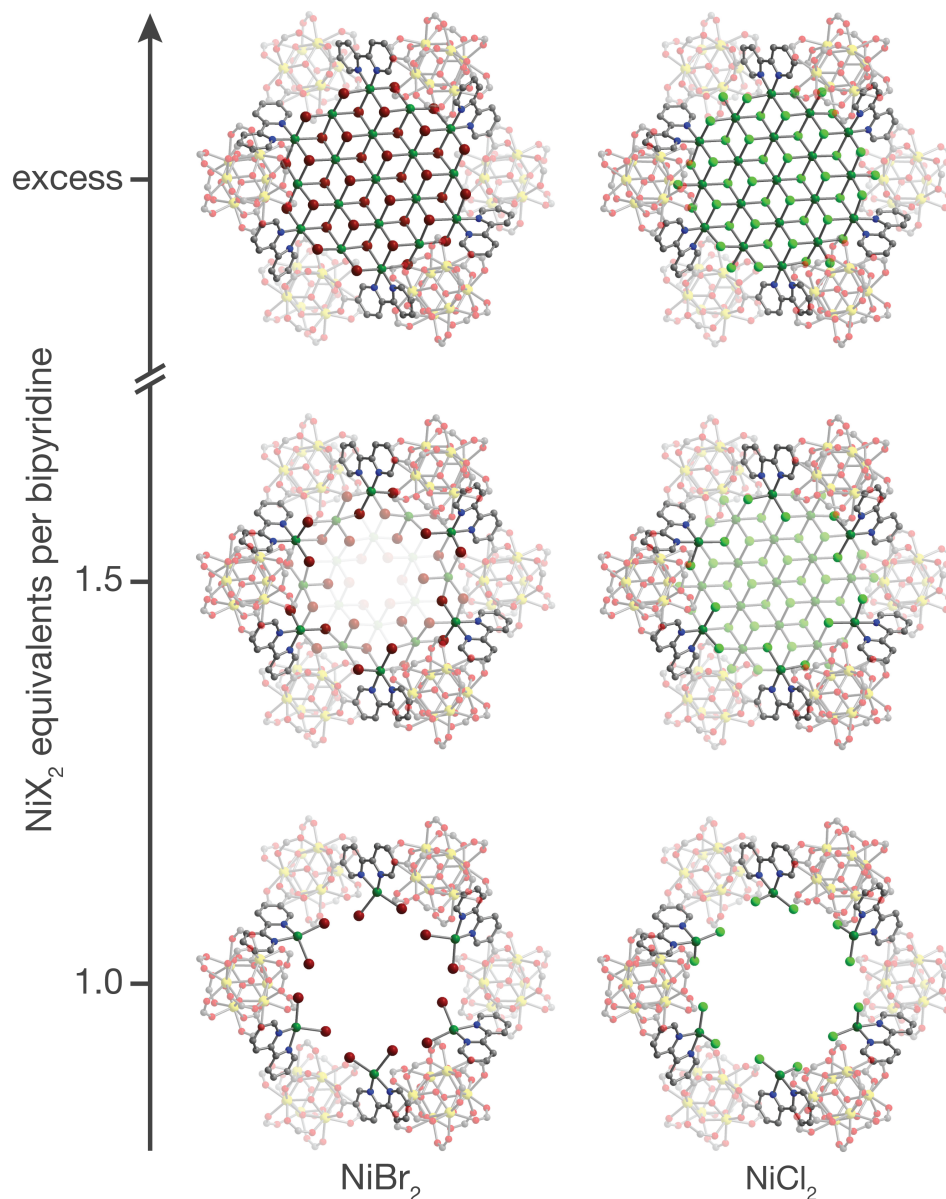
Bulk NiCl<sub>2</sub> adopts the same layered structure type as NiBr<sub>2</sub>, but with contracted lattice dimensions as a result of having shorter nickel–halide bonds.<sup>33</sup> To probe if **1** could also stabilize

nickel(II) chloride sheets, the framework was reacted with Ni(DME)Cl<sub>2</sub> under the same conditions used for nickel(II) bromide. The single-crystal structure of the resulting framework **1**(NiCl<sub>2</sub>)<sub>13</sub> at 100 K (Figures 6.2A and 6.S2) confirmed the formation of analogous nickel(II) chloride sheets. Significantly, the flexibility of the framework allows the bipyridine linkers to conform to the more compact nickel(II) chloride lattice. Consistent with its greater lattice stabilization energy,<sup>34</sup> nickel(II) chloride affords a higher Ni loading (69.9(4)%) compared to nickel(II) bromide under similar reaction conditions. Moreover, the nickel site occupancies range from 78.4(7)%, 67.1(0.7)%, 64.5(0.7)%, and 68.4(16)% going from Site I to IV and reveal that 65% of the octahedral cages contain full sheets, whereas only 3% hold partial clusters, suggesting that nickel(II) chloride preferentially forms complete clusters. Unlike the nickel(II) bromide structure, **1**(NiCl<sub>2</sub>)<sub>13</sub> features a slightly expanded average Ni···Ni separation (3.578(17) Å) in **1**(NiCl<sub>2</sub>)<sub>13</sub> in comparison to that of the bulk structure (3.483(6) Å), which likely reflects a subtle interplay between the stabilization gained from forming an ideal NiCl<sub>2</sub> lattice and the strain incurred upon contraction of the bipyridine linkers around the cluster.

Encouraged by the stabilization of nickel(II) halide clusters in **1**, we pursued extending this chemistry to cobalt(II) chloride and iron(II) chloride. Attempts to grow cobalt(II) chloride and iron(II) chloride clusters under similar conditions, however, resulted in metalation of only the bipyridine sites. Recognizing that an equilibrium between the metal(II) halide clusters and solvated metal species governs cluster assembly, we conducted reactions under reduced concentrations of coordinating solvent to drive equilibrium toward sheet formation. Specifically, reacting **1** with either CoCl<sub>2</sub> or FeCl<sub>2</sub> in a 10% (v/v) solvent mixture of 1,2-dimethoxyethane (DME) and 1,2-difluorobenzene (DFB) at 120 °C results in the growth of cobalt(II) and iron(II) chloride sheets in the frameworks **1**(CoCl<sub>2</sub>)<sub>14</sub> (Figures 6.2B and 6.S3) and **1**(FeCl<sub>2</sub>)<sub>17</sub> (Figures 6.2C and 6.S4). Close inspection of the cobalt and iron structures revealed tetrahedral metal sites (Site V) in addition to the four distinct octahedral sites located in the nickel(II) halide clusters. These tetrahedral complexes cap the edges of each sheet at Site II and likely represent a mixture of [MCl<sub>4</sub>]<sup>2-</sup> and M(DME)Cl<sub>2</sub> complexes; however, disorder of these species precludes unambiguous assignment of their identity. Site occupancies for the four octahedral sites in the cobalt and iron clusters were found to range from 60.5(12)–81.4(6)% for Co and 74.6(10)–88.5(5)% for Fe (Table 6.S1), while the tetrahedral sites were generally found to be only a third occupied. Both structures display relatively high metal loadings (74.7(4)% for Co and 91.6(3)% for Fe relative to a M<sub>19</sub>Cl<sub>38</sub> sheet), indicating that minimizing the amount of coordinating solvent strongly promotes cluster formation. As with the nickel(II) chloride structure, the cobalt and iron structures at 100 K contain sheets with slightly longer M···M separations between octahedral centers (Co···Co = 3.65(2) Å ; Fe···Fe = 3.680(12) Å) compared to those of their bulk counterparts (Co···Co = 3.553 Å; Fe···Fe = 3.603 Å).<sup>35</sup>

Microcrystalline powder samples of the MX<sub>2</sub>-loaded frameworks (MX<sub>2</sub> = NiBr<sub>2</sub>, NiCl<sub>2</sub>, CoCl<sub>2</sub>, and FeCl<sub>2</sub>) were prepared for further characterization of these materials. The powder X-ray diffraction patterns of these samples were all found to be consistent with patterns predicted from the single-crystal structures (Figures 6.S5–6.S8). Low-pressure N<sub>2</sub> adsorption measurements on desolvated powder samples at 77 K (Table 6.S2) reveal that the frameworks exhibit significantly reduced surface areas after cluster incorporation, consistent with the metal halide clusters filling a large portion of the framework pores. Indeed, analysis of the available void space in the structure predicts that complete loading of the metal(II) halide sheets would fill 77–99% of the pore volume and restrict all access between cages in the framework. As the formation of sheets close to the crystal exterior may hinder further diffusion of MX<sub>2</sub> units into the crystal, elemental

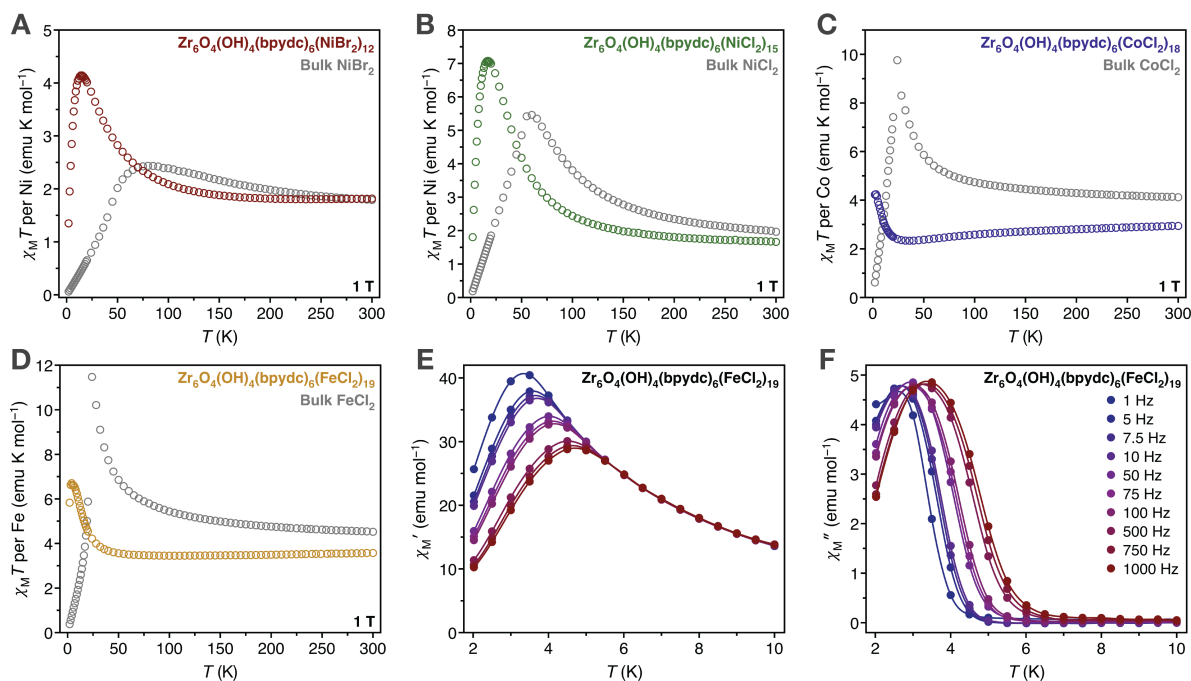
mapping was performed on the microcrystalline samples using scanning transmission electron microscopy energy-dispersive X-ray spectroscopy (STEM-EDS). These experiments reveal that the M and X spatial distributions of each variant match well with that of Zr (Figures 6.S9–6.S12), suggesting uniform dispersion of clusters throughout the crystal rather than their accumulation at regions near the surface. Notably, these observations imply that, under the reaction conditions, reversible cluster formation occurs through an equilibrium between the clusters and dissolved metal species, enabling migration of  $\text{MX}_2$  species to the crystal interior.



**Figure 6.3.** Stages of nickel(II) halide cluster growth based on crystal structures of **1** after reaction with 1.0, 1.5, and excess equivalents of  $\text{NiBr}_2$  and  $\text{NiCl}_2$ . The nickel(II) bromide structures correspond to  $\mathbf{1}(\text{NiBr}_2)_{5.6}$  (1.0 equiv),<sup>20</sup>  $\mathbf{1}(\text{NiBr}_2)_{7.2}$  (1.5 equiv), and  $\mathbf{1}(\text{NiBr}_2)_{15}$  (excess), while the nickel(II) chloride structures correspond to  $\mathbf{1}(\text{NiCl}_2)_{4.7}$  (1.0 equiv),  $\mathbf{1}(\text{NiCl}_2)_{7.8}$  (1.5 equiv), and  $\mathbf{1}(\text{NiCl}_2)_{13}$  (excess) as determined by single-crystal X-ray diffraction at 100 K. In the structures of  $\mathbf{1}(\text{NiBr}_2)_{6.7}$  (1.5 equiv) and  $\mathbf{1}(\text{NiCl}_2)_{7.8}$  (1.5 equiv), sections of the clusters are faded to illustrate their lower occupancies. Yellow, green, dark red, light green, red, blue, and gray spheres represent Zr, Ni, Br, Cl, O, N, and C atoms, respectively. Hydrogen atoms are omitted for clarity.

The formation of partially filled sheets in  $\mathbf{1}(\text{NiBr}_2)_{10}$  suggested that sheet growth could be monitored as a function of metal halide loading. Toward this end, single-crystal structures were collected at 100 K for samples of  $\mathbf{1}$  treated with increasing equivalents of  $\text{NiBr}_2$  or  $\text{Ni}(\text{DME})\text{Cl}_2$  relative to bipyridine (Figure 6.3). Reaction with one equivalent of either metal source exclusively results in metalation of the bipyridine linkers,<sup>20</sup> confirming that cluster nucleation occurs at these sites. For nickel(II) bromide, additional equivalents populate the rest of the sites, preferring edge sites over those at the interior (Figure 6.S13). This trend implies that nickel(II) bromide sheet formation initiates at the bipyridine sites, followed by growth toward the center. In contrast, the remaining sites in the nickel(II) chloride sheets fill at an even rate with increasing  $\text{NiCl}_2$  loading (Figure 6.S14), further indicating the preference of nickel(II) chloride to form completely filled sheets. Significantly, the framework surface area rises upon lowering the  $\text{NiBr}_2$  or  $\text{NiCl}_2$  loading (Table 6.S2), suggesting that the clusters in partially-loaded frameworks remain accessible for further interaction with guest molecules.

As the metal halide clusters represent fragments of metal halide monolayers, we anticipated that the magnetic behavior of each cluster would follow that of the corresponding bulk material. Conveniently, the magnetic coupling for these solids can be described by the same general model. Ferromagnetic coupling is dominant within monolayers, while antiferromagnetic coupling relates adjacent monolayers.<sup>35,36</sup> For each material, the molar magnetic susceptibility times temperature product ( $\chi_M T$ ) increases with decreasing temperature as spins within each monolayer align ferromagnetically. Below the Néel temperatures ( $T_N$ ) a sharp decrease in  $\chi_M T$  is observed as alternating monolayers adopt opposite spin orientations to form an antiferromagnetic ground state.<sup>35,36</sup>



**Figure 6.4.** Dc magnetic susceptibility data for  $\mathbf{1}(\text{NiBr}_2)_{12}$  (A),  $\mathbf{1}(\text{NiCl}_2)_{18}$  (B),  $\mathbf{1}(\text{CoCl}_2)_{18}$  (C),  $\mathbf{1}(\text{FeCl}_2)_{19}$  (D) under a 1 T applied field. Data is shown in red, green, purple, and orange symbols, respectively. Magnetic susceptibility for the corresponding bulk metal halide is shown in gray. Variable-temperature ac magnetic susceptibility data at zero dc magnetic field and in a 4 mT ac oscillating magnetic field for  $\mathbf{1}(\text{FeCl}_2)_{19}$  (E, F). Data under frequencies of 1–1,000 Hz is shown from blue to red. Lines are included to guide the eye.

To compare the behavior of the framework-confined clusters to that of their bulk counterparts,  $\chi_M T$  was measured as a function of temperature between 300 and 2 K at various applied fields. Room temperature measurements taken under a 1 T applied field revealed per metal susceptibilities commensurate to or slightly lower than those observed in the corresponding bulk material (Figure 6.4). For  $\text{FeCl}_2$  and  $\text{CoCl}_2$ , the tetrahedral metal complexes likely couple antiferromagnetically to neighboring sites and thereby suppress the per metal susceptibility.

Upon cooling,  $\chi_M T$  increases for all clusters. Analogous to the bulk metal halides, individual spins within each cluster align parallel to one another, coupling ferromagnetically to form a total cluster spin,  $S$ . Notably,  $\chi_M T$  continues to increase well below the Néel temperature for each corresponding bulk material, indicating suppression of the antiferromagnetic interlayer interaction present in the bulk metal(II) halides. While a steep decrease in  $\chi_M T$  is observed below 10 K for all clusters, we attribute this primarily to Zeeman splitting of the high-spin ground state,  $S$ , rather than intercluster interactions. Taken together, these findings suggest that the metal halide clusters mirror the magnetic structures of bulk metal halide monolayers.<sup>21</sup>

Given the large spin ground states of the ferromagnetically-coupled clusters, we anticipated that slow magnetic relaxation or single-molecule magnetism may be observed. Magnetic relaxation dynamics were initially probed through magnetic hysteresis measurements and by comparing zero-field-cooled (ZFC) and field-cooled (FC) susceptibilities. While  $\text{CoCl}_2$ ,  $\text{NiCl}_2$ , and  $\text{NiBr}_2$  clusters all exhibited closed hysteresis loops, the  $\text{FeCl}_2$  clusters exhibit a divergence between ZFC and FC susceptibilities at 3 K (Figure 6.S15), and open hysteresis loops at 2 K ( $H_C = 70$  mT at  $9 \text{ mT s}^{-1}$ ; Figure 6.S16). These results suggested unique relaxation dynamics, and ac susceptibility measurements were subsequently performed to further investigate the origins of this low temperature behavior.

Temperature dependent in-phase ( $\chi'$ ) and out-of-phase ( $\chi''$ ) susceptibilities were collected to investigate the magnetic relaxation dynamics of the  $\text{FeCl}_2$  clusters (Figures 6.4E and 6.4F). A peak maximum in  $\chi'$  was found to vary by 1.3 K over a frequency range of 1–1,000 Hz. The frequency dependence in  $\chi''$  precludes the existence of long-range magnetic ordering. Consequently, the low-temperature behavior can be attributed either to cluster-based superparamagnetism or to a glassy magnetic phase transition. The magnitude of the frequency shift can be quantified using the Mydosh parameter ( $\gamma$ ), which adopts characteristic values for different magnetic behaviors.<sup>37</sup> We find a Mydosh parameter of 0.14 for the  $\text{FeCl}_2$  clusters, consistent with superparamagnetism. Furthermore, Arrhenius fitting of the ac susceptibility affords physically meaningful values for the spin reversal barrier,  $U_{\text{eff}}$  ( $16 \text{ cm}^{-1}$ ) and relaxation time,  $\tau_0$  ( $10^{-10}$  s). These values are competitive with other iron(II) cluster-based single-molecule magnets, and highlight that these confined clusters can exhibit single-molecule magnet behavior.<sup>38,39</sup>

## 6.4. Conclusion

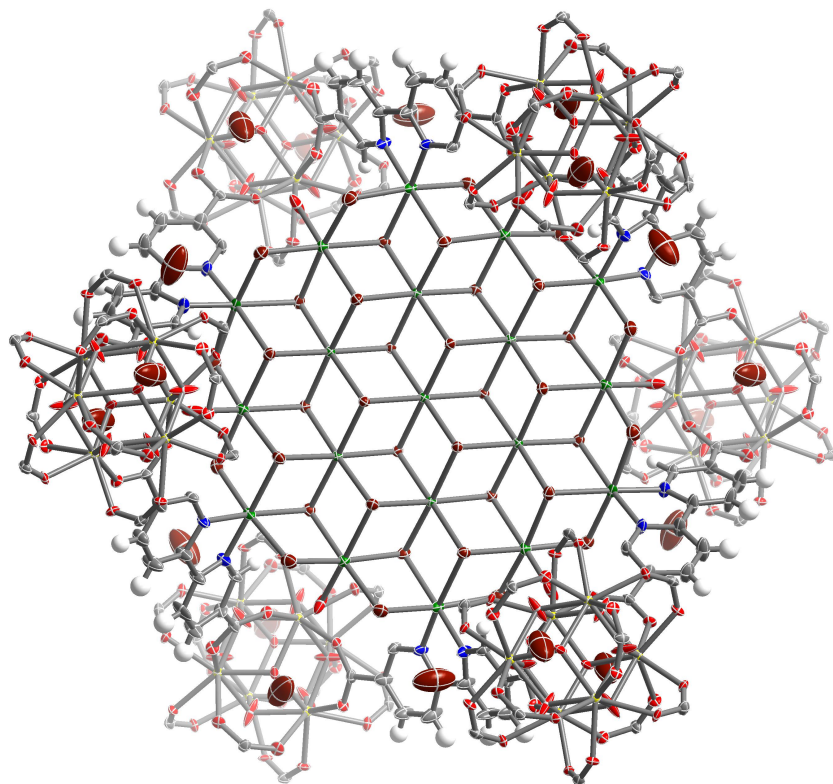
Altogether, these results clearly demonstrate that the pore environment of a metal–organic framework can be leveraged as a multidentate ligand scaffold to control the growth of inorganic clusters. Moreover, binding these clusters within a crystalline support enables their structural determination by single-crystal X-ray diffraction, which in turn affords detailed insight into their structure and the mechanism of their formation. Finally, magnetic measurements establish that these clusters display magnetic properties that arise directly from their confined size and shape.

## **6.5. Acknowledgements**

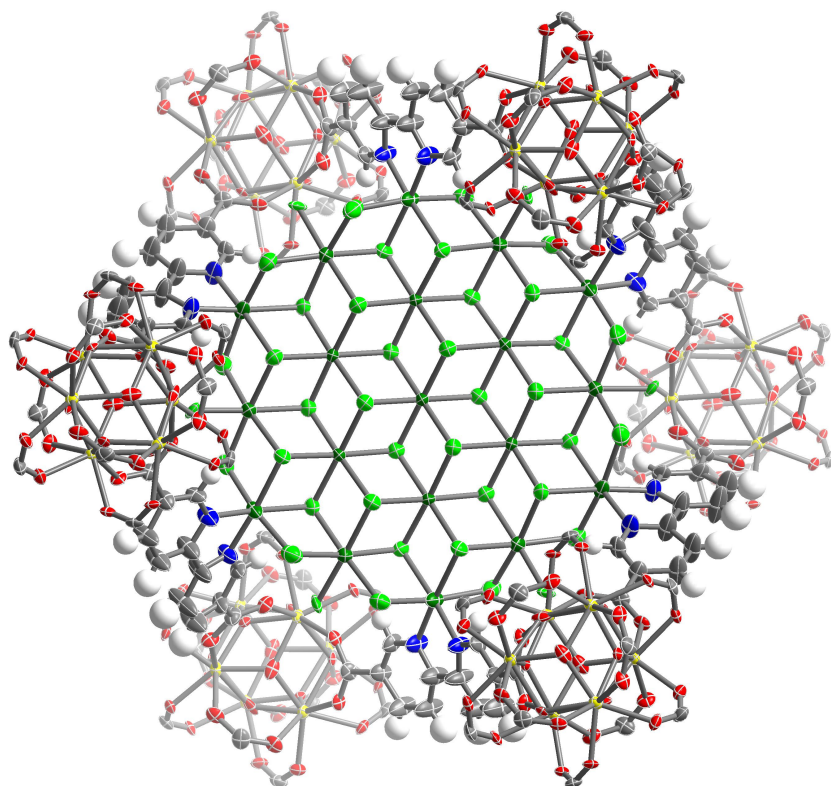
Additional data described in this paper are presented in the supporting online material. This research was supported through a Multidisciplinary University Research Initiatives Program funded by the U.S. Department of Defence, Office of Naval Research under Award N00014-15-1-2681. Single-crystal X-ray diffraction experiments were performed at beamline 11.3.1 at the Advanced Light Source at Lawrence Berkeley National Laboratory. The Advanced Light Source is supported by the Director, Office of Science, Office of Basic Energy Sciences, of the U.S. Department of Energy under Contract no. DE-AC02-05CH11231. Powder X-ray diffraction data were collected at beamline 17-BM-B at the Advanced Photon Source, a U.S. Department of Energy, Office of Science User Facility operated by the DOE Office of Science by Argonne National Laboratory under Contract No. DE-AC02-06CH11357. We thank Simon J. Teat for experimental assistance and helpful discussions.

## 6.6. Supplementary Information

### 6.6.1. Supplementary Figures

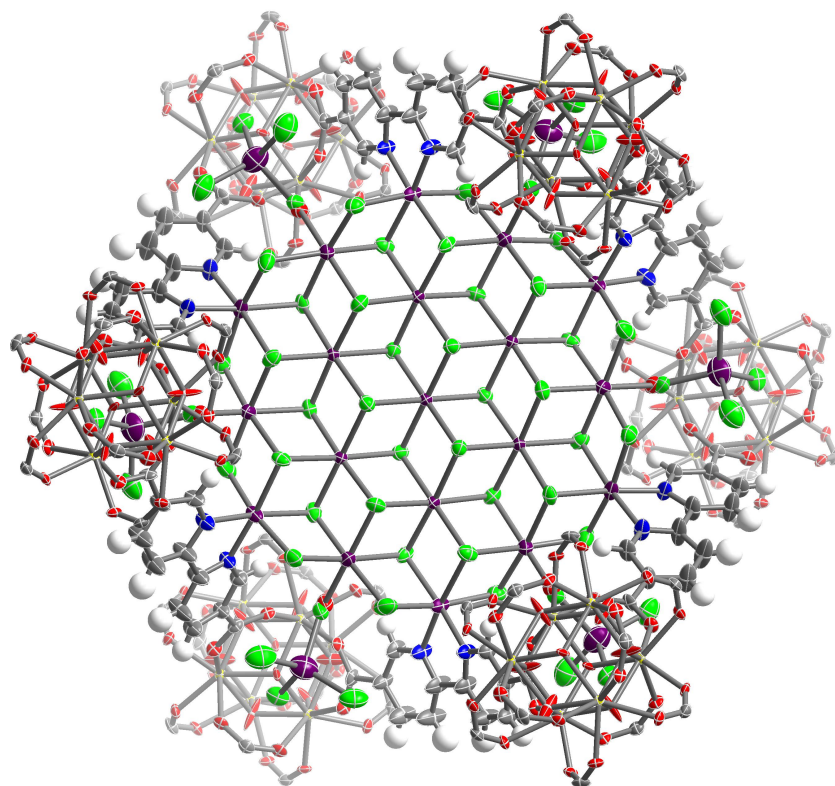


**Figure 6.S1.** Atomic displacement parameter plot of  $\text{Zr}_6\text{O}_4(\text{OH})_4(\text{bpydc})_6(\text{NiBr}_2)_{15}$  at 100 K drawn at 50% probability level as determined by single-crystal X-ray diffraction. An oxygen atom from a disordered solvent molecule likely completes the coordination sphere of the nickel center at Site II; however the rest of the molecule could not be modeled. Bromide anions balance the charge of the clusters were located near the bridging hydroxides of the zirconium clusters. Yellow, green, dark red, red, blue, gray, and white ellipsoids represent Zr, Ni, Br, O, N, C, and H atoms, respectively.

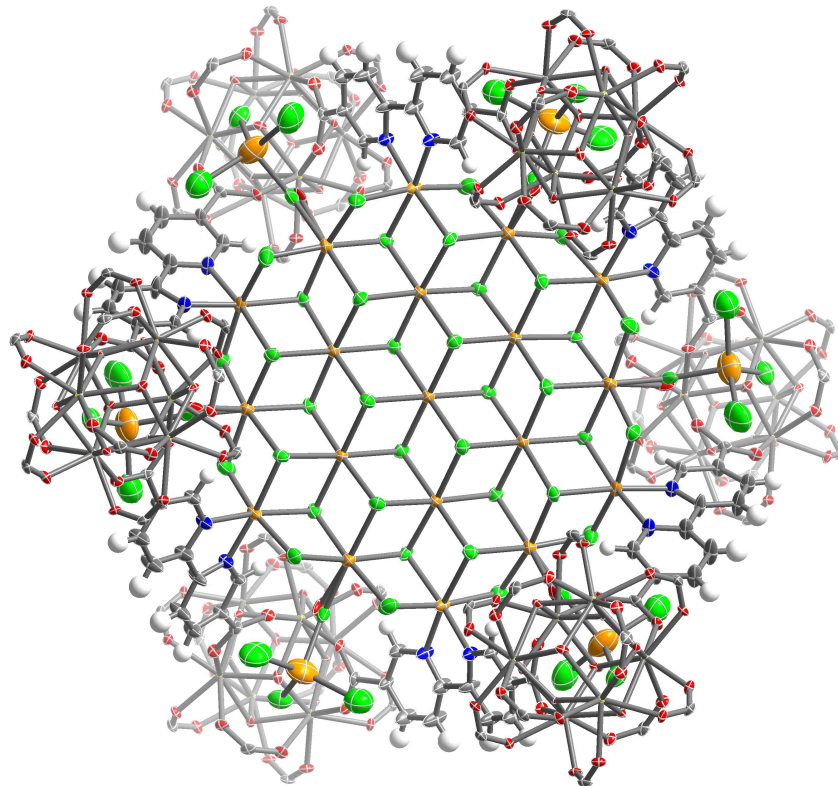


**Figure 6.S2.** Atomic displacement parameter plot of  $\text{Zr}_6\text{O}_4(\text{OH})_4(\text{bpydc})_6(\text{NiCl}_2)_{13}$  at 100 K drawn at 50% probability level as determined by single-crystal X-ray diffraction. Yellow, green, light green, red, blue, gray, and white ellipsoids represent Zr, Ni, Cl, O, N, C, and H atoms, respectively.

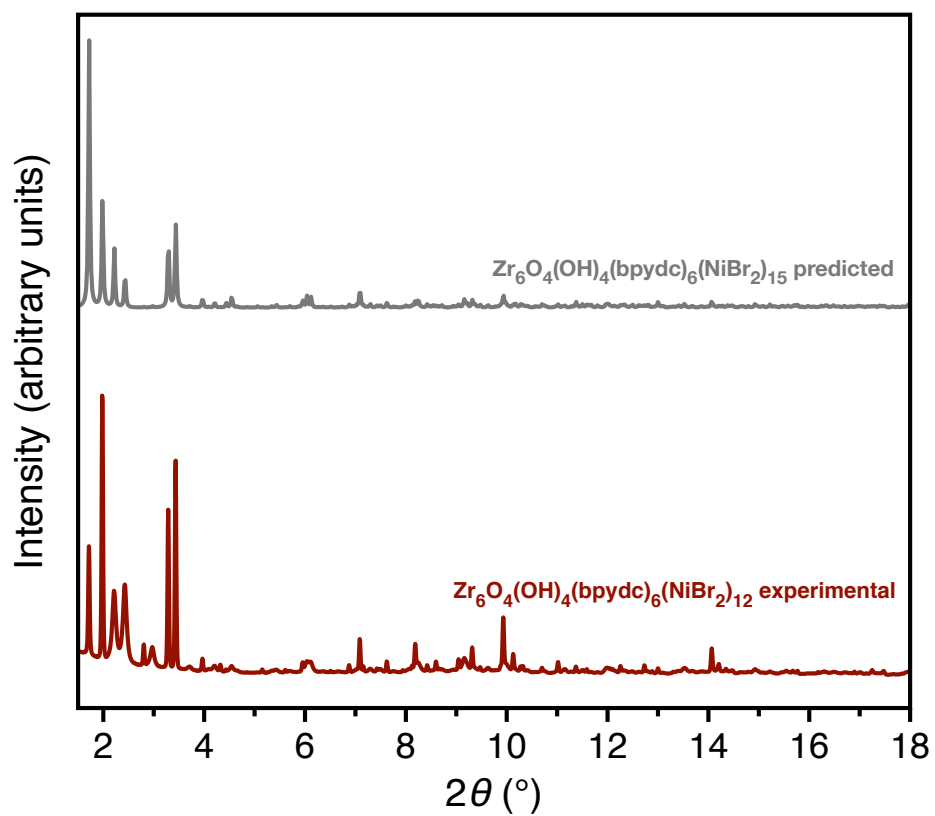




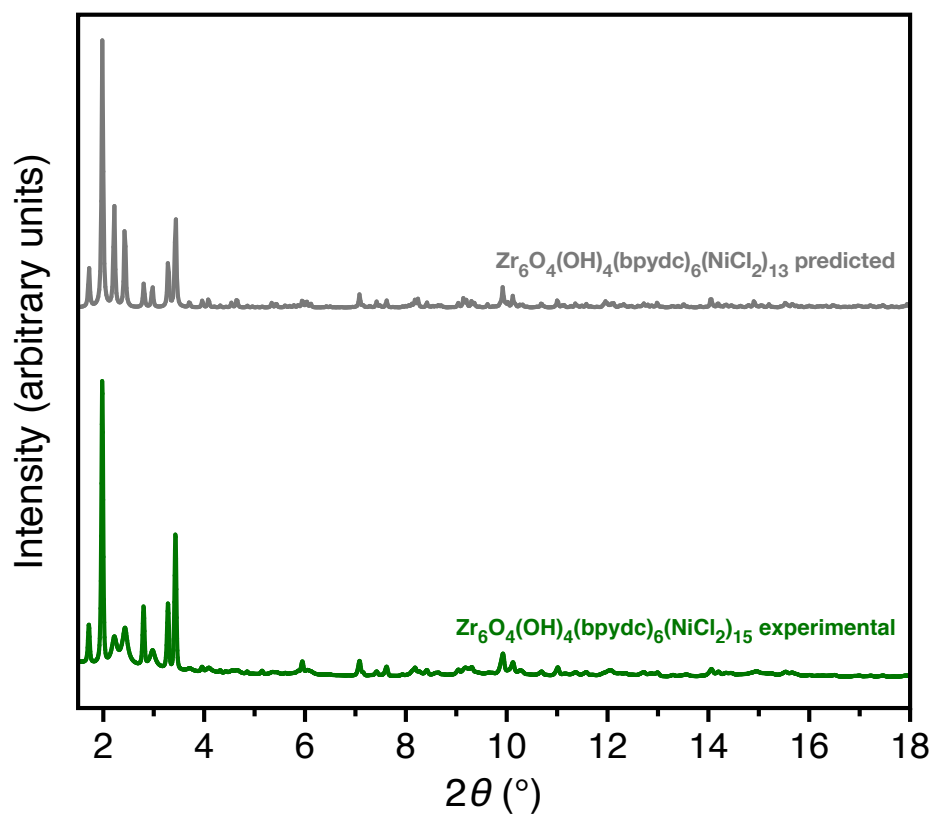
**Figure 6.S3.** Atomic displacement parameter plot of  $\text{Zr}_6\text{O}_4(\text{OH})_4(\text{bpydc})_6(\text{CoCl}_2)_{14}$  at 100 K drawn at 50% probability level as determined by single-crystal X-ray diffraction. Note that the tetrahedral metal complexes likely exist as a mixture of  $[\text{CoCl}_4]^{2-}$  and  $\text{Co}(\text{DME})\text{Cl}_2$  species based on relative occupancies of the  $\text{Cl}^-$  ligands, but the coordinated DME molecules could not be resolved due to disorder and weak scattering compared to  $\text{Cl}^-$ . Yellow, purple, light green, red, blue, gray, and white ellipsoids represent Zr, Co, Cl, O, N, C, and H atoms, respectively.



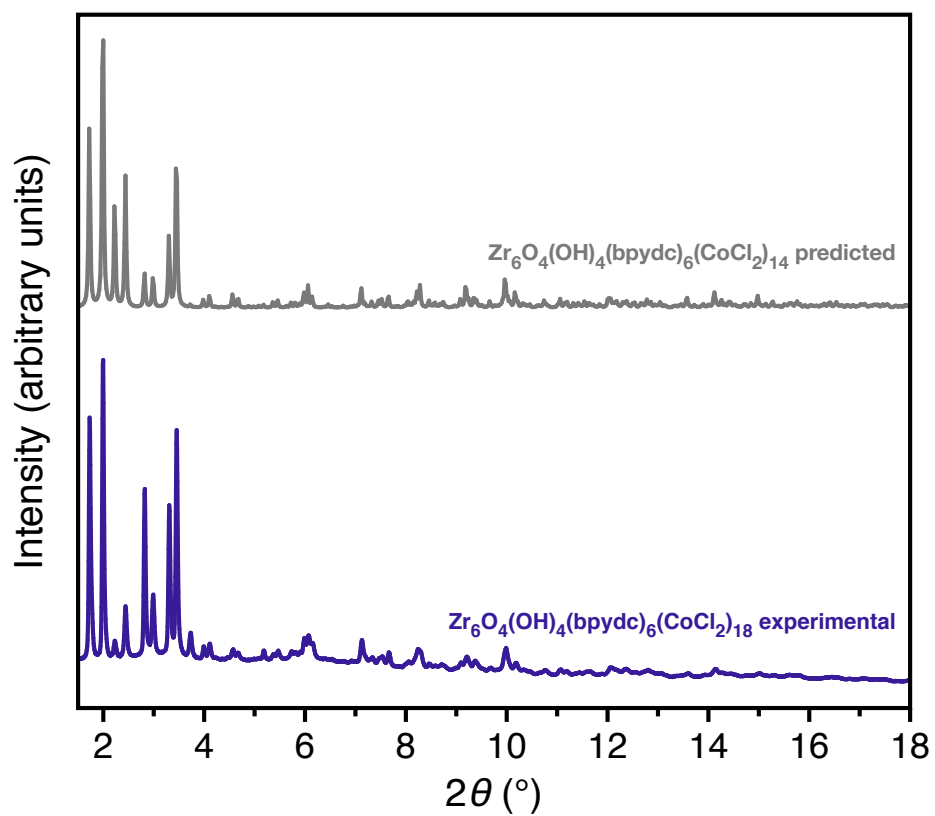
**Figure 6.S4.** Atomic displacement parameter plot of  $\text{Zr}_6\text{O}_4(\text{OH})_4(\text{bpydc})_6(\text{FeCl}_2)_{17}$  at 100 K drawn at 50% probability level as determined by single-crystal X-ray diffraction. Note that the tetrahedral metal complexes likely exist as a mixture of  $[\text{FeCl}_4]^{2-}$  and  $\text{Fe}(\text{DME})\text{Cl}_2$  species based on relative occupancies of the  $\text{Cl}^-$  ligands, but the coordinated DME molecules could not be resolved due to disorder and weak scattering compared to  $\text{Cl}^-$ . Yellow, orange, light green, red, blue, gray, and white ellipsoids represent Zr, Fe, Cl, O, N, C, and H atoms, respectively.



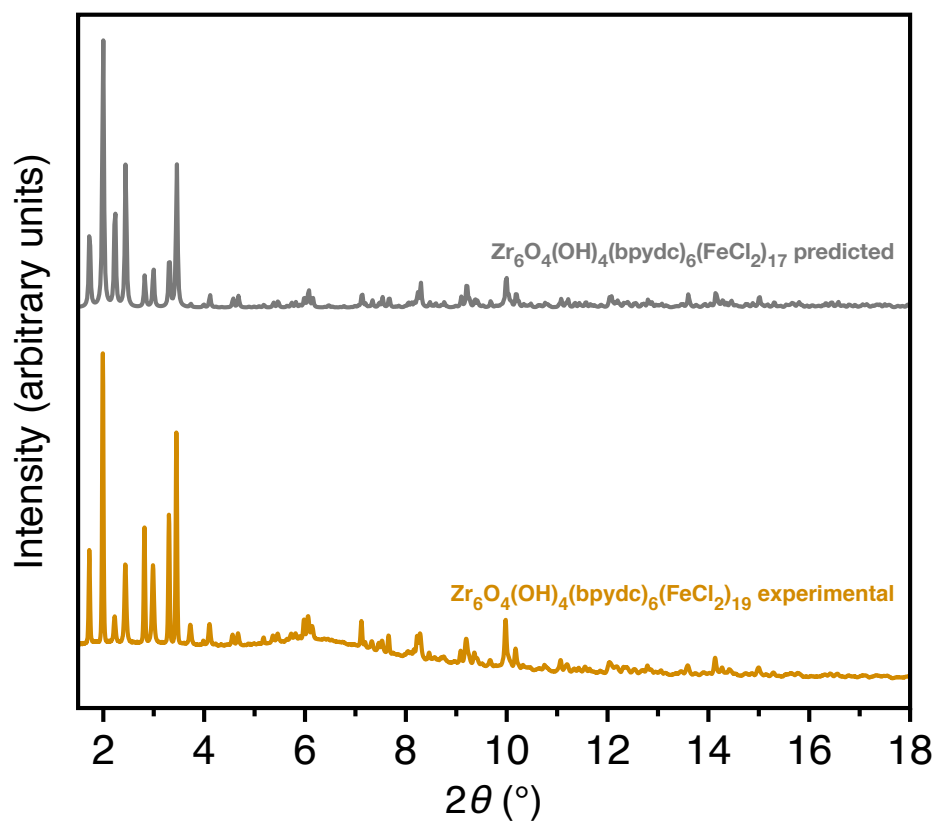
**Figure 6.S5.** Comparison of the predicted powder X-ray diffraction pattern for  $\text{Zr}_6\text{O}_4(\text{OH})_4(\text{bpydc})_6(\text{NiBr}_2)_{15}$  (light gray) and the experimental powder X-ray diffraction pattern for  $\text{Zr}_6\text{O}_4(\text{OH})_4(\text{bpydc})_6(\text{NiBr}_2)_{12}$  (red) at 298 K with a wavelength of 0.45241 Å.



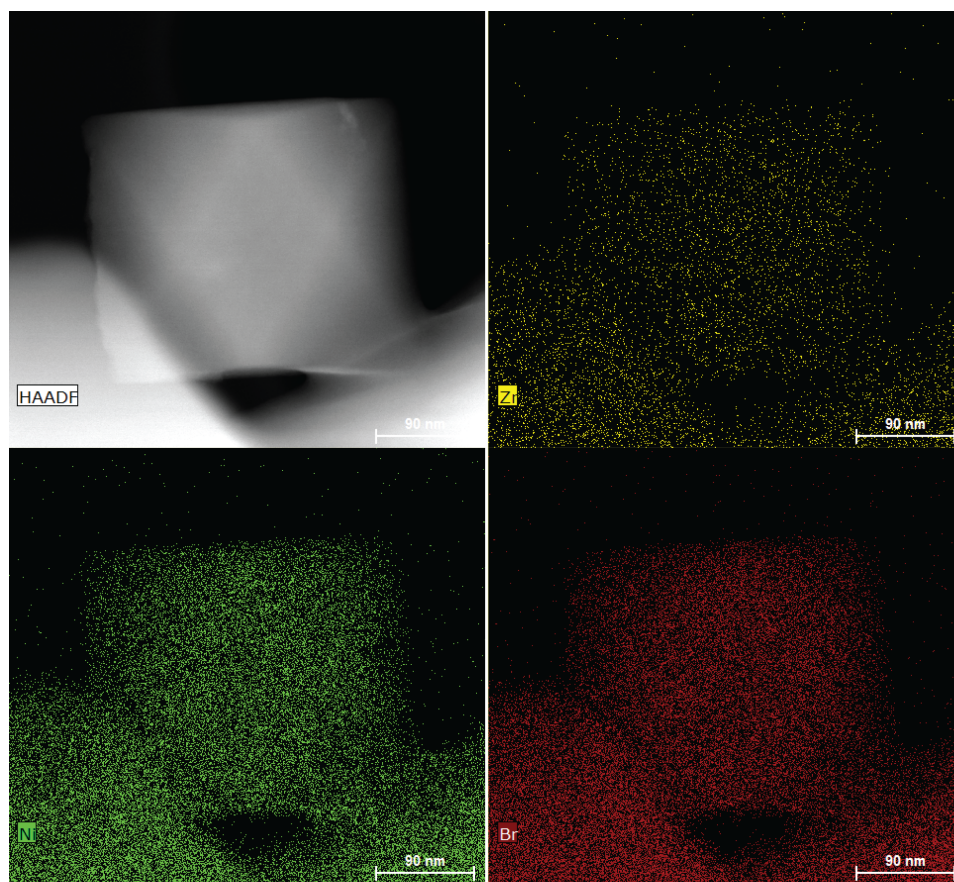
**Figure 6.S6.** Comparison of the predicted powder X-ray diffraction pattern for  $\text{Zr}_6\text{O}_4(\text{OH})_4(\text{bpydc})_6(\text{NiCl}_2)_{13}$  (light gray) and the experimental powder X-ray diffraction pattern for  $\text{Zr}_6\text{O}_4(\text{OH})_4(\text{bpydc})_6(\text{NiCl}_2)_{15}$  (green) at 298 K with a wavelength of 0.45241 Å.



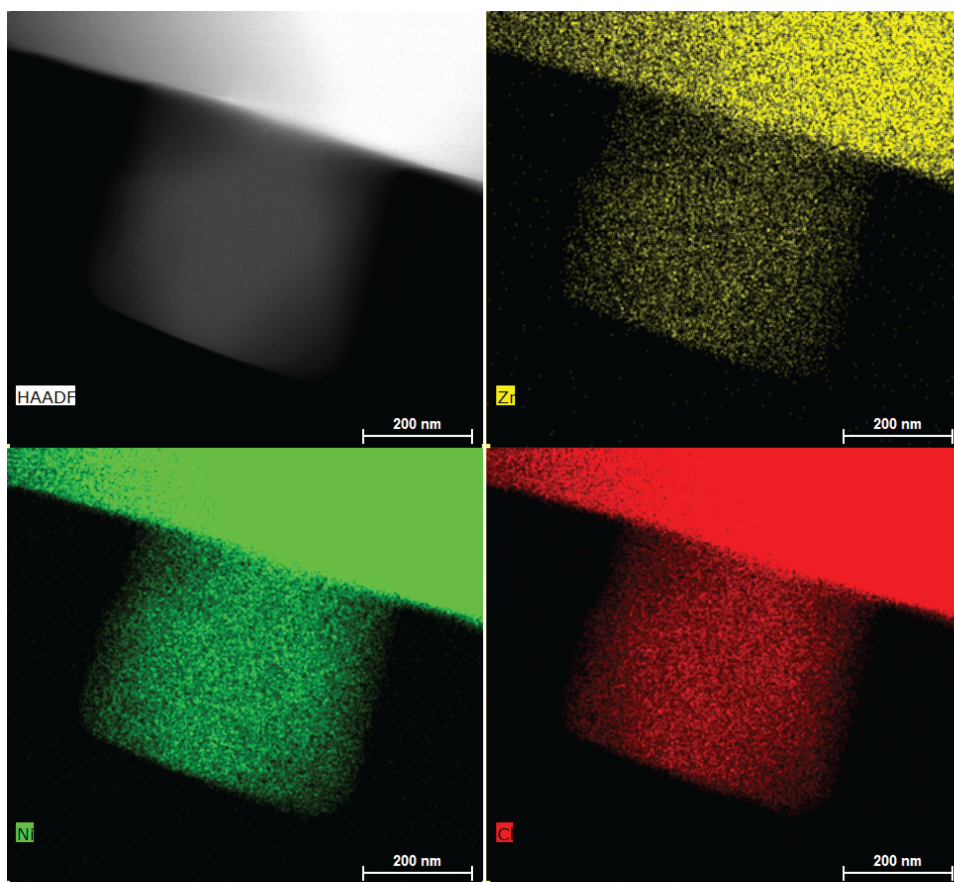
**Figure 6.S7.** Comparison of the predicted powder X-ray diffraction pattern for  $\text{Zr}_6\text{O}_4(\text{OH})_4(\text{bpydc})_6(\text{CoCl}_2)_{14}$  (light gray) and the experimental powder X-ray diffraction pattern for  $\text{Zr}_6\text{O}_4(\text{OH})_4(\text{bpydc})_6(\text{CoCl}_2)_{18}$  (violet) at 298 K with a wavelength of 0.45241 Å.



**Figure 6.S8.** Comparison of the predicted powder X-ray diffraction pattern for  $\text{Zr}_6\text{O}_4(\text{OH})_4(\text{bpydc})_6(\text{FeCl}_2)_{17}$  (light gray) and the experimental powder X-ray diffraction pattern for  $\text{Zr}_6\text{O}_4(\text{OH})_4(\text{bpydc})_6(\text{FeCl}_2)_{19}$  (orange) at 298 K with a wavelength of 0.45241 Å.

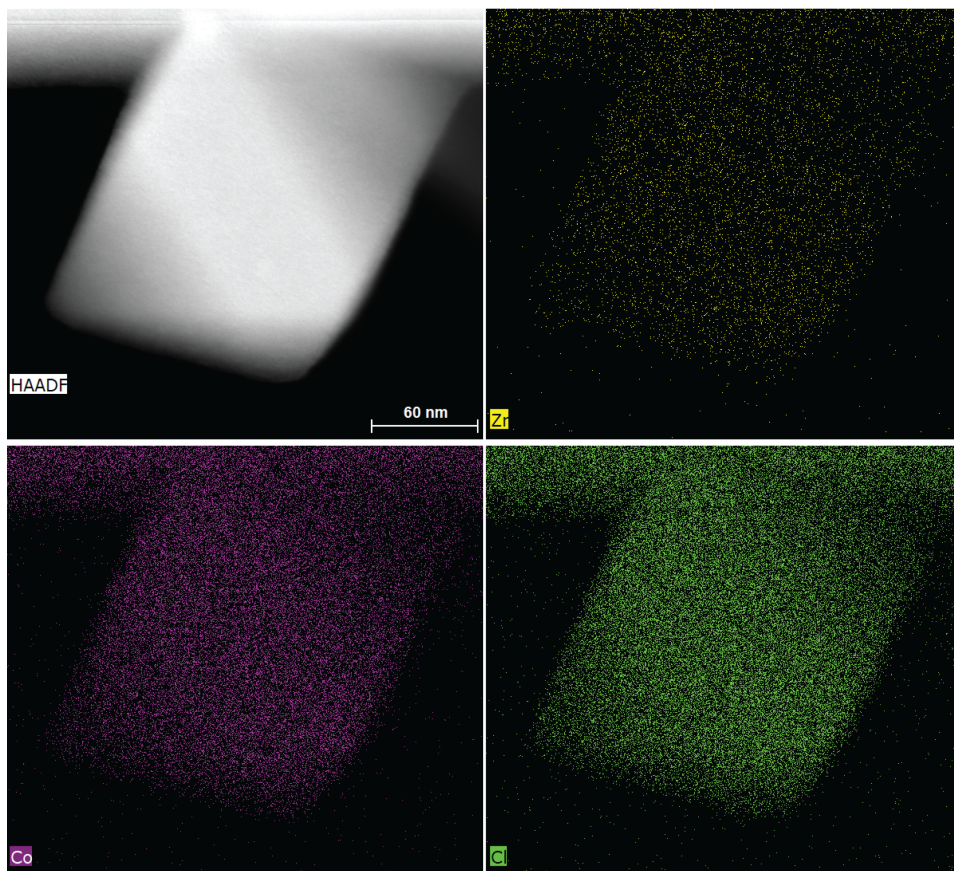


**Figure 6.S9.** High-angle annular dark field (HAADF) image (top left) and energy-dispersive X-ray spectroscopy (EDS) Zr (top right; yellow), Ni (bottom left; green), and Br (bottom right; red) mapping of a microcrystalline powder sample of  $1(\text{NiBr}_2)_{12}$ .

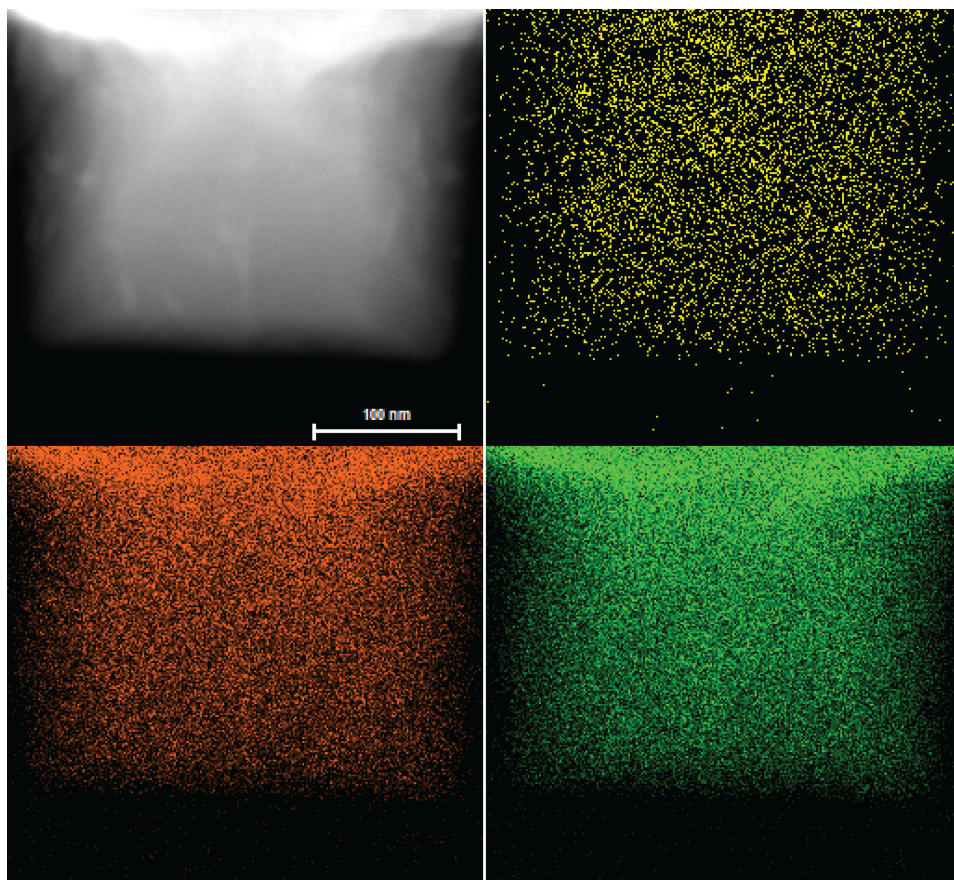


**Figure 6.S10.** High-angle annular dark field (HAADF) image (top left) and energy-dispersive X-ray spectroscopy (EDS) mapping Zr (top right; yellow), Ni (bottom left; green), and Cl (bottom right; red) of a microcrystalline powder sample of  $1(\text{NiCl}_2)_{15}$ .

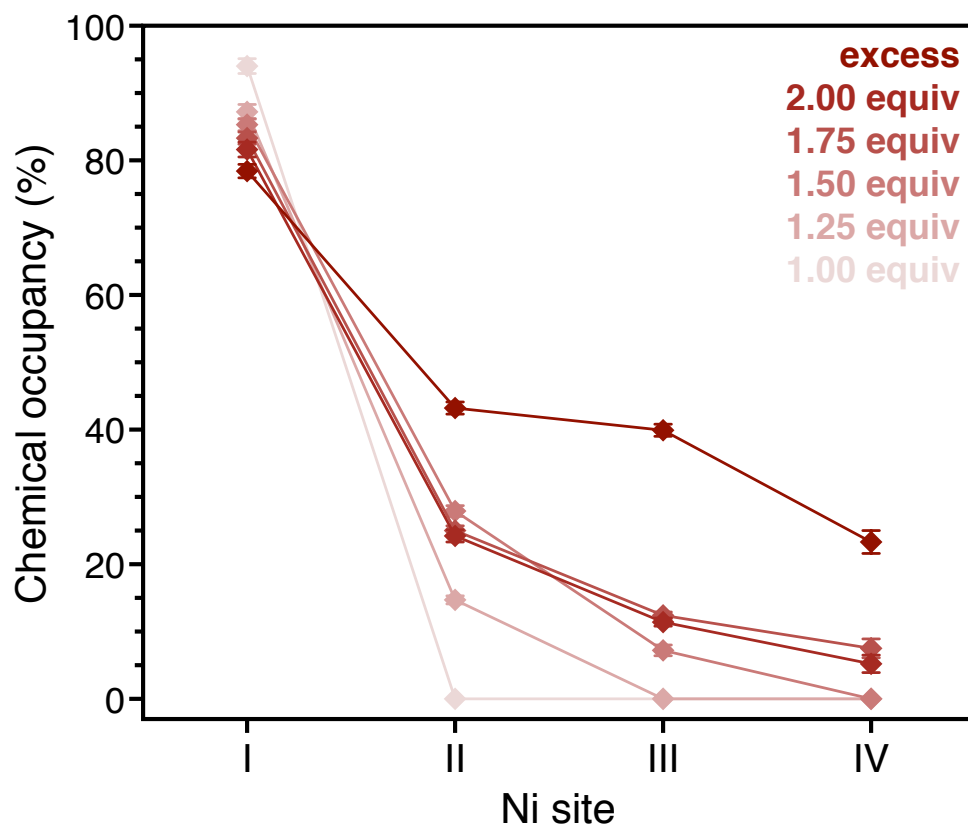




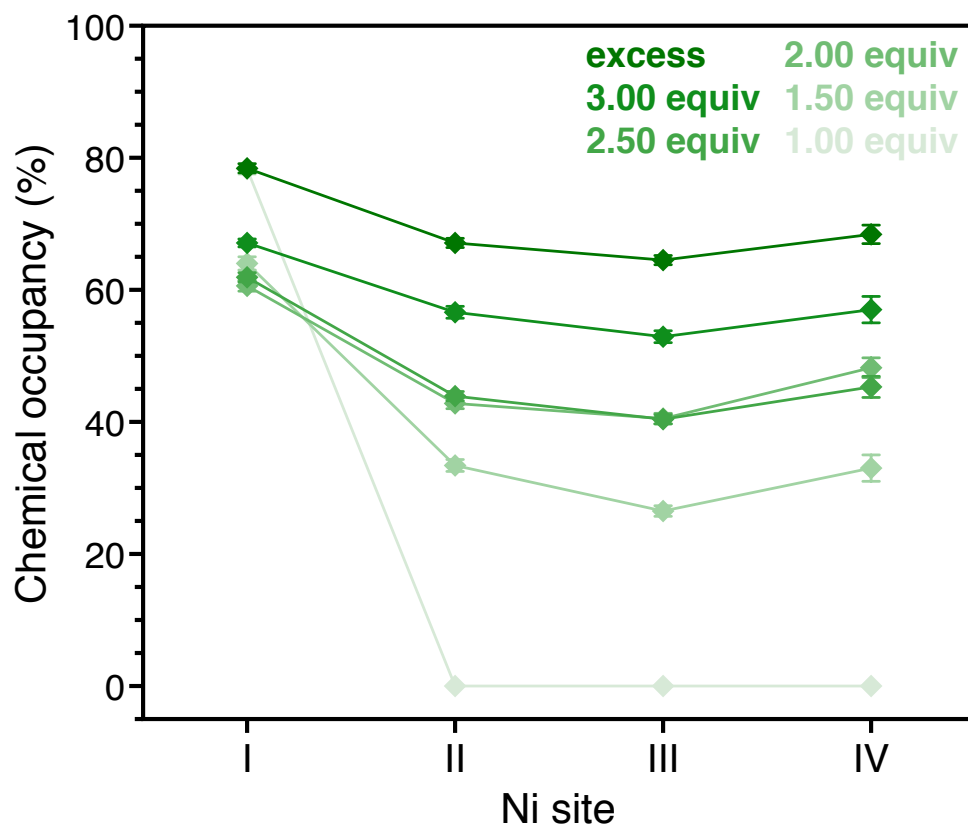
**Figure 6.S11.** High-angle annular dark field (HAADF) image (top left) and energy-dispersive X-ray spectroscopy (EDS) Zr (top right; yellow), Co (bottom left; violet), and Cl (bottom right; green) mapping of a microcrystalline powder sample of  $1(\text{CoCl}_2)_{14}$ .



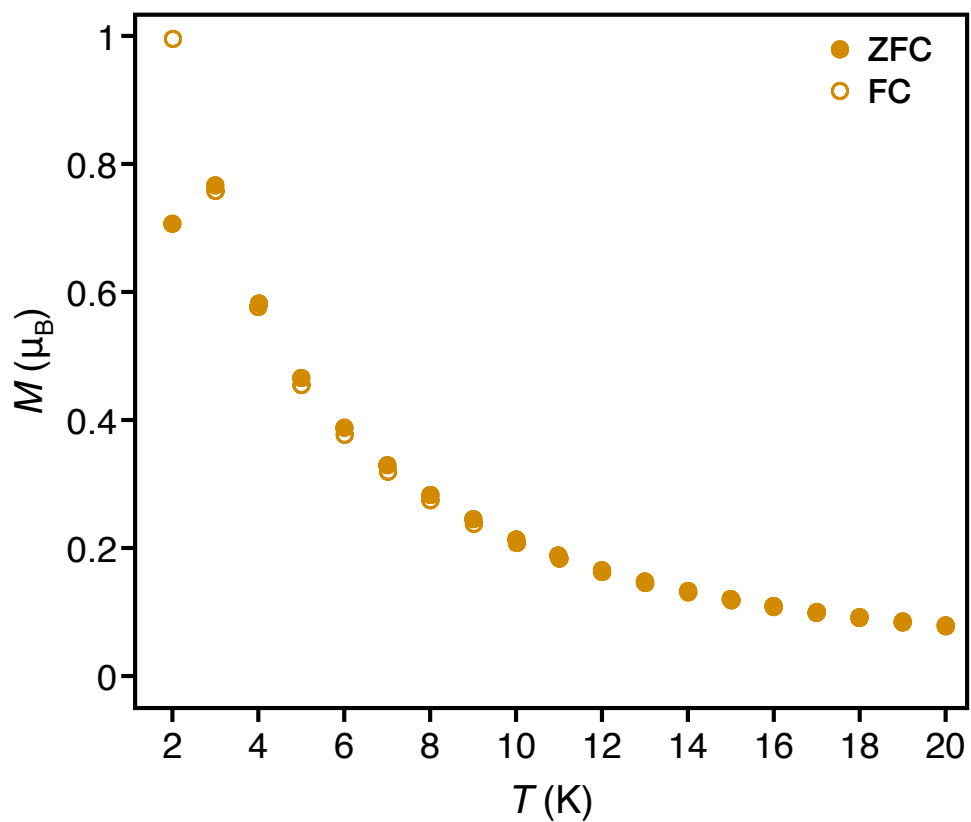
**Figure 6.S12.** High-angle annular dark field (HAADF) image (top left) and energy-dispersive X-ray spectroscopy (EDS) Zr (top right; yellow), Fe (bottom left; orange), and Cl (bottom right; green) mapping of a microcrystalline powder sample of  $1(\text{FeCl}_2)_{19}$ .



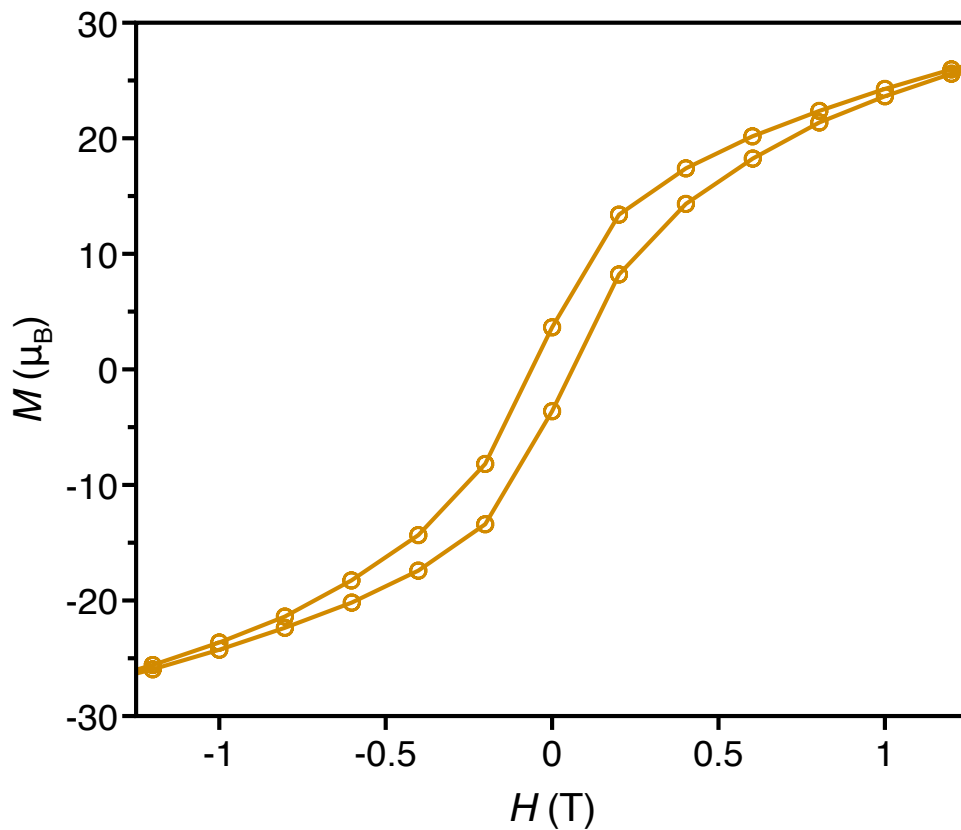
**Figure 6.S13.** Comparison of the Ni site occupancies for single-crystal structures of NiBr<sub>2</sub>-loaded **1** obtained by reaction of **1** with 1.00 equiv to excess (> 50 equiv) NiBr<sub>2</sub> (light to dark red) in diglyme. Solid lines are included to guide the eye.



**Figure 6.S14.** Comparison of the Ni site occupancies for single-crystal structures of NiCl<sub>2</sub>-loaded **1** obtained by reaction of **1** with 1.00 equiv to excess (> 50 equiv) Ni(DME)Cl<sub>2</sub> (light to dark green) in diglyme. Solid lines are included to guide the eye.



**Figure 6.S15.** Zero field-cooled (filled circles) and field-cooled (empty circles) magnetization ( $M$ ) versus temperature ( $T$ ) data for  $\mathbf{1(FeCl_2)_{19}}$  (orange). Data collected under an applied field of 0.01 T.



**Figure 6.S16.** Magnetization ( $M$ ) versus applied dc magnetic field ( $H$ ) data for  $1(\text{FeCl}_2)$  (orange) at 2 K. Hysteresis loops were recorded at a sweep rate of 9 mT/s. Solid lines are included as guides for the eye.

## 6.6.2. Supplementary Tables

**Table 6.S1.** Crystallographic site occupancy factors for MX<sub>2</sub>-loaded (MX<sub>2</sub> = NiBr<sub>2</sub>, NiCl<sub>2</sub>, CoCl<sub>2</sub>, FeCl<sub>2</sub>) metal–organic frameworks as determined by single-crystal X-ray diffraction.

Compound <sup>a</sup>	Metal source	Solvent	Site Occupancy (%)				
			Site I	Site II	Site III	Site IV	Site V
<b>1</b> (NiBr <sub>2</sub> ) <sub>9.9</sub>	Ni(DME)Br <sub>2</sub> (excess)	diglyme	78.4(10)	43.2(9)	39.9(9)	23.3(17)	–
<b>1</b> (NiBr <sub>2</sub> ) <sub>7.1</sub>	NiBr <sub>2</sub> (2.00 equiv)	diglyme	81.6(11)	24.2(9)	11.4(6)	5.2(11)	–
<b>1</b> (NiBr <sub>2</sub> ) <sub>7.3</sub>	NiBr <sub>2</sub> (1.75 equiv)	diglyme	83.3(9)	25.0(7)	12.4(5)	7.5(10)	–
<b>1</b> (NiBr <sub>2</sub> ) <sub>7.2</sub>	NiBr <sub>2</sub> (1.50 equiv)	diglyme	85.3(9)	27.9(8)	7.2(5)	0	–
<b>1</b> (NiBr <sub>2</sub> ) <sub>6.1</sub>	NiBr <sub>2</sub> (1.25 equiv)	diglyme	87.2(11)	14.7(6)	0	0	–
<b>1</b> (NiBr <sub>2</sub> ) <sub>5.6</sub> (ref. 20)	NiBr <sub>2</sub> (1.00 equiv)	diglyme	94.0	0	0	0	–
<b>1</b> (NiCl <sub>2</sub> ) <sub>13</sub>	Ni(DME)Cl <sub>2</sub> (excess)	diglyme	78.4(7)	67.1(7)	64.5(7)	68.4(16)	–
<b>1</b> (NiCl <sub>2</sub> ) <sub>11</sub>	Ni(DME)Cl <sub>2</sub> (3.0 equiv)	diglyme	67.1(6)	56.6(9)	52.9(9)	57(2)	–
<b>1</b> (NiCl <sub>2</sub> ) <sub>9.1</sub>	Ni(DME)Cl <sub>2</sub> (2.5 equiv)	diglyme	61.9(7)	43.9(7)	40.4(7)	45.3(16)	–
<b>1</b> (NiCl <sub>2</sub> ) <sub>9.2</sub>	Ni(DME)Cl <sub>2</sub> (2.0 equiv)	diglyme	60.6(8)	42.8(8)	40.5(8)	48.2(19)	–
<b>1</b> (NiCl <sub>2</sub> ) <sub>7.7</sub>	Ni(DME)Cl <sub>2</sub> (1.5 equiv)	diglyme	64(1)	33.4(9)	26.5(8)	33(2)	–
<b>1</b> (NiCl <sub>2</sub> ) <sub>4.7</sub>	Ni(DME)Cl <sub>2</sub> (1.0 equiv)	diglyme	78.3(7)	0	0	0	–
<b>1</b> (NiBr <sub>2</sub> ) <sub>15</sub>	Ni(DME)Br <sub>2</sub> (excess)	DME/DFB 10% (v/v)	87.1(6)	73.5(2)	80.5(6)	83.8(11)	–
<b>1</b> (NiBr <sub>2</sub> ) <sub>14</sub>	Ni(DME)Br <sub>2</sub> (3.25 equiv)	DME/DFB 10% (v/v)	83.2(6)	63.6(6)	68.4(6)	69.6(12)	–
<b>1</b> (CoCl <sub>2</sub> ) <sub>14</sub>	CoCl <sub>2</sub> (excess)	DME/DFB 10% (v/v)	81.4(6)	63.0(6)	56.3(6)	60.5(12)	24.8(9)
<b>1</b> (CoCl <sub>2</sub> ) <sub>15</sub>	CoCl <sub>2</sub> (3.25 equiv)	DME/DFB 10% (v/v)	83.6(6)	64.9(6)	63.1(6)	67.2(13)	30.6(9)
<b>1</b> (FeCl <sub>2</sub> ) <sub>17</sub>	FeCl <sub>2</sub> (excess)	DME/DFB 10% (v/v)	88.5(5)	79.7(5)	76.7(5)	74.6(10)	32.8(7)
<b>1</b> (FeCl <sub>2</sub> ) <sub>16</sub>	FeCl <sub>2</sub> (3.25 equiv)	DME/DFB 10% (v/v)	86.5(6)	68.1(6)	67.2(6)	67.8(13)	31(1)

<sup>a</sup>Formulas are reported based on the metal loading obtained by refinement of the metal site occupancy factors.

**Table 6.S2.** Metal loading and surface areas of metal–organic frameworks investigated in this work.

Compound <sup>a</sup>	Metal source	Solvent	Metal Loading (%) <sup>b</sup>		Surface Area (m <sup>2</sup> /g) <sup>c</sup>	
			Single Crystal	Powder	Langmuir	BET
<b>1</b> (ref. 19)	–	–	–	–	2770	2730
<b>1</b> (NiBr <sub>2</sub> ) <sub>9,9</sub>	Ni(DME)Br <sub>2</sub> (excess)	diglyme	52.2(5)	–	–	–
<b>1</b> (NiBr <sub>2</sub> ) <sub>9,1</sub>	NiBr <sub>2</sub> (3.00 equiv)	diglyme	–	48(2)	420	450
<b>1</b> (NiBr <sub>2</sub> ) <sub>9,1</sub>	NiBr <sub>2</sub> (2.00 equiv)	diglyme	37.3(5)	48(3)	600	520
<b>1</b> (NiBr <sub>2</sub> ) <sub>9,3</sub>	NiBr <sub>2</sub> (1.75 equiv)	diglyme	38.6(4)	48.8(12)	610	520
<b>1</b> (NiBr <sub>2</sub> ) <sub>7,3</sub>	NiBr <sub>2</sub> (1.50 equiv)	diglyme	38.0(4)	45.3(14)	620	520
<b>1</b> (NiBr <sub>2</sub> ) <sub>8</sub>	NiBr <sub>2</sub> (1.25 equiv)	diglyme	32.2(4)	42.1(17)	576	500
<b>1</b> (NiBr <sub>2</sub> ) <sub>6</sub> (ref. 20)	NiBr <sub>2</sub> (1.00 equiv)	diglyme	29.7	31.9(6)	650	550
<b>1</b> (NiCl <sub>2</sub> ) <sub>13</sub>	Ni(DME)Cl <sub>2</sub> (excess)	diglyme	69.9(4)	–	–	–
<b>1</b> (NiCl <sub>2</sub> ) <sub>15</sub>	Ni(DME)Cl <sub>2</sub> (3.0 equiv)	diglyme	58.9(5)	80.5(2)	150	90
<b>1</b> (NiCl <sub>2</sub> ) <sub>14</sub>	Ni(DME)Cl <sub>2</sub> (2.5 equiv)	diglyme	48.6(4)	73.2(7)	310	240
<b>1</b> (NiCl <sub>2</sub> ) <sub>12</sub>	Ni(DME)Cl <sub>2</sub> (2.0 equiv)	diglyme	48.0(4)	63.1(19)	470	410
<b>1</b> (NiCl <sub>2</sub> ) <sub>9,8</sub>	Ni(DME)Cl <sub>2</sub> (1.5 equiv)	diglyme	40.8(5)	51.8(8)	730	600
<b>1</b> (NiCl <sub>2</sub> ) <sub>4,7</sub>	Ni(DME)Cl <sub>2</sub> (1.0 equiv)	diglyme	24.7(2)	29.5(7)	860	770
<b>1</b> (NiBr <sub>2</sub> ) <sub>15</sub>	Ni(DME)Br <sub>2</sub> (excess)	DME/DFB 10% (v/v)	80.5(4)	–	–	–
<b>1</b> (NiBr <sub>2</sub> ) <sub>12</sub>	Ni(DME)Br <sub>2</sub> (3.25 equiv)	DME/DFB 10% (v/v)	71.6(3)	79.3(3)	130	110
<b>1</b> (CoCl <sub>2</sub> ) <sub>14</sub>	CoCl <sub>2</sub> (excess)	DME/DFB 10% (v/v)	74.7(4)	–	–	–
<b>1</b> (CoCl <sub>2</sub> ) <sub>18</sub>	CoCl <sub>2</sub> (3.25 equiv)	DME/DFB 10% (v/v)	80.0(4)	93(4)	50	50
<b>1</b> (FeCl <sub>2</sub> ) <sub>17</sub>	FeCl <sub>2</sub> (excess)	DME/DFB 10% (v/v)	91.6(2)	–	–	–
<b>1</b> (FeCl <sub>2</sub> ) <sub>19</sub>	FeCl <sub>2</sub> (3.25 equiv)	DME/DFB 10% (v/v)	83.4(5)	100(3)	10	50

<sup>a</sup>With the exception of the samples prepared from only single crystals, formulas are reported based on the metal loading of the powder samples. <sup>b</sup>Metal loadings are normalized with respect to the expected loading for full occupancy of a M<sub>19</sub>X<sub>38</sub> cluster. Single-crystal loadings were obtained by refinement of the metal site occupancy factors, while powder loadings were determined from analysis of the M:Zr ratio by ICP-OES. <sup>c</sup>Langmuir and BET (Brunauer–Emmett–Teller) surface areas were calculated from analysis of low-pressure N<sub>2</sub> adsorption isotherms at 77 K.



**Table 6.S3.** Crystallographic data for frameworks obtained from reaction of **1** with NiBr<sub>2</sub> sources in diglyme.

	<b>I</b> (NiBr <sub>2</sub> ) <sub>9,9</sub> (excess)	<b>I</b> (NiBr <sub>2</sub> ) <sub>7,1</sub> (2.00 equiv)	<b>I</b> (NiBr <sub>2</sub> ) <sub>7,3</sub> (1.75 equiv)	<b>I</b> (NiBr <sub>2</sub> ) <sub>7,2</sub> (1.50 equiv)	<b>I</b> (NiBr <sub>2</sub> ) <sub>6,1</sub> (1.25 equiv)
Formula	C <sub>72</sub> H <sub>36</sub> Br <sub>21.36</sub> N <sub>12</sub> Ni <sub>9.95</sub> O <sub>34.59</sub> Zr <sub>6</sub>	C <sub>63.29</sub> H <sub>31.64</sub> Br <sub>14.88</sub> N <sub>10.55</sub> Ni <sub>7.08</sub> O <sub>29.09</sub> Zr <sub>6</sub>	C <sub>62.38</sub> H <sub>31.19</sub> Br <sub>14.76</sub> N <sub>10.40</sub> Ni <sub>7.32</sub> O <sub>28.79</sub> Zr <sub>6</sub>	C <sub>69.44</sub> H <sub>34.60</sub> Br <sub>13.98</sub> N <sub>11.53</sub> Ni <sub>7.23</sub> O <sub>31.07</sub> Zr <sub>6</sub>	C <sub>65.69</sub> H <sub>32.85</sub> Br <sub>10.56</sub> N <sub>10.95</sub> Ni <sub>6.11</sub> O <sub>29.90</sub> Zr <sub>6</sub>
Temperature (K)	100(2)	100(2)	100(2)	100(2)	100(2)
Crystal System	Cubic	Cubic	Cubic	Cubic	Cubic
Space Group	<i>Pa</i> $\bar{3}$	<i>Pa</i> $\bar{3}$	<i>Pa</i> $\bar{3}$	<i>Pa</i> $\bar{3}$	<i>Pa</i> $\bar{3}$
<i>a</i> , <i>b</i> , <i>c</i> (Å)	26.208(3)	26.2991(6)	26.2940(11)	26.1253(9)	26.2931(8)
<i>a</i> , <i>β</i> , <i>γ</i> (°)	90	90	90	90	90
<i>V</i> (Å <sup>3</sup> )	18001(6)	18189.6(12)	18179(2)	17831.3(18)	18177.1(17)
<i>Z</i>	4	4	4	4	4
Radiation, <i>λ</i> (Å)	Synchrotron, 0.8856	Synchrotron, 0.8856	Synchrotron, 0.9537	Synchrotron, 0.9537	Synchrotron, 0.8856
2 $\theta$ Range for Data Collection (°)	4.33 to 52.53	4.316 to 52.58	4.159 to 64.76	2.958 to 70.426	4.316 to 46.66
Completeness to 2 $\theta$	99.9% (2 $\theta$ = 52.53°)	99.6% (2 $\theta$ = 52.58°)	100.0% (2 $\theta$ = 64.76°)	99.9% (2 $\theta$ = 69.81°)	99.9% (2 $\theta$ = 44.66°)
Data / Restraints / Parameters	3278 / 351 / 301	3309 / 526 / 303	4668 / 441 / 303	5704 / 78 / 290	2381 / 466 / 264
Goodness of Fit on F <sup>2</sup>	1.079	1.118	1.037	1.069	1.069
<i>R</i> <sub>1</sub> <sup>a</sup> , <i>wR</i> <sub>2</sub> <sup>b</sup> (1 > 2 $\sigma$ ( <i>I</i> ))	0.0697, 0.1877	0.0839, 0.2184	0.0769, 0.2105	0.0822, 0.2355	0.0693, 0.1970
<i>R</i> <sub>1</sub> <sup>a</sup> , <i>wR</i> <sub>2</sub> <sup>b</sup> (all data)	0.0798, 0.1942	0.0908, 0.2246	0.0872, 0.2224	0.0909, 0.2443	0.0726, 0.1907
Largest Diff. Peak and Hole (e Å <sup>-3</sup> )	1.387 and -1.138	1.385 and -0.826	1.360 and -1.008	2.065 and -1.092	1.040 and -0.628

$$^a R_1 = \frac{\sum |F_o| - |F_c|}{\sum |F_o|}, \quad ^b wR_2 = \left\{ \frac{\sum [w(F_o^2 - F_c^2)]}{\sum [w(F_o^2)]} \right\}^{1/2}$$

**Table 6.S4.** Crystallographic data for frameworks obtained from reaction of **1** with NiCl<sub>2</sub> sources in diglyme.

	<b>1</b> (NiCl <sub>2</sub> ) <sub>13</sub> (excess)	<b>1</b> (NiCl <sub>2</sub> ) <sub>11</sub> (3.00 equiv)	<b>1</b> (NiCl <sub>2</sub> ) <sub>9,2</sub> (2.50 equiv)	<b>1</b> (NiCl <sub>2</sub> ) <sub>9,2</sub> (2.00 equiv)	<b>1</b> (NiCl <sub>2</sub> ) <sub>7,8</sub> (1.50 equiv)	<b>1</b> (NiCl <sub>2</sub> ) <sub>4,7</sub> (1.00 equiv)
Formula	C <sub>58.97</sub> H <sub>29.48</sub> Cl <sub>127.90</sub> N <sub>9.83</sub> Ni <sub>13.29</sub> O <sub>30.23</sub> Zr <sub>6</sub>	C <sub>57.36</sub> H <sub>28.68</sub> Cl <sub>123.46</sub> N <sub>9.56</sub> Ni <sub>11.20</sub> O <sub>27.12</sub> Zr <sub>6</sub>	C <sub>55.71</sub> H <sub>27.85</sub> Cl <sub>119.10</sub> N <sub>9.28</sub> Ni <sub>9.23</sub> O <sub>26.57</sub> Zr <sub>6</sub>	C <sub>55.25</sub> H <sub>27.65</sub> Cl <sub>118.66</sub> N <sub>9.21</sub> Ni <sub>8.93</sub> O <sub>26.42</sub> Zr <sub>6</sub>	C <sub>58.38</sub> H <sub>29.19</sub> Cl <sub>116.12</sub> N <sub>9.73</sub> Ni <sub>7.82</sub> O <sub>27.46</sub> Zr <sub>6</sub>	C <sub>59.26</sub> H <sub>29.63</sub> Cl <sub>109.42</sub> N <sub>9.88</sub> Ni <sub>4.71</sub> O <sub>27.75</sub> Zr <sub>6</sub>
Temperature (K)	100(2)	100(2)	100(2)	100(2)	100(2)	100(2)
Crystal System	Cubic	Cubic	Cubic	Cubic	Cubic	Cubic
Space Group	<i>P</i> $\bar{a}$ $\bar{3}$	<i>P</i> $\bar{a}$ $\bar{3}$	<i>P</i> $\bar{a}$ $\bar{3}$	<i>P</i> $\bar{a}$ $\bar{3}$	<i>P</i> $\bar{a}$ $\bar{3}$	<i>P</i> $\bar{a}$ $\bar{3}$
<i>a</i> , <i>b</i> , <i>c</i> (Å)	26.1572(9)	26.1835(9)	26.2207(11)	26.1748(8)	26.1489(7)	26.0860(10)
$\alpha$ , $\beta$ , $\gamma$ (°)	90	90	90	90	90	90
<i>V</i> (Å <sup>3</sup> )	17896.7(18)	17950.8(19)	18027(2)	17932.9(16)	17879.7(14)	17751(2)
<i>Z</i>	4	4	4	4	4	4
Radiation, $\lambda$ (Å)	Synchrotron, 0.8856	Synchrotron, 0.8856	Synchrotron, 0.8856	Synchrotron, 0.8856	Synchrotron, 0.8856	Synchrotron, 0.8856
2 $\theta$ Range for Data Collection (°)	4.336 to 56.824	4.334 to 53.73	4.328 to 52.626	4.336 to 50.89	4.34 to 52.616	4.35 to 55.524
Completeness to 2 $\theta$	99.9% (2 $\theta$ = 56.824°)	99.9% (2 $\theta$ = 53.73°)	100.0% (2 $\theta$ = 52.626°)	99.9% (2 $\theta$ = 50.89°)	99.7% (2 $\theta$ = 55.616°)	99.9% (2 $\theta$ = 55.524°)
Data / Restraints / Parameters	4038 / 285 / 310	3483 / 249 / 289	3285 / 342 / 289	2990 / 345 / 289	3248 / 346 / 289	3754 / 303 / 214
Goodness of Fit on F <sup>2</sup>	1.150	1.132	1.085	1.125	1.113	1.111
<i>R</i> <sub>1</sub> <sup>a</sup> , <i>wR</i> <sub>2</sub> <sup>b</sup> (1 > 2 $\sigma$ ( <i>I</i> ))	0.0594, 0.1798	0.0809, 0.2230	0.0706, 0.1899	0.0754, 0.2134	0.0898, 0.2514	0.0711, 0.1988
<i>R</i> <sub>1</sub> <sup>a</sup> , <i>wR</i> <sub>2</sub> <sup>b</sup> (all data)	0.0668, 0.1881	0.1013, 0.2502	0.0887, 0.2121	0.0931, 0.2354	0.1064, 0.2748	0.0764, 0.2032
Largest Diff. Peak and Hole (e Å <sup>-3</sup> )	1.538 and -0.609	1.029 and -0.927	0.959 and -0.716	0.776 and -0.764	0.901 and -0.801	2.102 and -0.739

$$^a R_1 = \sum |F_o| - |F_c| / \sum |F_o|, \quad ^b wR_2 = \left\{ \frac{\sum [w(F_o^2 - F_c^2)]}{\sum [w(F_o^2)]} \right\}^{1/2}.$$

**Table 6.S5.** Crystallographic data for frameworks obtained from reaction of **1** with MX<sub>2</sub> (MX<sub>2</sub> = NiBr<sub>2</sub>, CoCl<sub>2</sub>, FeCl<sub>2</sub>) sources in 10% DME in DFB.

	<b>1</b> (NiBr <sub>2</sub> ) <sub>15</sub> (excess)	<b>1</b> (NiBr <sub>2</sub> ) <sub>11</sub> (3.25 equiv)	<b>1</b> (CoCl <sub>2</sub> ) <sub>14</sub> (excess)	<b>1</b> (CoCl <sub>2</sub> ) <sub>15</sub> (3.25 equiv)	<b>1</b> (FeCl <sub>2</sub> ) <sub>17</sub> (excess)	<b>1</b> (FeCl <sub>2</sub> ) <sub>16</sub> (3.25 equiv)
Formula	C <sub>62.40</sub> H <sub>31.20</sub> Br <sub>30.43</sub> N <sub>10.40</sub> Ni <sub>15.31</sub> O <sub>33.19</sub> Zr <sub>6</sub>	C <sub>62.40</sub> H <sub>31.20</sub> Br <sub>30.43</sub> N <sub>10.40</sub> Ni <sub>15.32</sub> O <sub>33.19</sub> Zr <sub>6</sub>	C <sub>63.60</sub> H <sub>31.80</sub> Cl <sub>29.28</sub> Co <sub>14.19</sub> N <sub>10.60</sub> O <sub>31.43</sub> Zr <sub>6</sub>	C <sub>64.45</sub> H <sub>32.22</sub> Cl <sub>31.09</sub> Co <sub>15.19</sub> N <sub>10.74</sub> O <sub>31.54</sub> Zr <sub>6</sub>	C <sub>65.69</sub> H <sub>32.85</sub> Cl <sub>35.76</sub> Fe <sub>17.40</sub> N <sub>10.95</sub> O <sub>32.72</sub> Zr <sub>6</sub>	C <sub>65.06</sub> H <sub>32.53</sub> Cl <sub>32.21</sub> Fe <sub>15.85</sub> N <sub>10.84</sub> O <sub>31.91</sub> Zr <sub>6</sub>
Temperature (K)	100(2)	100(2)	100(2)	100(2)	100(2)	100(2)
Crystal System	Cubic	Cubic	Cubic	Cubic	Cubic	Cubic
Space Group	<i>Pa</i> $\bar{3}$	<i>Pa</i> $\bar{3}$	<i>Pa</i> $\bar{3}$	<i>Pa</i> $\bar{3}$	<i>Pa</i> $\bar{3}$	<i>Pa</i> $\bar{3}$
<i>a</i> , <i>b</i> , <i>c</i> (Å)	26.0161(11)	26.1215(9)	26.0374(10)	26.0095(10)	25.9770(12)	25.9796(11)
<i>α</i> , <i>β</i> , <i>γ</i> (°)	90	90	90	90	90	90
<i>V</i> (Å <sup>3</sup> )	17609(2)	17823.6(18)	17652(2)	17595(2)	17529(2)	17535(2)
<i>Z</i>	4	4	4	4	4	4
Radiation, <i>λ</i> (Å)	Synchrotron, 0.9537	Synchrotron, 0.9537	Synchrotron, 0.8856	Synchrotron, 0.8856	Synchrotron, 0.8856	Synchrotron, 0.8856
2 $\theta$ Range for Data Collection (°)	2.97 to 73.324	2.092 to 74.484	2.756 to 70.334	2.76 to 68.148	2.762 to 72.558	2.762 to 71.464
Completeness to 2 $\theta$	100.0% (2 $\theta$ = 69.818°)	100.0% (2 $\theta$ = 69.81°)	99.9% (2 $\theta$ = 64.194°)	100.0% (2 $\theta$ = 64.194°)	99.9% (2 $\theta$ = 64.194°)	99.9% (2 $\theta$ = 64.194°)
Data / Restraints / Parameters	6246 / 0 / 298	6580 / 9 / 298	7011 / 48 / 328	6439 / 48 / 328	7535 / 60 / 346	7268 / 60 / 346
Goodness of Fit on F <sup>2</sup>	1.121	1.126	1.113	1.137	1.094	1.111
<i>R</i> <sub>1</sub> <sup>a</sup> , <i>wR</i> <sub>2</sub> <sup>b</sup> (I > 2 $\sigma$ ( <i>I</i> ))	0.0466, 0.1354	0.0549, 0.1553	0.0685, 0.1873	0.0638, 0.1808	0.0488, 0.1412	0.0593, 0.1805
<i>R</i> <sub>1</sub> <sup>a</sup> , <i>wR</i> <sub>2</sub> <sup>b</sup> (all data)	0.0587, 0.1487	0.0712, 0.1735	0.0781, 0.1993	0.0742, 0.1933	0.0560, 0.1484	0.0656, 0.1861
Largest Diff. Peak and Hole (e Å <sup>-3</sup> )	1.904 and -1.146	1.734 and -0.986	1.517 and -3.071	1.285 and -1.995	1.930 and -1.303	1.852 and -1.131

$$^a R_1 = \sum |F_o| - |F_c| / \sum |F_o|, \quad ^b wR_2 = \{ \sum [w(F_o^2 - F_c^2)^2] / \sum [w(F_o^2)^2] \}^{1/2}.$$

## 6.7. References

- (1) Bawendi, M. G.; Steigerwald, M. L.; Brus, L. E. *Annual Review of Physical Chemistry* **1990**, *41* (1), 477–496.
- (2) Billas, I. M.; Châtelain, A.; de Heer, W. A. *Science* **1994**, *265* (5179), 1682–1684.
- (3) Lee, S. C.; Holm, R. H. *Angew. Chem. Int. Ed.* **1990**, *29* (8), 840–856.
- (4) Gatteschi, D.; Caneschi, A.; Pardi, L.; Sessoli, R. *Science* **1994**, *265* (5175), 1054–1058.
- (5) Xia, Y.; Xiong, Y.; Lim, B.; Skrabalak, S. E. *Angew. Chem. Int. Ed.* **2008**, *48* (1), 60–103.
- (6) Papatriantafyllopoulou, C.; Moushi, E. E.; Christou, G.; Tasiopoulos, A. J. *Chem. Soc. Rev.* **2016**, *45* (6), 1597–1628.
- (7) Knickelbein, M. B. *J. Chem. Phys.* **2001**, *115* (5), 1983–1986.
- (8) Niemeyer, M.; Hirsch, K.; Zamudio-Bayer, V.; Langenberg, A.; Vogel, M.; Kossick, M.; Ebrecht, C.; Egashira, K.; Terasaki, A.; Möller, T.; Issendorff, B. V.; Lau, J. T. *Phys. Rev. Lett.* **2012**, *108* (5), 057201.
- (9) Kim, C. R.; Uemura, T.; Kitagawa, S. *Chem. Soc. Rev.* **2016**, *45* (14), 3828–3845.
- (10) Meilikhov, M.; Yusenko, K.; Esken, D.; Turner, S.; Van Tendeloo, G.; Fischer, R. A. *Eur. J. Inorg. Chem.* **2010**, *2010* (24), 3701–3714.
- (11) Lin, H.; Zhou, C.; Tian, Y.; Besara, T.; Neu, J.; Siegrist, T.; Zhou, Y.; Bullock, J.; Schanze, K. S.; Ming, W.; Du, M.-H.; Ma, B. *Chem. Sci.* **2017**, *8* (12), 8400–8404.
- (12) Chen, K.-J.; Perry, J. J., IV; Scott, H. S.; Yang, Q.-Y.; Zaworotko, M. J. *Chem. Sci.* **2015**, *6* (8), 4784–4789.
- (13) Gallington, L. C.; Kim, I. S.; Liu, W.-G.; Yakovenko, A. A.; Platero-Prats, A. E.; Li, Z.; Wang, T. C.; Hupp, J. T.; Farha, O. K.; Truhlar, D. G.; Martinson, A. B. F.; Chapman, K. W. *J. Am. Chem. Soc.* **2016**.
- (14) Braglia, L.; Borfecchia, E.; Lomachenko, K. A.; Bugaev, A. L.; Guda, A. A.; Soldatov, A. V.; Bleken, B. T. L.; Øien-Ødegaard, S.; Olsbye, U.; Lillerud, K. P.; Bordiga, S.; Agostini, G.; Manzoli, M.; Lamberti, C. *Faraday Discuss.* **2017**, *32*, 276.
- (15) An, B.; Zhang, J.; Cheng, K.; Ji, P.; Wang, C.; Lin, W. *J. Am. Chem. Soc.* **2017**, *139* (10), 3834–3840.
- (16) Chen, L.; Chen, H.; Luque, R.; Li, Y. *Chem. Sci.* **2014**, *5*, 3708–3714.
- (17) Umena, Y.; Kawakami, K.; Shen, J.-R.; Kamiya, N. *Nature* **2011**, *473* (7345), 55–60.
- (18) Kanady, J. S.; Tsui, E. Y.; Day, M. W.; Agapie, T. *Science* **2011**, *333* (6043), 733–736.
- (19) Gonzalez, M. I.; Bloch, E. D.; Mason, J. A.; Teat, S. J.; Long, J. R. *Inorg. Chem.* **2015**, *54* (6), 2995–3005.
- (20) Gonzalez, M. I.; Oktawiec, J.; Long, J. R. *Faraday Discuss.* **2017**, *201*, 363–379.
- (21) Ohhashi, K.; Tsujikawa, I. *Journal of the Physical Society of Japan* **1974**, *37* (1), 63–70.
- (22) Huang, B.; Clark, G.; Navarro-Moratalla, E.; Klein, D. R.; Cheng, R.; Seyler, K. L.; Zhong, D.; Schmidgall, E.; McGuire, M. A.; Cobden, D. H.; Yao, W.; Xiao, D.; Jarillo-Herrero, P.; Xu, X. *Nature* **2017**, *546* (7657), 270–273.
- (23) Rama, G.; Ardá, A.; Maréchal, J.-D.; Gamba, I.; Ishida, H.; Jiménez-Barbero, J.; Vázquez, M. E.; Vázquez López, M. *Chem. Eur. J.* **2012**, *18* (23), 7030–7035.
- (24) Bruker Analytical X-ray Systems, Inc. *SAINT and APEX 2 Software for CCD Diffractometers*; Bruker Analytical X-ray Systems, Inc.: Madison, WI, USA, 2000.
- (25) Sheldrick, G. M. *SADABS*; Bruker Analytical X-ray Systems, Inc.: Madison, WI, USA, 2014.

- (26) Sheldrick, G. M. *SHELXS*; University of Göttingen, Germany, 2014.
- (27) Sheldrick, G. M. *Acta Crystallogr., A, Found. Crystallogr.* **2008**, *64* (Pt 1), 112–122.
- (28) Sheldrick, G. M. *SHELXL*; University of Göttingen, Germany: University of Göttingen, Germany, 2014.
- (29) Dolomanov, O. V.; Bourhis, L. J.; Gildea, R. J.; Howard, J. A. K.; Puschmann, H. *Journal of Applied Crystallography* **2009**, *42* (2), 339–341.
- (30) Spek, A. L. *Acta Crystallogr C Struct Chem* **2015**, *71* (Pt 1), 9–18.
- (31) Spek, A. L. *Journal of Applied Crystallography* **2003**, *36* (1), 7–13.
- (32) Ketelaar, J. A. A. *Zeitschrift für Kristallographie - Crystalline Materials* **1934**, *88* (1-6).
- (33) Ferrari, A.; Braibanti, A.; Bigliardi, G.; IUCr. *Acta Crystallographica* **1963**, *16* (8), 846–847.
- (34) George, P.; McClure, D. S. *The Effect of Inner Orbital Splitting on the Thermodynamic Properties of Transition Metal Compounds and Coordination Complexes*; John Wiley & Sons, Inc.: Hoboken, NJ, USA, 1959; Vol. 1, pp 381–463.
- (35) Wilkinson, M. K.; Cable, J. W.; Wollan, E. O.; Koehler, W. C. *Physical Review* **1959**, *113* (2), 497–507.
- (36) Tsubokawa, I. *Journal of the Physical Society of Japan* **1960**, *15* (11), 2109–2109.
- (37) Mydosh, J. A. *Spin glasses*; Taylor & Francis: Abingdon, UK, 1993.
- (38) Milios, C. J.; Winpenny, R. E. P. In *Molecular Nanomagnets and Related Phenomena; Structure and Bonding*; Springer Berlin Heidelberg: Berlin, Heidelberg, 2014; Vol. 164, pp 1–109.
- (39) Neese, F.; Pantazis, D. A. *Faraday Discuss.* **2011**, *148*, 229–238.